



Article

Impacts of Extreme Space Weather Events on September 6th, 2017 on Ionosphere and Primary Cosmic Rays

Aleksandra Kolarski , Nikola Veselinović , Vladimir A. Srećković , Zoran Mijić * , Mihailo Savić
and Aleksandar Dragić

Institute of Physics Belgrade, University of Belgrade, Pregrevica 118, 11080 Belgrade, Serbia

* Correspondence: zoran.mijic@ipb.ac.rs; Tel.: +381-11-3713134

Abstract: The strongest X-class solar flare (SF) event in 24th solar cycle, X9.3, occurred on 6 September 2017, accompanied by earthward-directed coronal mass ejections (CMEs). Such space weather episodes are known to cause various threats to human activities ranging from radio communication and navigation disturbances including wave blackout to producing geomagnetic storms of different intensities. In this study, SFs' ionospheric impacts and effects of accompanied heliospheric disturbances on primary cosmic rays (CR) are investigated. This work offers the first detailed investigation of characteristics of these extreme events since they were inspected both from the perspective of their electromagnetic nature, through very low frequency (VLF) radio waves, and their corpuscular nature of CR by multi-instrumental approach. Aside data recorded by Belgrade VLF and CR stations, data from GOES and SOHO space probes were used for modeling and analysis. Conducted numerical simulations revealed a significant change of ionospheric parameters (sharpness and effective reflection height) and few orders of magnitude increase of electron density. We compared our findings with those existing in the literature regarding the ionospheric response and corresponding parameters. In addition, Forbush decrease (FD) magnitude, corrected for magnetospheric effect, derived from measurements, and one predicted from power exponents used to parametrize the shape of energetic proton fluence spectra at L1 were compared and found to be in good agreement. Presented findings could be useful for investigation of atmospheric plasma properties, particles' modeling, and prediction of extreme weather impacts on human activities.

Keywords: solar flares; coronal mass ejections; atmospheric ionization; sudden ionospheric disturbances; ionospheric parameters; solar energetic particles; secondary cosmic ray flux; Forbush decreases



Citation: Kolarski, A.; Veselinović, N.; Srećković, V.A.; Mijić, Z.; Savić, M.; Dragić, A. Impacts of Extreme Space Weather Events on September 6th, 2017 on Ionosphere and Primary Cosmic Rays. *Remote Sens.* **2023**, *15*, 1403. <https://doi.org/10.3390/rs15051403>

Academic Editors: Dario Sabbagh and Saioa A. Campuzano

Received: 17 January 2023

Revised: 23 February 2023

Accepted: 28 February 2023

Published: 2 March 2023



Copyright: © 2023 by the authors. Licensee MDPI, Basel, Switzerland. This article is an open access article distributed under the terms and conditions of the Creative Commons Attribution (CC BY) license (<https://creativecommons.org/licenses/by/4.0/>).

1. Introduction

As an important aspect of space weather applications, ionospheric responses to intense solar flares (SFs) and coronal mass ejections (CMEs) have been investigated for several decades [1–3]. Short in duration but huge explosive events on the Sun release high-energy particles and intense broad range radiation influencing the state of the Earth's upper atmosphere. While enhanced EUV radiation disturbs E and F regions of the ionosphere, during solar flares, X-ray radiation can increase by several orders of magnitude and cause an extra ionization within the ionospheric D-layer [4,5]. The increase in the rate of change of atmospheric ionization depends on both the flare class and the rate of change in flare radiations [6]. For the investigation of D-region behavior, radio wave measurements at very low and low frequencies (VLF-LF) are widely used [7–9]. SFs have a direct radio wave interference effect on Global Navigation Satellite System (GNSS) transmission and other radio systems [10–12]. High-frequency (HF) radio wave blackout and magnetic field variation have also been documented and studied [11,13].

Solar activity can produce extreme phenomena which are more likely around the maximum of the 11-year cycle. One such type of events are SFs that are, in most cases, followed by CMEs [14]. CME releases a large-scale flux of charged particles from solar

corona with an accompanying embedded magnetic field. This additional flux of charged particles emerging in interplanetary space is defined as interplanetary coronal mass ejection (ICME). When propagating with speed greater than magnetosonic wave speed (in solar wind reference frame), ICME can form a shock due to interaction with ambient solar wind. In situ measurements of the environment performed by space probes at different locations in the heliosphere can provide information about various solar weather parameters. They also include direct measurements of fast-moving energetic particles that can be in temporal correlation with CMEs and SFs [15]. These particles can originate from the Sun, in which case they are called solar energetic particles (SEPs) or can be accelerated locally by an ICME related shock when they are referred to as energetic storm particles (ESPs). Several space probes placed at Lagrange point 1 (L1) between the Sun and the Earth constantly monitor this flux, in addition to a number of probes at Earth's vicinity and elsewhere throughout the heliosphere [16]. Enhancement of interplanetary magnetic field (IMF) creates additional modulation of cosmic ray (CR) and can lead to one of the transient phenomena, Forbush decrease (FD). FD is a rapid depression of measured CR flux (typically occurring within a day), followed by a gradual recovery that can last for several days [17]. Correlation between FD parameters (magnitude of decrease, duration, time evolution) and various parameters of solar wind plasma have been studied in the past [18–20].

Extreme space weather events can have severe impacts on wide areas of human activities. Historically, such events are not very frequent, but the probability of their occurrence over the next decade is not negligible (i.e., for geomagnetic storms, it has been estimated to be about 12% [21]). Extreme events can cause significant damage to sensitive satellite components and increase absorbed radiation dose in space, which can pose a serious health hazard to astronauts. Energetic particle flux during extreme solar activity events is studied and different models of the space environment are proposed for forecasting schemes. Even though many studies have been carried out, still, only limited information is available on an approximate assessment of the direct impact such events can have on technological infrastructure and what the indirect associated expenses would be [22].

Study of ionospheric reaction to SFs is currently very relevant research, given the prospect of improving the capacity and reliability of anticipating space weather disturbances, which might affect the performance of a wide range of space-borne and ground-based technological systems and pose a danger to human health and safety [23,24].

The 24th solar cycle began in December 2008 and although approaching the solar minimum and the low solar activity, several strong SFs occurred in September 2017, including the X9.3 class flare, the strongest one in that cycle [25,26]. A lot of studies have been published analyzing different aspects of these extreme weather events. The SF effect on the chemical structure of the upper and middle atmosphere is reported in [27]. In the study presented in [28], the analysis of total electron content (TEC) and rate of change of TEC index to probe the storm-time ionospheric TEC irregularities in the Indian longitude sector during the space weather events of 6–10 September 2017 was presented. During the flares, the total radio fade-out in the range of 30 to 90 min at the Hermanus and Sao Luis ionosondes is reported [29]. It is also observed that SFs' effects on the ionosphere last longer than the effects on the Earth's magnetic field [30]. The effects of the strong X9.3 flare of 6 September 2017, following its impact on the ionosphere and the resulting difficulties for existing (e.g., precise positioning and GNSS navigation support services) and future technologies (e.g., autonomous car navigation) have been analyzed [10].

In this paper, X-class SFs of 6 September 2017 ionospheric impacts and the effects of accompanied heliospheric disturbances on primary cosmic rays are investigated. The atmospheric D-region parameters and electron density are obtained and analyzed along with various heliospheric parameters (associated with the accompanying ICME) measured in-situ at L1, as well as flux of secondary cosmic ray muons measured on the ground and shallow-underground levels. Since all empirical models are based upon data obtained through numerous studies, such as International Reference Ionosphere model [31], each

case study of extreme weather events is of great significance, not only for the atmospheric plasma properties investigations, but also for the particles' modeling procedures. With that goal, modulation of ionosphere and CR flux by intense X-class SF events was investigated through a multi-instrumental approach, by employing space- and ground-based observations on one hand, and by conducting proposed numerical simulations on the other hand, using both original VLF and CR measurements (from the same location in Belgrade) as well as data and results from other observing stations worldwide. Through extensive comparison, noticed agreements and disagreements between results are highlighted as well.

2. Materials and Methods

Galactic cosmic rays interact with interplanetary magnetic fields as they traverse our solar system. IMF is a solar magnetic field carried by the solar wind, a stream of charged particles propagating outward from the Sun. Interaction of CRs with IMF modulates CR flux as is also evident from measurements of CR flux intensity with Earth-based CR detectors [32]. Galactic cosmic rays, upon reaching Earth, interact with atmospheric atoms and molecule nuclei, generating a shower of secondary particles. Secondary CRs vertical flux, at the bottom of the atmosphere (at atmospheric depth 1000 g cm^{-2}), for particles' energies larger than 1 GeV, is composed mainly of muons ($\approx 90 \text{ m}^{-2} \text{ s}^{-1} \text{ sr}^{-1}$), protons and neutrons ($\approx 2 \text{ m}^{-2} \text{ s}^{-1} \text{ sr}^{-1}$), electrons and positrons ($\approx 0.2 \text{ m}^{-2} \text{ s}^{-1} \text{ sr}^{-1}$), and charged pions ($\approx 0.04 \text{ m}^{-2} \text{ s}^{-1} \text{ sr}^{-1}$) as well as neutrinos [33]. Observation of these secondary CRs can be conducted in the atmosphere, on the ground or even underground, detecting one or several different types of produced particles. A worldwide network of neutron monitors (NM) and ground detectors that detect hadronic components of secondary CRs have been in use for decades. NMs are sensitive to primary CRs with energies of about 0.5–20 GeV. Another type of widely used Earth-based CR detectors are muon monitors, focused on detecting the muon component of secondary CRs. Muon monitors are sensitive to higher energies of primary CRs, thus complementing NMs measurements [34].

Belgrade CRs station is a part of the Low-background Laboratory for Nuclear Physics (LBLNP) at the Institute of Physics Belgrade (IPB), Serbia. It has two identical detector set-ups placed on two different levels, one on ground level (GLL) and the other in shallow-underground (UL). Underground level is situated below 12 m of loess overburden (25-m water equivalent). This setup allows for monitoring of secondary CR's muons flux that originates from two different energy ranges under the same environmental conditions (such as geomagnetic location, atmospheric parameters, experimental setup). Altitude of the station is 78 m above sea level, with a geomagnetic latitude of $39^{\circ}32' \text{ N}$. Relation between the measured count rate of these energy-integrating detectors with flux of primary CRs at the top of the atmosphere was found using a calculated detector yield function. Additionally, due to the sensitivity of secondary muons to varying properties of the atmosphere, which acts as a moderator, correction of measured flux for atmospheric pressure and variation of temperature throughout the whole atmospheric column from the top of the atmosphere to the ground is needed. Details of the detector systems and response function of Belgrade CR station acquired using Monte Carlo simulation of CR transport, along with the description and results of atmospheric and efficiency corrections are presented in [35,36].

For inspection of the Earth's lower ionospheric response to intense solar activity during events of energetic solar outbursts (such as SFs and CMEs) during the descending branch of the 24th solar cycle, as in September 2017, VLF radio signal registrations from Belgrade's (BEL; 44.85° N , 20.38° E) Absolute Phase and Amplitude Logger (AbsPAL) station database were used. This system is a part of the Laboratory for Astrophysics and Physics of Ionosphere at the IPB, Serbia. Numerical simulations conducted in this paper rely on application of the well known and widely exploited technique of Long Wavelength Propagation Capability (LWPC) software [37] utilization on one hand, based on hop wave theory and the ionospheric exponential model [38,39], and on the FlarED' Method and Approximate Analytic Expression application [5,40] on the other hand: the novel approach based on retrieving ionospheric parameters directly from solar X-ray radiation spectral

components of soft range. Here, novel approach is applied on two cases of SF events within the strongest X-class (the weaker X2.2 and stronger X9.3), making the validation of the proposed approximate method firmly applicable and reliable across the entire X-class range, in addition to some previous recent research all regarding cases of weaker X-class SFs from the lower section of X-class range [5,8,40]. The methodology used relies on simultaneous monitoring of several VLF signals during regular and irregular ionospheric conditions, both for amplitude and phase, and obtaining properties of perturbations directly from observed recorded VLF data, by signal values' comparison between unperturbed and perturbed states. The details are presented in Section 3.2 and Supplementary Material.

3. Results

3.1. Solar Energetic Particles and Secondary Cosmic Ray Flux during and after Intense SF Events

The strongest flare of solar cycle 24 (classified as X9.3) happened in early September 2017 during the declining phase of this solar cycle. Active region AR12673 [41] was the cause of unusual and intensive solar activity. This region produced several more SFs around that time with the most intense one occurring on 6 September 2017. The flare was closely followed by a severe geomagnetic storm that began on 7 September. In total, four different possibly related CMEs erupted within several days. The first of these was a halo CME that happened on 4 September which, together with the second one, affected CR flux and produced an intense Forbush decrease on 7 September. Magnitude of FD for 10 GV rigidity primary CR corrected for magnetospheric effect (M_M) [18] was -7.7% (quoted from IZMIRAN database of FD parameters [42]).

Solar activity and the accompanying heliospheric disturbance during early September 2017 have been studied in detail in a number of published articles that indicate that successive CMEs between 4–6 September produced complex transients. Complex interactions caused by the passage of ICME are not so simple to model, one consequence being that it is not so straightforward to predict time of arrival of the disturbance on Earth [43]. However, in-situ measurements by space probes at L1 can help in this regard. Based on data from Solar and Heliospheric Observatory (SOHO)/Large Angle and Spectrometric Corona-graph (LASCO)/C2 [44] and analysis given in [45], the first CME from AR12673 with a moderate speed of approximately 710 km s^{-1} appeared on 4 September followed by a much faster (approx. 1350 km s^{-1}) second CME. These two CMEs merged in lower solar corona into a single structure producing single shock followed by a prolonged sheath region which was detected at L1 on 6 September. The second shock arrived at L1 on 7 September as a result of CME that occurred on 6 September. This CME had a high velocity of 1480 km s^{-1} and its eruption coincides with the X9.3 SF. This shock was followed by a turbulent sheath region and a magnetic cloud. One repository where such measurements can be found compiled in the form of low- and high-resolution OMNI data can be found at GSFC/Space Physics Data Facility [46]. Low-resolution OMNI data (used in this study) contains hourly values for various heliospheric and geomagnetic indices. One of the probes that monitors variation of energetic proton flux at L1 is the ERNE instrument onboard SOHO probe [47]. It consists of two separate particle detectors with complementing detector energy ranges (for lower and higher particle energies) and provides energetic particle flux measurements in 20 energy bins (ranging from 1.3 up to 130 MeV per nucleon) with a time resolution of one hour (data are available at [48]). Apart from providing insight into SF/CME/ICME induced disturbance in the heliosphere, measurements done by this instrument could be useful for predicting the effects that these phenomena have on cosmic rays, as some studies have shown [49]. Proton flux recorded during early September 2017 is showed in Figure 1 and Figures S1 and S2 in Supplementary Material. As it is often difficult to determine the acceleration mechanism related to violent events on the Sun (especially when accelerated particles are detected near Earth), for the sake of simplicity, going forward, we will refer to both solar energetic particles (accelerated near the Sun) and energetic storm particles (accelerated in interplanetary space) as SEP.

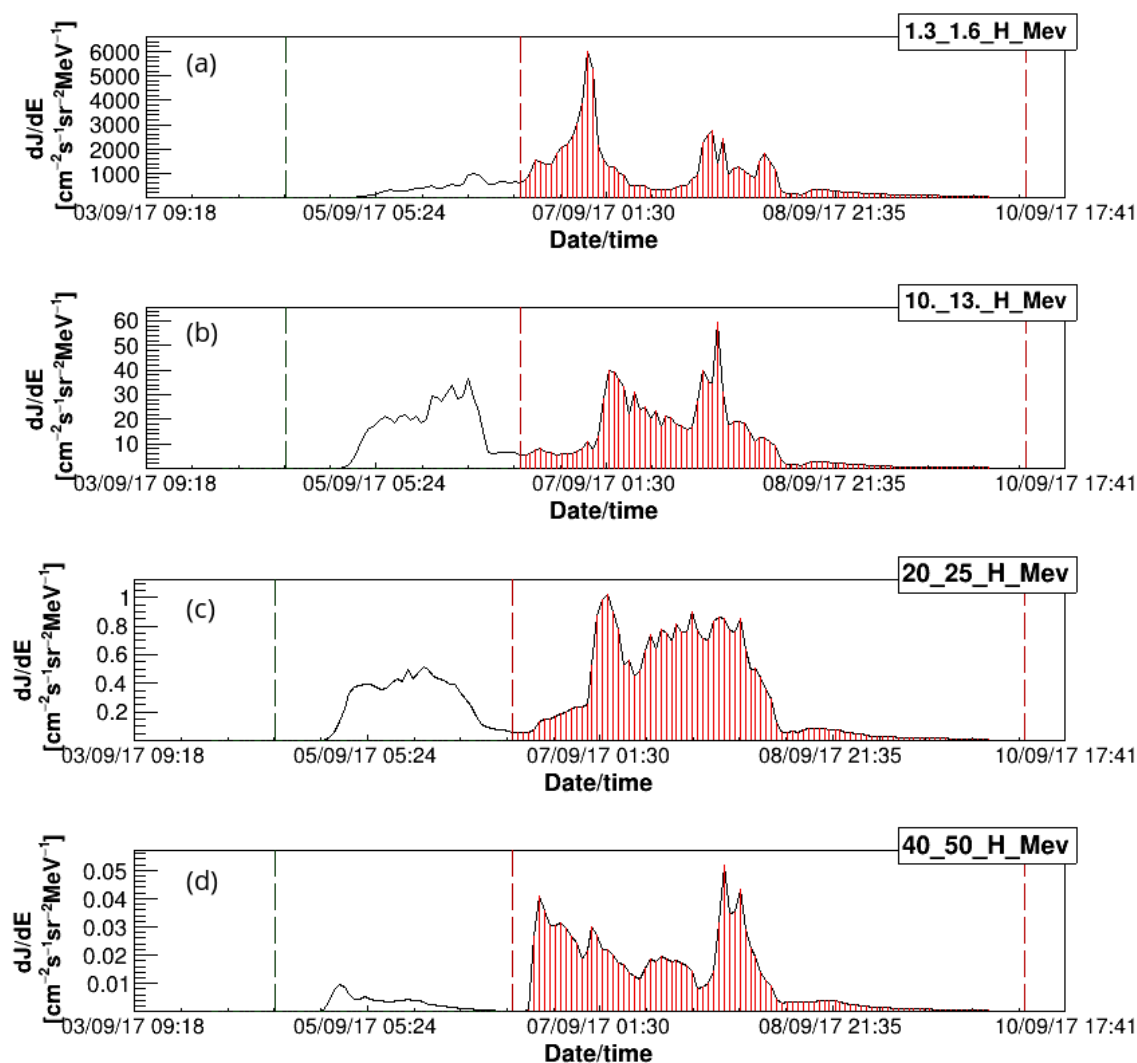


Figure 1. Hourly time series (UT) for several different proton channels from SOHO/ERNE ((a) 1.3–1.6 MeV, (b) 10–13 MeV, (c) 20–25 MeV, (d) 40–50 MeV channels' energy bands) for September 2017. Integration interval for spectral fluence is indicated with red vertical dashed lines.

In order to determine SEP fluence related to heliospheric disturbances and FD events during early September 2017, integration of SOHO/ERNE proton flux time series in separate energy channels is needed over the time period associated with a given FD event. Determination of this time period during complex solar activity in September 2017 is not simple or straightforward. Using procedures described in [36] that rely on the IZMIRAN database, as well as neutron monitor data and data measured at Belgrade muon station, we can determine optimal integration intervals more reliably.

Generally, SEP fluence spectrum exhibits a change of slope (sometimes referred to as a “knee”). Several different models are proposed to describe this characteristic shape [50–52]. We chose to use the double power law proposed in [53] given by Equation (1):

$$f(E) = \begin{cases} E^{-a} \exp\left(-\frac{E}{E_k}\right), & E < (b-a)E_k \\ E^{-b} [(b-a)E_k]^{b-a} \exp(a-b), & E > (b-a)E_k \end{cases} \quad (1)$$

where E is the particle energy, E_k is the “knee” energy (at which the break in the spectrum occurs), a and b are power exponents related to energy ranges below and above E_k , respectively. Exponents a and b are determined by fitting the proton fluence spectrum using Equation 1 and are used to parameterize its shape. E_k is set as a fixed parameter and

is determined from the known dependence of “knee” energy on integral fluence. More detailed description of the procedure can be found in [49]. The shape of fluence spectrum and fitted double power law for the September event are shown in Figure 2. Obtained values were -1.16 for exponent a and -2.5 for exponent b (taking 6.8 MeV as value for “knee” energy).

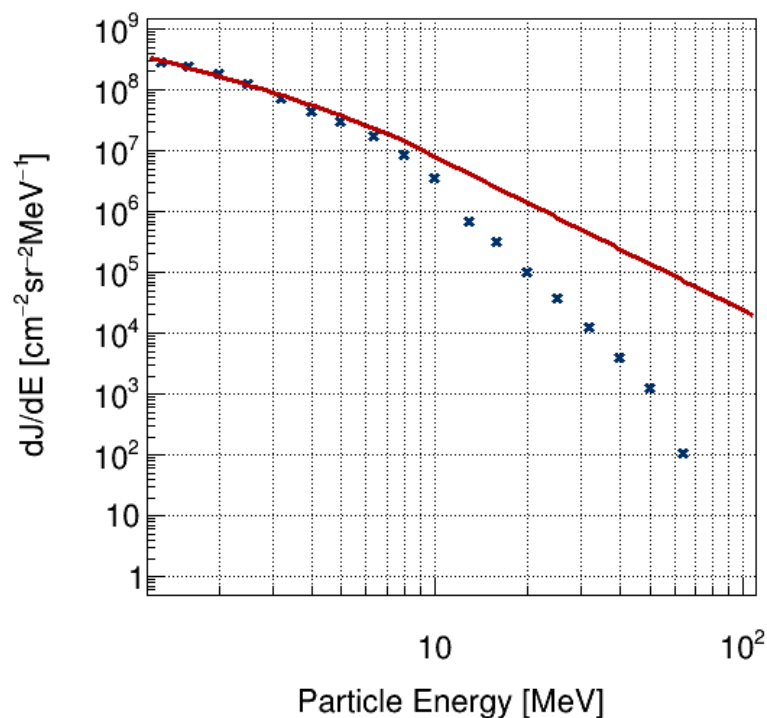


Figure 2. Fluence spectrum for energetic protons measured by SOHO/ERNE at L1 during FD in September 2017. Data points represent fluence integrated in different energy channels over time of duration of the event, while red line represents the fitted double power law.

Observed underestimate of fluence in higher energy channels can be explained by the assumption that there are contributions of low energy CR in these energy ranges that are suppressed with additional heliospheric disturbance and can be more pronounced for more extreme solar activity events. Additionally, this discrepancy between model and measured fluence can be due to saturation of high energy channels during events with greater SEP flux [54].

Contribution of these higher energy channels to integral flux is rather small and it does not significantly affect total flux, however, it does add to higher uncertainty of b , which is why this exponent is seldom used in analysis. Based on the established correlation between a exponent and FD magnitude corrected for magnetospheric effect [49], an estimated value of 8.3% was obtained for M_M , which is in reasonably good agreement with the value found in the IZMIRAN database. Large disturbances in the heliosphere in early September 2017 that cause large FD are part of a complex event that can lead to disturbance in the magnetosphere and primary CR flux variability, but also influence dynamic processes in the ionosphere.

3.2. Monitoring Low Altitude Mid-Latitude Ionosphere during intense SF events

Monitoring of the mid-latitude ionospheric D-region (50–90 km) from BEL station during September 2017 were simultaneously conducted for all VLF signals recorded by the AbsPAL system. Geographical position of BEL VLF system and the VLF transmitters (GQD/22.10 kHz, Anthorn UK and TBB/26.70 kHz, Bafa Turkey) are given in Figure S3. Both shown signals are of short great circle paths (GCPs) propagating mostly over land. In general, the GQD signal arrives to Belgrade from the north, in NW-SE direction, with

GCPGQD = 1982 km covering almost two time zones, while TBB signal arrives from the south, in SE-NW direction, with GCPTBB = 1020 km covering one time zone (Table 1). Corresponding incident solar X-ray flux data were obtained from the Geostationary Operational Environmental Satellite (GOES) database [55].

Table 1. VLF transmitting sites.

	Freq. (kHz)	Country	Latitude (°)	Longitude (°)	GCP (km)	Prop. Path Direction
Transmitter:						
GQD	22.10	UK	54.73 N	2.88 W	1982	NW to SE
TBB	26.70	Turkey	37.43 N	27.55 E	1020	SE to NW

We studied data from 6 September 2017 belonging to the descending branch of the 24th solar cycle, with the strongest SF event X9.3 reported during the last solar cycle and the earth-directed CME which produced FD. September 2017 was the most active month during 2017, with a total of 99 SFs reported, of which there were 68 C, 27 M, and four X class events. During 6 September 2017, there were seven SFs reported in total, of which there were two C, three M, and two X-class SFs. Such intense solar activity significantly affected Earth's lower ionosphere, which can be clearly observed both as amplitude and phase perturbations on sub-ionospheric propagating VLF signals and was documented on BEL AbsPAL recordings. The two strongest SFs reported on 6 September 2017, i.e., X2.2 and X9.3—overall the strongest SF from the last solar cycle, as observed on GQD and TBB signal traces, practically occurred during the established stable daytime ionospheric conditions, when both traces were entirely sunlit. BEL GQD data during the entire day of 6 September 2017, with the accompanying incident solar X-ray flux from soft spectral range (0.1–0.8 nm) are given in Figure S4. As the best representative quiet day, 3 September 2017 was chosen. As observed on GQD signal, solar-induced sudden ionospheric disturbances (SIDs) are denoted by black arrows accompanied with the time of each SF event's occurrence in UT. Both amplitude and phase perturbation follow the SF events' evolution, with time delays corresponding to the sluggishness of the ionosphere [56]. Oscillatory character of the perturbations characteristic for GQD signal registered by BEL station, can still be recognized on the signal's phase, especially in the case of the weaker SF, while in the case of the amplitude, this feature is no longer observable mostly due to inducing SF's intensity [5,7,57–59]. Although these two SF occurred back-to-back, it is possible to determine individual contributions of each SF on signal recordings. It can be stated that, although these SFs strongly impacted the Earth-ionosphere waveguide for several hours, as observed from BEL station, the mid-latitude lower ionosphere fully recovered and went back to its regular conditions. Preflare ionospheric state can be treated as quiet.

Comparison between GQD and TBB signal recordings, arriving from opposite directions to the BEL station, but both of short GCPs, is given in Figure 3, as an enlarged section related to time evolution of X2.2 and X9.3 SFs.

Amplitude change in both signals is of similar behavior, simply following the incident solar X-ray radiation, with similar relative change in the amplitude amount compared to unperturbed conditions $\Delta A \approx 7$ dB. However, in the case of the TBB signal, there is a more rapid decreasing trend after the peak value corresponding to the maximal amplitude change in both SF cases. In the case of the GQD signal, relative change in the phase amount compared to unperturbed conditions ΔPh (°) is several tens of degrees, with still recognizable oscillatory behavior characteristic for BELGQD. Unfortunately, in the case of the TBB signal, phase data were unusable so that further analysis, neither qualitative nor quantitative and neither any of the numerical simulations, were not possible to conduct. The TBB signal recordings given are purely interesting from the point of view of amplitude comparison with the GQD signal, with total opposite GCPs as recorded in Belgrade.

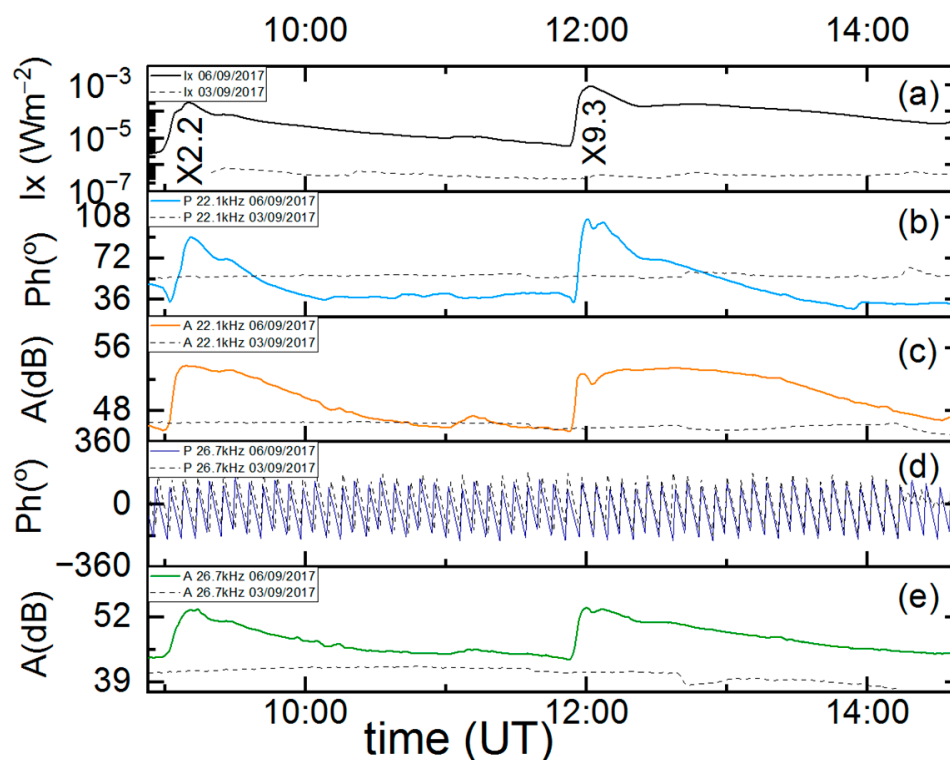


Figure 3. Simultaneous variations of X-ray flux (a) with phase delay, (b) amplitude delay, (c) variations of GQD/22.10 kHz and phase delay, (d) amplitude delay, (e) variations of TBB/26.70 kHz signals versus universal time UT during occurrence of X2.2 and X9.3 class SFs of 6 September 2017. Observed amplitude and phase perturbations with the quiet signal of 3 September 2017 (dashed black) are measured at Belgrade station. Time variation of soft X-ray irradiance is measured by GOES-15 satellite.

3.3. Analysis of Signal Propagation Parameters during Intense SF Events

SFs' occurrence time and evolution were both favorable regarding applied modeling procedures, due to stable daytime GQD waveguide conditions. This was particularly significant for application of the first of previously mentioned numerical procedures in the Methods section, i.e., application of Wait's theory through LWPC software utilization, based upon the two-component exponential model. VLF sub-ionospheric propagation simulations, depending on pair of so-called Wait's parameters β (km^{-1}) and H' (km) (representing time-dependent parameter of lower ionospheric boundary sharpness and VLF signal's reflection height), are conducted using Equation (2) valid for daytime ionosphere [39]:

$$N_e(h, H', \beta) = 1.43 \cdot 10^{13} \cdot e^{(-0.15 \cdot H')} \cdot e^{[(\beta - 0.15) \cdot (h - H')]} \text{, (m}^{-3}\text{)} \quad (2)$$

Parameters β and H' for unperturbed daytime ionospheric conditions are within software predefined as 0.3 km^{-1} and 74 km , respectively, while for each case of perturbed conditions, they must be individually modeled as input parameter pairs along GCP, depending on determined measured amplitude and phase perturbations. Modeling procedure is based on trial-and-error technique, with the goal of achieving the best fit between measured and simulated values of amplitude and phase perturbations obtained through modeling. Results from this numerical procedure in the case of X2.2 and X9.3 SFs of 6 September 2017, for their entire time evolution, are given in Figure 4. Both sharpness (Figure 4b) and effective reflection height (Figure 4a) are in correlation with incident soft X-ray flux (Figure 4c).

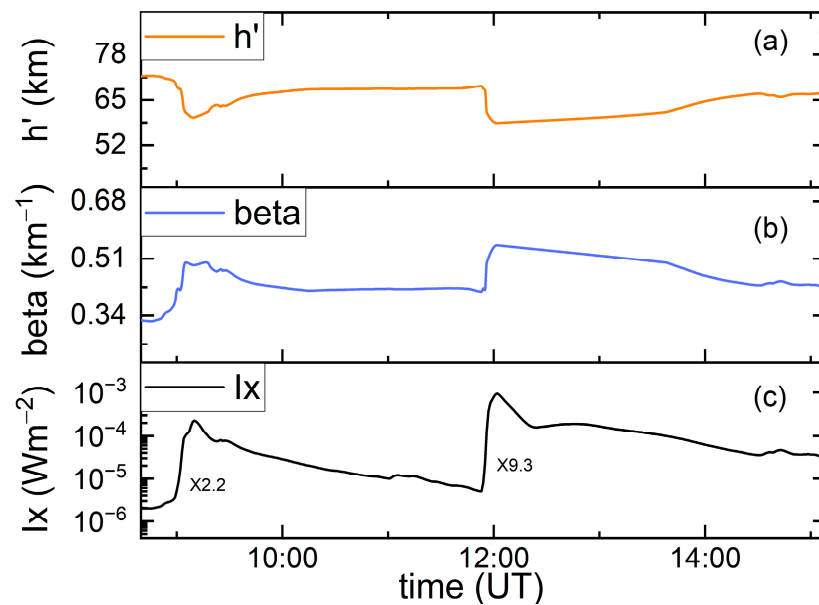


Figure 4. Simultaneous variations of the effective reflection height h' , (a) sharpness β , (b) and X-ray flux (c) during the occurrence of two successive X-ray flares of 6 September 2017.

Obtained modeled values of sharpness and reflection heights corresponding to X-ray flux peaks revealed: in the case of X2.2 SF at 09:10 UT with $I_{x_{\max}} = 2.2658 \cdot 10^{-4} \text{ Wm}^{-2}$, sharpness increased for amount of 0.13 km^{-1} and reflection height was lowered for 14 km, while in the case of X9.3 SF at 12:02 UT with $I_{x_{\max}} = 9.3293 \cdot 10^{-4} \text{ Wm}^{-2}$, sharpness increased for the amount of 0.25 km^{-1} and reflection height was lowered for 15.6 km, compared with their predefined unperturbed values.

Electron density was calculated at the reflection height, when $h = H'$ throughout altitude range corresponding to lower ionosphere (50–90 km), but it must be noted that at the range boundaries, results obtained from calculations should be taken with caution due to possible model failure. Electron density profiles corresponding to the influence of two X-class SFs from 6 September 2017, as observed on the GQD signal at BEL station, are given in Figure 5, in black and red for X2.2 and X9.3 SFs respectively, while quiet ionospheric conditions are given in blue. Conducted calculations indicate that N_e for these two SFs differ within one order of magnitude throughout the entire altitude range. Looking separately, at a height of 74 km, compared to unperturbed ionospheric state, N_e increased by almost three and about 3.5 orders of magnitude during the cases of weaker and stronger SF events respectively.

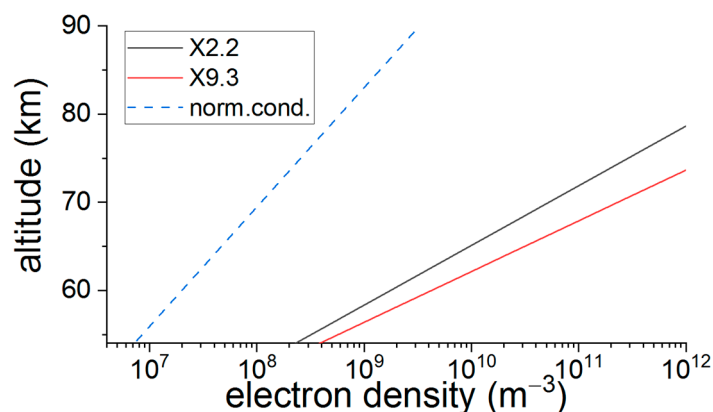


Figure 5. The height profile of electron density at peak time for two successive X-class SFs of 6 September 2017.

For time evolution of X2.2 and X9.3 SFs of 6 September 2017, during about 12 h, a novel approach for obtaining GQD signal propagation parameters, sharpness β and reflection height H' from incident solar X-ray irradiance, was applied by employing the FlarED' Method and Approximate Analytic Expression application, where electron density is calculated with simple logarithmic second-degree polynomial Equation (3) specially designed to take ionospheric response time delay through height-dependent coefficients into calculations (for more details see [5,40]):

$$\log Ne(h, Ix) = a_1(h) + a_2(h) \cdot \log Ix + a_3(h) \cdot (\log Ix)^2 \quad (3)$$

where $a_1(h)$, $a_2(h)$, and $a_3(h)$ are height-dependent coefficients, Ix is solar X-ray flux (Wm^{-2}), and h is height (km). Such calculated Ne values are in good agreement with those obtained using other simulation methods related to the two-component exponential model and VLF sub-ionospheric propagation simulations conducted through the use of LWPC software [40]. Figure 6 presents a 12-h variation of solar X-ray flux within two spectral bands provided by GOES-15 and -13 satellites (Figure 6a) and the corresponding Ne (m^{-3}) during these two X-class SFs (Figure 6b).

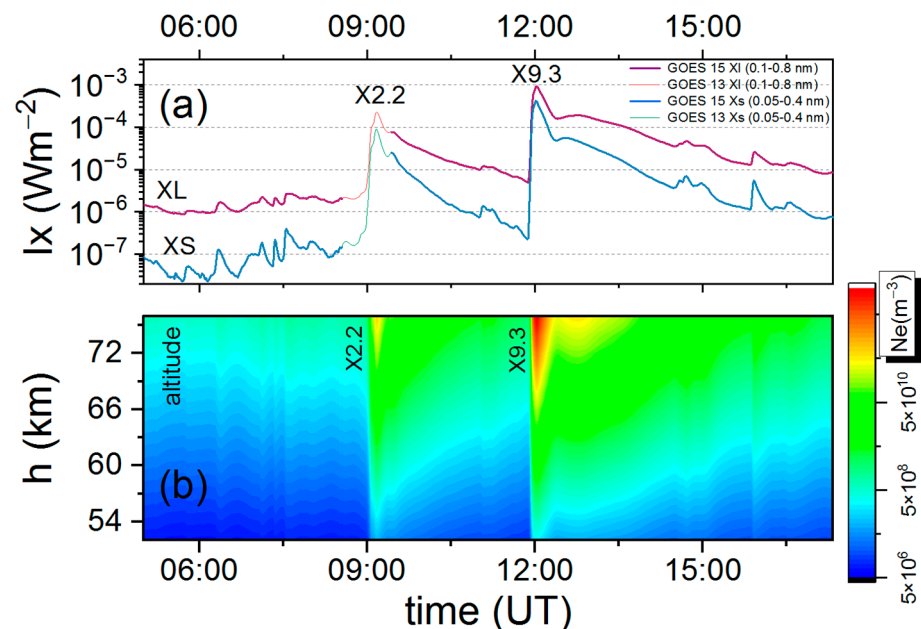


Figure 6. Variation of X-ray flux (a) as measured by GOES-15 and -13 satellites and the surface plot of corresponding electron density profile (b) versus universal time UT during two successive X-class SFs of 6 September 2017. The results are obtained using simple approximative Equation (3).

3.4. Analysis of Cosmic Ray Flux Registered by Belgrade Station during Early September 2017

As a result of solar activity at the beginning of September 2017, a strong FD was detected, resulting in a decrease of CR flux of close to 15% (as observed on the South Pole [60]). The effect was also detected on lower latitudes, being intense enough to be detected by underground muon monitors that are generally sensitive to higher energies of galactic CRs. To get a better perspective of data recorded by Belgrade muon station during this period (both by GLL and UL), we compared it against selected neutron monitor measurements (provided by the Neutron Monitor Database [61]). For this purpose, we chose three NMs: one on the opposite hemisphere with low effective vertical geomagnetic cutoff rigidity R_c , one near the North Pole, and one relatively close to Belgrade muon station with a comparable R_c . All selected stations have different asymptotic directions, R_c , and altitude and are generally sensitive to primary CR with lower median rigidity than CR detected by Belgrade muon station. Median rigidity (R_m) is the rigidity of primary CR where half of all contributions to detector count rate originates from primary CR with

rigidity lower than that specific value. Basic characteristics for NM stations are as follows: South Pole (SOPO, 90.00°S, altitude 2820 m, $R_c = 0.1$ GV, median rigidity $R_m = 10$ GV), Thule (THUL, 76.5°N, 68.7°W, 26 m, $R_c = 0.3$ GV, $R_m = 12.6$ GV), and Athens (ATHN, 37.97°N, 23.78°E, 260 m, $R_c = 8.53$ GV, $R_m = 25.1$ GV). Belgrade muon station, as mentioned before, measures muon flux on ground level (GLL, 44.85°N, 20.38°E, 75 m, $R_c = 5.3$ GV, $R_m = 63$ GV) and underground level (UL, 44.85°N, 20.38°E, 75 m, $R_c = 12$ GV, $R_m = 122$ GV). Median rigidity for NM stations is retrieved from [62]. For Belgrade muon station, R_m values for GLL and UL were determined using the response function obtained by means of Monte Carlo simulation for CR transport. Time series of detected flux for all stations during early September 2017 are given in Figure 7. Flux is normalized using a ten-day average before the FD. This longer interval was chosen due to unusually high solar activity during the period of interest.

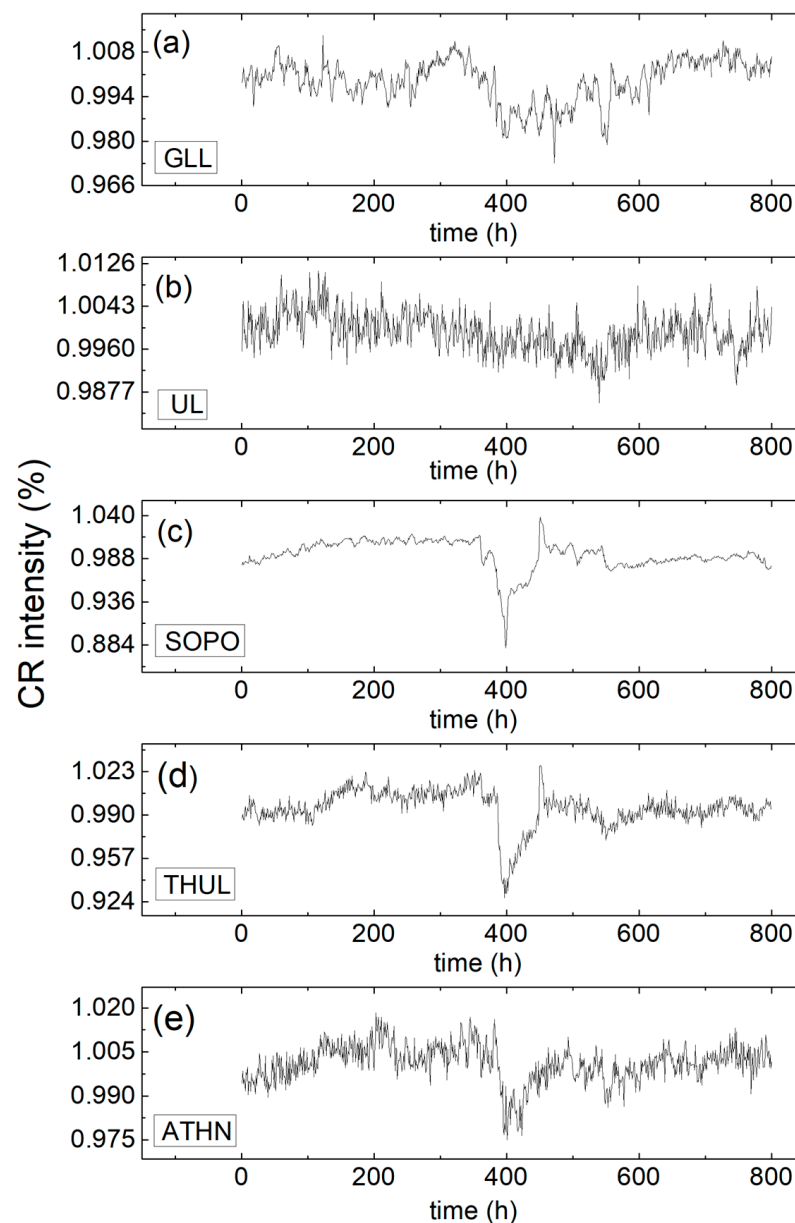


Figure 7. Normalized time series of secondary CR flux detected at several ground and one shallow-underground monitors: (a) ground (GLL) and (b) underground (UL) detector at Belgrade muon station, (c) South pole NM (SOPO), (d) Thule NM (THUL), and (e) Athens NM (ATHN).

Hourly time series show that all stations detected FD around the same time, however, time profiles are not the same. This is due to the specific sensitivity of selected CR stations to primary CR with different rigidities. Additionally, the measured magnitude of the FD is not the same for all detector stations. As expected, UL, GLL, and Athens, with higher cutoff and median rigidity, recovered from sharp depression sooner than stations at higher latitudes (with lower R_c). For a more quantitative description of the relationship between observations from selected monitors, cross-correlation analysis of hourly time series for different stations can be applied using Pearson coefficient with a 2-tail test for significance. Correlation coefficients between data recorded by these ground stations during September 2017 are given in Table 2.

Table 2. Statistical correlation between ground stations during September 2017.

Pearson Corr.	ATHN	SOPO	GLL	UL	THUL
ATHN	1	0.55084	0.43443	0.5056	0.61535
SOPO		1	0.18941	0.45194	0.81747
GLL			1	0.69325	0.36496
UL				1	0.51526
THUL					1

These ground (and one shallow-underground) stations have different locations, different cut-off rigidities, and different energy-dependent detection efficiency of the detectors. All these differences can lead to better understanding of these different correlation coefficients.

Further insight can be gathered by comparing variability of CR flux measured by different stations, as well as geomagnetic activity and selected space weather parameters for the early part of September, which are presented in Figure 8. One-hour time resolution was used for all data. The ICME list compiled by Richardson and Cane [63] and the CME list provided by SOHO/LASCO [64] were used to precisely time the near Earth passage of two ICMEs observed during this period (respective time intervals indicated in Figure 8 by dashed blue lines).

In the days following early September X-flares, two sudden storm commencements (SSCs), or two shocks, arrived during the last hours of 6–7 September (indicated by solid blue lines in Figure 8). They were followed by a sheath region and ICME ejecta. Interaction of shock and sheath region of ICME2 with ICME1 ejecta, visible in the sudden change of solar wind parameters, led to the observed intense geomagnetic activity and consequent FD. This CME-CME interaction with its complex structure was the main reason for the extensive geomagnetic storm [65] and a strong detected FD. With arrival of the first ICME, CR flux showed a small decrease detected as a low-magnitude FD by NM stations [66] (at 23:43:00 UT on 6 September, with magnitude of 1.8% according to IZMIRAN database).

When the second fast interplanetary shock arrived and interacted with ejecta from the previous ICME, a sharp decrease in CR flux and one of the largest FDs in solar cycle 24 was detected (at 23:00:00 UT on 7 September, with magnitude of 7.7% according to IZMIRAN database). Main FD was clearly visible even with muon detectors, which leads to the conclusion that inhomogeneities in the heliosphere created by interaction of these two ICMEs modulated CR extensively. The recovery phase of this FD was influenced by disturbed interplanetary condition, the effect being dependent on particle energy as was evident by comparing profiles of CR time series recorded by different stations. Before the end of the recovery phase, another flare (X8.2 of 10 September) led to a small ground level enhancement (GLE), the last one of solar cycle 24 (GLE #72). Recovery time of the main FD was approximately three days in total, which is a relatively short period for such a large CR modulation. Cross-correlation coefficients between CR time series measured by Belgrade muon station and selected space weather parameters for the period of six days (during 5–10 September) are given in Table 3.

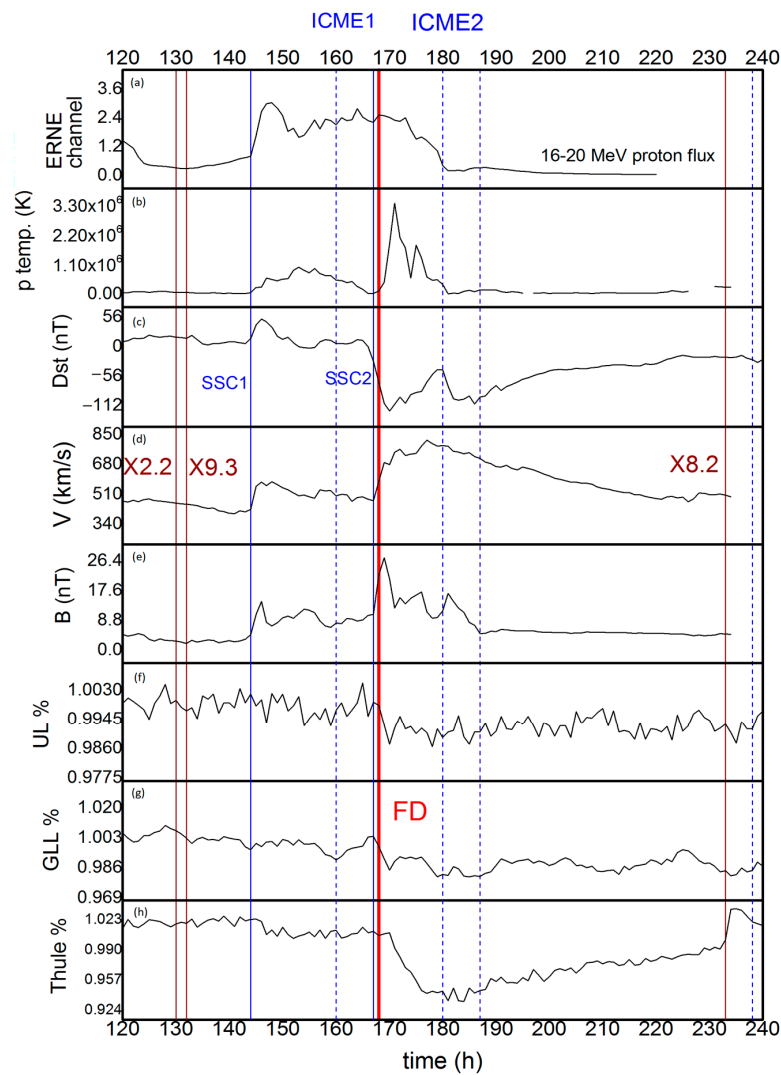


Figure 8. Hourly variation in CR intensity measured at ground station ((f) UL, (g) GLL, (h) Thule), (e) magnitude of interplanetary magnetic field B, (d) velocity of solar wind V, (c) Dst index, (b) proton temperature, and (a) one of the proton channels measured by ERNE/SOHO during early September 2017 (period 4th–10th).

Table 3. Statistical correlation (with significance) between time series of CR flux measured at ground stations and selected space weather parameters during 5–10 September 2017.

Pearson Corr.	Thule		GLL		UL	
Thule	1					
GLL	0.67213	(<10 ⁻⁶)	1			
UL	0.62741	(<10 ⁻⁶)	0.75552	(<10 ⁻⁶)	1	
Average B	-0.238	(<0.008)	-0.242	0.007	-0.243	<0.007
SW speed	-0.80562	(<10 ⁻⁶)	-0.62829	(<10 ⁻⁶)	-0.58503	(<10 ⁻⁶)
Dst Index	0.77923	(<10 ⁻⁶)	0.6979	(<10 ⁻⁶)	0.65494	(<10 ⁻⁶)
Proton Channel 16–20 MeV	0.43083	<10 ⁻⁵	0.38276	<10 ⁻⁴	0.31715	<10 ⁻³

During this period, apparent correlation can be established between selected parameters. This correlation is larger for Thule NM than in the case of Belgrade Muon monitor. Due to the short period, correlation between proton flux at L1 and detected CR flux on all stations is exaggerated.

4. Discussion

The cascade of strong solar activity from AR12673 that occurred in early September 2017 was among others characterized by a number of SFs. Several concurrent interconnecting CMEs/ICMEs emerged in a relatively short period, inducing a disturbance in the heliosphere. The complex structure of interacting CMEs/ICMEs produced an extensive geomagnetic storm and ionospheric disturbance and affected the flux of primary CR (visible as a FD). Additionally, the mentioned phenomena were responsible for the increased flux of energetic particles in interplanetary space. The origin and acceleration mechanism for energetic protons measured at L1 is not so straightforward to determine due to complicated interactions of all effects potentially involved. In case these particles originate from the Sun, correlation between SF properties and SEP fluence is supposed to be rather poor, although it is suggested that primary acceleration of SEP to higher energies occur in close proximity to the flare site [67,68]. If, on the other hand, these particles are accelerated in interplanetary space due to the passage of ICME shock, some correlation can be established (i.e., between measured proton fluence and CME/ICME velocity). However, regardless of their origin, the shape of energetic proton fluence spectrum can hold useful information about heliospheric disturbance and can even provide insight into the effect that this disturbance has on the flux of primary CR in interplanetary space (especially when more intense events are concerned). That was also demonstrated in this case, where the magnitude of the corresponding FD corrected for magnetospheric effect estimated from proton fluence spectra was in good agreement with the value for M_M calculated based on NM measurements.

Impacts of the soft range X-ray solar electromagnetic radiation released from two powerful SF events from 6 September 2017 onto the European mid-latitude ionospheric D-region were monitored and inspected based on recordings from BEL narrowband VLF receiving station, belonging to a global ground-based VLF network system. Lower ionospheric disturbances induced by incident soft range X-ray radiation were indirectly examined regarding simultaneous perturbations of VLF radio signals' propagation parameters within the Earth-ionosphere waveguide, with analysis conducted for signals with short GCPs (Table 1; Figure S3).

Aside from quiet ionospheric preflare conditions, SFs' occurrence times were also favorable in terms of applied modeling procedure using the LWPC software package, since analyzed signals on their GCPs towards BEL station were transmitted through waveguides under already established stable daytime ionospheric conditions. Since this procedure relies on trial-and-error technique in acquiring the best fitting pair of Wait's parameters for depicting real measured data with the modeled data, and from that, by obtaining information regarding lower ionospheric conditions based on modeled ones, both of these prerequisites significantly eased an already highly challenging task of modeling X-class SFs and especially those most energetic among them. In such disturbed conditions, both ionospheric plasma properties and related corresponding VLF signal propagation parameters are drastically changed compared with the regular state. Accordingly, electron density height profiles are also changed in regard to both time and space distributions. As expected, the evolution of observed VLF signals' perturbations was with similar characteristics, following a lower ionospheric response to incident solar X-ray flux with delay times corresponding to the sluggishness of the ionosphere and were of amounts expected for cases of such powerful events (Figure 3). Their back-to-back occurrence did not allow for individual duration specification of each SF's impact on analyzed VLF signals, however, their individual contribution was possible to determine. According to registered VLF BEL data, after a several-hour lasting disturbance, the lower ionosphere fully recovered (Figure S4).

For the state of maximal perturbation that corresponds to SFs' X-ray flux peaks, perturbed GQD signal's amplitudes are 118% and 117% of unperturbed, while phases are 165% and 192% of unperturbed. Wait's parameters are in correlation with incident soft X-ray flux and modeling results based upon exponential conductivity increase with height within the ionosphere suggesting that perturbed sharpnesses are 143.3% and 183.3% of unperturbed, while perturbed reflection heights are 81% and 78.9% of unperturbed,

respectively to SFs (Figure 4). As expected, in the case of the stronger SF event, propagation was more affected by the induced disturbance, causing the reflecting edge boundary to become significantly sharper, while reflecting edge height descended for 1.6 km^{-1} more than in case of the weaker one. Numerically, simulated ionospheric conditions fit well with observed ones, as indirectly obtained through GQD signal's amplitude and phase measurements. Due to its short GCP and stable daytime ionospheric conditions, averaged conditions that were held within the waveguide during the modeling procedure can be considered reliable. Electron densities calculated using Equation (2) for the D-region altitude range show about one order of magnitude difference between analyzed SFs at their peak, giving a reflection height of 74 km an increase in electron density of 82.1% compared between stronger and weaker events (Figure 5).

The effects on the ionosphere of the largest SF event of the last decade, X9.3 together with X2.2, occurred on 6 September 2017, observed through GQD VLF signal response in relation to the SF class, were compared with some other cases of strong SF events, including several major SFs (2003–2011 of class X28+–X6.9) and other SFs (from 2006–2017 of class X1–X9.3 and from period 1994–1998 in range X1–X5). Figure S5 provides a comparison of the results obtained in this study (black stars) and those available in the literature [5,7,8,69–77]. Presented ionospheric parameters (β and H') and corresponding electron densities are related to results from two hundred cases of SF events recorded in Belgrade on GQD trace in the period of 2003–2017 in other mid-latitudinal ionospheric sectors and the low-latitudinal ionospheric sector. In order to ensure better insight into the tendency of parameters with the SF events' strength, smaller diagrams containing the entire C–X-class range are embedded in Figure S5. It can be seen that values of signal parameters for some X-class events are quite scattered.

Our results fit well with the general trend (linear fit), considering that most of the available cases taken into consideration are from the mid-latitudinal sector. A significant discrepancy notable in the enlarged X-class section, related to results from [69] and [70], is probably caused by latitudinal factor (due to low-latitudinal observations likewise as suggested in [71] and similarly due to observations obtained more towards higher-latitude compared with Belgrade receiver site, respectively). A novel proposed approximate method that employs approximative Equation (3) for obtaining ionospheric parameters was validated both for cases of weaker and stronger SFs and expanded further towards the upper boundary of X-class range, as compared to recent previous studies employing this technique. Applied novel approach provides mapping of the entire ionospheric altitude range (Figure 6) in a simpler and easier to conduct manner. Results obtained in this study using this novel approach applied to X-class SFs could be useful for validation of the available ionospheric models and as input data for other climate models.

Furthermore, increased solar activity at the beginning of September 2017 had a significant effect on cosmic rays observed as a decrease in measured flux by all relevant CR stations. Intensity of the event was such that the energy range of affected primary CR was wide enough for the effect to be detected both by neutron monitors and muon detectors. The decrease was even observable in shallow-underground muon measurements, although to a much lesser extent. Temporal agreement between measurements taken by different detectors was good, while the shape of detected FD varied, as would be expected due to difference in location, instrument design, and sensitivity. Cross-correlation analysis of hourly time series for different stations (presented in Table 2) shows expected positive correlation, where obtained coefficients are consistent with values expected based on differences in detector location, particular setups, station specific environmental conditions, and most importantly, the energy (rigidity) range of primary CR they are sensitive to. GLL and UL have the same position, however, correlation is not so high (≈ 0.7) due to different R_c and R_m . Nevertheless, this correlation is higher than that between either of the detectors and any of the neutron monitor stations. NMs have more similar R_c and R_m values, so this correlation is greater despite their different location. As far as correlation between measured CR flux and selected space weather and geomagnetic parameters is concerned,

a larger correlation observed for NM (Table 3) can almost certainly be attributed to the fact that muon detectors are sensitive to higher energy CR (which are less modulated by disturbances in the heliosphere). Correlation between selected proton channel (particles with energy between 16 and 20 MeV) and CR flux is exaggerated as it is a consequence of a relatively short time interval taken for analysis. This value is greatly reduced if a longer interval is taken into consideration, even appearing as a small anticorrelation. This is expected as proton flux with its turbulent magnetic field scatters CR and thus can produce a decrease in detected CR flux. Inverse correlation of magnetic field and solar wind speed with CR flux is anticipated due to the same reason.

Forbush decrease in early September 2017 was caused by compound solar wind disturbance formed due to the interaction of several ICMEs. This time interval is particularly interesting because it happens in a descending-to-minimum phase of a solar cycle. The apparent multitude of solar activity is more characteristic to other phases. For example, similar series of successive CMEs led to FD in March 2012 [78] during the ascending phase of the solar cycle, but this heightened activity of the Sun, isolated between relatively quiet periods, allows for better study of the phenomena. Forecasting these multiple CME interaction events and predicting time of arrival is very difficult [45] but needed, so this series of events can be a good case study.

Although no apparent correlation between SF intensity and solar wind and FD parameters is clearly demonstrable, the majority of more intense FDs are caused by a CME/ICME following a significant SF, thus indicating a likely connection. For one such complex event, accompanying disturbances induced in the heliosphere, magnetosphere, and ionosphere are generally directly attributed to different sources and establishing clear relationships between various parameters used to describe them is far from straightforward. Yet, based on some general features, it is possible to make rudimentary event classification, where within certain classes, some of these relationships may be more pronounced. Strong flares do not necessarily produce a significant FD (although can have an associated GLE, as is the case for X14.4 flare that occurred on 15 April 2001), can produce both strong FDs and GLEs (e.g., GLE #69 on 20 January 2005, GLE #66 on 28 October and GLE #67 on 2 November 2003), or can produce strong FD but without associated GLE (e.g., 7 March 2012, related to X5.4 flare and September 2017 event studied here). It has been shown [49,79] that events that fall in this last category exhibit stronger correlations between FD magnitude and some space weather parameters, specifically average CME speed. More recently, a correlation between FD magnitude (especially in the case of more intense FDs) and shape of energetic proton spectra measured at L1 has been reported for this class of events. As the number of such events is relatively low, it is of significance that results presented in this work are consistent with the indicated relationship. For reference, dependence of FD magnitude on selected SF, CME, and geomagnetic parameters for some of the mentioned events is given in Figure S6.

5. Conclusions

The influence of severely disturbed space weather conditions of 6 September 2017 on parameters of the Earth's atmosphere was studied, in relation to the relatively close and far surroundings of the Earth. The influence of strong X-class SFs on the ionosphere and primary cosmic rays, based on space- and ground-based observations on one hand and simulations on the other hand, are presented. It contributes to better understanding of solar-terrestrial coupling processes and how primary cosmic rays and the ionosphere respond under conditions during the X-class SF events. Based on the results presented, the following conclusions can be drawn:

- SEP fluence during strongly disturbed conditions of the heliosphere in early September 2017 was calculated from SOHO/ERNE data and modeled using double power law. Relationships between power exponents used to parameterize the shape of fluence spectrum and FD magnitude corrected for magnetospheric effect are consistent with ones expected for this type of event. Hourly time series of secondary CR flux, detected by several ground-based monitors and one shallow-underground monitor, show that

- all stations detected FD at the same time. Cross-correlation between these time series, and between CR time series and some geomagnetic activity indices, as well as selected IMF and solar wind parameters, are presented. Sensitivity of different stations to primary CR with different rigidity results in different time profiles, maximal decreases, and duration of recovery phase of FD;
- We observed that a correlation between heliospheric and geomagnetic parameters decreases with increase of median energy of the CR detected by different stations and that shows an extension of CR modulation of complex CME-CME interaction structure initiated with strong SFs;
 - Impact of intense solar activity onto the Earth's lower ionosphere, through analyzed X-class SFs, was clearly observed (perturbed amplitudes are 118% and 117% of unperturbed, while perturbed phases are 165% and 192% of unperturbed, for X2.2 and X9.3, respectively). BEL AbsPAL recordings of registered VLF signals during SF events are in correlation with X-ray flux (with time delays corresponding to the sluggishness of the ionosphere). Although X2.2 and X9.3 occurred back-to-back, it was possible to determine individual contributions of each SF based upon registered VLF signals;
 - Numerical simulations were conducted through the application of the LWPC software package and the FlarED' Method and Approximate Analytic Expression application's novel approach. The ionospheric parameters (sharpness and effective reflection height) and electron density are in correlation with incident X-ray flux of soft range. N_e for these two SFs revealed the difference within one order of magnitude throughout the entire altitude range considered. Compared to quiet ionospheric conditions, N_e at the reference height increased by several orders of magnitude during both SF events. As monitored by BEL VLF station in the mid-latitudinal sector, both presented X-class SFs are common in properties and behavior, as could be expected for intense SF events, according to their strength. However, there is a significant difference in estimations of ionospheric parameters related to some other cases of reported X-class SFs from different sectors.

Although there are numerous papers related to the influence of SF events on Earth's ionosphere, the vast majority of present case studies of selected SF events, more or less are extensively related to numbers of examined cases. X-class SF events have never been systematically studied in terms of lower ionospheric response. Coupling processes between such extreme space weather events and the lower ionosphere are not well understood. In addition, many intense SF events are related to other energetic solar events like CMEs and SEPs. Comprehensive research is needed especially in terms of retrieving a global (worldwide) lower ionospheric response to such strong events from propagation parameters of radio signals as a remote sensing technique. Case studies, although restricted to some selected events and with great contribution of "local" components contained within obtained and presented results, would provide substantial contributions.

This study emphasized the relevance of the ionospheric response, which was analyzed using a multi-instrument method, and gave a comprehensive examination of the events from the Sun to the Earth. It gave an insight into the sudden increase in ionization during the storm and strong SFs from the beginning of September 2017 and the potential effects on radio communication. Since conditions in the D-region of the ionosphere have a dramatic effect on high frequency communications and low frequency navigation systems, the ionospheric responses (and its parameters like β , H' and N_e) to severe SFs are a key topic of study in ionospheric physics and are considered to be an important factor for space weather predictions, improvement of empirical models, and applications of machine learning techniques in atmospheric sciences.

Supplementary Materials: The following supporting information can be downloaded at: <https://www.mdpi.com/article/10.3390/rs15051403/s1>, Figure S1: Differential SEP fluxes during extreme solar event in September 2017, measured by SOHO/ERNE energetic particle sensors LET (Low Energy Detector) proton channels. Red vertical dashed lines indicate the time for the start and the end

of interval used to calculate the integral flux.; Figure S2: Differential SEP fluxes during extreme solar event in September 2017, measured by SOHO/ERNE energetic particle sensors HET (High Energy Detector) proton channels. Red vertical dashed lines indicate the time for the start and the end of interval used to calculate the integral flux.; Figure S3: The geographic position of Belgrade (BEL) VLF receiver and the GQD transmitter (54.73°N, 2.88°W), Anthorn UK and TBB transmitter (37.43°N, 27.55°E) Bafa Turkey with GCP of sub-ionospheric propagating VLF signals.; Figure S4: Simultaneous variations of X-ray flux (red), phase (blue), and amplitude (orange) of GQD/22.10 kHz signal versus universal time UT during occurrence of X2.2 and X9.3 class solar flares of 6 September 2017 (from upper to lower panel). Observed amplitude and phase perturbations on GQD radio signal, as well as quiet signal (dashed black), are measured at Belgrade station. Time variation of soft X-ray irradiance is measured by GOES-15 satellite.; Figure S5: Lower ionospheric response to SF events of different strength across X-class (shaded gray area), obtained indirect modeling of VLF signals' propagation parameters: (a) sharpness β (km^{-1}), and (b) effective reflection height H' , (km) and (c) estimated corresponding electron densities N_e (m^{-3}), in function of X-ray flux; results from our research are presented by black stars.; Figure S6: Magnitude of the FD versus the average CME velocity between the Sun and the Earth, calculated using the time of the beginning of the associated CME observations (a) Minimal Dst-index in the event, (b) maximal X-ray flare power (c) with associated flare indicated in red.

Author Contributions: Conceptualization, V.A.S.; writing—original draft preparation, V.A.S., A.K. and N.V.; writing—review and editing A.K., N.V., V.A.S., Z.M., M.S. and A.D. The authors had full access to the data and took responsibility for their integrity. All authors have read and agreed to the published version of the manuscript.

Funding: This work was funded by the Institute of Physics Belgrade, University of Belgrade, through a grant by the Ministry of Science, Technological Development and Innovations of the Republic of Serbia.

Data Availability Statement: VLF data were recorded at the Institute of Physics Belgrade, University of Belgrade and can be obtained upon request. Please contact V.A.S.

Acknowledgments: The article is based upon work from COST Action CA18212—Molecular Dynamics in the GAS phase (MD-GAS), supported by COST (European Cooperation in Science and Technology). Authors thank D. Šulić for instrumental set-up and useful discussions. OMNI data was made available by NASA/GSFC's Space Physics Data Facility's OMNIWeb service. This CME catalog is generated and maintained at the CDAW Data Center by NASA and The Catholic University of America in cooperation with the Naval Research Laboratory. SOHO is a project of international cooperation between ESA and NASA. We acknowledge the NMDB database, founded under the European Union's FP7 program (contract no.213007) for providing data. We also gratefully acknowledge using data from the catalogue of Forbush effects and interplanetary disturbances provided by Cosmic Ray Group at the IZMIRAN Space Weather Prediction Center at Pushkov Institute of Terrestrial Magnetism, Ionosphere, and Radio Wave Propagation of the Russian Academy of Sciences.

Conflicts of Interest: The authors declare no conflict of interest. The funders had no role in the design of the study; in the collection, analyses, or interpretation of data; in the writing of the manuscript, or in the decision to publish the results.

References

1. Manju, G.; Pant, T.K.; Devasia, C.V.; Ravindran, S.; Sridharan, R. Electrodynamical response of the Indian low-mid latitude ionosphere to the very large solar flare of 28 October 2003—A case study. *Ann. Geophys.* **2009**, *27*, 3853–3860. [[CrossRef](#)]
2. Fu, H.; Zheng, Y.; Ye, Y.; Feng, X.; Liu, C.; Ma, H. Joint Geoeffectiveness and Arrival Time Prediction of CMEs by a Unified Deep Learning Framework. *Remote Sens.* **2021**, *13*, 1738. [[CrossRef](#)]
3. Sahai, Y.; Becker-Guedes, F.; Fagundes, P.R.; Lima, W.L.C.; de Abreu, A.J.; Guarnieri, F.L.; Candido, C.M.N.; Pillat, V.G. Unusual ionospheric effects observed during the intense 28 October 2003 solar flare in the Brazilian sector. *Ann. Geophys.* **2007**, *25*, 2497–2502. [[CrossRef](#)]
4. Le, H.; Liu, L.; Chen, Y.; Wan, W. Statistical analysis of ionospheric responses to solar flares in the solar cycle 23. *J. Geophys. Res. Space Phys.* **2013**, *118*, 576–582. [[CrossRef](#)]
5. Srećković, V.A.; Šulić, D.M.; Ignjatović, L.; Vujčić, V. Low Ionosphere under Influence of Strong Solar Radiation: Diagnostics and Modeling. *Appl. Sci.* **2021**, *11*, 7194. [[CrossRef](#)]
6. Kelley, M.C. *The Earth's Ionosphere: Plasma Physics and Electrodynamics*; Academic Press: Cambridge, MA, USA, 2009.

7. Barta, V.; Natras, R.; Srećković, V.; Koroncay, D.; Schmidt, M.; Šulic, D. Multi-instrumental investigation of the solar flares impact on the ionosphere on 05–06 December 2006. *Front. Environ. Sci.* **2022**, *10*, 904335. [[CrossRef](#)]
8. Kolarski, A.; Srećković, V.A.; Mijić, Z.R. Response of the Earth's Lower Ionosphere to Solar Flares and Lightning-Induced Electron Precipitation Events by Analysis of VLF Signals: Similarities and Differences. *Appl. Sci.* **2022**, *12*, 582. [[CrossRef](#)]
9. Nina, A. Modelling of the Electron Density and Total Electron Content in the Quiet and Solar X-ray Flare Perturbed Ionospheric D-Region Based on Remote Sensing by VLF/LF Signals. *Remote Sens.* **2022**, *14*, 54. [[CrossRef](#)]
10. Berdermann, J.; Kriegel, M.; Banyś, D.; Heymann, F.; Hoque, M.M.; Wilken, V.; Borries, C.; Heßelbarth, A.; Jakowski, N. Ionospheric Response to the X9.3 Flare on 6 September 2017 and Its Implication for Navigation Services Over Europe. *Space Weather* **2018**, *16*, 1604–1615. [[CrossRef](#)]
11. Yasyukevich, Y.; Astafyeva, E.; Padokhin, A.; Ivanova, V.; Syrovatskii, S.; Podlesnyi, A. The 6 September 2017 X-Class Solar Flares and Their Impacts on the Ionosphere, GNSS, and HF Radio Wave Propagation. *Space Weather* **2018**, *16*, 1013–1027. [[CrossRef](#)]
12. De Paula, V.; Segarra, A.; Altadill, D.; Curto, J.J.; Blanch, E. Detection of Solar Flares from the Analysis of Signal-to-Noise Ratio Recorded by Digisonde at Mid-Latitudes. *Remote Sens.* **2022**, *14*, 1898. [[CrossRef](#)]
13. Demyanov, V.V.; Yasyukevich, Y.V.; Ishin, A.B.; Astafyeva, E.I. Ionospheric super-bubble effects on the GPS positioning relative to the orientation of signal path and geomagnetic field direction. *GPS Solut.* **2012**, *16*, 181–189. [[CrossRef](#)]
14. Yashiro, S.; Gopalswamy, N. Statistical relationship between solar flares and coronal mass ejections. *Proc. Int. Astron. Union* **2008**, *4*, 233–243. [[CrossRef](#)]
15. Desai, M.; Giacalone, J. Large gradual solar energetic particle events. *Living Rev. Sol. Phys.* **2016**, *13*, 3. [[CrossRef](#)]
16. Freiherr von Forstner, J.L.; Guo, J.; Wimmer-Schweingruber, R.F.; Dumbović, M.; Janvier, M.; Démoulin, P.; Veronig, A.; Temmer, M.; Papaioannou, A.; Dasso, S.; et al. Comparing the Properties of ICME-Induced Forbush Decreases at Earth and Mars. *J. Geophys. Res. Space Phys.* **2020**, *125*, e2019JA027662. [[CrossRef](#)]
17. Cane, H.V. Coronal Mass Ejections and Forbush Decreases. *Space Sci. Rev.* **2000**, *93*, 55–77. [[CrossRef](#)]
18. Belov, A.V.; Eroshenko, E.A.; Oleneva, V.A.; Struminsky, A.B.; Yanke, V.G. What determines the magnitude of forbush decreases? *Adv. Space Res.* **2001**, *27*, 625–630. [[CrossRef](#)]
19. Papaioannou, A.; Belov, A.; Abunina, M.; Eroshenko, E.; Abunin, A.; Anastasiadis, A.; Patsourakos, S.; Mavromichalaki, H. Interplanetary Coronal Mass Ejections as the Driver of Non-recurrent Forbush Decreases. *Astrophys. J.* **2020**, *890*, 101. [[CrossRef](#)]
20. Belov, A.; Shlyk, N.; Abunina, M.; Belova, E.; Abunin, A.; Papaioannou, A. Solar Energetic Particle Events and Forbush Decreases Driven by the Same Solar Sources. *Universe* **2022**, *8*, 403. [[CrossRef](#)]
21. Riley, P.; Love, J.J. Extreme geomagnetic storms: Probabilistic forecasts and their uncertainties. *Space Weather* **2017**, *15*, 53–64. [[CrossRef](#)]
22. Eastwood, J.P.; Biffis, E.; Hapgood, M.A.; Green, L.; Bisi, M.M.; Bentley, R.D.; Wicks, R.; McKinnell, L.A.; Gibbs, M.; Burnett, C. The Economic Impact of Space Weather: Where Do We Stand? *Risk Anal.* **2017**, *37*, 206–218. [[CrossRef](#)] [[PubMed](#)]
23. Kumar, A.; Kashyap, Y.; Kosmopoulos, P. Enhancing Solar Energy Forecast Using Multi-Column Convolutional Neural Network and Multipoint Time Series Approach. *Remote Sens.* **2023**, *15*, 107. [[CrossRef](#)]
24. Alabdulgader, A.; McCraty, R.; Atkinson, M.; Dobyns, Y.; Vainoras, A.; Ragulskis, M.; Stolc, V. Long-Term Study of Heart Rate Variability Responses to Changes in the Solar and Geomagnetic Environment. *Sci. Rep.* **2018**, *8*, 2663. [[CrossRef](#)] [[PubMed](#)]
25. Bruno, A.; Christian, E.R.; de Nolfo, G.A.; Richardson, I.G.; Ryan, J.M. Spectral Analysis of the September 2017 Solar Energetic Particle Events. *Space Weather* **2019**, *17*, 419–437. [[CrossRef](#)]
26. Chamberlin, P.C.; Woods, T.N.; Didkovsky, L.; Eparvier, F.G.; Jones, A.R.; Machol, J.L.; Mason, J.P.; Snow, M.; Thiemann, E.M.B.; Viereck, R.A.; et al. Solar Ultraviolet Irradiance Observations of the Solar Flares During the Intense September 2017 Storm Period. *Space Weather* **2018**, *16*, 1470–1487. [[CrossRef](#)]
27. Pikulina, P.; Mironova, I.; Rozanov, E.; Karagodin, A. September 2017 Solar Flares Effect on the Middle Atmosphere. *Remote Sens.* **2022**, *14*, 2560. [[CrossRef](#)]
28. Vankadara, R.K.; Panda, S.K.; Amory-Mazaudier, C.; Fleury, R.; Devanaboyina, V.R.; Pant, T.K.; Jamjareegulgarn, P.; Haq, M.A.; Okoh, D.; Seemala, G.K. Signatures of Equatorial Plasma Bubbles and Ionospheric Scintillations from Magnetometer and GNSS Observations in the Indian Longitudes during the Space Weather Events of Early September 2017. *Remote Sens.* **2022**, *14*, 652. [[CrossRef](#)]
29. Amaechi, P.O.; Akala, A.O.; Oyedokun, J.O.; Simi, K.G.; Aghogho, O.; Oyeyemi, E.O. Multi-Instrument Investigation of the Impact of the Space Weather Events of 6–10 September 2017. *Space Weather* **2021**, *19*, e2021SW002806. [[CrossRef](#)]
30. Curto, J.J.; Marsal, S.; Blanch, E.; Altadill, D. Analysis of the Solar Flare Effects of 6 September 2017 in the Ionosphere and in the Earth's Magnetic Field Using Spherical Elementary Current Systems. *Space Weather* **2018**, *16*, 1709–1720. [[CrossRef](#)]
31. Bilitza, D. IRI the International Standard for the Ionosphere. *Adv. Radio Sci.* **2018**, *16*, 1–11. [[CrossRef](#)]
32. Moraal, H. Cosmic-Ray Modulation Equations. *Space Sci. Rev.* **2013**, *176*, 299–319. [[CrossRef](#)]
33. Dorman, L.I. *Cosmic Rays in the Earth's Atmosphere and Underground*; Springer: Dordrecht, The Netherlands, 2004; Volume 303, p. 862.
34. Zhang, J.L.; Tan, Y.H.; Wang, H.; Lu, H.; Meng, X.C.; Muraki, Y. The Yangbajing Muon–Neutron Telescope. In *Nuclear Instruments and Methods in Physics Research Section A: Accelerators, Spectrometers, Detectors and Associated Equipment*; Elsevier: Amsterdam, The Netherlands, 2010; Volume 623, pp. 1030–1034. [[CrossRef](#)]

35. Veselinović, N.; Dragić, A.; Savić, M.; Maletić, D.; Joković, D.; Banjanac, R.; Udovičić, V. An underground laboratory as a facility for studies of cosmic-ray solar modulation. In *Nuclear Instruments and Methods in Physics Research Section A: Accelerators, Spectrometers, Detectors and Associated Equipment*; Elsevier: Amsterdam, The Netherlands, 2017; Volume 875, pp. 10–15.
36. Savić, M.; Maletić, D.; Dragić, A.; Veselinović, N.; Joković, D.; Banjanac, R.; Udovičić, V.; Knežević, D. Modeling Meteorological Effects on Cosmic Ray Muons Utilizing Multivariate Analysis. *Space Weather* **2021**, *19*, e2020SW002712. [[CrossRef](#)]
37. Ferguson, J. *Computer Programs for Assessment of Long-Wavelength Radio Communications, Version 2.0: User's Guide and Source Files*; Space and Naval Warfare Systems Center: San Diego, CA, USA, 1998.
38. Mitra, A.P. *Ionospheric Effects of Solar Flares*; Springer: Berlin/Heidelberg, The Netherlands, 1974; Volume 46.
39. Wait, J.R.; Spies, K.P. *Characteristics of the Earth-Ionosphere Waveguide for VLF Radio Waves*; US Department of Commerce, National Bureau of Standards: Gaithersburg, MD, USA, 1964; Volume 13.
40. Srećković, V.A.; Šulić, D.M.; Vujčić, V.; Mijić, Z.R.; Ignjatović, L.M. Novel Modelling Approach for Obtaining the Parameters of Low Ionosphere under Extreme Radiation in X-Spectral Range. *Appl. Sci.* **2021**, *11*, 11574. [[CrossRef](#)]
41. AR12673 History. Available online: http://helio.mssl.ucl.ac.uk/helio-vo/solar_activity/arstats/arstats_page4.php?region=12673 (accessed on 14 December 2022).
42. Space Weather Prediction Center (IZMIRAN). Available online: <http://spaceweather.izmiran.ru/eng/dbs.html> (accessed on 22 January 2022).
43. Wold, A.M.; Mays, M.L.; Taktakishvili, A.; Jian, L.K.; Odstrcil, D.; MacNeice, P. Verification of real-time WSA-ENLIL+Cone simulations of CME arrival-time at the CCMC from 2010 to 2016. *J. Space Weather Space Clim.* **2018**, *8*, A17. [[CrossRef](#)]
44. Gopalswamy, N.; Yashiro, S.; Michalek, G.; Stenborg, G.; Vourlidas, A.; Freeland, S.; Howard, R. The SOHO/LASCO CME Catalog. *Earth Moon Planets* **2009**, *104*, 295–313. [[CrossRef](#)]
45. Werner, A.L.E.; Yordanova, E.; Dimmock, A.P.; Temmer, M. Modeling the Multiple CME Interaction Event on 6–9 September 2017 with WSA-ENLIL+Cone. *Space Weather* **2019**, *17*, 357–369. [[CrossRef](#)]
46. SPDF - OMNIWeb Service. Available online: https://spdf.gsfc.nasa.gov/pub/data/omni/low_res_omni/ (accessed on 10 November 2022).
47. Torsti, J.; Valtonen, E.; Lumme, M.; Peltonen, P.; Eronen, T.; Louhola, M.; Riihonen, E.; Schultz, G.; Teittinen, M.; Ahola, K.; et al. Energetic particle experiment ERNE. *Sol. Phys.* **1995**, *162*, 505–531. [[CrossRef](#)]
48. Multi-Source Spectral Plots (MSSP) of Energetic Particle. Available online: https://omniweb.gsfc.nasa.gov/ftpbrowser/flux_spectr_m.html (accessed on 25 October 2022).
49. Savić, M.; Veselinović, N.; Dragić, A.; Maletić, D.; Joković, D.; Udovičić, V.; Banjanac, R.; Knežević, D. New insights from cross-correlation studies between solar activity indices and cosmic-ray flux during Forbush decrease events. *Adv. Space Res.* **2022**, *71*, 2006–2016. [[CrossRef](#)]
50. Band, D.; Matteson, J.; Ford, L.; Schaefer, B.; Palmer, D.; Teegarden, B.; Cline, T.; Briggs, M.; Paciesas, W.; Pendleton, G.; et al. BATSE Observations of Gamma-Ray Burst Spectra. I. Spectral Diversity. *Astrophys. J.* **1993**, *413*, 281. [[CrossRef](#)]
51. Ellison, D.C.; Ramaty, R. Shock acceleration of electrons and ions in solar flares. *Astrophys. J.* **1985**, *298*, 400–408. [[CrossRef](#)]
52. Mottl, D.A.; Nymmik, R.A.; Sladkova, A.I. Energy spectra of high-energy SEP event protons derived from statistical analysis of experimental data on a large set of events. *AIP Conf. Proc.* **2001**, *552*, 1191–1196. [[CrossRef](#)]
53. Zhao, L.; Zhang, M.; Rassoul, H.K. Double power laws in the event-integrated solar energetic particle spectrum. *Astrophys. J.* **2016**, *821*, 62. [[CrossRef](#)]
54. Miteva, R.; Samwel, S.W.; Zabunov, S.; Dechev, M. On the flux saturation of SOHO/ERNE proton events. *Bulg. Astron. J.* **2020**, *33*, 99.
55. NOAA National Centers for Environmental Information. Available online: <https://satdat.ngdc.noaa.gov/sem/goes/data/avg/> (accessed on 10 October 2022).
56. Žigman, V.; Grubor, D.; Šulić, D. D-region electron density evaluated from VLF amplitude time delay during X-ray solar flares. *J. Atmos. Sol.-Terr. Phys.* **2007**, *69*, 775–792. [[CrossRef](#)]
57. Kolarski, A.; Grubor, D. Sensing the Earth's low ionosphere during solar flares using VLF signals and goes solar X-ray data. *Adv. Space Res.* **2014**, *53*, 1595–1602. [[CrossRef](#)]
58. Kolarski, A.; Srećković, V.A.; Mijić, Z.R. Monitoring solar activity during 23/24 solar cycle minimum through VLF radio signals. *Contrib. Astron. Obs. Skaln. Pleso* **2022**, *52*, 105. [[CrossRef](#)]
59. Šulić, D.; Srećković, V.A.; Mihajlov, A.A. A study of VLF signals variations associated with the changes of ionization level in the D-region in consequence of solar conditions. *Adv. Space Res.* **2016**, *57*, 1029–1043. [[CrossRef](#)]
60. Dorman, L.; Tassev, Y.; Velinov, P.I.Y.; Mishev, A.; Tomova, D.; Mateev, L. Investigation of exceptional solar activity in September 2017: GLE 72 and unusual Forbush decrease in GCR. *J. Phys. Conf. Ser.* **2019**, *1181*, 012070. [[CrossRef](#)]
61. Neutron Monitor Database. Available online: <https://www.nmdb.eu/> (accessed on 20 October 2022).
62. Kojima, H.; Shibata, S.; Oshima, A.; Hayashi, Y.; Antia, H.; Dugad, S.; Fujii, T.; Gupta, S.K.; Kawakami, S.; Minamino, M.; et al. Rigidity Dependence of Forbush Decreases. In *Proceedings of the 33rd International Cosmic Ray Conference, Rio de Janeiro, Brazil, 2–9 July 2013*.
63. Near-Earth Interplanetary Coronal Mass Ejections Since January 1996. Available online: <https://izw1.caltech.edu/ACE/ASC/DATA/level3/icmetable2.htm> (accessed on 15 October 2022).

64. Soho Lasco Cme Catalog Cdaw Data Center. Available online: https://cdaw.gsfc.nasa.gov/CME_list/ (accessed on 10 November 2022).
65. Scolini, C.; Chané, E.; Temmer, M.; Kilpua, E.K.J.; Dissauer, K.; Veronig, A.M.; Palmerio, E.; Pomoell, J.; Dumbović, M.; Guo, J.; et al. CME–CME Interactions as Sources of CME Geoeffectiveness: The Formation of the Complex Ejecta and Intense Geomagnetic Storm in 2017 Early September. *Astrophys. J. Suppl. Ser.* **2020**, *247*, 21. [[CrossRef](#)]
66. Badruddin, B.; Aslam, O.P.M.; Derouich, M.; Asiri, H.; Kudela, K. Forbush Decreases and Geomagnetic Storms During a Highly Disturbed Solar and Interplanetary Period, 4–10 September 2017. *Space Weather* **2019**, *17*, 487–496. [[CrossRef](#)]
67. Miteva, R.; Klein, K.L.; Malandraki, O.; Dorrian, G. Solar Energetic Particle Events in the 23rd Solar Cycle: Interplanetary Magnetic Field Configuration and Statistical Relationship with Flares and CMEs. *Sol. Phys.* **2013**, *282*, 579–613. [[CrossRef](#)]
68. Ravishankar, A.; Michałek, G. Non-interacting coronal mass ejections and solar energetic particles near the quadrature configuration of Solar TERrestrial RELations Observatory. *Astron. Astrophys.* **2020**, *638*, A42. [[CrossRef](#)]
69. Pandey, U.; Singh, B.; Singh, O.P.; Saraswat, V.K. Solar flare induced ionospheric D-region perturbation as observed at a low latitude station Agra, India. *Astrophys. Space Sci.* **2015**, *357*, 35. [[CrossRef](#)]
70. Gavrilov, B.G.; Ermak, V.M.; Lyakhov, A.N.; Poklad, Y.V.; Rybakov, V.A.; Ryakhovsky, I.A. Reconstruction of the Parameters of the Lower Midlatitude Ionosphere in M- and X-Class Solar Flares. *Geomagn. Aeron.* **2020**, *60*, 747–753. [[CrossRef](#)]
71. Venkatesham, K.; Singh, R. Extreme space-weather effect on D-region ionosphere in Indian low latitude region. *Curr. Sci.* **2018**, *114*, 1923–1926. [[CrossRef](#)]
72. Thomson, N.R.; Rodger, C.J.; Clilverd, M.A. Large solar flares and their ionospheric D region enhancements. *J. Geophys. Res. Space Phys.* **2005**, *110*. [[CrossRef](#)]
73. Grubor, D.; Šulić, D.; Žigman, V. The response of the Earth-ionosphere VLF waveguide to the January 15–22 2005 solar events. In Proceedings of the IUGG XXIV General Assembly, Perugia, Italy, 2–13 July 2007.
74. Kolarski, A.; Grubor, D. Monitoring VLF signal perturbations induced by solar activity during January 2005. In Proceedings of the The XIX Serbian Astronomical Conference, Belgrade, Serbia, 13–17 October 2020; pp. 387–390.
75. Kumar, S.; Kumar, A.; Menk, F.; Maurya, A.K.; Singh, R.; Veenadhari, B. Response of the low-latitude D region ionosphere to extreme space weather event of 14–16 December 2006. *J. Geophys. Res. Space Phys.* **2015**, *120*, 788–799. [[CrossRef](#)]
76. Tan, L.M.; Thu, N.N.; Ha, T.Q.; Marbouti, M. Study of solar flare induced D-region ionosphere changes using VLF amplitude observations at a low latitude site. *Indian J. Radio Space Phys.* **2014**, *43*, 197–246.
77. McRae, W.M.; Thomson, N.R. Solar flare induced ionospheric D-region enhancements from VLF phase and amplitude observations. *J. Atmos. Sol.-Terr. Phys.* **2004**, *66*, 77–87. [[CrossRef](#)]
78. Zhao, L.L.; Zhang, H. Transient galactic cosmic-ray modulation during solar cycle 24: A comparative study of two prominent forbush decrease events. *Astrophys. J.* **2016**, *827*, 13. [[CrossRef](#)]
79. Lingri, D.; Mavromichalaki, H.; Belov, A.; Eroshenko, E.; Yanke, V.; Abunin, A.; Abunina, M. Solar Activity Parameters and Associated Forbush Decreases During the Minimum between Cycles 23 and 24 and the Ascending Phase of Cycle 24. *Sol. Phys.* **2016**, *291*, 1025–1041. [[CrossRef](#)]

Disclaimer/Publisher’s Note: The statements, opinions and data contained in all publications are solely those of the individual author(s) and contributor(s) and not of MDPI and/or the editor(s). MDPI and/or the editor(s) disclaim responsibility for any injury to people or property resulting from any ideas, methods, instructions or products referred to in the content.



New insights from cross-correlation studies between solar activity indices and cosmic-ray flux during Forbush decrease events

Mihailo Savić, Nikola Veselinović*, Aleksandar Dragić, Dimitrije Maletić, Dejan Joković
Vladimir Udovičić, Radomir Banjanac, David Knežević

Institute of Physics Belgrade, University of Belgrade, Pregrevica 118, 11080 Belgrade, Serbia

Received 1 April 2022; received in revised form 12 September 2022; accepted 27 September 2022

Available online 3 October 2022

Abstract

Observed galactic cosmic ray intensity can be subjected to a transient decrease. These so-called Forbush decreases are driven by coronal mass ejection induced shockwaves in the heliosphere. By combining in situ measurements by space borne instruments with ground-based cosmic ray observations, we investigate the relationship between solar energetic particle flux, various solar activity indices, and intensity measurements of cosmic rays during such an event. We present cross-correlation study done using proton flux data from the SOHO/ERNE instrument, as well as data collected during some of the strongest Forbush decreases over the last two completed solar cycles by the network of neutron monitor detectors and different solar observatories. We have demonstrated connection between the shape of solar energetic particles fluence spectra and selected coronal mass ejection and Forbush decrease parameters, indicating that power exponents used to model these fluence spectra could be valuable new parameters in similar analysis of mentioned phenomena. They appear to be better predictor variables of Forbush decrease magnitude in interplanetary magnetic field than coronal mass ejection velocities.

© 2022 COSPAR. Published by Elsevier B.V. All rights reserved.

Keywords: Cosmic rays; Forbush decrease; Solar energetic particles; Solar activity

1. Introduction

Cosmic rays (CRs) are high-energy charged particles that arrive at Earth from space, mainly originating from outside of our Solar system. CRs are modulated in the heliosphere (Heber et al., 2006) due to interaction with the interplanetary magnetic field (IMF) frozen in a constant stream of charged particles from Sun - the solar wind (SW). Transients in the heliosphere additionally modulate CRs. One type of transients are interplanetary coronal mass ejections (ICMEs), closely related to coronal mass ejections (CMEs).

ICMEs interact with SW, and as the speed of particles in ICME is different than the speed of SW particles, a bow shock can be created, affecting the CR flux (Belov et al., 2014). This interaction between ICMEs and residual solar wind can be one of the causes of short-term depression in CR flux, detectable at Earth (Subramanian et al., 2009). Such transient decrease in observed flux is known as a Forbush decrease (FD), a type of CR flux modulation that has been studied extensively since its initial discovery in the 1930s (Gopalswamy (2016) and references therein). There are two clearly distinguishable classes of Forbush decreases: recurrent and non-recurrent. Non-recurrent FDs, typically caused by ICMEs (Dumbovic et al., 2012), are mostly characterized by a sudden offset, which lasts about a day, followed by a gradual recovery phase within several days (Cane, 2000). Due to ICME sub-structures

* Corresponding author.

E-mail address: veselinovic@ipb.ac.rs (N. Veselinović).

(the sheath and the associated shock and magnetic cloud) FD can have one or two-step profile, which depends on transit of one or both structures to the observer (Richardson and Cane, 2011). Recurrent FDs have different profile, with gradual onset and decrease and symmetrical recovery caused by high-speed streams from coronal holes (Melkumyan et al., 2019). In this paper we will focus on non-recurrent ICME induced FDs.

Apart from FD profile, one of the main parameters that is used to describe a Forbush decrease is its magnitude. The effect is not the same for all CR particles, as it depends on their rigidity. Rigidity is defined as $R \equiv B\rho = p/q$, where ρ is gyroradius of the particle due to magnetic field B , p is particle momentum, and q is its charge. The higher the rigidity of a particle, the less it is affected by heliospheric inhomogeneities, hence the reduction in flux is less pronounced.

Another phenomenon that can accompany violent events on the Sun is emission of fast-moving particles, commonly known as solar energetic particles (SEP). The occurrence of such particles is typically related to eruptions on the surface of the Sun, which can be characterized by bursts of X-rays - solar flares (SF), and/or emission of coronal plasma - already mentioned CMEs. When excess of these solar energetic particles with high energy penetrates the geomagnetic field, it can cause a sudden and brief increase in measured CR flux at Earth - a ground level enhancement (GLE). Because GLEs can be harmful to human infrastructures (potentially damaging power lines, satellites in orbit, etc.), they have been studied in detail for decades.

Variations of CR flux have been monitored at Earth for decades using ground and underground-based detectors, primarily neutron monitors (NM) (Belov et al., 2000; Koldobskiy et al., 2019) and muon detectors (Mendonça et al., 2016; Veselinović et al., 2015). Different types of ground-based detectors complement each other in terms of their CR energy domain (Veselinovic et al., 2017), muon detectors being sensitive to energies higher than those detectable by NMs. In addition, CR flux is also (especially in the last couple of decades) directly measured in space using space-borne instruments (Dumbovic et al., 2020; von Forstner et al., 2020). In the MeV energy range most space probe particle detectors are sensitive to, enhancement of SEP flux can enshroud CR flux, thus making a task of establishing decoupled event-integrated energy spectra (or spectral fluences) for SEP and CRs a laborious task (Koldobskiy et al., 2021; Bruno and Richardson, 2021).

Many authors have studied the connection between SFs, CMEs/ICMEs and SEP, consequential effects on the geomagnetic field and compound effect of the IMF and geomagnetic field disturbances on CRs. Most relevant for our analysis is work that studied connection between different FD and ICME parameters (Belov et al. (2000), Belov (2008), Papaioannou et al. (2020) and references therein), which has among other, shown significant correlation between CME speeds and FD magnitudes. More precisely, CME speeds have been established as the best predictor

variables of FD magnitudes for primary CR particles with 10GV rigidity detected at Earth. Also of interest is the work that studied the connection between the disturbance of geomagnetic field and CR flux measured at Earth (Alhassan et al., 2021; Badruddin et al., 2019), where a significant correlation between FD magnitude and different geomagnetic parameters due to common solar or interplanetary origin has been established.

SF, CME/ICME, SEP and FD events are very often related processes that occur either simultaneously or in succession, in which case can be thought of as different components of one more complex event. CMEs (along with their interplanetary counterparts ICMEs) have been recognized as the main driver of FDs, while on the other hand there has been plenty of evidence for the relationship between CMEs with SEP. Namely, there are two different known mechanism for SEP acceleration: acceleration during magnetic-reconnection events usually resulting in solar flares (which produce short impulsive SEP events), and acceleration caused by CME induced shock waves (which result in gradual SEP events) (Reames, 1999). For this study the second class is of interest. Another type of closely related events that are important for this analysis are energetic storm particle (ESP) events, which represent particles accelerated locally by interplanetary shocks driven by fast CMEs (Desai and Giacalone, 2016). Even though details of the mechanism and the precise role of CME induced shock in the evolution of SEP events are not fully understood (Anastasiadis et al., 2019), we believe that analysis of how SEP/ESP events relate to CME, geomagnetic and FD events could provide some valuable new insight. We are especially interested in, and will concentrate the most on, the possibility of the last of these connections. To do so, we have decided to look into the shape of SEP/ESP fluence spectra and analyze how it relates to different CME, geomagnetic and especially FD parameters.

It should be noted that different mentioned types of events, even when related, do not need to occur at the same place nor at the same time. This is due to the fact that SEP travel along magnetic field lines, while CME/ICME shocks travel mostly directly away from the Sun. Furthermore, modulation of primary CR, detected as FD upon their arrival at Earth, can happen anywhere in the heliosphere. Hence, in general case, detection of these events should not necessarily be simultaneous. However, we believe that for the class of events selected for this analysis we can assume that they occur and are detected within a certain time window. We will elaborate more on this in Section 2.3.

The article is structured as follows: first we list various sources of data and justify the selection of solar cycle 23 and 24 FD events to be used in the analysis; then we describe parametrization of SEP events (involving calculation and parametrization of SEP fluence spectra); finally we perform correlative analysis between established SEP parameters and various CME, FD and geomagnetic indices and discuss the observed dependencies.

2. Data

Sources of SEP proton flux, various solar and space weather parameters, as well as ground CR measurements and different FD parameters used in this study are listed below. Different criteria for FD event selection are also described.

2.1. Solar energetic particle flux data

The source for SEP flux data was the ERNE instrument (Torsti et al., 1995) onboard the Solar and Heliospheric Observatory (SOHO). Instrument consists of two separate particle detectors. The Low-Energy Detector (LED) and the High-Energy Detector (HED). Former covers ion fluxes and count rates in the 1.3 – 13 MeV/nucleon energy range, and latter ion fluxes and count rates in the 13 – 130 MeV/nucleon energy range. Both ranges are separated in ten energy channels. SOHO has been making in situ observation from Lagrangian point L1 for the last three solar cycles (data available at https://omniweb.gsfc.nasa.gov/ftpbrowser/flux_spectr_m.html). ERNE data for solar cycles 23, 24 and current cycle 25 allows the study of variations of proton fluences in SEP events during this period (Paassilta et al., 2017; Belov et al., 2021). Higher channels are more correlated with measured CR flux (Veselinovic et al., 2021) and it appears as if flux in these channels is a mixture of CR and energetic proton fluxes of particles with the same energy. Important feature of HED detector is that, due to rather large geometric factor, during large intensity proton events SOHO/ERNE data have been subject to saturation effects in higher energy channels (Valtonen and Lehtinen, 2009; Miteva et al., 2020).

2.2. IZMIRAN directory of Forbush decreases

IZMIRAN database is an online repository developed at the Institute of Terrestrial Magnetism, Ionosphere and Radiowave Propagation (IZMIRAN) at Moscow Troitsk, Russia. It contains an extensive list of Forbush decreases and various parameters from solar, space weather, cosmic ray and geomagnetic measurements, spanning from the late 1950s (<http://spaceweather.izmiran.ru/eng/dbs.html>). Database has been compiled from a number of sources, such as measurements by ground-based detectors, instruments mounted on various satellites, as well as public data provided by different agencies specializing in monitoring solar, space and atmospheric weather and geomagnetism. Extensive list of sources and data repositories used to compile this database are referenced in a number of publications listed on the IZMIRAN internet site (IZMIRAN Space Weather Prediction Center, 2016).

We have decided to use IZMIRAN database as our primary source of data for Forbush decrease parameters as well as for selected variables, parameters and indices that describe associated space weather and geomagnetic

phenomena. Selection of parameters pertinent to our analysis was mostly based on previous work by other authors (i.e. Belov (2008), Lingri et al. (2016)), where they established which quantities are most relevant in these types of studies.

Chosen parameters fall into three categories (abbreviations to be used throughout the text are given in parentheses). First category are FD related parameters - Forbush decrease magnitude for 10GV rigidity primary particles (M) and Forbush decrease magnitude for 10GV rigidity primary particles corrected for magnetospheric effect using Dst index (M_M). These magnitudes are determined using global survey method (GSM). GSM combines measurements from a world-wide network of neutron monitors (NMs), takes into account different anisotropies, disturbances of atmospheric and geomagnetic origin, as well as apparatus-specific features, and produces an estimated hourly variation of CR flux outside Earth's atmosphere and magnetosphere (Belov et al., 2018). Specifically, correction for magnetospheric effect takes into account the fact that geomagnetic disturbances affect the effective cutoff threshold rigidities and effective asymptotic directions of primary particles for different NM stations (Belov et al., 2005).

Second group of parameters used from IZMIRAN database are CME and SW related parameters - the average CME velocity between the Sun and the Earth, calculated using the time of the beginning of the associated X-ray flare (V_{mean}), the average CME velocity between the Sun and the Earth, calculated using the time of the beginning of the associated CME observations (V_{meanC}) and maximal hourly solar wind speed in the event (V_{max}). Izmiran DB authors have matched detected FD events with associated CMEs using a SOHO LASCO CME catalog (Belov et al., 2014). Catalog includes a comprehensive list of CME events along with some of most relevant parameters, i.e. speeds calculated by tracking CME leading edge (as described in Yashiro et al. (2004), further sources available at https://cdaw.gsfc.nasa.gov/CME_list/catalog_description.htm).

Final group of parameters from IZMIRAN database used in this analysis are related to geomagnetic field - maximal Kp index in the event (Kp_{max} - based on data from NOAA Space Weather Prediction Center, <https://www.swpc.noaa.gov/products/planetary-k-index>), maximal 3-h Ap index in the event (Ap_{max} - defined as the mean value of the variations of the terrestrial magnetic field, derived from Kp index) and minimal Dst index in the event (Dst_{min} - calculated using data provided by World Data Center for Geomagnetism, Kyoto, <http://wdc.kugi.kyoto-u.ac.jp/dst/dir/index.html>).

2.3. Selection of FD events

Time interval used for this analysis was dictated by the period of operation of SOHO/ERNE device, which was commissioned in December 1995 (data available from June 1996) and is still operational. That coincides with the

beginning of solar cycle 23 and lasts through cycle 24, so we considered all FD events that occurred in this period, concentrating on events with magnitudes for 10 GV particles larger 4% in the analysis. There are several reasons for such magnitude cut, primary reason being that even though we often reference neutron monitor data in the analysis, CR related research in our laboratory is mainly based on muons detectors, which are generally less sensitive to FDs of smaller magnitude and GLE events. Additionally, it is known that all larger FDs (i.e. with magnitudes greater than 5%) are caused by CMEs (Belov, 2008). Since we use CME speed as a reference parameter in the analysis, introducing such cut made event selection simpler, as practically all considered FD events would have an associated CME. Finally, CME speed is less reliably determined in the case of weaker CME events (Yashiro et al., 2004).

One important step in the event selection procedure is to make sure that for each global event both proton flux increase detected by SOHO/ERNE and FD are related to the same CME. As mentioned in the introduction, detection of these separate events is not necessarily simultaneous. However, we have checked the direction of CMEs/ICMEs for all events for which such information was available, and in all these cases they moved directly toward Earth. This would imply that detection of the increase of energetic particles, Forbush decrease and geomagnetic storm associated with a given CME should be detectable within a relatively small time window. To illustrate this, on Fig. 1 we have shown time series for proton flux (in

one selected energy channel), CR flux and *Dst* index for one such event. Furthermore, because of large magnitudes of FDs selected for the analysis, we believe it to be the case for all events.

Another important point is that we cannot say with certainty what is the exact origin of detected proton flux solely based on SOHO/ERNE data. They could be of solar origin (SEP), particles accelerated locally at shock in interplanetary space (ESP), or combination of both. For the sake of simplicity we have decided to use the somewhat more general term SEP for these energetic particles, having mentioned limitation of its use in mind.

As determination of SEP fluence is not a straightforward procedure (as explained in more detail in Section 3.1), from the initial set of events we discarded all for which fluence value was difficult to determine or had a large uncertainty due to overlap and unclear separation of proton flux time series of successive events. That set was then further reduced based on the quality of FD identification flag assigned to each event in the IZMIRAN database, taking into account only events where identification was confident or reliable enough. Applying mentioned selection criteria resulted in the final set of 21 events, presented in Table 1 with some of the parameters of interest.

3. Parametrization of SEP fluence energy spectra

Parametrization procedure for any of the selected FD events can be broken down into two steps: 1 - calculation

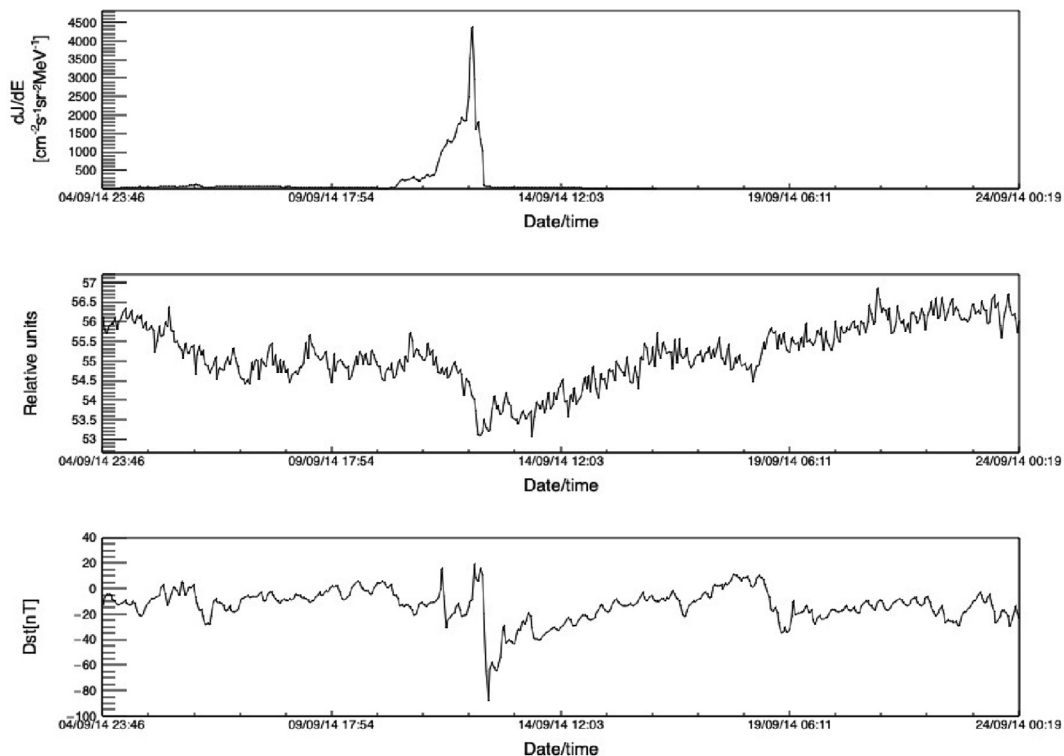


Fig. 1. Time series of hourly data for the same time interval around FD event of 12 September 2014: proton flux in the 1.3 – 1.6 MeV channel (top), Athens neutron monitor count rate (middle), and *Dst* index (bottom).

Table 1

Forbush decrease events from solar cycles 23 and 24 selected for the analysis, along with some of the FD, CME and geomagnetic field parameters of interest.

Date/Time	M [%]	M_M [%]	X flare	V_{mean} [km s^{-1}]	V_{meanC} [km s^{-1}]	V_{max} [km s^{-1}]	Kp_{max}	Ap_{max}	Dst_{min} [nT]
2001.09.29 09:40:00	4.3	4.4	M 1.0/	852.0	831	694.0	5.33	56.0	−56.0
2001.10.11 17:01:00	7.0	6.9	M 1.4/2F	766.0	769	572.0	6.0	80.0	−71.0
2001.10.21 16:48:00	5.4	7.3	X 1.6/2B	855.0	858	677.0	7.67	179.0	−187.0
2001.11.24 05:56:00	9.2	9.8	M 9.9/	1323.0	1366	1024.0	8.33	236.0	−221.0
2002.04.17 11:07:00	6.2	7.0	M 1.2/SF	742.0	745	611.0	7.33	154.0	−127.0
2002.09.07 16:36:00	4.6	5.1	C 5.2/SF	860.0	863	550.0	7.33	154.0	−181.0
2003.10.30 16:19:00	14.3	9.4	X10.0/2B	2109.0	2140	1876.0	9.0	400.0	−383.0
2003.11.20 08:03:00	4.7	6.8	M 3.2/2N	854.0	872	703.0	8.67	300.0	−422.0
2004.07.26 22:49:00	13.5	14.4	M 1.1/1F	1279.0	1290	1053.0	8.67	300.0	−197.0
2004.09.13 20:03:00	5.0	5.3	M 4.8/SX	945.0	948	613.0	5.33	56.0	−50.0
2005.05.15 02:38:00	9.5	12.2	M 8.0/SX	1207.0	1231	987.0	8.33	236.0	−263.0
2006.12.14 14:14:00	8.6	9.6	X3.4/4B	1154.0	1165	955.0	8.33	236.0	−146.0
2011.02.18 01:30:00	5.2	4.7	X2.2/	579.0	579	691.0	5.0	48.0	−30.0
2011.08.05 17:51:00	4.3	4.8	M 9.3/	1089.0	1104	611.0	7.67	179.0	−115.0
2011.10.24 18:31:00	4.9	6.5	-	-	633	516.0	7.33	154.0	−147.0
2012.03.08 11:03:00	11.7	11.2	X5.4/	1187.0	1188	737.0	8.0	207.0	−143.0
2012.07.14 18:09:00	6.4	7.6	X 1.4/	822.0	834	667.0	7.0	132.0	−127.0
2013.06.23 04:26:00	5.9	5.3	M 2.9/	832.0	844	697.0	4.33	32.0	−49.0
2014.09.12 15:53:00	8.5	5.9	X1.6/2B	893.0	897	730.0	6.33	94.0	−75.0
2015.06.22 18:33:00	8.4	9.1	M2.6/	1027.0	1040	742.0	8.33	236.0	−204.0
2017.09.07 23:00:00	6.9	7.7	X9.3/	-	1190	817.0	8.33	236.0	−124.0

of SEP fluence in different energy channels and 2 - determination of power exponents for SEP fluence spectra.

3.1. SEP fluence calculation

SEP fluence is calculated by integrating SOHO/ERNE proton flux time series in separate energy channels over time period associated with a given FD event. First step in this procedure is to determine this time period (and hence integration boundaries) as precisely as possible. Most more energetic events we considered for this analysis have a strong SF associated with them. This may lead to a complex picture, as FD event of interest often occurs in the middle of a turbulent period where additional FDs (sometimes associated with other CMEs) precede or follow it. As a consequence, clear separation of successive events and determination of optimal integration boundaries may not be simple nor straightforward. To make this procedure more reliable, we have used IZMIRAN database and neutron monitor data (courtesy of the Neutron Monitor Database (Neutron Monitor Database, 2022)) in parallel with SOHO/ERNE proton time series, trying to identify prominent features in all three sources, so we could separate events of interest in all energy channels as clearly as possible.

Baseline for integration was determined based on a data interval of at least one (but preferably several) days, where proton flux was negligibly different from zero relative to the flux during the event. If possible, time interval before the event was taken for the calculation of baseline unless there was a preceding disturbance, in which case quiet interval following the event was taken instead. Integration of fluence for several selected SOHO/ERNE energy channels

for the event of 12 September 2014 is shown on Fig. 2. Integration interval is indicated with vertical dashed lines and baseline value with a horizontal dashed line.

One interesting feature that can be observed in SOHO/ERNE data time series is that in some cases proton flux in the highest energy channels can dip below the baseline after the initial increase. For a number of events such behavior is even more pronounced, where in extreme cases it can happen that no flux increase is observed, but rather just the decrease. We believe this indicates that the highest energy channels have non-negligible contribution of low-energy cosmic rays, which can increase uncertainty for fluence calculation. We will refer to this again when discussing fluence spectra in Section 3.2.

To make fluence calculation procedure more reliable we have assigned a quality flag to each event, based on our estimate of the uncertainty of integration, and decided on a quality cut we deemed acceptable for further analysis. As mentioned in Section 2.3, 21 events have passed this criterion. Even then, for a number of events calculated fluence proved to be sensitive to small variations of integration boundaries, which makes it especially difficult to give a reliable estimate of the error for the integration procedure and should be kept in mind when discussing the results.

3.2. Determination of SEP fluence spectra power exponents

Fluence energy spectra for all selected events were formed using values for different energy channels, calculated as explained in the previous section. The choice of parameters to be used to describe their shape and characteristics depends on the analytic expression used to model

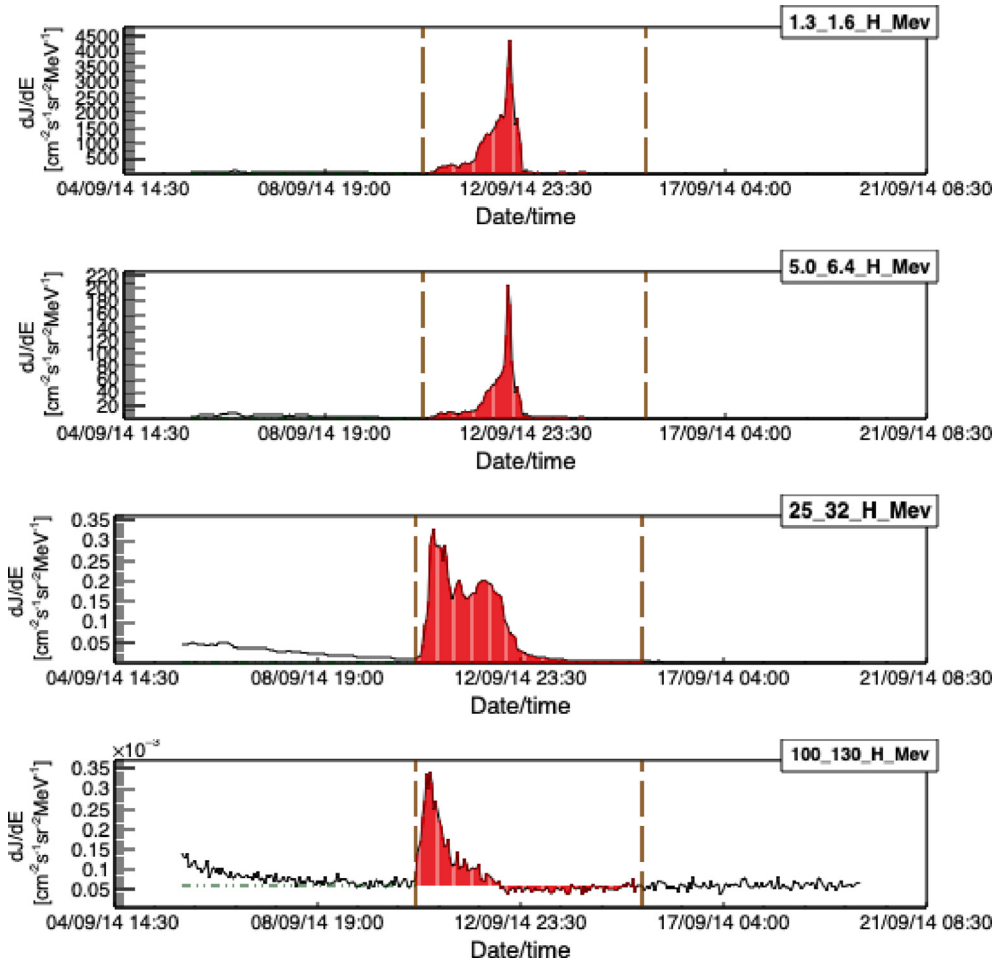


Fig. 2. Solar proton flux for four selected energy channels during FD event of 12 September 2014. Vertical dashed lines indicate integration interval, horizontal dashed line indicates the baseline value, while areas shaded red correspond to result of the integration used to calculate the SEP fluence.

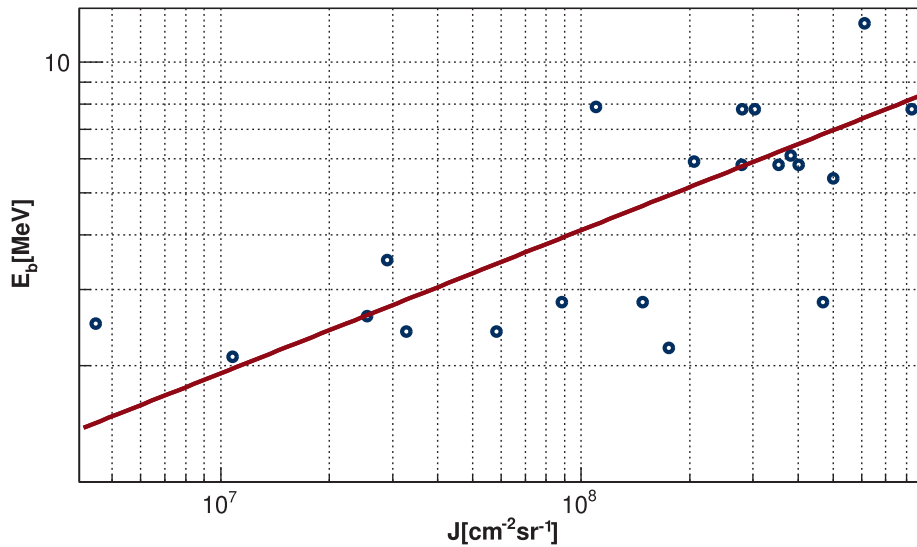


Fig. 3. “Knee” energy dependence on SEP fluence (integrated over full energy range) for selected events. Power function fit is indicated by the red line.

the spectrum. In general, during a SEP event spectra exhibit a characteristic “bend” or a “knee”, which is not so straightforward to describe theoretically. Various expressions were proposed to model this observed feature (Ellison and Ramaty, 1985; Mottl et al., 2001), out of which we have decided to use the following double power law one (Band et al., 1993; Zhao et al., 2016), as we feel it is well suited for our analysis:

$$\frac{dJ}{dE} = \begin{cases} E^{-\alpha} \exp\left(-\frac{E}{E_b}\right) & E \leq (\beta - \alpha)E_b, \\ E^{-\beta} [(\beta - \alpha)E_b]^{\beta - \alpha} \exp(\alpha - \beta) & E > (\beta - \alpha)E_b, \end{cases} \quad (1)$$

where E_b is knee energy at which the break occurs, while α and β are power-law exponents that describe energy ranges below and above the break respectively, and consequently are variables we chose to parametrize the SEP event.

These power-law exponents obtained by fitting fluence spectra with Expression 1 can be very sensitive to variation of knee energy, so some care needs to be taken in order to determine E_b as accurately as possible.

Determination of knee energy using “by eye” method proved to be uncertain enough for us to decide on using a more quantitative approach, which is based on the fact that knee energy generally depends on the integral fluence of the event (as described in Nymmik (2013) and Miroshnichenko and Nymmik (2014)). In accordance with this, we firstly determined the knee energy “by eye”, plotted it against integral fluence and then fitted this dependence with a power function in the form of $E_b = aJ^b$ (Fig. 3), where E_b is the knee energy, J integral fluence, and a and b are fit parameters. We then used these fit parameters to determine E_b for each event. In several cases where there has been some overlap of proton flux time series profiles associated with different successive events, small correction for integral fluence was introduced, which also affected the knee energy value.

Fluence spectra were then fitted with expression given in Eq. 1, using thusly calculated knee energy. On Fig. 4 we can see two characteristic examples that illustrate how well this expression actually models the fluence spectrum during a SEP event. In case of 11 October 2001 event (Fig. 4a) we see that the theoretical model fits the experimental data reasonably well, except for some small disagreement in the highest energy channels (feature we believe can be explained by our assumption that there is a non-negligible contribution of low-energy CR in this energy range). On the other hand, for a number of events with greater SEP flux higher energy channels tend to get saturated (as mentioned in Section 2.1). This in turn leads to an underestimated fluence and consequently poorer fit in this energy range, as can be seen for the 24 November 2001 event shown on Fig. 4b. Contribution of flux in these high-energy channels to integral fluence is very small, so this underestimated value does not significantly affect the value of knee energy or uncertainty of the exponent α . However,

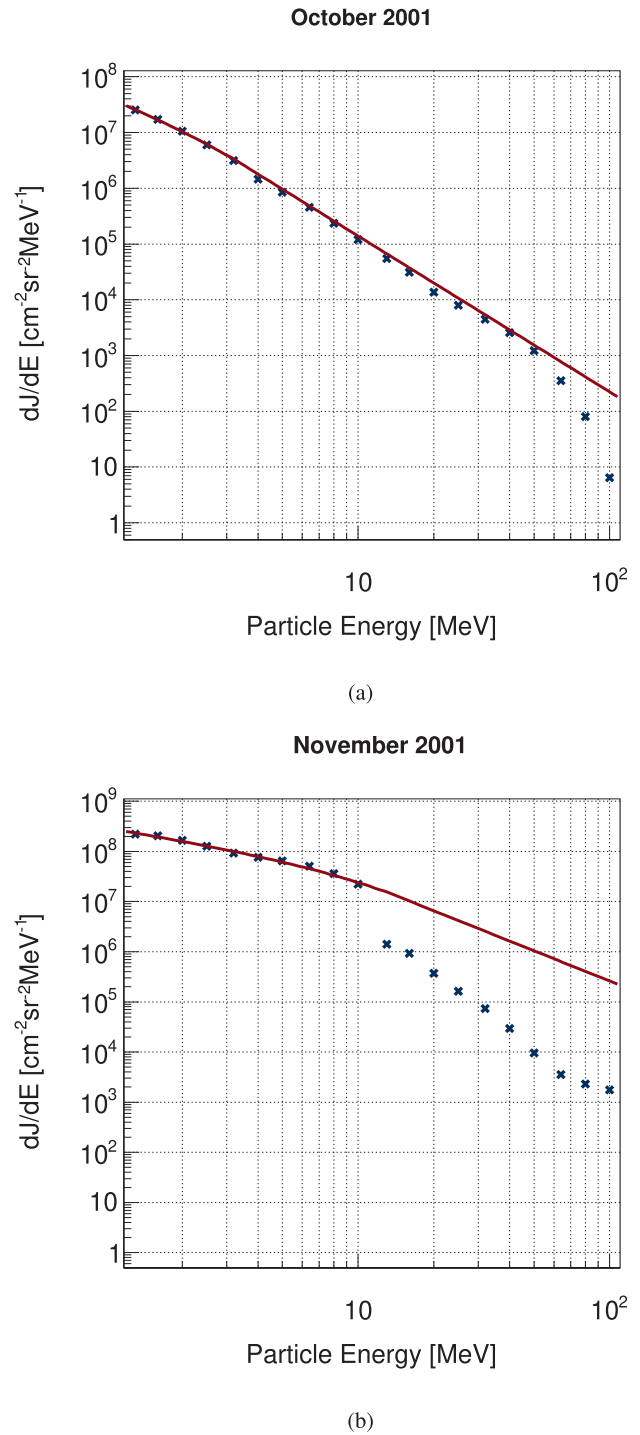


Fig. 4. SEP fluence energy spectra for the: (a) 11 October 2001 event, (b) 24 November 2001 event. Red lines indicate the double power law fit.

the uncertainty of exponent β is more significantly affected and for this reason in further analysis we will rely on exponent α more for the parametrization of fluence spectra.

4. Correlative analysis

We have performed correlative analysis between power exponents chosen to parametrize SEP fluence and selected

Table 2

Correlation coefficients (r) between SEP fluence spectra power exponents and selected FD, CME and geomagnetic field indices.

	α	β	M	M_M	V_{meanC}	V_{mean}	V_{max}	Kp_{max}	Ap_{max}	Dst_{min}
α	1.00	0.96	0.67	0.64	0.77	0.75	0.66	0.40	0.53	-0.40
β	0.96	1.00	0.67	0.67	0.72	0.70	0.60	0.44	0.50	-0.38
M	0.67	0.67	1.00	0.84	0.79	0.79	0.79	0.53	0.65	-0.41
M_M	0.64	0.67	0.84	1.00	0.57	0.57	0.53	0.69	0.69	-0.46
V_{meanC}	0.77	0.72	0.79	0.57	1.00	1.00	0.92	0.61	0.77	-0.58
V_{mean}	0.75	0.70	0.79	0.57	1.00	1.00	0.92	0.62	0.78	-0.60
V_{max}	0.66	0.60	0.79	0.53	0.92	0.92	1.00	0.49	0.71	-0.58
Kp_{max}	0.40	0.44	0.53	0.69	0.61	0.62	0.49	1.00	0.94	-0.78
Ap_{max}	0.53	0.50	0.65	0.69	0.77	0.78	0.71	0.94	1.00	-0.87
Dst_{min}	-0.40	-0.38	-0.41	-0.46	-0.58	-0.60	-0.58	-0.78	-0.87	1.00

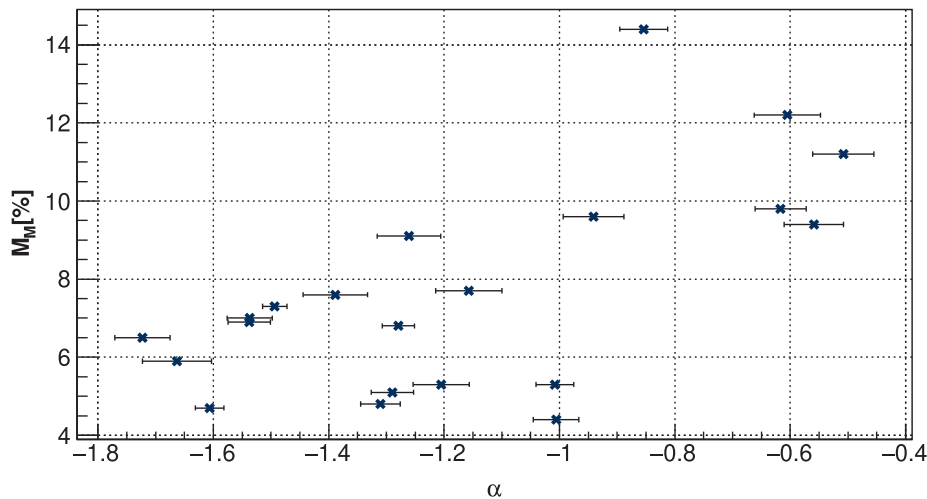


Fig. 5. Dependence of FD magnitude for particles with 10GV rigidity corrected for magnetospheric effects (M_M) on power exponent α .

parameters from Izmiran database. The results are presented in Table 2. Worth noting is the slightly lower statistics for V_{mean} due to exclusion of two events for which this parameter was not available.

Strong correlation between FD magnitude for particles with 10GV rigidity (M) and mean CME (V_{meanC} , V_{mean}) and maximum SW (V_{max}) velocities illustrates the important role these parameters have in driving FD events, as has been discussed in detail by several authors (i.e. Belov et al. (2014)). On the other hand, correlation between these velocities and parameter M_M is noticeably smaller. M_M is FD magnitude for particles with 10GV rigidity corrected for magnetospheric effect (using Dst index), so we could approximate it as an estimated measure of the FD magnitude in interplanetary magnetic field.

If we now look at how SEP fluence spectra power exponents relate to other parameters in Table 2, we observe the best correlation with mean CME velocities, while it is somewhat smaller with maximum SW velocity. Correlation with FD magnitude (M) is smaller than for CME velocities, however interestingly the correlation with the corrected FD magnitude (M_M) appears larger than in the case of CME velocities. One possible explanation for this could be that the shape of SEP fluence spectrum is more related to CR disturbance induced in interplanetary magnetic and less

to one induced in geomagnetic field. What could support this assumption further is the fact that we observe smaller correlation between α and β exponents and geomagnetic indices Kp_{max} , Ap_{max} and Dst_{min} than between these indices and CME velocities.

It should be said that even though SEP fluence spectra power exponents are not directly measured independent variables, the procedure to calculate them is relatively simple, while procedure used to calculate FD magnitudes (using GSM approach) is somewhat less straightforward and accessible. Hence, these exponents could be used to give a first estimate of Forbush decrease magnitudes outside atmosphere and magnetosphere. Having this in mind, we could conclude that SEP fluence power exponents could be better predictor variables (in the sense described above) of FD magnitude in interplanetary space than CME velocities are, while they are less reliable predictor variables of FD magnitude observed at Earth. If true, this could possibly lead us a small step closer to empirically decoupling the effects of IMF and geomagnetic fields on CR.

To further examine how FD magnitude corrected for magnetospheric effects is related to the shape of SEP fluence spectra, we have analyzed their dependence, which is plotted on Fig. 5. Both power exponents exhibit similar dependence, but only plot for α is shown, as it has consid-

Table 3

Correlation coefficients (r) between FD magnitudes for particles with 10GV rigidity (uncorrected M and corrected for magnetospheric effect M_M) and SEP fluence spectra power exponents, selected FD, CME and geomagnetic field indices for particles with $M_M \geq 6\%$ (left) and particles with $M_M < 6\%$ (right).

	$M_M \geq 6\%$					$M_M < 6\%$				
	α	β	V_{meanC}	V_{mean}	V_{max}	α	β	V_{meanC}	V_{mean}	V_{max}
M	0.82	0.76	0.84	0.85	0.78	-0.55	-0.25	-0.08	-0.10	0.62
M_M	0.77	0.76	0.52	0.49	0.55	-0.38	0.01	0.23	0.19	0.17

erably smaller uncertainty (as mentioned in Section 3.2) and we believe it to be a more reliable parameter. We can see that the graph is fairly linear, as could be expected based on the correlation coefficients, but on closer inspection it appears as if there are two separate classes of events with somewhat different behavior. If we loosely divide all FD events into low-magnitude set (with M_M less than 6%) and high-magnitude set (with M_M greater or equal to 6%), we can observe much weaker dependence of corrected FD magnitude on power exponent α for the first class than for the second one.

To check if this observation is well founded, we look into the correlation coefficients for these two separate classes, which are shown in Table 3.

We can see that correlation coefficients for these two sets are indeed very different. While in case of FDs with M_M equal or greater than 6% we observe an even larger correlation than before between power exponents α and β and both FD magnitude and corrected FD magnitude (approaching the values of correlation coefficients for CME velocities), coefficients for FDs with M_M less than 6% have very different values, correlation even being negative. Although statistics for this second set of events is rather small (and hence the uncertainty for correlation coefficients might be large), it appears that the assumption about two classes of events does stand. What is more, we observe a similarly drastic difference in correlation coefficients between FD magnitudes and mean CME velocities (with little to none correlation for events with $M_M < 6\%$), also pointing to the existence of two separate classes of events. This could need to be further confirmed using larger statistics, i.e. by including FD events with magnitudes smaller than 4%.

5. Conclusions

We analyzed the connection between CME, SEP and FD events, investigating how the shape of SEP fluence spectra during the global disturbance relates to different CME and FD parameters typically used in such analysis. We fitted SEP fluence spectra with double power law and used power exponents (α and β) from these fits to parameterize the shape of SEP fluence spectra.

By the means of correlative analysis we investigated the connection between SEP fluence spectra power exponents and selected CME and SW parameters (mean CME and maximum SW velocities), as well as selected FD parameters (magnitude for 10GV particles and magnitude for

10GV particles corrected for magnetospheric effect) and various parameters of geomagnetic activity (Kp , Ap and Dst indices).

We observed largest correlation between power exponents and CME velocities. The correlation between power exponents and FD magnitude (M) is significant yet smaller than in case of mean CME velocities (V_{meanC} , V_{mean}) and FD magnitude. On the other hand, the correlation between FD magnitude corrected for magnetospheric effects (M_M) and power exponents is larger than between these magnitudes and mean CME velocities.

The dependence of corrected FD magnitude on power exponent α possibly indicates two separate classes of events in terms of corrected magnitude value, rough boundary being corrected FD magnitude value of 6%. Events with corrected FD magnitude larger than 6% show increased correlation with power exponent α , while for the set of events with this magnitude smaller than 6% correlation even has opposite sign. Similarly considerable difference between two classes of events can be observed in correlations of mean CME velocities and corrected FD magnitude. Even taking into account smaller number of events used in the analysis, this could be an indication of these two groups of events exhibiting different behavior.

With everything considered, we believe we have demonstrated an important connection of the shape of SEP fluence spectra with CME and FD events, and that power exponents α and β can be valuable new parameters to be used in the future study of mentioned phenomena. They seem to be better predictor variables of FD magnitude (and hence CR disturbance) in interplanetary magnetic field than CME velocities, especially in the case of events where FD magnitude corrected for magnetospheric effect is larger than 6%.

Declaration of Competing Interest

The authors declare that they have no known competing financial interests or personal relationships that could have appeared to influence the work reported in this paper.

Acknowledgments

The authors acknowledge funding provided by the Institute of Physics Belgrade, through the grant by the Ministry of Education, Science and Technological Development of the Republic of Serbia.

OMNI data was made available by NASA/GSFC's Space Physics Data Facility's OMNIWeb service. Data from the SOHO experiment, an international collaboration between ESA and NASA, was kindly provided by ERNE team from Turku University, Finland. Neutron monitor data is available online through the use of excellent NEST tool, provided by the Neutron Monitor Database. We would also like to express our gratitude to the cosmic ray group at the IZMIRAN Space Weather Prediction Center at Pushkov Institute of Terrestrial Magnetism, Ionosphere and Radio Wave Propagation of the Russian Academy of Sciences for kindly providing catalogue of Forbush-effects and interplanetary disturbances.

Finally, we would like to thank the Reviewers for constructive comments and useful suggestions that significantly contributed to the quality of the manuscript.

References

- Alhassan, J.A., Okike, O., Chukwude, A.E., 2021. Testing the effect of solar wind parameters and geomagnetic storm indices on galactic cosmic ray flux variation with automatically-selected forbush decreases. *Res. Astron. Astrophys.* 21 (9), 234. <https://doi.org/10.1088/1674-4527/21/9/234>.
- Anastasiadis, A., Lario, D., Papaioannou, A., et al., 2019. Solar energetic particles in the inner heliosphere: status and open questions. *Philosoph. Trans. Roy. Soc. A: Mathe. Phys. Eng. Sci.* 377 (2148), 20180100. <https://doi.org/10.1098/rsta.2018.0100>, URL: <https://royalsocietypublishing.org/doi/abs/10.1098/rsta.2018.0100>.
- Badruddin, B., Aslam, O.P. M., Derouich, M. et al., 2019. Forbush decreases and geomagnetic storms during a highly disturbed solar and interplanetary period, 4–10 september 2017. *Space Weather*, 17(3), 487–496. URL: <https://agupubs.onlinelibrary.wiley.com/doi/abs/10.1029/2018SW001941>. <https://doi.org/10.1029/2018SW001941>.
- Band, D., Matteson, J., Ford, L., et al., 1993. BATSE Observations of Gamma-Ray Burst Spectra. I. Spectral Diversity. *Astrophys. J.* 413, 281–292. <https://doi.org/10.1086/172995>.
- Belov, A., 2008. Forbush effects and their connection with solar, interplanetary and geomagnetic phenomena. *Proc. Int. Astron. Union* 4 (S257), 439–450. <https://doi.org/10.1017/S1743921309029676>.
- Belov, A., Abunin, A., Abunina, M., et al., 2014. Coronal mass ejections and non-recurrent forbush decreases. *Sol. Phys.* 289, 3949–3960. <https://doi.org/10.1007/s11207-014-0534-6>.
- Belov, A., Baisultanova, L., Eroshenko, E., et al., 2005. Magnetospheric effects in cosmic rays during the unique magnetic storm on november 2003. *J. Geophys. Res.: Space Phys.* 110 (A09S20). <https://doi.org/10.1029/2005JA011067>.
- Belov, A., Eroshenko, E., Oleneva, V., et al., 2000. What determines the magnitude of forbush decreases? *Adv. Space Res.* 27 (3), 625–630. [https://doi.org/10.1016/S0273-1177\(01\)00095-3](https://doi.org/10.1016/S0273-1177(01)00095-3), URL: <https://www.sciencedirect.com/science/article/pii/S0273117701000953>.
- Belov, A., Eroshenko, E., Yanke, V., et al., 2018. The Global Survey Method Applied to Ground-level Cosmic Ray Measurements. *Sol. Phys.* 293 (4), 68. <https://doi.org/10.1007/s11207-018-1277-6>.
- Belov, A., Papaioannou, A., Abunina, M., et al., 2021. On the rigidity spectrum of cosmic-ray variations within propagating interplanetary disturbances: Neutron monitor and SOHO/EPHIN observations at ~1–10 GV. *Astrophys. J.* 908 (1), 5. <https://doi.org/10.3847/1538-4357/abd724>.
- Bruno, A., Richardson, I.G., 2021. Empirical model of 10–130 mev solar energetic particle spectra at 1 au based on coronal mass ejection speed and direction. *Sol. Phys.* 296 (36). <https://doi.org/10.1007/s11207-021-01779-4>.
- Cane, H., 2000. Coronal mass ejections and forbush decreases. *Space Sci. Rev.* 93 (1), 55–77. <https://doi.org/10.1023/A:1026532125747>.
- Desai, M., Giacalone, J., 2016. Large gradual solar energetic particle events. *Living Rev. Sol. Phys.* 13 (3). <https://doi.org/10.1007/s41116-016-0002-5>.
- Dumbovic, M., Vršnak, B., Calogovic, J., et al., 2012. Cosmic ray modulation by different types of solar wind disturbances. *A&A* 538, A28. <https://doi.org/10.1051/0004-6361/201117710>.
- Dumbovic, M., Vršnak, B., Guo, J., et al., 2020. Evolution of coronal mass ejections and the corresponding forbush decreases: Modeling vs. multi-spacecraft observations. *Sol. Phys.* 295 (104). <https://doi.org/10.1007/s11207-020-01671-7>.
- Ellison, D.C., Ramaty, R., 1985. Shock acceleration of electrons and ions in solar flares. *Astrophys. J.* 298, 400–408. <https://doi.org/10.1086/163623>.
- Freiherr von Forstner, J.L., Guo, J., Wimmer-Schweingruber, R.F., et al., 2020. Comparing the properties of icme-induced forbush decreases at earth and mars. *J. Geophys. Res.: Space Phys.* 125(3), e2019JA027662. URL: <https://agupubs.onlinelibrary.wiley.com/doi/abs/10.1029/2019JA027662>. <https://doi.org/10.1029/2019JA027662>. E2019JA027662 10.1029/2019JA027662.
- Gopalswamy, N., 2016. History and development of coronal mass ejections as a key player in solar terrestrial relationship. *Geosci. Lett.* 3 (8), 18. <https://doi.org/10.1186/s40562-016-0039-2>.
- Heber, B., Fichtner, H., Scherer, K., 2006. Solar and heliospheric modulation of galactic cosmic rays. *Space Sci. Rev.* 125 (1), 81–91. <https://doi.org/10.1007/s11214-006-9048-3>.
- IZMIRAN Space Weather Prediction Center, 2016. Izmiran space weather prediction center. URL: <http://spaceweather.izmiran.ru/eng/about.html> [Online; accessed 29-January-2022].
- Koldobskiy, S.A., Bindi, V., Corti, C., et al., 2019. Validation of the neutron monitor yield function using data from ams-02 experiment, 2011–2017. *J. Geophys. Res.: Space Phys.* 124 (4), 2367–2379. <https://doi.org/10.1029/2018JA026340>, URL: <https://agupubs.onlinelibrary.wiley.com/doi/abs/10.1029/2018JA026340>.
- Koldobskiy, S., Raukunen, O., Vainio, R., et al., 2021. New reconstruction of event-integrated spectra (spectral fluences) for major solar energetic particle events. *Astron. Astrophys.* 647, A132. <https://doi.org/10.1051/0004-6361/202040058>.
- Lingri, D., Mavromichalaki, H., Belov, A., et al., 2016. Solar activity parameters and associated forbush decreases during the minimum between cycles 23 and 24 and the ascending phase of cycle 24. *Sol. Phys.* 291, 1025–1041. <https://doi.org/10.1007/s11207-016-0863-8>.
- Melkumyan, A., Belov, A., Abunina, M., et al., 2019. On recurrent Forbush Decreases. In: Lagutin, A., Moskalenko, I., Panasyuk, M. (Eds.), *Journal of Physics Conference Series*, IOP Publishing, Bristol, United Kingdom volume 1181 of *Journal of Physics Conference Series*. p. 012009, <https://doi.org/10.1088/1742-6596/1181/1/012009>.
- de Mendonça, R.R. S., Braga, C.R., Echer, E., et al., 2016. The temperature effect in secondary cosmic rays (Muons) observed at the ground: analysis of the global muon detector network data. *Astrophys. J.* 830(2), 88. <https://doi.org/10.3847/0004-637x/830/2/88>.
- Miroshnichenko, L., Nymmik, R., 2014. Extreme fluxes in solar energetic particle events: Methodological and physical limitations. *Radiation Measur.* 61, 6–15. <https://doi.org/10.1016/j.radmeas.2013.11.010>, URL: <https://www.sciencedirect.com/science/article/pii/S1350448713003806>.
- Miteva, R., Samwel, S.W., Zabunov, S., et al., 2020. On the flux saturation of SOHO/ERNE proton events. *Bulgarian Astron. J.* 33, 99.
- Mottl, D.A., Nymmik, R. A., Sladkova, A.I., 2001. Energy spectra of high-energy SEP event protons derived from statistical analysis of experimental data on a large set of events. In: El-Genk, M.S., Bragg, M.J. (Eds.), *Space Technology and Applications International Forum - 2001*, AIP Publishing LLC., New York volume 552 of *American Institute of Physics Conference Series*, pp. 1191–1196, <https://doi.org/10.1063/1.1358071>.

- Neutron Monitor Database, 2022. Neutron Monitor Database. URL: <https://www.nmdb.eu/>.
- Nymmik, R., 2013. Charge states of heavy ions, as determined from the parameters of solar energetic particle spectra. *Bull. Russian Acad. Sci.: Phys.* 77, 490–492. <https://doi.org/10.3103/S1062873813050419>.
- Paassilta, Miiikka, Raukunen, Osku, Vainio, Rami, et al., 2017. Catalogue of 55–80 mev solar proton events extending through solar cycles 23 and 24. *J. Space Weather Space Clim.* 7, A14. <https://doi.org/10.1051/swsc/2017013>.
- Papaioannou, A., Belov, A., Abunina, M., et al., 2020. Interplanetary coronal mass ejections as the driver of non-recurrent forrush decreases. *Astrophys. J.* 890 (2), 101. <https://doi.org/10.3847/1538-4357/ab6bd1>.
- Reames, D.V., 1999. Particle acceleration at the sun and in the heliosphere. *Space Sci. Rev.* 90 (3), 413–491. <https://doi.org/10.1023/A:1005105831781>.
- Richardson, I.G., Cane, H.V., 2011. Galactic Cosmic Ray Intensity Response to Interplanetary Coronal Mass Ejections/Magnetic Clouds in 1995–2009. *Sol. Phys.* 270 (2), 609–627. <https://doi.org/10.1007/s11207-011-9774-x>.
- Subramanian, P., Antia, H.M., Dugad, S.R., et al., 2009. Forrush decreases and turbulence levels at coronal mass ejection fronts. *A&A* 494 (3), 1107–1118. <https://doi.org/10.1051/0004-6361:200809551>.
- Torsti, J., Valtonen, E., Lumme, M., et al., 1995. Energetic particle experiment erne. *Sol. Phys.* 162 (1–2), 505–531. <https://doi.org/10.1007/BF00733438>.
- Valtonen, E., Lehtinen, I.-V., 2009. Solar energetic particle fluences from soho/erne. *Acta Geophys.* 57, 116–124. <https://doi.org/10.2478/s11600-008-0056-4>.
- Veselinovic, N., Dragic, A., Savić, M., et al., 2017. An underground laboratory as a facility for studies of cosmic-ray solar modulation. *Nucl. Instrum. Methods Phys. Res. Section A: Accelerat. Spectromet. Detectors Assoc. Equip.* 875, 10–15. URL: <https://www.sciencedirect.com/science/article/pii/S0168900217309634>. <https://doi.org/10.1016/j.nima.2017.09.008>.
- Veselinovic, Nikola, Savić, Mihailo, Dragic, Aleksandar, et al., 2021. Correlation analysis of solar energetic particles and secondary cosmic ray flux. *Eur. Phys. J. D* 75 (6), 173. <https://doi.org/10.1140/epjd/s10053-021-00172-x>.
- Veselinović, N., Dragić, A., Maletić, D., et al., 2015. Cosmic rays muon flux measurements at Belgrade shallow underground laboratory. In: Trache, L., Chesneanu, D., Alexandru Ur, C. (Eds.), *Exotic Nuclei and Nuclear/Particle Astrophysics (V) From Nuclei to Stars: Carpathian Summer School of Physics 2014*, AIP Publishing LLC., New York volume 1645 of American Institute of Physics Conference Series, pp. 421–425. <https://doi.org/10.1063/1.4909614>.
- Yashiro, S., Gopalswamy, N., Michalek, G., et al., 2004. A catalog of white light coronal mass ejections observed by the soho spacecraft. *J. Geophys. Res.: Space Phys.* 109 (A7). <https://doi.org/10.1029/2003JA010282>.
- Zhao, L., Zhang, M., Rassoul, H.K., 2016. Double power laws in the event-integrated solar energetic particle spectrum. *Astrophys. J.* 821 (1), 62. <https://doi.org/10.3847/0004-637x/821/1/62>.

Space Weather



RESEARCH ARTICLE

10.1029/2020SW002712

Key Points:

- Correction of meteorological effects on muon component of secondary cosmic rays significantly extends the usability of muon monitors
- A new method for modeling of meteorological effects utilizing multivariate analysis and machine learning techniques is presented
- Correction efficiency of the best performing algorithm is greater than for other commonly used methods

Correspondence to:


M. Savić,
msavic@ipb.ac.rs

Citation:

Savić, M., Maletić, D., Dragić, A., Veselinović, N., Joković, D., Banjanac, R., et al. (2021). Modeling meteorological effects on cosmic ray muons utilizing multivariate analysis. *Space Weather*, 19, e2020SW002712. <https://doi.org/10.1029/2020SW002712>

Received 30 DEC 2020
 Accepted 13 JUL 2021

Modeling Meteorological Effects on Cosmic Ray Muons Utilizing Multivariate Analysis

M. Savić¹ , D. Maletić¹, A. Dragić¹, N. Veselinović¹, D. Joković¹, R. Banjanac¹, V. Udovičić¹, and D. Knežević¹

¹Institute of Physics Belgrade, University of Belgrade, Belgrade, Serbia

Abstract Correction of meteorological effects on muon component of secondary cosmic rays significantly extends the usability of muon monitors. We propose a new data driven empirical method for correction of meteorological effects on muon component of secondary cosmic rays, based on multivariate analysis. Several multivariate algorithms implemented in Toolkit for Multivariate Data Analysis with ROOT framework are trained and then applied to correct muon count rate for barometric and temperature effects. The effect of corrections on periodic and aperiodic cosmic ray variations is analyzed and compared with integral correction method, as well as with neutron monitor data. The best results are achieved by the application of linear discriminant method, which increases sensitivity of our muon detector to cosmic ray variations beyond other commonly used methods.

Plain Language Summary Primary cosmic rays are energetic particles that arrive at Earth from space. On their journey toward Earth they are affected by the solar wind (a stream of charged particles emanating from the sun), which has information about various solar processes embedded in it. In top layers of the atmosphere primary cosmic rays interact with nuclei of air molecules and produce large number of secondary particles that propagate toward Earth's surface. These secondary particles preserve information about variations of primary cosmic rays, which allows for the study of solar processes using Earth based detectors. One type of secondary particles that can be detected on the ground are muons. However, muons are affected by the conditions in the atmosphere, which can disturb the information about variations of primary cosmic rays. That is why it is important to model these atmospheric effects on cosmic ray muons as well as possible so they can be corrected for. In this study, we present a new method for modeling and correction of atmospheric effects on cosmic ray muons, that is based on multivariate analysis utilizing machine learning algorithms. This method increases sensitivity of our muon detector to cosmic ray variations beyond other commonly used methods.

1. Introduction

Meteorological effects on muon component of secondary cosmic rays have been known and studied for almost a century. A number of meteorological parameters contribute to variation of muon flux in the atmosphere, but two are the most significant: atmospheric pressure and atmospheric temperature.

Aperiodic fluctuations of intensity, discovered in the very early cosmic ray measurements, were eventually attributed to the variation of atmospheric pressure by Myssowsky & Tuwim (1926) (associated effect dubbed *barometric*), while *temperature effect* has been discovered more than a decade later and has two components: *negative* (first quantitatively described by Blackett, 1938) and *positive* (suggested by Forró, 1947). Barometric effect represents variation of muon flux due to variation of the mass of the absorber (air column) above the detector. Negative temperature effect is a consequence of dependence of effective height of muon generation level on the atmospheric temperature, resulting in longer muon path and increased probability of decay with higher temperature. Positive temperature effect has to do with positive correlation between atmospheric temperature and air density, decreasing the probability of nuclear interactions and increasing the probability of decay of muon-generating pions with the increase of temperature.

In order to study variations of primary cosmic rays (CR) using Earth based muon detectors, it is of the utmost importance to describe these meteorological effects as precisely as possible so they can be corrected for. A precise correction for meteorological effects significantly increases sensitivity of muon detectors to CR variations, making them a more usable counterpart to neutron monitors (the other widely used type of

© 2021. The Authors.

This is an open access article under the terms of the [Creative Commons Attribution-NonCommercial-NoDerivs License](https://creativecommons.org/licenses/by-nc-nd/4.0/), which permits use and distribution in any medium, provided the original work is properly cited, the use is non-commercial and no modifications or adaptations are made.

ground based cosmic ray detectors), as muon detectors are normally responsive to higher energy primary cosmic rays. Additionally, muon monitors have a unique application in diagnostics of the atmosphere, allowing for prediction of atmospheric temperatures provided a good model of meteorological effects is available (Belov et al., 1987; Kohno et al., 1981).

Several empirical and theoretical models of meteorological effects have been proposed over the years, based on which corrections can be performed. Even though full set of meteorological effects is larger, in this analysis we will concentrate on the correction of temperature and barometric effect only, so results can be more easily compared to other methods.

Some of the most commonly used methods for temperature correction are: method of effective level of generation, introduced by Duperier (1949), integral method, developed by Feinberg (1946), Dorman (1954), and others (Maeda & Wada, 1954; Wada, 1962), method of mass-averaged temperature developed by Dvornikov et al. (1976), and method of effective temperature (mostly applicable to underground detectors) (Barrett et al., 1952).

Each of these methods have their own advantages, but in this study, we have decided to use the integral method as a reference against which to compare the results of our analysis. Main reason being is that it is derived from the theory of meteorological effects, which involves the most detailed analysis, as well as it being the least approximative. According to this approach, relative variation of muon count rate due to the temperature effect can be expressed as:

$$\left(\frac{\delta I}{I}\right)_{temp} = \int_0^{h_0} \alpha(h) \cdot \delta T(h) \cdot dh, \quad (1)$$

where α is temperature coefficient density function, δT is temperature variation and h_0 is atmospheric depth of the observation level expressed in g/cm^2 . Temperature coefficient density function is calculated theoretically, while temperature variation is calculated relative to some reference temperature for the period, usually mean temperature. In practical application, integration in Equation 1 is substituted with a sum, taking into account some finite number of isobaric levels.

Analysis of barometric effect is also included in the theory of meteorological effects, but barometric coefficient is rarely calculated theoretically. Most commonly it is determined using linear regression, assuming linear dependence between atmospheric pressure and muon flux:

$$\left(\frac{\delta I}{I}\right)_{pres} = \beta \cdot \delta P, \quad (2)$$

where β is barometric coefficient, and δP represents atmospheric pressure variation.

Each of the mentioned methods is at least in some part approximative, so the idea behind this work is to introduce a new empirical method for correction of meteorological effects that would be data driven, assuming as little as possible upfront. Other advantages of such approach are that it does not depend on the design of the detector, location of the site or topology of the surrounding terrain (as these would ideally be factored in by the model), and that it can be applied in near-real time. Additionally, proposed method can be used in the analysis and potential correction of temperature effect of neutron component of cosmic rays, as part of detected neutrons can originate from cosmic ray muons captured in the nuclei of the shielding of a neutron monitor detector (Dorman, 2004). Finally, in principle it can easily be generalized to take wider set of meteorological parameters into account.

As the presented problem is multidimensional, involving a relatively large number of correlated variables, we have decided to employ multivariate analysis, relying on machine learning techniques. In some recent work (Morozova et al., 2017; Savic et al., 2019) decorrelation of atmospheric variables and numerical modeling has been successfully applied to the study of interaction of cosmic rays with Earth's atmosphere, so utilizing adaptive and flexible machine learning methods could possibly yield further improvement, potentially revealing additional dependencies and taking higher order effects into account. This approach involves application of a number of multivariate algorithms, more or less rooted in statistical machine learning, to our problem and comparing their consistency and effectiveness with selected reference results.

Large part of variations observed in continuous cosmic ray measurements can be attributed to different space weather phenomena, due to modulation of primary cosmic rays in the heliosphere. In terms of temporal properties, they can be classified as periodic or aperiodic. We will test how newly introduced methods for correction of meteorological effects affect the sensitivity for detection of both periodic as well as aperiodic variations of muon flux of nonterrestrial origin, and how it ultimately compares to the sensitivity of neutron monitors.

2. Data

For the analysis of meteorological effects both muon flux and meteorological data are needed. Muon flux was measured experimentally in the Low Background Laboratory at the Institute of Physics Belgrade, while meteorological data is a combination of modeled atmospheric temperature profiles, and atmospheric pressure and ground level temperature measured locally.

2.1. CR Muon Data

Low Background Laboratory (LBL) is located on the grounds of the Institute of Physics Belgrade. Geographical coordinates for the laboratory are $44^{\circ}51'N$ and $20^{\circ}23'E$, with elevation of 75 m and geomagnetic cutoff rigidity of 5.3 GV. Detector system is comprised of a $100 \times 100 \times 5$ cm plastic scintillator with accompanying read-out electronics. Median energy for the detector system is (59 ± 2) GeV (Veselinović et al., 2017), with muon flux of $(1.37 \pm 0.06) \times 10^{-2}$ per cm^2 s. Electron contamination determined for a previously used experimental setup was $\sim 24\%$ (Dragić et al., 2008), and is assumed to be comparable for the current one (Joković, 2011). More detailed description of the laboratory and the experimental setup can be found elsewhere (Dragić et al., 2011). Native muon count rate data has time resolution of 5 min, but hour sums are also frequently used in analysis.

Continuous cosmic ray muon flux measurements have been ongoing in LBL since 2002, current setup being utilized since 2009. Data are available to public via an online interface on the Belgrade Cosmic Ray Station internet site (Low Background Laboratory for Nuclear Physics, 2020).

As with any long-term measurement, some shorter interruptions and inconsistencies are unavoidable, hence when choosing the interval to be used for the analysis we decided to use a one-year period from June 1, 2010 to May 31, 2011, where measurements had the most continuity and consistency. Additionally, using a one-year period should remove any potential bias, primarily due to annual temperature variation.

2.2. Meteorological Data

Meteorological parameters needed for the analysis come from two sources: Atmospheric temperature profile data are produced by an atmospheric numerical model, while atmospheric pressure and ground temperature data come from local measurements.

Meteorological balloon soundings above Belgrade done by Republic Hydro-meteorological Service of Serbia (RHMZ, 2020) are not frequent enough for the purposes of this analysis, so modeled data for atmospheric temperature profile are used instead. Several numerical atmospheric models can provide such data. In this work, we have chosen Global Forecast System (GFS) produced by National Centers for Environmental Prediction (GFS, 2020), which has been found to be in best agreement with balloon soundings done above Belgrade. Comparison was done where soundings data were available, as described in our previous study (Savić et al., 2019). GFS provides a large number of modeled atmospheric parameters among which are atmospheric temperatures for different isobaric levels. Modeled data sets are being produced four times per day (at hours 00:00, 06:00, 12:00, and 18:00). In addition, analysis data are also available, reprocessed *post festum* and taking into account real data measured by world network of meteorological services. In this analysis, we have been using such reprocessed atmospheric temperatures for the following isobaric levels: 10, 20, 30, 50, 70, 100, 150, 200, 250, 300, 350, 400, 450, 500, 550, 600, 650, 700, 750, 800, 850, 900, 925, and 975 mb. Data are available with spatial resolution of 0.5° of geographical longitude/latitude, so coordinates closest to the laboratory coordinates were chosen. Data were then interpolated with cubic spline, similar as in Berkova et al. (2012), and sampled in finer time resolution needed for the analysis.

Atmospheric pressure and ground temperature data are compiled from different meteorological stations in and around Belgrade, and then interpolated as described in more detail elsewhere (Savic et al., 2016). Finally, unique time series of combined modeled and measured meteorological data, with finest time resolution of 5 min, is assembled to be used in the analysis.

3. Methodology

The use of machine learning has seen an unprecedented expansion in the last decade. The main strength of such approach being that it does not assume any a priori model, but is data driven and thus able to potentially discover hidden dependencies. This is especially true when applied to large data sets with many correlated variables. In this study, we want to establish whether such approach would yield any improvements when applied to the problem of meteorological effect on cosmic ray muons.

To test this, we have decided to use toolkit for multivariate analysis (TMVA) package which provides a ROOT-integrated environment for application of multivariate classification and regression techniques (Hoecker et al., 2007). The package has been developed for the use in high-energy physics and contains implementation of a number of supervised learning algorithms, which utilize training and testing procedures on a sample data set to determine the mapping function. Mapping function maps the input parameters to output target value, trying to model the actual functional dependence (“target” function) as accurately as possible. The structure of the mapping function is algorithm specific, and can be a single global function or a set of local models. Trained algorithm is then applied to the full data set and provides either a signal/background separation (in case of classification) or prediction of target value (in case of regression).

For us, the later application is especially interesting. The idea is to train the mapping function, using meteorological parameters as input variables, and muon count rate as the regression target, and use trained function to produce the predicted target output for a larger data set. In principle, implementation of this procedure is specific for different analysis frameworks. TMVA provides template code for the training and application of multivariate methods, where optimal parameters obtained in the training/testing phase are stored in “weight” files to be used in the application phase. Thusly predicted muon count rate would ideally contain only variations related to meteorological effects, while the residual difference between modeled and measured muon count rate would contain variations of non-meteorological origin. We would apply this procedure for a number of algorithms implemented in TMVA, compare their performance and efficiency based on several criteria, and finally suggest the methods best suited for the modeling, and ultimately the correction, of meteorological effects.

Corrected muon count rate would be calculated according to the following equation:

$$N_{\mu}^{(corr)} = \Delta N_{\mu} + \langle N_{\mu} \rangle, \quad (3)$$

where

$$\Delta N_{\mu} = N_{\mu}^{(mod)} - N_{\mu} \quad (4)$$

is the difference between the modeled and measured muon count rate.

Not all machine learning methods are equally suited for all types of problems and selection of the optimal method for a particular application is rarely straightforward. The efficiency of different algorithms depends on a number of factors: Whether they are used for classification or regression, is correlation between parameters linear or nonlinear, what is the general complexity of the problem and required level of optimization, and so on. One can only assume the efficiency of any given algorithm upfront but there is no clear general rule which one will perform best in a particular situation. Often, several algorithms with specific strengths and weaknesses can be applied to the same problem and only through analysis of the final result the optimal one can be determined. For this reason, in our analysis we have decided to indiscriminately include the largest number of algorithm classes available in TMVA, and only after extensive parallel testing narrow the selection down to the optimal one.

We will briefly describe different classes of multivariate methods available in TMVA, as well as list specific algorithms that were chosen as representative for each class. First class are methods based on probability

density estimation (PDE) techniques, where actual probability density function is estimated based on the available data. Here we have selected to test two specific multidimensional implementations, somewhat similar in nature: PDE range-search (PDE-RS) and k-nearest neighbor (KNN) algorithms. Examples of use of this approach for multivariate regression are scarce, but the success with which PDERS was applied in classification problems in high-energy physics (Carli & Koblitz, 2003) motivated its use here. Second class are methods based on function discriminant analysis. These methods are widely used for dimensionality reduction and classification. Here, we selected the linear discriminant (LD) algorithm which shares some similarities in the approach with principal component analysis (PCA), in that it maps a space of potentially correlated input variables onto a smaller space of uncorrelated variables, but in addition to PCA it also maximizes the separation between output classes, making it a natural choice for application to our problem. Algorithms that employ higher order functions were also tested, but as could be expected performed more poorly. Application of artificial neural networks (ANN) to multivariate regression problems has seen expansion in recent years, where ANN methods often perform better than more straightforward regression techniques, especially if some degree of nonlinearity is present. Even though the dependence of cosmic ray muon flux on atmospheric temperatures is linear, we felt it is certainly worth investigating how ANN methods would perform when applied to this problem, and if any additional hidden dependence would be revealed. We have chosen to apply the MLP, as it is the fastest and most flexible available ANN algorithm in TMVA. Finally, method of boosted regression trees (BDT) employs a larger number (*forest*) of binary decision trees, which split the phase space of input variables based on a yes/no decision to a series of sequential cuts applied, so to predict a specific value of the output variable. They have been very successfully applied to classification problems in high-energy physics (Lalchand, 2020), but can also be used for multivariate regression with the similar rationale as for the ANN. We have selected two representative algorithms for testing: boosted decision tree (BDT) and gradient boosted decision tree (BDTG).

In this analysis, the procedure is applied to correction of barometric and temperature effect but it is easy to see how it can be extended to include more atmospheric variables, especially as such data is readily available from atmospheric numerical models.

3.1. Training Procedure

For the training/testing data subset we have selected data for the 10 geomagnetically quietest days of each month (list provided by GFZ German Research Center for Geosciences, GFZ Potsdam, 2020), as we expect variations due to meteorological effects to be more pronounced here. This subset was then further split into training and testing data set, where 70% of randomly selected data was used for training while remaining 30% was used for testing. Data time resolution used was 5 min as it gave us a larger statistics for training.

There is a number of settings that can be manipulated for each of the multivariate algorithms used. They vary from some basic parameters, to selection of different subalgorithms or various options that can be turned on or off. For each algorithm, we have selected the optimal set of parameters. The criterium for optimal performance was minimizing the average quadratic deviation of the modeled output versus the target value. Also, where allowed by the algorithm, input variables were decorrelated prior to further processing.

Table 1 shows the values of average quadratic deviation for the modeled output (modeled muon count rate) versus the target value (measured muon count rate) for different algorithms. First two columns refer to the training data subset while second two columns refer to the testing data subset. First and third column represent average quadratic deviation defined as $(\sum(f_{MVA} - f_{target})^2)^{1/2}$ (where f_{MVA} and f_{target} represent modeled and measured count rates, respectively), while second and fourth columns represent truncated average quadratic deviation which takes into account 90% of data with least deviation. As previously mentioned, the criterium for selection of optimal parameters for every algorithm is the minimal value of average quadratic deviation for the test data subset.

3.2. Algorithm Performance Analysis

All presented multivariate algorithms have no built in knowledge about the studied effect, so in addition to quantitative test mentioned in the section above, we introduce some qualitative analysis designed to estimate the integrity of modeled data. Prime concern here would be to test whether the suggested procedure

Table 1
Average Quadratic Deviation for Selected Multivariate Methods

Method	Training		Testing	
	Average deviation (counts/5 min)	Truncated deviation (counts/5 min)	Average deviation (counts/5 min)	Truncated average (counts/5 min)
PDERS	234	185	258	201
KNN	224	177	233	185
LD	286	225	284	223
MLP	228	180	234	186
BDT	219	182	237	188
BDTG	223	174	236	187

Abbreviations: BDT, boosted decision tree; BDTG, gradient boosted decision tree; KNN, k-nearest neighbor; LD, linear discriminant.

for the correction of barometric and temperature effect (PT correction) removes these meteorological effects only, while leaving all other features nonperturbed. To this end, we will analyze several distributions of modeled data, compare them with raw and reference PT corrected data (obtained using the integral method) and look for possible anomalous features.

First, we will look into structure of distributions of difference between modeled and measured muon count rate as a function of measured count. We want to make comparison between these distributions in the training phase (for the test data subset) and after the trained algorithm was applied to the full data set. We would expect these distributions to be consistent, and appearance of some new structures or strong trends would point to some perturbation in the application phase. We have selected two examples to illustrate the difference in consistency of application of trained algorithms—BDTG and PDERS, their distributions shown in Figure 1.

We can see that distributions for BDTG algorithm for test data subset (Figure 1a) and full data set (Figure 1b) are fairly similar, and any structures and trends in the test distributions are mostly well replicated in the full data set distributions (different statistics taken into account). This is the case for most applied algorithms except for PDERS, where some dependence of the count rate, negligible for the test data distribution (Figure 1c), exists for the full data set distribution (Figure 1d).

Another, more important feature, is that for some algorithms distributions we analyzed in the previous paragraph are not smooth, but rather display some structures. To get further insight into these structures, for all featured methods we plotted distributions of modeled muon count rate along with the distribution of raw count rate on the same graph, as shown in Figure 2.

In order to better understand shapes of distributions and any structures observed in plots in Figure 2, it would be helpful to compare them to equivalent plots for muon count rates corrected for pressure and temperature effects using a well-established reference method. However, before we take a look at these distributions, we will first briefly describe procedures used to obtain reference PT correction.

Temperature and barometric effect are typically corrected for independently, where one of several methods mentioned in Section 1 is used for temperature correction, and barometric coefficient for pressure correction is determined empirically. Integral method for correction of temperature effect is widely accepted as the most accurate one. It is based on the theory of meteorological effects and takes complete atmospheric temperature profile and relevant processes into account. Most thorough description of the theory of meteorological effects is given by Dorman (2004), where temperature coefficient density function $\alpha(h)$ in Equation 1 is given in its integral form. In order to be applied, this function is then calculated through integration, substituting parameters specific to the location of the experiment. Temperature coefficient density functions for the location of Low Background Laboratory for Nuclear Physics were calculated using Monte Carlo integration technique. In order to determine barometric coefficient, temperature corrected muon data were plotted as a function of atmospheric pressure (using entries for 10 geomagnetically quietest days

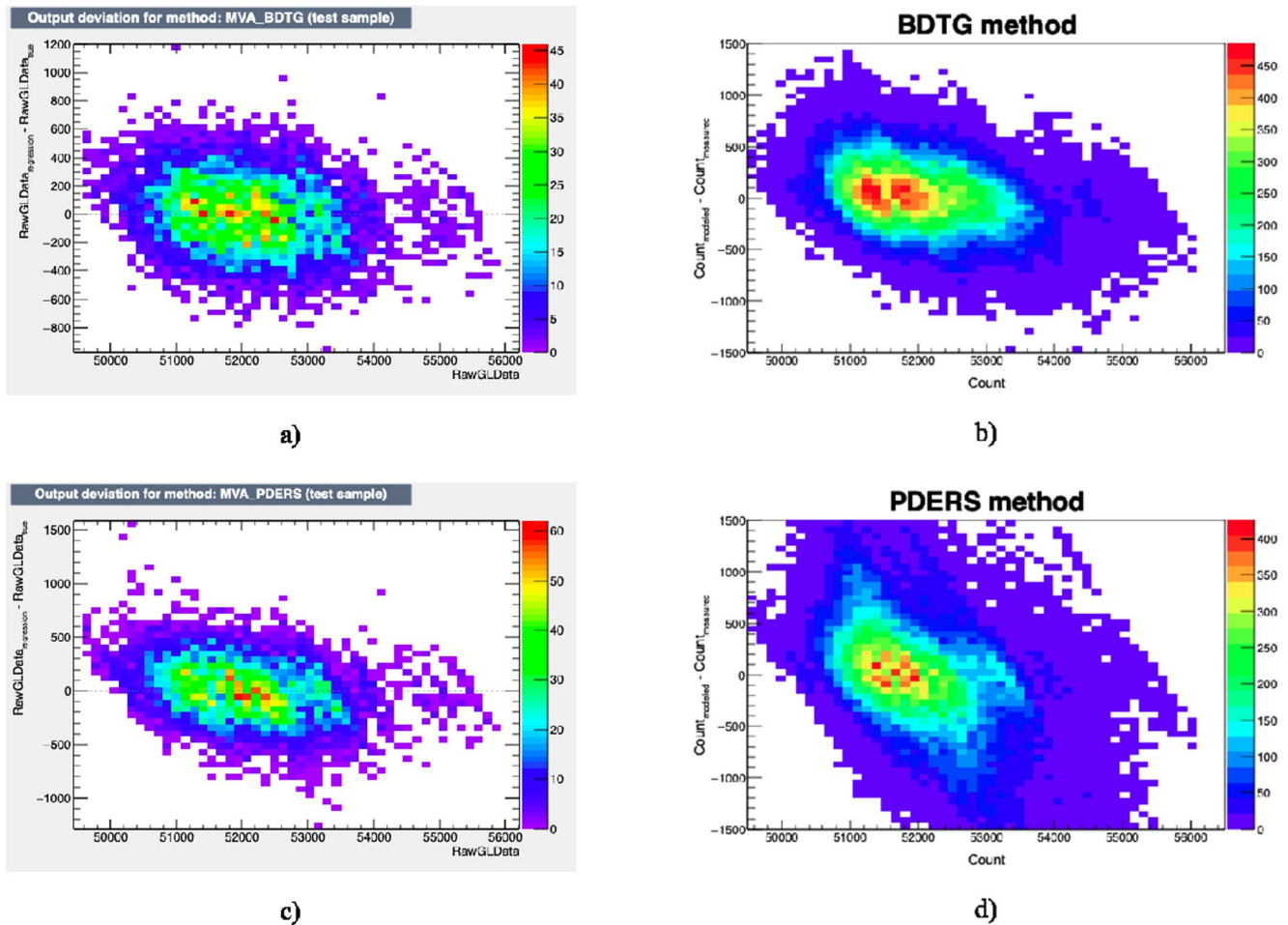


Figure 1. Distribution of difference between modeled (regression) and measured (true) muon count rate as a function of measured muon count rate for: (a) gradient Boosted decision tree (BDTG)—test data set, (b) BDTG—full data set, (c) PDERS—test data set, and (d) PDERS—full data set.

of each month only), coefficient determined via linear regression separately for each calendar year. Both procedures are presented in greater detail in our previous work (Savic et al., 2016).

Distributions equivalent to ones shown in Figures 1 and 2 were plotted for reference pressure and temperature corrected data, as shown in Figure 3. The analog for the modeled muon count rate is calculated from the variation due to pressure and temperature effects calculated based on the integral method. It is worth pointing out that distributions for reference PT corrected data are noticeably less smooth, which can be mostly attributed to lower statistics used as only hour summed data was available for this correction.

Based on these plots, we can conclude that we should not expect a significant deviation between raw and corrected data and that corresponding distributions should not have any characteristic structures. Most plots in Figure 2 are consistent with this expectation, however, some structures can be observed in KNN plots, and to a degree in BDT plots, while distribution plotted for PDERS algorithm does not have these structures but appears to somewhat deviate from raw data distribution.

Another insight into performance and consistency of different multivariate algorithms when applied to the modeling of meteorological parameters can be gathered by the way of spectral analysis of PT corrected data. Pressure and temperature corrected muon count rate was determined for all selected algorithms using modeled data, as described in Section 3. Since some gaps exist in our muon data, Lomb-Scargle algorithm was used to obtain the power spectra, as it is less sensitive to uneven data sampling (Press et al., 2007). Figure 4 shows power spectra for raw and muon count rates corrected for pressure and temperature effects using integral and two illustrative examples of multivariate methods. Full spectrum as well as selected interval

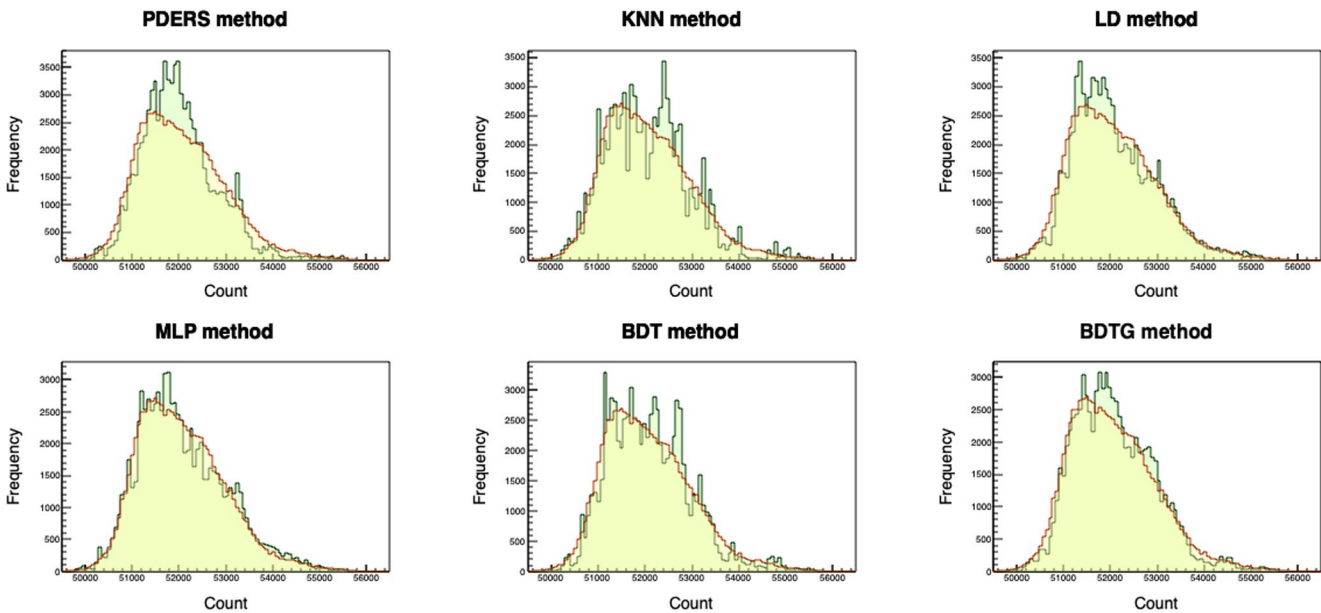


Figure 2. Comparison between distributions of raw (yellow) and muon count rate modeled by selected multivariate methods (green).

of frequencies around the periodicity of one day are shown, red dashed line indicating significance level of 0.01.

If integral method is again used as a reference, we can see that thus obtained PT correction does not remove daily variation, but rather makes it more pronounced. This should not come as a surprise, as only smaller part of the diurnal variation can be attributed to meteorological effects (Quenby & Thambyahpillai, 1960), while larger part is of nonmeteorological origin. Hence, removing variation due to atmospheric pressure would make daily variation more prominent. LD, and to a degree BDT/BDTG methods, have an effect on daily variation similar to the integral method, but for BDT method (bottom right in Figure 4) we observe emergence of some frequencies with significant power that cannot be associated with any known periodicity of cosmic rays, and probably have artificial origin. Such features are even more pronounced for the remaining multivariate algorithms, where in addition an over-reduction of power frequency corresponding to diurnal variation to can be observed. Over-reduction of daily variation coupled with introduction of artificial variations with significant powers points to possible inadequateness or overtraining of some of the multivariate methods.

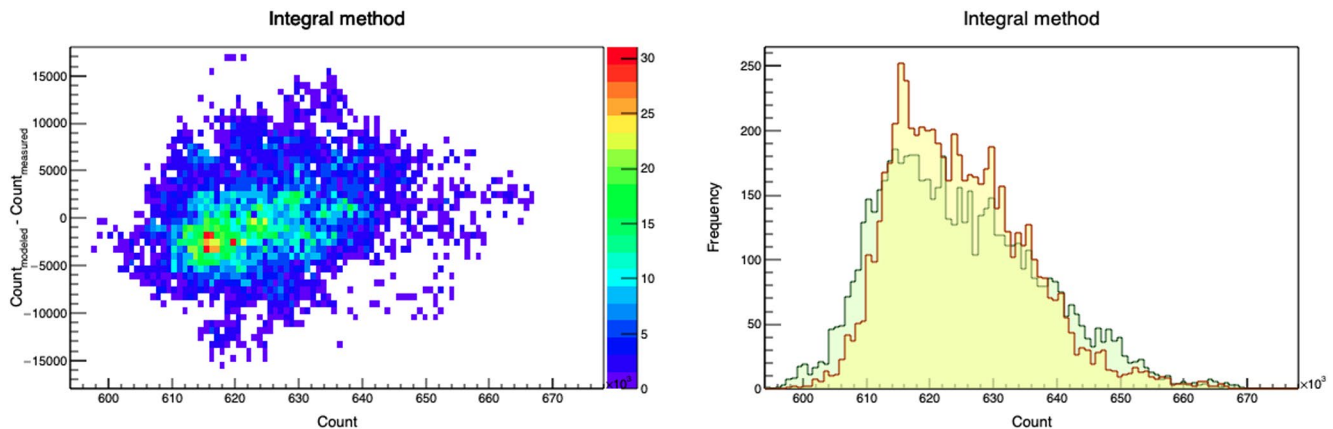


Figure 3. Distribution of difference between muon count rate calculated from the variation due to pressure and temperature effect using integral method and measured muon count rate as a function of measured muon count rate (left), and comparison between distributions of raw (yellow) and calculated muon count rate (green) shown on the right.

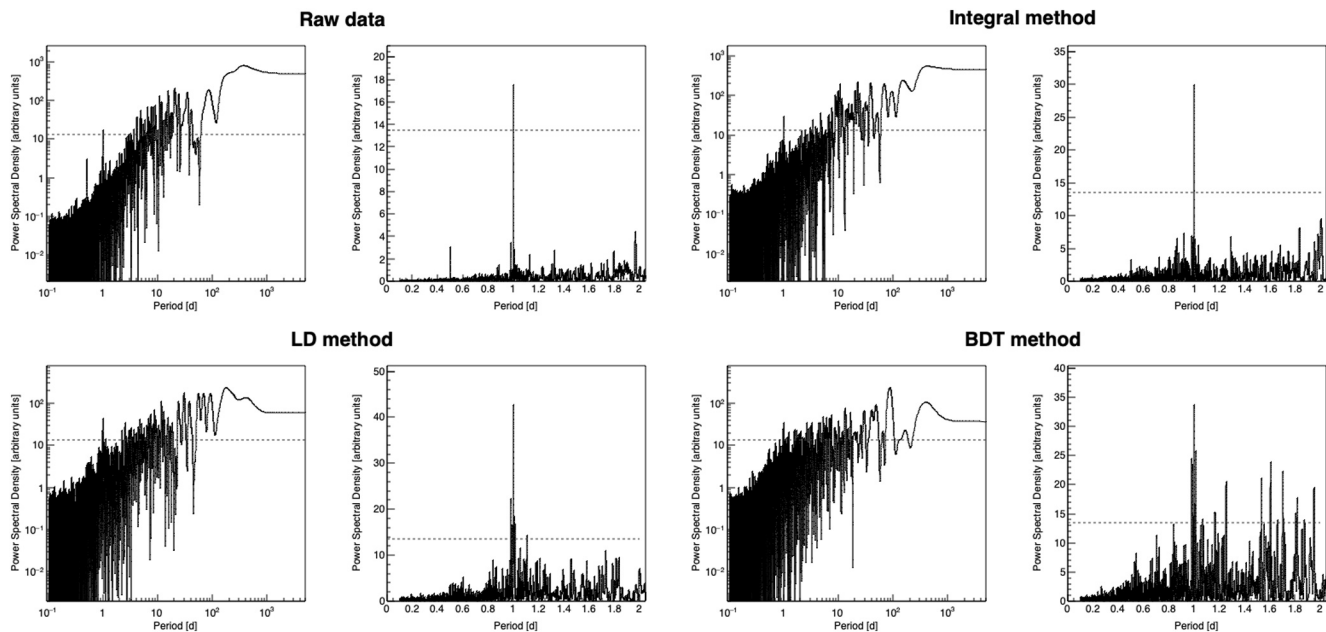


Figure 4. Power spectra for raw data (top left), PT corrected data using integral method (top right), and PT corrected data using selected multivariate methods (second row). For each method, both full spectrum and a range of frequencies around periodicity of one day are shown. Significance level of 0.01 is indicated by the red dashed line.

The effect on annual variation is difficult to determine based on the spectral analysis as period of only one year is analyzed, but we will introduce some quantitative tests in the next section that will help us with this estimate.

4. Results

We will use two criteria to estimate the efficiency of newly introduced methods for PT corrections. One will rely on the effectiveness with which the multivariate algorithms remove the annual variation and reduce variance, while the other will be based on the effect the correction has on detection sensitivity for aperiodic events, such as Forbush decreases (Forbush, 1937). In both cases, we will compare the results with the ones obtained by the integral method.

4.1. Effects of PT Correction on Periodic CR Variations

Significant part of the annual variation of cosmic ray muon flux can be attributed to the variation of atmospheric temperature (Hess, 1940). As mentioned before, the effectiveness with which this effect is corrected for will affect the detector sensitivity to variations of primary cosmic rays of non-atmospheric origin.

We will examine time series for pressure and temperature corrected data and compare them with raw and pressure corrected time series, especially taking note of how PT correction affects the annual variation. In order to estimate this effect, we fit the time series (except for raw data) with sine function with a period of one year. The amplitude of pressure corrected data determined from such fit will be used as an estimate of the annual muon flux variation, and serve as a reference against which to compare the effect of PT correction by different methods. In Figure 5 time series for raw, pressure corrected and pressure and temperature corrected data are shown. For the sake of simplicity, not all time series for data PT corrected using multivariate algorithms are shown, but rather only characteristic ones. Table 2 shows values for the annual variation amplitude for pressure and PT corrected time series, as well as possibly more informative reduction of annual variation calculated relative to the amplitude of the pressure corrected muon flux.

While, time series in Figure 5 for data PT corrected using integral, LD and BDTG methods do not seem to have some unexpected fluctuations, that is not the case for MLP method, where one can observe some

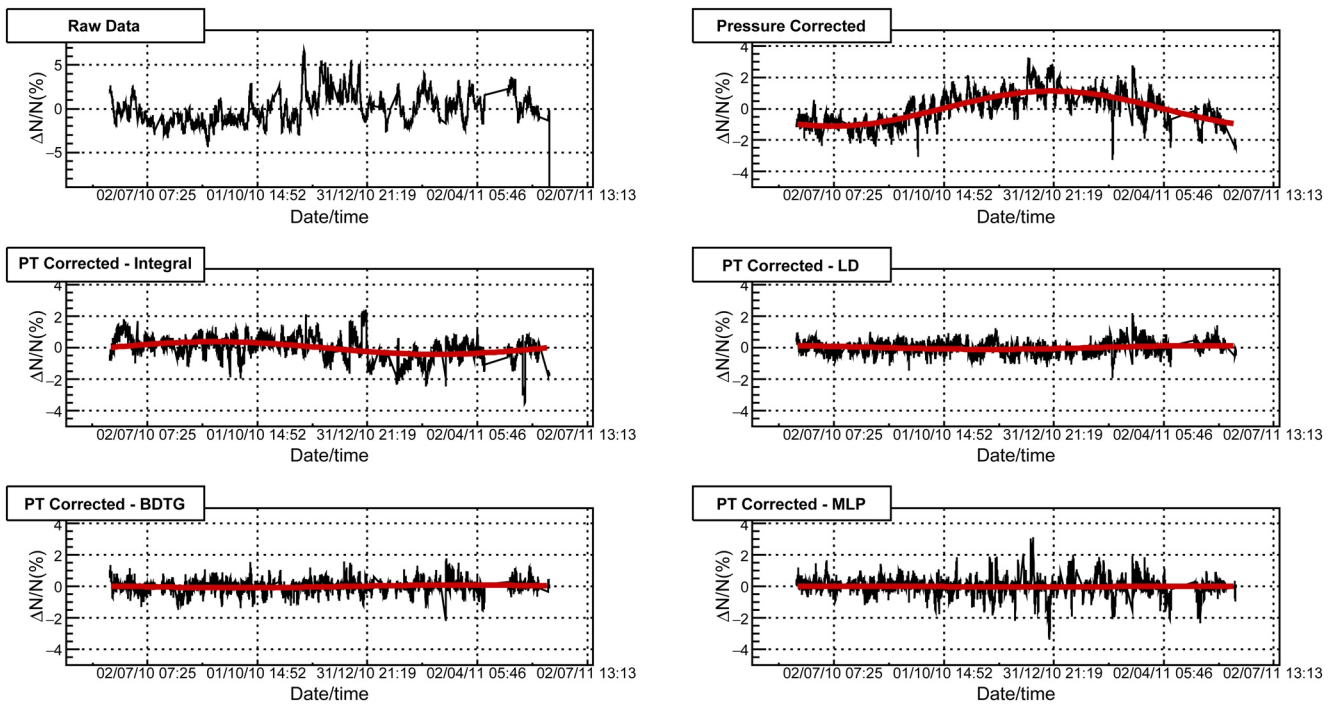


Figure 5. Muon count rate time series for the period from June 1, 2010 to May 31, 2011: raw data (top left), pressure corrected data (top right), PT corrected data using integral method (second row left) and data PT corrected using selected multivariate methods.

data that appears to deviate from the mean more significantly than what would be intuitively expected. For remaining multivariate algorithms this is even more the case. In order to try and quantify this visual comparison, we will analyze the effect corrections have on standard deviation of the data. If calculated relative to the mean muon flux for the whole period, standard deviation would be sensitive to the residual annual variation. To make standard deviation independent of the seasonal variation, we used a moving ten-day window to determine the mean value and then calculated the standard deviation relative to it.

Figure 6 shows distributions of relative variation of muon flux in respect to the moving window mean value for raw data and PT corrected data using integral, LD and MLP methods. It is based on these distributions that standard deviation was determined and results are presented in Table 3. Comparing standard deviations for PT corrected muon flux obtained by multivariate methods with the one obtained by the integral method, we can see that for LD, BDT, and BDTG algorithms they have comparable values. The difference is somewhat larger in the case of MLP, which is in accordance with features observed in Figure 6, while it is significantly larger for the remaining algorithms. This indicates that PT correction performed using KNN and PDERS (and possibly MLP) algorithms probably introduces some artificial features into PT corrected muon flux data.

One way to evaluate the effectiveness of different algorithms in reduction of the seasonal variation even better, would be to compare the PT corrected muon data to pressure corrected time series for selected neutron monitor detectors. The reasoning is based on a well-known fact that meteorological effects on the neutron component of secondary cosmic rays are dominated by the barometric effect. Temperature effect does exist for the secondary cosmic ray neutrons, but whether calculated theoretically (Dorman, 2004) or determined experimentally (Kaminer et al., 1965), it is still an order of magnitude smaller than for the muon component and typically not corrected for in neutron monitor data. Based on this, we

Table 2
Amplitude and Reduction of the Amplitude of Annual Variation Relative to Pressure Corrected Data (P Corrected) for PT Corrected Data (Using Integral and Selected Multivariate Methods)

Method	Amplitude (%)	Relative reduction (% of P corrected)
P corrected	1.11 ± 0.09	/
Integral	0.40 ± 0.03	64 ± 6
PDERS	0.09 ± 0.02	92 ± 3
KNN	0.24 ± 0.04	79 ± 5
LD	0.11 ± 0.03	90 ± 4
MLP	0.03 ± 0.01	98 ± 2
BDT	0.12 ± 0.03	89 ± 4
BDTG	0.086 ± 0.009	92 ± 2

Abbreviations: BDT, boosted decision tree; BDTG, gradient boosted decision tree; KNN, k-nearest neighbor; LD, linear discriminant.

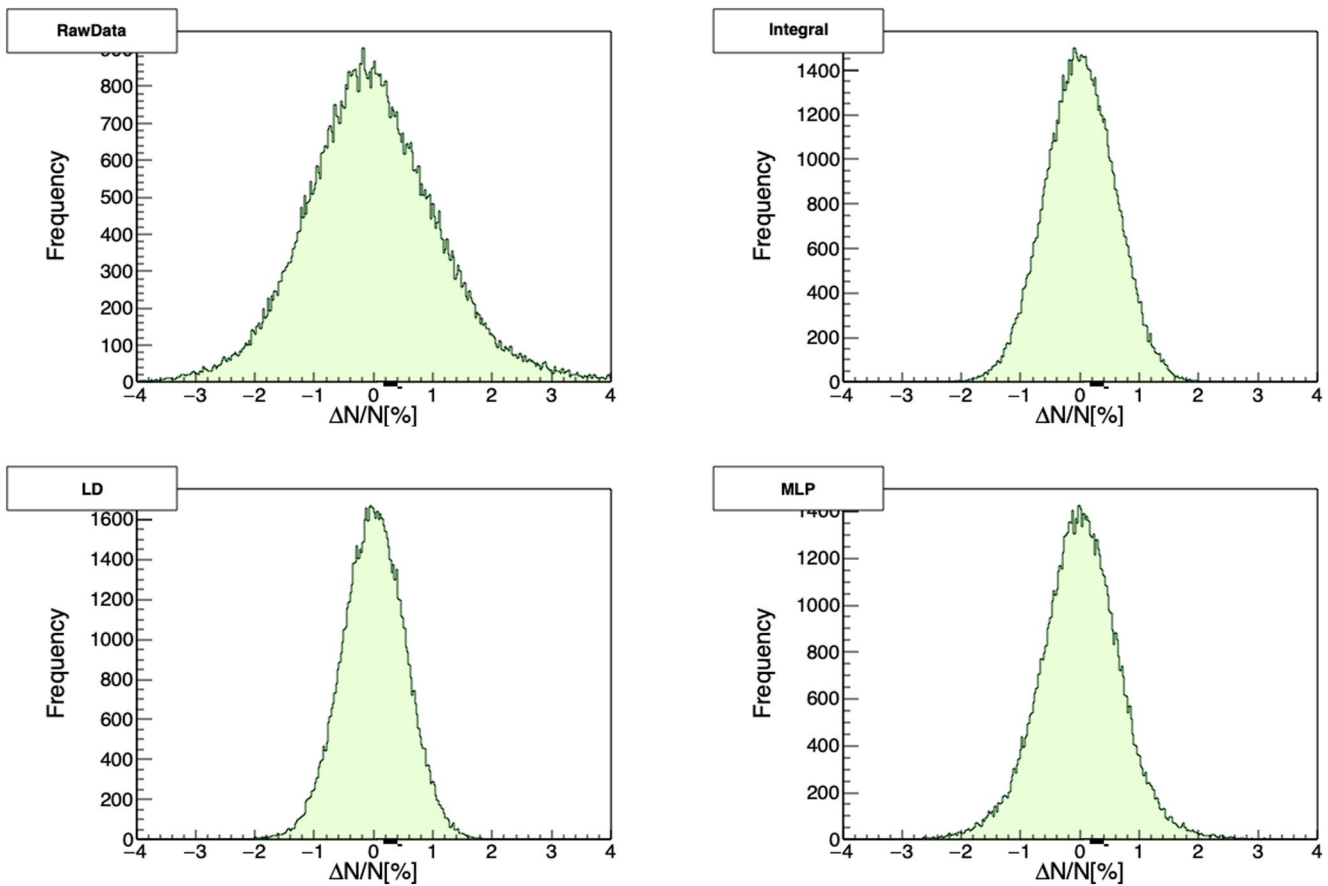


Figure 6. Relative variation of muon count rate calculated in respect to mean count in the ten-day moving window, for raw data (top left), PT corrected using integral method (top right), and data PT corrected using selected multivariate methods (second row).

believe pressure corrected neutron monitor data to be (in the first approximation) independent from meteorological effects, and hence a good reference for the evaluation of effectiveness of different methods for PT corrections of muon flux data.

For this comparison, we have chosen neutron monitors located in Athens and Rome, as they had the most consistent operation in the period we use for the analysis. Respective geomagnetic cutoff rigidities for these neutron monitors are 8.53 and 6.27 GV. Pressure and efficiency corrected relative neutron count rate was acquired via Neutron Monitor Database (NEST, 2020), presented for the said period in Figure 7. As for the muon flux data, relative neutron count rate time series were fitted with sinusoidal function, with a period of one year, to obtain the amplitude used as an estimate of the annual variation. Neutron monitors are more sensitive to lower energy secondaries than muon detectors so their time series can exhibit larger variations, which in turn can affect the fitting algorithm. However, in this case the fits seem to be dominantly affected by the relatively stable period between June and November 2010, hence we believe them to be a reliable estimate of the seasonal variation amplitude. Thus acquired annual variation amplitude for Rome neutron monitor is $(0.29 \pm 0.01)\%$, while for the Athens neutron monitor it is $(0.17 \pm 0.05)\%$.

Table 3
Standard Deviation of Relative Variation of Muon Count Rate for Raw and Data Corrected for Pressure and Temperature Effect (Using Integral and Selected Multivariate Methods)

Method	Raw	Integral	PDERS	KNN	LD	MLP	BDT	BDTG
Relative deviation (%)	1.117	0.592	0.990	0.785	0.533	0.687	0.607	0.551

Abbreviations: BDT, boosted decision tree; BDTG, gradient boosted decision tree; KNN, k-nearest neighbor; LD, linear discriminant.

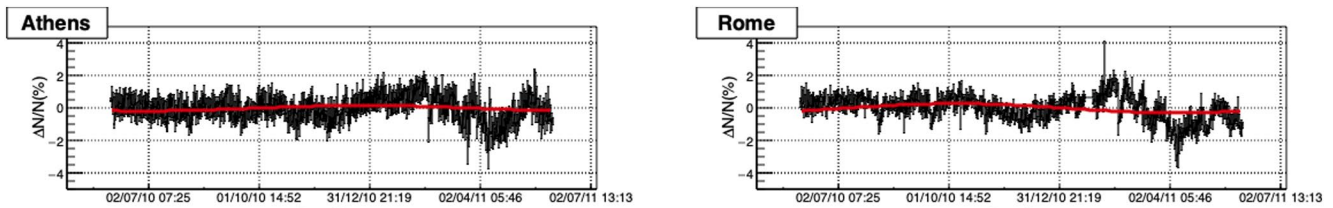


Figure 7. Relative neutron count rate time series for the period from June 1, 2010 to May 31, 2011 for Athens (left) and Rome (right) neutron monitors.

Comparing these values with the ones in Table 2, we see that methods KNN, LD, and BDT yield the most similar results. PDERS and MLP seem to underestimate the annual variation, while the integral method estimates a somewhat larger value.

Observed overall poor performance of KNN and PDERS algorithms could possibly be explained by the fact that these algorithms perform best when applied to problems involving strong nonlinear correlations, and are less efficient when dependencies between variables are dominantly linear (Hoecker et al., 2007). Additionally, these algorithms typically need a large training sample, so possibly statistics in our analysis was inadequate. However, artificial neural networks (such as MLP) should in principle be well suited for multivariate linear regression, and perform better than observed results suggest. Most likely, using minimization of the average quadratic deviation as a sole criterium for the selection of optimal parameters in the training phase may lead to overtraining (Montgomery et al., 2006), and additional qualitative criteria (i.e., ones introduced here) and more careful parameter control should also be used. BDT and BDTG algorithms performed reasonably well even though they are not optimized for treatment of linear multivariate problems, however, spectral analysis indicates a further improvement can be made. Additionally, all algorithms would probably benefit from a longer data interval of several years being used.

4.2. Effects of PT Correction on Aperiodic CR Variations

As mentioned before, apart from increasing sensitivity of muon detectors to periodic variations of primary cosmic rays, correcting raw muon flux data for meteorological parameters also affects detector sensitivity to aperiodic events which occur due to heliospheric modulation of primary cosmic rays. Here, we will analyze the effect PT correction, performed by application of different multivariate algorithms, has on detection of Forbush decrease events. We have chosen to concentrate on Forbush decreases as our muon detector is much less sensitive to other aperiodic events, such as ground level enhancements (GLE).

Forbush decrease (FD) events are typically characterized by their amplitude, so it could be a natural choice for a parameter to be used as a measure of detection sensitivity. However, another requirement for definition of sensitivity could be that detected signal significantly deviates from random fluctuations. That is, why we have decided to use the ratio of the amplitude to the standard deviation of muon flux, or relative amplitude, as an estimate of sensitivity to aperiodic events, rather than the actual amplitude. As we primarily focus on the magnitude of Forbush decreases, when we mention an FD event in the following text it mainly refers to the decrease phase and not the recovery phase.

To determine the amplitude, we have used a method proposed by Barbashina et al. (2009). The idea is to make the result independent from different trends leading up to, and following the actual FD. To do this, two intervals are defined: one i days before the onset of the FD, where i can have value $(1, \dots, n)$ days, and the other p days after the end of the decrease, where p can have value $(1, \dots, m)$ days. These intervals are then detrended using fit parameters obtained from linear regression. Mean count is determined for the detrended time series before the onset of FD for j days (where $j = 1, \dots, i$), and for the detrended time series during recovery stage for q days (where $q = 1, \dots, p$). Thus, in total we obtain $n!$ values for mean detrended count before the onset of FD, and $m!$ values for mean detrended count for the recovery stage. FD amplitude estimate is then calculated for each combination of “before” and “after” values according to the following formula:

$$A_{ij}^{pq} = \frac{\langle I_{before}^{(i,j)} \rangle - \langle I_{after}^{(p,q)} \rangle}{\langle I_{before}^{(i,j)} \rangle} \times 100\%, \quad (5)$$

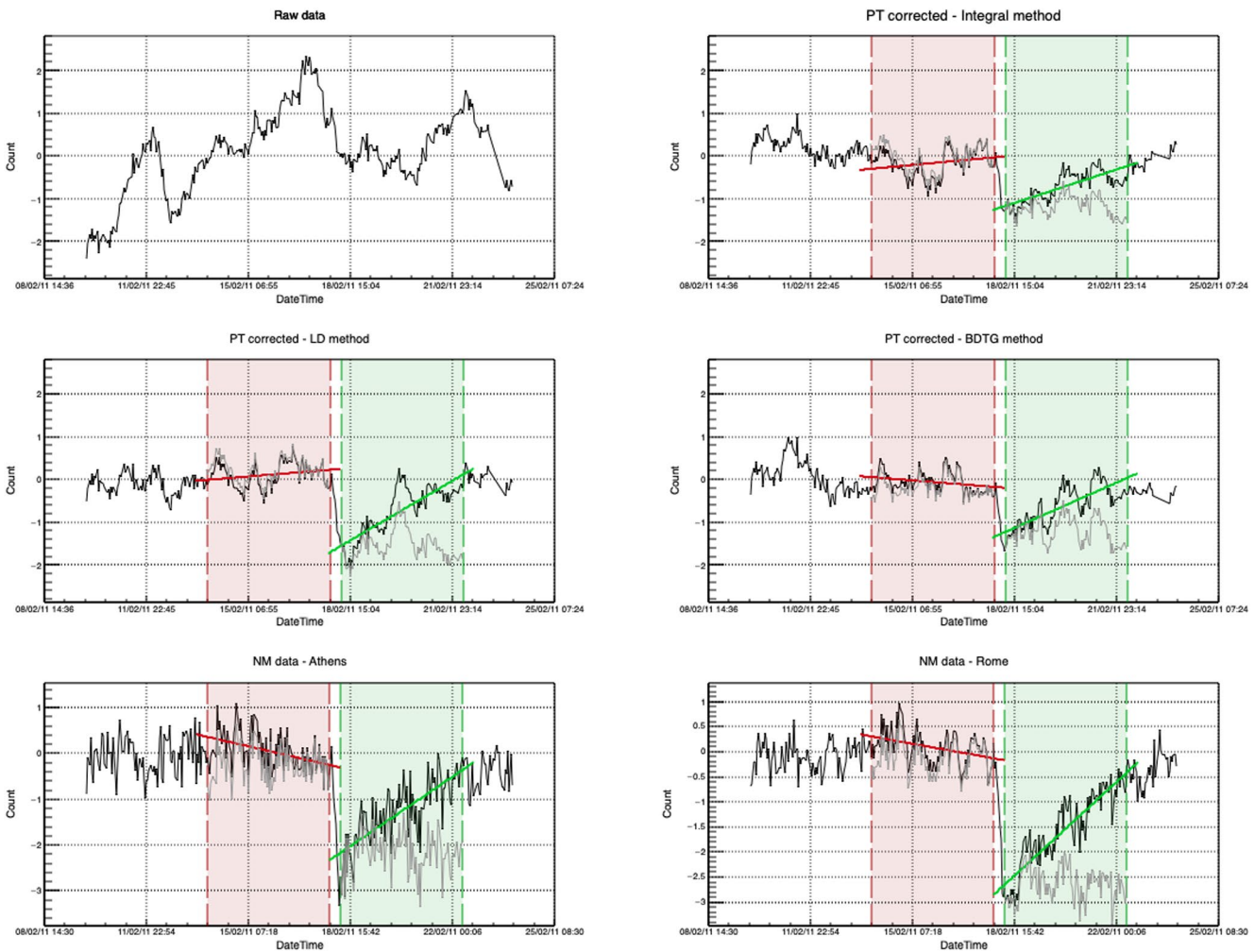


Figure 8. Time series for the interval around Forbush decrease of February 18, 2011: raw muon data (top left), PT corrected muon data using integral (top right), linear discriminant (center left) and gradient boosted decision tree (center right) methods, and neutron monitor data for Athens (bottom left) and Rome (bottom right) neutron monitors. Interval leading into (red) and following the Forbush decrease (FD) (green) are highlighted, as well as detrended intervals used to determine FD amplitude (gray).

where I_{before} and I_{after} are respective values for mean detrended count for intervals before the onset and after the end of the Forbush decrease. Finally, FD amplitude is calculated as the average of individual A_{ij}^{pq} values, rms deviation from the mean of the distribution used as an error estimate.

During the one-year period we used for the analysis there was a large number of Forbush events, but most of them had rather small amplitudes. We have analyzed several, however, here we will focus on the one with the largest magnitude as the results are most easily interpreted. The event is a Forbush decrease that occurred on February 18, 2011 in relation to X2.2 solar flare, and according to IZMIRAN space weather database (IZMIRAN, 2020) had 10 GV rigidity particle variation magnitude of 5.4. In Figure 8, we have shown plots that represent procedure described in the previous paragraph, applied to PT corrected datasets using integral method and selected multivariate algorithms. Procedure is also applied to pressure and efficiency corrected data for Athens and Rome neutron monitors, raw data also presented for reference. On the plots, interval leading into the onset of FD is indicated by red dashed lines, while recovery interval after the decrease is indicated by green dashed lines. We have chosen the lengths of both intervals to be four days ($n = m = 4$). Linear fits are represented by solid red and green lines, respectively, while detrended intervals are plotted using gray lines. Amplitudes and relative amplitudes calculated from the differences of means of detrended intervals are shown in Table 4.

Table 4
Amplitudes and Relative Amplitudes for the Forbush Decrease of February 18, 2011 for PT Corrected Muon Data and Selected Neutron Monitors

Method/NM monitor	Integral	LD	BDTG	Athens	Rome
FD amplitude (%)	1.38 ± 0.14	1.96 ± 0.18	1.10 ± 0.13	1.97 ± 0.15	2.68 ± 0.15
Relative FD amplitude	4.31 ± 0.44	7.09 ± 0.65	4.78 ± 0.56	5.30 ± 0.40	8.65 ± 0.48

Abbreviations: BDTG, gradient boosted decision tree; FD, Forbush decrease; LD, linear discriminant.

We see that relative amplitudes for this Forbush decrease, calculated based on data corrected for pressure and temperature using LD and BDTG algorithms, have sensitivity that is comparable or better than the sensitivity of integral method, even approaching the sensitivity of reference neutron monitors in the case of LD algorithm. However, when LD algorithm is concerned, such result can be at least in part explained by the fact that the calculated absolute FD amplitude is larger than expected for a muon detector. We would expect this value to be comparable to the value calculated based on the integral method. The reason for this discrepancy could be systematic, but also could be somewhat related to features of the studied FD event. Ideally, we should extend this analysis to more events, but selected time period was relatively calm in terms of solar activity, and February 2011 event was the only significant one with magnitude for 10 GV rigidity particles larger than five. Preliminary analysis done on Forbush decrease events of larger magnitude, that are outside the period used for analysis in this work, does show somewhat smaller effect for LD method, so that could be one of the focuses in the continuation of this work. We have excluded plots for the remaining multivariate algorithms as the results were either poorer (in the case of BDT and MLP) or inconsistent (in the case of PDERS and KNN).

5. Conclusions

We have selected a number of multivariate algorithms included in the TMVA package to apply for the correction of barometric and temperature effect on cosmic ray muons. Optimal parameters were determined for each algorithm based on the average quadratic deviation of modeled from measured data. Different distributions of modeled data for training phase and after the application of trained methods were compared to estimate the performance of selected algorithms. Pressure and temperature correction was done and spectral analysis performed to further test the algorithm consistency. The effect of the correction was analyzed for long-term (annual) and short-term (Forbush decrease) cosmic ray variations. In both cases, the efficiency of multivariate algorithms was compared to integral method and pressure corrected neutron monitor data.

Multidimensional probability density estimator algorithms (PDERS and KNN) appear not to be well suited for the modeling of pressure and temperature effect, most likely due to highly linear correlations between variables. MLP seems to have underperformed, while methods based on boosted decision trees (particularly BDTG) proved to be more successful, especially when effect on aperiodic variations was concerned. It should be expected that both MLP and BDT(G) methods can be improved if a longer period is used for analysis and parameters beyond average quadratic deviation of modeled data are used for algorithm optimization during training phase. Out of presented algorithms, LD proved to be the most consistent and effective in removing the pressure and temperature effects. In terms of the effect of PT correction on annual and aperiodic variations, this method matched or outperformed the integral method, while the effect it had on aperiodic effects was somewhat overestimative. This could give us grounds to assume at least part of the temperature effect is not taken into account by the integral method, and that there could be room for further improvement in modeling of meteorological effects beyond what theory currently provides.

Data Availability Statement

Raw muon count rate data set used in this study are publicly available online on the Belgrade Cosmic Ray Station site (<http://www.cosmic.ipb.ac.rs/>). Modeled atmospheric temperature data are available online on the NOAA GFS page (<https://www.ncdc.noaa.gov/data-access/model-data/model-datasets/global-forecast>

system-gfs). Latest atmospheric pressure and ground temperature data are available online on the site of Republic Hydro-meteorological Service of Serbia (<http://www.hidmet.gov.rs/>). List of international geomagnetically quiet days can be downloaded from the GFZ site (<https://www.gfz-potsdam.de/en/kp-index/>). Neutron monitor data can be accessed online via NEST browser interface (<http://www01.nmdb.eu/nest/>).

Acknowledgments

The authors acknowledge funding provided by the Institute of Physics Belgrade, through the grant by the Ministry of Education, Science and Technological Development of the Republic of Serbia.

References

- Barbashina, N., Dmitrieva, A., Kompaniets, K., Petrukhin, A., Timashkov, D., Shutenko, V., et al. (2009). Specific features of studying Forbush decreases in the muon flux. *Bulletin of the Russian Academy of Sciences: Physics*, 73, 343–346. <https://doi.org/10.3103/S1062873809030198>
- Barrett, P. H., Bollinger, L. M., Cocconi, G., Eisenberg, Y., & Greisen, K. (1952). Interpretation of cosmic-ray measurements far underground. *Reviews of Modern Physics*, 24, 133–178. <https://doi.org/10.1103/RevModPhys.24.133>
- Belov, A., Blokh, Y., Dorman, L., & Rogovaya, S. (1987). The temperature diagnostics of the atmosphere allowing for the temperature of the near-surface layer. *International Cosmic Ray Conference*, 4, 263.
- Berkova, M., Belov, A., Eroshenko, E., & Yanke, V. (2012). Temperature effect of muon component and practical questions of how to take into account in real time. *Astrophysics and Space Sciences Transactions*, 8, 41–44. <https://doi.org/10.5194/astra-8-41-2012>
- Blackett, P. M. S. (1938). On the instability of the Barytron and the temperature effect of cosmic rays. *Physical Review*, 54, 973–974. <https://doi.org/10.1103/PhysRev.54.973>
- Carli, T., & Koblitz, B. (2003). A multi-variate discrimination technique based on range-searching. *Nuclear Instruments and Methods in Physics Research Section A: Accelerators, Spectrometers, Detectors and Associated Equipment*, 501, 576–588. [https://doi.org/10.1016/S0168-9002\(03\)00376-0](https://doi.org/10.1016/S0168-9002(03)00376-0)
- Dorman, L. I. (1954). On the temperature effect of the hard component of cosmic rays. *Reports of Academy of Sciences of USSR (DAN SSSR)*, 95, 49–52.
- Dorman, L. I. (2004). *Cosmic rays in the Earth's atmosphere and underground*. Springer. Retrieved from <https://books.google.rs/books?id=mKlv68WBU5kC>
- Dragić, A., Joković, D., Banjanac, R., Udovičić, V., Panić, B., Puzović, J., & Aničin, I. (2008). Measurement of cosmic ray muon flux in the Belgrade ground level and underground laboratories. *Nuclear Instruments and Methods in Physics Research Section A: Accelerators, Spectrometers, Detectors and Associated Equipment*, 591(3), 470–475.
- Dragic, A. L., Udovicic, V. I., Banjanac, R., Jokovic, D. R., Maletic, D. M., Veselinovic, N. B., et al. (2011). The new set-up in the Belgrade low-level and cosmic-ray laboratory. *Nuclear Technology & Radiation Protection*, 26(3), 181–192. <https://doi.org/10.2298/NTRP1103181D>
- Duperier, A. (1949). The meson intensity at the surface of the Earth and the temperature at the production level. *Proceedings of the Physical Society Section A*, 62(11), 684–696. <https://doi.org/10.1088/0370-1298/62/11/302>
- Dvornikov, V. M., Krestyannikov, Y. Y., & Sergeev, A. (1976). Determination of the mass-average temperature on the cosmic ray intensity data. *Geomagnetism and Aeronomy*, 16, 923–925.
- Feinberg, E. L. (1946). On the nature of cosmic ray barometric and temperature effects. *Reports of Academy of Sciences of USSR (DAN SSSR)*, 53, 421–424. <https://doi.org/10.1038/157421a0>
- Forbush, S. E. (1937). On the effects in cosmic-ray intensity observed during the recent magnetic storm. *Physical Review*, 51, 1108–1109. <https://doi.org/10.1103/PhysRev.51.1108.3>
- Forró, M. (1947). Temperature effect of cosmic radiation at 1000-m water equivalent depth. *Physical Review*, 72, 868–869. <https://doi.org/10.1103/PhysRev.72.868>
- GFS. (2020). Retrieved from <https://www.ncdc.noaa.gov/data-access/model-data/model-datasets/global-forecast-system-gfs>
- GFZ Potsdam. (2020). Retrieved from <https://www.gfz-potsdam.de/en/kp-index/>
- Hess, V. F. (1940). On the seasonal and the atmospheric temperature effect in cosmic radiation. *Physical Review*, 57, 781–785. <https://doi.org/10.1103/PhysRev.57.781>
- Hoecker, A., Speckmayer, P., Stelzer, J., Therhaag, J., von Toerne, E., Voss, H., & Zemla, A. (2007). *Tmva—Toolkit for multivariate data analysis*. Ithaca, NY: Cornell University.
- IZMIRAN. (2020). Retrieved from <http://spaceweather.izmiran.ru/eng/dbs.html>
- Joković, D. (2011). *Detekcija i spektroskopija miona iz kosmičkog zračenja plastičnim scintilacionim detektorima (Detection and spectroscopy of cosmic ray muons with plastic scintillation detectors) (Doctoral dissertation)*. Faculty of Physics, University of Belgrade. Retrieved from <http://www.cosmic.ipb.ac.rs/documents/jokovic-thesis.pdf>
- Kaminer, N. S., Ilgatch, S. F., & Khadakhanova, T. S. (1965). Temperature effect of the cosmic ray neutron component. In *Proceedings of the 9th International Cosmic Ray Conference* (Vol. 1, p. 486).
- Kohno, T., Imai, K., Inue, A., Kodama, M., & Wada, M. (1981). Estimation of the vertical profile of atmospheric temperature from cosmic-ray components. In *Proceedings of the 17th International Cosmic Ray Conference* (Vol. 10, p. 289).
- Lalchand, V. (2020). Extracting more from boosted decision trees: A high energy physics case study. In *33rd Annual Conference on Neural Information Processing Systems* (Vol. 1).
- Low Background Laboratory for Nuclear Physics. (2020). Retrieved from <http://www.cosmic.ipb.ac.rs/>
- Maeda, K., & Wada, M. (1954). Atmospheric temperature effect upon the cosmic ray intensity at sea level. *Journal of the Scientific Research Institute*, 48, 71–79.
- Montgomery, D. C., Peck, E. A., & Vining, G. G. (2006). *Introduction to linear regression analysis* (4th ed.). Hoboken, NJ: Wiley & Sons.
- Morozova, A. L., Blanco, J. J., & Ribeiro, P. (2017). Modes of temperature and pressure variability in midlatitude troposphere and lower stratosphere in relation to cosmic ray variations. *Space Weather*, 15(5), 673–690. <https://doi.org/10.1002/2016SW001582>
- Myssowsky, L., & Tuwim, L. (1926). Unregelmäßige intensitätsschwankungen der höhenstrahlung in geringer seehöhe. *Zeitschrift für Physik*, 39, 146–150. <https://doi.org/10.1007/BF01321981>
- NEST. (2020). Retrieved from <http://www01.nmdb.eu/nest/>
- Press, W. H., Teukolsky, S. A., Vetterling, W. T., & Flannery, B. P. (2007). *Numerical recipes 3rd edition: The art of scientific computing* (3rd ed.). New York: Cambridge University Press.
- Quenby, J. J., & Thamyahpillai, T. (1960). Atmospheric temperature effects on the solar daily variation of cosmic ray intensity. *The Philosophical Magazine: A Journal of Theoretical Experimental and Applied Physics*, 5(54), 585–600. <https://doi.org/10.1080/14786436008241210>
- RHMZ. (2020). Retrieved from <http://www.hidmet.gov.rs/index-eng.php>

- Savic, M., Dragic, A., Veselinovic, N., Udovicic, V., Banjanac, R., Jokovic, D., & Maletic, D. (2016). Effect of pressure and temperature corrections on muon flux variability at ground level and underground. In *25th European cosmic ray Symposium*.
- Savic, M. R., Dragic, A. L., Maletic, D. M., Veselinovic, N. B., Banjanac, R. M., Jokovic, D. R., & Udovicic, V. I. (2019). A novel method for atmospheric correction of cosmic-ray data based on principal component analysis. *Astroparticle Physics*, *109*, 1–11. <https://doi.org/10.1016/j.astropartphys.2019.01.006>
- Veselinović, N., Dragić, A., Savić, M., Maletić, D., Joković, D., Banjanac, R., & Udovičić, V. (2017). An underground laboratory as a facility for studies of cosmic-ray solar modulation. *Nuclear Instruments and Methods in Physics Research Section A: Accelerators, Spectrometers, Detectors and Associated Equipment*, *875*, 10–15. <https://doi.org/10.1016/j.nima.2017.09.008>
- Wada, M. (1962). Atmospheric effects on the cosmic-ray meson intensity. *Journal of the Physical Society of Japan Supplement*, *17*, 508. <https://doi.org/10.1143/jpsj.17.1805>



Rigidity dependence of Forbush decreases in the energy region exceeding the sensitivity of neutron monitors

M. Savić, N. Veselinović*, A. Dragić, D. Maletić, D. Joković, R. Banjanac, V. Udovičić

Institute of Physics, University of Belgrade, Pregrevica 118, 11080 Zemun, Serbia

Received 2 May 2018; received in revised form 14 September 2018; accepted 24 September 2018

Available online 28 September 2018

Abstract

Applicability of our present setup for solar modulation studies in a shallow underground laboratory is tested on four prominent examples of Forbush decrease during solar cycle 24. Forbush decreases are of interest in space weather application and study of energy-dependent solar modulation, and they have been studied extensively. The characteristics of these events, as recorded by various neutron monitors and our detectors, were compared, and rigidity spectrum was found. Linear regression was performed to find power indices that correspond to each event. As expected, a steeper spectrum during more intense extreme solar events with strong X-flares shows a greater modulation of galactic cosmic rays. Presented comparative analysis illustrates the applicability of our setup for studies of solar modulation in the energy region exceeding the sensitivity of neutron monitors.

© 2018 COSPAR. Published by Elsevier Ltd. All rights reserved.

Keywords: Forbush decrease; Muon CR station; Median rigidity

1. Introduction

Galactic cosmic rays (GCRs) traverse the heliosphere; this leads to variation in the cosmic ray (CR) flux due to solar activity. The influence of solar and heliospheric modulation is pronounced for primary CR particles with low rigidity or momentum over unit charge. CRs interact, upon arrival, with Earth's atmosphere causing electromagnetic and hadronic showers. A network of ground-based CR detectors, neutron monitors (NMs), and muon detectors, located at various locations around the globe, as well as airborne balloons and satellites, provide valuable data to study the effect of these modulations on the integrated CR flux with time. Energies of the primary particles in NMs are sensitive to the state of solar activity and reach up to 40 GeV. Muon detectors have a significant response from 10 GeV up to several hundred GeV for surface, and

one order of magnitude greater for underground detectors, depending on the depth (Duldig, 2000). This energy interval allows muon detectors to monitor not only modulation effects on lower-energy CRs but also galactic effects on primary CRs with high energies where solar modulation is negligible. Because of the sensitivity to different energies of the primary particle flux, observations of muon detectors complement those of NMs in studies of long-term CR variations, CR anisotropy, and gradients or rigidity spectrum of Forbush decreases (FDs).

FDs (Forbush, 1954) represent decreases of the observed GCR intensity under the influence of coronal mass ejections (CMEs) and interplanetary counterparts of coronal mass ejections (ICMEs) and/or high-speed streams of solar wind (HSS) from the coronal holes (Belov, 2008). FDs belong to two types depending on the drivers: non-recurrent and recurrent decreases. This work addresses several non-recurrent FDs.

These sporadic FDs are caused by ICMEs. As the matter with its magnetic field moves through the solar system,

* Corresponding author.

E-mail address: veselinovic@ipb.ac.rs (N. Veselinović).

it suppresses the CR intensity. FDs of this kind have an asymmetric profile, and the intensity of GCRs has a sudden onset and recovers gradually. Sometimes an early phase of FD prior to the dip (precursor of FD) shows an increase in CR intensity. These precursors of FDs are caused by GCR acceleration at the front of the advancing disturbance on the outer boundary of the ICME, as the primary CR particles are being reflected from the approaching shock (Papailiou et al., 2013). The FD profile depends on the area, velocity, and intensity of CME magnetic field produced in extreme events that originate at the Sun (Chauhan et al., 2008).

Data from observed modulation of GCR intensity contain information regarding the transport of GCRs through the interplanetary environment. GCR transport parameters are connected with the interplanetary magnetic field (IMF) in the heliosphere. It is empirically established that the radial diffusion coefficient is proportional to the rigidity of CR (Ahluwalia, 2005). In this article, we present an analysis of the amplitude of FD during four events, which were recorded by plastic scintillator muon detectors, located at the Belgrade muon station, as well as by a network of NMs.

2. Belgrade CR station

The Low-Background Laboratory for Nuclear Physics (LBNP) is a part of the Institute of Physics, University of Belgrade. It is composed of two separate laboratory facilities, ground-level laboratory (GLL) and underground laboratory (UL), dug into a cliff. The overburden of the UL is approximately 12 m of loess soil, which is equivalent to 25 m of water (m.w.e). Laboratory is dedicated to measurements of low radiation activities and studies of muon and electromagnetic components of CRs at ground and shallow underground levels. The geographic position of the laboratory is at 75 m a.s.l., at 44°51'N latitude and 20°23'E longitude; geomagnetic vertical rigidity cutoff is 5.3 GV at the surface. The equipment was upgraded in 2008, and now, it consists of two identical sets of detectors and accompanying data processing electronics: one is situated in GLL and the other in UL. Detectors are a pair of plastic scintillator detectors, with dimensions of 100 cm × 100 cm × 5 cm and four PMTs that are directly coupled to the corners. Signals from two opposite PMTs on a single detector are summed, and the coincidence of the two diagonals is found. Fig. 1 presents the coincident sum spectra of two diagonals of large scintillator detectors.

Summing over diagonals suppresses the acquisition of electromagnetic component of the secondary CR shower and collects mainly the muon component of secondary CRs. A well-defined peak in the energy spectra corresponds to a muon energy loss of ~11 MeV. The average muon flux measured in the laboratory is 137(6) muons/m²s for GLL and 45(2) muons/m²s for UL. For more detailed description, see Dragić et al. (2011). Integral of this distribution, without low energy part, is used to form time series of this

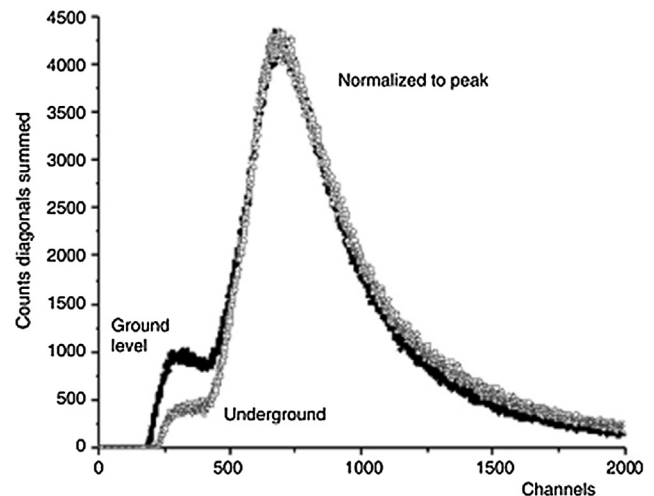


Fig. 1. The coincident spectra of two diagonals of large plastic detectors in UL and GLL normalized for comparison.

CR muons spectrum integrated over different time intervals. This time series is then corrected for efficiency, atmospheric pressure, and temperature (Savić et al., 2015).

The CR flux measured at the ground level varies because of changes in atmospheric conditions. Effects of the atmospheric pressure can be easily accounted for, similar like for NMs, but the temperature effect is somewhat more difficult to treat. The difficulties arise from the interplay of positive and negative temperature effects. With temperature increase, the atmospheric density decreases; hence, less pions interact and more muons are created from decay. The result is a positive effect of more muons at the ground level. On the other hand, the altitude of muon production level is high due to the expansion of the atmosphere when the temperature is high, muon path length is long, and decay probability of muons is high before they reach the ground level. Negative effect is dominant for low-energy muons (mostly detected in GLL) and positive for high-energy muons. A proper treatment of the temperature effect requires knowledge of the entire temperature profile of the atmosphere. This meteorological variation must be corrected to study CR variations originating outside the atmosphere.

For ground (and underground)-based CR detectors, the response function, i.e., the relation between particles of GCR spectra at the top of the atmosphere and recorded secondary particles at the surface level, should be accurately known. The total detector count rate can be expressed as follows (Caballero-Lopez and Moraal, 2012):

$$\begin{aligned} N(R_0, h, t) &= \sum_i \int_{R_0}^{\infty} (S_i(R, h) j_i(R, t)) dR \\ &= \int_{R_0}^{\infty} W(R, h, t) dR \end{aligned} \quad (1)$$

where $N(R_0, h, t)$ is the detector counting rate, R_0 is the geomagnetic cutoff rigidity, h is the atmospheric depth, and t represents time. $S_i(R, h)$ represents the detector yield

function for primary particles of type i and $j_i(R, t)$ represents the primary particle rigidity spectrum of type i at time t . The total response function $W(R, h, t)$ is the sum of $S_i(R, h)$ and $j_i(R, t)$. The maximum value of this function is in the range of 4–7 GV at sea level, depending on the solar modulation epoch at time t (Clem and Dorman, 2000). One of the methods to find this response function is to use the numerical simulation of propagation of CRs through the atmosphere. CORSIKA simulation package (Heck et al., 1998) was to simulate CR transport through the atmosphere and GEANT4 (Agostinelli et al., 2003) to simulate the propagation of secondary CRs through overburden and response of the detectors to find the relationship between the count rate at our site and the flux of primary particles on top of the atmosphere.

The excellent agreement of the simulated and measured flux (Fig. 2) allows us to establish that the cutoff energy for primary CR protons for showers detected in GLL is caused by its geomagnetic rigidity, and the median energy is ~ 60 GeV. For UL, the cutoff energy due to earth overburden is 12 GeV, and the median energy is ~ 120 GeV. These values give us opportunity to study solar modulation at energies exceeding energies detected with a NM. Observation of the solar activity and related magnetic disturbances in the heliosphere that create transient CR intensity variation at several different energies can provide an energy-dependent description of these phenomena.

3. Data analysis

The new setup in the LBLNP, presented by Dragić et al. (2011) coincides with the start of the 24th solar cycle, thus allowing us to observe the increase and decrease in solar activity and the effect of solar modulation at energies higher than ones studied using NMs.

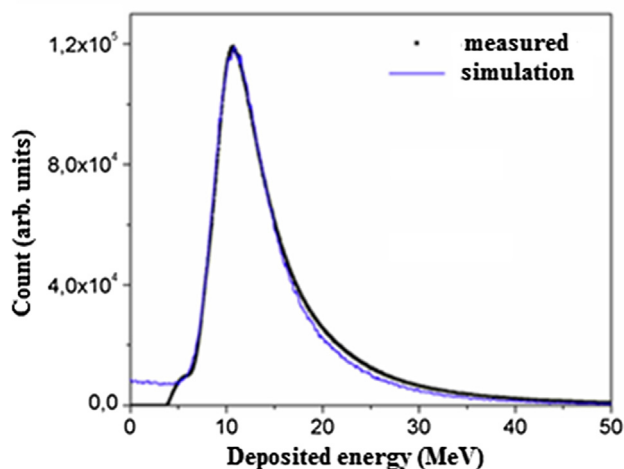


Fig. 2. Simulated (blue line) and measured spectra (black line) for muon detectors in UL. (For interpretation of the references to colour in this figure legend, the reader is referred to the web version of this article.)

Muon time series was searched for days where the average muon flux was significantly lower than the background level. The background level is determined from the moving averages of hourly count rates 10 days before the event. These decreases in the count rate, in GLL and UL, are then compared with space weather events of solar cycle 24. Data collected in UG and GLL are compared with four NM stations from the neutron monitor database [<http://www.nmdb.eu/>]. Three of these NMs (Athens, Rome, and Jungfraujoch) have cutoff rigidity and geographic proximity similar to the Belgrade CR station.

A high correlation is found between the count rates measured by the NMs in the LBLNP in March 2012 (Table 1), but for GLL and UL, as the cutoff energy of the primary flux increases, the correlation slightly decreases.

3.1. Selected Forbush decreases

The Belgrade CR station has detected, both in GLL and UL, several significant structures connected to some extreme solar effects. Several, more prominent, Forbush decreases occurred in March 2012, September 2014, June 2015, and most recently in September 2017.

The FD that occurred on March 8, 2012 was recorded at the Belgrade CR station as well as at other stations (Fig. 3). This FD was separated into two following two CMEs. These CMEs produced an intense disturbance in the interplanetary space and caused a severe geomagnetic storm when the shockwave reached Earth on March 8, 2012. During this event, a very complex combination of modulation occurs (Lingri et al., 2016). Two CMEs from the same active region as the September 10 (X1.6) flare produced FD on September 12, 2014. There was a relatively fast partial halo CME and a larger and rapidly moving halo CME trailing behind the first one on September 10. These two gave rise to the FD that was first detected by NMs on September 12, 2014. This FD was not a classical two-step FD as expected, probably due to the interaction of slower and faster CMEs. The FD profile (Fig. 3) showed a small second step several hours after the first, similar to the FD that occurred in February 2011 (Papaioannou et al., 2013). In June 2015, a large activity occurred in the Sun from powerful AR 2371 that produced several CMEs from the Sun. These CMEs induced a complex modulation of GCRs that led to an FD occurrence on June 22, 2015 with an unusual structure (Samara et al., 2018).

A sudden burst of activity from the Sun early in September 2017, after a prolonged period of low solar activity, produced several flares, including the largest solar flare seen from Earth since 2006, an X9.3 flare. This activity produced several Earth-directed CMEs. Throughout this time, Earth experienced a series of geomagnetic storms, which started promptly after the first CME. This unusual activity produced an FD, which was recorded with detectors in terms of ground level enhancement (GLE) on Earth and Mars (Guo et al., 2018).

Table 1

Correlation matrix of the linear correlation coefficient (in%) for recorded hourly flux at the Belgrade CR station with its temperature- and pressure-corrected underground and ground-level detectors (UL_tpc and GLL_tpc), only pressure-corrected detectors (UL_pc, GLL_pc), and raw data detectors (UL_raw and GLL_raw) and recordings at Rome, Oulu, Jungfraujoch (Jung.) and Athens NMs for March 2012.

UL_tpc	75	81	80	81	76	73	78	86	97	100
UL_pc	77	83	83	83	73	78	72	84	100	97
UL_raw	57	71	70	74	94	49	51	100	84	86
GLL_tpc	86	86	84	83	59	90	100	51	72	78
GLL_pc	90	92	90	89	56	100	90	49	78	73
GLL_raw	63	79	78	81	100	56	59	94	73	76
Oulu	90	98	98	100	81	89	83	74	83	81
Jung.	91	98	100	98	78	92	84	70	83	80
Rome	91	100	98	98	79	92	86	71	83	81
Athens	100	91	91	90	63	90	86	57	77	75
	Athens	Rome	Jung.	Oulu	GLL_raw	GLL_pc	GLL_tpc	UL_raw	UL_pc	UL_tpc

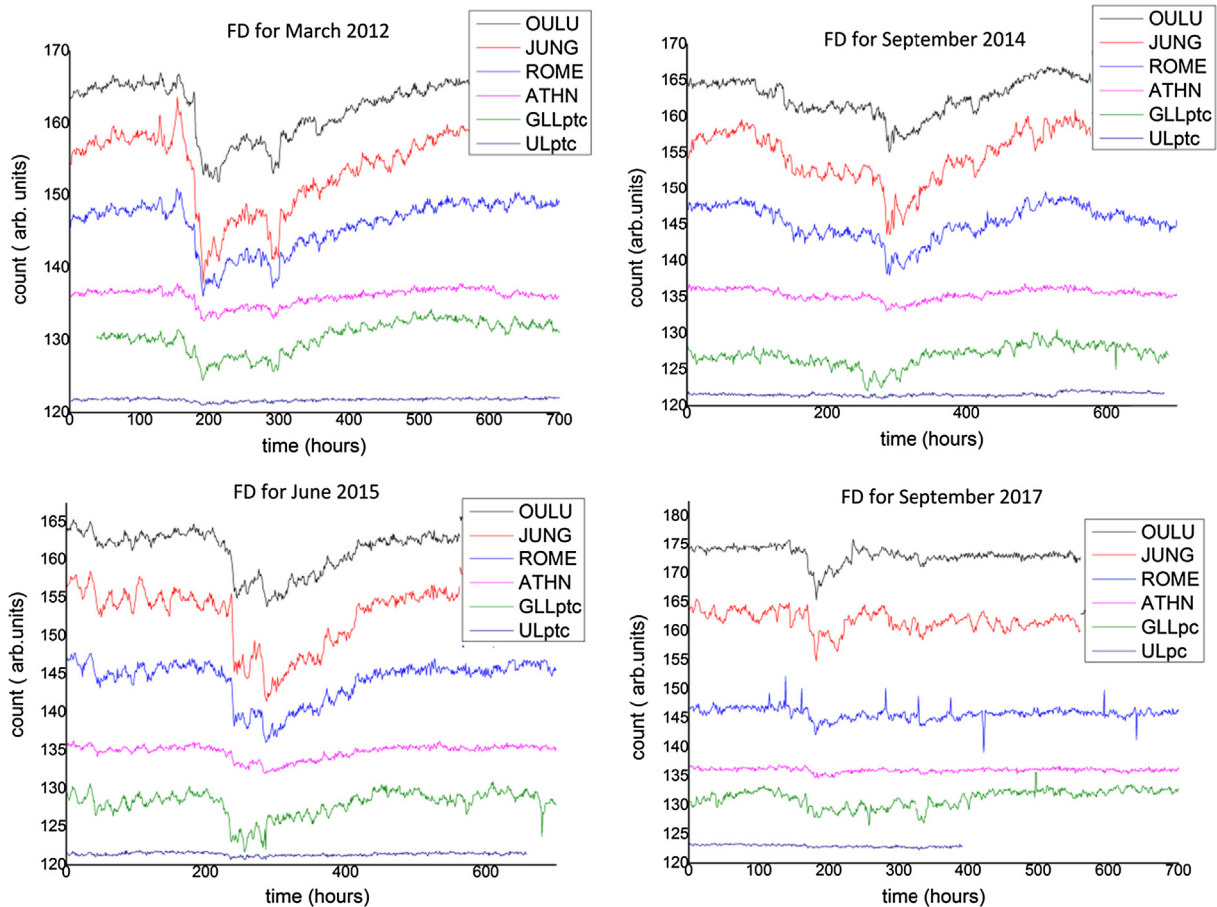


Fig. 3. Comparison of hourly time series over a one month period for pressure- and temperature-corrected count rates of the Belgrade muon monitor station (GLL_{ptc} and UL_{ptc}) and NMs at Athens (ATHN), Rome (ROME), Jungfraujoch (JUNG), and Oulu (OULU) for extreme solar events in March 2012, September 2014, and June 2015. Count rates are shifted for comparison. For extreme solar event in September 2017, for GLL and UL, the count rate is pressure-corrected only.

4. FD and median rigidity

For each event, we study the energy dependence of FD amplitude. The energy dependence of FD amplitude is

expected to follow the power law: $\Delta N/N \sim R^{-\gamma}$ (Cane, 2000). To obtain reliable values of amplitudes, we defined amplitude as a relative decrease in the hourly count rate of the minimum compared with the average of seven days'

Table 2
Median and cutoff rigidity for several stations.

Stations	Median rigidity R_m (GV)	Min. rigidity R_0 (GV)
Athens	25.1	8.53
Mexico	25.1	8.28
Almaty	15.8	6.69
Lomnický štít	12.6	3.84
Moscow	15.8	2.43
Kiel	15.8	2.36
Yakutsk	12.6	1.65
Apatity	12.6	0.65
Inuvik	12.6	0.3
Mc Murdo	12.6	0.3
Thule	12.6	0,3
South Pole	10	0.1
UL	122	12.3
GLL	63	5.3

count rate before FDs (not including possible precursory increases). Such a long base period was used because of the higher activity of the Sun prior to registered FDs and sensitivity of the muon detectors.

Amplitudes are determined for two of our detectors and for 12 NMs. To investigate the rigidity spectrum of

Table 3
Power indices of the median rigidity dependence of the dip of the FD. Power indices are obtained for NMs only, NMs and the Belgrade muon station, and Belgrade station only.

γ	NM only	NM + Belgrade	Belgrade station only
March 2012	0.82 ± 0.08	0.78 ± 0.03	0.715
Sept. 2014	0.79 ± 0.16	0.67 ± 0.06	0.744
June 2015	0.57 ± 0.05	0.58 ± 0.02	0.764
Sept. 2017	1.27 ± 0.16	0.86 ± 0.07	0.739

mentioned FDs, the median rigidity R_m is defined. R_m is the rigidity of the response of the detector to GCR spectrum where 50% of the detector counting rate lies below R_m (Ahluwalia and Fikani, 2007). For this study, we used a list of R_m for 12 NM stations given by Minamino et al. (2014). For an NM, the median rigidity can be computed from the detector response function derived from surveys for particulate station, usually around the minima of solar activity; this is because the intensity of lowest rigidity GCRs is maximum at that time.

For the Belgrade muon station, R_m was found using the response function acquired by the Monte Carlo method of

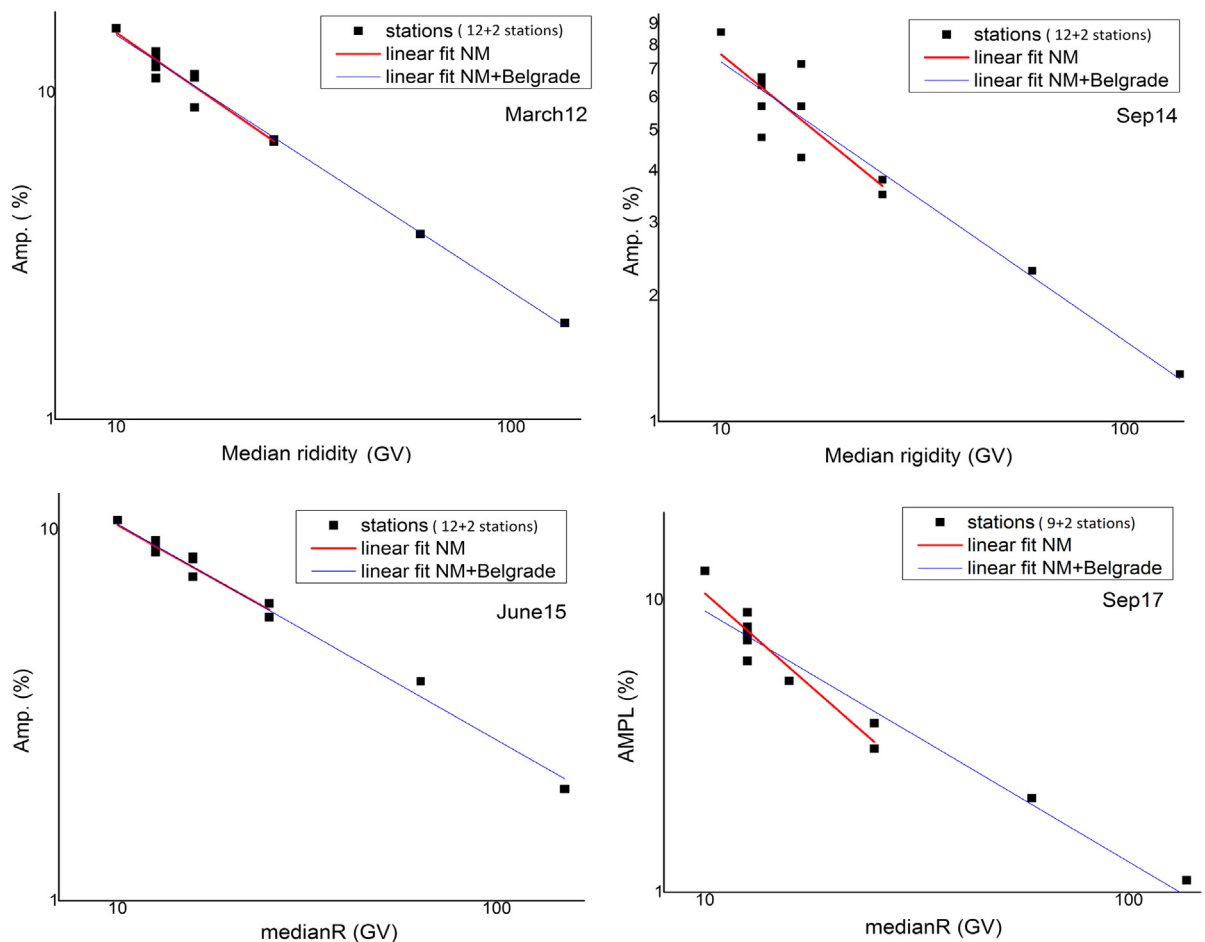


Fig. 4. Rigidity spectrum of FD from March 8, 2012, September 12, 2014, June 22, 2015, and September 8, 2017. Points represent the amplitude of the event as seen by NMs and the Belgrade CR station.

CR transport. Approximate values of R_m for the detectors used in this study are provided in Table 2.

For every selected event, a scatter plot is drawn (Fig. 4). All plots show, plotted in log-log scale, a clear median rigidity dependence of the amplitude of FD decrease.

Linear regression was performed to find power indices corresponding to each event. Power indices are given in Table 3.

Higher power indices can be due to more complex variations in GCRs. This more complex variation is a result of a series of CMEs during this event that leads to large compound ICME structure with multiple shocks and transient flow (Zhao and Zhang, 2016). Results obtained from the power law are generally consistent with those obtained in previous studies (Ahluwalia and Fikani, 2007, Lingri et al., 2016, Klyueva et al., 2017) conducted for NMs only.

A more significant difference observed for indices during the 2017 event was because we used only pressure-corrected data for the muon flux recorded at the Belgrade station. For all other events and data, we performed both pressure and temperature correction. Without temperature corrections, variation in the count rate in muon detectors is higher and it can affect the results.

We expect that when the newly improved, internally developed technique for temperature correction of the CR flux is implemented, the amplitude of the FD measured at the Belgrade muon station will be more consistent with other events and measurements. More data points on the graphs are needed to understand indices better, particularly in an energy region between NM and our laboratory. Similar work (Braun et al., 2009) discussed the extension up to 15 and 33 GeV, but there are no data available for FDs during cycle 24 and cannot be incorporated into this work. As for other operating muon telescopes, there is an agreement between the data obtained at our stations data and the URAGAN data for FD in June 2015 (Barbashina et al., 2016), but we have no data on other FDs and/or median energies of other stations. Our new experimental setup described elsewhere (Veselinović et al. 2017) will provide two additional median energies (121 and 157 GeV) to monitor variations in the CR flux.

5. Conclusion

The Belgrade CR station, with both ground level and underground setups, monitors the effect of solar modulation on the CR flux since 2008. Extreme solar events, like Forbush decreases, were detected during solar cycle 24 at the site, suggesting that these phenomena can be studied at energies higher than typical ones detected with NMs. GLL and UL data, as well as data from several NM stations, were used to analyze four intense FDs. The magnitude of FDs is energy (rigidity) dependent and follows the power law. Data used to find the rigidity dependence of these transient solar modulation of GCR were obtained over much higher range of rigidities than region NMs are

sensitive in, thus allowing more extensive studies of CR solar modulation processes.

Acknowledgements

We acknowledge the NMDB (www.nmdb.eu), founded under the European Union's FP7 programme (contract no. 213007), for providing data. We acknowledge individual monitors for following the information given on the respective station information page. *Athens NM data were kindly provided by the Physics Department of the National and Kapodistrian University of Athens. Jungfrauoch NM data were kindly provided by the Physikalisches Institut, University of Bern, Switzerland. Oulu NM data were kindly provided by <http://cosmicrays oulu.fi> and Sodankylä Geophysical Observatory. Rome NM data were kindly provided by SVIRCO NM, supported by INAF/IAPS-UNIRoma3 COLLABORATION.* We thank the anonymous referees for useful advices.

The present work was funded by the Ministry of Education, Science and Technological Development of the Republic of Serbia, under Project No. 171002.

References

- Agostinelli, S., et al., GEANT4—A Simulation Toolkit, 2003. Nuclear Instruments and Methods in Physics Research Section A 506, pp. 250–303. [https://doi.org/10.1016/S0168-9002\(03\)01368-8](https://doi.org/10.1016/S0168-9002(03)01368-8).
- Ahluwalia, H.S., 2005. Cycle 20 solar wind modulation of galactic cosmic rays: understanding the challenge. *J. Geophys. Res.* 110, A10106. <https://doi.org/10.1029/2005JA011106>.
- Ahluwalia, H.S., Fikani, M.M., 2007. Cosmic ray detector response to transient solar modulation: Forbush decreases. *J. Geophys. Res.* 112 (A8), A08105. <https://doi.org/10.1029/2006JA011958>.
- Barbashina, N.S., Ampilogov, N.V., Astapov, I.I., Borog, V.V., Dmitrieva, A.N., Petrukhin, A.A., Sitko, O.A., Shutenko, V.V., Yakovleva, E.I., 2016. Characteristics of the Forbush decrease of 22 June 2015 measured by means of the muon hodoscope URAGAN. *J. Phys.: Conf. Ser.* 675 (3). <https://doi.org/10.1088/1742-6596/675/3/032038>, article id. 032038.
- Belov, A.V., 2008. Forbush effects and their connection with solar, interplanetary and geomagnetic phenomena. In: *Proceedings of the International Astronomical Union 4.S257*, pp. 439–450. <https://doi.org/10.1017/S1743921309029676>.
- Braun, I., Engler, J., Hörandela, J.R., Milke, J., 2009. Forbush decreases and solar events seen in the 10–20 GeV energy range by the Karlsruhe Muon Telescope. *Adv. Space Res.* 43 (4), 480–488. <https://doi.org/10.1016/j.asr.2008.07.012>.
- Caballero-Lopez, R.A., Moraal, H., 2012. Cosmic-ray yield and response functions in the atmosphere. *J. Geophys. Res. Space Phys.* 117 (A12), 7461–7469. <https://doi.org/10.1029/2012JA017794>.
- Cane, H.V., 2000. Coronal mass ejections and Forbush decreases. *Space Sci. Rev.* 93 (1–2), 55–77. <https://doi.org/10.1023/1026532125747>.
- Chauhan, M.L., Jain Manjula, S.K., Shrivastava, S.K., 2008. Study of two major Forbush decrease events of 2005. In: *Proceedings of the 30th International Cosmic Ray Conference, Mexico City*, vol. 1 (SH), pp. 307–310. <https://doi.org/10.7529/ICRC2011/V10/0097>.
- Clem, J.M., Dorman, L.I., 2000. Neutron monitor response functions, cosmic rays and earth. *Space Sci. Rev.* 93 (1/2), 335–359. <https://doi.org/10.1023/A:1026515722112>.
- Dragić, A., Udovičić, V., Banjanac, R., Joković, D., Maletić, D., Veselinović, N., Savić, M., Puzović, J., Aničin, I.V., 2011. The new setup in the Belgrade low-level and cosmic-ray laboratory. *Nucl.*

- Technol. Radiat. Protect. 26 (3), 181–192. <https://doi.org/10.2298/NTRP1101064N>.
- Duldig, M.L., 2000. Muon observations. In: Bieber, J.W., Eroshenko, E., Evenson, P., Flückiger, E.O., Kallenbach, R. (Eds.), *Cosmic Rays and Earth*. Space Sciences Series of ISSI. Springer, Dordrecht, pp. 207–226. https://doi.org/10.1007/978-94-017-1187-6_1.
- Forbush, S.E., 1954. World-wide cosmic ray variations, 1937–1952. *J. Geophys. Res.* 59 (4), 525–542. <https://doi.org/10.1029/JZ059i004p00525>.
- Guo, J., Dumbović, M., Wimmer-Schweingruber, R.F., Temmer, M., Lohf, H., Wang, Y., Veronig, A., Hassler, D.M., Leila, M., Mays, L. M., Zeitlin, C., Ehresmann, B., Witasse, O., Freiherr von Forstner, J. L., Heber, B., Holmström, M., Posner, A., 2018. Modeling the evolution and propagation of the 2017 September 9th and 10th CMEs and SEPs arriving at Mars constrained by remote-sensing and in-situ measurement. Also Available at: arXiv preprint arXiv:1803.00461.
- Heck, D., Knapp, J., Capdevielle, J.N., Schatz, G., Thouw, T., 1998. *CORSIKA: a Monte Carlo code to simulate extensive air showers*. Forschungszentrum Karlsruhe GmbH, p. V +90, TIB Hannover, D-30167 Hannover.
- Klyueva, A.I., Belov, A.V., Eroshenko, E.A., 2017. Specific features of the rigidity spectrum of Forbush effects. *Geomag. Aeron.* 57 (2), 177–189. <https://doi.org/10.1134/S0016793217020050>.
- Lingri, D., Mavromichalaki, H., Belov, A., Eroshenko, E., Yanke, V., Abunin, A., Abunina, M., 2016. Solar activity parameters and associated Forbush decreases during the minimum between cycles 23 and 24 and the ascending phase of cycle 24. *Sol. Phys.* 291 (3), 1025–1041. <https://doi.org/10.1007/s11207-016-0863-8>.
- Minamino, Mohanty, Morishita, et al. for the GRAPES-3 Collaboration, 2014. Rigidity Dependence of Forbush Decreases, Poster #654. In: *Proceedings of the 33rd International Cosmic Ray Conference*, Rio de Janeiro, Brazil, pp. 3612–3615.
- Papailiou, M., Mavromichalaki, H., Abunina, M., Belov, A., Eroshenko, E., Yanke, V., Kryakunova, O., 2013. Forbush decreases associated with western solar sources and geomagnetic storms: a study on precursors. *Sol. Phys.* 283 (2), 557–563. <https://doi.org/10.1007/s11207-013-0231-x>.
- Papaioannou, A., Belov, A.A., Mavromichalaki, H., Eroshenko, E., Yanke, V., Asvestari, E., Abunin, A., Abunina, M., 2013. The first Forbush decrease of solar cycle 24. *J. Phys. Conf. Ser.* 409 (1). <https://doi.org/10.1088/1742-6596/409/1/012202>.
- Samara, E., Smpontias, I.A., Lytrosyngounis, I., Lingri, D., Mavromichalaki, H., Sgouropoulos, C., 2018. Unusual cosmic ray variations during the Forbush decreases of June 2015. *Sol. Phys.* 293 (67). <https://doi.org/10.1007/S11207-018-1290-9>.
- Savić, M., Maletić, D., Joković, D., Veselinović, N., Banjanac, R., Udovičić, V., Dragić, V., 2015. Pressure and temperature effect corrections of atmospheric muon data in the Belgrade cosmic-ray station. *J. Phys. Conf. Ser.* 632 (1). <https://doi.org/10.1088/1742-6596/632/1/012059>, article id. 012059.
- Veselinović, N., Dragić, A., Savić, M., Maletić, D., Joković, D., Banjanac, R., Udovičić, V., 2017. An underground laboratory as a facility for studies of cosmic-ray solar modulation. *Nucl. Instrum. Meth.* A875, 10–15. <https://doi.org/10.1016/j.nima.2017.09.008>.
- Zhao, L.-L., Zhang, H., 2016. Transient galactic cosmic-ray modulation during solar cycle 24: a comparative study of two prominent forbush decrease events. *Astrophys. J.* 827 (1). <https://doi.org/10.3847/0004-637X>.



Study of gamma transitions and level scheme of ^{94}Nb using the $^{93}\text{Nb}(n_{th}, 2\gamma)$ reaction

David Knezevic^{a,b,*}, Nikola Jovancevic^b, Anatoly M. Sukhovoj^c, Aleksandar Dragic^a, Liudmila V. Mitsyna^c, László Szentmiklósi^d, Tamás Belgya^d, Stephan Oberstedt^e, Miodrag Krmar^b, Ilija Arsenic^f, Vu D. Cong^{c,g}

^a University of Belgrade, Institute of Physics Belgrade, Pregrevica 118, 11080 Zemun, Serbia

^b University of Novi Sad, Faculty of Science, Department of Physics, Trg Dositeja Obradovica 3, 21000 Novi Sad, Serbia

^c Joint Institute for Nuclear Research, 141980 Moscow region, Dubna, Russia

^d Centre for Energy Research, Hungarian Academy of Sciences, Budapest, Hungary

^e European Commission, Joint Research Centre, Directorate G – Nuclear Safety and Security, Unit G.2, Retieseweg 111, B-2440 Geel, Belgium

^f University of Novi Sad, Faculty of Agriculture, Trg Dositeja Obradovica 8, 21000 Novi Sad, Serbia

^g Vietnam Academy of Science and Technology, Institute of Physics, Hanoi, Viet Nam

Received 21 February 2019; received in revised form 18 March 2019; accepted 9 April 2019

Available online 17 October 2019

Abstract

In this paper, we present new spectroscopic information on ^{94}Nb from the $^{93}\text{Nb}(n_{th}, 2\gamma)$ reaction. The intensities of the two-step gamma cascades in the compound nucleus ^{94}Nb to the final levels, with excitation energies below 400 keV, were derived from experimental spectra recorded at the PGAA facility of Centre for Energy Research (MTA EK), Budapest, Hungary. The intensities, energies of primary and secondary transitions of 216 energy-resolved cascades as well as intermediate cascade levels were determined. The part of the level scheme of ^{94}Nb was obtained from analyzing the intensity spectra of the strongest cascades. The results were compared to the existing data in the ENSDF database. We concluded that 27 primary transitions, 29 intermediate cascades levels as well as 183 secondary transitions can be recommended as new nuclear data.

* Corresponding author at: University of Belgrade, Institute of Physics Belgrade, Pregrevica 118, 11080 Zemun, Serbia. E-mail address: davidk@ipb.ac.rs (D. Knezevic).

© 2019 Elsevier B.V. All rights reserved.

Keywords: Gamma spectrometry; Thermal neutron capture; Level scheme; Gamma cascades

1. Introduction

Knowledge of the nuclear level scheme plays an important role in the understanding of the nuclear properties. In this work, the niobium nucleus (^{94}Nb) was chosen for a study, because it has been already applied in the nuclear technology and, due to niobium's high temperature resistance and relatively low cross section for a capture of thermal neutrons, it is expected to be increasingly utilized in innovative nuclear reactors. New accurate spectroscopic data on ^{94}Nb , as it is an odd-odd nucleus, can also be interesting from a theoretical point of view, for studying the level density and the radiative strength function [1–5].

The properties of ^{94}Nb nucleus have been studied using different methods, such as IT decay of ^{94}Nb [6–14], $^{93}\text{Nb}(^{16}\text{O}, ^{15}\text{O})$, $^{82}\text{Se}(^{19}\text{F}, 3n\alpha\gamma)$ and $^{92}\text{Zr}(\alpha, d)$ reactions for high-spin states [1, 15, 16], stripping reaction $^{93}\text{Nb}(d, p)$ [17–20], $^{93}\text{Nb}(p, n\gamma)$ reaction using protons of various energies [21–26], reactions with resonance capture of neutrons [27–31] as well as thermal neutron capture [2, 18, 27, 31, 32]. The latter reaction was used in this paper, too.

One of the most suitable techniques for determining the required nuclear parameters is the two-step gamma-cascade method based on measurements of coincident prompt gamma-rays following thermal neutron capture [33–36]. The objective of this experiment was the detection of two-step gamma cascades following thermal neutron captures on ^{93}Nb nuclei, $^{93}\text{Nb}(n_{th}, 2\gamma)^{94}\text{Nb}$. Niobium lies in the region of atomic masses suitable for a study by two-step gamma-cascades method, but is yet unexplored by it. For mono-isotopic niobium (^{93}Nb), the data analysis is simplified and, moreover, preparation of a high-purity target for the experiment is considerably easier. An advantage of the two-step gamma-cascades technique is a low Compton background in obtained spectra owing to usage of the background-subtraction algorithm [33]. The background in the two-step-cascade (TSC) spectra of mono-isotopic niobium is practically absent.

In this paper, we present new spectroscopic information for the ^{94}Nb nucleus (levels, gamma transitions and their intensities per capture) and compare the results with the existing ENSDF data [37]. As the two-step gamma-cascades method provides the possibility to estimate simultaneously the nuclear level density and radiative strength functions, in a future work, these nuclear parameters may be obtained for the ^{94}Nb as well [38–43].

2. Experimental setup and measurement

The experiment was carried out at the PGAA station of MTA EK in Budapest, Hungary [44, 45]. The niobium target, with purity of 99.9%, a mass of 10.82 g and $25 \times 25 \times 2 \text{ mm}^3$ was used. The target was mounted at the plane orthogonal to the beam line. Two HPGe detectors, with relative efficiencies of 23% and 27%, were used. The detectors were placed one next to the other, facing the target. Each detector was put at an $\pm 11.6^\circ$ angle relative to the axis normal to the beam line, which passed through the target, as depicted in Fig. 1. The detectors were at 7.5 cm distance from the center of niobium target. Close geometry was used in order to record as many coincident events as possible. Both detectors were shielded from background gamma radiation

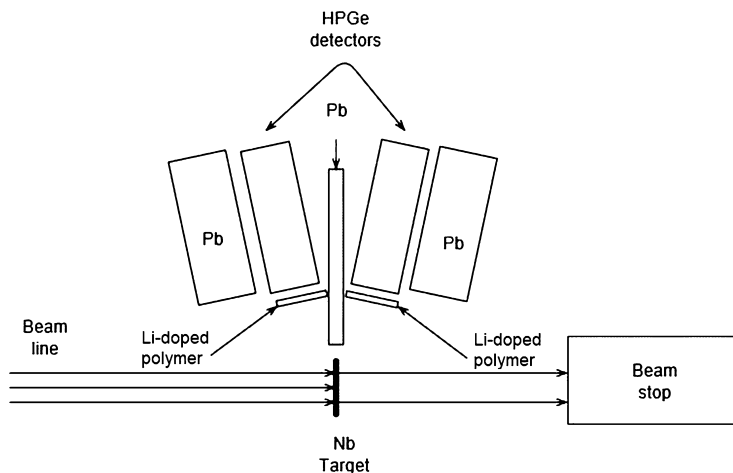


Fig. 1. Experimental setup for two-step gamma cascades measurement at the PGAA station of MTA EK, Budapest, Hungary.

with lead, and from neutrons with a 2 mm thick ^6Li doped polymer layer that was placed in front of the detector caps.

Experimental data were collected with a 4 channel CAEN N6724 digitizer [46]. The digitizer collected information on the energy and time of the gamma-coincidence events from both HPGe detectors, and stored it in list mode for offline analysis. The relative efficiency of the detectors was determined from single gamma-ray spectra accumulated using a PVC target (the $^{35}\text{Cl}(n,\gamma)^{36}\text{Cl}$ reaction) [47]. Niobium two-gamma events were recorded for 506 ks.

3. Result and discussion

The detailed procedures to extract the cascade events and intensities were described in Ref. [33], therefore, only a short description of the applied procedure will be presented here.

Fig. 2 shows the most important part of the spectrum of sums of amplitudes for coincident pulses (SACP). The coincidence time window was 40 ns. The seven marked peaks in Fig. 2 present the two-step cascade peaks of ^{94}Nb for transitions from the neutron binding energy (7227.0(5) keV) to the ground state and to the first six excited states with the energies 40.9, 58.7, 113.4, 140.3, 311.8 and 396.2 keV. Core information about these seven peaks is presented in Table 1.

The remaining unmarked peaks in SACP spectrum correspond to background events (Fig. 2). They may come from recording of coincidences of the first with the third or fourth quantum of the multiple-step gamma cascades or from neutron interaction with surrounding materials.

The next step was to obtain two-step-cascade (TSC) spectra for seven energy-resolved amplitude peaks. The obtained TSC spectra represent the cascades from the initial state to the defined final levels of the ^{94}Nb nucleus. The elimination of Compton background and random coincidences was done by gating on the region nearby the peaks of interest in Fig. 2. Figs. 3 and 4 show the examples of the obtained TSC spectra for cascade sum energies of 7087 and 7169 keV.

The mirror-symmetrical peaks [34] in the TSC spectra represent primary and secondary transitions of the investigated two-step gamma cascade. The peaks' positions correspond to the

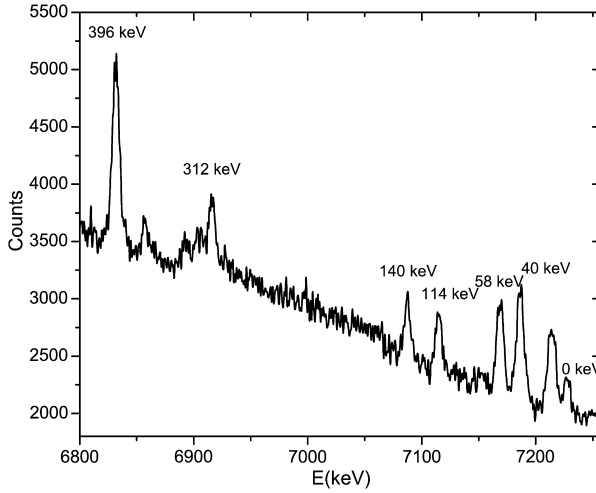


Fig. 2. Spectrum of sums of amplitudes for coincident pulses (SACP) at the radiative capture of thermal neutrons in ^{93}Nb nucleus. Peaks of the full capture of two quanta are labeled by energy of the final level of the resolved cascades.

Table 1

Information about the two-step cascades to the ground state and the first six excited states collected in the experiment.

Gamma cascade total energy (keV)	Final level (E_f) of the cascade (keV)	Spin of level E_f	Part of resolved cascade intensity	Full intensities % per decay
7227	0	6+	0.25(2)	5.4(20)
7186	40.9	3+	0.71(2)	6.2(15)
7169	58.7	(4)+	0.60(1)	7.0(11)
7114	113.4	(5)+	0.42(2)	5.3(15)
7087	140.3	(2)-	0.84(1)	2.7(9)
6916	311.8	(4,5)+	0.57(3)	3.2(10)
6831	396.2	(3)-	0.51(3)	5.4(11)
Sum of total			0.56(2)	35.2(40)

energies, E_1 and E_2 , of primary and secondary quanta of the cascades. The relative intensity of each peak is proportional to its area. The intensities of 216 resolved cascades are determined from seven TSC distributions. In all investigated cascades, primary transitions (except for 26 of them) have the higher energy in comparison with the energy of secondary quanta. Details of the method and the maximum likelihood function used to determine the energies of primary and secondary cascade transitions were presented in [36]. All detected primary and secondary gamma transitions and their intensities as well as the energy of intermediate levels are presented in Table 2.

In order to compare the data of the cascade spectra (Figs. 3 and 4) with the library data for strongest primary transitions with $E_1=5997.0$, 5898.0, 5591.6, 5496.5, 5369.7, 5364.9, 5103.5 and 5070.4 keV, the branching coefficients of their secondary transitions I_2 were obtained independently, from ENSDF database, which gave data of absolute intensity of the cascades for normalization of the data from Table 2. The values of the total intensity of two-step gamma cascades, $I_{\gamma\gamma}$, obtained in such a way (Table 1), which include both the resolved cascades and

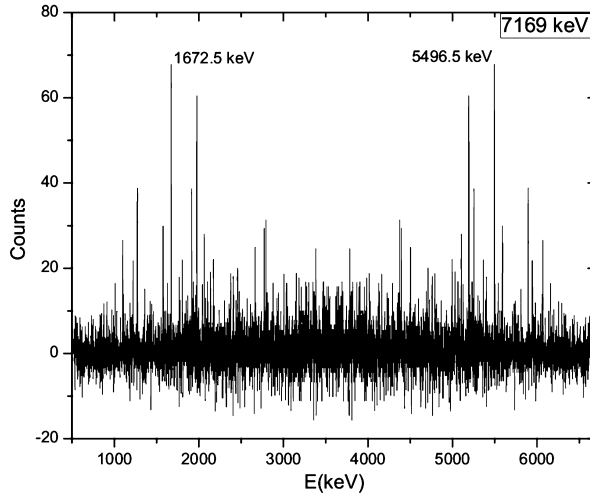


Fig. 3. TSC spectrum with the total energy of 7169 keV. The final level of the cascade is 58.708(10) keV. This spectrum represents the TSC spectrum with high number of cascades (36 pairs of gammas). The energies of the most intense pair of gammas are labeled.

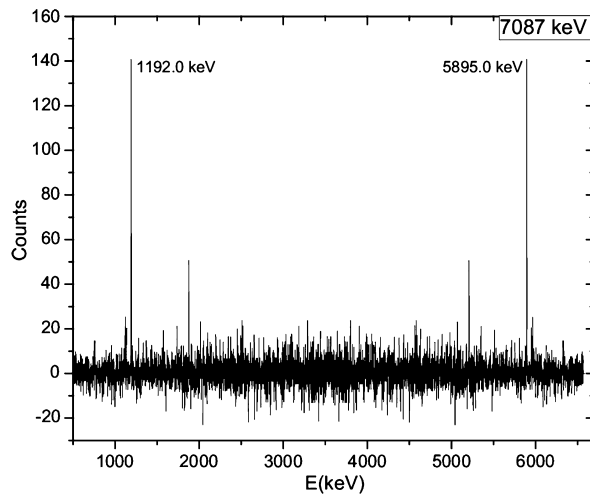


Fig. 4. TSC spectrum with the total energy of 7087 keV. The final level of the cascade is 140.298(12) keV. This spectrum represents the TSC spectrum with low number of cascades (18 pairs of gammas). The energies of the most intense pair of gammas are labeled.

unresolved cascade continuum with sub-threshold intensity, show that, for the investigated nucleus, we have obtained in this experiment 35% of total intensity of all two-step cascades. 56% of the obtained intensity $I_{\gamma\gamma}$ falls to the share of the energy-resolved cascades (Table 2).

The data was compared with the existing data from the ENSDF database [37]. From this comparison 107 primary transitions that existed in the ENSDF data set were determined. 27 primary transitions, which are not included in the ENSDF library, can be therefore considered as new data. 104 intermediate levels are identified in our experiment and already listed in the

Table 2

Comparison of the experimental data with the ENSDF database. E_1 and E_2 are the energies of the first and second quanta of the cascade, respectively, E_i is the energy of the intermediate level and E_f are the final levels of the two step gamma cascade. $I_{\gamma\gamma}$ is the intensity of the cascade (per 100 decays) observed in the experiment. The experimental uncertainty of E_2 has the same values as for E_1 (listed in the table). Values in bold are values for which there is no data in the ENSDF library.

Present work				ENSDF			
E_1 (keV)	E_2 (keV)	E_i (keV)	$I_{\gamma\gamma}$	E_f (keV)	E_1 (keV)	E_2 (keV)	E_i (keV)
6917.90(19)	251.1	309.10(21)	0.32(15)	58.708(10)	6915.73(4)	253.115(5)	311.821(10)
6835.00(15)	334.1	392.10(17)	0.26(24)	58.708(10)	6831.18(4)	337.529(8)	396.227(12)
6835.00(9)	279.1	392.1(9)	0.098(24)	113.4009(8)	6831.18(4)	–	396.227(12)
6833.9(5)	253.1	393.1(5)	2.1(3)	140.298(12)	6831.18(4)	253.113(5)	396.227(12)
6435.3(7)	751.7	791.7(7)	0.08(4)	40.892(12)	6434.78(6)	751.78(7)	792.595(16)
6410.9(10)	776.1	816.1(10)	0.05(4)	40.892(12)	6410.64(14)	775.99(6)	816.83(3)
6332.0(14)	755.0	895.0(14)	0.06(4)	140.298(12)	6331.74(7)	755.28(7)	895.650(14)
6332.0(6)	499.0	895.0(6)	0.36(14)	396.227(12)	6331.74(7)	499.426(8)	895.650(14)
6292.7(5)	894.3	934.3(5)	0.26(8)	40.892(12)	6292.19(7)	894.24(5)	936.036(20)
6271.8(6)	955.2	955.3(6)	0.11(4)	g.s.	6270.57(11)	957.34(5)	957.34(5)
6246.3(8)	867.7	980.7(8)	0.038(20)	113.4009(8)	–	–	979.29(18)
6187.3(10)	1039.7	1039.7(10)	0.050(27)	g.s.	–	–	–
6188.8(11)	642.2	1038.2(11)	0.07(5)	396.227(12)	–	–	–
6160.0(19)	954.1	1067.1(19)	0.016(11)	113.4009(8)	–	–	–
6136.0(10)	695.0	1091.0(10)	0.12(8)	396.227(12)	–	–	–
6068.9(5)	1118.1	1158.1(5)	0.14(5)	40.892(12)	6068.44(8)	1118.00(25)	1158.71(4)
6068.9(4)	1100.1	1158.1(4)	0.13(6)	58.708(10)	6068.44(8)	1100.11(15)	1158.71(4)
6058.1(7)	1055.9	1168.9(7)	0.047(23)	113.4009(8)	6058.16(9)	1056.39(15)	1169.88(6)
6050.9(10)	1176.1	1176.1(10)	0.05(3)	g.s.	–	1179.61(6)	1179.61(6)
6029.6(10)	1197.4	1197.4(10)	0.044(28)	g.s.	–	–	–
5997.0(7)	834.0	1230.0(7)	0.32(13)	396.227(12)	5995.67(9)	835.72(3)	1231.92(3)
5981.1(9)	1187.9	1245.9(9)	0.057(26)	58.708(10)	5980.20(9)	1188.3(4)	1247.26(7)
5964.3(5)	1122.7	1262.7(5)	0.17(5)	140.298(12)	5964.34(8)	1122.65(25)	1262.82(7)
5964.3(13)	866.7	1262.7(13)	0.068(27)	396.227(12)	5964.34(8)	–	1262.82(7)
5952.8(6)	1161.2	1274.0(6)	0.07(3)	113.4009(8)	5952.94(10)	1160.0(5)	1272.83(4)
5952.8(6)	878.2	1274.0(6)	0.12(8)	396.227(12)	5952.94(10)	879.75(14)	1272.83(4)
5945.3(7)	1281.7	1281.7(7)	0.11(4)	g.s.	5946.33(9)	1281.44(11)	1281.44(11)
5945.3(7)	1223.7	1281.7(7)	0.10(4)	58.708(10)	5946.33(9)	1222.98(12)	1281.44(11)
5895.00(25)	1292.0	1332.00(26)	0.38(8)	40.892(12)	5894.93(8)	1291.3(5)	1332.6(3)
5895.0(4)	1274.0	1332.0(4)	0.25(6)	58.708(10)	5894.93(8)	1273.4(5)	1332.6(3)
5895.0(9)	1219.0	1332.0(9)	0.049(24)	113.4009(8)	5894.93(8)	1220.1(5)	1332.6(3)
5895.00(21)	1192.0	1332.00(22)	0.83(11)	140.298(12)	5894.93(8)	1192.2(5)	1332.6(3)
5835.1(4)	1391.9	1391.9(4)	0.17(6)	g.s.	5834.74(11)	–	1392.73(12)
5819.9(11)	1294.1	1407.0(11)	0.028(16)	113.4009(8)	–	–	1405.0(10)
5808.6(9)	1305.4	1418.4(9)	0.058(27)	113.4009(8)	–	1304.8(5)	–
5808.6(10)	1022.4	1418.4(10)	0.13(9)	396.227(12)	–	–	–
5770.7(11)	1060.3	1456.3(11)	0.15(9)	396.227(12)	5769.77(9)	1061.45(11)	1458.12
5730.4(9)	1100.6	1496.6(9)	0.09(6)	396.227(12)	5727.98(11)	–	1499.92
5708.3(8)	1460.7	1518.7(8)	0.063(24)	58.708(10)	5708.73(11)	1459.6(14)	1519.0(10)

Table 2 (continued)

Present work				ENSDF			
E_1 (keV)	E_2 (keV)	E_i (keV)	$I_{\gamma\gamma}$	E_f (keV)	E_1 (keV)	E_2 (keV)	E_i (keV)
5708.3(9)	1405.7	1518.7(9)	0.056(28)	113.4009(8)	5708.73(11)	–	1519.0(10)
5647.4(8)	1439.6	1579.6(8)	0.038(21)	140.298(12)	5645.94(11)	–	1581.95(14)
5647.4(8)	1183.6	1579.6(8)	0.14(8)	396.227(12)	5645.94(11)	1185.1(3)	1581.95(14)
5617.0(7)	1552.0	1610.0(7)	0.059(22)	58.708(10)	–	–	1609.6(12)
5614.2(6)	1216.8	1612.8(6)	0.14(6)	396.227(12)	5612.72(11)	–	–
5607.6(7)	1307.4	1619.4(7)	0.09(4)	311.821(10)	5607(30)	1304.8(5)	1620.6(4)
5591.6(4)	1577.4	1635.4(4)	0.15(4)	58.708(10)	5591.32(10)	–	1636.14(11)
5591.6(6)	1239.4	1635.4(6)	0.29(12)	396.227(12)	5591.32(10)	1239.38(25)	1636.14(11)
5572.5(7)	1654.5	1654.5(7)	0.08(4)	g.s.	5572.33(11)	–	1655.09(17)
5572.5(7)	1541.5	1654.5(7)	0.08(4)	113.4009(8)	5572.33(11)	–	1655.09(17)
5511.6(6)	1575.4	1715.4(6)	0.09(3)	140.298(12)	5511.28(11)	–	1716.66(19)
5508.3(8)	1678.7	1718.7(8)	0.07(4)	40.892(12)	5507.80(11)	–	1720.1(3)
5496.50(27)	1672.5	1730.50(28)	0.39(6)	58.708(10)	5496.15(10)	–	1731.4(13)
5496.5(6)	1590.5	1730.5(6)	0.065(28)	140.298(12)	5496.15(10)	–	1731.4(13)
5496.5(4)	1418.5	1730.5(4)	0.23(6)	311.821(10)	5496.15(10)	1419.6(13)	1731.4(13)
5496.5(5)	1334.5	1730.5(5)	0.47(16)	396.227(12)	5496.15(10)	1334.6(5)	1731.4(13)
5453.3(10)	1461.7	1773.7(10)	0.052(29)	311.821(10)	5450.98(11)	1459.6(14)	1776.92(14)
5448.3(7)	1778.7	1778.7(7)	0.12(5)	g.s.	5447.18(13)	–	1779.72(5)
5448.3(16)	1466.7	1778.7(16)	0.029(21)	311.821(10)	5447.18(13)	–	1779.72(5)
5448.3(10)	1382.7	1778.7(10)	0.08(3)	396.227(12)	5447.18(13)	–	1779.72(5)
5414.2(9)	1772.8	1812(9)	0.06(3)	40.892(12)	5412.20(15)	–	1815.75(18)
5407.8(12)	1779.2	1819.2(12)	0.038(24)	40.892(12)	5406.92(18)	–	1821.2(7)
5369.7(9)	1545.3	1857.3(9)	0.08(4)	311.821(10)	5368.98(11)	–	1859.75(11)
5364.9(6)	1822.1	1862.1(6)	0.10(4)	40.892(12)	5363.80(11)	–	1864.13(14)
5364.9(5)	1804.1	1862.1(5)	0.12(4)	58.708(10)	5363.80(11)	–	1864.13(14)
5364.9(8)	1749.1	1862.1(8)	0.08(4)	113.4009(8)	5363.80(11)	–	1864.13(14)
5364.9(7)	1550.1	1862.1(7)	0.14(5)	311.821(10)	5363.80(11)	–	1864.13(14)
5364.9(9)	1466.1	1862.1(9)	0.10(10)	396.227(12)	5363.80(11)	–	1864.13(14)
5349.0(8)	1820.0	1878.0(8)	0.045(20)	58.708(10)	5348.56(11)	–	1879.35(14)
5349.0(8)	1738.0	1878.0(8)	0.13(5)	140.298(12)	5348.56(11)	–	1879.35(14)
5309.8(8)	1877.2	1917.2(8)	0.13(5)	40.892(12)	–	–	–
5307.3(8)	1523.7	1919.7(8)	0.11(6)	396.227(12)	5307.93(11)	–	1920.0(4)
5304.9(14)	1882.1	1922.1(14)	0.06(4)	40.892(12)	–	–	–
5300.5(10)	1886.5	1926.5(10)	0.080(28)	40.892(12)	5301.22(12)	–	1926.8(4)
5300.5(7)	1813.5	1926.5(7)	0.11(4)	113.4009(8)	5301.22(12)	–	1926.8(4)
5300.5(7)	1614.5	1926.5(7)	0.08(4)	311.821(10)	5301.22(12)	–	1926.8(4)
5284.0(6)	1885.0	1943.0(6)	0.041(19)	58.708(10)	5284.14(12)	–	1943.76(23)
5278.5(9)	1636.5	1948.5(9)	0.046(24)	311.821(10)	5277.43(19)	–	1950.4(3)
5270.4(9)	1916.6	1956.6(9)	0.044(25)	40.892(12)	5271.19(20)	–	1956.73(22)
5270.4(6)	1843.6	1956.6(6)	0.058(28)	113.4009(8)	5271.19(20)	–	1956.73(22)
5270.4(12)	1816.6	1956.6(12)	0.08(5)	140.298(12)	5271.19(20)	–	1956.73(22)
5270.4(6)	1644.6	1956.6(6)	0.08(5)	311.821(10)	5271.19(20)	–	1956.73(22)
5253.2(3)	1915.8	1973.8(3)	0.20(5)	58.708(10)	5252.51(12)	–	1975.5(4)
5212.8(6)	1702.2	2014.2(6)	0.059(26)	311.821(10)	5213.76(15)	–	2014.19(20)

(continued on next page)

Table 2 (continued)

Present work				ENSDF			
E_1 (keV)	E_2 (keV)	E_i (keV)	$I_{\gamma\gamma}$	E_f (keV)	E_1 (keV)	E_2 (keV)	E_i (keV)
5207.6(5)	1879.4	2019.4(5)	0.30(10)	140.298(12)	5207.94(12)	–	2020.0(3)
5206.8(12)	1623.4	2019.4(12)	0.05(3)	396.227(12)	5207.94(12)	–	2020.0(3)
5193.7(9)	2033.3	2033.3(9)	0.07(4)	g.s.	5193.37(12)	–	2033.6(3)
5193.7(9)	1975.3	2033.3(9)	0.36(7)	58.708(10)	5193.37(12)	–	2033.6(3)
5193.7(9)	1920.3	2033.3(9)	0.25(7)	113.4009(8)	5193.37(12)	–	2033.6(3)
5193.7(9)	1721.3	2033.3(9)	0.30(7)	311.821(10)	5193.37(12)	–	2033.6(3)
5179.9(10)	2007.1	2047.1(10)	0.042(22)	40.892(12)	5179.99(12)	–	2047.94(15)
5179.9(11)	1907.1	2047.1(11)	0.09(5)	140.298(12)	5179.99(12)	–	2047.94(15)
5179.9(7)	1651.1	2047.1(7)	0.13(5)	396.227(12)	5179.99(12)	–	2047.94(15)
5131.0(10)	1983.0	2096.0(10)	0.052(29)	113.4009(8)	5129.15(13)	–	2098.78(16)
5120.7(8)	1993.3	2106.3(8)	0.07(3)	113.4009(8)	–	–	–
5104.1(7)	2122.9	2122.9(7)	0.08(3)	g.s.	5103.33(12)	–	2124.62(15)
5104.1(6)	2082.9	2122.9(6)	0.12(4)	40.892(12)	5103.33(12)	–	2124.62(15)
5104.1(4)	2064.9	2122.9(4)	0.14(4)	58.708(10)	5103.33(12)	–	2124.62(15)
5104.1(8)	2009.9	2122.9(8)	0.12(5)	113.4009(8)	5103.33(12)	–	2124.62(15)
5104.1(7)	1726.9	2122.9(7)	0.29(13)	396.227(12)	5103.33(12)	–	2124.62(15)
5071.1(8)	2015.9	2155.9(8)	0.08(5)	140.298(12)	5070.26(12)	–	2157.67(15)
5071.1(4)	1759.9	2155.9(4)	0.26(10)	396.227(12)	5070.26(12)	–	2157.67(15)
5066.8(9)	2047.2	2160.2(9)	0.06(3)	113.4009(8)	5065.65(13)	–	2162.28(16)
5058.3(10)	2128.7	2168.7(10)	0.040(25)	40.892(12)	5059.7(3)	–	2168.2(3)
5053.8(7)	2173.2	2173.2(7)	0.11(4)	g.s.	5052.88(15)	–	2175.4(24)
5053.8(10)	2115.2	2173.2(10)	0.040(25)	58.708(10)	5052.88(15)	–	2175.4(24)
5031.8(10)	2195.2	2195.2(10)	0.07(3)	g.s.	5032.07(13)	–	2195.86(16)
5031.8(5)	2155.2	2195.2(5)	0.068(29)	40.892(12)	5032.07(13)	–	2195.86(16)
5031.8(6)	2137.2	2195.2(6)	0.13(4)	58.708(10)	5032.07(13)	–	2195.86(16)
5031.8(11)	1883.2	2195.2(11)	0.038(26)	311.821(10)	5032.07(13)	–	2195.86(16)
5019.4(10)	2167.6	2207.6(10)	0.040(22)	40.892(12)	5020.9(3)	–	2207.0(3)
5008.4(9)	2178.6	2218.6(9)	0.07(3)	40.892(12)	5006.76(22)	–	2221.16(24)
4998.3(6)	2228.7	2228.7(6)	0.14(5)	g.s.	4997.96(14)	–	2229.98(17)
4984.0(6)	2103.0	2243.0(6)	0.058(28)	140.298(12)	4982.50(13)	–	2245.3(5)
4984.0(5)	1847.0	2243.0(5)	0.13(6)	396.227(12)	4982.50(13)	–	2245.3(5)
4947.7(9)	2221.3	2279.3(9)	0.041(21)	58.708(10)	4949.72(17)	–	2278.5(7)
4890.0(12)	1941.0	2337.0(12)	0.05(3)	396.227(12)	4891.2(9)	–	2336.7(7)
4886.4(6)	2200.6	2340.6(6)	0.057(26)	140.298(12)	–	–	–
4861.6(13)	2325.4	2365.4(13)	0.05(3)	40.892(12)	4864.40(19)	–	2363.54(21)
4833.0(10)	1998.0	2394.0(10)	0.09(5)	396.227(12)	4834.8(4)	–	2393.1(4)
4827.8(10)	2341.2	2399.2(10)	0.06(3)	58.708(10)	4827.62(14)	–	2398.6(15)
4827.8(6)	2286.2	2399.2(6)	0.10(4)	113.4009(8)	4827.62(14)	–	2398.6(15)
4791.8(10)	2435.2	2435.2(10)	0.06(4)	g.s.	4791.59(14)	–	2436.5(5)
4791.8(6)	2395.2	2435.2(6)	0.15(5)	40.892(12)	4791.59(14)	–	2436.5(5)
4791.8(7)	2377.2	2435.2(7)	0.09(4)	58.708(10)	4791.59(14)	–	2436.5(5)
4760.6(14)	2426.4	2466.4(14)	0.046(29)	40.892(12)	–	–	–
4760.6(14)	2408.4	2466.4(14)	0.041(28)	58.708(10)	–	–	–
4760.6(8)	2353.4	2466.4(8)	0.051(26)	113.4009(8)	–	–	–

Table 2 (continued)

Present work				ENSDF			
E_1 (keV)	E_2 (keV)	E_i (keV)	$I_{\gamma\gamma}$	E_f (keV)	E_1 (keV)	E_2 (keV)	E_i (keV)
4760.6(9)	2070.4	2466.4(9)	0.08(3)	396.227(12)	–	–	–
4756.2(10)	2430.8	2470.8(10)	0.06(3)	40.892(12)	4756.27(15)	–	2471.68(17)
4734.7(11)	2352.3	2492.3(11)	0.048(29)	140.298(12)	–	–	–
4711.9(9)	2457.1	2515.1(9)	0.05(4)	58.708(10)	4711.62(14)	–	2516.38(18)
4711.9(6)	2203.1	2515.1(6)	0.17(5)	311.821(10)	4711.62(14)	–	2516.38(18)
4700.1(10)	2486.9	2526.9(10)	0.06(3)	40.892(12)	4699.7(4)	–	2528.3(4)
4691.5(9)	2495.5	2535.5(9)	0.051(27)	40.892(12)	4691.1(4)	–	2537.3(7)
4691.5(13)	2477.5	2535.5(13)	0.046(29)	58.708(12)	4691.1(4)	–	2537.3(7)
4682.4(12)	2486.6	2544.6(12)	0.037(23)	58.708(12)	4681.96(15)	–	2545.93(25)
4682.4(6)	2431.6	2544.6(6)	0.11(4)	113.4009(8)	4681.96(15)	–	2545.93(25)
4682.4(7)	2232.6	2544.6(7)	0.11(4)	311.821(10)	4681.96(15)	–	2545.93(25)
4674.5(9)	2512.5	2552.5(9)	0.07(4)	40.892(12)	4672.15(15)	–	2555.80(17)
4674.5(12)	2156.5	2552.5(12)	0.06(4)	396.227(12)	4672.15(15)	–	2555.80(17)
4660.8(7)	2526.2	2566.2(7)	0.07(3)	40.892(12)	4662.31(16)	–	2565.63(18)
4641.5(6)	2545.5	2585.5(6)	0.08(3)	40.892(12)	4642.2(4)	–	2585.8(4)
4635.8(18)	2591.2	2591.2(18)	0.04(5)	g.s.	4635.42(15)	–	2592.54(17)
4631.2(7)	2555.8	2595.8(7)	0.057(28)	40.892(12)	4629.89(15)	–	2598.07(17)
4631.2(8)	2537.8	2595.8(7)	0.08(3)	58.708(10)	4629.89(15)	–	2598.07(17)
4595.0(15)	2632.0	2632.0(15)	0.08(5)	g.s.	4594.44(15)	–	2633.52(17)
4595.0(10)	2592.0	2632.0(10)	0.06(3)	40.892(12)	4594.44(15)	–	2633.52(17)
4595.0(7)	2574.0	2632.0(7)	0.08(4)	58.708(10)	4594.44(15)	–	2633.52(17)
4595.0(8)	2519.0	2632.0(8)	0.07(3)	113.4009(8)	4594.44(15)	–	2633.52(17)
4560.4(11)	2626.6	2666.6(11)	0.04(8)	40.892(12)	4558.51(16)	–	2669.45(18)
4560.4(8)	2270.6	2666.6(8)	0.076(27)	396.227(12)	4558.51(16)	–	2669.45(18)
4557.0(10)	2612.0	2670.0(10)	0.045(24)	58.708(10)	4558.51(16)	–	2669.45(18)
4541.2(8)	2627.8	2685.8(8)	0.055(27)	58.708(10)	4543.2(3)	–	2685.0(4)
4512.7(8)	2714.3	2714.3(8)	0.13(6)	g.s.	–	–	–
4501.6(7)	2667.4	2725.4(7)	0.07(3)	58.708(10)	4501.41(16)	–	2726.55(18)
4428.0(7)	2799.0	2799.0(7)	0.10(5)	g.s.	–	–	–
4395.9(10)	2791.1	2831.1(10)	0.05(3)	40.892(12)	4395.05(16)	–	2832.91(18)
4395.9(11)	2773.1	2831.1(11)	0.041(26)	58.708(10)	4395.05(16)	–	2832.91(18)
4385.7(10)	2783.3	2841.3(10)	0.046(24)	58.708(10)	4384.25(18)	–	2843.73(20)
4385.7(9)	2728.3	2841.3(9)	0.07(3)	113.4009(8)	4384.25(18)	–	2843.73(20)
4363.2(9)	2823.8	2863.8(9)	0.042(25)	40.892(12)	–	–	–
4363.2(9)	2805.8	2863.8(9)	0.07(3)	58.708(12)	–	–	–
4330.9(10)	2896.1	2896.1(10)	0.08(5)	g.s.	4330.80(17)	–	2897.17(19)
4309.7(13)	2917.3	2917.3(13)	0.06(4)	g.s.	–	–	–
4304.4(11)	2922.6	2922.6(11)	0.06(4)	g.s.	4304.75(17)	–	2923.22(19)
4285.3(8)	2828.7	2941.7(8)	0.06(3)	113.4009(8)	4285.18(23)	–	2942.79(25)
4259.1(8)	2927.9	2967.9(8)	0.07(3)	40.892(12)	4260.77(17)	–	2967.3(6)
4259.1(8)	2827.9	2967.9(8)	0.10(5)	140.298(12)	4260.77(17)	–	2967.3(6)
4225.6(7)	2961.4	3001.4(7)	0.13(5)	40.892(12)	–	–	3003.6(8)
4225.6(9)	2888.4	3001.4(9)	0.06(3)	113.4009(8)	–	–	3003.6(8)
4217.3(8)	2969.7	3009.7(8)	0.058(26)	40.892(12)	4220.92(21)	–	3007.09(23)

(continued on next page)

Table 2 (continued)

Present work				ENSDF			
E_1 (keV)	E_2 (keV)	E_i (keV)	$I_{\gamma\gamma}$	E_f (keV)	E_1 (keV)	E_2 (keV)	E_i (keV)
4194.7(14)	3032.3	3032.3(14)	0.06(3)	g.s.	4196.67(18)	–	3031.21(20)
4194.7(7)	2992.3	3032.3(7)	0.07(3)	40.892(12)	4196.67(18)	–	3031.21(20)
4190.4(12)	2724.6	3036.6(12)	0.039(26)	311.821(10)	4191.04(20)	–	3036.8(3)
4154.1(8)	3032.9	3072.9(8)	0.10(4)	40.892(12)	4153.8(2)	–	3074.18(22)
4154.1(10)	2959.9	3072.9(10)	0.06(3)	113.4009(8)	4153.8(2)	–	3074.18(22)
4139.6(10)	2974.4	3087.4(10)	0.035(23)	113.4009(8)	4139.5(2)	–	3088.48(22)
4100.9(9)	3013.1	3126.1(9)	0.06(3)	113.4009(8)	4101.2(2)	–	3126.78(22)
4092.4(9)	3134.6	3134.6(9)	0.06(3)	g.s.	4090.5(2)	–	3137.6(3)
4071.7(9)	3155.3	3155.3(9)	0.06(3)	g.s.	4074.6(4)	–	3153.4(4)
4014.5(11)	3172.5	3212.5(11)	0.07(4)	40.892(12)	4015.9(2)	–	3212.09(22)
3960.5(8)	3226.5	3266.5(8)	0.06(3)	40.892(12)	3960.3(3)	–	3267.0(14)
3953.2(10)	3233.8	3273.8(10)	0.046(28)	40.892(12)	3955.7(2)	–	3272.29(22)
3947.7(10)	3239.3	3279.3(10)	0.06(4)	40.892(12)	3946.2(2)	–	3281.79(22)
3931.2(10)	3255.8	3295.8(10)	0.09(4)	40.892(12)	3931.7(2)	–	3296.29(22)
3920.8(8)	3266.2	3306.2(8)	0.09(4)	40.892(12)	3919.6(2)	–	3308.39(22)
3909.6(7)	3277.4	3317.4(7)	0.09(4)	40.892(12)	3912.7(2)	–	3315.29(22)
3891.9(6)	3295.1	3335.1(6)	0.15(6)	40.892(12)	3892.8(2)	–	3335.19(22)
3883.3(9)	3343.7	3343.7(9)	0.12(6)	g.s.	3885.9(2)	–	3342.09(22)
3867.3(10)	3319.7	3359.7(10)	0.06(3)	40.892(12)	3867.5(20)	–	3360.49(22)
2940.9(7)	4286.1	4286.1(7)	0.04(4)	g.s.	–	–	–
2940.9(7)	4246.1	4286.1(7)	0.07(3)	40.892(12)	–	–	–
2940.9(12)	4146.1	4286.1(12)	0.06(4)	140.298(12)	–	–	–
2784.6(11)	4402.4	4442.4(11)	0.05(3)	40.892(12)	–	–	–
2784.6(6)	4329.4	4442.4(6)	0.12(5)	113.4009(8)	–	–	–
2657.7(10)	4529.3	4569.3(10)	0.048(27)	40.892(12)	–	–	–
2657.7(7)	4456.3	4569.3(7)	0.07(3)	113.4009(8)	–	–	–
2412.5(11)	4765.5	4814.5(11)	0.06(3)	58.708(10)	2412.1(3)	–	–
2412.5(25)	4701.5	4814.5(25)	0.024(20)	113.4009(8)	2412.1(3)	–	–
2347.3(9)	4839.7	4879.7(9)	0.08(4)	40.892(12)	2346.3(5)	–	–
2347.3(9)	4739.7	4879.7(9)	0.06(3)	140.298(12)	2346.3(5)	–	–
2312.6(5)	4914.4	4914.4(5)	0.27(8)	g.s.	2314.32(16)	–	–
2312.6(10)	4874.4	4914.4(10)	0.05(3)	40.892(12)	2314.32(16)	–	–
2293.1(11)	4621.9	4933.9(11)	0.037(22)	311.821(10)	2291.8(10)	–	–
2293.1(7)	4537.9	4933.9(7)	0.07(4)	396.227(12)	2291.8(10)	–	–
1976.4(7)	5210.6	5250.6(7)	0.11(4)	40.892(12)	1975.41(15)	–	–
1976.4(10)	5137.6	5250.6(10)	0.07(4)	113.4009(8)	1975.41(15)	–	–
1858.3(4)	5368.7	5368.7(4)	0.21(6)	g.s.	1858.93(14)	–	–
1858.3(9)	5310.7	5368.7(9)	0.049(21)	58.708(10)	1858.93(14)	–	–
1858.3(8)	5255.7	5368.7(8)	0.07(4)	113.4009(8)	1858.93(14)	–	–
1784.5(7)	5402.5	5442.5(7)	0.11(4)	40.892(12)	–	–	–
1784.5(8)	5329.5	5442.5(8)	0.052(27)	113.4009(8)	–	–	–
1767.6(5)	5401.4	5459.4(5)	0.14(4)	58.708(10)	–	–	–
1767.6(7)	5147.4	5459.4(7)	0.052(24)	311.821(10)	–	–	–
1713.1(14)	5513.9	5513.9(14)	0.037(29)	g.s.	–	–	–
1713.1(6)	5400.9	5513.9(6)	0.10(4)	113.4009(8)	–	–	–

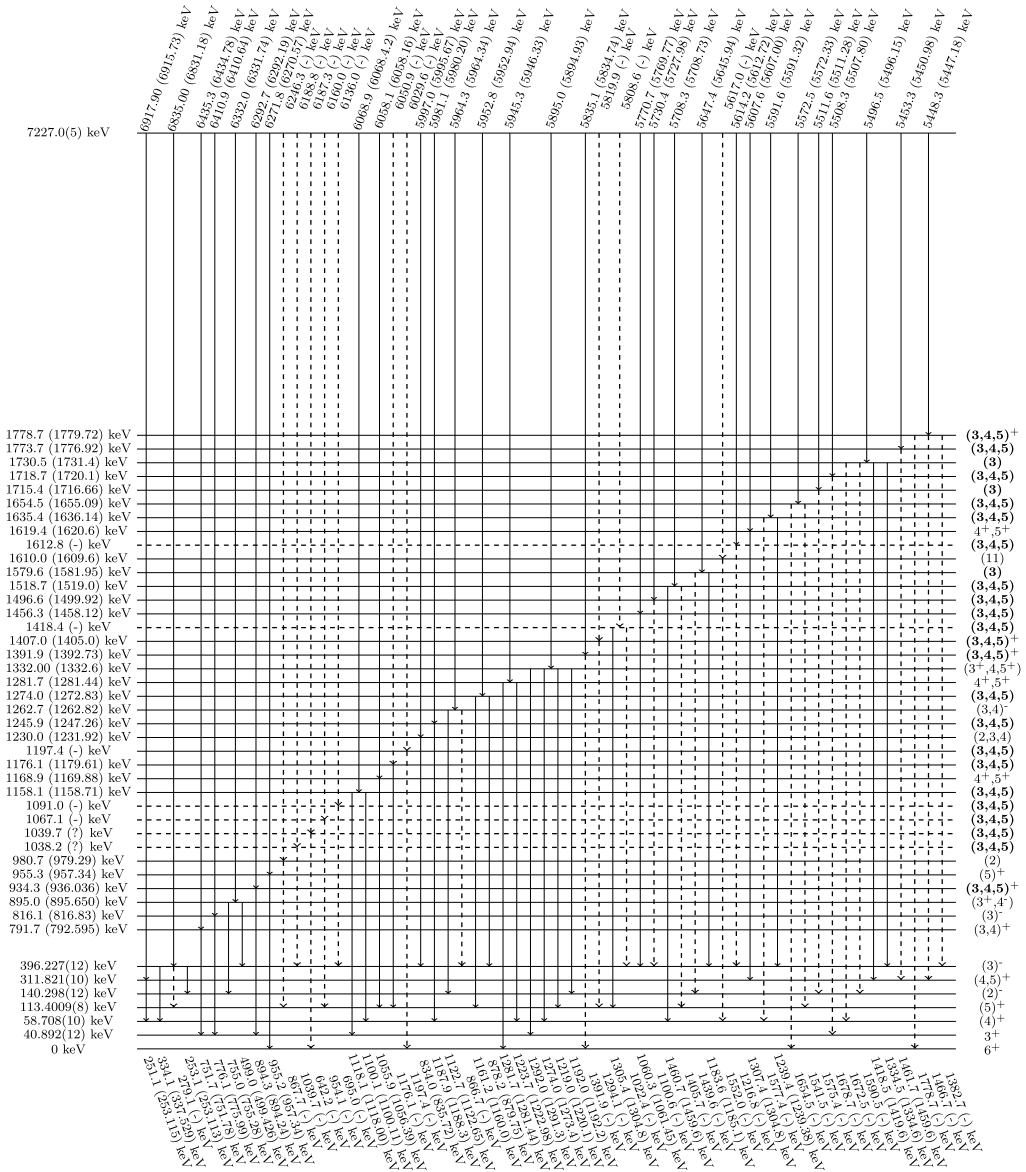


Fig. 5. Experimental level scheme of ^{94}Nb with intermediate level energies up to 1800 keV. Dashed lines - levels and gammas not found in the ENSDF library; bold spin values - values suggested by the authors for the levels without spin information in the ENSDF library. All energy values, except the energy values for the first 7 low lying levels are given in the form: Experimental value (ENSDF value).

ENSDF database. However, for 29 levels observed in this study, there is no data in the ENSDF library yet. In this work, we observed 183 secondary gamma transitions for which there is no information in the ENSDF database. 136 of these new observed secondary transitions come from the levels already in the ENSDF library, and 47 from levels determined for the first time in this work. Among secondary transitions, the ones with energies 879.75, 1061.45, 1185.1, 1304.8 and

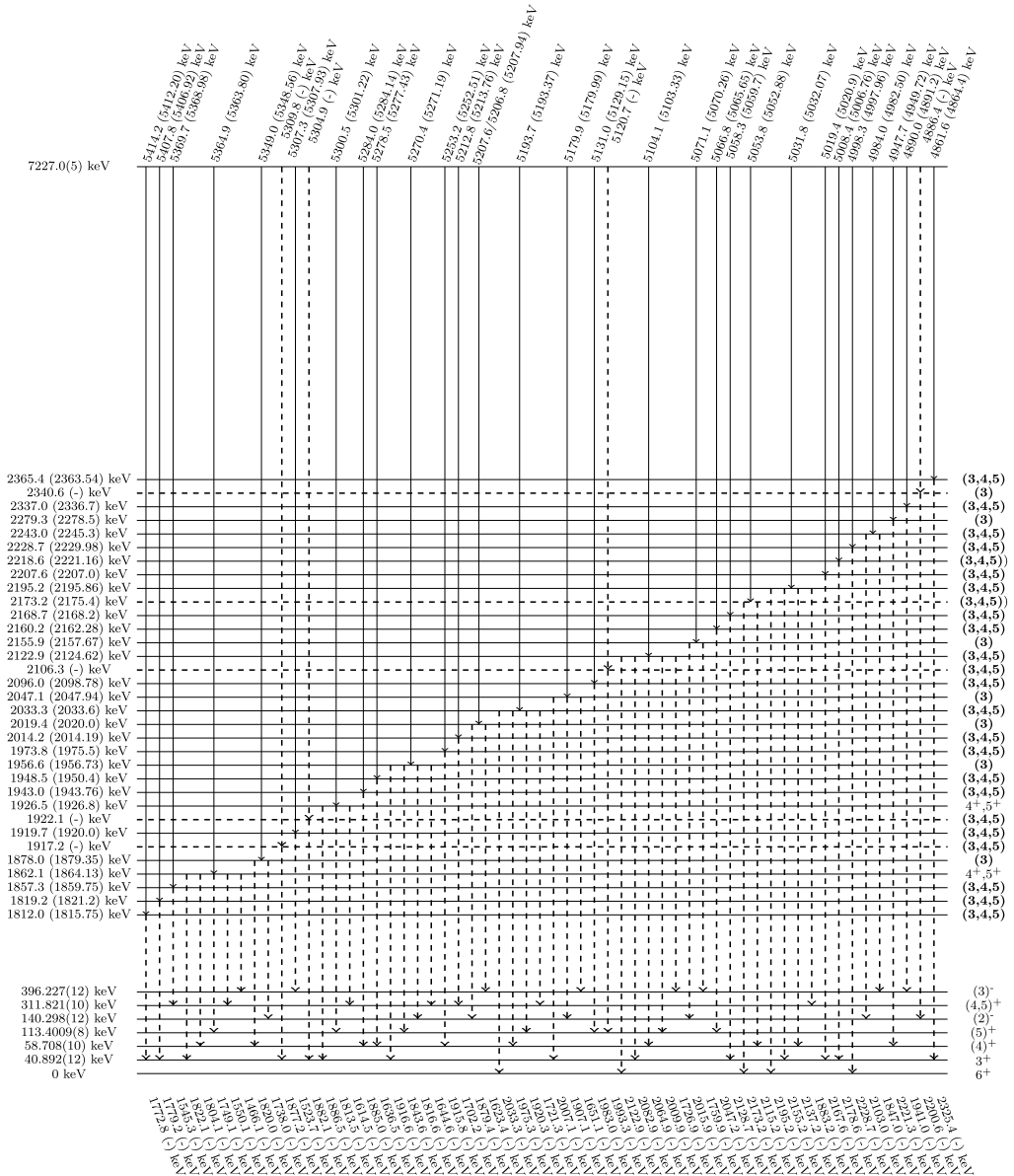


Fig. 6. Experimental level scheme of ^{94}Nb with intermediate level energies from 1800 to 2390 keV. Dashed lines - levels and gammas not found in the ENSDF library; bold spin values - values suggested by the authors for the levels without spin information in the ENSDF library. All energy values, except the energy values for the first 7 low lying levels are given in the form: Experimental value (ENSDF value).

1334.6 keV are included in the ENSDF database, but until now, they have not been placed into the decay scheme, and can also be considered as new data.

The comparison of determined energies of levels and gammas with the ones from the ENSDF database shows an average deviation of about 0.9 keV. For 104 levels and gammas, the deviation is larger than 1.5 keV. In those cases, ENSDF values were assigned tentatively by the authors.

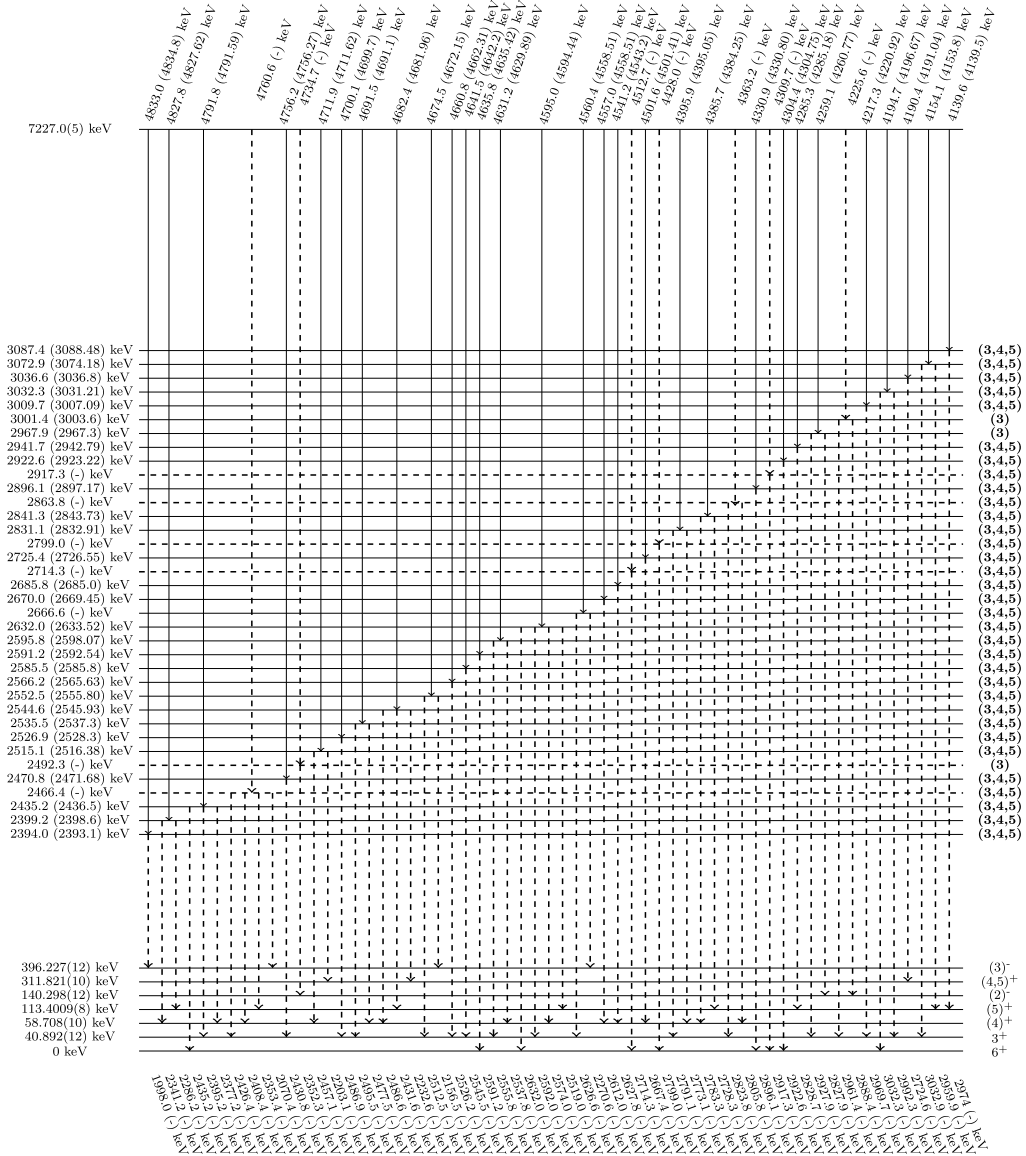


Fig. 7. Experimental level scheme of ^{94}Nb with intermediate level energies from 2390 to 3100 keV. Dashed lines - levels and gammas not found in the ENSDF library; bold spin values - values suggested by the authors for the levels without spin information in the ENSDF library. All energy values, except the energy values for the first 7 low lying levels are given in the form: Experimental value (ENSDF value).

This relatively large discrepancy can be explained by insufficient statistics in the present TSC spectra, which can cause uncertainty in the determination of the energy. For more precise data a longer time of measurements would be required.

The level scheme of ^{94}Nb obtained in this work is presented in Figs. 5 to 8. As it is known from [30], spin of the initial level of a cascade at a capture of thermal neutron in most cases

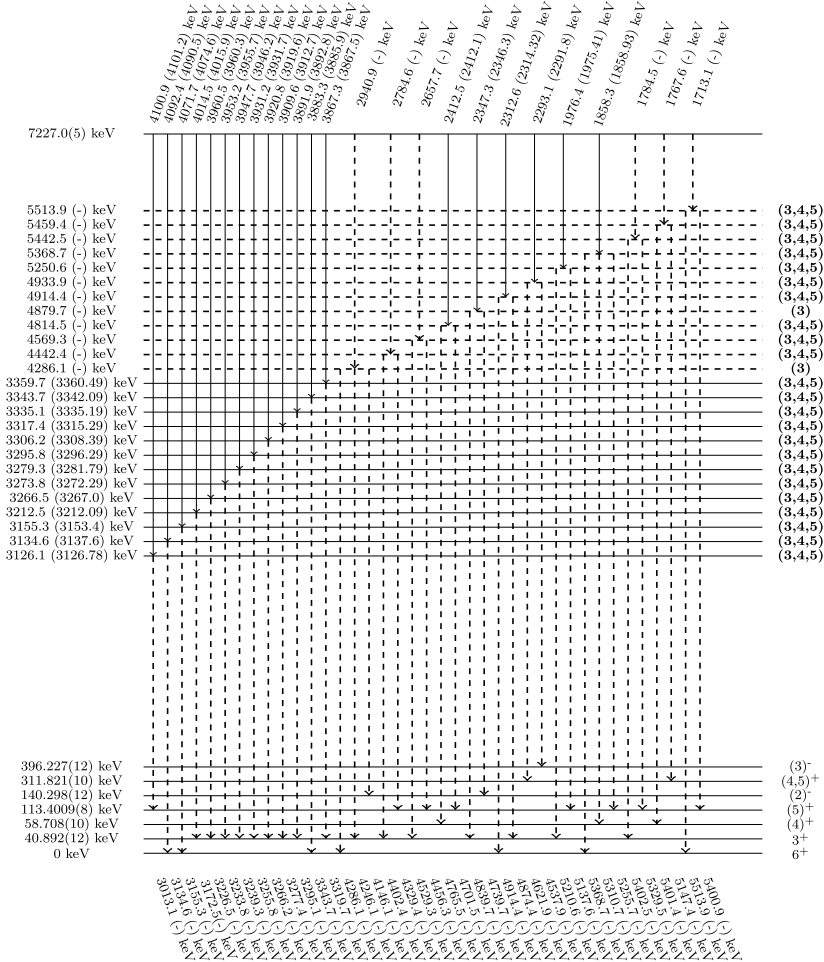


Fig. 8. Experimental level scheme of ^{94}Nb with intermediate level energies from 3100 to 5520 keV. Dashed lines - levels and gammas not found in the ENSDF library; bold spin values - values suggested by the authors for the levels without spin information in the ENSDF library. All energy values, except the energy values for the first 7 low lying levels are given in the form: Experimental value (ENSDF value).

($\sim 96\%$) is 4^+ and only in some ($\sim 4\%$) instances $J=5^+$. Thus, spin of an intermediate cascade level can take the values of $J = 3, 4$ and 5 , with the exception of the cascade with the energy of final level $E_f = 140$ keV, for which $J = 3$ is most likely. Among the peaks presented in Fig. 2, there are no cascades with a spin difference $\delta J \geq 3$ between initial and final levels, so the nature of the major part of the cascade quanta is E1 or M1. Also, for 5 final levels of cascades with positive parity, both transitions are either magnetic or electric that can have an influence on the emission spectrum, if the investigated nucleus is to be compared with other odd-odd nuclei.

4. Conclusion

In this paper, we presented the spectroscopic information obtained by investigating two-step gamma cascades following thermal-neutron capture on ^{93}Nb . As a result, the level scheme for the

^{94}Nb nucleus was obtained. Our data are in good agreement with the data in the ENSDF library. 29 new levels were observed with 27 new primary and 183 secondary gamma transitions in the energy range between 0.2 MeV and 7 MeV. These results will be useful for future investigations of nuclear structure parameters such as level density and radiative strength function.

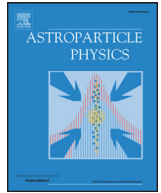
Acknowledgements

The authors are indebted to the CHANDA Program for funding the experiment in Budapest. Project ID: Fission-2013-4.1.2 call, grant number 605203.

References

- [1] N. Mărginean, D. Bucurescu, G. Căta-Danil, I. Căta-Danil, M. Ivaşcu, C. Ur, High-spin states in the ^{94}Nb nucleus, *Phys. Rev. C* 62 (3) (2000) 034309.
- [2] U. Gruber, R. Koch, B. Maier, O. Schult, J. Ball, K. Bhatt, R.K. Sheline, Energies and character of low-lying levels in Nb-94, *Nucl. Phys.* 67 (2) (1965) 433–442.
- [3] D. Goldberg, G. Dicker, S. Worcester, Niobium and niobium alloys in nuclear power, *Nucl. Eng. Des.* 22 (1) (1972) 124–137.
- [4] V. Likhanskii, I. Evdokimov, T. Aliev, V. Kon'kov, V. Markelov, V. Novikov, T. Khokhunova, Corrosion model for zirconium-niobium alloys in pressurized water reactors, *At. Energy* 116 (3) (2014) 186–193.
- [5] R.D. Mariani, P.G. Medvedev, D.L. Porter, S.L. Hayes, J.I. Cole, X.-M. Bai, Novel Accident-Tolerant Fuel Meat and Cladding, Tech. rep., Idaho National Laboratory (INL), 2013.
- [6] R.L. Caldwell, The internal conversion electrons of several short-lived neutron induced radioactivities, *Phys. Rev.* 78 (4) (1950) 407.
- [7] L. Ciuffolotti, C. Giori, M. Bettoni, K-conversion coefficient of the isomeric transition of nb94m, *Energia Nucleare* 8 (1961) 422.
- [8] P. Kilian, H. Langhoff, A. Flammersfeld, Der Zerfall von Nb-94m, *Z. Phys.* 169 (1) (1962) 23–31.
- [9] L. Yin, R.E. Sund, R.G. Arns, M.L. Wiedenbeck, Decay of Nb-94 and Nb-94m, *Nucl. Phys.* 34 (3) (1962) 588–592.
- [10] K. Sastry, R. Fink, P. Rao, K-conversion coefficient for 40.95-keV M3 transition in 6.3-min decay of Nb-94m, in: *Bulletin of the American Physical Society*, vol. 14, Amer. Inst. Physics Circulation Fulfillment Div., 500 Sunnyside Blvd., Woodbury . . . , 1969, p. 18.
- [11] R. Gehrke, R. Lokken, Calibration of the efficiency of a Si(Li) photon spectrometer in the energy region 5 to 125 keV, *Nucl. Instrum. Methods* 97 (2) (1971) 219–228.
- [12] M. De Bruin, P. Korthoven, Low-energy gamma rays from isotopes produced by (n, γ) reactions, *J. Radioanal. Chem.* 10 (1) (1972) 125–135.
- [13] M.O. Krause, Atomic radiative and radiationless yields for k and l shells, *J. Phys. Chem. Ref. Data* 8 (2) (1979) 307–327.
- [14] H. Muller, Nuclear data sheets for A=94, *Nucl. Data Sheets (United States)* 44 (2) (1985) 277–406.
- [15] M.S. Zisman, F. Becchetti, B. Harvey, D. Kovar, J. Mahoney, J. Sherman, Heavy-ion-induced single-nucleon transfer reactions in the Zr-Mo region, *Phys. Rev. C* 8 (5) (1973) 1866.
- [16] M. Zisman, B. Harvey, High-spin levels of Nb 92, 93, 94, 95, 96 and Tc 94 populated with (α, d) and (α, t) reactions at 50 MeV, *Phys. Rev. C* 5 (3) (1972) 1031.
- [17] R.K. Sheline, R.T. Jernigan, J.B. Ball, K.H. Bhatt, Y.E. Kim, J. Vervier, The $^{93}\text{Nb}(d, p)^{94}\text{Nb}$ reaction and the low-lying states of ^{94}Nb , *Nucl. Phys.* 61 (2) (1965) 342–351.
- [18] E. Jurney, H. Motz, R. Sheline, E. Shera, J. Vervier, Energy levels and configurations in ^{94}Nb , *Nucl. Phys. A* 111 (1) (1968) 105–128.
- [19] J. Moorhead, R. Moyer, Nuclear-structure studies in Mo and Nb isotopes via stripping reactions at 12 MeV, *Phys. Rev.* 184 (4) (1969) 1205.
- [20] R. Diehl, B. Cohen, R. Moyer, L. Goldman, Spectroscopic studies of molybdenum isotopes with (d, t) reactions, *Phys. Rev. C* 1 (6) (1970) 2132.
- [21] I. Fedorets, Y. Antufev, I. Zalyubovskii, A. Popov, V. Storizhko, Excited-states of Nb-94 in reaction of Zr-94 $(p, n \gamma)$ Nb-94, *Izv. Akad. Nauk SSSR, Ser. Fiz.* 40 (6) (1976) 1260–1265.
- [22] E. Hagen, B. Kern, F. Snyder, D. Miracle, Low-lying levels of Nb 94, *Phys. Rev. C* 13 (2) (1976) 620.

- [23] I. Fedorets, V. Mishchenko, A. Popov, V. Storizhko, Angular correlations in the reaction $94\text{Zr}(p, n\gamma)94\text{Nb}$, *Bull. Acad. Sci. USSR, Phys. Ser.* 43 (5) (1979) 38.
- [24] D. Miracle, B. Kern, Multipolarities of γ -rays from 92, 94-Nb and 94, 95, 96, 97, 98Tc, *Nucl. Phys. A* 320 (2) (1979) 353–372.
- [25] H. Miska, B. Norum, M. Hynes, W. Bertozzi, S. Kowalski, F. Rad, C. Sargent, T. Sasanuma, B. Berman, Precise measurement of the charge-distribution differences of the oxygen isotopes, *Phys. Lett. B* 83 (2) (1979) 165–168.
- [26] Y. Guyash, Z. Dombradi, E. Koltai, A. Krasnakhorkai, T. Fenesh, 94Nb levels excited in the reaction $94\text{Zr}(p, n\gamma)94\text{Nb}$, *Bull. Acad. Sci. USSR, Phys. Ser.* 44 (5) (1980) 118.
- [27] R. Chrien, K. Rimawi, J. Garg, Resonance neutron capture in Nb 93, *Phys. Rev. C* 3 (5) (1971) 2054.
- [28] R. Chrien, M. Bhat, G. Cole, Channel spin components of p-wave neutron widths in niobium, *Phys. Rev. C* 8 (1) (1973) 336.
- [29] T. Haste, B. Thomas, Investigations of resonance capture γ -ray spectra in the $93\text{Nb}(n, \gamma)94\text{Nb}$ reaction, *J. Phys. G, Nucl. Phys.* 1 (9) (1975) 967.
- [30] S.F. Mughabghab, *Neutron Resonance Parameters and Thermal Cross Section, Part A, Z=1-60, vol. 1*, Academic Press, 1981.
- [31] T. Kennett, W. Prestwich, J. Tsai, Energy levels of 94Nb populated directly via the (n, γ) reaction, *Can. J. Phys.* 66 (11) (1988) 947–959.
- [32] M. B., et al., Low-lying states of 94Nb , *Fizika (Zagreb)* 17 (1985) 219.
- [33] S. Boneva, E. Vasil'eva, Y.P. Popov, A. Sukhovoï, V. Khitrov, Two-quantum cascades of radiative neutron capture 1. Spectroscopy of excited states of complex nuclei in the neutron binding energy region, *Sov. J. Part. Nucl. (English Transl.)* 22 (2) (1991) 232–248.
- [34] Y.P. Popov, A. Sukhovoï, V. Khitrov, Y.S. Yazvitskij, Study on the γ decay of 165Dy with the help of the $(n, 2\gamma)$ reaction, *Izv. Akad. Nauk SSSR, Ser. Fiz.* 48 (5) (1984) 891–900.
- [35] A. Sukhovoï, V. Khitrov, Method of improving the amplitude resolution of the spectra of gamma-transition cascades in the computer processing of encoded coincidence data, *Instrum. Exp. Tech.* 27 (5) (1985) 1071–1074.
- [36] E. Vasilieva, A. Sukhovoï, V. Khitrov, Direct experimental estimate of parameters that determine the cascade gamma decay of compound states of heavy nuclei, *Phys. At. Nucl.* 64 (2) (2001) 153–168.
- [37] <https://www.nndc.bnl.gov/ensdf/>.
- [38] V. Khitrov, A. Sukhovoï, New technique for a simultaneous estimation of the level density and radiative strength functions of dipole transitions at $E_{\text{ex}} < B_{\text{n}} - 0.5$ MeV, arXiv preprint, arXiv:nucl-ex/0110017.
- [39] A. Sukhovoï, L. Mitsyna, N. Jovancevic, Overall picture of the cascade gamma decay of neutron resonances within a modified practical model, *Phys. At. Nucl.* 79 (3) (2016) 313–325.
- [40] D. Vu, A. Sukhovoï, L. Mitsyna, S. Zeinalov, N. Jovancevic, D. Knezevic, M. Krmar, A. Dragic, Representation of radiative strength functions within a practical model of cascade gamma decay, *Phys. At. Nucl.* 80 (2) (2017) 237–250.
- [41] A. Sukhovoï, New model of the cascade gamma decay of neutron resonances for practitioners: basic concepts and attainable precision, *Phys. At. Nucl.* 78 (2) (2015) 230–245.
- [42] A.M. Sukhovoï, L.V. Mitsyna, The next-generation practical model of the cascade gamma-decay of neutron resonance and expected parameters for an arbitrary nucleus, in: *Proceedings, 22nd International Seminar on Interaction of Neutrons with Nuclei: Fundamental Interactions and Neutrons, Nuclear Structure, Ultracold Neutrons, Related Topics*, ISINN 22, Dubna, Russia, May 27–30, 2014, 2015.
- [43] S. Boneva, V. Khitrov, A. Sukhovoï, A. Vojnov, Excitation study of high-lying states of differently shaped heavy nuclei by the method of two-step cascades, *Nucl. Phys. A* 589 (2) (1995) 293–306.
- [44] L. Szentmiklósi, T. Belgya, Z. Révay, Z. Kis, Upgrade of the prompt gamma activation analysis and the neutron-induced prompt gamma spectroscopy facilities at the Budapest research reactor, *J. Radioanal. Nucl. Chem.* 286 (2) (2010) 501–505.
- [45] L. Szentmiklósi, Z. Kasztovszky, T. Belgya, Z. Révay, Z. Kis, B. Maróti, K. Gméling, V. Szilágyi, Fifteen years of success: user access programs at the Budapest prompt-gamma activation analysis laboratory, *J. Radioanal. Nucl. Chem.* 309 (1) (2016) 71–77.
- [46] <https://www.caen.it/products/n6724/>.
- [47] B. Krusche, K. Lieb, H. Daniel, T. Von Egidy, G. Barreau, H. Börner, R. Brissot, C. Hofmeyr, R. Rascher, Gamma ray energies and 36Cl level scheme from the reaction $35\text{Cl}(n, \gamma)$, *Nucl. Phys. A* 386 (2) (1982) 245–268.



A novel method for atmospheric correction of cosmic-ray data based on principal component analysis

M. Savić, A. Dragić*, D. Maletić, N. Veselinović, R. Banjanac, D. Joković, V. Udovičić

Institute of Physics, University of Belgrade, Pregrevice 118, Zemun 11080, Serbia



ARTICLE INFO

Article history:

Received 23 August 2018
 Revised 8 December 2018
 Accepted 29 January 2019
 Available online 29 January 2019

Keywords:

Cosmic rays
 Muons
 Atmospheric corrections
 Principal component analysis

ABSTRACT

A new method for atmospheric correction of cosmic ray data is designed. It's fully empirical, based on the principal component analysis. The method requires knowledge of the pressure and the temperature profile of the atmosphere. It's applicable to all muon detectors. The method is tested on muon data from two detectors in Belgrade cosmic ray station, one located on the ground level and the other at the depth of 25 mwe. Correction reduces variance by 64.5% in ground level detector data and 38.1% in underground data. At the same time, the amplitude of the annual variation is reduced by 86.0% at ground level and 54.9% underground. With the same data sets the presented method performs better than the integral correction method.

© 2019 Elsevier B.V. All rights reserved.

1. Introduction

Count rates of ground based or underground cosmic-ray (CR) muon detectors are affected by atmospheric parameters (air pressure and temperature at different heights). The proper description of atmospheric effects is necessary for understanding primary CR variations, originating outside of the atmosphere.

Early studies in CR temporal variations [1,2] revealed the existence of a variation caused by the change of air pressure, the so called "barometric effect". With the increase in pressure the atmosphere represents thicker absorber, resulting in reduced number of muons reaching the ground level. Therefore, muon flux is expected to be anti-correlated with atmospheric pressure.

Observed negative correlation between muon flux and atmospheric temperature, the so called "negative temperature effect", has been explained by Blackett [3] to be a consequence of muon decay. During warm periods the atmosphere is expanded and the main layer of muon production (~100 mb) is higher, resulting in longer muon path and lower surviving probability to the ground level. Low energy muons are more affected, while the flux of high energy muons, capable of penetrating great depth, does not suffer. At deep underground experiments another type of temperature effect, "positive temperature effect" is pronounced [4]. Development of nuclear emulsions capable of detecting energetic charged particles lead to discovery of charged pions in CRs and $\pi - \mu$ decay [5–7]. The positive temperature effect is interpreted as a conse-

quence of latter process [8,9]. Pions created in the interactions of primary CR particles with the atmospheric nuclei can decay into muons or interact with air nuclei. Higher temperature in the production layer means lower air density and consequently, lower interaction probability and higher muon production.

In most cases linear regression is sufficient to account for the barometric effect. The temperature effects are treated by empirical and theoretical methods. In addition to the barometric coefficient β , **the method of effective level of generation** [8] introduces two empirical parameters: α_H to encounter for muon intensity variations δI_μ correlated with the change of the height of generation level δH (negative effect) and α_T for the changes of the temperature of this level (positive temperature effect).

$$\delta I_\mu = \beta \delta p + \alpha_H \delta H + \alpha_T \delta T \quad (1)$$

Duperier method has been successfully used in many studies for the atmospheric corrections of muon data ([10–15] etc.).

It's been argued [16,17] that for correct temperature correction of muon detectors count rate the vertical temperature profile of the entire atmosphere needs to be known. In the so called **integral method** the muon intensity variations caused by the temperature are described by the equation:

$$\frac{\delta I_\mu}{I_\mu} = \int_0^{h_0} W_T(h) \delta T(h) dh \quad (2)$$

where $\delta T(h)$ is the variation of temperature at isobaric level h with respect to the referent value and $W_T(h)$ is the temperature coefficient density. The coefficients are calculated theoretically and the best known calculations are given in references [18,19].

* Corresponding author.

E-mail address: dragic@ipb.ac.rs (A. Dragić).

The **mass-average temperature method** [20] is a variant of the integral method, based on the assumption of small changes of the temperature coefficient density $W_T(h)$ with the atmospheric depth h allowing its average value \overline{W}_T to be put in front of the integral in the Eq. (2) and on determination of the mass-averaged temperature T_m :

$$\frac{\delta I_\mu}{I_\mu} = \overline{W}_T(h) \int_0^{h_0} \delta T(h) dh = \overline{W}_T(h) \cdot \delta T_m \quad (3)$$

The method was used in numerous studies ([21–23] to name a few).

Another form of the integral method is **the effective temperature method** [24]. By introducing the temperature coefficient α_T :

$$\alpha_T = \int_0^{h_0} W_T(h) dh$$

the Eq. (2) can be normalized as:

$$\frac{\delta I_\mu}{I_\mu} = \int_0^{h_0} W_T(h) dh \cdot \frac{\int_0^{h_0} W_T(h) \delta T(h) dh}{\int_0^{h_0} W_T(h) dh} = \alpha_T \cdot \delta T_{eff} \quad (4)$$

where the effective temperature T_{eff} is defined as:

$$T_{eff} = \frac{\int_0^{h_0} W_T(h) T(h) dh}{\int_0^{h_0} W_T(h) dh}$$

The latter method is popular with the underground muon telescopes [25,26].

Different methods of atmospheric correction might be compared on the basis of several criteria. One is requirement of the lowest variance of corrected data. Since the most prominent temperature effect on CR time series is seasonal variation, another criterion is the smallest residual amplitude of seasonal variation after correction is applied. The latter does not take into account possible genuine seasonal variation of non-atmospheric origin.

Early studies comparing Duprier's empirical and Dorman's theoretical methods ([27] and references therein) found similar accuracy of two methods, with essentially the same corrections at sea level, but with the integral method overestimating the temperature effect.

A more recent study [28] compared different methods of atmospheric correction for data from Nagoya and Tibet supertelescopes, as well as Yakutsk, Moscow and Novosibirsk telescopes. They found the mass-averaged temperature method to practically coincide with the integral method. On the other hand, the effective level of generation method for Nagoya shows discrepancy from the integral method in winter time, being able to eliminate only 50% of the temperature effect. Even with the integral method in the case of Tibet muon telescope the removal of temperature effect is achieved with the density of temperature coefficients 3 times higher than calculated ones. The precise origin of disagreement is unknown.

The method of the effective level of generation takes care of key physical causes of the temperature effect. However, it does not make optimal use of the temperature data. Also, the assumption of a single level of main muon production is a simplification. Detailed CORSIKA simulation of the shower development in the atmosphere reveals the actual distribution of the muon generation heights (see Fig. 1).

Different implementations of the integral method exist, employing different approximations, choice of parameters, models of the atmosphere, whether kaon contribution is taken into account, leading to differences in calculated density temperature coefficients (see for instance discussion in [29]). As already mentioned, on the case of Tibet telescope [28] theoretical calculations do not fully correspond to the local experimental conditions and the origin of disagreement is difficult to trace.

The effective temperature method lacks universality, since it works best with the data from deep underground detectors.

Here we propose a new method for atmospheric corrections. It's fully empirical, makes use of the available temperature data through entire atmosphere and it's applicable to arbitrary detector irrespective to energy sensitivity and is simple to implement. The method is based on the principal component analysis, thus reducing dimensionality of the problem, exploiting correlations between atmospheric variables and ensuring mutual independence of correction parameters. The price is loss of clear physical interpretation of these parameters, since the pressure and the temperature at different levels are treated on equal footing.

2. Method description

2.1. Meteorological data

Set of variables that enter principal component decomposition consists of atmospheric temperature profile for the given location as well as locally measured atmospheric pressure. Meteorological balloon soundings for Belgrade are not done frequently enough to be used for suggested analysis. As a consequence, modeled temperatures were used instead. However, there were enough balloon sounding data for testing consistency of the modeled temperatures.

There are several weather and global climate numerical models available today. Here, Global Forecast System [30] data was used. GFS is a weather forecast model, developed by National Centers for Environmental Prediction [31], which is able to predict large number of atmospheric and land-soil parameters. Apart from forecast data, GFS also provides retrospective data produced taking into account most recent measurements by a world wide array of meteorological stations. Retrospective data are produced four times a day at 00:00, 06:00, 12:00 and 18:00 UTC. Data with finer temporal resolution are obtained by cubic spline interpolation. Temperatures for the following 25 isobaric levels (in mb) were used for initial analysis: 10, 20, 30, 50, 70, 100, 150, 200, 250, 300, 350, 400, 450, 500, 550, 600, 650, 700, 750, 800, 850, 900, 925, 975, 1000. Horizontal spatial resolution for modeled data is 0.5 degrees, so coordinates closest to the experiment location (latitude 44.86, longitude 20.39), were selected with this precision. Before any further analysis was done, GFS modeled temperature profiles were compared to local meteorological balloon soundings for Belgrade, where balloon data was available. Fig. 2 shows profile of differences between modeled and measured values for different isobaric levels. Disagreement was found between measured and modeled temperature at the lowest level. As a result, it was decided not to use temperature data for isobaric level of 1000 mb in further analysis. Ground temperature data measured by local meteorological stations was used for lowest layer instead. Similar problem with the GFS data was reported before by [28] who found 5°C deviation in the summer time near ground level at Yakutsk location.

Atmospheric pressure and ground level temperature from the Republic Hydro-meteorological Service of Serbia was used to compose unique local pressure and temperature time series.

2.2. Cosmic-ray data

The analysis is performed on data from Belgrade muon detectors. The Belgrade cosmic-ray station, together with the present detector arrangement is described in details elsewhere [32]. Two muon detectors are located in the laboratory, one at the ground level and the other at the depth of 25 mwe. Data are recorded on the event-by event basis and can be integrated into the time series with the arbitrary time resolution. For most purposes hourly data are used. Muon detectors are sensitive to primary cosmic rays

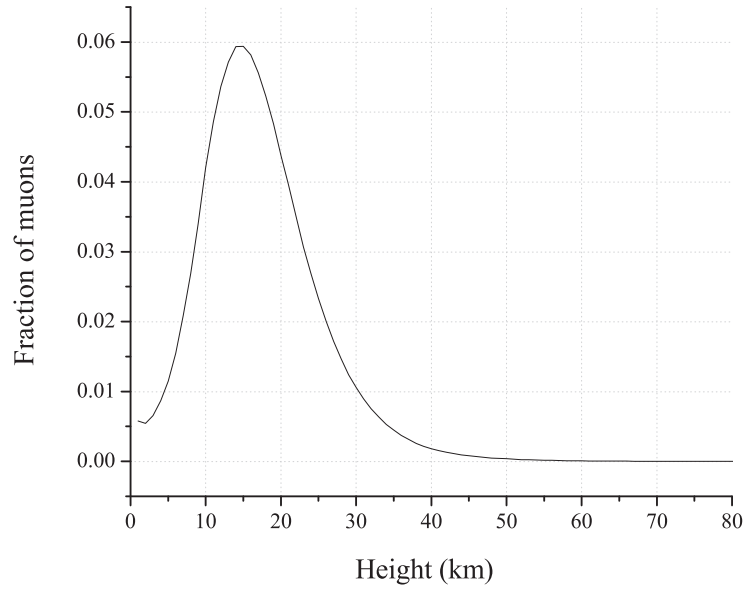


Fig. 1. Distribution of muon generation at different heights in the atmosphere, according to CORSIKA simulation.

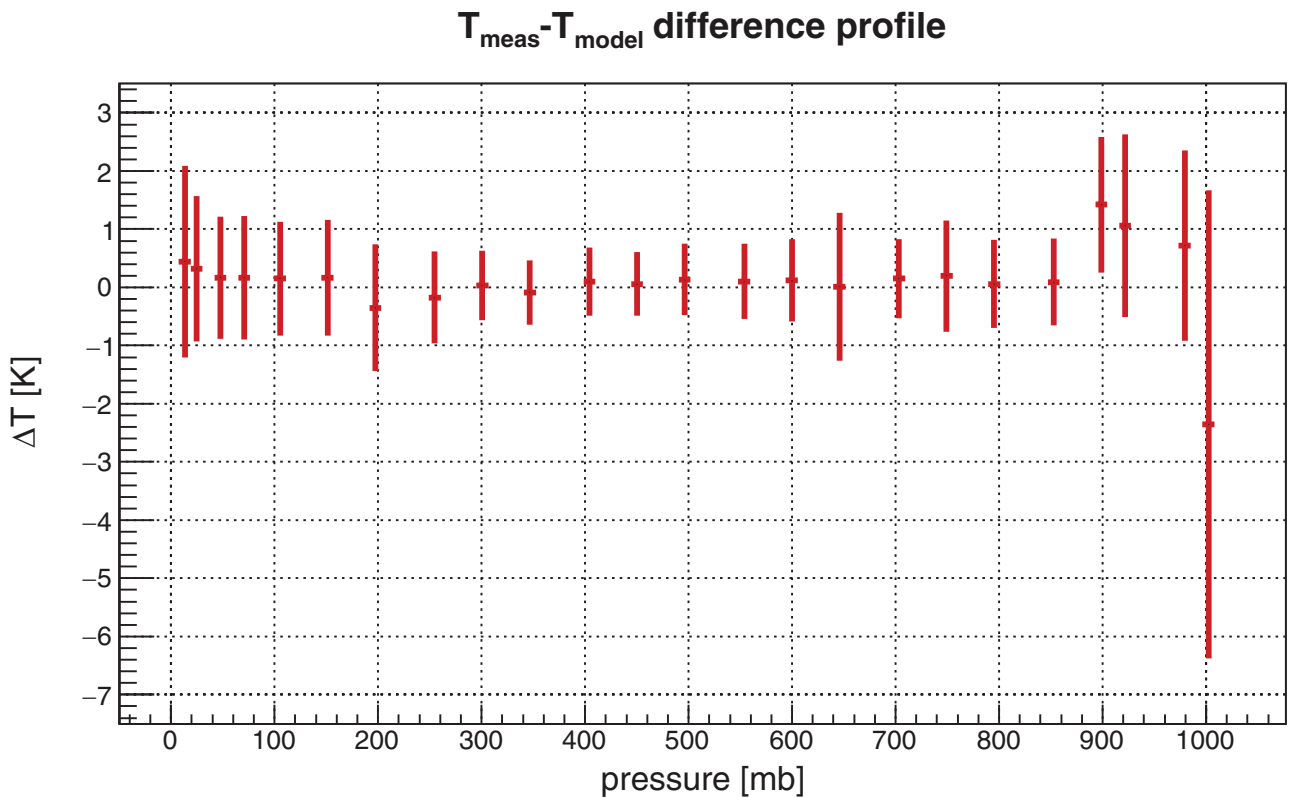


Fig. 2. Distribution of differences between measured temperatures and modeled by GFS.

of 59 GeV median energy in the case of ground level detector and 137 GeV for underground detector.

2.3. Principal component decomposition

Principal component analysis is a convenient and widely used data reduction method when dealing with strongly correlated

data. It transforms the original set of variables into a set of uncorrelated variables (called principal components (PC)). The principal components are ordered according to decreasing variance. In our case, there are 26 input variables: 24 modeled temperatures (isobaric level 1000 mb temperature excluded), locally measured ground level temperature and local atmospheric pressure. Initial variables were centered and normalized before

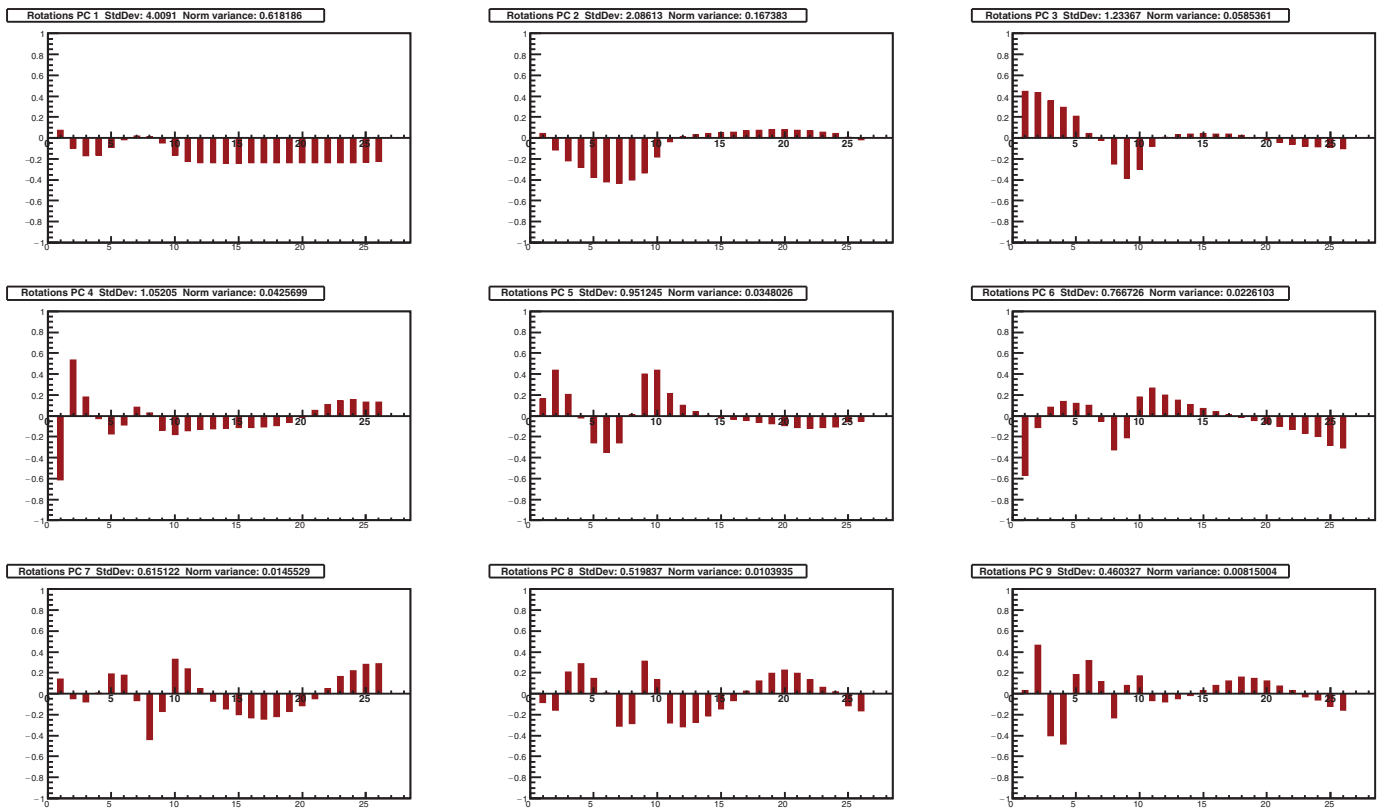


Fig. 3. Composition of nine principal components with largest variance (in decreasing order). Input variables are displayed on X-axis: 1 being pressure, 2 temperature of 10 mb isobaric level, 26 being local ground level temperature. Y-axis represents rotations.

decomposition. After decomposition, a new set of 26 principal components was obtained. Decomposition should not be regarded as universal, but it should be redone for every location and period under study.

One year was selected as a suitable time period for the analysis, in order to reduce possible seasonal bias, due to atmospheric temperature annual variation. Additional criteria were quality and consistency of muon data. Taking this into account, final time interval selected for analysis was from 01.06.2010 to 31.05.2011.

Fig. 3 shows composition plots for the first nine principal components, that account for 98% of total variance. X-axis represents input atmospheric variables, first being atmospheric pressure, followed by 10 mb layer temperature, last being ground level local temperature. Y-axis represents decomposition rotations for a given principal component. Interesting features observed on these plots are that first two principal components depend almost exclusively on temperature. The first one is mostly combination of temperatures in the troposphere (isobaric levels 250–1000 mb) with almost equal weights. The second eigenvector accounts for significant variance of temperatures in higher atmospheric levels (10–250 mb), with the strongest contribution centered in the tropopause. Components 3 to 6 have mixed p-T composition. The correlation of atmospheric pressure and temperature at different heights is not surprising. The diurnal and semi-diurnal oscillations of pressure are attributed to the warming of the upper atmosphere by the Sun [33]. This correlation makes it impossible to define a single barometric parameter in PCA based method of atmospheric corrections. It's worth mentioning that Dorman [34] recognizes three different barometric effects: absorption, decay and genera-

tion effect. It also indicates that empirical methods with separated pressure and temperature corrections might lead to overcorrection.

The values of the eigenvectors for these first nine components are also given in Table 1.

Fig. 4 shows plot of proportion of variance as well as plot of cumulative variance for obtained principal components. Corresponding numerical values are given in Table 2.

Usually, only a first few principal components (containing high fraction of total variance) are of practical interest. There are various different methods and rules for choosing how many PCs to retain in the analysis, none completely free of subjectivity (see for example a thorough discussion in [35]). A rule based on cumulative percentage of total variation usually recommends to retain PCs responsible for 70–90% of total variation. When one or two components are dominant, higher value (95%) is appropriate. In our case it would mean keeping first 6 PCs. According to Kaiser's rule only PCs with the eigenvalue $\lambda > 1$ should be retained. Jolliffe [35] suggested 0.7 as correct level, exceeded by six of our PCs. Another rule proposes to retain components with the eigenvalue above mean, a condition satisfied by first seven of our PCs. Another popular model is broken stick, but in application to our problem is too restrictive, leading to only two relevant PCs. The scree graph or log-eigenvalue diagram don't provide clean cut with our set of PCs.

To test the meaningfulness of potentially relevant PCs, the time series from PC data are constructed and tested whether they are distinguishable from white noise. The procedure is often done when principal component analysis is applied to atmospheric physics problems [36]. The time series with hourly resolution for the first three PCs are plotted on Fig. 5.

Table 1
Definition of first nine principal components.

Variables	Principal components								
	PC1	PC2	PC3	PC4	PC5	PC6	PC7	PC8	PC9
<i>p</i>	0.07699	0.04117	0.44694	-0.61285	0.16301	-0.57121	0.14028	-0.08106	0.03443
<i>T</i> (10)	-0.0947	-0.11603	0.43488	0.5344	0.43741	-0.11036	-0.04499	-0.15825	0.46469
<i>T</i> (20)	-0.16947	-0.21766	0.35754	0.18029	0.20527	0.08546	-0.07719	0.20635	-0.40309
<i>T</i> (30)	-0.16476	-0.27825	0.29593	-0.02505	-0.02204	0.14134	0.00634	0.28574	-0.47812
<i>T</i> (50)	-0.09124	-0.37682	0.20969	-0.17322	-0.25798	0.12084	0.19349	0.14645	0.18493
<i>T</i> (70)	-0.01483	-0.42304	0.04507	-0.08651	-0.3472	0.09965	0.18155	0.01024	0.31886
<i>T</i> (100)	0.02192	-0.43132	-0.02451	0.08228	-0.25692	-0.04937	-0.06464	-0.3103	0.1183
<i>T</i> (150)	0.01487	-0.40127	-0.24673	0.03037	0.012	-0.32566	-0.43658	-0.28393	-0.23316
<i>T</i> (200)	-0.04737	-0.33404	-0.38636	-0.13563	0.40141	-0.2069	-0.16852	0.31181	0.07995
<i>T</i> (250)	-0.16218	-0.17984	-0.29739	-0.18123	0.43708	0.18013	0.32866	0.13662	0.17389
<i>T</i> (300)	-0.22473	-0.03266	-0.07561	-0.14073	0.21179	0.26504	0.23807	-0.27931	-0.06785
<i>T</i> (350)	-0.2369	0.01439	0.00488	-0.12991	0.0998	0.1988	0.05306	-0.31612	-0.0771
<i>T</i> (400)	-0.23956	0.03362	0.02958	-0.12159	0.04075	0.14932	-0.06959	-0.27189	-0.04852
<i>T</i> (450)	-0.24028	0.04271	0.0402	-0.11503	0.00384	0.10744	-0.14772	-0.21165	-0.01823
<i>T</i> (500)	-0.24005	0.04935	0.0428	-0.11304	-0.02187	0.07218	-0.19893	-0.14512	0.03068
<i>T</i> (550)	-0.23958	0.05695	0.03965	-0.11295	-0.03254	0.0388	-0.23263	-0.06843	0.08056
<i>T</i> (600)	-0.23881	0.06549	0.03681	-0.10649	-0.04369	0.01102	-0.24562	0.02401	0.12499
<i>T</i> (650)	-0.23854	0.07279	0.0236	-0.09184	-0.06132	-0.01542	-0.21788	0.12597	0.15977
<i>T</i> (700)	-0.23835	0.0801	0.00429	-0.06052	-0.07601	-0.04668	-0.16785	0.19559	0.14932
<i>T</i> (750)	-0.23842	0.08071	-0.01837	-0.01332	-0.09245	-0.07308	-0.11295	0.22563	0.12401
<i>T</i> (800)	-0.23814	0.07557	-0.03907	0.05036	-0.10989	-0.09943	-0.04696	0.19596	0.07735
<i>T</i> (850)	-0.23701	0.0675	-0.06202	0.1081	-0.11988	-0.12745	0.04989	0.13672	0.0304
<i>T</i> (900)	-0.23535	0.05462	-0.07977	0.14776	-0.11454	-0.16955	0.16551	0.06204	-0.02952
<i>T</i> (925)	-0.23414	0.04606	-0.08313	0.15641	-0.10257	-0.19925	0.21877	0.01715	-0.05804
<i>T</i> (975)	-0.23108	0.00789	-0.08827	0.13022	-0.05888	-0.28046	0.284	-0.11523	-0.12249
<i>T</i> (1000)	-0.22494	-0.01582	-0.10092	0.13401	-0.04977	-0.30749	0.28553	-0.16516	-0.15908

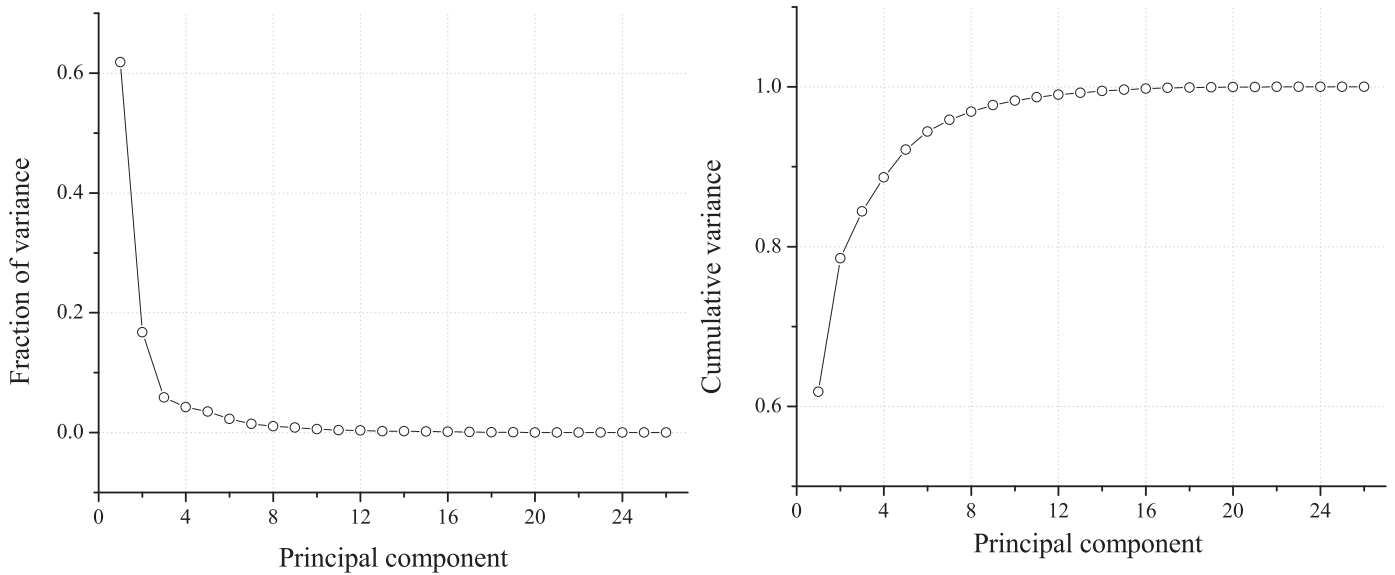


Fig. 4. Proportion of variance (left) and cumulative proportion of variance (right) for all 26 principal components.

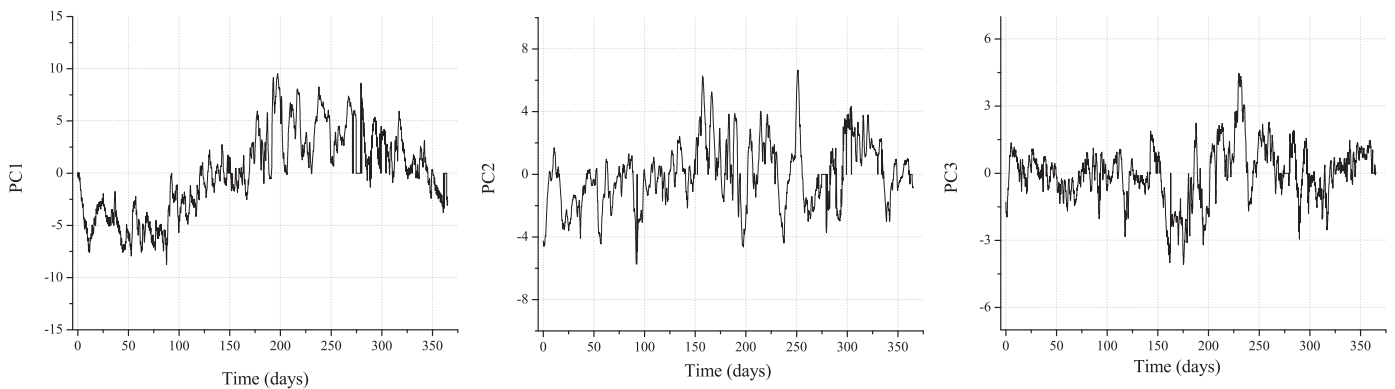


Fig. 5. Time series of the first 3 PCs.

Table 2
Variance (individual and cumulative) for all 26 PCs.

Principal component	Eigenvalue	Percentage of variance	Cumulative variance (%)
1	4.0091	0.618186	0.618186
2	2.08613	0.167383	0.785569
3	1.23367	0.0585361	0.844105
4	1.05205	0.0425699	0.886675
5	0.951245	0.0348026	0.921478
6	0.766726	0.0226103	0.944088
7	0.615122	0.0145529	0.958641
8	0.519837	0.0103935	0.969034
9	0.460327	0.00815004	0.977184
10	0.382006	0.00561263	0.982797
11	0.32832	0.00414592	0.986943
12	0.294489	0.00333553	0.990278
13	0.247876	0.00236317	0.992642
14	0.239462	0.00220546	0.994847
15	0.206157	0.00163465	0.996482
16	0.184453	0.00130857	0.99779
17	0.144657	8.04834E-4	0.998595
18	0.119676	5.5086E-4	0.999146
19	0.0938189	3.38538E-4	0.999485
20	0.0739496	2.10328E-4	0.999695
21	0.0586253	1.32189E-4	0.999827
22	0.0414996	6.62391E-5	0.999893
23	0.0338811	4.41511E-5	0.999937
24	0.0281359	3.04472E-5	0.999968
25	0.0219102	1.84637E-5	0.999986
26	0.0188263	1.36319E-5	1

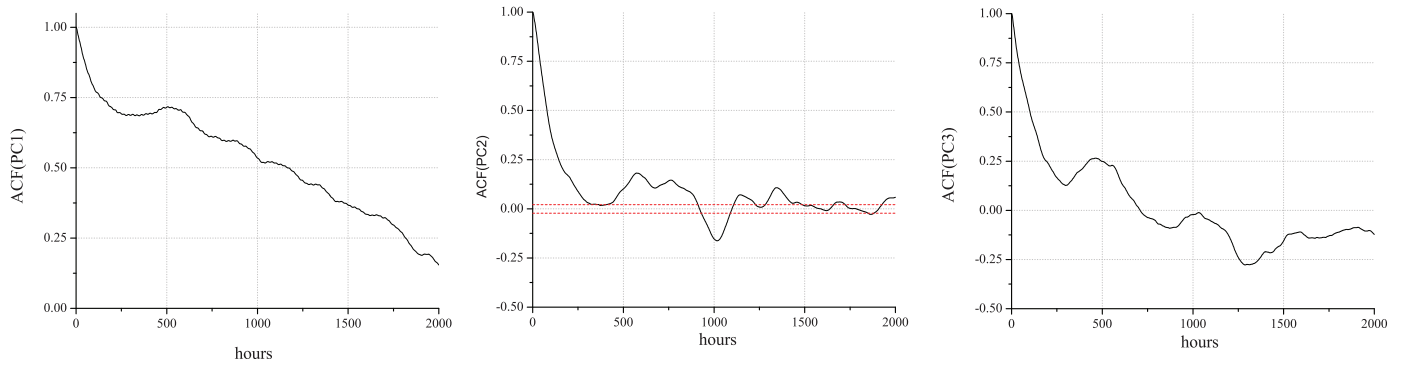


Fig. 6. Autocorrelation function of the first 3 PCs. Time lag is given in hours. In the case of PC2, 95% significance level is indicated by dashed red line. (For interpretation of the references to color in this figure legend, the reader is referred to the web version of this article.)

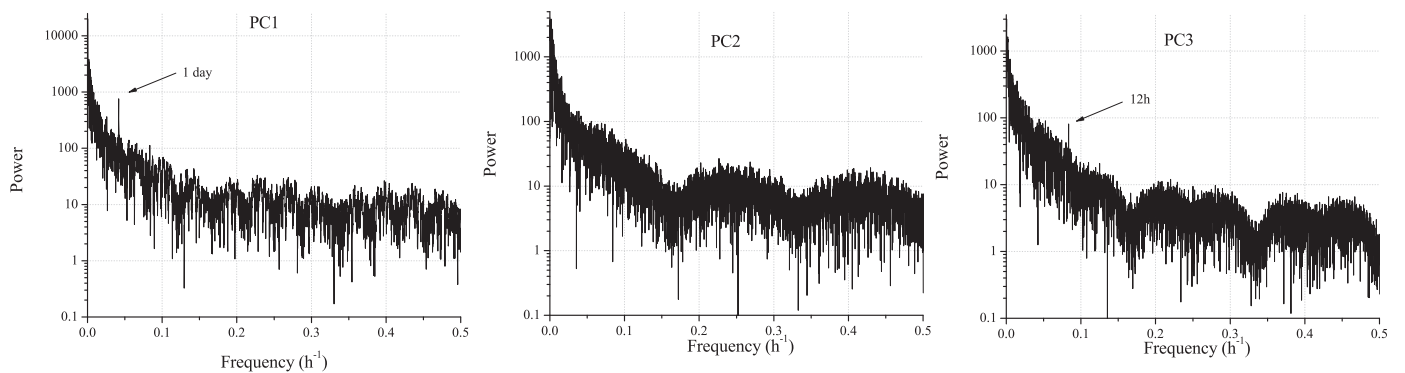


Fig. 7. Spectral analysis of time series of the first 3 PCs.

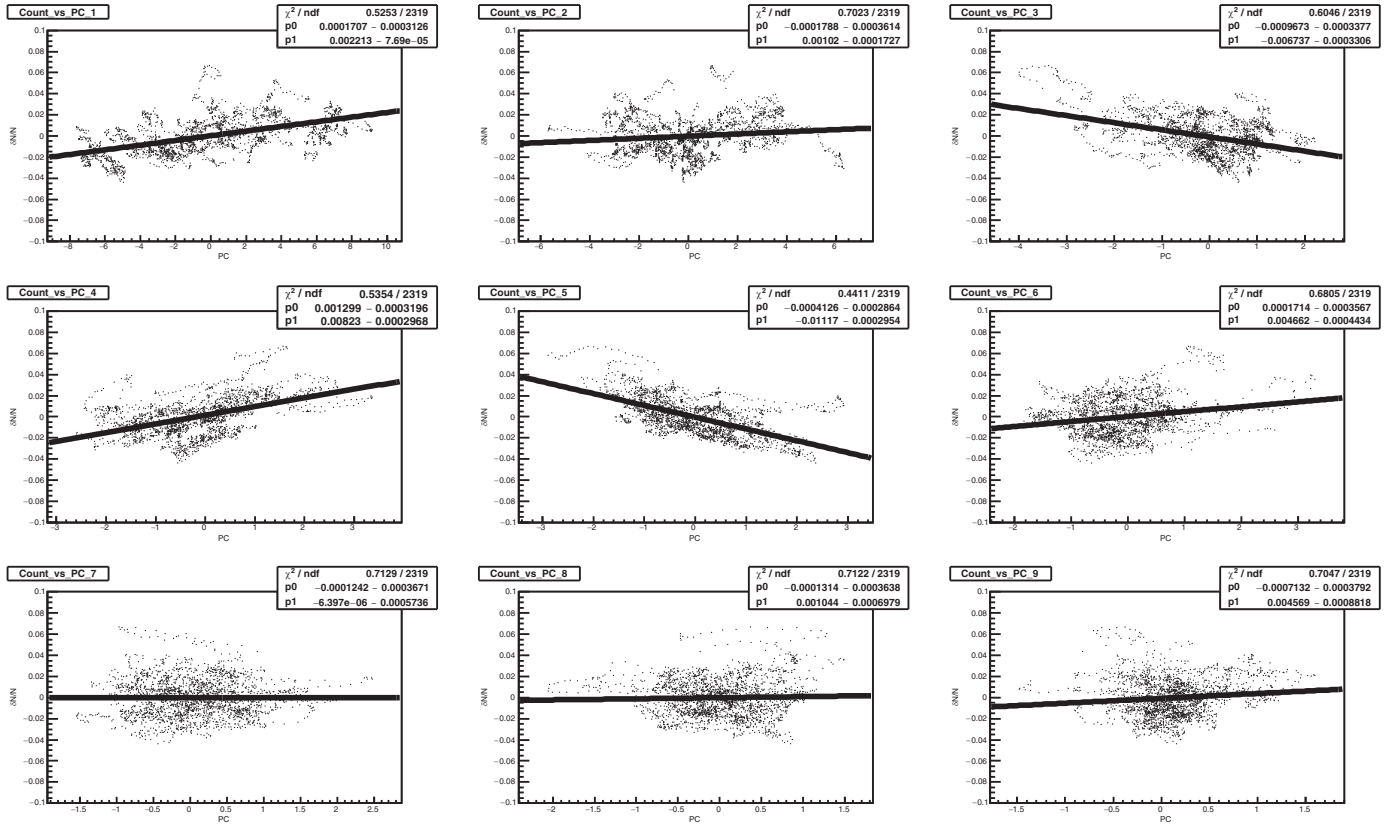


Fig. 8. Muon count dependence on principal components for the first nine principal components (GLL).

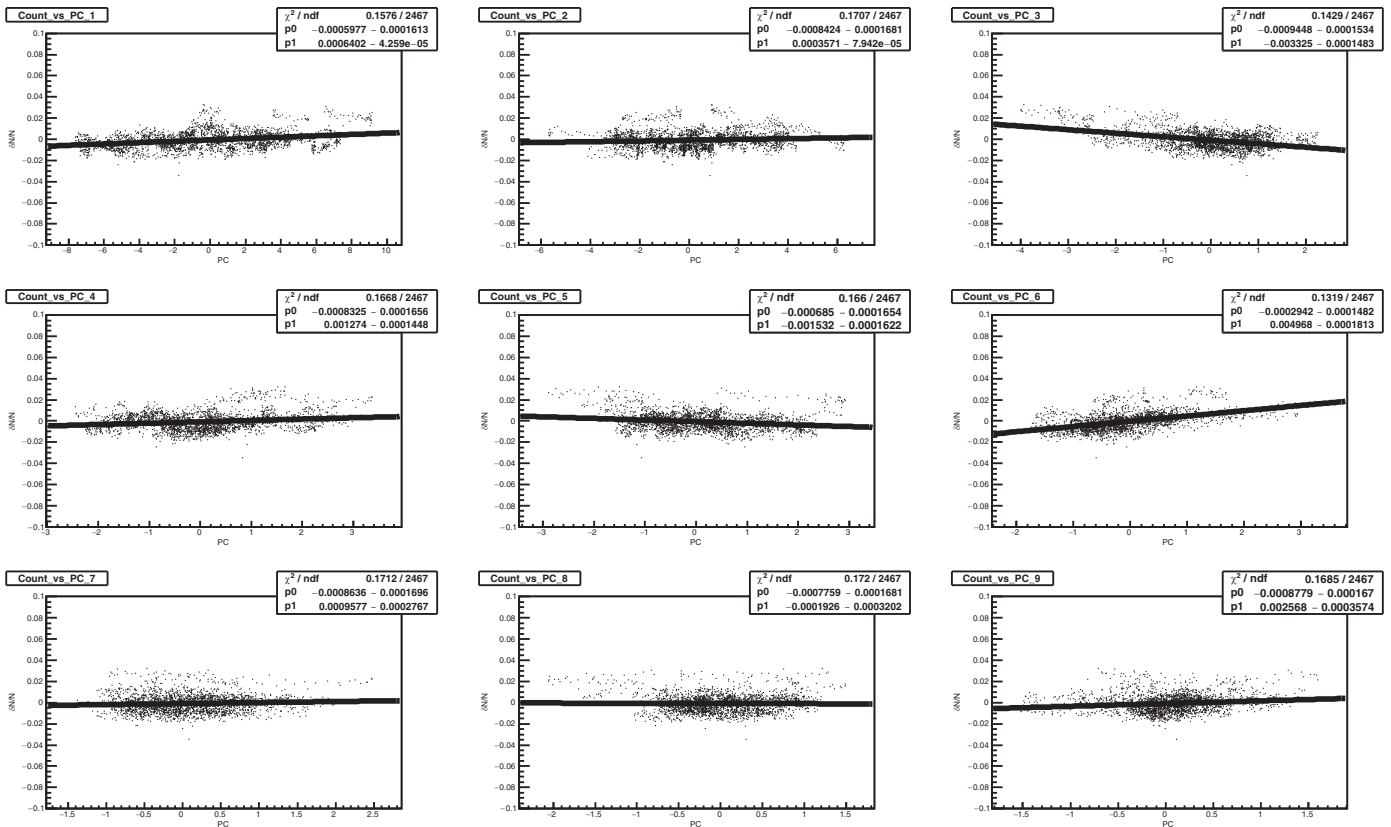


Fig. 9. Muon count dependence on principal components for the first nine principal components (UL).

The subsequent temperature and pressure measurements are highly correlated, as evident from autocorrelation function plot for selected PCs (Fig. 6).

The spectral analysis of the PC time series reveals, for PCs with the strong pressure component, semi-diurnal periodicity in addition to diurnal (Fig. 7).

Since our purpose is the regression of muon data with principal components, selecting the components with significantly high variance is not the main issue. It is more important to identify PCs with high correlation with CR data. Components with relatively low variance, can have high predictive power.

2.4. Correlation of principal components with CR muon count rate and correction of muon data

Scatter plot of muon count rate vs. PCs, together with the linear fit for the first nine principal components are shown on Fig. 8 (GLL) and Fig. 9 (UL). In the analysis hourly summed muon counts and principal component values for the respective hour were used. To minimize the effect of geomagnetic disturbances, only data for International Quiet Days were taken into account. The International Quiet Days are the days with minimum geomagnetic activity for each month. The selection of quiet days is deduced from K_p index. In our analysis 5 quietest days for each month are considered. The values of correlation coefficients are listed in Table 3.

Principal components PC1, PC3, PC4, PC5 and PC6 have been identified as ones with significant contribution to the muon flux variation. Interestingly enough, the PC2, responsible for 16.7% variance of the meteorological data has very little effect on muon flux, at neither ground nor underground level. Ground level muon flux variation is more affected by the first principal component, depending chiefly on the temperature in the troposphere. The finding agrees with usual negative temperature effect. The other PCs are difficult to compare with traditional correction parameters. Yet, the effect of PC3, that is composed more from upper atmosphere temperatures and hence could be loosely associated with positive temperature effect, is more pronounced for the underground muon flux. Fourth and fifth principal components with strong pressure contribution affect more ground level muon flux. On the other hand, PC6, also the one with high pressure component, has more pronounced influence on underground muon flux.

Gradients obtained from the fits for the significant principal components 1, 3, 4, 5 and 6 were then used to calculate the PCA corrected muon count according to the formula:

$$N_{\mu}^{(corr)} = N_{\mu} - \langle N_{\mu} \rangle \sum_i k_i PC_i, \quad i = 1, 3, 4, 5, 6 \quad (5)$$

where $N_{\mu}^{(corr)}$ corr is the corrected muon count, N_{μ} is the raw muon count, $\langle N_{\mu} \rangle$ is the mean count for the whole period, k_i are the gradients and PC_i are the corresponding principal components. Resulting corrected muon count time series are plotted on Figs. 10 (GLL) and 11 (UL) along with raw and pressure only corrected time series. Pressure corrected time series are produced for reference. Barometric coefficient was determined by applying linear regression to the same data set used for PCA. Data was previously corrected for temperature effect using integral method, as in Ref. [37]. Pressure corrected and PCA corrected time series are fitted with sine function with annual period in order to illustrate how PCA correction affects yearly variation induced by temperature effect.

PCA based atmospheric corrections remove 64.5% of total variance in GLL time series and 38.1% in UL time series. Pressure corrected CR time series exhibit annual variation, a consequence of

Table 3
Correlation coefficients between principal components and muon count rate in the ground level laboratory (GLL) and underground laboratory (UL).

PC	1	2	3	4	5	6	7	8	9	10	11	12	13	14	15	16	17	18	19	20	21	22	23	24	25	26
GLL	0.43	0.01	-0.37	0.48	-0.55	0.30	-0.01	0.03	-0.01	0.06	0.00	-0.04	0.00	0.01	0.02	-0.01	0.00	-0.01	-0.01	0.03	-0.03	0.00	0.02	-0.01	0.04	0.02
UL	0.26	0.02	-0.48	0.21	-0.19	0.52	0.02	0.04	0.07	0.04	0.01	-0.04	-0.07	0.06	-0.02	-0.05	0.04	0.04	-0.02	-0.02	0.00	0.01	0.00	-0.03	0.01	0.01

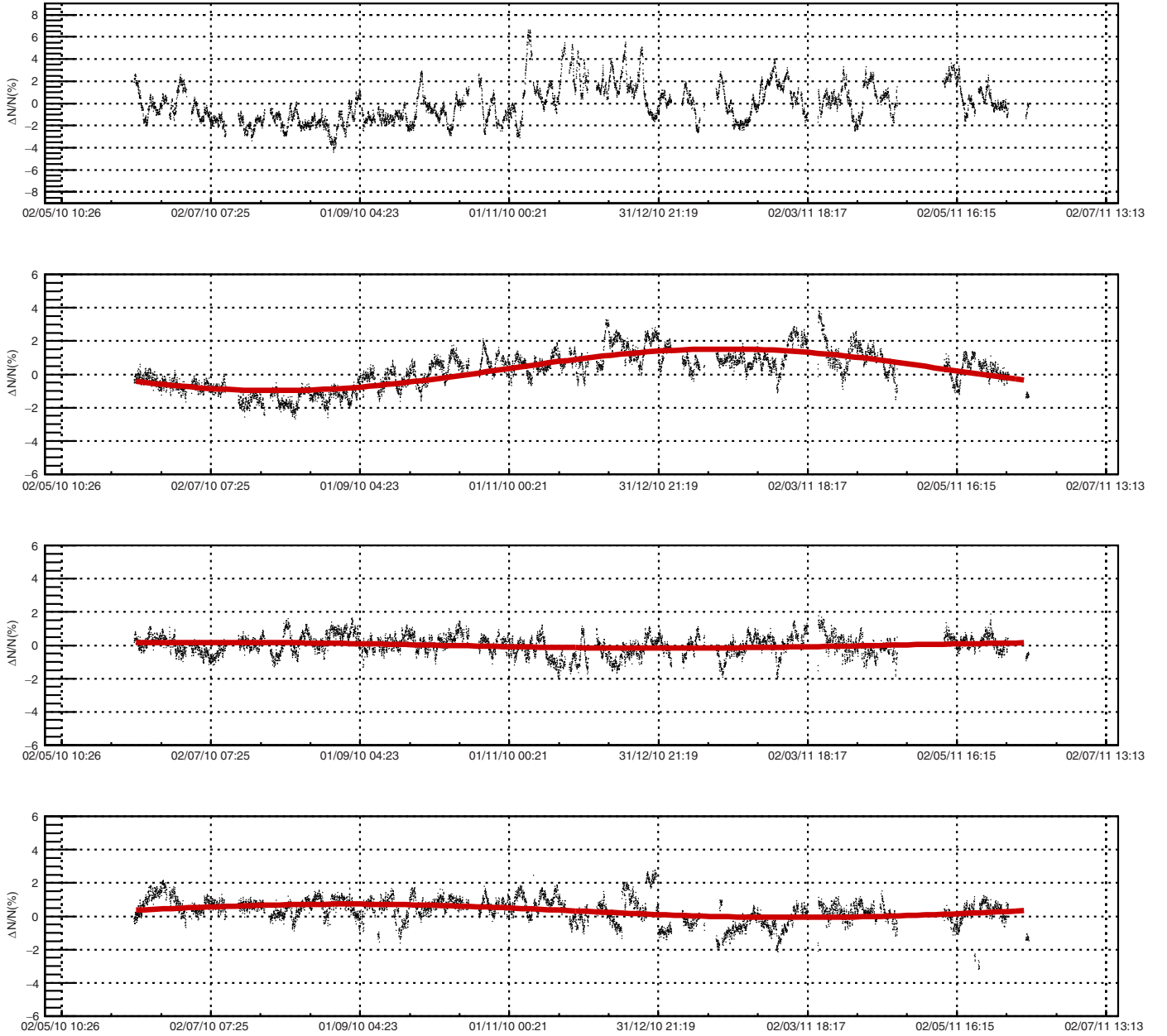


Fig. 10. Raw (upper panel), pressure corrected (middle panel), pressure+temperature corrected with PCA method (3rd panel from the top) and pressure+temperature corrected with integral method (lower panel) normalized muon count rate for GLL. The sine function with one year period is fitted to the data.

the temperature effect. The performance of the temperature correction may be tested by comparing the amplitude of the annual variation before and after correction. With presented method the amplitude of the annual variation is reduced by 86% (54.9%) in the case of GLL (UL) with respect to the pressure only corrected time series.

To further test the new method, the atmospheric correction of GLL data are performed by the integral method. The correction resulted in 56.25% of variance reduction and 68.1% of reduction of the amplitude of the annual wave. At least in the case of our CR data set the new method performs somewhat better than the integral method.

3. Conclusion

The principal component analysis is successfully used to construct a new empirical method for the atmospheric corrections of CR muon data. The method is equally applicable to all muon detectors, irrespective to location: ground level, shallow or deep underground. It requires knowledge of the atmospheric pressure and temperatures along the entire atmosphere, which is nowadays available in databases such as GFS. The method is suitable for the near real-time correction, with the delay defined by the availability of the atmospheric data (one day in the case of present GFS data). When applied to Belgrade muon data from two detectors

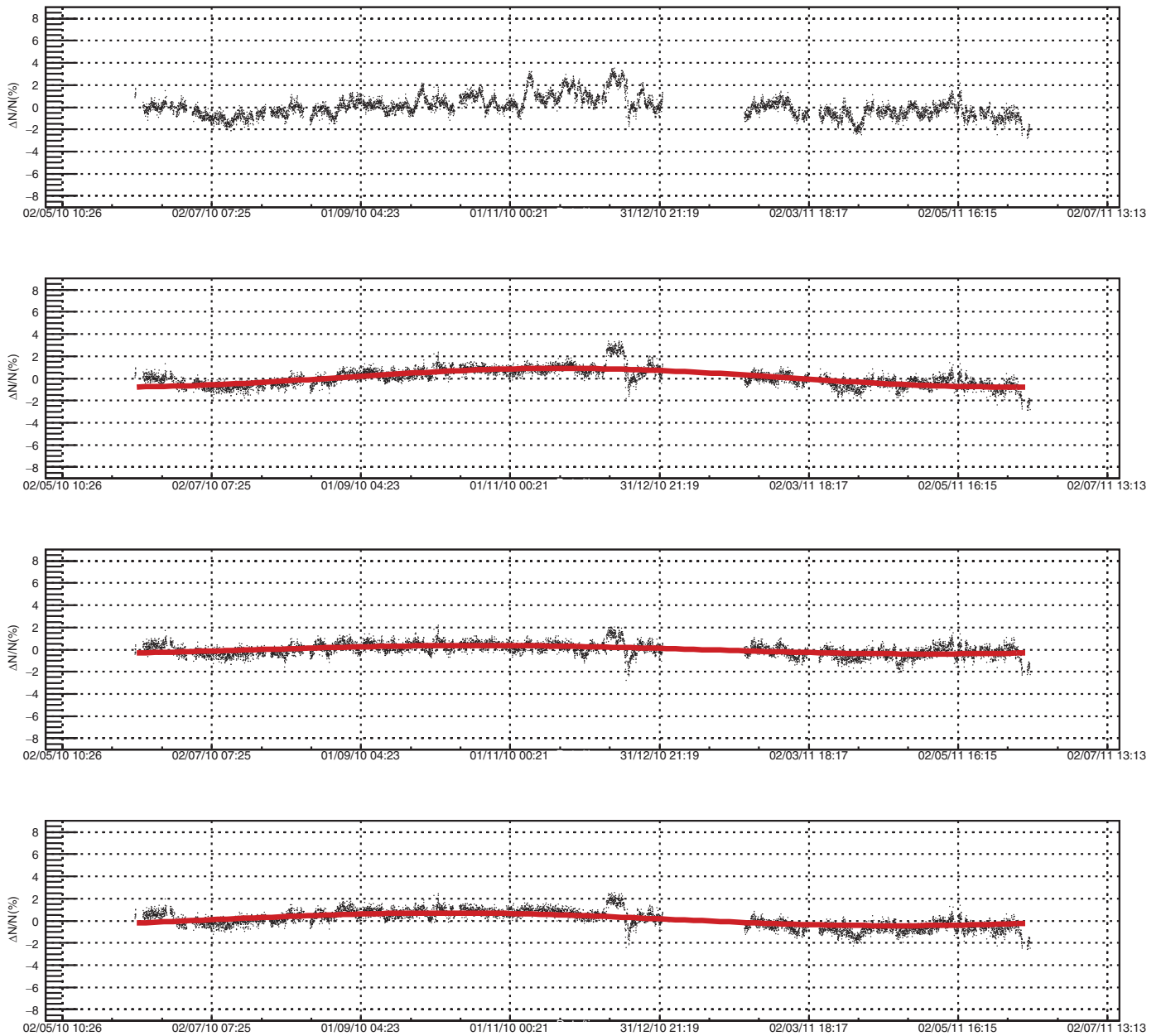


Fig. 11. Raw (upper panel), pressure corrected (middle panel), pressure+temperature corrected with PCA method (3rd panel from the top) and pressure+temperature corrected with integral method (lower panel) normalized muon count rate for UL. The sine function with one year period is fitted to the data.

(ground level and at 25 mwe), the method requires correction to five parameters, determined from linear regression. With the same CR dataset, the present method yields results superior to the integral method in terms of variance reduction and reduction of the annual variation. The new method is also suitable for temperature corrections of the neutron monitor data, which is seldom done in practice.

Acknowledgments

The authors are deeply grateful to Dr. Viktor Yanke for the encouragement and useful advice. The present work was funded by the Ministry of Education, Science and Technological Development of the Republic of Serbia, under the Project no. 171002.

References

- [1] L. Myssowsky, L. Tuwim, Unregelmäßige intensitätsschwankungen der höhenstrahlung in geringer seehöhe, *Zeitsch. Phys.* 39 (2–3) (1926) 146–150.
- [2] E. Steinke, Über schwankungen und barometereffekt der kosmischen ultrastrahlung im meeresniveau, *Zeitsch. Phys.* 64 (1–2) (1930) 48–63.
- [3] P.M. Blackett, On the instability of the barytron and the temperature effect of cosmic rays, *Phys. Rev.* 54 (11) (1938) 973.
- [4] M. Forro, Temperature effect of cosmic radiation at 1000-m water equivalent depth, *Phys. Rev.* 72 (9) (1947) 868.
- [5] C.M.G. Lattes, G.P. Occhialini, C.F. Powell, Observations on the tracks of slow mesons in photographic emulsions, *Nature* 160 (4067) (1947) 486.
- [6] C.M.G. Lattes, H. Muirhead, G.P. Occhialini, C.F. Powell, Processes involving charged mesons, *Nature* 159 (4047) (1947) 694.
- [7] G. Occhialini, C. Powell, Nuclear disintegrations produced by slow charged particles of small mass, *Nature* 159 (4032) (1947) 186.
- [8] A. Duperier, The meson intensity at the surface of the earth and the temperature at the production level, *Proc. Phys. Soc. Lond. Sect. A* 62 (11) (1949) 684.
- [9] A. Duperier, Temperature of the upper atmosphere and meson production, *Nature* 167 (4243) (1951) 312.

- [10] C. Baker, D. Hall, J. Humble, M. Duldig, Atmospheric correction analysis for the Mawson muon telescopes, in: International Cosmic Ray Conference, 3, 1993, p. 753.
- [11] A. Maghrabi, M. Almutayri, Atmospheric effect on cosmic ray muons at high cut-off rigidity station, *Adv. Astron.* 2016 (2016).
- [12] C.R. Braga, A. Dal Lago, T. Kuwabara, N.J. Schuch, K. Munakata, Temperature effect correction for the cosmic ray muon data observed at the Brazilian Southern Space Observatory in São Martinho da Serra, *J. Phys.* 409 (2013) 012138 IOP Publishing..
- [13] G.C. Castagnoli, M. Dodero, Temperature effect of the muon component underground and pion attenuation length, *Il Nuovo Cimento B* (1965–1970) 51 (2) (1967) 525–534.
- [14] A. Fenton, R. Jacklyn, R. Taylor, Cosmic ray observations at 42 m we underground at hobart, tasmania, *Il Nuovo Cimento* (1955–1965) 22 (2) (1961) 285–295.
- [15] M. Zazyan, M. Ganeva, M. Berkova, V. Yanke, R. Hippler, Atmospheric effect corrections of mustang data, *J. Space Weather Space Clim.* 5 (2015) A6.
- [16] L. Dorman, The temperature effect of the hard component of cosmic rays, *Doklady Akad. Nauk SSSR* 95 (1954).
- [17] E. Feinberg, On the nature of cosmic ray barometric and temperature effects, *DAN SSSR* 53 (5) (1946) 421–424.
- [18] L.I. Dorman, Cosmic ray variations, Technical Report, Foreign Technology Div Wright-Patterson AFB OHIO, 1957.
- [19] K. Maeda, M. Wada, Atmospheric temperature effect upon the cosmic-ray intensity at sea level, *J. Sci. Res. Inst.* 48 (1954).
- [20] V. Dvornikov, Y.Y. Krest'yannikov, A. Sergeev, Determination of the variation of average-mass temperature of the atmosphere by data of cosmic ray intensity, *Geomag. Aeron.* 16 (1976) 923–925.
- [21] V. Yanchukovsky, G.Y. Filimonov, R. Hisamov, Atmospheric variations in muon intensity for different zenith angles, *Bull. Russ. Acad. Sci.* 71 (7) (2007) 1038–1040.
- [22] R. De Mendonça, C. Braga, E. Echer, A. Dal Lago, K. Munakata, T. Kuwabara, M. Kozai, C. Kato, M. Rockenbach, N. Schuch, et al., The temperature effect in secondary cosmic rays (muons) observed at the ground: analysis of the Global MUON Detector Network data, *Astrophys. J.* 830 (2) (2016) 88.
- [23] A. Dmitrieva, I. Astopov, A. Kovylyaeva, D. Pankova, Temperature effect correction for muon flux at the earth surface: estimation of the accuracy of different methods, *J. Phys.* 409 (2013) 012130. IOP Publishing.
- [24] P.H. Barrett, L.M. Bollinger, G. Cocconi, Y. Eisenberg, K. Greisen, Interpretation of cosmic-ray measurements far underground, *Rev. Mod. Phys.* 24 (3) (1952) 133.
- [25] S. Tilav, P. Desiati, T. Kuwabara, D. Rocco, F. Rothmaier, M. Simmons, H. Wising, et al., Atmospheric variations as observed by IceCube, arXiv:1001.0776 (2010).
- [26] P. Adamson, C. Andreopoulos, K. Arms, R. Armstrong, D. Auty, D. Ayres, C. Backhouse, J. Barnett, G. Barr, W. Barrett, et al., Observation of muon intensity variations by season with the Minos far detector, *Phys. Rev. D* 81 (1) (2010) 012001.
- [27] H. Carmichael, M. Bercovitch, J.F. Steljes, Introduction of meteorological corrections into meson monitor data, *Tellus* 19 (1) (1967) 143–160, doi:10.1111/j.2153-3490.1967.tb01468.x.
- [28] M.D. Berkova, A.V. Belov, E.A. Eroshenko, V.G. Yanke, Temperature effect of the muon component and practical questions for considering it in real time, *Bull. Russ. Acad. Sci.* 75 (6) (2011) 820–824, doi:10.3103/S1062873811060086.
- [29] A. Dmitrieva, R. Kokoulin, A. Petrukhin, D. Timashkov, Corrections for temperature effect for ground-based muon hodoscopes, *Astropart. Phys.* 34 (6) (2011) 401–411, doi:10.1016/j.astropartphys.2010.10.013.
- [30] Global forecast system (GFS), <https://www.ncdc.noaa.gov/data-access/modeldata/model-datasets/global-forecast-system-gfs>.
- [31] National centers for environmental prediction (NCEP), <http://www.ncep.noaa.gov/>.
- [32] A. Dragić, V. Udovičić, R. Banjanac, D. Joković, D. Maletić, N. Veselinović, M. Savić, J. Puzović, I.V. Aničin, The new setup in the Belgrade low-level and cosmic-ray laboratory, *Nucl. Technol. Radiat. Protect.* 26 (3) (2011) 181–192.
- [33] B. Haurwitz, The diurnal surface-pressure oscillation, *Arch. Meteorol. Geophys. Bioklimatol. Ser. A* 14 (4) (1965) 361–379, doi:10.1007/BF02253483.
- [34] L.I. Dorman, Cosmic Rays in the Earth's Atmosphere and Underground, Springer Netherlands, 2004, doi:10.1007/978-1-4020-2113-8.
- [35] I. Jolliffe, Principal Component Analysis, Springer-Verlag, 2002, doi:10.1007/b98835.
- [36] R.W. Preisendorfer, D.M. Curtis, Principal component analysis in meteorology and oceanography, Elsevier, Amsterdam, 1988.
- [37] M. Savić, D. Maletić, D. Joković, N. Veselinović, R. Banjanac, V. Udovičić, A. Dragić, Pressure and temperature effect corrections of atmospheric muon data in the belgrade cosmic-ray station, *J. Phys. Conf. Ser.* 632 (1) (2015) 012059.



Correlation analysis of solar energetic particles and secondary cosmic ray flux

Nikola Veselinović^a, Mihailo Savić, Aleksandar Dragić, Dimitrije Maletić, Radomir Banjanac, Dejan Joković, David Knežević, and Vladimir Udovičić

Institute of Physics Belgrade, University of Belgrade, Pregrevica 118, Belgrade 11080, Serbia

Received 31 January 2021 / Accepted 5 May 2021 / Published online 8 June 2021
© The Author(s), under exclusive licence to EDP Sciences, SIF and Springer-Verlag GmbH Germany, part of Springer Nature 2021

Abstract. Galactic cosmic rays entering heliosphere are modulated by interplanetary magnetic field which is carried away from the Sun by the solar wind. Cosmic rays are additionally modulated by coronal mass ejections and shock waves, which can produce Forbush decrease, a transient decrease in the observed galactic cosmic ray intensity. Measurements of magnetic field and plasma parameters in near-Earth space detect regularly coronal mass ejections, so it is important to understand the correlation between near-Earth particles fluxes associated with these coronal mass ejections and Forbush decreases. By combining in situ measurements of solar energetic particles with ground-based observations by the Belgrade muon detector, we analysed the dynamics of the variation of galactic cosmic rays. Correlation between variations of the flux of the cosmic rays and average in situ particle fluxes was investigated during Forbush decreases. Correlation exhibited dependence on the energy of solar wind particles, but also on cut-off rigidities of cosmic rays detected on the ground. The goal of cross-correlation analysis is to help in better understanding of how coronal mass ejections affect space weather as well as the effects they have on primary cosmic ray variations as detected by ground-based cosmic ray detectors.

1 Introduction

Space weather has been widely used as a term to define impact of the Sun, heliosphere and geomagnetic field on our biosphere and our technological systems. Understanding space weather is a matter of both scientific interest and practical importance as its impact could potentially be hazardous to our civilisation. Cosmic ray (CR) observations can also be used to study space weather. Primary (or galactic) CRs are high-energy nuclei (mainly protons) that originate from outside of our solar system. Their flux and energy range is covering several tens of orders of magnitude (flux from 10^{-28} up to 10^4 ($\text{m}^2 \text{sr sec eV/nucleon}$)⁻¹ and energy range up to 10^{21} eV [10]). As charged particles, CRs are sensitive to magnetic field, so often it is more convenient to use geomagnetic rigidity instead of energy to characterise primary CRs. Geomagnetic rigidity is defined as $R = B\rho = pq$, where B is the magnetic field, ρ is the gyroradius of the particle due to this field, p is the particle momentum and q is its charge [14]. As they traverse interplanetary space, galactic CRs interact with helio-

spheric magnetic field. The heliosphere is the region of space around the Sun dominated by the solar wind and the interplanetary magnetic field (IMF). The solar wind is a stream of supersonic plasma blowing outward from the Sun. IMF represents solar magnetic field carried by highly conducting solar wind plasma. Interaction of CRs with this large-scale field modulates CRs flux intensity measured on Earth, which is nested deep inside the heliosphere. Interaction with the heliosphere causes gradient and curvature drift motion of CRs and scattering by the magnetic irregularities embedded in the solar wind [19]. Variations in the solar magnetic field directly affect the heliosphere, most prominent being the solar cycle variation with a period of about 11 years. Solar cycle affects activity of the Sun which is visible in varying number of sunspots, solar flares (SFs) and coronal mass ejections (CMEs). Coronal mass ejection is an extreme solar activity event, followed by significant release of charged particles and accompanying magnetic field from solar corona. Intensity of measured CRs flux anticorrelates with the activity of the Sun, with lower intensity during maximum of the solar cycle and higher intensity during minimum of solar activity.

One of the transient phenomena of this interaction is the Forbush decrease (FD), which represents a rapid depression in CR flux. It is usually characterised by a sudden decrease reaching minimum within one day, followed by a subsequent gradual recovery phase, which

Supplementary information The online version of this article (<https://doi.org/10.1140/epjd/s10053-021-00172-x>) contains supplementary information, which is available to authorized users.

^a e-mail: veselinovic@ipb.ac.rs (corresponding author)

can last for several days. Typical causes of FD are transient interplanetary events related to interplanetary coronal mass ejections (ICMEs). If the speed of the ICME is greater than fast magnetosonic wave speed in the solar wind reference frame, ambient solar wind plasma will be compressed. The shock can be formed, which is driven ahead of ICME and can cause enhancement of IMF. FD can also be formed due to corotating interaction regions between different solar wind streams with different speed [2]. In this paper, we will only focus on ICME induced FDs, of which we will study four cases.

Correlation between parameters characterising FDs (like magnitude of the decrease, duration, one-step or two-step FDs, etc.) and solar wind parameters has been studied for some time. There is reasonable evidence for correlation between FD magnitude and amplitude of magnetic field enhancement B , velocity of CME, maximum solar wind velocities and other parameters as shown in [7, 22]. Also, profile of FDs is modelled and compared with CME magnetic structure, starting from the simple force-free flux rope with circular cross section, but it can deviate from this ideal concept. FD magnitude is explained with cumulative effect of diffusion of CRs through the turbulent sheath region [3, 11]. FD is also energy dependent, where amplitude of decrease is typically around several percent. Higher-rigidity CRs only weakly interact with magnetic disturbances, so no significant change of the flux can be expected for CRs with rigidity of several dozen GV [9]. In order to detect FD at any location, larger statistics are needed for CRs of lower energy. CRs also interact with geomagnetic field which imposes the minimal rigidity CRs must have in order to reach Earth's surface. This geomagnetic cut-off rigidity depends on geomagnetic latitude. It is smaller at the poles and increases with latitude, with some exceptions due to deviation of Earth's magnetic field from the magnetic dipole model (i.e., South Atlantic anomaly [4]).

Primary CRs arriving at Earth interact with atoms and molecules in Earth's atmosphere. CRs with energy above 300–400 MeV/nucleon generate showers of secondary particles. These secondary CRs consist of electrons and photons (electromagnetic component) and harder, in terms of energy, nuclear component of the cascade. Nuclear component, at the bottom of the atmosphere, is composed mainly of muons, protons, neutrons and neutrinos. Secondary CRs can be observed with detectors in the atmosphere (balloon probes), on the ground or even underground. High-energy muons can penetrate deep underground and can be an important component of the background in experiments requiring high sensitivity (dark matter search, proton decay, etc.).

There is a well-known correlation between parameters of solar wind plasma and CR flux, and the goal of this paper is to extend the study of FDs, specifically its magnitude and time evolution, to wider range of parameters of the heliosphere measured routinely with satellites. We concentrate our study on previously scarcely used parameters of the solar wind, particularly flux of

charged particles of different energies. These particles are the source of inhomogeneity in the IMF, so the goal is to try and find distinguishing characteristics of FDs, like magnitude of decrease and FD profile that can be related to the satellite proton flux data, and examine their potential correlation with other space weather parameters. This additional information can be useful in finding explicit connection between parameters of solar wind and CR flux and can lead to better understanding of these complex processes.

2 CR data

In order to provide higher count rate, detector on Earth has to be omnidirectional and to detect integral flux over different range of energies. For the last seventy years secondary CRs are measured using standard ground-based neutron monitors (NMs) [6]. There is a worldwide network of NMs (<http://www01.nmdb.eu/>) that measures flux of secondary CRs originated from primary CRs with rigidity range approximately between 1 GV and 20 GV. Every node of the worldwide network of ground stations has its unique cut-off rigidity depending on its geomagnetic coordinates and height. The other type of widely used ground-based CR detectors are muon monitors. Muon monitors are sensitive to primary CRs of higher rigidity and complement NMs measurements [26]. Worldwide network of these muon stations is still rudimentary, but it can provide insight into flux variation of primary CRs with energies higher than CRs detected by NMs. Since both NMs and muon detectors are energy-integrating detectors and use entire atmosphere above it as a moderator, it is not trivial to relate count rate of these detectors to the flux or energy spectrum of primary CRs at the top of the atmosphere. One needs to know the response of a detector to a unit flux of CRs with the given energy, the so-called detector yield function. Yield functions can be calculated either theoretically, using a numerical simulation of the nucleonic cascade caused by energetic cosmic rays in the Earth's atmosphere, e.g., [8], or semi-empirically, for example based on a latitudinal survey [16].

As flux of secondary cosmic rays is also sensitive to varying properties of the atmosphere through which these CRs propagate, it is necessary to conduct flux correction of the measured flux for atmospheric parameters, where atmospheric pressure correction is the most important. In addition to atmospheric pressure, CR muons are sensitive to temperature variations in the atmosphere, starting from the top of the atmosphere all the way to the ground level. There are several procedures for corrections of these effects which are regularly used. Most commonly used are the integral method and the method of effective level of generation, but some novel techniques have also been introduced in recent years [25]. Correction for these atmospheric parameters is necessary in order to increase detector sensitivity to

Table 1 Properties of primary CR flux related to muons detected at Belgrade CR station

Detector	Muon flux 1/(m ² s)	$E_{0.05}$ (GeV)	E_{med} (GeV)	$E_{0.95}$ (GeV)	Cut-off rigidity (GV)
GLL	137(6)	11	59(2)	915	5.3
UL	45(2)	31	137(5)	1811	12

variations of primary CRs flux and more precisely study the influence of solar modulation on galactic CRs.

Belgrade CR station started collecting data with the current experimental set-up in 2009. The station consists of two separate detector units: one placed on ground level (GLL) and the other in shallow underground (UL), both utilising the same experimental set-up. Such configuration provides opportunity to monitor muon fluxes in two different energy ranges with all other external parameters (such as atmospheric parameters, geomagnetic location and experimental set-up) being the same. Underground part of the station detects muons originated from primary CRs with higher energy because of the layer of soil overburden (13 m of loess) which absorbs lower-energy muons. Details of the detector systems at the Belgrade CRs station as well as calculated response functions are presented in [29]. The station is situated at the Laboratory for Nuclear Physics at the Institute of Physics Belgrade, Serbia. The altitude of the station is 78 m above sea level. Its geographic coordinates are: 44°51' N and 20°23' E, with geomagnetic latitude of 39°32' N. Sensitivity of Belgrade CR detectors to galactic CRs is given in Table 1, where primary CRs with the energy below $E_{0.05}$ (and above $E_{0.95}$) contribute with 5% to the count rate of the corresponding detector, and E_{med} is median energy based on simulation. In preparation for the analysis, detected muon count rates are corrected for efficiency, as well as for barometric and atmospheric temperature effects. Temperature effect correction is done using integral method [24].

3 Satellite data

In recent years, satellites provide new direct measurements of primary CRs flux in the heliosphere and the geomagnetic field. Also, detectors mounted on spacecraft allow us to probe even further, as Voyager recently crossed heliospheric boundary and for the first time galactic CRs flux was measured outside the heliosphere. The problem with such measurements is limitation to the size of the detectors, due to constraints of the construction of the satellites. In order to have valid statistics and good resolution, only low-energy particle flux can be measured. These low-energy particles are sensitive to geomagnetic field, which can introduce additional perturbation. Also, measurements of low-energy CRs can be masked by the increased flux of low-energy solar energetic particles (SEPs) in the MeV energy range. FDs detected by ground-based detectors are measured in energy range several orders of

magnitude higher than the energy range available to satellites measurements. (NMs detect flux that originate from ~ 10 GeV, single muon detectors higher than that up to ~ 100 GeV, while solar weather satellite measurements range up to several 100 MeV.) SEP occurrence is sporadic and depends on which part of the solar cycle we are in, so long-term studies with stable data quality are necessary if we are to study solar modulation of CRs. Such long-term measurements have been performed with various spacecrafts during the last four decades. Data measured on different interplanetary locations are then used for modelling of the heliosphere, which is important for understanding and forecasting space weather. This is a relatively new and dynamic field that is still expanding. More in situ measurements that can be catalogued [17] and compared with data from ground based stations will improve our understanding of near space environment.

In this paper, we use proton data from ERNE (Energetic and Relativistic Nuclei and Electron experiment) detector at the SOHO (Solar and Heliospheric Observatory) (https://omniweb.gsfc.nasa.gov/ftpbrowser/flux_spectr_m.html), which has been performing measurements in Lagrangian point L1 for the last quarter of a century described in [13] and references therein. Experiments that collect in situ particles data are ERNE and COSTEP (Comprehensive SupraThermal and Energetic Particle analyser), where data are combined to meet requirements of the mission. ERNE detector provides proton flux data in relatively large energy range (1.6 to 131 MeV) separated in several energy channels (1.3–1.6, 1.6–2.0, 2.0–2.5, 2.5–3.2, 3.2–4.0, 4.0–5.0, 5.0–6.4, 6.4–8.0, 8.0–10, 10–13, 13–16, 16–20, 20–25, 25–32, 32–40, 40–50, 50–64, 64–80, 80–100, 100–130 MeV). Measurements are taken with two different detectors: LED (low-energy detector) covers lower-energy and HED (high-energy detector) which covers higher-energy channels [28]. Satellites, including SOHO, also measure in situ parameters of the space environment and gather data about magnetic field, solar wind and concentration and flux of various types of particles on the location. Satellite data relevant to heliospheric studies are, among other places, available at GSFC/Space Physics Data Facility, in the form of low- and high-resolution OMNI data (https://spdf.gsfc.nasa.gov/pub/data/omni/low_res_omni/). In this study, we used the low-resolution OMNI data that contain hourly data for the solar wind magnetic field and plasma parameters, energetic proton fluxes, and geomagnetic and solar activity indices for different regions in proximity to Earth [12].

4 Four prominent FD events during rising phase of solar cycle 24

Previous (24th) solar cycle started in December 2008 and ended in November 2019 (as available from Sunspot Index and Long-term Solar Observations database <http://www.sidc.be/silso/node/167>). It had an unusually weak maximum, with smoothed maximum international sunspot number of 116. For comparison, in cycles 22 and 23 this number was 214 and 180, respectively (as available from Sunspot Index and Long-term Solar Observations database <http://sidc.be/silso/home>). Same period was also characterised by smaller number of FDs, especially ones with larger amplitudes.

There were fifteen strong FDs (with magnitude of decrease larger than 5% for particles with 10 GV rigidity) recorded in the rising phase of solar cycle 24, however in this study we will limit our analysis to four events detected by the Belgrade Cosmic Ray Station (<http://www.cosmic.ipb.ac.rs/>). Other prominent FDs that occurred in this period have not being detected by either GLL or UL detector due to discontinuity of operation, so they have been omitted from this study. All four events followed ejections from an active region on the Sun, accompanied by a solar flare with interplanetary shock wave and sudden storm commencing (SSC), and disturbance in the geomagnetic field. All of these FDs were seen by the NM detector network as well.

First significant FD of solar cycle 24 was recorded on 18 February 2011 and has been caused by a CME heading directly towards Earth [20]. It has been detected by most ground stations around the world. Its morphology is influenced by the interaction of two CMEs, first slower and the second faster (with respective speeds of 390 km/s and 1020 km/s), that occurred a day apart [27]. Geomagnetic activity has been relatively weak due to orientation of the magnetic field of the ejecta [21].

Second event was observed on 7 March 2012. It included an X-class flare (X5.4), that occurred in NOAA AR 11429 with an intense halo CME, followed by several smaller flares and another partial CME. It caused one of the strongest FDs of the last solar cycle. Observed solar activity was also related to the intense geomagnetic storm that followed [15].

A strong SF (X1.6) was detected by several spacecrafts during 10 September 2014, originating from active region NOAA AR 2158. Based on the SOHO coronagraph images, this flare was associated with a CME that was aimed towards Earth, where it arrived on September 12. This activity resulted in a major geomagnetic storm, one of the strongest in 2014.

In the second half of June 2015, solar activity was very intense, since a number of CMEs and flares were produced from the powerful AR 12371, which dominated solar activity during that period [23]. The impact of these CMEs on the Earth's magnetosphere resulted in a moderate to severe G4-class geomagnetic storm that occurred on the summer solstice. The result was a very interesting and unusual modulation galactic CRs flux, which appeared as a series of FDs.

For the study of FD events and their relationship with IMF and geomagnetic disturbances, researchers from IZMIRAN (Pushkov Institute of Terrestrial Magnetism, Ionosphere and Radio Wave Propagation, Russian Academy of Sciences) created an FD database (<http://spaceweather.izmiran.ru/eng/dbs.html>) which contains various FD parameters, as well as their relationship with heliospheric and geomagnetic parameters covering several solar cycles [1]. Properties of the four selected FDs, taken from the IZMIRAN database, are given in Table 2.

5 Data analysis

In order to establish the usability of SOHO SEP flux data in the study of CR variations, we will first analyse how muon count rate time series compare with some of the IMF parameters more commonly used in the analysis of solar activity-induced CR variations. To this end, we compare hourly muon count rates (measured by Belgrade muon station and corrected for atmospheric effects) with time series for selected parameters from OMNI database. To give more weight to this qualitative analysis, we concentrate only on periods of extreme solar activity, in particular periods of the occurrence of four FD events described in Sect. 4. We then examine the relationship between measured muon count rates and the SOHO/ERNE SEP flux data and analyse any discerning features in comparison with the ones observed in OMNI data time series. The period selected for this analysis is approximately one solar rotation of 27 days. All probes at L1 are about an hour upstream of the magnetosphere so all their data are interspersed with data from spacecraft close to Earth (e.g., IMP 8). In order to compute hourly averages “at Earth” this time shift has to be taken into account (https://omniweb.gsfc.nasa.gov/html/ow_data.html).

Next, we investigate the short-term correlation between SEP flux and muon count rate data during time periods of four selected FDs. Muon time series for this procedure were selected for times where average muon flux was significantly lower than the background level. Background level was determined from moving averages for hourly count rates 10 days before the event. We then perform correlative analysis between SOHO SEP flux data and muon count rates for a period of one year (from 01.06.2010 to 31.05.2011), in order to establish the long-term relationship. For further insight, we also look into the correlation between these variables during the periods of reduced geomagnetic activity (International Quiet Days) and increased geomagnetic activity (International Disturbed Days).

Finally, we look in greater detail into SOHO SEP flux time series. In order to perform more quantitative analysis, time-integrated flux is calculated for SEP data for different SOHO energy bins and for the duration of selected FD events. In order to provide a parameter for characterisation for different FD events, calculated integral flux is plotted as a function of proton energy and

Table 2 Selected FD and interplanetary disturbance parameters (taken from IZMIRAN database)

Parameter	FD 1	FD 2	FD 3	FD 4	Parameter comment
Date of FD	18.2.2011.	8.3.2012.	12.9.2014.	22.6.2015.	
Date of parent solar event	15.2.2011.	7.3.2012.	10.9.2014.	21.6.2015.	
AR number	1158	11429	2158	12371	NOAA active region
V_{meanC}	584	1198	906	1040	The average ICME velocity between the Sun and the Earth, calculated using the time of the beginning of the associated CME observations (in km/s)
V_{max}	691	737	730	742	Maximal hourly solar wind speed in the event (in km/s)
B_{max}	31	23.1	31.7	37.7	Maximal hourly IMF strength in the event (in nT)
B_{zmin}	- 5.5	- 16.1	- 9.5	- 26.3	Minimal hourly Bz component of the IMF in the event (in nT)
R_{bulk}	72.25	146.2	131.35	171.25	An estimate of the maximum proton rigidity (in GV) that can be reflected by the total magnetic field, integrated from the event onset to the FD minimum
Magn	5.2	11.7	8.5	8.4	FD magnitude for particles with 10 GV rigidity, calculated as maximal range CRs density variations in the event, obtained by GSM from NM network data (in %)
MagnM	4.7	13.1	6.9	10.4	FD magnitude for particles with 10 GV rigidity, corrected on magnetospheric effect with Dst-index (in %)
TminM	7	20	9	11	Time from the FD onset to minimum, calculated from the data corrected for magnetospheric effect
Kp_{max}	5	8	6.33	8.33	Maximal Kp-index in the event
Ap_{max}	48	207	94	236	Maximal 3-hour Ap-index in the event
Dst_{min}	- 30	- 143	- 75	- 204	Minimal Dst-index in the event (in nT)
Flare class	X2.2	X5.4	X1.6	M2.6	Associated X-ray flare data
SSN	85	97	126	56	Number of sunspot at the FD onset day

fitted with a power function. Dependence of magnitude for selected FDs on the exponents obtained from fitted distributions is then analysed.

6 Results and discussion

Comparison between time series of selected IMF parameters from OMNI database and muon count rate time

series during the periods of four selected FD events is shown in Fig. 1. Observed anticorrelation between muon count rates and proton flux and temperature, as well as with the overall IMF magnetic field and detected plasma speed, is in agreement with previously stated evidence in the literature [30].

Similar comparison between muon count rate time series and selected channels of SOHO/ERNE proton flux data for the same time intervals is shown in Fig.

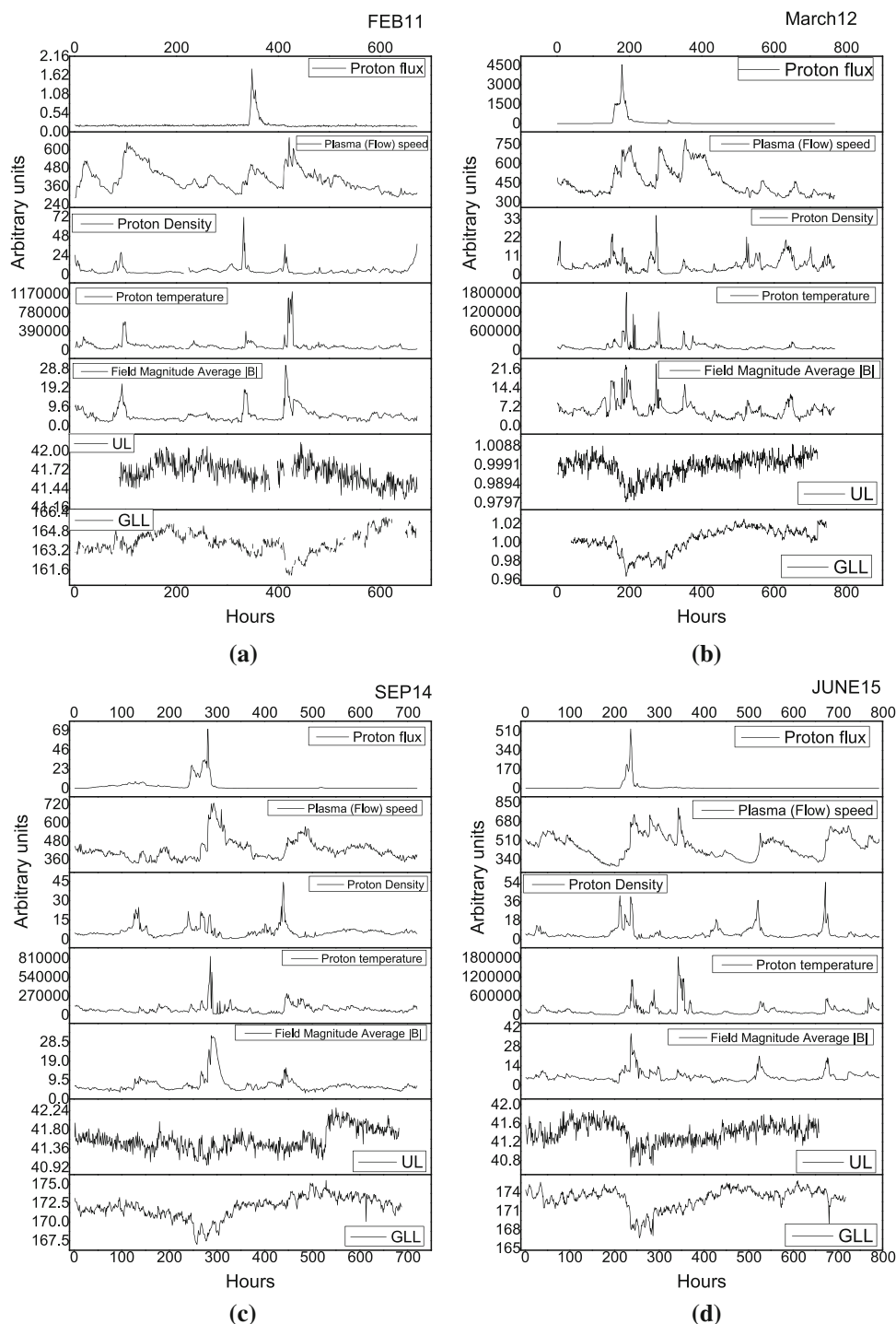


Fig. 1 Time series for particle and plasma parameters (taken from OMNI database) in the time interval of approximately one month around the occurrence of four selected FD events: **a** February 2011 (start of time interval on 1 February), **b** March 2012 (start of time interval on 1 March), **c** September 2014 (start of time interval on 1 September) and **d** June 2015 (start of time interval on 13 June)

2. For the sake of clarity, we chose three energy channels (1.6–2 MeV, 16–20 MeV, 100–130 MeV), approximately one order of magnitude apart, where first channel is measured with LED and the other two with HED detector on SOHO/ERNE instrument. In case of the

February 2011 event, there is an observable time lag (≈ 55 h) between the increase of measured proton flux at low-energy channels (1.6–2 MeV and 16–20 MeV energy channels) and the beginning of FD recorded at ground station. This time lag is also present between

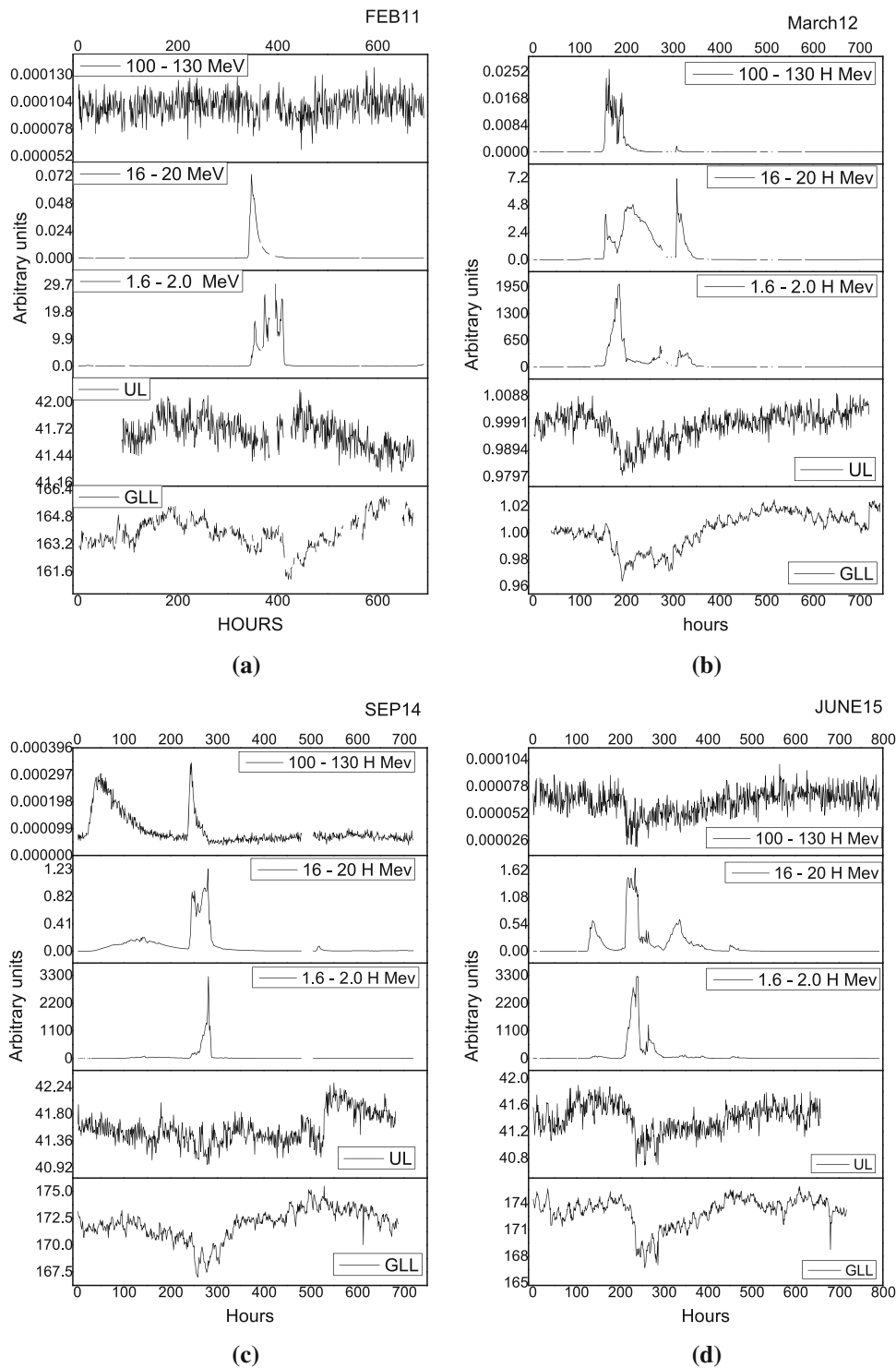


Fig. 2 Hourly time series for different proton channels from SOHO/ERNE and two muon detectors at Belgrade CR station, in the time interval of approximately one month around the occurrence of four selected FD events: **a**) February (start of time interval on 1 February) 2011, **b** March 2012 (start of time interval on 1 March), **c** September 2014 (start of time interval on 1 September) and **d** June 2015 (start of time interval on 13 June)

OMNI proton flux data and ground station measurements for this FD alone. FD is a complex modulation of CR flux that depends on a lot of parameters, like magnitude of magnetic field and its components,

speed of solar wind and CMEs (with CME average speed ≈ 490 km/s), most of which are listed in Table 2. Parameter values for all four ICMEs are mostly comparable, but one difference that stands out is the discrep-

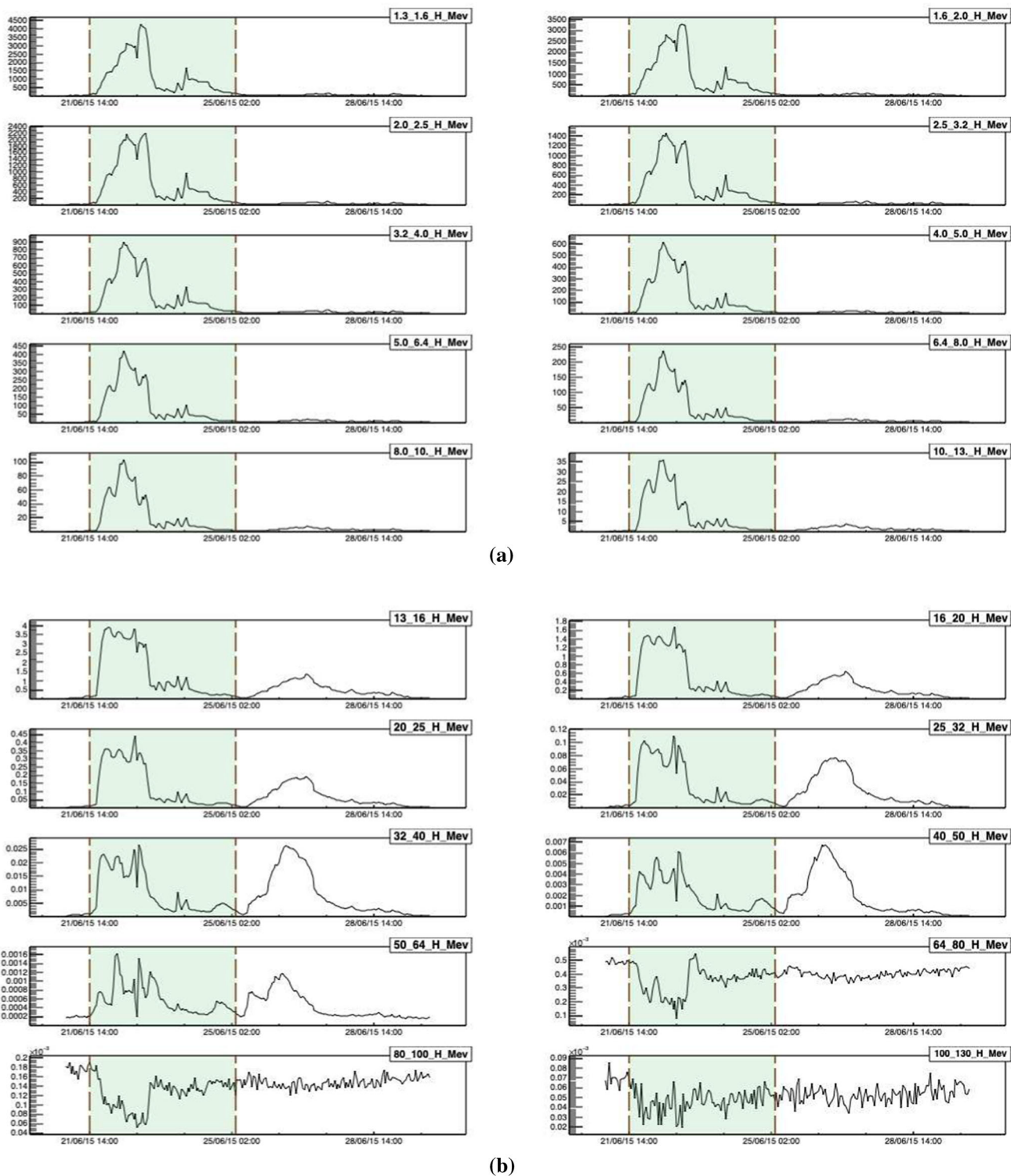


Fig. 3 Differential SEP fluxes during extreme solar event in June 2015, measured by SOHO/ERNE proton channels. Vertical dashed lines indicate the time for the start and the end of interval used to calculate the integral flux

ancy in average CME velocity (584 km/s from Table 2.) for the FD of February 2011, which can possibly explain the observed time lag for this particular FD.

Based on the observed time lag and other coincident features, we can establish good agreement between

SOHO low-energy channel data and OMNI data time series. As for high-energy channels, SEP time series in 100–130 MeV energy range for February 2011 and June 2015 events appear to correlate with muon count rate measurements on the ground. One possible explanation

Table 3 Statistical correlation between Belgrade CR station and SOHO/ERNE measurements during the periods of four selected FD events

FD	Energy range (MeV)	GLL		UL	
		Pearson coefficient	<i>P</i> value	Pearson coefficient	<i>P</i> value
FEB 11	1.6–2.0 H	– 0.10877	0.01	– 0.05285	0.2
	16–20 H	– 0.18384	2×10^{-5}	– 0.10732	0.01
	100–130 H	0.24204	$< 10^{-6}$	– 0.13212	0.02
MAR 12	1.6–2.0 H	– 0.48477	$< 10^{-6}$	– 0.43994	$< 10^{-6}$
	16–20 H	– 0.72033	$< 10^{-6}$	– 0.68221	$< 10^{-6}$
	100–130 H	– 0.29172	$< 10^{-6}$	– 0.27822	$< 10^{-6}$
SEP 14	1.6–2.0 H	– 0.2839	$< 10^{-6}$	– 0.48052	$< 10^{-6}$
	16–20 H	– 0.37814	$< 10^{-6}$	– 0.63735	$< 10^{-6}$
	100–130 H	– 0.04951	0.007	– 0.10466	0.2
JUN 15	1.6–2.0 H	– 0.3921	$< 10^{-6}$	– 0.27531	$< 10^{-6}$
	16–20 H	– 0.31229	$< 10^{-6}$	– 0.17113	$< 10^{-6}$
	100–130 H	0.48588	$< 10^{-6}$	0.39296	$< 10^{-6}$

could be that in addition to SEP these energy channels are also populated by very low-energy CRs.

We can further investigate this assumption by looking more closely into SOHO SEP flux time series for one of the two weaker FD events. We have selected June 2015 event, as time series for higher-energy channels appear to be slightly more informative. Figure 3 shows proton flux series for all energy channels measured by SOHO/ERNE detector. From these plots, it is apparent that proton fluxes for energies larger than 64 MeV exhibit different dynamic relative to fluxes of lower energies, and seem to be in anticorrelation with them. This indeed supports the assumption these channels are populated by low-energy CR.

Another way we can illustrate this observation more quantitatively is by performing relative analysis. Firstly, we will look into short-term correlations between proton flux and muon count rate time series during four selected FD events. Correlation between respective time series was found using Pearson correlation coefficient. For significance two-tailed test is used. Correlation coefficient and its significance level between ground station and in situ measurement from SOHO/ERNE instrument is given in Table 3.

Due to higher energy of the primary CRs detected in UL, the correlation between SEPs and measured flux in UL is smaller than correlation between SEPs and flux measured in GLL. The greatest anticorrelation (i.e., between GLL and UL data and 16–20 MeV protons ≈ -0.7) is observed for the strongest ICME (and corresponding FD) of March 2012, and this anticorrelation is observed in all energy channels. However, for lower-intensity events of June 2015 and February 2011, correlations between detected CR flux in GLL and highest energy channel (100–130 MeV) are mostly positive. These observations further confirm the assumption about high-energy channels being populated by low-energy CR, which is especially evident in case of low-intensity FD events.

Table 4 Pearson correlation coefficient for the correlation between CR flux detected at Belgrade CR station (GLL detector) and flux of protons of different energies detected with SOHO/ERNE detector, for the period of one year (from June 2010 May 2011)

	GLL	
	Pearson coefficient	<i>P</i> value
H 1.3–1.6 MeV	– 0.02	0.13
H 1.6–2.0 MeV	– 0.02	0.16
H 2.0–2.5 MeV	– 0.02	0.20
H 2.5–3.2 MeV	– 0.01	0.27
H 3.2–4.0 MeV	– 0.01	0.36
H 4.0–5.0 MeV	– 0.01	0.57
H 5.0–6.4 MeV	< 0.01	0.75
H 6.4–8.0 MeV	< 0.01	1.00
H 8.0–10 MeV	< 0.01	0.78
H 10–13 MeV	0.01	0.57
H 13–16 MeV	0.01	0.41
H 16–20 MeV	0.01	0.31
H 20–25 MeV	0.01	0.26
H 25–32 MeV	0.01	0.24
H 32–40 MeV	0.01	0.27
H 40–50 MeV	0.01	0.46
H 50–64 MeV	< 0.01	0.80
H 64–80 MeV	0.05	< 0.01
H 80–100 MeV	0.12	< 0.01
H 100–130 MeV	0.07	< 0.01

Similar results, with even greater correlation between the entire time profile for flux measured with NMs and solar wind speed and magnetic field during ICME, are reported for stronger FDs during solar cycle 23 [5].

Next, we will analyse long-term correlations between SOHO proton flux and measured muon count rates. Pearson coefficients for this correlation over a period of one year (from June 2010 May 2011), when activity of the Sun was low at the commencement of the 11-years cycle, are presented in Table 4. Here we see very

Table 5 Pearson correlation coefficient for the correlation between CR flux detected at Belgrade CR station (GLL detector) and flux of protons of different energies detected with SOHO/ERNE detector, during international geomagnetically quiet and disturbed days for the period of one year (from June 2010 May 2011)

	GLL Quiet days		GLL Disturbed days	
	Pearson coefficient	<i>P</i> value	Pearson coefficient	<i>P</i> value
H 1.3–1.6 MeV	0.01	0.61	– 0.05	0.13
H 1.6–2.0 MeV	0.01	0.80	– 0.05	0.14
H 2.0–2.5 MeV	0.02	0.30	– 0.05	0.13
H 2.5–3.2 MeV	0.03	0.11	– 0.05	0.12
H 3.2–4.0 MeV	0.04	0.04	– 0.05	0.10
H 4.0–5.0 MeV	0.05	0.02	– 0.06	0.08
H 5.0–6.4 MeV	0.05	0.01	– 0.06	0.07
H 6.4–8.0 MeV	0.06	0.01	– 0.06	0.06
H 8.0–10 MeV	0.06	0.01	– 0.06	0.06
H 10–13 MeV	0.06	0.01	– 0.06	0.07
H 13–16 MeV	0.06	< 0.01	– 0.06	0.08
H 16–20 MeV	0.06	< 0.01	– 0.05	0.10
H 20–25 MeV	0.06	< 0.01	– 0.05	0.12
H 25–32 MeV	0.06	< 0.01	– 0.05	0.15
H 32–40 MeV	0.06	< 0.01	– 0.04	0.20
H 40–50 MeV	0.06	< 0.01	– 0.02	0.57
H 50–64 MeV	0.07	< 0.01	0.07	0.03
H 64–80 MeV	0.25	< 0.01	0.08	0.02
H 80–100 MeV	0.38	< 0.01	0.11	< 0.01
H 100–130 MeV	0.15	< 0.01	0.09	0.01

little correlation between CR and proton fluxes in all but the highest energy channels (above 64 MeV).

Table 5 shows the same correlation analysis if only data for 10 geomagnetically quietest or 5 geomagnetically most disturbed days of each month (http://isgi.unistra.fr/events_qdays.php) are used. The fact that we observe a significant increase of positive correlation coefficients in the case of geomagnetically quiet days, further corroborates the assumption about the mixed nature of particles that populate higher-energy channels. Consequentially, care should be taken how data from these channels are treated in analysis.

To provide further quantitative support for the use of SOHO SEP flux measurements in the analysis of FD events, we will calculate integral proton flux in all energy channels for the four selected FDs. Integration intervals are selected to include the period of increased proton flux that corresponds to a particular FD, but not to extend the interval to include potential follow-up structures that cannot be associated with the event. One such selection for all energy channels, for June 2015 event, is indicated by dashed lines in Fig. 3. In Fig. 4, we show thusly calculated integral flux as a function of particle energy (where lower boundary values from SOHO SEP energy bins are taken), using both linear and log scale for clarity.

One feature that can be noticed from plots in Fig. 4 is that integral flux drops off is more steeply in February 2011 than for others studied FDs, where a change in the trend between high-energy and low-energy range can be observed. FD that occurred in March 2012 was the longest and the most intensive of the four. Steepness of

the integral flux for this FD shows relatively more populated proton channels with higher energies compared to weaker FD. This is in agreement with strongest modulation of CRs flux during this FD. There is a discontinuity in the integral flux between proton energy channel 13–16 MeV and 16–20 MeV due to different acquisition method from different instruments, and possibly because of degradation of the detectors on board the spacecraft [13] and saturation of the instrument due to high intensity of solar protons [18].

One simple way to characterise relative abundance of SEP particles of different energies for a given event would be to fit described integral flux distribution with a power function, where (in a simple approximation) larger exponent would indicate greater relative abundance of lower-energy particles, while smaller exponent would point to greater relative abundance of higher-energy particles. Distributions were fitted with a power function given by the formula $I(E) = a * E^b$ (where I is the integral flux and E is particle energy), resulting fits represented by red lines in Fig. 4, while values for the exponents of power function fits are represented in Table 6.

If SOHO protons flux measurements are to be proved useful in the analysis of FD events, SEP flux characteristics should correlate with some of the FD and interplanetary disturbance parameters. To test this, we have analysed dependence of different FD parameters on the exponent of the integral proton flux power distribution (labelled b in the formula in previous paragraph). We have found some correlation for most tested parameters, most striking being one between the magnitude

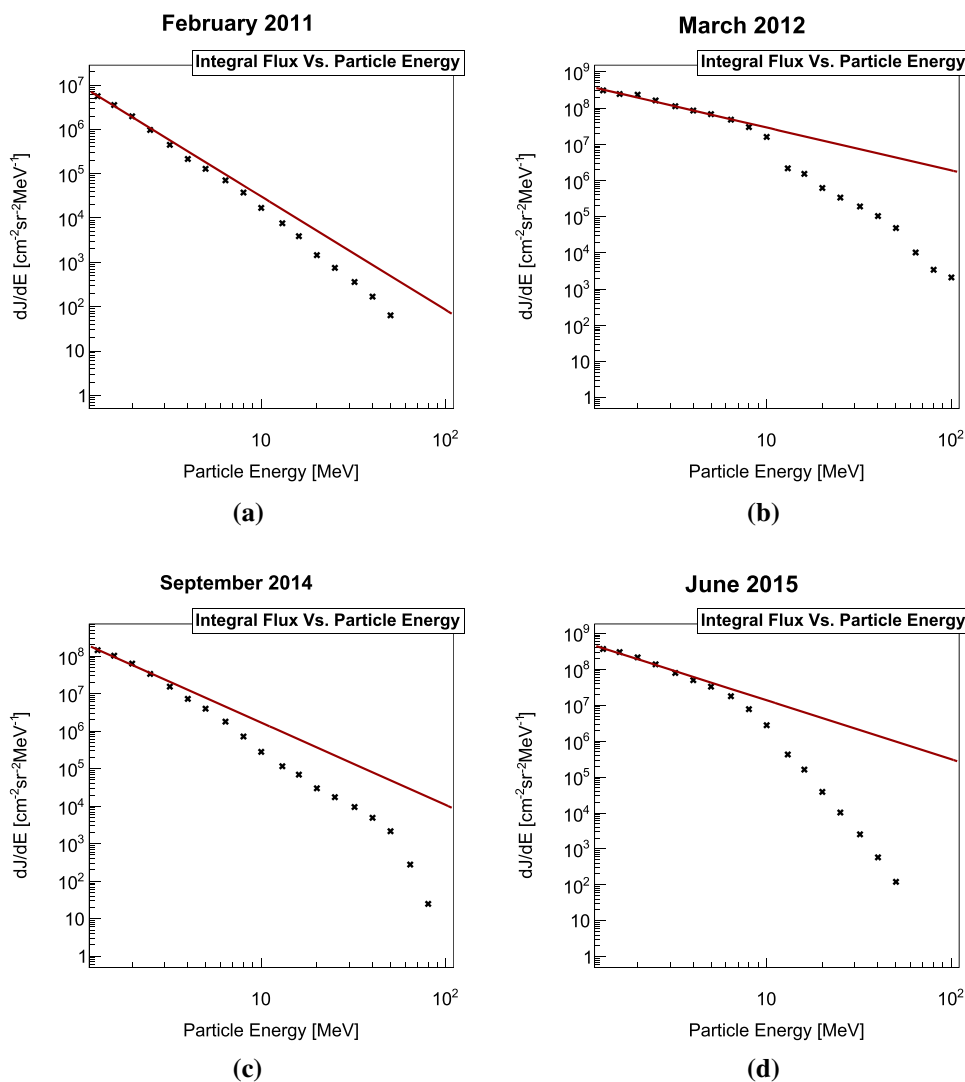


Fig. 4 Time-integrated flux of differential SEP fluxes during the four selected FD events: **a** February 2011, **b** March 2012, **c** September 2014 and **d** June 2015, in linear and logarithmic scale. Power function fits are represented by red lines

Table 6 Exponent values of power function fits of integral proton flux distributions

FD	Power function exponent values
FEB 2011	- 2.56
MAR 2012	- 1.18
SEP 2014	- 2.20
JUN 2015	- 1.64

of FD for particles with 10 GV rigidity (corrected for magnetospheric effect) and the exponent of the integral flux. This dependence (strictly for illustrative purposes fitted with linear fit) is shown in Fig. 5.

Observed strong dependence is potentially a very good indicator that SOHO SEP flux measurements can be a valid source of data to be used in the analysis of

interplanetary disturbances and their interaction with cosmic rays.

7 Conclusions

Analysing strong aperiodic variations of cosmic ray flux, such as Forbush decreases, allows us to study violent processes that occur on the Sun, and corresponding perturbations in the heliosphere, using Earth-based detectors. In addition to cosmic ray flux and magnetic field data commonly used to study such events, we have extended analysis to include proton flux measurements, obtained using spacecraft mounted detectors. Based on the analysis of four selected Forbush decrease events, we have found SOHO/ERNE proton flux measurements to be consistent with solar plasma parameters, as well as with observations by the ground-based muon detectors.

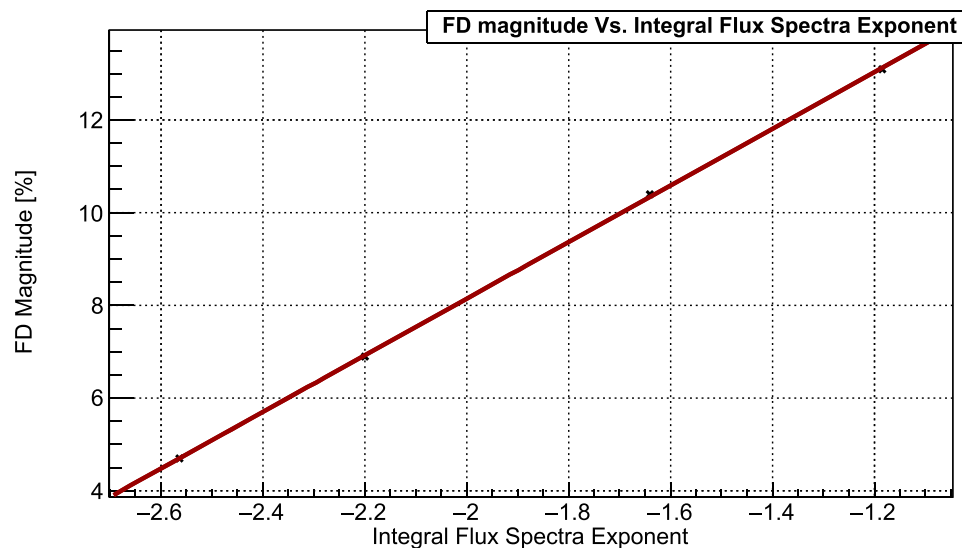


Fig. 5 Dependence of FD magnitude, corrected for magnetospheric effect with Dst-index for particles with 10 GV rigidity, on the power exponent of the integral SEP flux, four selected FD events: **a** February 2011, **b** March 2012, **c** September 2014 and **d** June 2015. Linear fit (for illustrative purposes) is indicated by the red line

We have concluded that during Forbush decrease events lower-proton-energy channels are dominated by SEP particles, while in higher-energy channels there is a contribution of low-energy cosmic rays, especially apparent during less intense events. We have found a clear correlation between Forbush decrease magnitude (corrected for magnetospheric effect with Dst-index for particles with 10 GV rigidity) and power exponent of the integral flux of SOHO/ERNE measurements. This result gives grounds to further pursue the analysis of heliospheric proton flux data, as it may yield additional valuable information. Such information can potentially help us to classify and study in greater detail the dynamics of interaction of cosmic rays in the heliosphere.

Acknowledgements The authors acknowledge funding provided by the Institute of Physics Belgrade, through the grant by the Ministry of Education, Science and Technological Development of the Republic of Serbia. We also acknowledge use of NASA/GSFC's Space Physics Data Facility's OMNIWeb (or CDAWeb or ftp) service and OMNI data as well as team behind SOHO, which is a project of international collaboration between ESA and NASA. We would also like to thank the referees for constructive and useful advice.

Data Availability Statement "This manuscript has data included as electronic supplementary material".

References

1. A.A. Abunin, M.A. Abunina, A.V. Belov, S.P. Gaidash, E.A. Eroshenko, I.I. Pryamushkina, L.A. Trefilova, E.I. Gamza, *J. Phys. Conf. Ser.* **1181**, 012062 (2019). <https://doi.org/10.1088/1742-6596/1181/1/012062>
2. K.P. Arunbabu, H.M. Antia, S.R. Dugad, S.K. Gupta, Y. Hayashi, S. Kawakami, P.K. Mohanty, T. Nonaka, A. Oshima, P. Subramanian, *A and A* **555**, A139 (2013). <https://doi.org/10.1051/0004-6361/201220830>
3. K.P. Arunbabu, H.M. Antia, S.R. Dugad, S.K. Gupta, Y. Hayashi, S. Kawakami, P.K. Mohanty, A. Oshima, P. Subramanian, *A and A* **580**, A41 (2015). <https://doi.org/10.1051/0004-6361/201425115>
4. C.R.A. Augusto, V. Kopenkin, C.E. Navia, K.H. Tsui, H. Shigueoka, A.C. Fauth, E. Kemp, E.J.T. Manganote, M.A. Leigui de Oliveira, P. Miranda, R. Ticona, A. Velarde, *ApJ* **759**, 143 (2012). <https://doi.org/10.1088/0004-637X/759/2/143>
5. A. Bhaskar, G. Vichare, K.P. Arunbabu et al., *Astrophys. Space Sci.* **361**, 242 (2016). <https://doi.org/10.1007/s10509-016-2827-8>
6. V. Belov, *SpaceSci. Rev.* **93**(1), 79–105 (2000). <https://doi.org/10.1023/A:1026584109817>
7. H.V. Cane, *Space Sci. Rev.* **93**, 55–77 (2000). <https://doi.org/10.1023/A:1026532125747>
8. J.M. Clem, L.I. Dorman, *Space Sci. Rev.* **93**, 335–359 (2000). <https://doi.org/10.1023/A:1026508915269>
9. E.S. Comedi, A.S. Elias, B.S. Zossi, S. Bruno, *JASTP* **211**, 105475 (2020). <https://doi.org/10.1016/j.jastp.2020.105475>
10. M. Duldig, *Science* **314**(5798), 429–430 (2006). <https://doi.org/10.1126/science.1134046>
11. M. Dumbović, B. Vršnak, J. Guo et al., *Sol. Phys.* **295**, 104 (2020). <https://doi.org/10.1007/s11207-020-01671-7>
12. J.H. King, N.E. Papitashvili, *J. Geophys. Res.* **110**, A02104 (2005). <https://doi.org/10.1029/2004JA010649>
13. P. Kühl, B. Heber, R. Gómez-Herrero, O. Malandraki, A. Posner, H. Sierks, *J. Space Weather Space Clim.* (2020). <https://doi.org/10.1051/swsc/2020056>
14. S.Y. Lee, *Accelerator Physics*, 2nd edn. (World Scientific, Singapore, 2004)

15. M. Livada, H. Mavromichalaki, C. Plainaki, *Astrophys. Space Sci.* **363**, 8 (2018). <https://doi.org/10.1007/s10509-017-3230-9>
16. R.A. Caballero-Lopez, H. Moraal, *JGR Space Phys.* **117**, A12 (2012). <https://doi.org/10.1029/2012JA017794>
17. R. Miteva, S.W. Samwel, M.V. Costa-Duarte, *JASTP* (2018). <https://doi.org/10.1016/j.jastp.2017.05.003>
18. R. Miteva, D. Danov, in *Proceedings of the tenth Workshop 'Solar Influences on the Magnetosphere, Ionosphere and Atmosphere', Primorsko, Bulgaria*, ed. by K. Georgieva, B. Kirov, D. Danov, 2018. <https://doi.org/10.31401/WS.2018.proc>
19. H. Moraal, *Space Sci. Rev.* **176**, 299–319 (2013). <https://doi.org/10.1007/s11214-011-9819-3>
20. S.Y. Oh, Y. Yi, *A Sol. Phys.* **280**, 197–204 (2012). <https://doi.org/10.1007/s11207-012-0053-2>
21. A. Papaioannou, A. Belov, H. Mavromichalaki et al., *J. Phys. Conf. Ser.* **409**, 012202 (2013). <https://doi.org/10.1088/1742-6596/409/1/012202>
22. A. Papaioannou, M. Belov, E. Abunina, A. Eroshenko, A. Abunin, S. Anastasiadis, Patsourakos, H. Mavromichalaki, *ApJ* **890**, 101 (2020). <https://doi.org/10.3847/1538-4357/ab6bd1>
23. E. Samara, A. Smponias, I. Lytrosyngounis et al., *Sol. Phys.* **293**, 67 (2018). <https://doi.org/10.1007/s11207-018-1290-9>
24. M. Savić, A. Dragić, N. Veselinović et al., *XXV ECRS 2016 Proceedings—eConf C16-09-04.3*, e-Print: 1701.00164 [physics.ins-det], [arXiv:1701.00164v1](https://arxiv.org/abs/1701.00164)
25. M. Savić, A. Dragić, D. Maletić et al., *Astropart. Phys.* (2019). <https://doi.org/10.1016/j.astropartphys.2019.01.006>
26. M. Savić, N. Veselinović, A. Dragić et al., *ASR* **63**, 4 (2019). <https://doi.org/10.1016/j.asr.2018.09.034>. ISSN 0273-1177
27. M. Temmer, A.M. Veronig, V. Peinhart, B. Vršnak, *ApJ* **785**, 85 (2014). <https://doi.org/10.1088/0004-637X/785/2/85>
28. J. Torsti, E. Valtonen, M. Lumme et al., *Sol. Phys.* **162**, 505–531 (1995). <https://doi.org/10.1007/BF00733438>
29. N. Veselinović, A. Dragić, M. Savić, D. Maletić, D. Joković, R. Banjanac, V. Udovičić, *NIM A* **875**, 1 (2017). <https://doi.org/10.1016/j.nima.2017.09.008>. ISSN 0168-9002
30. L.-L. Zhao, H. Zhang, *ApJ* **827**, 13 (2016). <https://doi.org/10.3847/0004-637X>

See discussions, stats, and author profiles for this publication at: <https://www.researchgate.net/publication/341642542>

Radon variability due to floor level in two typical residential buildings in Serbia

Article in *Nukleonika* · May 2020

DOI: 10.2478/nuka-2020-0019

CITATIONS

4

READS

83

9 authors, including:



Vladimir Udovičić

Institute of Physics Belgrade

68 PUBLICATIONS 378 CITATIONS

[SEE PROFILE](#)



Nikola Veselinović

Institute of Physics Belgrade

30 PUBLICATIONS 117 CITATIONS

[SEE PROFILE](#)



Dimitrije M Maletić

Institute of Physics Belgrade

132 PUBLICATIONS 8,539 CITATIONS

[SEE PROFILE](#)



A. Dragić

Institute of Physics Belgrade

71 PUBLICATIONS 331 CITATIONS

[SEE PROFILE](#)

Some of the authors of this publication are also working on these related projects:



IAEA Regional project RER9136 "Reducing Public Exposure to Radon by Supporting the Implementation and Further Development of National Strategies" [View project](#)



ATLAS Project 2020 [View project](#)



Radon variability due to floor level in two typical residential buildings in Serbia

Vladimir Udovicic ,
Nikola Veselinovic,
Dimitrije Maletic,
Radomir Banjanac,
Aleksandar Dragic,
Dejan Jokovic,
Mihailo Savic,
David Knezevic,
Maja Eremic Savkovic

Abstract. It is well known that one of the factors that influence the indoor radon variability is the floor level of the buildings. Considering the fact that the main source of indoor radon is radon in soil gas, it is expected that the radon concentration decreases at higher floors. Thus at higher floors the dominant source of radon is originating from building materials, and in some cases there may be deviations from the generally established regularity. In such sense, we chose one freestanding single-family house with loft and other 16-floor high-rise residential building for this study. The indoor radon measurements were performed by two methods: passive and active. We used passive devices based on track-etched detectors: Radtrak² Radonova. For the short-term indoor radon measurements, we used two active devices: SN1029 and SN1030 (manufactured by Sun Nuclear Corporation). The first device was fixed in the living room at the ground level and the second was moved through the floors of the residential building. Every measuring cycle at the specified floor lasted seven days with the sampling time of 2 h. The results show two different indoor radon behaviours regarding radon variability due to floor level. In the single-family house with loft we registered intense difference between radon concentration in the ground level and loft, while in the high-rise residential building the radon level was almost the same at all floors, and hence we may conclude that radon originated mainly from building materials.

Keywords: Radon variability • Time series

Introduction

Radon sources in the buildings are primarily from soil, building materials and water. Considering the nature of the occurrence and all the sources, the concentration of radon is higher in the ground-floor rooms compared with that in the higher floors of the dwellings in apartments. In the literature one can find a lot of papers dealing with the influence of various factors, including the floor levels, on the radon concentration and variability. In one group of the articles, investigation of the indoor radon concentration distribution due to floor levels of the buildings is the part of the data analysis which was drawn from the national or regional radon surveys [1–6] and others are dedicated to these specific studies [7–11]. In the case of the big buildings with a several number of floors a deviation from the general regularity can be observed, since the dominant source of indoor radon at higher floors is building materials. On the other hand, the radon variability due to floor level, especially in big cities with a much higher number of high-rise buildings and population density compared with rural environments, may have an impact on the assessments of the effective dose from radon exposure at the national level. Usually, the indoor radon map represents the arithmetic mean value of indoor radon concentration on the ground floor, and thus it is not

V. Udovicic✉, N. Veselinovic, D. Maletic, R. Banjanac,
A. Dragic, D. Jokovic, M. Savic, D. Knezevic
Institute of Physics Belgrade
University of Belgrade
Pregrevica 118 St., 11080 Belgrade, Serbia
E-mail: udovicic@ipb.ac.rs

M. Eremic Savkovic
Serbian Radiation and Nuclear Safety and Security
Directorate
Masarikova 5 St., 11000 Belgrade, Serbia

Received: 30 November 2019
Accepted: 17 January 2020

representative of the radon exposure to all citizens since most people do not live on the ground floor. So, it is necessary to convert indoor radon map to a dose map. One of the examples is presented as a plan to develop models that allow correction from ground-floor dwellings to the real situation, accounting data from the national buildings database [12]. In Serbia, national typology of residential buildings is based on the results from the monography “National typology of residential buildings of Serbia” by a group of authors from the Faculty of Architecture [13]. There are six types of the residential buildings in Serbia: two for family housing – freestanding single-family house and single-family house in a row and four types for multifamily housing – freestanding residential building and residential building (lamella) (apartment block with repeated multiple lamellar cores and separate entrances), residential building in a row, and high-rise residential building. Distribution of buildings by type at the national level shows that 97% of all residential buildings are family housing. Also, for all defined types of buildings, number of floors ranges from one to eight above the ground level. Freestanding family houses are mostly ground floor (37%) or ground floor with loft in use (26%), while there is a very low representation of houses that have more than two floors (5%), with average floor level of family buildings of 1.4 [13]. In such sense, we chose one freestanding single-family house with loft with well-known radon characteristics [14] and one 16-floor high-rise residential building for this study.

Materials and methods

Two housing units were selected, one from the family housing group and one high-rise residential building from the collective housing group. The family house has a characteristic construction style in which the house has been built for several years with constant upgrading, which can potentially be a source of radon entry into such houses. The house has a basement and is made of standard materials (brick block, concrete, plaster). Finally, insulation was made using 5-cm thick styrofoam. Long-term measurements of radon concentrations have been carried out in this house by various methods, and several scientific papers have been published so far [14–16].

From the group of residential buildings for collective housing, we chose high-rise building in New Belgrade. It was built in the 1960s as block type. The soliter has a basement, while on the ground floor there are outlets and business premises. The apartments are located in the first floor upward. The soliter has 16 floors. One of the important parameters in the selection of building in municipality New Belgrade is the fact that this municipality is the most populated in Serbia.

The long-term radon measurements were performed with passive device Radtrak² Radonova based on CR-39 track detector. The detectors were exposed for three months from March to June. In the high-rise building, passive radon detectors were deployed at some of the floors in one or several apartments. Time series of measured radon concentrations in the studied residential buildings were obtained using two active devices: SN1029 with the following characteristics declared by the manufacturer – the measurement ranging from 1 Bq·m⁻³ to 99.99 kBq·m⁻³, accuracy equal to ±25%, sensitivity of 0.16 counts/h/Bq·m⁻³ and SN1030 with the following characteristics – the measurement ranging from 1 Bq·m⁻³ to 99.99 kBq·m⁻³, accuracy equal to ±20%, sensitivity of 0.4 counts/h/Bq·m⁻³. SN1029 device were calibrated at the accredited metrological Lab (SUJCHBO Kamenna, Czech Republic) in 2015 and model SN1030 were calibrated by the manufacturer in 2017. The both instruments participated in 2018 NRPI Intercomparisons of radon gas continuous monitors and also, SN1029 device participated in 2015 NRPI Intercomparisons of radon gas measurement devices at SURO v.v.i. Institute, Prague, Czech Republic within the IAEA Technical Cooperation Projects RER 9153 and RER 9127, with excellent results. These are measuring devices of simple construction and practical application. It is a counter with the addition of a sensor for measuring meteorological parameters. The operator can adjust the time sequences from 0.5 h to 24 h. One measurement cycle can take 1000 h or a total of 720 time sequences (the number of successive measurements, i.e. points in a time series). The devices were set to operate in a 2-h time sequence. One was fixed in the downstairs living room and the other was fixed in repositioning floors in apartment buildings. Each measurement cycle on a given floor lasted seven days.

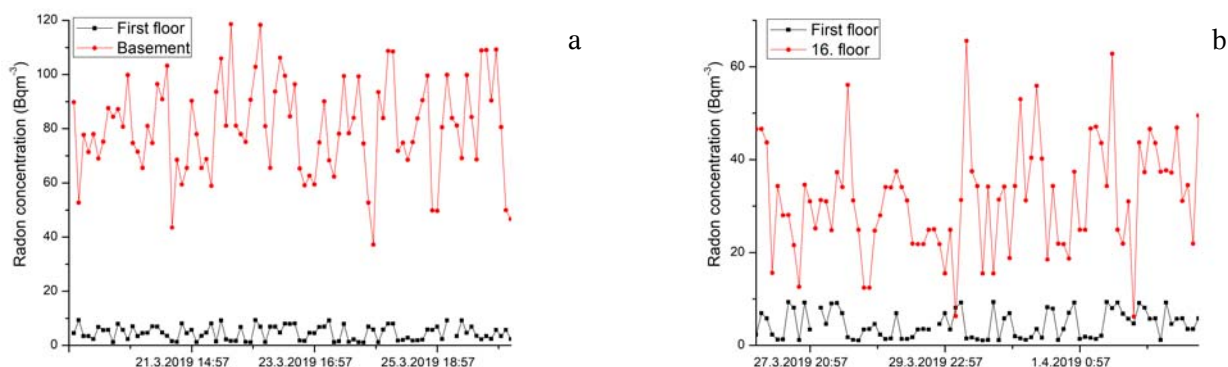


Fig. 1. The time series of the radon concentrations at the first floor vs. basement (a) and 16th floor (b) in the big residential building.

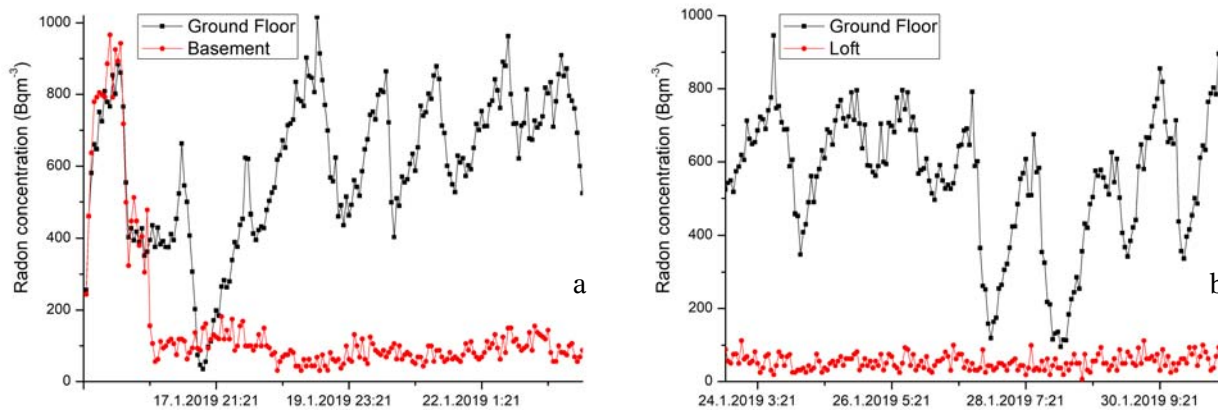


Fig. 2. The time series of the radon concentrations at the first floor vs. basement (a) and loft (b) in the single-family house.

Table 1. Results of indoor radon measurements in the high-rise residential building using passive (Radtrak² Radonova) and active radon devices

Floor level	Radon concentration/ Passive device (Radtrak ²) [Bq·m ⁻³]	Average radon concentration per floor level (Radtrak ²) [Bq·m ⁻³]	Arithmetic mean (standard deviation) radon concentration over measuring cycle [Bq·m ⁻³]
Basement	52 ± 10	53.5	81(17)
	69 ± 12		
	38 ± 10		
	55 ± 10		
1	<10	14	5(3)
	14 ± 8		
2	17 ± 8	17	24(9)
3			25(10)
4	21 ± 8	20.5	26(11)
	20 ± 8		
5	11 ± 8	19	
	27 ± 10		
6	22 ± 8	17	
	12 ± 8		
7	17 ± 8	23	25(10)
	23 ± 8		
8	22 ± 8	22	
9	15 ± 8	17.7	24(10)
	16 ± 8		
10	22 ± 8	17.5	
	15 ± 8		
11	20 ± 8	16	
	16 ± 8		
12	<10	<10	
14	20 ± 8	18.5	29(9)
	17 ± 8		
15	15 ± 8	15.5	
	16 ± 8		
16	31 ± 8	31	32(12)
Overall mean	24	21.6	30

Results and discussions

Figure 1 shows the illustrative examples that show radon time series from high-rise building, and Fig. 2 originates from the observed single-family house.

The arithmetic mean radon concentrations obtained from long- and short-term measurements are shown in Tables 1 and 2 for high-rise building and single-family house with loft, respectively.

In the family house, it is possible to notice marked variations in radon concentration with 1-day periodicity. Also interesting is the ratio of radon concentration on the ground floor to the basement of the house, which is the opposite of the usual situation in houses with a basement. This inverse behaviour can be explained by the fact that the basement does not cover the whole ground floor but a smaller part of it. The rest of the ground floor is covered by a concrete slab as a substrate, but cracks and poor joint with the walls are potential sources of elevated radon. Also, the differences in the results between two methods, passive and active devices, are due to the fact that presented radon values are measured in different seasons. With high-rise residential building, the situation is the opposite and it can be considered from the first floor that the dominant source of radon is the building material. There may even be a slight increase in the mean radon concentration on the higher floors. Also, the results show very low radon level on the first floor (well below the outdoor values) in the apartment. In such sense, we performed test intercomparison radon measurements for two active devices SN1029 and SN1030 in well-defined and controlled radon atmosphere (radon concentration below 30 Bq·m⁻³) in the Underground Low-background Laboratory in the Institute of Physics Belgrade [17, 18]. Additional testing includes the same place and time of the measurements but different sampling time set to 1, 2, 4, 8 and 12 h. The results are shown in Table 3.

In the above performed measurements, both devices show significant differences in the low-level radon range, which may originate from individual instruments characteristics presented in the “Materials and methods” section.

Table 2. Results of indoor radon measurements in the single-family house with loft using passive (Radtrak² Radonova) and active radon devices

Floor level	Radon concentration/Passive device (Radtrak ²) [Bq·m ⁻³]	Arithmetic mean (standard deviation) radon concentration over measuring cycle [Bq·m ⁻³]
Basement		160(202)
Ground level	330 ± 50	579(194)
Loft	18 ± 8	53(21)

Table 3. Test intercomparison indoor radon measurements with active radon devices SN1029 and SN1030

	Arithmetic mean (standard deviation) radon concentration over measuring cycle [Bq·m ⁻³]				
Sampling time [h]	1	2	4	8	12
SN1029	28(12)	28(11)	27(7)	23(6)	32(14)
SN1030	12(6)	14(7)	10(3)	12(5)	14(6)

Conclusions

The results show that the radon behaviour in two different residential buildings is diametrically opposite. In the single-family house with loft we registered intense difference between radon concentration in the ground level and loft, while in the high-rise residential building the radon level was almost the same at all floors and hence we may conclude that radon originated mainly from building materials. However, the results from the high-rise building can be predicted on the basis of work of a group of authors who have determined the internal exposure from construction material used in Serbia which originates from the exhalation of radon and thoron [19] and the study presented in this article [10]. We can expect similar results in any other multistorey buildings in Serbia. In the future work, we will focus on the additional radon measurements in the typical residential buildings from other types of houses.

Acknowledgments. The authors acknowledge funding provided by the Institute of Physics Belgrade through the grant by the Ministry of Education, Science and Technological Development of the Republic of Serbia.

ORCID

V. Udovicic  <http://orcid.org/0000-0002-7839-1537>

References

- Bochicchio, F., Campos-Venuti, G., Piermattei, S., Nucetelli, C., Risica, S., Tommasino, L., Torri, G., Magnoni, M., Agnesod, G., Sgorbati, G., Bonomi, M., Minach, L., Trotti, F., Malisan, M. R., Maggiolo, S., Gaidolfi, L., Giannardi, C., Rongoni, A., Lombardi, M., Cherubini, G., D'Ostilio, S., Cristofaro, C., Pugliese, M., Martucci, V., Crispino, A., Cuzzocrea, P., Sansone Santamaria, A., & Cappai, M. (2005). Annual average and seasonal variations of residential radon concentration for all the Italian Regions. *Radiat. Meas.*, *40*, 686–694.
- Friedmann, H. (2005). Final results of the Austrian Radon Project. *Health Phys.*, *89*(4), 339–348.
- Du, L., Prasauskas, T., Leivo, V., Turunen, M., Pekkonen, M., Kiviste, M., Aaltonen, A., Martuzevicius, D., & Haverinen-Shaughnessy, U. (2015). Assessment of indoor environmental quality in existing multi-family buildings in North-East Europe. *Environ. Int.*, *79*, 74–84.
- Cucoş (Dinu), A., Cosma, C., Dicu, T., Begy, R., Moldovan, M., Papp, B., Niță, D., Burghel, B., & Sainz, C. (2012). Thorough investigations on indoor radon in Băița radon-prone area (Romania). *Sci. Total Environ.*, *431*, 78–83.
- Yarmoshenko, I., Vasilyev, A., Malinovsky, G., Bossew, P., Žunić, Z. S., Onischenko, A., & Zhukovsky, M. (2016). Variance of indoor radon concentration: Major influencing factors. *Sci. Total Environ.*, *541*, 155–160.
- Kropat, G., Bochud, F., Jaboyedoff, M., Laedermann, J. P., Murith, C., Palacios, M., & Baechler, S. (2014). Major influencing factors of indoor radon concentrations in Switzerland. *J. Environ. Radioact.*, *129*, 7–22.
- Borgoni, R., De Francesco, D., De Bartolo, D., & Tzavidis, N. (2014). Hierarchical modeling of indoor radon concentration: how much do geology and building factors matter? *J. Environ. Radioact.*, *138*, 227–237.
- Xie, D., Liao, M., & Kearfott, K. J. (2015). Influence of environmental factors on indoor radon concentration levels in the basement and ground floor of a building – A case study. *Radiat. Meas.*, *82*, 52–58.
- Man, C. K., & Yeung, H. S. (1999). Modeling and measuring the indoor radon concentrations in high-rise buildings in Hong Kong. *Appl. Radiat. Isot.*, *50*, 1131–1135.
- Vukotić, P., Zekić, R., Antović, N. M., & Andjelić, T. (2019). Radon concentrations in multi-story buildings in Montenegro. *Nucl. Technol. Radiat. Prot.*, *34*, 165–174.
- Lorenzo-González, M., Ruano-Ravina, A., Peón, J., Piñeiro, M., & Barros-Dios, J. M. (2017). Residential radon in Galicia: a cross-sectional study in a radon-prone area. *J. Radiol. Prot.*, *37*(3), 728–741.
- Elío, J., Cinelli, G., Bossew, P., Gutiérrez-Villanueva, J. L., Tollefsen, T., De Cort, M., Nogarotto, A., & Braga, R. (2019). The first version of the Pan-European Indoor Radon Map. *Nat. Hazards Earth Syst. Sci.*, *19*, 2451–2464.
- Jovanović Popović, M., Ignjatović, D., Radivojević, A., Rajčić, A., Čuković Ignjatović, N., Đukanović, Lj., & Nedić, M. (2013). *National typology of residential*

- buildings in Serbia*. Belgrade: Faculty of Architecture University of Belgrade.
14. Udovičić, V., Maletić, D., Banjanac, R., Joković, D., Dragić, A., Veselinović, N., Živanović, J., Savić, M., & Forkapić, S. (2018). Multiyear indoor radon variability in a family house—A case study in Serbia. *Nucl. Technol. Radiat. Prot.*, 33(2), 174–179.
 15. Maletić, D., Udovičić, V., Banjanac, R., Joković, D., Dragić, A., Veselinović, N., & Filipović, J. (2014). Comparison of multivariate classification and regression methods for indoor radon measurements. *Nucl. Technol. Radiat. Prot.*, 29, 17–23.
 16. Filipović, J., Maletić, D., Udovičić, V., Banjanac, R., Joković, D., Savić, M., & Veselinović, N. (2016). The use of multivariate analysis of the radon variability in the underground laboratory and indoor environment. *Nukleonika*, 61(3), 357–360. DOI: 10.1515/nuka-2016-0059.
 17. Udovičić, V., Aničin, I., Joković, D., Dragić, A., Banjanac, R., Grabež, B., & Veselinović, N. (2011). Radon time-series analysis in the Underground Low-level Laboratory in Belgrade, Serbia. *Radiat. Prot. Dosim.*, 145(2/3), 155–158.
 18. Udovičić, V., Filipović, J., Dragić, A., Banjanac, R., Joković, D., Maletić, D., Grabež, B., & Veselinović, N. (2014). Daily and seasonal radon variability in the underground low-background laboratory in Belgrade, Serbia. *Radiat. Prot. Dosim.*, 160(1/3), 62–64.
 19. Ujić, P., Čeliković, I., Kandić, A., Vukanac, I., Đurašević, M., Dragosavac, D., & Žunić, Z. S. (2010). Internal exposure from building materials exhaling ^{222}Rn and ^{220}Rn as compared to external exposure due to their natural radioactivity content. *Appl. Radiat. Isot.*, 68, 201–206.

SPECTROSCOPY OF NEUTRON INDUCED REACTIONS WITH THE ν -BALL SPECTROMETER*

N. JOVANČEVIĆ^{a,b}, M. LEBOIS^{a,b}, J.N. WILSON^{a,b}, D. THISSE^{a,b}, L. QI^{a,b}, I. MATEA^{a,b},
 F. IBRAHIM^{a,b}, D. VERNEY^{a,b}, M. BABO^{a,b}, C. DELAFOSSE^{a,b}, F. ADSLEY^{a,b},
 G. TOCABENS^{a,b}, A. GOTTARDO^{a,b}, Y. POPOVITCH^{a,b}, J. NEMER^{a,b}, R. CANAVAN^{c,d},
 M. RUDIGIER^{c,d}, K. BELVEDERE^{c,d}, A. BOSO^{c,d}, P. REGAN^{c,d}, Zs. PODOLYAK^{c,d},
 R. SHEARMAN^{c,d}, M. BUNCE^{c,d}, P. INAVOV^{c,d}, S. OBERSTEDT^e, A. LOPEZ-MARTENS^f,
 K. HAUSCHILD^f, J. LJUNGVALL^f, R. CHAKMA^f, R. LOZEVA^f, P.-A. SÖDERSTRÖM^g,
 A. OBERSTEDT^g, D. ETASSE^h, D. RALET^h, A. BLAZHEVⁱ, R.-B. GERSTⁱ, G. HAFNERⁱ,
 N. CIEPLICKA-ORYŃCZAK^j, L.W. ISKRA^j, B. FORNAL^j, G. BENZONI^k, S. LEONI^k,
 S. BOTTONI^k, C. HENRICH^l, P. KOSEOGLOU^l, J. WIEDERHOLD^l, I. HOMM^l, C. SURDER^l,
 T. KROLL^l, D. KNEZEVIC^m, A. DRAGIC^m, L. CORTESⁿ, N. WARRⁱ, K. MIERNIK^o,
 E. ADAMSKA^o, M. PIERSA^o, K. REZYNKINA^p, L. FRAILE^q, J. BENITO GARCIA^q,
 V. SANCHEZ^q, A. ALGORA^r, P. DAVIES^s, V. GUADILLA-GOMEZ^t, M. FALLOT^t,
 T. KURTUKIAN-NIETO^u, C. SCHMITT^u, M. HEINE^u, D. REYGADAS TELLO^v, M. YAVACHOVA^w,
 M. DIAKAKI^x, F. ZEISER^y, W. PAULSON^y, D. GESTVANG^y

^aIPN Orsay, 15 rue G. Clémenceau, 91406 Orsay, France

^bUniv. Paris-Saclay, 15 rue G. Clémenceau, 91406 Orsay Cedex, France

^cDepartment of Physics, Univ. of Surrey, Guildford, GU2 7XH, UK

^dNational Physical Laboratory, Teddington, Middlesex, TW11 0LW, UK

^eEuropean Commission, Joint Research Centre, Directorate G
Retieseweg 111, 2440 Geel, Belgium

^fCSNSM Orsay, Bat. 104, 91405 Orsay, France

^gHoria Hulubei National Institute of Physics and Nuclear Engineering (IFIN-HH)
077125 Bucharest, Romania

^hLaboratoire de Physique Corpusculaire de Caen

6 Bvd. du maréchal Juin, 14050 CAEN CEDEX 4, France

ⁱInstitut für Kernphysik, Zulpicher Strasse 77, 50937 Köln, Germany

^jH. Niewodniczański Institute of Nuclear Physics, PAN

Radzikowskiego 152, 31-342 Kraków, Poland

^kDipartimaneto di Fisica, Univ. degli Studi di Milano, 20133 Milano, Italy

^lInstitut für Kernphysik, TU Darmstadt, Schlossgartenstrasse 9, 64289 Darmstadt, Germany

^mInstitute of Physics Belgrade, Pregrevica 118, Belgrade, Serbia

ⁿRIKEN, 2-1 Hirosawa, Wako, Saitama 351-0198, Japan

^oUniv. of Warsaw, Faculty of Physics, 02-093 Warszawa, Poland

^pKU Leuven, 3000 Leuven, Belgium

^qUniv. Complutense de Madrid, Avda. de Séneca, 2 Ciudad Universitaria, 28040 Madrid, Spain

^rInstituto de Fisica Corpuscular, 46980 Paterna, Spain

^sThe University of Manchester, Oxford Rd, Manchester, M13 9PL, UK

^tSubatech, 4 rue Alfred Kastler — La Chantrerie — BP 20722, 44307 Nantes cedex 3, France

^uCentre d'Etudes Nucleaires de Bordeaux Gradignan

19 Chemin du Solumium CS 10120, 33175 Gradignan Cedex, France

^vUniv. of Brighton, Mithras House Lewes Road, Brighton BN2 4AT, UK

^wBulgarian Academy of Sciences, 15th November 1, Sofia, Bulgaria

^xEuropean Organization for Nuclear Research (CERN), Geneva, Switzerland

^yUniv. of Oslo, Department of Physics, P.O. Box 1048, Blindern 0316 Oslo, Norway

(Received December 19, 2018)

* Presented at the Zakopane Conference on Nuclear Physics “Extremes of the Nuclear Landscape”, Zakopane, Poland, August 26–September 2, 2018.

The ν -ball is a high-efficiency hybrid spectrometer which consists of both germanium (Ge) detectors and associated anti-Compton BGO shields, coupled to lanthanum bromide (LaBr₃) detectors. The hybrid configuration provides a combination of both excellent energy and timing resolutions. The ν -ball geometry allows the coupling with the LICORNE directional neutron source at the ALTO facility of the IPN, Orsay. This opens the possibility to perform precise spectroscopy of neutron induced reactions and was used for two experiments during the recent experimental campaign. These two experiments are described here: 1. Spectroscopy of the neutron-rich fission fragments produced in the $^{238}\text{U}(n, f)$ and $^{232}\text{Th}(n, f)$ reactions; 2. Spectroscopy above the shape isomer in ^{238}U . The $^{238}\text{U}(n, f)$ and $^{232}\text{Th}(n, f)$ reactions produce hundreds of neutron-rich nuclei on which gamma-ray spectroscopy can be performed. The main goal of the experiment aiming to populate the shape isomer in ^{238}U is the measurement of the gamma-ray and fission decay branches as well as determination of level scheme in the super-deformed minimum. The shape isomer is populated by $^{238}\text{U}(n, n')$ reaction, which gives a very advantageous population cross section over other reactions. More detailed descriptions of these two ν -ball experiments will be presented here.

DOI:10.5506/APhysPolB.50.297

1. Introduction

The ν -ball spectrometer was recently constructed at the ALTO facility of the IPN, Orsay. ν -ball is a hybrid device consisting of 24 clovers and 10 coaxial Ge detectors (and associated anti-Compton BGO shields) with excellent energy resolution and up to 20 LaBr₃ detectors with excellent timing resolution. The main goals were to perform spectroscopy of neutron-rich nuclei and fission shape isomers as well as extract information about nuclear moments or deformations with high sensitivity using fast timing techniques. The unique possibility of coupling the ν -ball spectrometer to the LICORNE (Lithium Inverse Cinematiques ORsay NEutron source) directional neutron source at the ALTO facility [1] was exploited. This opens up the possibility for detailed spectroscopic studies of neutron induced reactions. Two experiments of this type were performed: 1. Spectroscopy of the neutron-rich fission fragments produced in the $^{238}\text{U}(n, f)$ and $^{232}\text{Th}(n, f)$ reactions [2]; 2. Spectroscopy above the shape isomer in ^{238}U [3]. The $^{238}\text{U}(n, f)$ and $^{232}\text{Th}(n, f)$ reactions give a possibility for production and study of hundreds of neutron-rich nuclei, hence many different physics cases are addressed simultaneously. The main goal of the spectroscopy above the shape isomer in ^{238}U is the measurement of population and decay of this long-lived superdeformed state in a nucleus that has a significant gamma branch to the normal deformed potential minimum. The hope is to determine the level scheme in the super-deformed minimum.

2. Coupling the ν -ball spectrometer and LICORNE neutron source

The combination of LaBr₃ and Ge detectors provide excellent timing and energy resolution. The measured timing resolution of LaBr₃ detectors was ≈ 250 ps and timing resolution of Ge detectors was about ≈ 12 ns. The Ge detectors provide in average energy resolution of 2.8 keV at 1.33 MeV energy in comparison with 2.6% at 662 keV for the LaBr₃. Total efficiency was simulated and confirmed by measurements to be $\approx 6.2\%$ for Ge and $\approx 0.8\%$ for LaBr₃ detectors. One of the main characteristics of the ν -ball is full digitization of all signals from detectors including BGO detectors. The FASTER digital data acquisition system was used with a total of up to 200 channels [4]. Since the BGO detectors were used without collimation, calorimetric measurement by determination of full energy deposited in the spectrometer was possible. Calorimetric measurement in combination with the determination of gamma multiplicity is a powerful tool for selection of the events coming from different processes, for example separation of fission events and beta decay. The LICORNE neutron source [1] provides intensely focused quasi-monoenergetic neutron beams produced by the inverse kinematic reaction $p(^7\text{Li},n)^7\text{Be}$. The neutron energy is constrained between 0.5 MeV and 4.0 MeV and is suitable for gamma-spectroscopy measurements of fast neutron induced reactions, particularly fission.

3. Spectroscopy of the neutron-rich fission fragments produced in the $^{238}\text{U}(n, f)$ and $^{232}\text{Th}(n, f)$ reactions

The collection of spectroscopic information about neutron-rich nuclei is very important for many different reasons such as the nuclear structure studies (for example, testing of different theoretical models) or better understanding of astrophysical processes in which neutron-rich nuclei can be produced. Coupling of the ν -ball spectrometer with the LICORNE neutron source gave us possibility to populate and study neutron-rich nuclei. The production mechanism was fission of ^{238}U and ^{232}Th induced by the fast neutrons of incident energy around 2 MeV. The fast fission reaction provides on average higher ratios of neutrons to protons (N/Z) in the reaction products with less emitted neutrons per fission in contrast to thermal neutron-induced fission of ^{235}U , ^{241}Pu and spontaneous fission of ^{248}Cm , ^{252}Cf . This is a clear advantages of these population mechanisms in comparison to ones used previously [5, 6]. Two targets of ^{238}U (81 g) and ^{232}Th (129 g) provide the possibility to perform cross checking of data. Many different physics cases will be studied. The first part of the experiment using the cylindrical shape ^{238}U target was performed in February 2018. The lithium primary beam energy was 16.4 MeV and pulsed with 400 ns period. The experiment lasted

for two weeks. The second part of the experiment was performed in April 2018. The target was a conical shaped aluminum shell housing 9 samples of ^{232}Th of different diameters and thickness of 0.1 mm and an average density of 1 g/cm^3 to reduce attenuation of low-energy gamma rays. The primary lithium beam energy was 16.75 MeV, again with pulsation of 400 ns period. The measurement was three weeks duration. All data were collected in triggerless mode with all gamma ray hits in the detectors stored on disk for later offline analysis. The most important task in the data analysis is to obtain very good selectivity for the particular events of interest. The pulsed neutron beam with period of 400 ns and pulse width of 2 ns, allows separation of prompt and delayed gamma rays and gives access to time correlations. In Figs. 1 and 2, the matrices of energy *versus* time for the Ge and LaBr_3 detectors are presented. Another possibility to increase selectivity comes from

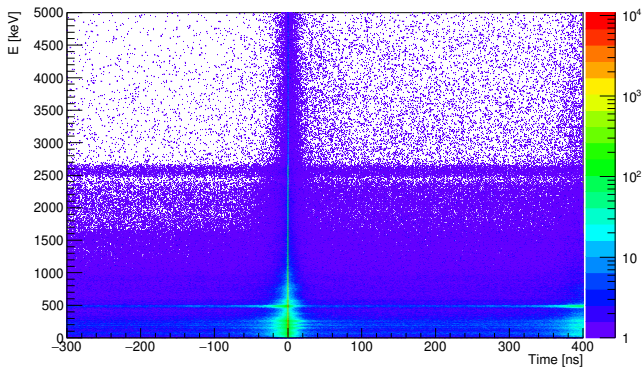


Fig. 1. Energy *versus* time for the LaBr_3 detectors during measurements with ^{232}Th target.

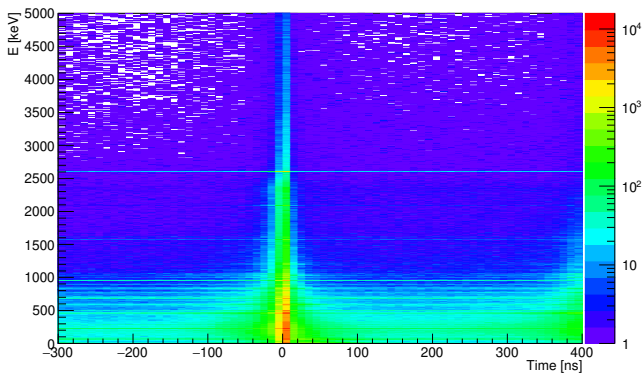


Fig. 2. Energy *versus* time for the Ge detectors during measurements with ^{232}Th target.

the fast timing of the LaBr₃ detectors as well as energy selection with excellent resolution of the Ge detectors. Finally, further selectivity is provided by calorimetric measurement. By analyzing sum-energy and gamma multiplicity (Fig. 3), it is possible to distinguish between events with different multiplicities and total sum energy.

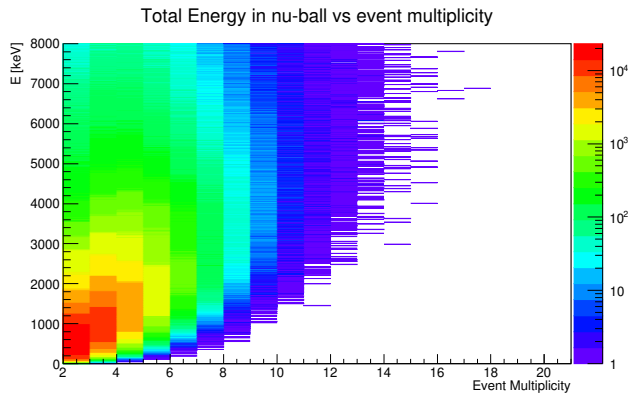


Fig. 3. Multiplicity *versus* total deposited energy in ν -ball spectrometer during activation of the ^{232}Th target.

4. Spectroscopy above the shape isomer in ^{238}U

Study of fission shape isomers can provide information about the fission barrier energy landscape as well as characteristic of super-deformed state of atomic nuclei. In this work, we decided to study the shape isomer in ^{238}U . The goal of the experiment was to obtain information about population of the fission shape isomer, its decay, branching ratio, half life and fission barrier penetrability. Study of shape isomer in ^{238}U has some advantages for experimental work. First of all, it is known that the ground state in the super deformed minimum has energy of 2.558 MeV. Also, two isomeric transitions (IT) to the normal deformed states with energy of 1878 keV and 2513 keV are identified in previous works [7, 8]. The measured half life of that IT decay is 195(30) ns [7, 8]. Decay of this state can occur through IT or isomeric fission (IF) with ratio of IT/IF = 95/5 [8]. With an incident neutron energy between 3 MeV and 5 MeV, the ratio of the prompt fission to delayed fission is $\approx 10^{-4}$ [9]. Taking into account the prompt fission cross section and the IT/IF ratio, the cross section for population of superdeformed isomeric state in ^{238}U can be expected to be ≈ 1.5 mb. Because of this high cross section, the $^{238}\text{U}(n, n')$ reaction is ideal to populate the shape isomer. The LICORNE incident neutron energy was, therefore, arranged to be 3.5 MeV which will give the possibility to populate energy levels up to 1 MeV above the shape isomer in the superdeformed well. Using

the ν -ball spectrometer with the LICORNE pulsed neutron beam gives the possibility first, to study IT decay of fission isomer and then, to study its population to obtain information about level scheme above the shape isomer. The experiment used the same cylindrical ^{238}U target of mass of 81 g used in the previous experiment. However, the lithium primary beam energy was higher, at 18.5 MeV. The measured LICORNE neutron energy spectrum (from TOF) is presented in Fig. 4. Data were collected over a period of approximately 6 days. Prompt and delayed gamma spectra (from 100 ns to 300 ns after beam pulse) for a part of collected data are presented in Fig. 5.

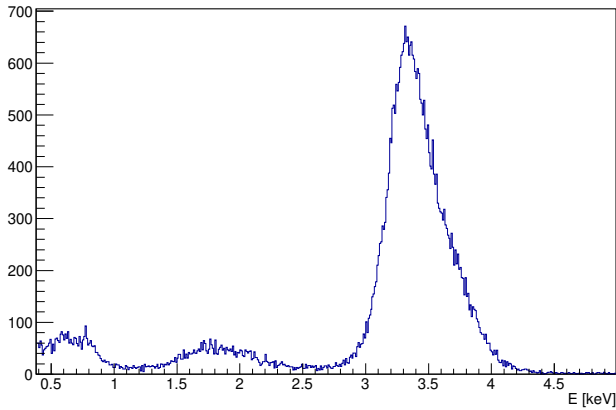


Fig. 4. Measured LICORNE neutron spectrum during the measurement of spectroscopy above the shape isomer in ^{238}U .

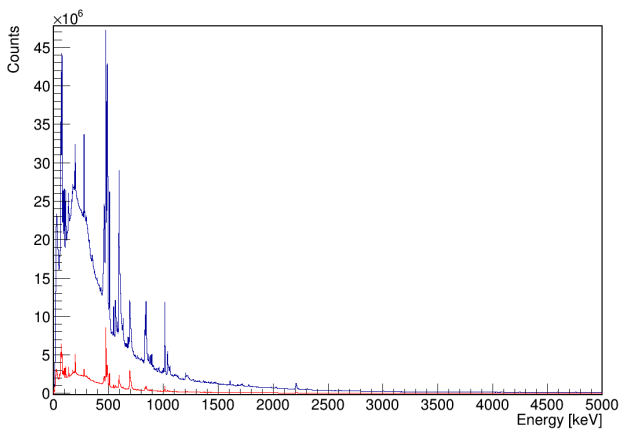


Fig. 5. (Color online) Prompt spectrum (top/blue line) and delay spectrum (bottom/red line) of Ge detectors during the measurement of spectroscopy above the shape isomer in ^{238}U .

The ability to make a selection of different events based on detected gamma multiplicity is presented in Fig. 6. No significant difference in the spectra (Fig. 6) is seen, which requires a further investigation.

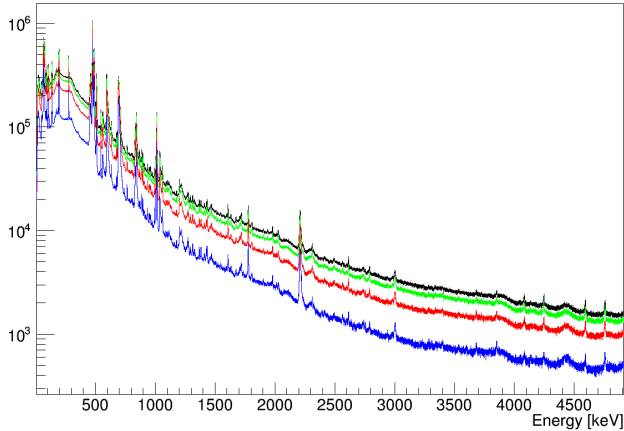


Fig. 6. (Color online) Delayed gamma spectra during the measurement of spectroscopy above the shape isomer in ^{238}U (from 100 ns to 300 ns after beam pulse) with prompt gamma multiplicity equal to or less than 1 and delay gamma multiplicity: equal or less than 1 (bottom/blue line), equal or less than 2 (second from the bottom/red line), equal or less than 3 (second from the top/green line) and equal or less than 4 (top/black line).

5. Conclusion

The coupling of the ν -ball hybrid spectrometer with the LICORNE neutron source was performed at the ALTO facility of the IPN Orsay. Two experiments concerning the gamma-ray spectroscopy of neutron-induced reactions were performed and the main ideas and experimental conditions have been described. The analysis of the collected data is in progress. New information about the structure of neutron-rich nuclei and the fission shape isomer in ^{238}U is expected.

REFERENCES

- [1] M. Lebois *et al.*, *Nucl. Instrum. Methods Phys. Res. A* **735**, 145 (2014).
- [2] J.N. Wilson *et al.*, *Acta Phys. Pol. B* **48**, 395 (2017).
- [3] D.N. Poenaru, M.S. Ivascu, D. Mazilu, *Chapter 2: Fission Isomer*, in: *Particle Emission from Nuclei, Volume II, Fission and Beta-delayed Decay Models*, D.N. Poenaru, M.S. Ivascu (Eds.), CRC PRESS, 1989, ISBN 0-8493-4646-3.

- [4] FASTER DAQ, <http://faster.in2p3.fr>
- [5] J.K. Hwang *et al.*, *Phys. Rev. C* **57**, 2250 (1998).
- [6] A.G. Smith *et al.*, *Phys. Rev. C* **60**, 064611 (1999).
- [7] P. Russo, J. Pedersen, R. Vandenboch, *Nucl. Phys. A* **240**, 13 (1975).
- [8] J. Kantele *et al.*, *Phys. Rev. C* **29**, 1693 (1984).
- [9] K.L. Wolf, J.W. Meadows, *Bull. Am. Phys. Soc.* **19**, KH1 595 (1974).

Study of Nuclear Structure Parameters by Using the (n_{th} , 2γ) Reaction

N. JOVANČEVIĆ*

*University of Novi Sad, Faculty of Science, Department of Physics,
Trg Dositeja Obradovica 3, 21000 Novi Sad, Serbia*

L. V. MITSYNA and A. M. SUKHOVOJ

Joint Institute for Nuclear Research, Dubna, 141980, Russia

D. KNEŽEVIĆ

*University of Novi Sad, Faculty of Science, Department of Physics,
Trg Dositeja Obradovica 3, 21000 Novi Sad, Serbia and
Institute of Physics Belgrade, Pregrevica 118, 11080 Zemun, Serbia*

M. KRMAR and J. PETROVIĆ

*University of Novi Sad, Faculty of Science, Department of Physics,
Trg Dositeja Obradovica 3, 21000 Novi Sad, Serbia*

S. OBERSTEDT

*European Commission, Joint Research Centre, Institute for Reference
Materials and Measurements (IRMM), Retieseweg 111, B-2440 Geel, Belgium*

A. DRAGIĆ

Institute of Physics Belgrade, Pregrevica 118, 11080 Zemun, Serbia

F. -J. HAMBSCH

*European Commission, Joint Research Centre, Institute for Reference
Materials and Measurements (IRMM), Retieseweg 111, B-2440 Geel, Belgium*

V. D. CONG

*Joint Institute for Nuclear Research, Dubna, 141980, Russia and
Vietnam Atomic Energy Institute, Vietnam*

(Received 22 January 2019, in final form 11 March 2019)

The empirical Dubna model for investigating of the cascade gamma-decay of the neutron resonance allows a simultaneous determination of the level density and radiative strengths in a region up to the binding neutron energy for any nucleus. Data can be obtained by determining the intensities of two-step cascades between a decaying compound-state and a group of low-lying levels of the nucleus and describing these intensities by using the most appropriate models prescribed parametrically. For evaluation and minimization of systematical errors of the models used for the level density and radiative strengths for primary gamma transitions spectroscopic information about quanta sequence for observed resolved cascades must be obtained and at least two different sets of models must be used for verification of derivable nuclear parameters. The step-wise structure, which was observed in the energy dependence of the level density for more than 40 investigated nuclei, shows that the structure of a nucleus modifies by excitation.

PACS numbers: 27.30.+t, 21.10.Ma, 21.10.Pc, 21.60.Cs, 23.20.Lv, 28.20.Np

Keywords: Neutron capture, Two-step gamma cascades, Level density, Radiative strength function

DOI: 10.3938/jkps.75.100

*E-mail: nikola.jovancevic@df.uns.ac.rs

I. INTRODUCTION

A study of the process of step-by-step gamma emission requires experimental technique, that would allow on investigation of the properties of any nucleus at its excitation from the ground-state energy up to the energy of gamma emission when a neutron is captured [1–8]. All experiments that investigate the structure of an excited nucleus are based on measuring the spectra, *i.e.*, the cross sections. For a complete and reliable study of gamma-decay processes, the experiment has to allow both the level density, ρ , and the emission widths for products of the nuclear reaction Γ to be obtained, for all excited levels from the measured intensities of the spectra [9]. The present practical model for describing cascade gamma decay of neutron resonances makes possible the simultaneous determination of the ρ and Γ parameters, from an approximation of the intensities of two-step cascades [10–14].

If an emission spectrum is to be obtained, the total energy of gamma transitions must be recorded using multi-detector systems (calorimeters). As for a majority of stable isotopes, a capture reaction is usually accompanied by a wide spectrum of gammas, and the best calorimeters for this type of the experiment are HPGe detectors with high efficiency. In the analysis of total gamma-spectrum, problems and difficulties always exist owing to extracting the required nuclear parameters from the data from an indirect experiment. An acceptable model representation of the required nuclear parameters is always needed to obtain the values of ρ and Γ from a description of the experimental intensity gamma-spectrum. At that, a careful examination of the relation between the relative uncertainties of the experimental spectra δS and the errors of the determined parameter $\delta\rho$ and $\delta\Gamma$, which can an order of magnitude greater than δS , is necessary.

Objective information about ρ and Γ can be obtained only from the data on a gamma spectrum of $M = 2$ multiplicity. At present, establishing a gamma-quantum sequence in the cascade experimentally and obtaining the nuclear parameters for all decaying levels is not possible, as no suitable experimental equipment is available. This is due to the absence of spectrometers with an energy resolution $FWHM < D_i$ (for any spacing D_i between intermediate levels), and with picosecond time resolution for any excitation energy of the investigated nucleus. Because of these limitations only an average number of excited levels and an average value of the partial widths in fixed energy intervals can be measured. Moreover, if the two-step cascade has only two variants of the quanta sequence, then for three quanta $3! = 6$ sequence variants exist. That is, at this time, obtaining reliable information about gamma decay from spectra with multiplicities $M \leq 3$ is not possible.

At that, one should take into account that even in the spectrum of two-step gammas, two sequences of gamma-quanta are possible, one of which is false and must be

removed from the analysis. When solving the nonlinear system of equations, that connect the strongly correlated ρ and Γ values with the experimental two-step cascade intensity, the intensifying of both primary and secondary transitions have an infinite number of solutions. That means that the two-step cascade intensity can be described with the same accuracy by using an infinite number of pairs of essentially different ρ and Γ functions. However, a solution region of the system of equations for the intensity of only primary transitions is bounded for any chosen pair of ρ and Γ model functions. Then, if reliable nuclear parameters are to be obtained, secondary transitions must be removed from the spectrum of the cascade intensity of all gamma transitions.

As the level density (the number of levels in the energy interval δE) increases, on average, exponentially when the nuclear excitation energy goes up, the wave functions of each level must be considered individually in the process of constructing the level-density function. The components of the wave function for each nuclear level increase in number with increasing excitation energy while the absolute values of these components decrease [15,16]. This effect is explained in the theory of the nucleus in the framework of the quasi-phonon model [17–19]. Undoubtedly, this effect plays the leading role when investigating the behavior of nuclear matter.

Thus, in the proposed analysis, for any pair of parametrical representations of the ρ and the Γ values, the most probable parameters of these two functions are determined describing the experimental sum of the intensities of primary transitions of the cascade with the use of the likelihood method. At present, our analysis is based on a modern model of the density of n -quasiparticle levels [31], the balance of the changes in the entropy and excitation energy of quasiparticle levels [9], the level density of collective (vibrational) states [32], and tested ideas about the shape of the energy dependence of the radiative strength functions.

1. Methods for determination of the nuclear parameters

Nuclear parameters extracted from the measured spectra describe the process of emission of the reaction products. Two different procedures usually named as “one-step” [20–25] and “two-step” reactions [1–8], are used for the studying the nuclear structure.

In the case of the one-step reaction, any gamma quanta (or nucleon) of the compound-state decay is recorded irrespective of the energy of the excited level (the total energy of all reaction products is equal to the compound-state excitation energy). In the two-step reaction, a coincidence of two gamma-quanta of the same cascade is recorded. For that, the secondary gamma transitions of the cascade to a group of low-lying levels (including the ground state of the nucleus) are also recorded. Only in

the two-step experiment is information about the energies of intermediate levels included in the data treatment process.

The fundamental difference between one-step and two-step experiments becomes evident when the level density is obtained from the evaporated spectra. As the correlations of the level density and the penetrability coefficients on the wave function of excited level are not taken into account in the one-step experiment, only the product of the ρ and the Γ functions can be determined. Additionally, because of the strong anti-correlation of the ρ and the Γ functions, an unknown systematic uncertainty of their determination appears.

Only in two-step experiments can the uncertainties in the ρ and the Γ determinations be reduced, as they are described by appreciably different functions. A decrease in the methodical errors occurs due to the fact that the intensity $I_{\gamma\gamma}(E_1)$ as a function of the primary transition energy E_1 is, in essence, a convolution of two practically independent experiments; *i.e.*, we can consider the spectrum of primary transitions and the branching ratio distribution of secondary transitions as independent distributions.

An increase the quality of the data from the two-step experiments is obtained by using the following procedures: (1) digital improvement of the energy resolution without any reduction in the efficiency of the cascade recording [3] and (2) an algorithm for determining a sequence of the resolved cascade quanta in any given interval of energies of their primary transitions by using the methods and the results of nuclear spectroscopy [4]. For the first time, procedure to extract the level density and the partial widths of γ -emission from the $(n, 2\gamma)$ reaction investigation was developed in Dubna, Refs. 6,7. From the measured spectrum of the two-step cascade, the intensity $I_{\gamma\gamma}(E_1)$, which links the neutron resonance λ (with the excitation energy E_{ex}) to the group of final levels f via intermediate levels i by dipole transitions, is determined. This can be represented by the following equation:

$$\begin{aligned}
 I_{\gamma\gamma}(E_1) &= \sum_{\lambda,f} \sum_i \frac{\Gamma_{\lambda i} \Gamma_{i f}}{\Gamma_{\lambda} \Gamma_i} \\
 &= \sum_{\lambda,f} \sum_j \frac{\Gamma_{\lambda j}}{\langle \Gamma_{\lambda j} \rangle m_{\lambda j}} n_j \frac{\Gamma_{j f}}{\langle \Gamma_{j f} \rangle m_{j f}} \quad (1)
 \end{aligned}$$

where the sum of partial widths of primary transitions $\sum_i \Gamma_{\lambda i}$ to $M_{\lambda i}$ intermediate levels i is $\langle \Gamma_{\lambda i} \rangle M_{\lambda i}$, and this sum for secondary transitions to $m_{i f}$ intermediate levels is $\langle \Gamma_{i f} \rangle m_{i f}$ (as $\langle \Gamma_{\lambda i} \rangle = \sum_i \Gamma_{\lambda i} / M_{\lambda i}$ and $\langle \Gamma_{i f} \rangle = \sum_i \Gamma_{i f} / m_{i f}$). The sums of intermediate levels in small energy intervals ΔE_j are $n_j = \rho \Delta E_j$. The branching ratios for primary $[\Gamma_{\lambda j} / (\langle \Gamma_{\lambda j} \rangle M_j)]$ and secondary $[\Gamma_{j f} / (\langle \Gamma_{j f} \rangle m_{\lambda j})]$ transitions are fixed for each ΔE_j .

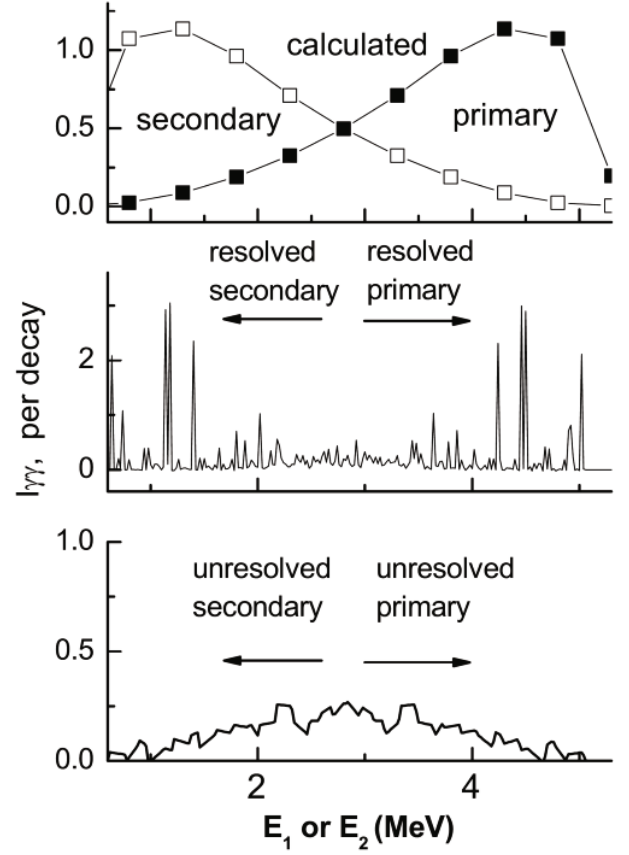


Fig. 1. Distribution of the intensity of the 5731 keV cascade for ^{185}W calculated by using the models (top picture) in Refs. 26,27, with a 500 keV averaging energy interval. Experimental distribution of resolved peaks of the cascade transitions (middle picture) and unresolved continuum (bottom picture; the average energy interval is 10 keV).

2. The $I_{\gamma\gamma}(E_1)$ spectra preparation

The division of the experimental spectra into two mirror distributions (dependent on the energies of only primary, E_1 , and only secondary, E_2 , cascade gamma-quanta) is performed using spectroscopic information. The dividing procedure [6] is based on two facts: (1) the shapes of the intensity dependencies on energy for primary and secondary transitions in the same cascade are mirror - symmetrical and (2) the resolved peaks of the intensity spectrum of the two-step cascade contain no less than half of the total intensity (this fact was confirmed experimentally for all investigated nuclei).

Figure 1 illustrates the possibility of such a division of the spectra of intensity. In the top panel of Fig. 1, the calculated intensity distribution of the cascade with the total energy $E_1 + E_2 = 5731$ keV for ^{185}W [5] is presented, as an example. For our calculations, we used the back shift Fermi-gas model [27] and the model presented in Ref. 26. The calculated intensity shows a division of the spectrum into two parts. As can be seen, the peaks

of the primary and the secondary γ -transitions of the cascade are located symmetrically in opposite parts of the interval E_γ for all γ -quanta energies (for example see Fig. 2).

The experimental distribution of the intensities of resolved peaks and the continuum of unresolved peaks are shown in Fig. 1 in the middle and the bottom panels, respectively. A combination of “primary resolved” and “primary unresolved” parts of the cascade intensity is just the desired $I_{\gamma\gamma} = f(E_1)$ distribution. The determination of the “unresolved” spectrum, where primary transitions are located, was done based on the fact that the total level density increases with the increasing excitation energy.

The calculated intensity of this cascade is about 5% per decay, and the corresponding experimental value is about 11%; thus, resolved peaks account for 8.4% of the experimental intensity, and the unresolved continuum contains 2.6% of the intensity. In addition to that, the shape of the experimental distribution noticeably differs from the calculated one; *i.e.*, description of the intensity spectrum by the statistical model is not satisfactory. As in the center of the experimental spectrum (near half the neutron binding energy $0.5B_n$), the intensity is noticeably smaller than it is for the calculated spectrum, we have a good reason to believe that the separation of $I_{\gamma\gamma}(E_1)$ from the experimented spectrum was performed with a higher accuracy than could have been expected in the framework of the statistical model of the nucleus. The experiment modeling shows that a methodical error of this dividing procedure is caused only by the inaccurate allocation of some cascades (when $E_2 > E_1$) near $0.5B_n$, but this does not change the sum of intensities.

3. Location areas of nuclear parameters

The system of nonlinear equations, Eq. (1), designed for the search of unknown functions $\rho = f(E_{ex})$ and $\Gamma = \Phi(E_1)$ is completely degenerate. Nevertheless, these functions can be defined, but only as possible values in some finite areas. Because of the nonlinearity of these functions, their values cannot be infinite. When the procedure for extracting the ρ and the Γ values was created [7], a set of possible functions, $\rho = f(E_{ex})$ and $\Gamma = \Phi(E_1)$, that describe the $I_{\gamma\gamma}$ intensity with practically zero uncertainty, had already been specified. At an arbitrary choice of the initial ρ and Γ values for fitting the system in Eq. (1), we used, in particular, the model of the Fermi gas and the extrapolation of the tail of the Giant dipole resonance. Small, local distortions of the ρ and the Γ functions were made in each iteration step in order to get a minimal χ^2 . In such a way, this reusable procedure was implemented with different independent initial ρ and Γ values and deviations of the random components of the correction vector until χ^2 minimization was reached. This approach is rather stable, when any

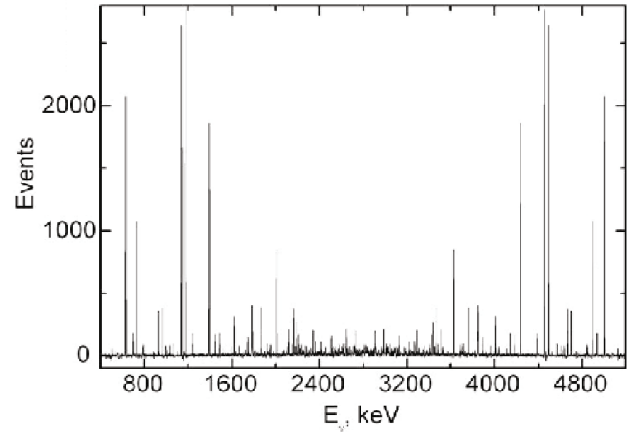


Fig. 2. Experimental distribution of intensities of two-step cascades between a neutron resonance and the first excited state of ^{185}W taking into account the detector efficiency. The spectrum is normalized to the sum of recorded events [5].

noticeable anti-correlation between the ρ and the Γ values is absent, which is ensured by the branching coefficient for the second step of the cascade, which, in turn, depends on the ratio of the partial width Γ_{if} of the secondary transition to the total gamma-width Γ_i of the decayed intermediate levels i (see Eq. (1)). Different energy dependencies for the spectra of primary quanta and the secondary ones, with the branching coefficients, allow us to bound the area of random ρ and Γ functions. A well-defined step-like structure of the level density [7, 8] has resulted from fittings with any initial parameters.

Such a step-like structure of the level density (it can be explained by the breaking of nucleon Cooper pairs in the nucleus) nowise contradicts the smoothness of the experimental spectra obtained from the nucleon reactions, when the ρ and the Γ values are connected and their product is a smooth function. Nevertheless, in this case, the location areas of the ρ and the Γ functions (for an accurate description of the experimental intensity) become bigger, as shown in Ref. 30.

The relative uncertainties, $\delta\rho/\rho$ and $\delta\Gamma/\Gamma$, always exceed $\delta I_{\gamma\gamma}/I_{\gamma\gamma}$. For the lowest energies of the primary transitions of cascades, such an excess may even reach several orders of magnitude. However, the real transfer coefficients of the uncertainties of the functions $\rho = f(E_{ex})$ and $\Gamma = \Phi(E_1)$ to the $I_{\gamma\gamma}(E_1)$ uncertainty must be analyzed. When the accuracy of the $I_{\gamma\gamma}(E_1)$ description is about a few percent, as has resulted from our analysis (see Figs. 3, 5, 6, 7, 8), the accuracies of the ρ and the Γ determinations will be a few tens of percent. The reader should note that the small number of bins in Figs. 3, 6, 7, 8 is the result of averaging multiple bins in order to show graphically the dynamics of the change in the nuclear structure. The actual bin size for the calculation was 50 keV.

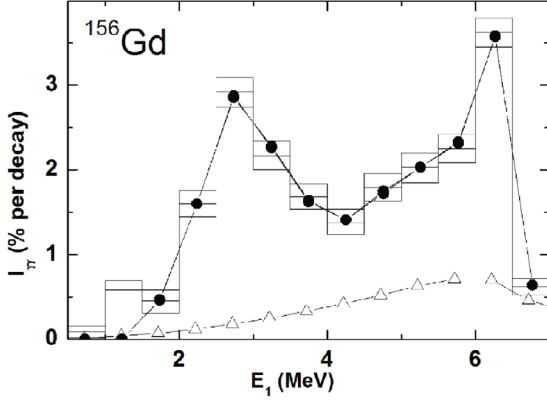


Fig. 3. Measured $I_{\gamma\gamma}(E_1)$ with uncertainties (histogram) for ^{156}Gd . Points - the fit for the practical model; triangles - $I_{\gamma\gamma}$ calculated by using the models in Refs. 26, 27. The threshold for recorded cascade gammas is $E_\gamma = 520$ keV.

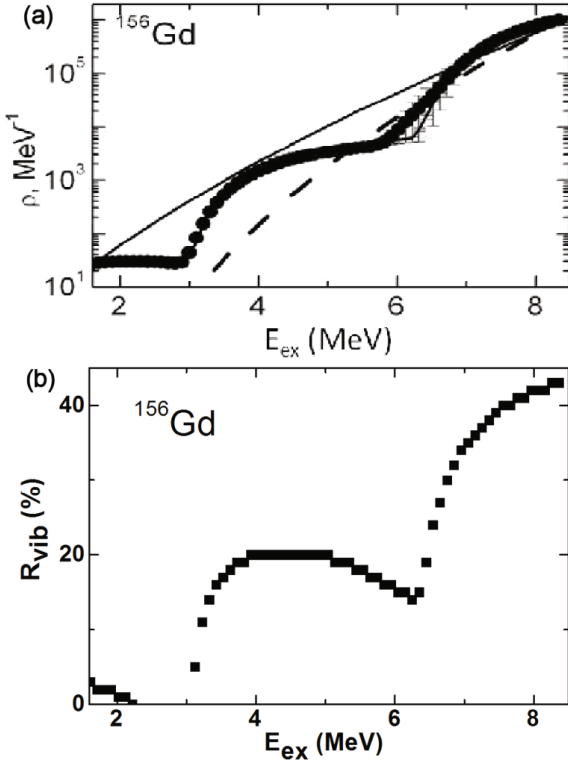


Fig. 4. Level density of ^{156}Gd . (a) Points are the fit for level density (uncertainties are scatters of fits in the case of different sets of initial parameters); dashed and solid lines are the level densities obtained from the model of Ref. 27 with the shell correction $\delta E(6)$ and without δE , respectively. (b) The ratio of collective levels density to the total level density.

II. BASIS OF THE PROPOSED MODEL

The development and the refinement of the model presented in Ref. 7 was done at the Frank Laboratory of Neutron Physics (FLNP), JINR [10–14]. We present here the basic idea and improvement of the model.

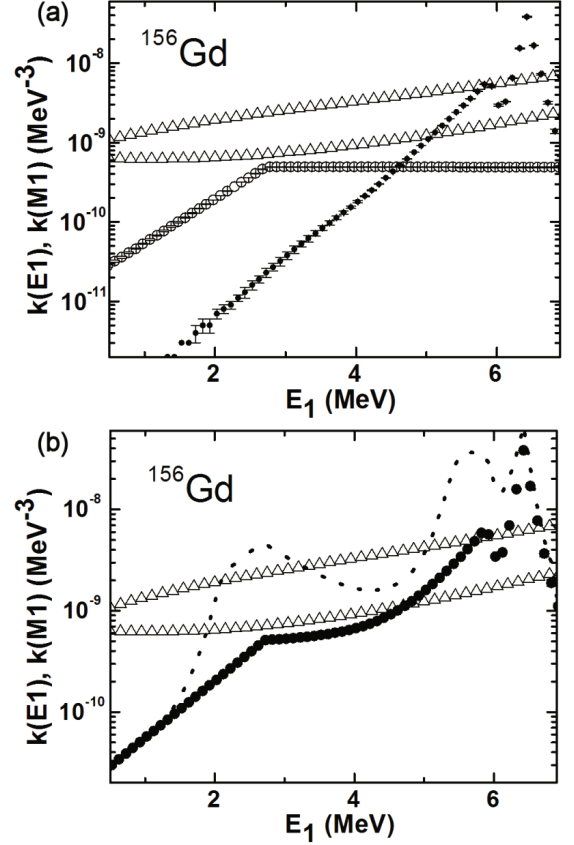


Fig. 5. Radiative strength function for ^{156}Gd . (a) Solid points are the fit of the radiative strength function for $E1$ -transitions; open points are the fit of the radiative strength function for $M1$ -transitions. (b) Solid points are the sum of $E1$ - and $M1$ -radiative strength functions. The dash line is the sum of radiative strength functions multiplied by the ρ_{mod}/ρ_{exp} ratio [27]. Lower triangles are the calculations using the model of Ref. 26 with $k(M1) = \text{const}$; upper triangles are the calculations using the model of Refs. 28, 29 with $k(M1) = \text{const}$.

1. The level density

An expression for the density ρ_l for fermionic-type levels was described by using the model [31] of the density Ω_n of n -quasi-particle states:

$$\rho_l = \frac{(2J+1) \cdot \exp\left(-\frac{(J+1/2)^2}{2\sigma^2}\right)}{2\sqrt{2\pi}\sigma^3} \cdot \Omega_n(E_{ex}),$$

$$\Omega_n(E_{ex}) = \frac{g^n (E_{ex} - U_l)^{n-1}}{\left(\left(\frac{n}{2}\right)!\right)^2 (n-1)!},$$
(2)

where E_{ex} is the excitation energy, $g = 6a/\pi^2$ is the density of single-particle states near the Fermi surface (a is a parameter from the model of a back-shifted Fermi

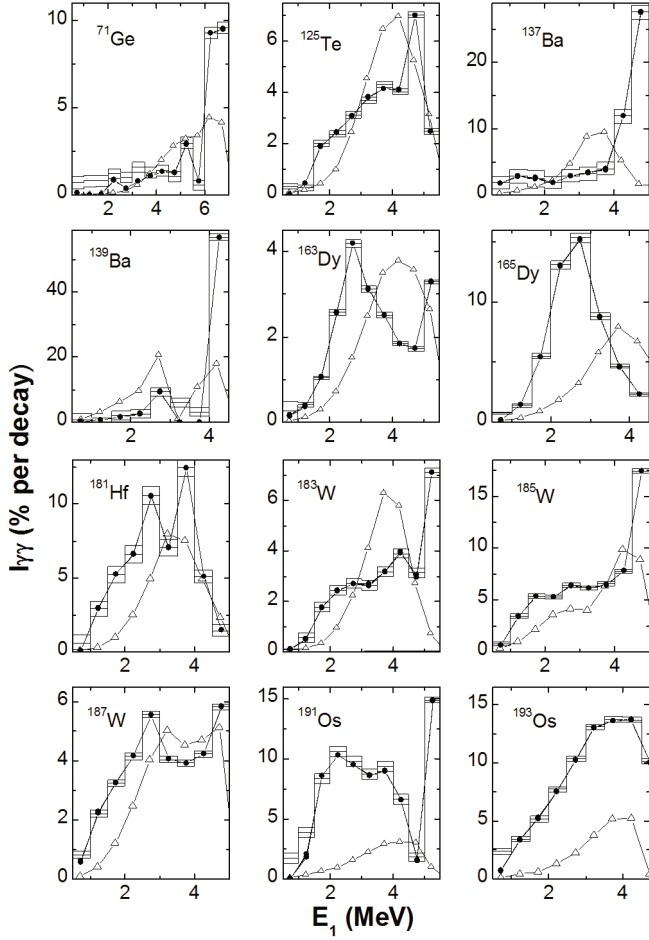


Fig. 6. Histograms are the sums of the measured cascades's intensities with their small errors in 0.5 MeV bins for even-odd nuclei. Solid points are the best fits and triangles are the spectra calculated using the models from Refs. 26,27 with $k(M1) = \text{const.}$

gas [31,32]), U_l is the energy for the l -th Cooper pair breaking threshold. The cut-off factor σ of the spin J for the excited state of a compound nucleus above the maximal excitation energy E_d of the "discrete" level area is also taken from the model of Fermi gas.

For a given E_{ex} , the coefficient of the collective enhancement of the vibrational level density (or both vibrational and rotational ones in the case of a deformed nucleus) C_{col} , was obtained from the theoretical description in Ref. 9. This description gives the following equation:

$$C_{\text{col}} = A_l \cdot \exp\left(\sqrt{(E_{\text{ex}} - U_l)/E_\nu} - (E_{\text{ex}} - U_l)/E_\mu\right) + \beta. \quad (3)$$

In the above equation, A_l are parameters for the densities of the vibrational levels above the breaking point for l -th Cooper pair. The changes in the nuclear entropy and the quasi-particles excitation energies are determined by E_μ and E_ν , respectively. The parameters A_l are fitted

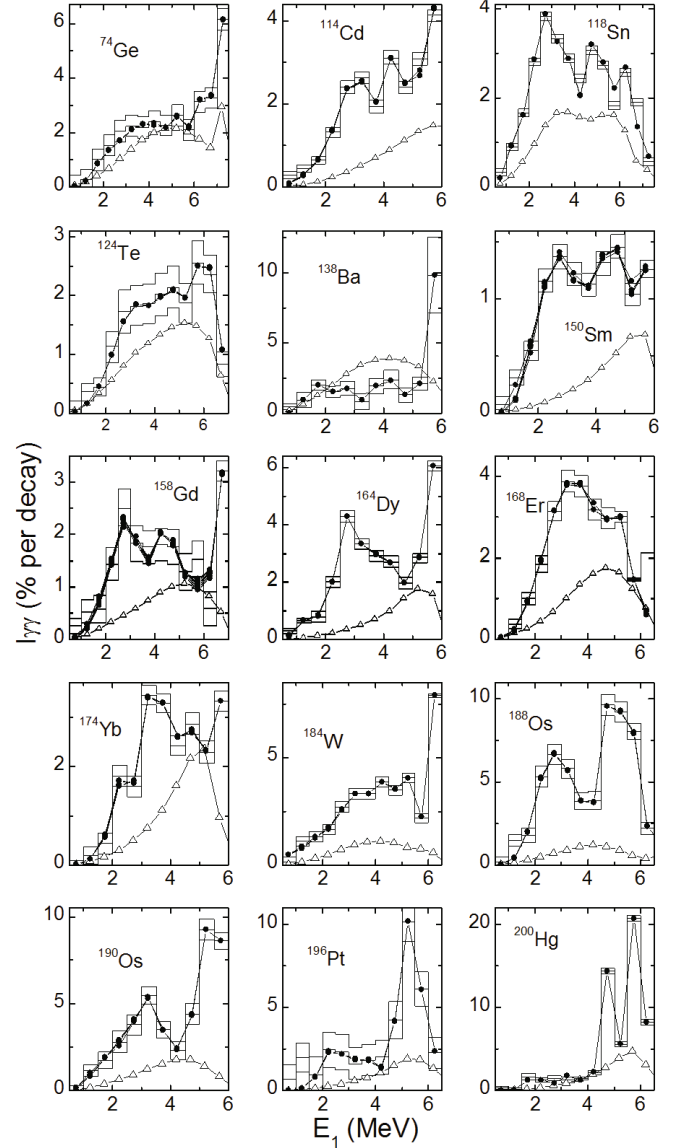


Fig. 7. Histograms are the sums of the measured cascades's intensities with their small errors in 0.5 MeV bins for even-even nuclei. Solid points are the best fits and triangles are the spectra calculated using the models from Refs. 26,27 with $k(M1) = \text{const.}$

independently for different pairs, as in Refs. 10–12. The parameter β describes for the level density of rotation levels.

2. Radiative strength function

The radiative strength functions,

$$k = \Gamma / \left(A^{2/3} E_\gamma^3 D_\lambda \right), \quad (4)$$

for $E1$ -transitions are determined in Ref. 26:

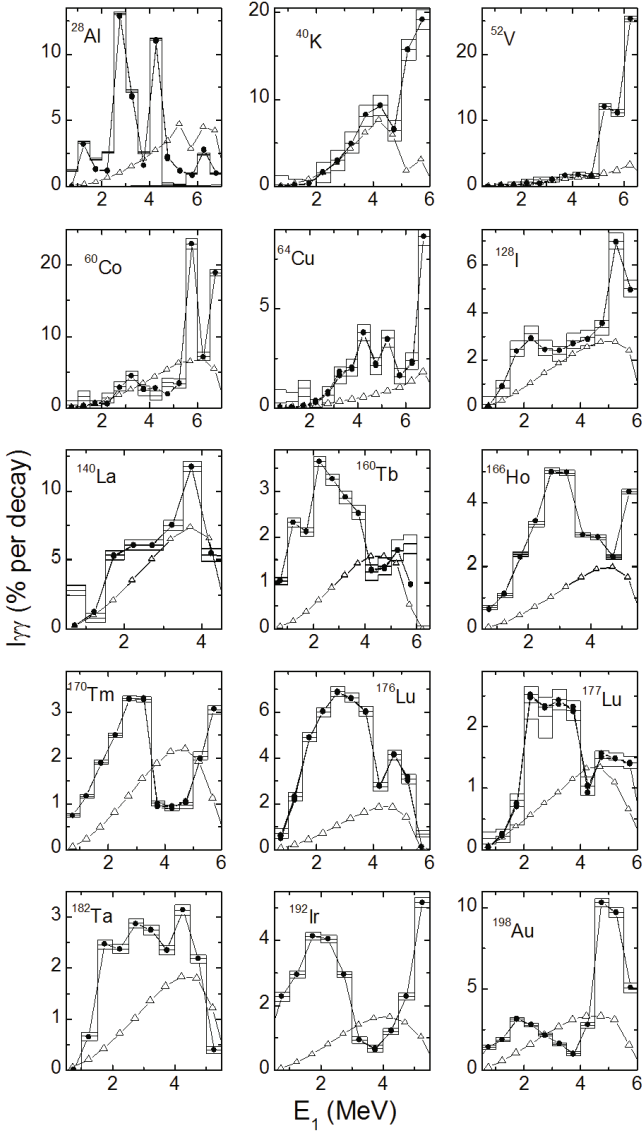


Fig. 8. Histograms are the sums of the measured cascades's intensities with their small errors in 0.5 MeV bins for odd-odd nuclei. Solid points are the best fits and triangles are the spectra calculated using the models from Refs. 26,27 with $k(M1) = \text{const}$.

$$k(E_1, E_\gamma) = w \frac{1}{3\pi^2 \hbar^2 c^2 A^{2/3}} \frac{\sigma_G \Gamma_G^2 (E_\gamma^2 + \kappa 4\pi^2 T^2)}{(E_\gamma^2 + E_G^2)^2 + E_\gamma^2 \Gamma_\gamma^2} + P\delta^- \exp(\alpha_p (E_\gamma - E_p)) + P\delta^+ \exp(\beta_p (E_p - E_\gamma)), \quad (5)$$

with the thermodynamic temperature T , the fitting normalization parameter w and the coefficient κ . Cascades with pure quadrupole transitions were not observed in our experiments, and the radiation strength functions for $M1$ -transitions were obtained for fitting in a similar manner.

The position of the giant dipole resonance E_G , its width Γ_G and its cross section σ_G in the maximum were taken from Ref. 33 for each nucleus. The results of analyses done in Ref. 34 showed the need to add peaks to the radiative strength function. We described the shape of each peak in a different ways. The presented analysis was done by using two exponential functions corresponding to the left and the right slopes of the peak, which correspond to the energies below and above the maximum, Eq. (5). E_p , the amplitude P and the slope parameters α_p and β_p are fitted for each peak independently. At $E_1 \approx B_n$, the fitted ratios Γ_{M1}/Γ_{E1} of the $E1$ - and the $M1$ - radiative strength functions were normalized to the experimental values. Their sum, Γ_λ , was normalized to the total radiation width of the resonance.

3. Parameters for fitting

The set of fitting parameters (see Eqs. (2), (3) and (5)) of all cascades in our model is as follows: the energy thresholds for breaking of Cooper pairs U_l up to $l = 4$, the E_μ and E_ν parameters, parameters A_l , parameters w , κ , β , P , E_p , α_p and β_p and the ratio of the levels density for levels with negative parity to the total level density, r . By using this set of parameters in the framework of the proposed model, we were able to describe the intensity $I_{\gamma\gamma}(E_1)$ for 43 nuclei in the mass interval $28 \leq A \leq 200$.

III. PRACTICAL MODEL IMPROVEMENTS

Significant disagreement is seen between the measured cascade intensities and the ones calculated using the statistical model [10,11]. If the most reliable information about the nuclear matter properties is to be obtained several models for ρ and Γ [32] would be combined.

The Dubna model is based on the conclusion of the theoretical analysis [35], concerning the fragmentation of different quasi-particle states in a nuclear potential, that Cooper pair breaking during nuclear excitation is a sequential process. Thus, the Dubna model allows us to examine two opposite hypotheses (the particular cases of above-mentioned theory): that the nucleus is a pure fermion system or that a phase transition to a nucleus consisting of bosons occurs at some excitation energy.

No known fully precise and correct models about the behavior of nuclear matter in excited nuclei are available. The singular verifiable hypothesis, which arose from nuclear superfluidity studies, is an increase in the total level density, which grows in a manner taken into account by the C_{col} coefficient.

At first, in our practical model [10,11], we assumed that the E_μ and the E_ν parameters of the vibrational

Table 1. Values used in the analysis (the maximal excitation energy E_d of the “discrete” level area, the energy E_{max} of the final level of the cascade, the shell correction δE for the density of quasi-particle levels and the intensity $I_{\gamma\gamma}$ of the two-step cascade and the number of discrete levels) for the investigated nuclei.

Nucleus	E_d (MeV)	E_{max} (MeV)	Shell correction δE (MeV)	I (%)	Spins of state λ	Number of discrete levels
²⁸ Al	2.486	0.972	-11.1	49(1)	2,3	11
⁴⁰ K	2.985	1.64	-3.1	67(3)	1,2	21
⁵² V	0.846	0.147	-5.0	60(2)	3,4	8
⁶⁰ Co	1.515	1.5	-5.9	71(3)	3,4	22
⁶⁴ Cu	0.926	0.278	-3.2	30(6)	1,2	13
⁷¹ Ge	1.298	0.0	-3.5	32(2)	1/2	18
⁷⁴ Ge	2.963	2.165	-3.0	36(2)	4,5	26
¹¹⁴ Cd	2.316	0.558	-1.0	26(1)	0,1	17
¹¹⁸ Sn	2.930	1.230	-1.8	31(1)	0,1	17
¹²⁴ Te	2.702	0.603	-0.3	20(2)	0,1	23
¹²⁵ Te	1.319	0.671	-2.3	31(1)	1/2	18
¹²⁸ I	0.434	0.434	-1.0	33(2)	2,3	21
¹³⁷ Ba	2.662	0.279	-6.3	59(4)	1/2	11
¹³⁸ Ba	2.780	1.436	-8.2	26(5)	1,2	12
¹³⁹ Ba	1.748	1.082	-6.0	81(6)	1/2	8
¹⁴⁰ La	0.658	0.322	-4.0	48(2)	3,4	18
¹⁵⁰ Sm	1.927	0.773	3.0	12(1)	3,4	25
¹⁵⁶ Gd	1.638	0.288	2.4	23(5)	1,2	25
¹⁵⁸ Gd	1.517	0.261	-0.2	19(2)	1,2	20
¹⁶⁰ Tb	0.279	0.279	0.12	23(3)	1,2	21
¹⁶³ Dy	1.055	0.250	-3.0	22(1)	1/2	18
¹⁶⁴ Dy	1.808	0.242	-2.0	29(1)	2,3	26
¹⁶⁵ Dy	0.738	0.184	-3.6	53(1)	1/2	16
¹⁶⁶ Ho	0.522	0.522	-1.5	31(1)	3,4	24
¹⁶⁸ Er	1.719	0.995	-2.3	27(4)	3,4	25
¹⁷⁰ Tm	0.715	0.648	-1.3	23(2)	0,1	21
¹⁷⁴ Yb	1.949	0.253	-3.5	22(1)	2,3	29
¹⁷⁶ Lu	0.688	0.595	-1.8	44(1)	3,4	23
¹⁷⁷ Lu	0.854	0.637	0.25	16(1)	$6\frac{1}{2}, 7\frac{1}{2}$	22
¹⁸¹ Hf	1.154	0.332	-3.1	52(4)	1/2	9
¹⁸² Ta	0.480	0.360	-2.4	19(1)	3,4	15
¹⁸³ W	1.471	0.209	-4.0	28(1)	1/2	13
¹⁸⁴ W	1.431	0.364	-2.4	35(1)	0,1	16
¹⁸⁵ W	1.106	1.068	-0.9	62(1)	1/2	24
¹⁸⁷ W	1.083	0.303	-2.6	34(1)	1/2	24
¹⁸⁸ Os	1.764	0.633	-0.2	59(3)	0,1	16
¹⁹⁰ Os	1.682	0.756	-0.7	49(3)	1,2	12
¹⁹¹ Os	0.815	0.815	-3.5	76(2)	1/2	27
¹⁹² Ir	0.415	0.415	-0.3	27(6)	1,2	30
¹⁹³ Os	1.288	0.889	-3.8	80(1)	1/2	20
¹⁹⁶ Pt	1.998	0.688	-3.7	37(5)	0,1	26
¹⁹⁸ Au	0.528	0.495	-5.6	42(1)	1,2	23
²⁰⁰ Hg	1.972	0.368	-8.0	59(2)	0,1	20

level density vary for different broken Cooper pairs independently and that the density g of the single-particle

states is constant near the Fermi surface for any given nucleus. However, results from Ref. 12 showed that E_μ

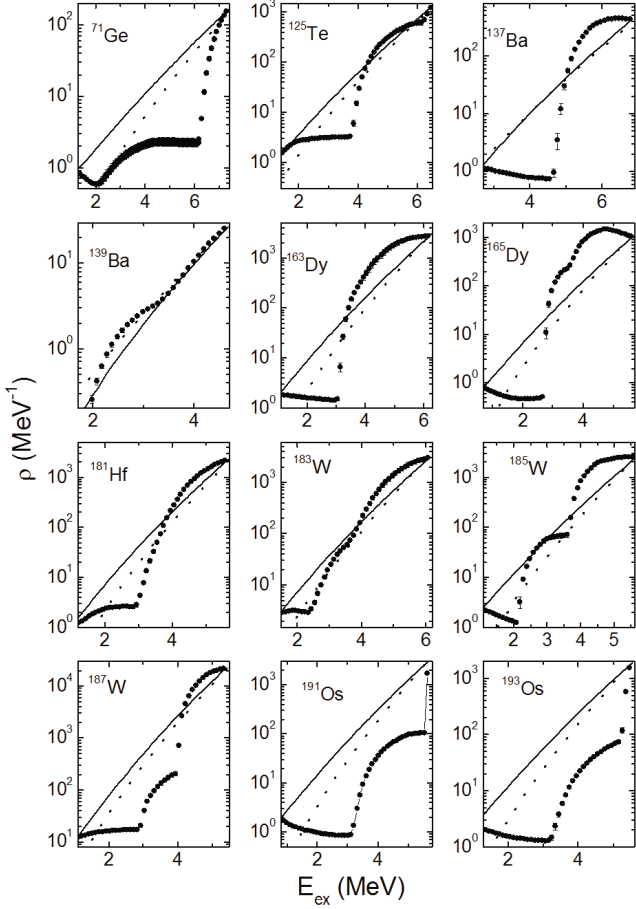


Fig. 9. Most probable densities for intermediate levels of two-step cascades (solid points) for even-odd nuclei and their variations in different fits with the lowest χ^2 . Dashed lines shows the level density obtained using the model of Ref. 27 with the shell correction δE (6); solid lines show the level density obtained using the model of Ref. 27 without the shell correction δE (6).

and E_ν can be replaced by the same parameter, (*i.e.*, $E_\mu = E_\nu$), which allowed us to decrease the number of model parameters. Moreover, an analysis of scores of fittings showed that this common parameter could be taken for all broken pairs in a given nucleus. According to the results of theoretical investigations [9], an influence of the shell inhomogeneity of a single-particle spectrum on the obtained ρ and Γ values must be considered.

An interval of the approximation is specified taking into account two factors: the cascade-quantum energy must be more than 0.52 MeV and the number of levels in the bin below E_d must be less than 5. In the former case, we avoid the problem of taking into account the line shapes of annihilation peak, and, in the latter case, we diminish the strong fluctuations of the intensities of the discrete levels.

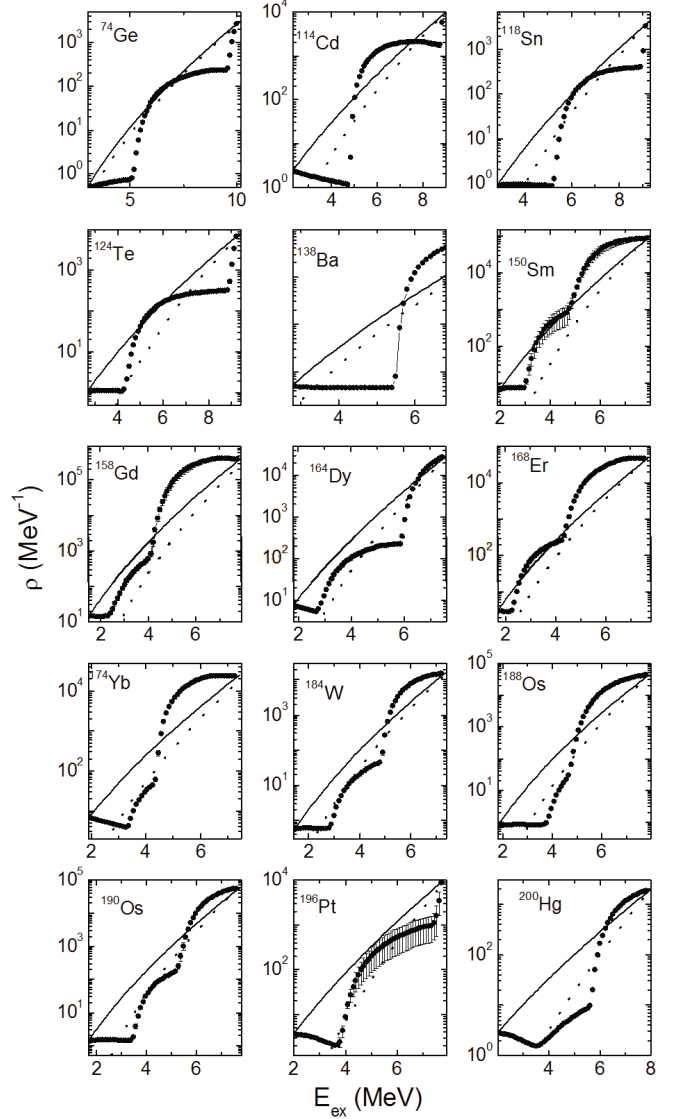


Fig. 10. Most probable densities for intermediate levels of two-step cascades (solid points) for even-even nuclei and their variations in different fits with the lowest χ^2 . Dashed lines show the level density obtained using the model of Ref. 27 with the shell correction δE (6); solid lines show the level density obtained using the model of Ref. 27 without the shell correction δE (6).

IV. CORRECTION FOR SHELL INHOMOGENEITIES

In this work, the theoretical predictions for the dependence of the density of the quasi-particle levels on the shell correction δE were tested for 43 nuclei. The testing was performed by using the parameter $a(A)$, which depended on the excitation energy, included linearly in the parameter of the single-particle density g (see Eq. (2)). $a(A)$ for a nucleus with mass A and excitation energy

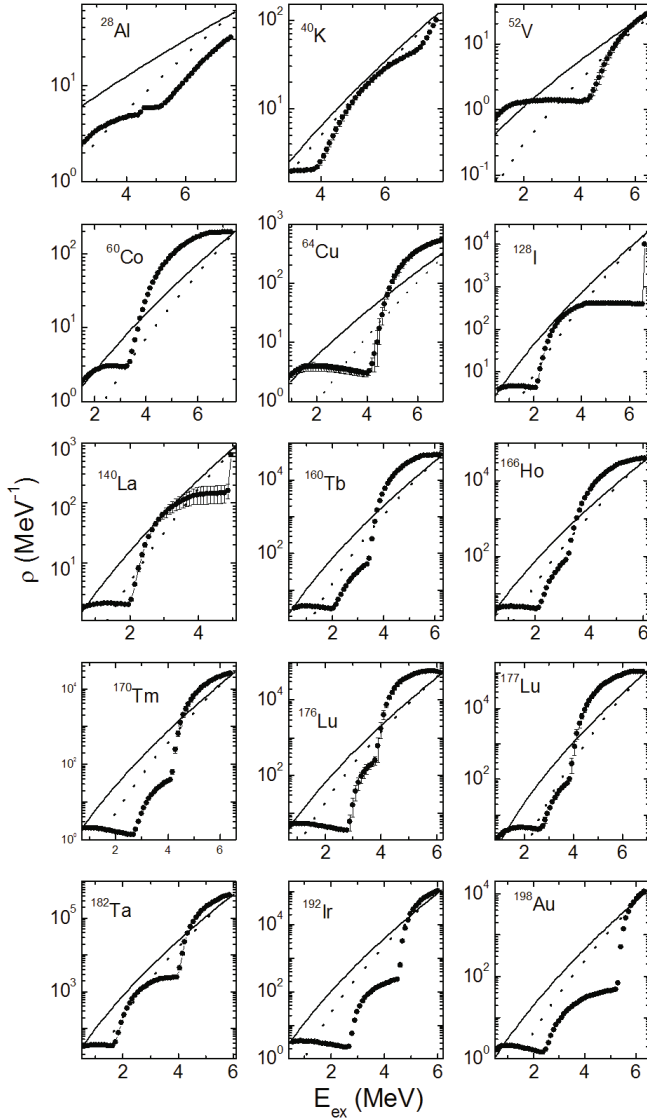


Fig. 11. Most probable densities for intermediate levels of two-step cascades (solid points) for ^{177}Lu and odd-odd nuclei and their variations in different fits with the lowest χ^2 . Dashed lines show the level density obtained using the model of Ref. 27, with the shell correction δE (6); solid lines show the level density obtained using the model of Ref. 27 without the shell correction δE (6).

E_{ex} , is given by [9]:

$$a(A) = \tilde{a} (1 + ((1 - \exp(\gamma E_{ex})) \cdot \delta E / E_{ex})) \quad (6)$$

where asymptotic value $\tilde{a} = 0.114 \cdot A + 0.162 \cdot A^{2/3}$ and $\gamma = 0.054$. For keeping and taking into account the average spacing between neutron resonances [10–12], we varied the δE values slightly relative to their calculations [9]. The shell corrections, used for fitting the parameters of the Dubna model, are presented in the Table 1.

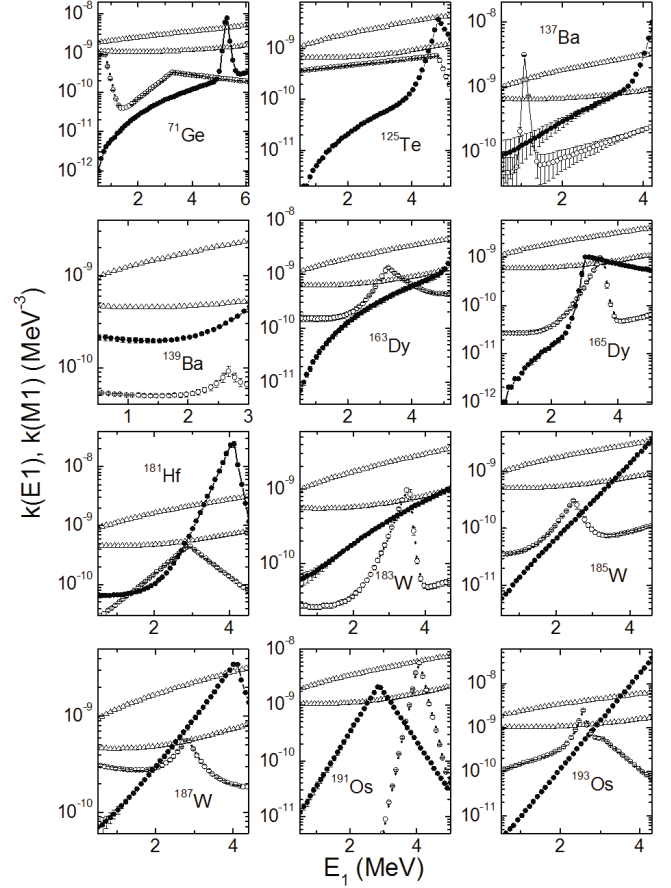


Fig. 12. Radiative strength functions of $E1$ -transitions (closed points) and of $M1$ -transitions (open points) in the case of even-odd nuclei (the best fits). The top line of triangles depicts the model calculation from Ref. 28 while the bottom line represents the model calculation of Ref. 26 in sum for $k(M1) = \text{const.}$

V. RESULTS AND DISCUSSION

The data on the energies E_{max} of the final level of the cascades and the sums of the experimental intensities are shown in Table 1. For almost half of the investigated nuclei, the intensities of the measured two-step cascades contain $\approx 50\%$ (or more) of the total intensities of all cascade transitions to the final levels. Consequently, for these nuclei the systematic uncertainties in the ρ and Γ determinations are minimized, which means that the fits for the ρ and the Γ values are the best ones. In all calculations for $E_{ex} \leq E_d$ (E_d is the maximal excitation energy of the “discrete” level area) the data on excitation energies and decay modes of low-lying levels from Ref. 36 were used. The number of discrete levels (below E_d) is presented in Table 1.

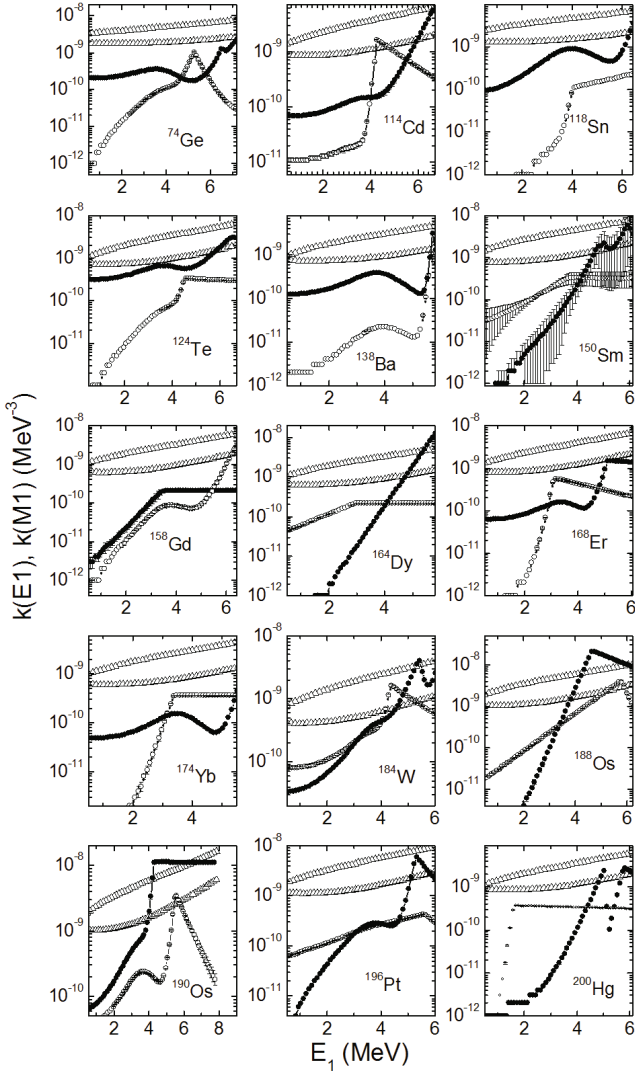


Fig. 13. Radiative strength functions of $E1$ -transitions (closed points) and of $M1$ -transitions (open points) in the case of even-even nuclei (the best fits). The top line of triangles depicts the model calculation from Ref. 28 while the bottom line represents the model calculation of Ref. 26 in sum for $k(M1) = \text{const}$.

1. Characteristics of the fitting procedure

The experimental distributions of the cascade intensities are usually measured in energy intervals with a width of 1 keV and can include from 5000 to 10000 channels (Fig. 2), for each M investigated cascade ($2 \leq M \leq 16$). The basis equations, Eqs. (2)–(5), contain on the average, ≈ 20 parameters, which are fitted for all recorded cascades of the investigated nucleus. In practice, for obtaining the fitted parameters, averaging the energy intervals of primary transitions for excitation energies over 50 keV is reasonable.

The Monte Carlo method was used to solve Eq. (1). The non-linearity of the strongly correlated equations of

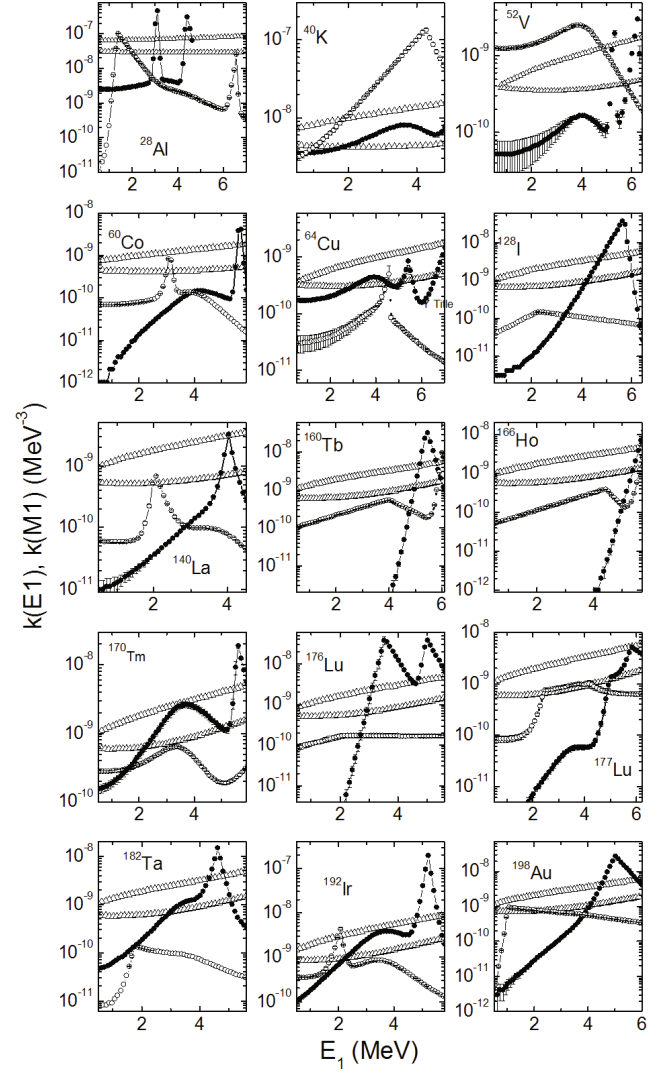


Fig. 14. Radiative strength functions of $E1$ -transitions (closed points) and of $M1$ -transitions (open points) in the case of ^{177}Lu and odd-odd nuclei (the best fits). The top line of triangles depicts the model calculation from Ref. 28 while the bottom line represents the model calculation of Ref. 26 in sum for $k(M1) = \text{const}$.

the system has an influence on the uncertainty for extracting the ρ and the Γ parameters from $I_{\gamma\gamma}$. The existence of false local minima of χ^2 is inevitable for the system of nonlinear equations in Eq. (1), and this occurrence makes a precise determination of the ρ and the Γ values harder. The probability of getting a false minimum of χ^2 sometimes amounts to 20%. Nevertheless, all accumulated data (see Table 1) provide new and very important information.

Experimental data on $I_{\gamma\gamma}(E_1)$ are usually obtained with a small total uncertainty and averaged over 500 keV energy intervals. In Figs. 3–5 the results for ^{156}Gd are presented in more detail. The best fits to $I_{\gamma\gamma}(E_1)$, the fitted level densities, and the radiative strength functions

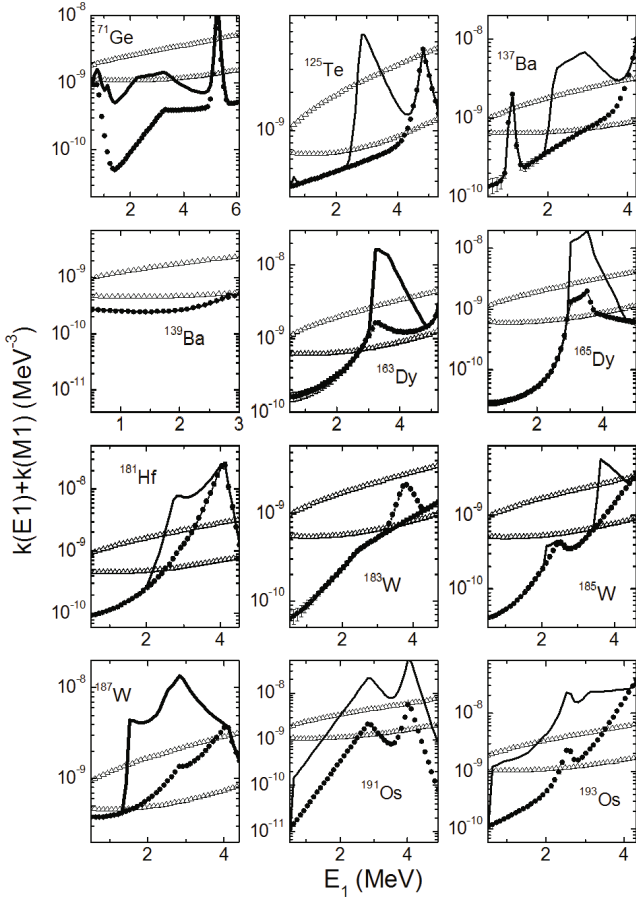


Fig. 15. Sum of radiative strength functions of $E1$ - and $M1$ -transitions (closed points) for even-odd nuclei (the best fits). The solid line is the same multiplied by $\rho_{\text{mod}}/\rho_{\text{exp}}$ [27]. The top line of triangles depicts the model calculation from Ref. 28 while the bottom line represents the model calculation of Ref. 26 in sum with $k(M1) = \text{const}$.

are compared to values obtained by using the statistical model. The results and the corresponding calculations for the rest of the investigated nuclei are presented in Figs. 6–8 (the cascade intensities), in Figs. 9–11, (the level densities), in Figs. 12–14 (the radiative strength functions of $E1$ - and $M1$ -transitions), in Figs. 15–17 (sums of the strength functions) and in Figs. 18–20 (the ratios of the density of vibrational levels to the total level density). The spectra in Figs. 3, 6–8 were calculated using functions shown as solid lines in Figs. 15–17.

2. Resulting parameters

The various shapes of the $I_{\gamma\gamma}$ distributions for different nuclei (Figs. 3, 6, 7 and 8) are most likely determined by the diverse wave functions of the excited levels. In a similar manner, for example, the very strong dependences of the neutron strength functions on nuclear mass [37] or

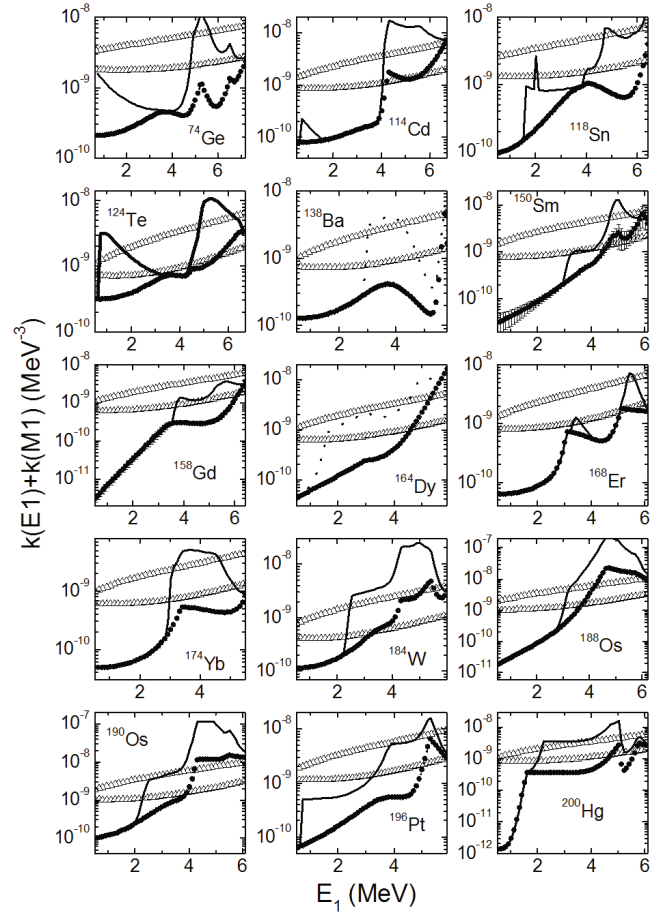


Fig. 16. Sum of radiative strength functions of $E1$ - and $M1$ -transitions (closed points) for even-even nuclei (the best fits). The solid line is the same multiplied by $\rho_{\text{mod}}/\rho_{\text{exp}}$ [27]. The top line of triangles depicts the model calculation from Ref. 28 while the bottom line represents the model calculation of Ref. 26 in sum with $k(M1) = \text{const}$.

the dependences of spectroscopic factors of reactions (d, p) and (d, t) on the locations of low-lying levels (relative to the Fermi-surface) [38] are explained.

The level densities in Figs. 4, 9, 10, and 11 demonstrate that, if the shell inhomogeneities of single-particle spectra are taken into account, the single-particle densities are noticeably reduced in comparison to the ones calculated using the hypothesis $a = \text{const}$. Thus, level densities obtained in our model change slightly when the shell corrections are taken into account. Thus, in Figs. 4, 9, 10, and 11, the curves that describe the calculated single-particle density (using Eq. (6)) and the ones for the fitted level density, for all investigated nuclei, became closer to one another.

The main source of the large fluctuations in the radiative strength functions (see Figs. 5, 12, 13, and 14) is their anti-correlation with the level density in every energy range. Average sums of the strength functions of $E1$ - and $M1$ -transitions for $E_1 = 520$ keV are 0.80(8),

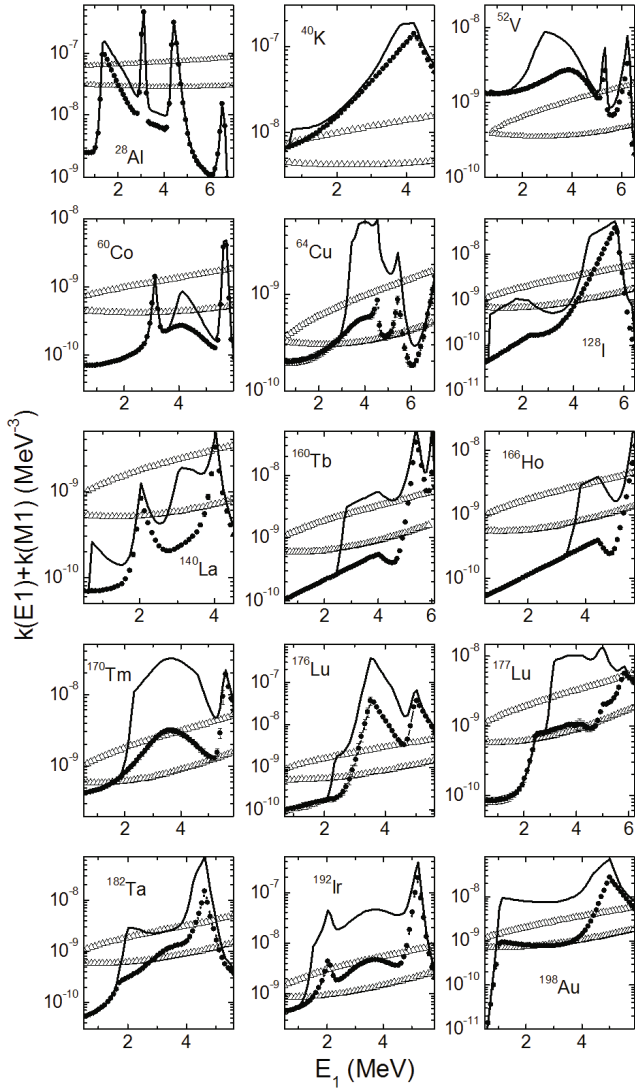


Fig. 17. Sum of radiative strength functions of $E1$ - and $M1$ -transitions (closed points) for ^{177}Lu and odd-odd nuclei (the best fits). The solid line is the same multiplied by $\rho_{\text{mod}}/\rho_{\text{exp}}$ [27]. The top line of triangles depicts the model calculation from Ref. 28 while the bottom line represents the model calculation of Ref. 26 in sum with $k(M1) = \text{const}$.

$2.1(2)$ and $2.5(3) \cdot 10^{-10} \text{ MeV}^{-3}$ for even-even, even-odd and odd-odd nuclei, respectively. Thus, the summation noticeably reduces the above-mentioned scatter and allows us to assert that the sum strength function decreases with decreasing energy of the primary transition.

The contributions of the levels of a vibrational type in the total level density (Figs. 18–20) for all nuclei decrease near the U_l points. For a majority of the nuclei the part of the vibrational levels below B_n is about 40%, which does not contradict the results of the analysis of distributions of the total radiative widths above B_n [39]. Calculations of the distributions of random deviations for the total radiative widths of s-resonances, executed in Ref. 39, showed a superposition of at least four distri-

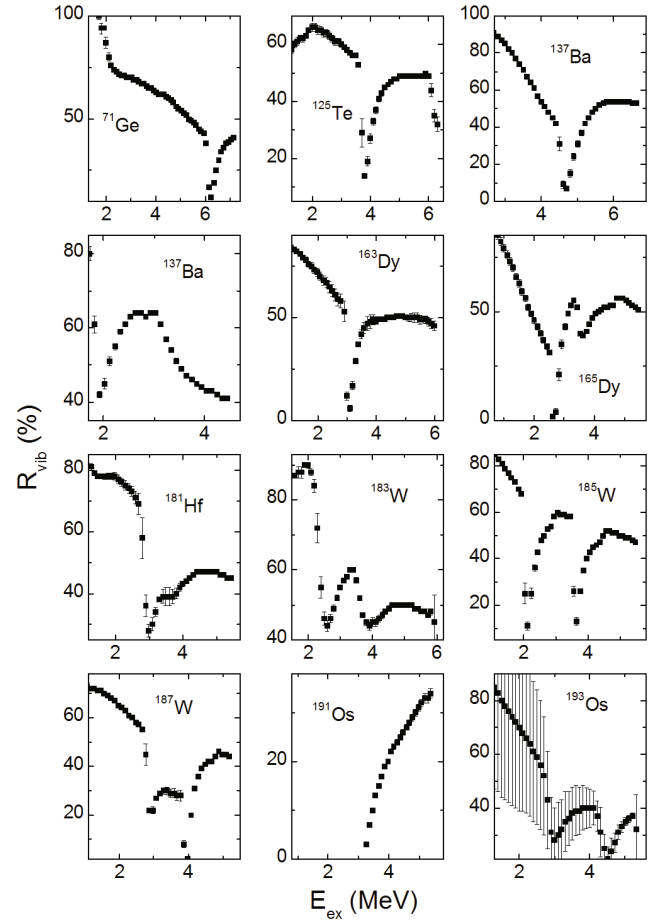


Fig. 18. Part of the vibrational levels R_{vib} in the total density of excited levels for even-odd nuclei at excitation energy E_{ex} .

butions with different averages $\langle \Gamma_\gamma \rangle$.

When the gamma-decay process is investigated, the problem of describing of special points (of the breaking of the Cooper pairs) appears. As anti-correlation between ρ and Γ values can be different to a greater or lesser extent in all excitation energy ranges, it can be maximal just at the points of breaking the Cooper pairs. A noticeable dependence of the resulting strength functions on the local jumps in the level density is seen. Then as already pointed out, in order to prevent a contradiction between the data of the two-step experiment and one-step experiment, one must to take into account the connection between the ρ and the Γ values. We investigated such an anti-correlation by multiplying the phenomenological expression, Eq. (5), for the strength function by the $\rho_{\text{mod}}/\rho_{\text{exp}}$ ratio, which inserts an additional fitted correlation. Here, ρ_{exp} is taken from the best fit obtained while solving the system in Eq. (1), and ρ_{mod} was taken from the model of a back-shifted Fermi gas [27]. The function ρ_{mod} represents smoothed density for fermion-type levels and describes both a neutron resonance density and the cumulative sum of known nuclear levels at

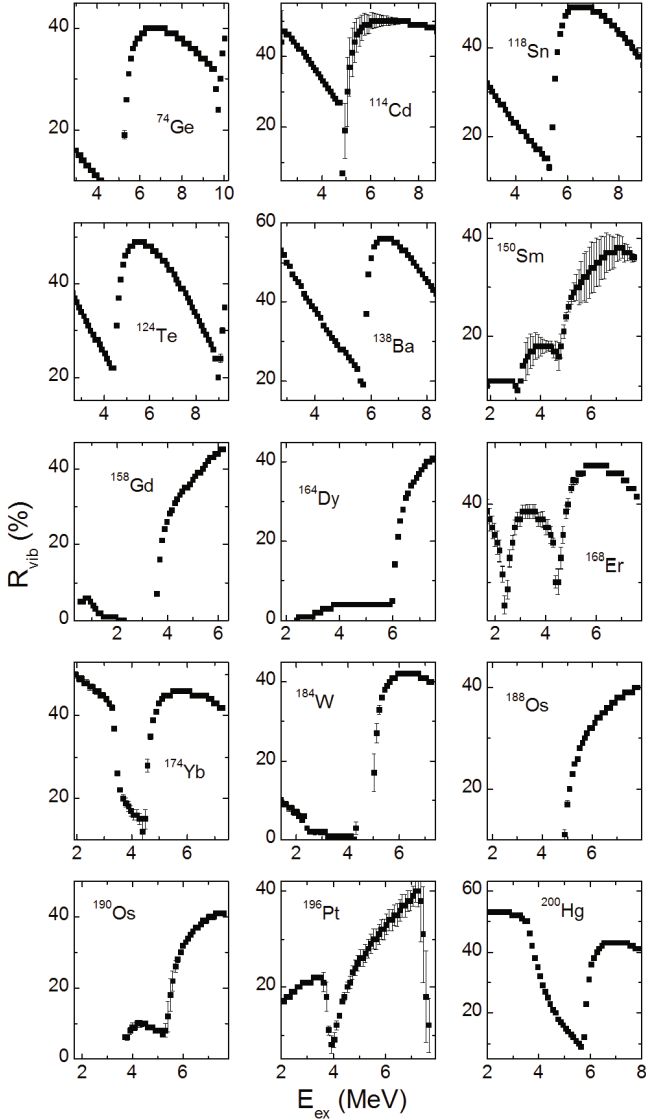


Fig. 19. Part of the vibrational levels R_{vib} in the total density of excited levels for even-even nuclei at excitation energy E_{ex} .

$E_{\text{ex}} \leq E_d$ (E_d was taken from Ref. 36). The limiting condition $1 \leq \rho_{\text{mod}}/\rho_{\text{exp}} \leq 10$ from Refs. 10 and [11] was implemented in this analysis.

The coefficient $\rho_{\text{mod}}/\rho_{\text{exp}}$ was introduced to the phenomenological formula for the strength function, which makes the residual anti-correlation of the fitted ρ and Γ demonstrable, to test its influence on the shape of the strength functions of the step-like structure of fitted level density distribution. Simultaneously, it was a test of the invariability of this step-like structure.

The data in Fig. 21 show that the above-mentioned hypothesis about equality of the E_μ and E_ν parameters and about their independence from the number of breakup pairs does not make the fitting quality worse for any investigated nuclei. Therefore, the energy slope of

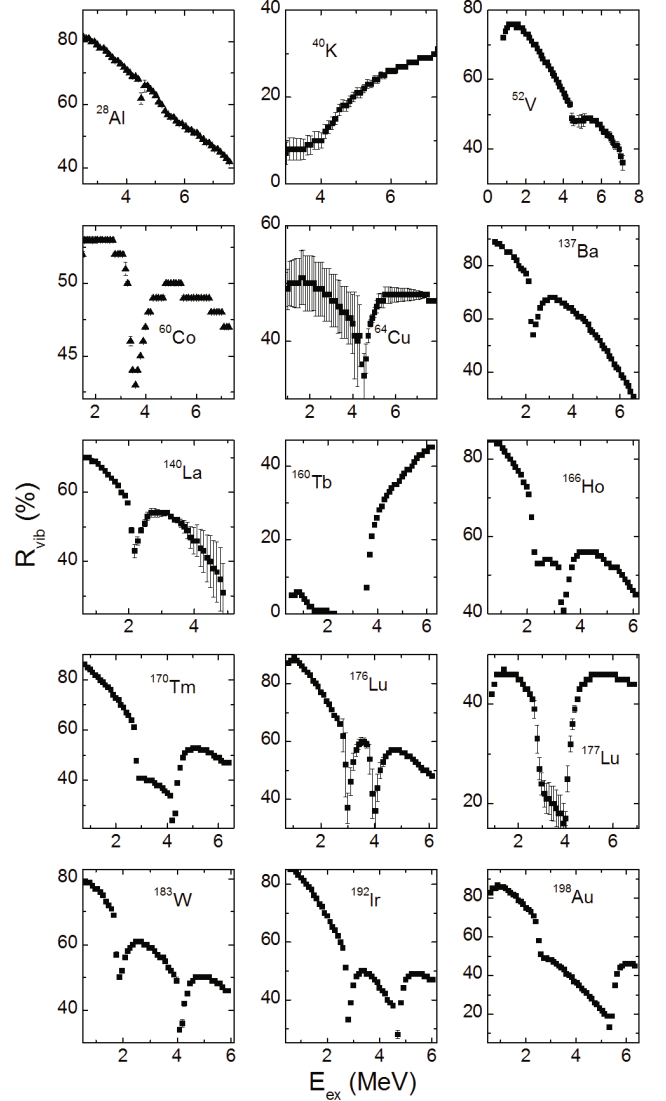


Fig. 20. Part of the vibrational levels R_{vib} in the total density of excited levels for ^{177}Lu and odd-odd nuclei at excitation energy E_{ex} .

the vibrational level density is rather dominantly determined by the Δ_0 value. In our analysis of all investigated nuclei, that the coefficients E_μ and E_ν from Eq. (1) turn out to lie near 1 and to be randomly scatter relative to the average. Because of that, Fig. 21 is clear proof of the validity of the vibrational-increase accounting in the level density.

3. The Cooper-pairs-breaking thresholds

Our previous studies have shown the existence of a connection between the shape of the nucleus and the Cooper-pairs-breaking thresholds [11, 13, 14]. These results were also confirmed in this work. Figure 22 presents the dependence of the binding energy to Δ_0 on nuclei

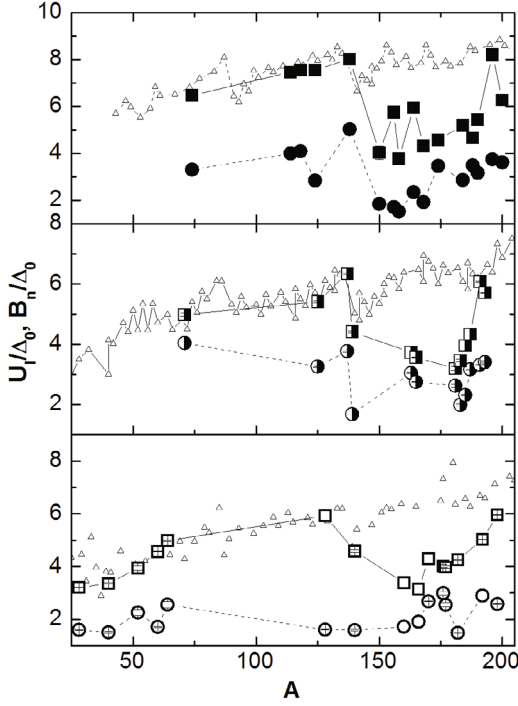


Fig. 21. Dependence of the E_μ and the E_ν (same) model parameters on the nuclear mass A . (Black points-even-even nuclei, black-white-even-odd nuclei and white points-odd-odd nuclei.)

mass and the dependencies of the ratios for the break up thresholds of the second and the third Cooper pairs to Δ_0 on nuclei mass. We should mention that the Cooper-pairs-breaking thresholds are different for nuclei with different nucleon parities and depend on the pairing energy (Δ_0) for the last nucleon. Results presented in Fig. 22 show a significant differences in the ratios U_2/Δ_0 and U_3/Δ_0 for deformed and spherical nuclei, in contrast to B_n/Δ_0 ratio.

4. Level parity

The obtained values for the ratio $r = \rho(\pi-)/(\rho(\pi-) + \rho(\pi+))$ of levels $\rho(\pi-)$ with negative parity to the total level density are presented in Fig. 23. The average values of this ratio are 0.61(22) for even-even, 0.25(28) for even-odd and 0.16(16) for odd-odd nuclei (for odd-even ^{177}Lu , it is 0.65(1)). Those results suggest that the gamma-decay process depends on various nucleon parities. The calculation of the ratio $r = \rho(\pi-)/(\rho(\pi-) + \rho(\pi+))$ was done using a linear extrapolation of the r value in the $E_d \leq E_{ex} \leq B_n$ energy region. In the B_n energy point it was used accepted assumption, that $\rho(\pi-) = 0.5 \cdot (\rho(\pi-) + \rho(\pi+))$, the $\rho(\pi-)$ value in this point was fixed, and at the E_d energy the $\rho(\pi-)$ varied.

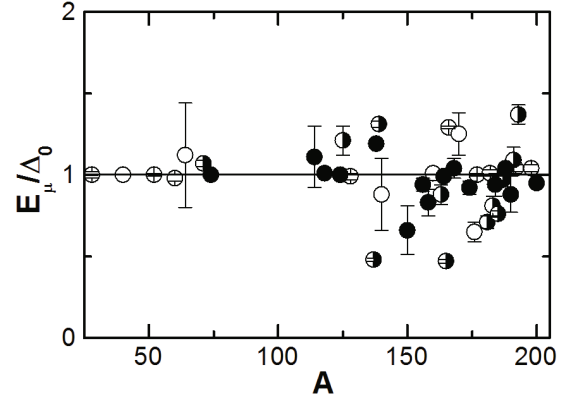


Fig. 22. Dependence of the ratios, U_i/Δ_0 , of break-up thresholds to the average pairing energy of the last nucleon on the nuclear mass A , for the second (points) and the third (squares) Cooper pairs. (Black points-even-even nuclei, black-white-even-odd nuclei and white points-odd-odd nuclei.) Triangles show the dependence of B_n/Δ_0 ratio on mass.

VI. POSSIBLE EXPERIMENTS FOR A STUDY OF SUPERFLUIDITY

Experiments on recording the cascades of two-gamma transitions of radiative capture of thermal neutrons were carried out in Dubna (Russia), Riga (Latvia), Rez (Czech Republic) and Dalat (Vietnam). Unfortunately, gamma-ray cascades at thermal neutron capture allow the determination of ρ and Γ only for a fixed area of nuclear excitations, for a certain spin interval, and for a given parity of the decaying resonance (Table 1).

Until now, in all analyses, a nucleus was usually imagined as a statistical system. The real uncertainty of this nuclear model is still unknown; therefore, new experiments (*e.g.*, as in Ref. 10) are needed. Such experiments can be carried out not only by using beams of thermal and resonance neutrons but also by utilizing any accelerators of charged particles, if provides the scattering of energies of excited levels λ in the target and the energy resolution of the HPGe - detectors are comparable.

The best approach to studying cascades of gamma transitions of decaying levels excited by gamma quanta can be achieved using any source of gamma radiation (*e.g.* ELBE [40] or S-DALINAC [41]) with a fixed energy. At fixed energy E_{max} of the gamma beam, the model of Ref. 10 can be applied in the interval of excitation energies of the decaying levels from E_{max} to $E_{max} - 511$ keV, which would allow for the cascade decay process to become clearer.

The background conditions during cascade recordings for a beam of gamma quanta are essentially better than those for neutron beams. For experiments of the types seen in Refs. 40, 41, a singular requirement is needed: detectors must be placed close to the target, in a back hemisphere relative to it. In such an experiment the ra-

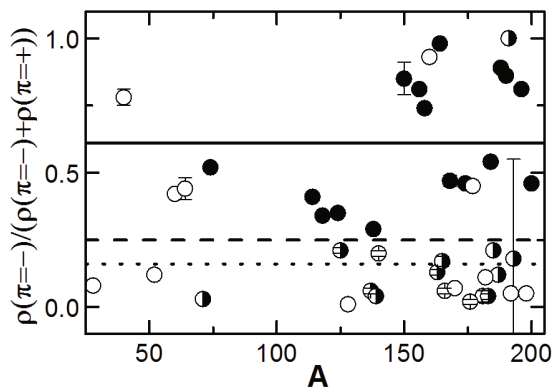


Fig. 23. Mass dependence of the ratio $r = \rho(\pi-)/(\rho(\pi-)+\rho(\pi+))$ at the upper energy border for the discrete region of levels (E_d) and their averaged values for even-even (solid lines), even-odd (dashed lines) and odd-odd nuclei (dotted lines). (Black points-even-even nuclei, black-white-even-odd nuclei and white points-odd-odd nuclei.)

diative strength functions for gamma transitions both to the ground state of the target nucleus, and to its' excited levels can be determined separately. The information content of such an experiment will exceed the results of $(n, 2\gamma)$ reaction investigations by at least ten times.

Unlike the cascades of gamma transitions, cascades with nucleon emission provide significant statistical improvements due to the high efficiency of recording the charged products of the reaction. Mathematically, the spectrum of primary gamma transitions of decaying levels below the emission threshold for nucleon products of the reaction and the spectrum of evaporated nucleons (light nuclei) above the binding energy are identical. Therefore, the analysis of a cascade of evaporated nucleon and gamma quanta is similar to the analysis of the cascade of two-gamma transitions. Nevertheless the intensity of a cascade of nucleon and gamma quantum to low-lying levels can be depend strongly on the orbital moment of the evaporated nucleon.

VII. CONCLUSION

In order to obtain reliable values of ρ and Γ , we used an effective practical model that takes into account the interaction of the fermion and the boson components in the nuclear matter. The need to take into account the corrections for the shell inhomogeneities of single-particle spectrum on the level density was demonstrated when comparing the parameters obtained under two different conditions: at a constant density of single-particle states near the Fermi surface and at $g \neq \text{const}$. The results obtained using the shell corrections were closer to the existing representations. Nevertheless, we cannot describe the cascade intensities without taking into account the strong influence of the nuclear superfluidity on

the gamma-decay process. The results about the Cooper pair break-up energies showed a dependence of the dynamics for interactions between superfluid and normal nuclear matter phases on the shape of nucleus. Those data were obtained with high accuracy.

Our model allows for a separate determination of the density of vibrational levels between the breaking thresholds of the Cooper pairs. In two-step gamma-decay, a common result for nuclei with different parity of nucleons is a decrease in the sum k of radiative strength functions when the energy of primary transitions decreases. When one analyzes the set of investigated nuclei, the average sums are almost equal for odd-odd and even-odd nuclei, while the k values are two times smaller for the even-even nuclei.

Unfortunately, the existence of errors for the ρ and the Γ functions is a fundamental problem. This is important for any model used for an analysis of experimental data, as well as for calculations of cross sections or spectra. The systematic uncertainties also come from fluctuations in the intensities of the gamma decay transitions in different nuclei. However, the results presented here gave a possibility for describing of the data obtained in two-step cascades experiments with a satisfactory accuracy that is higher the statistical one.

ACKNOWLEDGMENTS

We wish to express our gratitude to Dr. Petar Mali for helpful advice and discussions.

REFERENCES

- [1] S. Valenta *et al.*, Phys. Rev. C **92**, 064321 (2015).
- [2] J. Honzatko *et al.*, Nucl. Inst. Meth. A **376**, 434 (1996).
- [3] A. M. Sukhovojev and V. A. Khitrov, Instrum. Exp. Tech., **27**, 1071 (1984).
- [4] Yu. P. Popov, A. M. Sukhovojev, V. A. Khitrov and Yu. S. Yazvitsky, Bull. Acad. Sci. USSR Phys. Ser. **48(5)**, 53 (1984).
- [5] V. A. Bondarenko *et al.*, Fizika B (Zagreb) **11**, 201 (2002).
- [6] S. T. Boneva, A. M. Sukhovojev and V. A. Khitrov, Nucl. Phys. A **589**, 293 (1995).
- [7] E. V. Vasilieva, A. M. Sukhovojev and V. A. Khitrov, Phys. At. Nucl. **64**, 153 (2001).
- [8] A. M. Sukhovojev and V. A. Khitrov, Phys. Part. Nucl. **36**, 359 (2005).
- [9] V. Ignatyuk, Report INDC-233(L), IAEA, Vienna (1985).
- [10] A. M. Sukhovojev, Phys. Atom. Nucl. **78**, 230 (2015).
- [11] A. M. Sukhovojev and L. V. Mitsyna, in *Proceedings of XXII International Seminar on Interaction of Neutrons with Nuclei* (Dubna, May 2014, Preprint N E3-2015-13, 2015), p. 245, <http://isinn.jinr.ru/past-isinns.html>.

- [12] A. M. Sukhovoĵ, L. V. Mitsyna and N. Jovancevic, in *XXIII International Seminar on Interaction of Neutrons with Nuclei* (Dubna, May 2015, JINR preprint E3-2016-12, Dubna, 2015), p. 299.
- [13] D. C. Vu *et al.*, Phys. Atom. Nucl. **80**, 237 (2017).
- [14] A. M. Sukhovoĵ, L. V. Mitsyna and N. Jovancevic, Phys. Atom. Nucl. **79**, 313 (2016).
- [15] V. G. Soloviev, Nucl. Phys. A **586**, 265 (1995).
- [16] V. G. Soloviev, Sov. J. Phys. Part. Nucl. **60**, 390 (1972).
- [17] V. G. Soloviev, Theory of Atomic Nuclei. Quasi-particle and Phonons, IPP, Bristol and Philadelphia, 1992.
- [18] H. A. Weidenmuller and G. E. Mitchell, Rev. Mod. Phys. **81** (2009).
- [19] F. Iachello and A. Arima, *The Interacting Boson Model* (Cambridge University Press, Cambridge, 1987).
- [20] H. Vonach, in *Proc. IAEA Advisory Group Meeting on Basic and Applied Problems of Nuclear Level Densities* (New York, 1983), INDC(USA)-092/L, p. 247.
- [21] B. V. Zhuravlev, Bull. Rus. Acad. Sci. Phys. **63**, 123 (1999).
- [22] G. A. Bartholomew *et al.*, Adv. Nucl. Phys. **7**, 229 (1973).
- [23] A. Schiller *et al.*, Nucl. Instrum. Meth. A **447**, 498 (2000).
- [24] A. C. Larsen *et al.*, Phys. Rev. **76**, 044303 (2007).
- [25] A. C. Larsen *et al.*, Phys. Rev. **83**, 034315 (2011).
- [26] S. G. Kadenskij, V. P. Markushev and W. I. Furman, Sov. J. Nucl. Phys. **37**, 165 (1983).
- [27] W. Dilg, W. Schantl, H. Vonach and M. Uhl, Nucl. Phys. A **217**, 269 (1973).
- [28] P. Axel, Phys. Rev. **126**, 671 (1962).
- [29] D. M. Brink, Ph. D. Thesis, Oxford University, 1955.
- [30] N. Jovancevic, A. M. Sukhovoĵ, W. I. Furman and V. A. Khitrov, in *Proceedings of XX International Seminar on Interaction of Neutrons with Nuclei* (Dubna, May 2012, Preprint N E3-2013-22, Dubna, 2013), p. 157.
- [31] V. M. Strutinsky, in *Proceedings of the International Congress on Nuclear Physics* (Paris, France, 1958), p. 617.
- [32] Reference Input Parameter Library RIPL-2, *Handbook for Calculations of Nuclear Reaction Data* (IAEA-TECDOC, 2002).
- [33] S. S. Dietrich and B. L. Berman, Atom. Data Nucl. Data Tab. **38**, 199 (1988).
- [34] A. M. Sukhovoĵ, V. A. Khitrov and W. I. Furman, Phys. Atom. Nucl. **71**, 982 (2008).
- [35] L. A. Malov and V. G. Soloviev, Sov. J. Nucl. Phys. **26**, 384 (1977).
- [36] <http://www-nds.iaea.org/ENDSF>.
- [37] A. Bohr and B. R. Mottelson, *Nuclear Structure* (W. A. Benjamin, New York; Amsterdam, 1969), Vol. 1.
- [38] V. A. Bondarenko *et al.*, Nucl. Phys. A **762**, 167 (2005).
- [39] A. M. Sukhovoĵ and V. A. Khitrov, Phys. Atom. Nucl. **76**, 68 (2013).
- [40] A. Makinaga *et al.*, Phys. Rev. C **90**, 044301 (2014).
- [41] B. Özel-Tashenov *et al.*, Phys. Rev. C **90**, 024304 (2014).

MULTIYEAR INDOOR RADON VARIABILITY IN A FAMILY HOUSE – A CASE STUDY IN SERBIA

by

**Vladimir I. UDOVIČIĆ^{1*}, Dimitrije M. MALETIĆ¹, Radomir M. BANJANAC¹,
Dejan R. JOKOVIĆ¹, Aleksandar L. DRAGIĆ¹, Nikola B. VESELINOVIĆ¹,
Jelena Z. ŽIVANOVIĆ¹, Mihailo R. SAVIĆ¹, and Sofija M. FORKAPIĆ²**

¹Institute of Physics, University of Belgrade, Belgrade, Serbia

²Department of Physics, Faculty of Science, University of Novi Sad, Novi Sad, Serbia

Scientific paper

<http://doi.org/10.2298/NTRP1802174U>

The indoor radon behavior has complex dynamics due to the influence of the large number of different parameters: the state of indoor atmosphere (temperature, pressure, and relative humidity), aerosol concentration, the exchange rate between indoor and outdoor air, construction materials, and living habits. As a result, indoor radon concentration shows variation, with the usual periodicity of one day and one year. It is well-known that seasonal variation of the radon concentration exists. It is particularly interesting to investigate indoor radon variation at the same measuring location and time period, each year, due to estimation of individual annual dose from radon exposure. The long-term indoor radon measurements, in a typical family house in Serbia, were performed. Measurements were taken during 2014, 2015, and 2016, in February and July, each year. The following measuring techniques were used: active and charcoal canisters methods. Analysis of the obtained results, using multivariate analysis methods, is presented.

Key words: radon variability, multivariate regression analysis, multi-seasonal radon measurements, indoor radon

INTRODUCTION

The research of the dynamics of radon in various environments, especially indoors, is of great importance in terms of protection against ionizing radiation and in designing of measures for its reduction. Published results and development of many models to describe the behavior of indoor radon, indicates the complexity of this research, especially with models for prediction of the variability of radon [1-3]. This is because the variability of radon depends on a large number of variables such as local geology, permeability of soil, building materials used for the buildings, the state of the indoor atmosphere (temperature, pressure and relative humidity), aerosol concentration, the exchange rate between indoor and outdoor air, construction materials, as well as the living habits of people. It is known that the indoor radon concentration variation has periodicity of one day and one year. It is also well-known that the seasonal variation of the radon concentration exists. This is why it is particularly interesting to investigate indoor radon variation at the same measuring location and time period, year after

year, in order to estimate the individual annual dose from radon exposure. In that sense, we performed long-term indoor radon measurements in a typical family house in Serbia. Measurements were taken during the 2014, 2015, and 2016, in February and July, each year. We used the following measuring techniques: active and charcoal canisters methods. The detailed analysis of the obtained results using multivariate analysis (MVA) methods is presented in this paper.

First, MVA methods were tested on the radon variability studies in the Underground Low Background Laboratory in the Institute of Physics, Belgrade [4, 5]. Several climate variables: air temperature, pressure, and humidity were considered. Further advance was made by using all the publicly available climate variables monitored by nearby automatic meteorological station. In order to analyze the dependence of radon variation on multiple variables, multivariate analysis needs to be used. The goal was to find an appropriate method, out of the wide spectrum of multivariate analysis methods that are developed for the analysis of data from high-energy physics experiments, to analyze the measurements of variations of radon concentrations in indoor spaces. Previous

* Corresponding author; e-mail: udovicic@ipb.ac.rs

analysis were done using the maximum of 18 climate parameters and use and comparison of 8 different multivariate methods. In this paper the number of variables is reduced to the most important ones and new derived variables, like vapor pressure, simple modeled solar irradiance and simple modeled precipitation, which were introduced in the multivariate analysis.

INDOOR RADON MEASUREMENTS METHODS

Depending on the integrated measurement time, methods of measurement of the indoor radon concentrations may be divided into long-term and short-term ones. The device for the performed short-term radon measurements is SN1029 radon monitor (manufactured by the Sun Nuclear Corporation, NRSB approval-code 31822) with the following characteristics: the measurement range from 1 Bqm^{-3} to 99.99 kBqm^{-3} , accuracy equal to $+25 \%$, sensitivity of $0.16 \text{ counts hour per Bqm}^{-3}$. The device consists of two diffused junction photodiodes as the radon detector which is furnished with sensors for temperature, barometric pressure, and relative humidity. The sampling time was set to 2 h. The method for Charcoal Canister used is: EERF Standard Operating Procedures for Radon-222 Measurement Using Charcoal Canisters [6], also used by major laboratories which conduct radon measurements in Serbia [7]. Exposure time of the charcoal canisters was 48 h. The connection between short term and long term measurements has attracted some interest previously [8].

The family house, selected for the measurements and analysis of variations of radon concentrations, is a typical house in Belgrade residential areas, with requirement of existence of cellar. House is built on limestone soil. Radon measurements were carried out in the living room of the family house, which is built of standard materials (brick, concrete, mortar) and isolated with styrofoam. During the period of measurements (winter-summer 2014, 2015, and 2016), the house was naturally ventilated and air conditioning was used in heating mode at the beginning of the measurement period. During the winter period measurements, the electrical heating was used in addition to air conditioning. Measured radon concentrations, room temperature (T_{id}), atmospheric pressure (P_{id}) and relative humidity (H_{id}) inside the house, were obtained using radon monitor. Values of meteorological variables, in the measurement period, were obtained from an automatic meteorological station, located near the house in which the measurement was performed. We used the following meteorological variables: external air temperature (T), also at height of 5cm, pressure (P) and humidity (H), solar irradiation, wind speed, precipitation, temperature of the soil at depths of 10 cm, 20 cm and 50 cm. The natural ventilation routine was not monitored. Since the ventilation is of

crucial importance for the level of radon indoors [9], Multivariate regression analysis was used mainly for winter periods.

MULTIVARIATE REGRESSION ANALYSIS

In many fields of physics, especially in high-energy physics, there is the demand for detailed analyses of a large amount of data. For this purpose, the data analysis environment ROOT [10], is developed. ROOT is modular scientific software framework, which provides all the functionalities needed to deal with big data processing, statistical analysis, visualization and storage. A specific functionality gives the developed Toolkit for Multivariate Analysis (TMVA) [11]. The TMVA provides an environment for the processing, parallel evaluation and application of multivariate regression techniques.

TMVA is used to create, test and apply all available regression multivariate methods, implemented in ROOT, in order to find methods which are the most appropriate and yield maximum information on the dependence of indoor radon concentrations on the multitude of meteorological variables. Regression methods are used to find out which regression method can, if any, on the basis of input meteorological variables only, give an output that would satisfactorily close match the observed variations of radon concentrations. The output of usage of multivariate regression analysis methods has mapped functional behavior, which can be used to evaluate the measurements of radon concentrations using input meteorological variables only. All the methods make use of training events, for which the desired output is known and is used for training of Multivariate regression methods, and test events, which are used to test the MVA methods outputs.

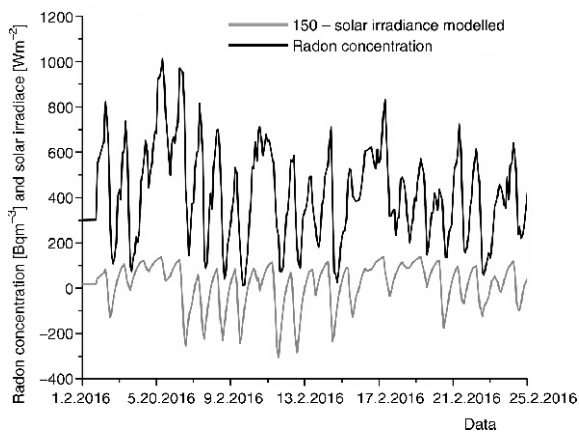
RESULTS

Measurements were performed during February and July in 2014, 2015, and 2016 using radon monitor and charcoal canister measurements. The descriptive results are summarized in tab. 1. The measurements using radon monitor and charcoal canisters are in good agreement.

Previous work done by researchers from the Low Background Laboratory, Institute of Physics, Belgrade, using the MVA analysis in search of connections between radon concentration and meteorological variables, included only one period of measurement, February or July 2014 [4]. Now the MVA analysis is using all the measured data February/July 2014-2016. New variables introduced in MVA analysis are modeled solar irradiance, modeled precipitation and vapor

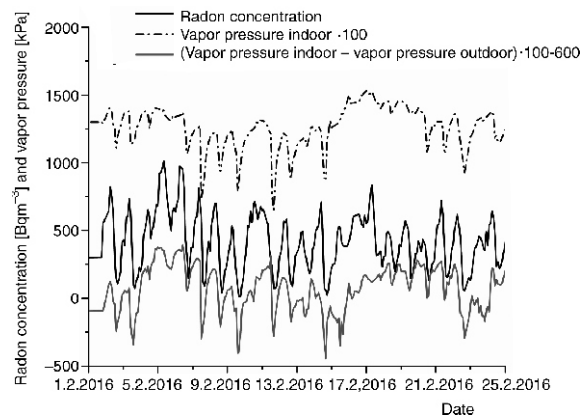
Table 1. Descriptive results of February and July 2014, 2015, and 2016 measurements, using radon monitor and charcoal canisters (only in February)

Results of measurements	2014		2015		2016	
	Feb.	July	Feb.	July	Feb.	July
Minimal radon activity using radon monitor [Bqm^{-3}]	15	0	28	0	12	3
Maximal radon activity using radon monitor [Bqm^{-3}]	1000	286	915	88	1013	262
Median radon activity using radon monitor [Bqm^{-3}]	418	25	524	22	412	28
Arithmetic mean of radon activity using radon monitor (standard deviation) [Bqm^{-3}]	402 (216)	40 (41)	508 (207)	27 (18)	423 (214)	39 (32)
Room temperature using radon monitor (standard deviation) [$^{\circ}\text{C}$]	20.4 (0.8)	24.7 (0.9)	21.2 (0.6)	24.9 (0.8)	22.3 (0.6)	24.6 (0.8)
Relative humidity using radon monitor (standard deviation) [%]	67.4 (5.7)	67.8 (4.8)	68.2 (4.8)	51.5 (4.7)	64.0 (6.4)	58.9 (7.5)
Radon activity using charcoal canister (standard deviation) [Bqm^{-3}]	432 (10)	/	518 (6)	/	407 (5)	/

**Figure 1. Modeled solar irradiance in comparison with measured radon concentration during February 2016**

pressure. In order to make use of intensity of solar irradiance during the whole day and night, the solar irradiance is modeled so that it includes 80 % of solar irradiance value from the previous measurement (previous hour) with addition of solar irradiance value for the actual hour of measurement (fig. 1). The value of 80 % is chosen so that the modeled solar irradiation has the best correlation with the radon measurements. Similar model of precipitation was used in this analysis. The next new variable is vapor pressure. The vapor pressure variable is calculated using the slope $s(T)$, of the relationship between saturation vapor pressure and air temperature and is given by [12, 13], so that the vapor pressure equals relative humidity times saturation vapor pressure, fig. 2.

Before the start of training of Multivariate regression methods using TMVA toolkit in ROOT, the description of input meteorological variables is performed, mainly by looking into inter-correlations of input variables and their connections with the measured radon concentrations. The MVA is using all the measured data. Table 2 presents the meteorological variables and their module value of correlation with the measured radon concentrations (target), which is indicative in finding linear dependence of radon mea-

**Figure 2. Vapor pressure in comparison with measured radon concentration during February 2016**

surements and input variables. The second column in tab. 2 presents us with correlation ratio values which indicate if there are some functional dependence (not only linear) between input variables and radon concentration, and the last column presents the mutual information which indicates if there is a non-functional dependence of input variables and radon measurements [11].

From tab. 2 it can be noticed that linear correlated values are not the only ones which can be used in MVA analysis, for example variable solar irradiance has high mutual information with the radon measurements.

In the data preparation for MVA training the whole dataset is consisting of many events. An event includes time of measurement, radon measurement and meteorological variables. The dataset is randomly split in two halves, one half of the events will be used for training of multivariate regression methods, and the other half of events for testing of methods, mainly to compare the measured and MVA evaluated values for radon concentration.

It turns out that the methods best suited for our purpose is the Boosted Decision Trees (BDT) method. This means that BDT gives the smallest difference be-

Table 2. Input variable rank and values for correlation, correlation ratio and mutual information, all with the measured radon concentrations (target) for February and July 2014-2016 measurements

Variable	Correlation with target		Correlation ratio		Mutual information	
	Rank	Value	Rank	Value	Rank	Value
Soil temperature depth 20 cm [°C]	1	0.87	1	0.60	13	1.48
Soil temperature depth 50 cm [°C]	2	0.86	2	0.57	14	1.31
Soil temperature depth 10 cm [°C]	3	0.82	3	0.54	9	1.84
Temperature outdoor [°C]	4	0.82	5	0.53	8	1.85
Vapor indoor – vapor od [mbar]	5	0.81	9	0.41	11	1.73
Temperature od – temperature id [°C]	6	0.80	4	0.53	6	1.92
Temperature height 5 cm [°C]	7	0.77	8	0.48	7	1.91
Vapor od [mbar]	8	0.76	10	0.41	5	1.92
Temperature id [°C]	9	0.75	7	0.49	17	1.16
Solar irradiance [Wm ⁻²]	10	0.61	6	0.50	2	2.23
Humidity indoor [%]	11	0.45	11	0.26	1	2.26
Humidity outdoor [%]	12	0.31	13	0.20	10	1.76
Air pressure outdoor [mbar]	13	0.27	17	0.07	12	1.55
Wind speed [ms ⁻¹]	14	0.22	16	0.01	16	1.28
Air pressure indoor [mbar]	15	0.17	18	0.04	15	1.31
Humidity od – Humidity id [%]	16	0.10	14	0.19	4	2.11
Precipitation [Lm ⁻²]	17	0.01	15	0.19	18	1.13
Vapor indoor [mbar]	18	0.002	12	0.02	3	2.17

tween the measured radon concentration from test sample and the evaluation of value of radon concentration using input variables only. This can be seen in fig. 3, which shows the distribution of BDT and BDTG regression method outputs (evaluated values) in comparison with the measured radon concentration during February 2016.

Since TMVA has 12 different regression methods implemented, only some of those will give useful results when evaluating the radon concentration measurements. Table 4 summaries the results of MVA analysis. It shows the MVA methods RMS of difference of evaluated and measured radon concentration. Also, tab. 4 shows the mutual information of measured and MVA evaluated radon concentration. Besides

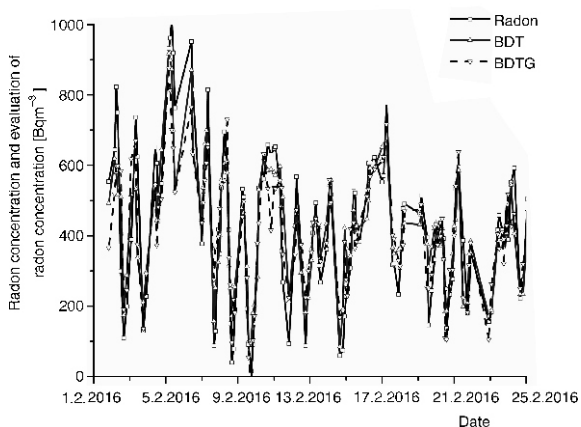


Figure 3. Comparison of MVA evaluated radon concentration and measured one from the test sample of events during February 2016

BDT, the Multi-Layer Perceptron (MLP) [10], an implementation of Artificial Neural Network multivariate method, also gives good results.

The MVA regression analysis results in mapped functional behavior and, as opposed to possible existence of theoretical modeling, which is independent of the number of measurements, MVA depends on the number of events. More events, the better mapped function we get as a result. In this sense, if the number of measurements is not great, multivariate analysis can be used only as help, to indicate which variables are more important to be used in theoretical modeling, for comparison of mapped and modeled functions, and modeled function test.

CONCLUSION

Indoor radon variation at one location in the same periods (February and July), was investigated for three years. Long-term indoor radon measurements show intense seasonal variation. The results obtained with different measuring methods are in good agreement. The radon behavior in the house is almost the same and shows good reproducibility year by year. The small variations in the year by year dynamics are originated mostly from the variations in meteorological variables during winter seasons and mostly due to ventilation habits during summer season. Ventilation habits were not monitored nor taken into account in MVA regression analysis. The preliminary results using multivariate analysis methods in TMVA are shown. Main output of Multivariate regression analy-

Table 3. Input variable correlation with the measured radon concentrations for February and July 2016

Correlation with target			
February 2016		July 2016	
Variable	Value	Variable	Value
Vapor id-vapor od [mbar]	0.58	Soil temperature depth 20 cm [°C]	0.46
Humidity id [%]	0.54	Soil temperature depth 50 cm [°C]	0.42
Vapor id [mbar]	0.52	Solar irradiance	0.32
Solar irradiance [Wm ⁻²]	0.48	Temperature id [°C]	0.30
Temperature od – temperature id [°C]	0.46	Soil temperature depth 10 cm [°C]	0.24
Temperature [°C]	0.44	Temperature od [°C]	0.21
Soil temperature depth 10 cm [°C]	0.43	Humidity od [%]	0.20
Soil temperature depth 20 cm [°C]	0.42	Humidity id [%]	0.19
Humidity [%]	0.38	Air pressure [mbar]	0.17
Temperature height 5 cm [°C]	0.32	Precipitation [Lm ⁻²]	0.17
Temperature id [°C]	0.29	Temperature od – temperature id [°C]	0.16
Air pressure od [mbar]	0.23	Air pressure id [mbar]	0.16
Air pressure id [mbar]	0.21	Humidity od – humidity id [%]	0.14
Soil temperature depth 50 cm [°C]	0.20	Wind speed [ms ⁻²]	0.13
Precipitation [Lm ⁻²]	0.19	Temperature height 5 cm [°C]	0.12
Humidity od – humidity id [%]	0.15	Vapor id [mbar]	0.06
Vapor od [mbar]	0.08	Vapor od [mbar]	0.03
Wind speed [ms ⁻¹]	0.05	Vapor id – vapor od [mbar]	0.02

Table 4. RMS of MVA method's evaluation error and mutual information; February/July 2014-2016

MVA method	RMS [Bqm ⁻³]	Mutual information
BDT	85.5	1.477
BDTG	92.1	1.614
MLP	101	1.401

sis is the initial version of *mapped* function of radon concentration dependence on multitude of meteorological variables. Simplification of MVA methods can be made by choosing only the most important input variables and exclude the other variables.

ACKNOWLEDGEMENTS

The authors acknowledge the financial support of the Ministry of Science, Technology and Development of Serbia within the projects: Nuclear Methods Investigations of Rare Processes and Cosmic Rays (grant number 171002) and Biosensing Technologies and Global System for Continuous Research and Integrated Management (grant number 43002).

AUTHORS' CONTRIBUTIONS

The idea for this paper came as a result of discussions of V. I. Udovičić, R. M. Banjanac, D. R. Joković, A. L. Dragić, and D. M. Maletić. Gathering climate data and MVA analysis was done by D. M. Maletić and V. I. Udovičić. Performed indoor radon measurements were done by V. I. Udovičić and S. M. Forkapić. Writing of the paper was done by D. M. Maletić and V. I. Udovičić. A. L. Dragić gave idea about using MVA

methods in cosmic and radon measurements. N. B. Veselinović and M. R. Savić analyzed and validated climate data. J. Z. Živanović helped with MVA analysis. D. R. Joković helped with data analysis and paper technical preparation.

REFERENCES

- [1] Collignan, B., *et al.*, Development of a Methodology to Characterize Radon Entry in Dwellings, *Building and Environment*, 57 (2012), Nov., pp. 176-183
- [2] Li, F., Baixeras, C., The RAGENA Dynamic Model of Radon Generation, Entry and Accumulation Indoors, *Science of the Total Environment*, 307 (2003), 1-3, pp. 55-69
- [3] Jelle, B. P., *et al.*, Development of a Model for Radon Concentration in Indoor Air, *Science of the Total Environment*, 416 (2012), Jan., pp. 343-350
- [4] Maletić, D., *et al.*, Comparison of Multivariate Classification and Regression Methods for Indoor Radon Measurements, *Nucl Technol Radiat*, 29 (2014), 1, pp. 17-23
- [5] Udovičić, V., *et al.*, Radon Problem in an Underground Low-Level Laboratory, *Radiation Measurements*, 44 (2009), 9-10, pp. 1009-1012
- [6] ***, EPA 520/5-87-005, Gray D.J, Windham S.T, United States Environmental Protection Agency, Montgomery, 1987
- [7] Živanović, M. Z., *et al.*, Radon Measurements with Charcoal Canisters, *Nucl Technol Radiat*, 31 (2016), 1, pp. 65-72
- [8] Stojanovska, Z., *et al.*, Prediction of Long-Term Indoor Radon Concentrations Based on Short-Term Measurements, *Nucl Technol Radiat*, 32 (2017), 1, pp. 77-84
- [9] Nikolić, M. D., *et al.*, Modelling Radiation Exposure in Homes from Siporex Blocks by Using Exhalation Rates of Radon, *Nucl Technol Radiat*, 30 (2015), 4, pp. 301-305
- [10] Brun, R., Rademakers, F., ROOT – An Object Oriented Data Analysis Framework, *Nucl. Inst. Meth. in Phys. Res.*, A 389 (1997), 1-2, pp. 81-86

- [11] Hoescker, A., et al., TMVA – Toolkit for Multivariate Data Analysis, PoS ACAT 040, arXiv:physics/070303, 2007
- [12] Murray, F. W., On the Computation of Saturation Vapor Pressure, *J. Applied Meteorology*, 6 (1967), 1, pp. 203-204

- [13] Tetens, O., About Some Meteorological Aspects (in German), *Z. Geophys*, 6 (1930), pp. 207-309

Received on October 6, 2018

Accepted on June 8, 2018

**Владимир И. УДОВИЧИЋ, Димитрије М. МАЛЕТИЋ, Радомир М. БАЊАНАЦ,
Дејан Р. ЈОКОВИЋ, Александар Л. ДРАГИЋ, Никола Б. ВЕСЕЛИНОВИЋ,
Јелена З. ЖИВАНОВИЋ, Михаило Р. САВИЋ, Софија М. ФОРКАПИЋ**

**СТУДИЈА СЛУЧАЈА ВИШЕГОДИШЊЕ ВАРИЈАБИЛНОСТИ РАДОНА
У ПОРОДИЧНОЈ КУЋИ У СРБИЈИ**

Понашање радона у затвореном простору има сложену динамику због утицаја великог броја различитих параметара који утичу на његову варијабилност: метеоролошких (температура, притисак и релативна влажност), концентрације аеросола, брзине размене између унутрашњег и спољашњег ваздуха, грађевинских материјала и животних навика. Као резултат, концентрација радона у затвореним просторијама показује варијацију, уз стандардну периодичност од једног дана и једне године. Годишња варијабилност је добро позната сезонска варијација концентрације радона. Посебно је интересантно пратити вишегодишње варијације концентрације радона на истој мерној локацији и временском периоду, пре свега због процене индивидуалних годишњих доза од изложености радону. У типичној породичној кући у Србији извршена су дуготрајна мерења радона у дневном боравку. Мерења су рађена током 2014, 2015, и 2016. године, у фебруару и јулу, сваке године. Коришћене су следеће мерне технике: активна и метода коришћења угљених канистера. Добијени резултати анализирани су коришћењем мултиваријантне регресионе анализе.

Кључне речи: варијабилност радона, мултиваријантна регресиона анализа, радон у затвореним просторијама, вишегодишње мерење радона

New empirical methods for correction of meteorological effects on cosmic ray muons

M. Savić,^{a,*} A. Dragić,^a D. Maletić,^a N. Veselinović,^a D. Joković,^a R. Banjanac,^a V. Udovičić^a and D. Knežević^a

^a*Institute of Physics Belgrade,
Pregrevica 118, 11080 Belgrade, Serbia
E-mail: msavic@ipb.ac.rs*

Flux of muon component of secondary cosmic rays is affected by varying conditions in the atmosphere. Dominant effects are barometric and temperature effect, which reflect variations of atmospheric pressure and atmospheric temperature respectively. Precise modelling and correction for these meteorological effects significantly increases sensitivity of Earth-based muon detectors to variations of primary cosmic ray flux. We are presenting two recently developed empirical methods for correction of meteorological effects on cosmic ray muons. First method is based on principal component analysis, while second employs multivariate analysis using machine learning techniques. Both methods are applied for correction of barometric and temperature effects, but can easily be generalised to take more atmospheric parameters into account. We apply these corrections to muon count rates measured by Belgrade cosmic ray station and study their effect on sensitivity of detection of periodic and aperiodic flux variations of primary cosmic rays. Comparison with the most widely used method for correction of meteorological effects – integral method, as well as with neutron monitor data, demonstrates very high effectiveness of presented methods.

*37th International Cosmic Ray Conference (ICRC 2021)
July 12th – 23rd, 2021
Online – Berlin, Germany*

*Presenter

1. Introduction

Cosmic ray muons (hard component of secondary cosmic rays) are affected by variations of atmospheric parameters as they propagate toward Earth. There are a number of meteorological effects that affect cosmic ray muon flux, most prominent being the *barometric (pressure) effect* and the *temperature effect*, which depend on atmospheric pressure and atmospheric temperature respectively. Apart from fundamental, precise modelling of these effects also has practical importance, as it allows for correction that significantly increases the sensitivity of ground based muon monitors to variations of primary cosmic rays.

A number of methods for correction of barometric and temperature effect have been developed over the years. Some (i.e. method of effective level of generation [1]) are empirical in nature, while others (most notably integral method) rely on the theory of meteorological effects, developed by Dorman [2] among others. All these methods are at least in some part approximative, but for all intents and purposes we have decided to use the integral method as a reference in our analysis, as it gives the most complete treatment of the problem.

The idea behind the work presented here is to try and develop a new, easy to use empirical method, less approximative in nature, compare it to the reference integral method, and investigate whether a more precise model of meteorological effects can be constructed, and possibly some additional information extracted. In order to most completely treat the meteorological effects, both atmospheric pressure and full atmospheric temperature profile need to be taken into account. For analysis that involves that many potentially highly correlated input variables, we have decided to employ modern techniques used for decorrelation and dimensionality reduction, and introduce two new methods for modelling and correction of meteorological effects - *PCA method* based on principal component analysis (PCA), and *MVA method* based on multivariate analysis (MVA) via use of machine learning. Though these two are somewhat similar in nature, a more "hands on" approach of the PCA method can offer a somewhat different insight than the more "blackbox" machine learning approach.

2. Data

2.1 CR data

Muon count rates used in this analysis were measured in the Ground Level Laboratory (GLL) of the Low Background Laboratory for Nuclear Physics, at the Institute of Physics Belgrade [3]. More detailed description of the laboratory and current detector system can be found in some of our previous work [4]. Muon count rates can have arbitrary time resolution but five-minute and hour sums were used in the analysis. For quality and consistency of data reasons, and to remove potential biases due to annual variation, data for a period of one year (from 01.06.2010 to 31.05.2011) were selected.

2.2 Meteo data

This analysis requires information about both atmospheric pressure and vertical atmospheric temperature profile. Data about atmospheric pressure is readily available from the Republic Hydro-meteorological Servis of Serbia. As for the vertical temperature profile data, temperatures for 24

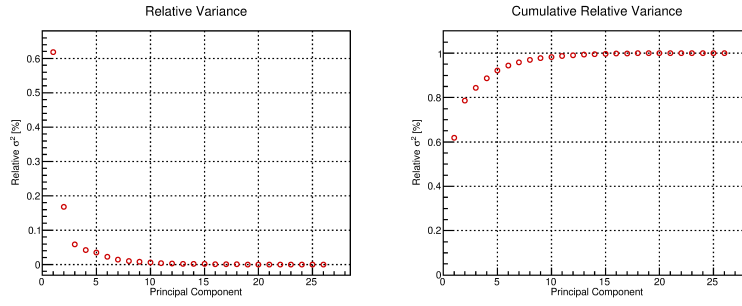


Figure 1: Relative variance (left) and cumulative relative variance (right) for all 26 principal components.

isobaric levels modelled by the Global Forecast System (GFS) [5] were used, starting from the top layer of the atmosphere (10 mb), to the level just above ground level (975 mb). For the above ground layer, locally measured temperature was used as the model was performing poorly there. More details about the preparation of meteorological data is available elsewhere [7].

3. Methodology

3.1 PCA method

Principal component analysis is a well established technique for dimensionality reduction of complex problems that involve large number of correlated variables, and as such very well suited for application to our problem. Using principal component decomposition we have transformed the initial set of correlated meteorological variables (locally measured atmospheric pressure, 24 modelled temperatures, and locally measured ground temperature) to a set of 26 uncorrelated principal components.

Using a series of tests typically used in such analysis (cumulative percentage rule, modified Kaiser's rule, mean eigenvalue rule, ...), we have determined that the first six components (responsible for close to 95% of total variance, as seen on Figure 1) are significant. Composition of the these components is shown on Figure 2, where variables on the x-axis are atmospheric pressure followed by atmospheric temperatures, starting from the top layer of the atmosphere.

Correlative analysis of muon count rate and significant principal components showed practically no correlation between measured muon count rate and the second principal component, further reducing the set of principal components to five. This is an interesting results as this component, mainly composed of lower stratosphere and upper troposphere temperatures, is responsible for close to 17% of total variation of meteorological variables.

Finally, we have determined the muon count rate corrected for meteorological effects according to formula:

$$N_{\mu}^{(corr)} = N_{\mu} - \langle N_{\mu} \rangle \sum_i k_i PC_i, \quad i = 1, 3, 4, 5, 6 \quad (1)$$

where $N_{\mu}^{(corr)}$ is corrected, N_{μ} measured and $\langle N_{\mu} \rangle$ mean muon count rate, while k_i , that correspond to principal components PC_i , are coefficients determined by linear regression, as shown on Figure 3. Full analysis and results are presented in more detail in our other work [8].

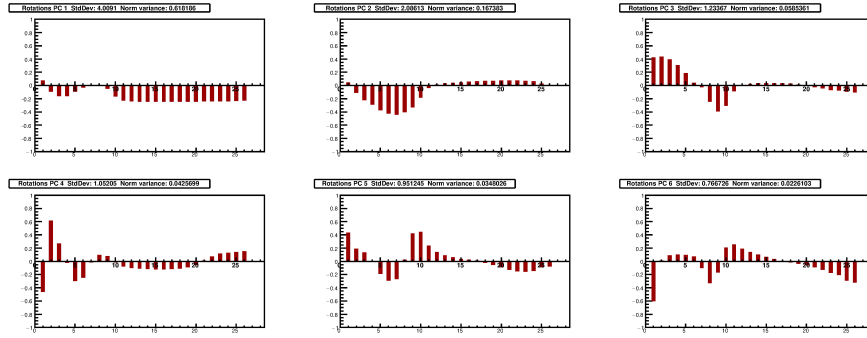


Figure 2: Composition for six most significant principal components. Meteorological variables are on the x-axis, first one being atmospheric pressure, followed by atmospheric temperatures (starting with the top layer of the atmosphere and ending with the ground level).

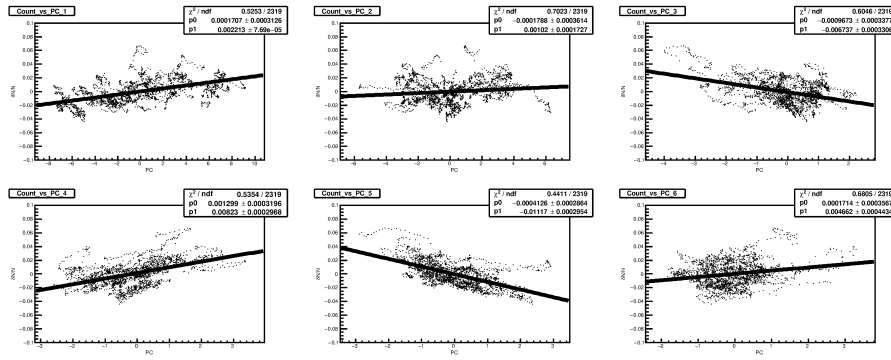


Figure 3: Muon count rate dependence on principal components for six most significant components, distributions fitted with linear function.

3.2 MVA method

Multivariate analysis utilising machine learning techniques can be a powerful tool for modelling of highly correlated systems. We have tested a number of algorithms implemented in Toolkit for Multivariate Data Analysis (TMVA), which has been successfully used for classification and regression problems in particle physics. For us, regression application is of greater interest, as the idea is to train and test multivariate algorithms on a subset of data (for geomagnetically quiet days), where most of the variation can be attributed to atmospheric effects, using meteorological variables as input and muon count rate as the target value. Trained algorithms can be then used on a full data set to predict the muon count rate (which would ideally depend only on meteorological parameters), and corrected muon count rate can be calculated using the formula:

$$N_{\mu}^{(corr)} = \Delta N_{\mu} + \langle N_{\mu} \rangle, \quad \Delta N_{\mu} = N_{\mu}^{(mod)} - N_{\mu}, \quad (2)$$

where $N_{\mu}^{(corr)}$ is corrected, N_{μ} measured, $N_{\mu}^{(mod)}$ modelled, and $\langle N_{\mu} \rangle$ is mean muon count rate.

Minimal average quadratic deviation of modelled from measured value was the only criterion used for optimisation of algorithm parameters in the training phase, so a series of tests have been

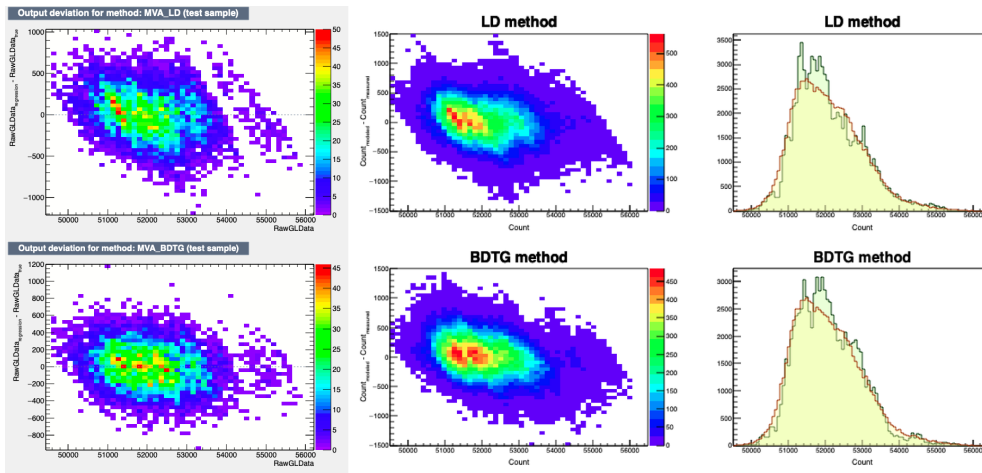


Figure 4: Modelled count rate and its deviation from measured count rate as a function of measured count rate for LD (top) and BDTG (bottom) algorithms. Deviation distributions for test data set are on left, for the full data set are in the middle, while distributions of modelled count rate (compared with the measured one) are on the right.

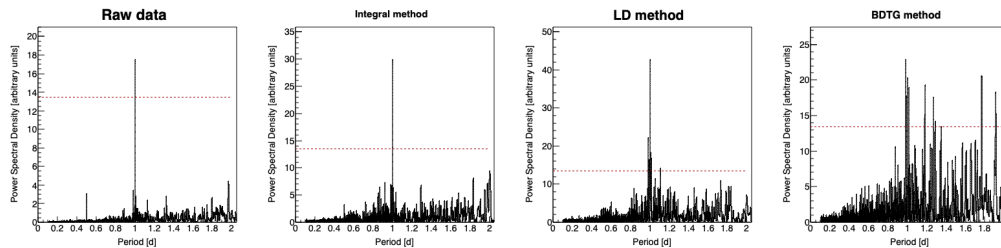


Figure 5: Power spectra for periods in the interval [0, 2] days, for measured data (far left), and data corrected using integral (central left), LD (central right) and BDTG (far right) methods.

devised in order to investigate the consistency of application of trained algorithms and minimise the possibility of artificial features being introduced.

Some of the tests included comparison of distributions of residual deviation of modelled from measured data for the test and full data set, or looking for anomalous features in distributions of modelled count in comparison with measured count distribution (both types of distributions for selected algorithms shown in Figure 4).

Based on these tests, the best performing algorithm proved to be LD (Linear Discriminant method), which is closely related to PCA approach. The second best potential candidate was BDTG (Gradient Boosted Decision Tree method), but there are probably some limits to its applicability, as indicated by spectral analysis (Figure 5). From the remaining tested methods, algorithms based on probability density techniques performed more poorly, which was not that surprising as the problem analysed here involves highly linear dependencies, but poor performance of methods based on neural networks was not expected, and possibly some improvement can be made there.

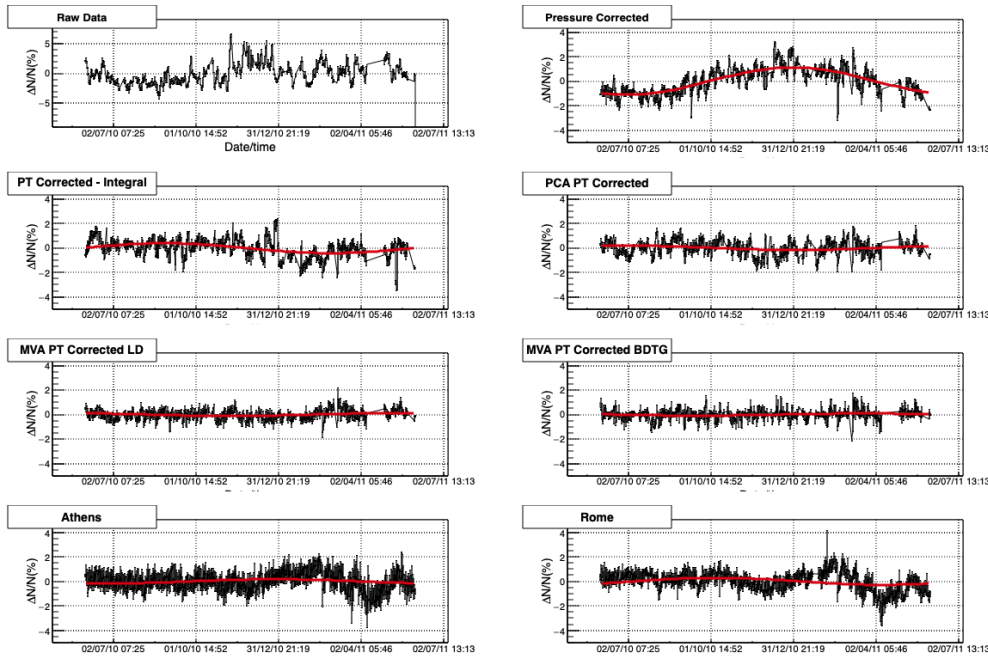


Figure 6: Muon count rate time series and reference neutron monitor data for the period of one year (01.06.2010-31.05.2011), fitted with sine function with a period of one year.

4. Results

4.1 Effect of corrections on periodic CR variations

One way to assess the performance of different methods for correction of meteorological effects could be to compare the efficiency with which they remove the annual variation due to temperature variation. In order to determine this variation, we have fitted pressure corrected data with a sine function, with a period of one year. Amplitude determined from such fit is then used as an estimate of magnitude of the annual variation. The same procedure was used to determine the residual annual variation after the correction via use of different methods (Figure 6). As neutron monitor count rates are usually considered to negligibly depend on atmospheric temperature (at least in the first approximation), we can treat their time series the same way in order to estimate the expected annual variation magnitude.

Table 1 shows amplitudes for the annual variation calculated based on plots in Figure 6, as well as reduction in annual variation relative to pressure corrected data. As can be seen, values for PCA and LD methods are closer to the estimates based on the neutron monitor data than the integral method value, while for BDTG method the value is somewhat smaller.

4.2 Effect of corrections on aperiodic CR variations

To study the effect of corrections on aperiodic variations we have selected the most intense Forbush decrease event in the one year period used for the analysis. For the event that occurred on 18.02.2011, we determined the amplitude of decrease for data corrected via different methods and reference neutron monitors, using procedure suggested by Barbashina et al. [9] (as shown on

Method/ Neutron monitor	P corr.	Integral	PCA	LD	BDTG	Athens	Rome
Annual amplitude [%]	1.11(9)	0.40(3)	0.18(5)	0.11(3)	0.086(9)	0.17(5)	0.29(1)
Relative reduction [% of P corrected]	-	64(10)	84(28)	90(30)	92(30)	-	-

Table 1: Amplitude and reduction of the amplitude of annual variation relative to pressure corrected data (P corr.) for pressure and temperature corrected data (using integral and selected multivariate methods). Athens and Rome neutron monitor data also included for reference

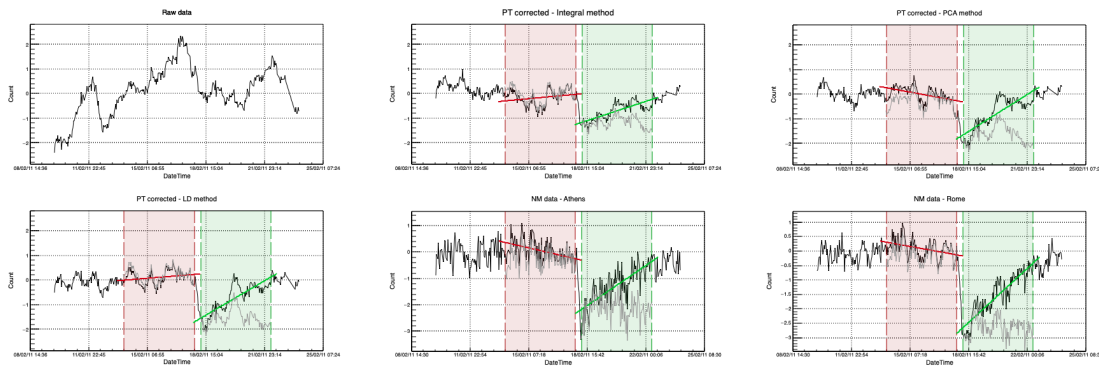


Figure 7: Muon count rate time series and reference neutron monitor data for the period around the Forbush decrease event of 18.02.2011. Highlighted intervals are used for detrending and calculation of decrease amplitude.

Method/ Neutron monitor	Integral	PCA	LD	BDTG	Athens	Rome
FD amplitude [%]	1.38(14)	1.52(21)	1.96(18)	1.10(13)	1.97(15)	2.68(15)
Relative FD amplitude	4.31(44)	4.90(66)	7.09(65)	4.78(56)	5.30(40)	8.65(48)

Table 2: Amplitudes and relative amplitudes for the Forbush decrease event of 18.02.2011 for pressure and temperature corrected muon data and reference neutron monitors

Figure 7). Additionally, as a measure of sensitivity to such events, we have introduced amplitude calculated relative to standard deviation of count rates leading up to the event.

Values for thusly calculated amplitudes and relative amplitudes are shown in Table 2. LD algorithm has values comparable to neutron monitor values, but that is at least in part due to somewhat larger calculated amplitude. This is most likely a feature pertaining to the specific event, as preliminary results for other events outside the interval used in this work show values closer to expected.

5. Conclusions

Two new methods for correction of meteorological effects on cosmic ray muons are introduced. Both are fully empirical, require knowledge about the atmospheric pressure and atmospheric temperature profile and can be applied to any muon monitor. The effect on reduction of the annual variation of CR data, as well as the effect on sensitivity of FD event detection was compared to the integral method and reference neutron monitor data. Their effectiveness was comparable or possibly better than for the integral method, allowing for the possibility that a part of meteorological effects is not taken into account by theory.

References

- [1] A Duperier, "The Meson Intensity at the Surface of the Earth and the Temperature at the Production Level", in Proceedings of the Physical Society. Section A, volume 62, number 11, pages 684, year 1949, doi: 10.1088/0370-1298/62/11/302
- [2] Dorman, L. I., "On the temperature effect of the hard component of cosmic rays", in Reports of Academy of Sciences of USSR (DAN SSSR), volume 95, issue 1, pages 49 - 52, year 1954b
- [3] Low Background Laboratory for Nuclear Physics, url: <http://www.cosmic.ipb.ac.rs/>
- [4] Dragic Aleksandar, Udovicic Vladimir, Banjanac Radomir, Jokovic Dejan, Maletic Dimitrije, Veselinovic Nikola, Savic Mihailo, Puzovic Jovan, Anicin Ivan, "The New Set-Up in the Belgrade Low-Level and Cosmic-Ray Laboratory", in NUCLEAR TECHNOLOGY AND RADIATION PROTECTION, volume 26, number 3, pages 181-192, year 2011, doi: 10.2298/NTRP1103181D
- [5] GFS, url: <https://www.ncdc.noaa.gov/data-access/model-data/model-datasets/global-forecast-system-gfs>
- [6] Berkova M., Belov A., Eroshenko E., Yanke Victor, "Temperature effect of muon component and practical questions of how to take into account in real time", in Astrophysics and Space Sciences Transactions, year 2012, pages 41-44, volume 8, doi: 10.5194/astra-8-41-2012
- [7] Savic Mihailo, Dragic Aleksandar, Veselinovic Nikola, Udovicic Vladimir, Banjanac Radomir, Jokovic Dejan, Maletic Dimitrije, "Effect of pressure and temperature corrections on muon flux variability at ground level and underground", in "25th European Cosmic Ray Symposium", Torino, Italy, eprint: 1701.00164, year 2016
- [8] Savic Mihailo, Dragic Aleksandar, Maletic Dimitrije, Veselinovic Nikola, Banjanac Radomir, Jokovic Dejan, Udovicic Vladimir, "A novel method for atmospheric correction of cosmic-ray data based on principal component analysis", in ASTROPARTICLE PHYSICS, volume 109, pages 1-11, year 2019, doi: 10.1016/j.astropartphys.2019.01.006
- [9] Barbashina N., Dmitrieva Anna, Kompaniets K., Petrukhin A., Timashkov D., Shutenko V., Yakovleva Elena, Yashin, Igor, "Specific features of studying Forbush decreases in the muon flux", in Bulletin of The Russian Academy of Sciences: Physics, year 2009, pages 343-346, volume 73, doi: 10.3103/S1062873809030198

Determination of the nuclear level densities and radiative strength function for 43 nuclei in the mass interval $28 \leq A \leq 200$

David Knezevic^{1,5}, Nikola Jovancevic^{1,*}, Anatoly M. Sukhovoij², Ludmila V. Mitsyna², Miodrag Krmar¹, Vu D. Cong², Franz-Josef Hamsch⁴, Stephan Oberstedt⁴, Zsolt Revay³, Christian Stieghorst³, and Aleksandar Dragic⁵

¹University of Novi Sad, Faculty of Science, Department of Physics, Trg Dositeja Obradovica 3, 21000 Novi Sad, Serbia

²Joint Institute for Nuclear Research, 141980 Moscow region, Dubna, Russia

³Technische Universität München, Forschungsneutronenquelle Heinz Maier-Leibnitz (FRM II), Lichtenbergstr. 1, 85747 Garching, Germany

⁴European Commission, Joint Research Centre, Directorate G – Nuclear Safety and Security, Unit G.2, Retieseweg 111, 2440 Geel, Belgium

⁵Institute of Physics Belgrade, Pregrevica 118, 11080 Zemun, Serbia

Abstract. The determination of nuclear level densities and radiative strength functions is one of the most important tasks in low-energy nuclear physics. Accurate experimental values of these parameters are critical for the study of the fundamental properties of nuclear structure. The step-like structure in the dependence of the level densities ρ on the excitation energy of nuclei E_{ex} is observed in the two-step gamma cascade measurements for nuclei in the $28 \leq A \leq 200$ mass region. This characteristic structure can be explained only if a co-existence of quasi-particles and phonons, as well as their interaction in a nucleus, are taken into account in the process of gamma-decay. Here we present a new improvement to the Dubna practical model for the determination of nuclear level densities and radiative strength functions. The new practical model guarantees a good description of the available intensities of the two step gamma cascades, comparable to the experimental data accuracy.

1 Introduction

The development of theoretical models of nuclear structures requires a set of experimental information of the excited levels density, ρ , (with given quantum numbers) and of the values of the partial width (radiative strength function), Γ , of all possible decay channels. Correct interpretation of the dynamics of the nuclear transitions, in a broad variety from the simple low-lying levels (e.g., quasi-particle or phonon structure) to the very complex compound-states is possible by the theoretical calculations if those experimental data are available. One of the most suitable techniques for determination of required nuclear mater parameters (ρ and Γ) is the two-step gamma cascades methods based on measurement of gamma coincidences following neutron capture [1].

*e-mail: nikola.jovancevic@df.uns.ac.rs

Based on the experimental data collected by two-step gamma cascades experiment a model for description the gamma-decay of neutron resonance was developed at JINR, Dubna [2, 3]. In this model the level density ρ of quasi-particles in any nucleus is defined using the known model of n -quasi-particle levels. Here we presented the improved version of this model taking into account shell inhomogeneities of the single-particle level spectra and their influence on the functions: $\rho = \varphi(E_{ex})$ and $\Gamma = \psi(E_1)$, where E_{ex} is the excitation energy and E_1 is primary transition energy. The experimental results of two step gamma cascades intensity for 43 nuclei in the $28 \leq A \leq 200$ mass region were fitting by this model. This provide us possibility to extract parameters of nuclear structure such as breaking thresholds of the second and the third Cooper pairs, ratio of the collective level density to the total one or level parity.

2 Dubna two-step gamma cascades method

The two-step gamma-cascades method for obtaining information about the nuclear structure parameters following the thermal neutron captures was developed at FLNP, JINR, DUBNA [2, 3]. From amount of gamma-gamma coincidences the method allows to choose registration events of full energy of two-gamma transition cascade with a sufficiently low background. And the experimental intensity distributions of cascades to the final levels of compound-nucleus with excited energy below ~ 500 – 800 keV are obtained from these coincidences. Using the nuclear spectroscopy procedures allows decomposing the initial spectrum on primary and secondary transmission components of cascades with an acceptable uncertainty [2, 3].

The basic idea of this method comes from specific dependence of the two-step gamma- cascade intensity on the partial radiative width Γ and the density of excited levels:

$$I_{\gamma\gamma} = \sum_{\lambda,f} \sum_i \frac{\Gamma_{\lambda i} \Gamma_{if}}{\Gamma_{\lambda} \Gamma_i} = \sum_{\lambda,f} \frac{\Gamma_{\lambda i}}{\langle \Gamma_{\lambda i} \rangle m_{\lambda i}} n_{\lambda i} \frac{\Gamma_{if}}{\langle \Gamma_{if} \rangle m_{if}} \quad (1)$$

where $\Gamma_{\lambda i}$ and Γ_{if} are the partial radiative widths corresponding to the primary and to the secondary transitions; $n_{\lambda i} = \rho \Delta E_i$ is the number of the excited intermediate levels in a certain interval of the excitation energy ΔE_i ; $\langle \Gamma_{\lambda i} \rangle$ and $\langle \Gamma_{if} \rangle$ are the average values of the corresponding intervals of the nucleus excitation energy widths; $m_{\lambda i}$ and m_{if} are the number of levels in the same intervals. When this method was developed for the first time it was based on an interactive calculation. Using iterative process with “randomly” chosen functions ρ and Γ , it is possible to obtain the most probable values of level density and radiative width (or radiative strength function).

3 Model of the gamma-decay of neutron resonance

Here we present improved version of the model for the gamma-decay of neutron resonance [2] which can explain the experimental data based on combination of phenomenological and theoretical representations.

The level density, described by an expression for density ρ_l of Fermi levels, was taken from the model of density Ω_n of n -quasi-particle states [4]:

$$\rho_l = \frac{(2J + 1) \exp\left(- (J + 1/2)^2 / 2\sigma^2\right)}{2 \sqrt{2\pi}\sigma^3} \cdot \Omega_n(E_{ex}), \Omega_n(E_{ex}) = \frac{g^n (E_{ex} - U_l)^{n-1}}{((n/2)!)^2 (n-1)!} \quad (2)$$

Here J is the spin quantum number, $g = 6a/\pi^2$ is the density of the single-particle states near Fermi-surface, σ is the cut-off factor (a and σ values were taken from the back-shifted Fermi-gas model

[5]), and U_l , is the energy of the l -th Cooper pair breaking threshold. The effect of the collective enhancement was also included in this model by the coefficient C_{col} of the collective enhancement of the vibrational level density (or both vibrational and rotational ones for deformed nuclei). For a given excitation energy, E_{ex} , the phenomenological coefficient is determined by a theoretical description that can be found in Ref. [3]:

$$C_{coll} = A_l \exp(\sqrt{(E_{ex} - U_l)/E_v} - (E_{ex} - U_l)/E_\mu) + \beta \quad (3)$$

where A_l are parameters of density for the vibrational levels above the breaking point for each l -th Cooper pair, E_μ and E_v determine the change in the nuclear entropy and the change of the quasi-particles excitation energies, respectively. Coefficients A_l for different pairs are fitted independently, as it was done in Ref. [2]. Coefficient β is used for a description of the rotation level density.

Radiative strength functions for $E1$ - and $M1$ -transitions are determined in this model by Ref. [6]:

$$k(E1, E_\gamma) + k(M1, E_\gamma) = w \frac{1}{3\pi^2 \hbar^2 c^2 A^{2/3}} \frac{\sigma_G \Gamma_G^2 (E_\gamma^2 + \kappa 4\pi^2 T^2)}{(E_\gamma^2 - E_G^2)^2 + E_\gamma^2 \Gamma_G^2} + P\delta^- \exp(\alpha_p(E_\gamma - E_p)) + P\delta^+ \exp(\beta_p(E_p - E_\gamma)) \quad (4)$$

with fitting normalization parameter w and coefficient κ ; thermodynamic temperature T ; the location of the center of the giant dipole resonance E_G , with width Γ_G and cross section σ_G in the maximum for each nucleus. For description of experimental data of Ref. [3] it is necessary to add one or several narrow peaks to the strength function is based on the data of Ref. [3]. The second summand of Eq. (5) corresponds to the left slope of the peak (energies below the maximum), and the third summand is the right slope (energies above the maximum). Position E_p in the energy scale, amplitudes $P\delta^+$ and $P\delta^-$ and slope parameters α_p and β_p are fitted for each peak independently. At $E_1 \approx B_n$ the fitted ratios Γ_{M1}/Γ_{E1} of $E1$ - and $M1$ -strength functions are normalized to known experimental values, and their sum Γ_λ is normalized to the total radiation width of the resonance.

The influence of the shell correction δE on the density of the quasi-particle levels were tested in this work. It was done by using the $a(A)$ value, which depends on the excitation energy, included linearly in the parameter of the single-particle density g (see Eq. (2)). For a nucleus with mass A and excitation energy E_{ex} , $a(A)$ is expressed, as [3]:

$$a(A) = \tilde{a}(1 + ((1 - \exp(\gamma E_{ex}))\delta E/E_{ex})) \quad (5)$$

where asymptotic value is $\tilde{a} = 0.114 \cdot A + 0.162 \cdot A^{2/3}$ and $\gamma = 0.054$. The δE values slightly varied relative to their evaluations [3] in order to keep an average spacing between neutron resonances (see [2]).

In our model the set of common parameters for fitting (see Eqs. (2, 3)) were:

- 1) the break up thresholds energies U_l up to $l=4$,
- 2) the E_μ and E_v parameters, which are common for all Cooper pairs
- 3) the mutually independent parameters A_l of the density of vibrational levels above the break up threshold U_l
- 4) the coefficients w , κ and β
- 5) the ratio r of negative parity and the total level density.

Those parameters were used for the description of the intensity $I_{\gamma\gamma}(E_1)$ for 43 nuclei, in the framework of the proposed model.

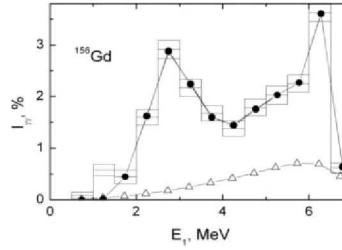


Figure 1. Histogram - experimental cascade intensity and its uncertainties for ^{156}Gd as function of primary cascade quanta E_1 . Points - the best fit of the presented practical model; triangles - a calculation of $I_{\gamma\gamma}$ using models of Ref. [5, 6]. Recorded threshold for cascade gammas is $E_\gamma = 520$ keV.

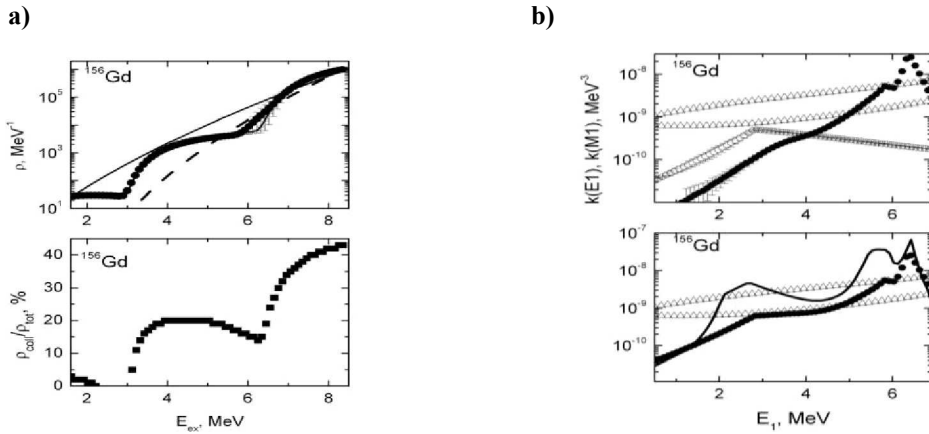


Figure 2. a) Level density of ^{156}Gd . *Top*: points are the best fit of level density (uncertainties – scatter of fits for different sets of initial parameters); dashed and solid lines are the level density calculated using the model of Ref. [5], with taking into account the shell correction δE (6) and without δE , correspondingly. *Bottom*: fitted ratio of density of collective levels to the total level density. **b)** Strength function for ^{156}Gd . *Top*: solid points are the best fit of the strength function of $E1$ -transitions; open points are the best fit of the strength function of $M1$ -transitions. *Bottom*: solid points are a sum of $E1$ - and $M1$ - strength functions; dash line is the sum of strength functions multiplied by $\rho_{\text{mod}}/\rho_{\text{exp}}$ ratio (Ref. [7]). Calculations using the model of Ref. [6] (lower triangles) and using the model of Ref. [8] (upper triangles) were fulfilled with $k(M1) = \text{const}$.

4 Results and discussion

A solution of the system of Eq. (1) is performed by the Monte-Carlo method. The nonlinearity of the strongly correlated equations of the system (1) produces an uncertainty of extracting the ρ and Γ parameters from $I_{\gamma\gamma}$ intensities.

Experimental data on $I_{\gamma\gamma}(E_1)$ are usually obtained with a small total uncertainty and averaged over 500 keV energy intervals. The results for ^{156}Gd are shown, in more detail, in Figs. 1–2. The best fits to $I_{\gamma\gamma}(E_1)$, as well as the fitted level densities and strength functions, are compared to corresponding values calculated using the statistical model. The results and corresponding calculations of level density and radiative strength function for the rest of the investigated nuclei will not be shown in

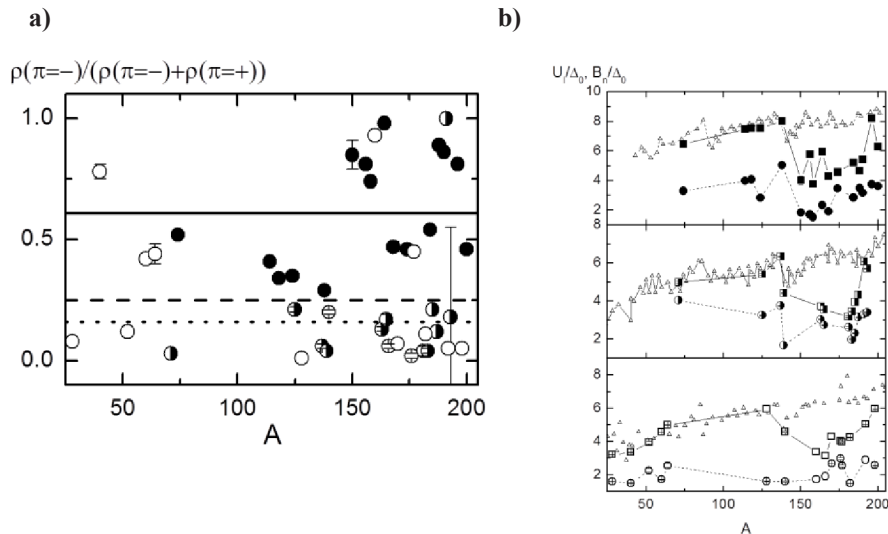


Figure 3. **a)** A-dependence of the ratios U_i/Δ_0 , for the second (points) and the third (squares) Cooper pairs. Full points – even-even, half-open points are even-odd and open points are odd-odd compound nuclei. Triangles – the mass dependence of B_n/Δ_0 ratio. **b)** Mass dependence of the ratio of the level density with negative parity to the total level density at the upper energy border of the E_d and their averages for even-even nuclei (solid lines), even-odd (dashed lines) and odd-odd nuclei (dotted lines). Full points – even-even, half-open points – even-odd and open points – odd-odd compound nuclei.

this publication. However, we are presented here obtained results for some of parameters of nuclear structure.

One important parameter is the breaking thresholds for Cooper pairs. In the present analysis was confirmed the previous results about the connection between the shape of the investigated nucleus and the breaking thresholds. That was established for the first time in our prior analysis [3]. As the breaking thresholds differ for nuclei with various nucleon parities and depend on the average pairing energy (Δ_0) of the last nucleon, the mass dependencies for the ratios of the break up thresholds of the second and the third Cooper pairs to Δ_0 , as well as the mass dependence of the binding energy to Δ_0 , are presented in Fig. 3. As it can be seen in Fig. 3, there is a noticeable difference in U_2/Δ_0 and U_3/Δ_0 ratios for spherical and deformed nuclei in contrast to B_n/Δ_0 .

In this work it was also obtained information about levels parity. For determination of the part $r = \rho(\pi-)/(\rho(\pi-) + \rho(\pi+))$ of levels $\rho(\pi-)$ with negative parity, a linear extrapolation for r value was applied in the $E_d \leq E_{ex} \leq B_n$ energy interval. At that, in the B_n point we use generally accepted assumption, that $\rho(\pi-) = 0.5(\rho(\pi-) + \rho(\pi+))$, and $\rho(\pi-)$ value in this energy point was fixed, and at the E_d energy the $\rho(\pi-)$ value varied.

The calculated ratios of density of the levels with negative parity to the total level density are shown in Fig. 3. The averages of these ratios are 0.61(22), 0.25(28) and 0.16(16) for even-even, even-odd and odd-odd nuclei, respectively (and for odd-even ^{177}Lu it is 0.65(1)). Hence, the behavior of the gamma-decay process is different for nuclei of various nucleon parities.

5 Conclusion

In this work we presented new variant of model for gamma decay of neutron resonance, taking into account shell inhomogeneities of the single-particle level spectra. We used this model for fitting the experimental intensity of two-step gamma cascades and to obtain information about parameters of nuclear structure.

The data on Cooper pair break-up energies, obtained with a high accuracy, are sufficient to conclude that the dynamics of interaction between superfluid and normal phases of a nucleus depends on its' shape. Our model allows for a separate determination of the density of vibrational levels between the breaking thresholds of the Cooper pairs.

Unfortunately, an existence of the sources of uncertainties of the sought ρ and Γ functions is a fundamental problem, and it is inevitable for any nuclear model used for experimental data analysis and for predictions of the spectra and cross sections. There are also fluctuations of the intensities of gamma-transitions in different nuclei, which has a contribution to the systematical error. Nevertheless, the practical model showed one possibility to describe the data of the two-step experiments with the accuracy that exceeds the statistical one.

For future development of reliable model of cascade gamma decay new experimental data are necessary. Because of that, ^{108}Ag , ^{110}Ag , ^{104}Rh and ^{56}Mn nuclei will be investigated by two step gamma cascade method.

References

- [1] V.G. Soloviev, Nuclear Physics A **586**(2), 265 (1995)
- [2] A.M. Sukhovoj, Phys. Atom. Nucl. **78**, 230 (2015)
- [3] A.M. Sukhovoj, L.V. Mitsyna, N. Jovancevic, Phys. Atom. Nucl. **79**, 313 (2016)
- [4] V.M. Strutinsky, in Proceedings of the International Congress on Nuclear Physics, Paris, France, p. 617 (1958)
- [5] W. Dilg, W. Schantl, H. Vonach, and M. Uhl, Nucl. Phys. A **217**, 269 (1973)
- [6] S.G. Kadenskij, V.P. Markushev and W.I. Furman, Sov. J. Nucl. Phys. **37**, 165 (1983)
- [7] N. Jovancevic, A.M. Sukhovoj, W.I. Furman, and V.A. Khitrov, in Proceedings of XX ISINN, Preprint E3-2013-22, p. 157 (Dubna, 2013); <http://isinn.jinr.ru/past-isinns.html>
- [8] P. Axel, Phys. Rev. **126**, 671 (1962)



An underground laboratory as a facility for studies of cosmic-ray solar modulation



N. Veselinović, A. Dragić*, M. Savić, D. Maletić, D. Joković, R. Banjanac, V. Udovičić

Institute of Physics, University of Belgrade, Pregrevica 118, 11080 Zemun, Serbia

ARTICLE INFO

Keywords:

Cosmic ray muons
Forbush decrease
Response function

ABSTRACT

The possibility of utilizing a shallow underground laboratory for the study of energy dependent solar modulation process is investigated. The laboratory is equipped with muon detectors at ground level and underground (25mwe), and with an underground asymmetric muon telescope to have a single site detection system sensitive to different median energies of primary cosmic-ray particles. The detector response functions to galactic cosmic rays are determined from Monte Carlo simulation of muon generation and propagation through the atmosphere and soil, based on CORSIKA and GEANT4 simulation packages. The present setup is suitable for studies of energy dependence of Forbush decreases and other transient or quasi-periodic cosmic-ray variations.

© 2017 Elsevier B.V. All rights reserved.

1. Introduction

Galactic cosmic rays (GCR) arriving at Earth after propagating through the heliosphere interact with nuclei in the atmosphere. These interactions of primary CRs lead to production of a cascade (shower) of secondary particles: hadrons, electrons, photons, muons, neutrinos. Ground based CR detectors are designed to detect some species of secondary cosmic radiation. Widely in use are neutron monitors [1,2], muon telescopes [3,4], various types of air shower arrays [5], γ -ray air Cherenkov detectors [6], air fluorescence detectors [7] etc.

The flux and energy spectra of GCR are modulated by the solar magnetic field, convected by the solar wind. Particularly affected are GCR at the low energy side of the spectrum (up to ~ 100 GeV). Therefore, secondary CRs generated in the atmosphere can be used for studying solar and heliospheric processes. Among the best known effects of the solar modulation are CR flux variations with 11 year period of the solar cycle, 22 year magnetic cycle, diurnal variation and Forbush decrease. The so called corotation with the solar magnetic field results in the flux variation with the 27-day period of solar rotation.

Modulation effects have been studied extensively by neutron monitors (NM) [8,9], sensitive up to several tens of GeV, depending on their geomagnetic location and atmospheric depth. Muon detectors at ground level are sensitive to primary particles of higher energies than NMs. Underground muon detectors correspond to even higher energy primaries. For this reason muon observations complement NM observations in studies of long-term CR variations, CR anisotropy and gradients

or rigidity spectrum of Forbush decreases. However, muon observations suffer from difficulties to disentangle variations of atmospheric origin. While the effect of atmospheric pressure is similar to NMs and easy to account for, the temperature effect is more complicated. The entire temperature profile of the atmosphere is contributing, with different net temperature effect on muon flux at different atmospheric layers, as a result of interplay of positive and negative temperature effects. The positive temperature effect is a consequence of reduced atmospheric density with the temperature increase, resulting in less pion interactions and more decays into muons [10]. The negative temperature effect comes from the increased altitude of muon production at the periods of high temperature, with the longer muon path length and the higher decay probability before reaching the ground level [11]. Both effects are accounted for by the integral method of Dorman [12]. The negative temperature effect is dominant for low energy muons (detected at ground level) and the positive for high energy muons (detected deep underground). At shallow depth of several tens of meters of water equivalent both temperature effects contribute to the overall temperature effect. Several detector systems with different sensitivity to primaries at the same location have the advantage of sharing common atmospheric and geomagnetic conditions.

Belgrade CR station is equipped with muon detectors at ground level and at the depth of 25 m.w.e. Underground laboratory is reached only by muons exceeding energy threshold of 12 GeV. The existing detectors are recently amended by additional setup in an attempt to fully exploit laboratory's possibilities to study solar modulation at different

* Corresponding author.

E-mail address: dragic@ipb.ac.rs (A. Dragić).

median rigidities. In the present paper the detector systems at the Belgrade CR station are described. Response functions of muon detectors to galactic cosmic rays are calculated. The detector system represents useful extension of modulation studies with neutron monitors to higher energies, as it is demonstrated in the case of a recent Forbush event.

2. Description of Belgrade CR station

The Belgrade cosmic-ray station, situated at the Low Background Laboratory for Nuclear Physics at Institute of Physics, is located at near-sea level at the altitude of 78 m a.s.l. Its geographic position is: latitude 44°51'N and longitude 20°23'E, with vertical cut-off rigidity 5.3 GV. It consists of the ground level lab (GLL) and the underground lab (UL) which has useful area of 45 m², dug at a depth of 12 m. The soil overburden consists of loess with an average density 2.0 ± 0.1 g/cm³. Together with the 30 cm layer of reinforced concrete the laboratory depth is equivalent to 25 m.w.e. At this depth, practically only the muonic component of the atmospheric shower is present [13].

2.1. Old setup

The experimental setup [14] consists of two identical sets of detectors and read out electronics, one situated in the GLL and the other in the UL. Each setup utilizes a plastic scintillation detector with dimensions 100 cm × 100 cm × 5 cm equipped with 4 PMTs optically attached to beveled corners of a detector. Preamplifier output of two diagonally opposing PMTs are summed and fed to a digitizer input (CAEN FADC, type N1728B). FADC operates at 100 MHz frequency with 14 bit resolution. The events generating enough scintillation light to produce simultaneous signals in both inputs exceeding the given threshold are identified as muon events. The simulated total energy deposit spectrum is presented on the left panel of Fig. 1. After the appropriate threshold conditions are imposed on the signals from two diagonals, the spectrum is reduced to the one represented on the right panel of the same figure. Contribution from different CR components are indicated on both graphs and experimentally recorded spectrum is plotted as well.

Particle identification is verified by a two-step Monte Carlo simulation. In the first step development of CR showers in the atmosphere is traced, starting from the primary particles at the top of the atmosphere by CORSIKA simulation package. CORSIKA output contains information on generated particles (muons, electrons, photons, etc.) and their momenta at given observation level. More details on CORSIKA simulation will be given in Section 3. This output serves as an input for the second step in simulation, based on GEANT4. In the later step energy deposit by CR particles in the plastic scintillator detector are determined, together with the light collection at PMTs. Contributions from different CR components to recorded spectrum are also shown in Fig. 1.

According to the simulation, 87.5% of events in the coincident spectrum originate from muons. To account for the contribution from other particles to the experimental spectrum not all the events in the spectrum are counted when muon time series are constructed. Muon events are defined by setting the threshold corresponding to muon fraction of recorded spectrum. Threshold is set in terms of “constant fraction” of the spectrum maximum, which also reduces count rate fluctuations due to inevitable shifts of the spectrum during long-term measurements.

2.2. Upgrade of the detector system

Existing detectors enable monitoring of CR variations at two different median energies. An update is contemplated that would provide more differentiated response. Two ideas are considered. First one was to extend the sensitivity to higher energies with detection of multi-muon events underground. An array of horizontally oriented muon detectors ought to be placed in the UL. Simultaneous triggering of more than

one detector is an indication of a multi-muon event. The idea was exploited in the EMMA underground array [15], located at the deeper underground laboratory in Pyhasalmi mine, Finland, with the intention to reach energies in the so called knee region. For a shallow underground laboratory, exceeding the energy region of solar modulation would open the possibility to study CR flux variations originating outside the heliosphere. Second idea is an asymmetric muon telescope separating muons with respect to zenith angle. Later idea is much less expensive to be put into practice.

Both ideas will be explained in detail and response function to GCR for existing and contemplated detectors calculated in the next section.

3. Calculation of response functions

Nature of variations of primary cosmic radiation can be deduced from the record of ground based cosmic ray detectors provided relation between the spectra of primary and secondary particles at surface level are known with sufficient accuracy. Relation can be expressed in terms of rigidity or kinetic energy.

Total detector count rate can be expressed as:

$$N(E_{th}, h, t) = \sum_i \int_{E_{th}}^{\infty} Y_i(E, h) \cdot J_i(E, t) dE \quad (1)$$

where E is primary particle energy, i is type of primary particle (we take into account protons and α particles), $J_i(E, t)$ is energy spectrum of primary particles, h is atmospheric depth and $Y_i(E, h)$ is the so called yield function. E_{th} is the threshold energy of primary particles. It depends on location (geomagnetic latitude and atmospheric altitude) and detector construction details. At a given location on Earth, only particles with rigidity above vertical rigidity cut-off contribute to the count rate. Also, detector construction often prevents detection of low energy particles. For instance, muon detectors are sometimes covered with a layer of lead. In present configuration our detectors are lead free.

Historically, yield functions were calculated empirically, often exploiting the latitude variations of neutron and muonic CR component [16–18]. With the advancement of computing power and modern transport simulation codes it became possible to calculate yield functions from the interaction processes in the atmosphere [19,20]. The yield function for muons is calculated as:

$$Y_i(E, h) = \int_{E_{th}}^{\infty} \int S(\theta, \phi) \cdot \Phi_{i,\mu}(E_i, h, E, \theta, \phi) dE d\Omega \quad (2)$$

where $S(\theta, \phi)$ is the effective detector area and integration is performed over upper hemisphere. $\Phi_{i,\mu}(E_i, h, E, \theta, \phi)$ is the differential muon flux per primary particle of the type i with the energy E_i .

Total differential response function:

$$W(E, h, t) = \sum_i Y_i(E, h) \cdot J_i(E, t) \quad (3)$$

when normalized to the total count rate gives the fraction of count rate originating from the primary particles with the energy in the infinitesimal interval around E . Integration of differential response function gives the cumulative response function.

The response functions of our CR detectors are calculated using Monte Carlo simulation of CR transport through the atmosphere with CORSIKA simulation package. Simulation was performed with protons and α -particles as primary particles. They make ~94% (79% + 14.7%) of all primaries [21]. Implemented hadron interaction models were FLUKA for energies below 80 GeV, and QGSJET II-04 for higher energies. If the old version of QGSJET is used, a small discontinuity in response function is noticed at the boundary energy between two models. Geomagnetic field corresponds to the location of Belgrade $B_x = 22.61$ μ T, $B_z = 42.27$ μ T. Power law form of differential energy spectrum of galactic cosmic rays $J_p(E) \sim E^{-2.7}$ is assumed. Energy range of primary particles is between 1 GeV and $2 \cdot 10^7$ GeV. Interval of zenith angles is $0^\circ < \theta < 70^\circ$. Low energy thresholds for secondary particles are: 150 MeV for hadrons and muons and 15 MeV for electrons

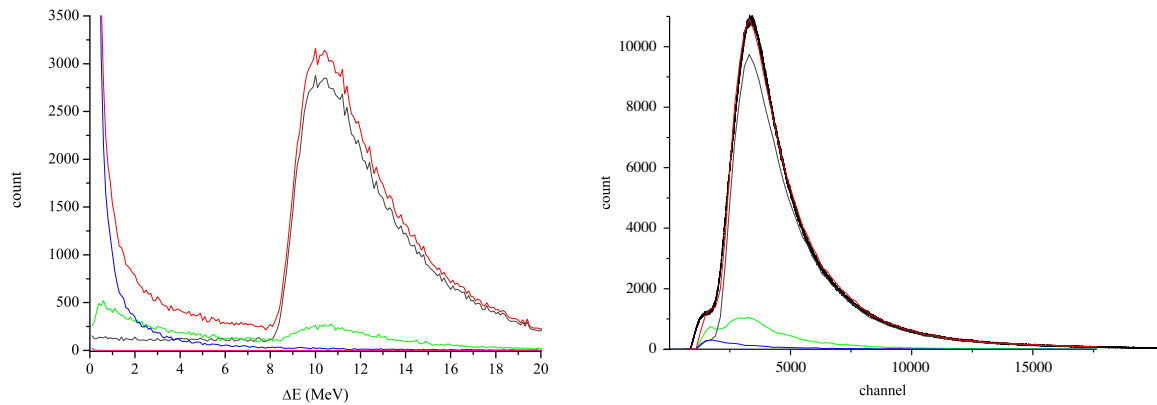


Fig. 1. Left — ΔE spectrum in the plastic scintillator detector, derived from GEANT simulation; right — the same, but for the events exceeding threshold on both diagonals. Contribution of different CR components to the total energy deposit in the detector: muons-gray line, photons-blue line, electrons-green line and sum of all contributions — red line. The black curve on the right panel is the experimental spectrum. (For interpretation of the references to color in this figure legend, the reader is referred to the web version of this article.)

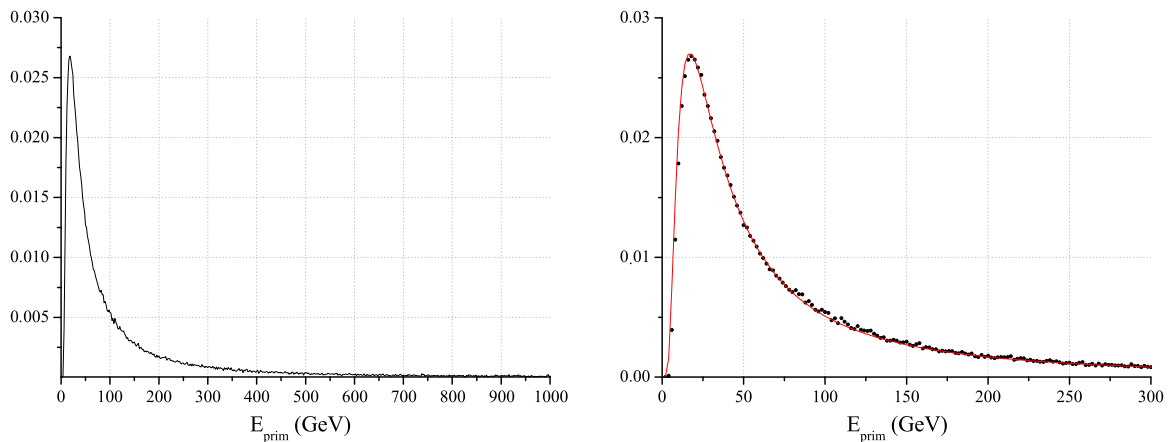


Fig. 2. Left: normalized total response function of ground level muon detector to galactic cosmic rays; right: same as left, fitted with Dorman function (red line). (For interpretation of the references to color in this figure legend, the reader is referred to the web version of this article.)

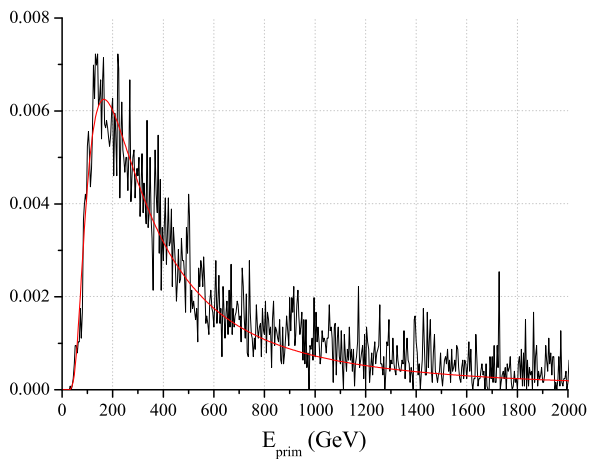


Fig. 3. Response function for multi-muon events in UL to galactic cosmic rays.

and photons. Selected atmospheric model is AT511 (Central European atmosphere for May 11 1993). Observational level is at 78m a.s.l.

For calculation of response functions for underground detectors, simulation of particle propagation through the soil overburden is performed using the code based on GEANT4 package. For precise calculation of energy loss, chemical composition of the soil needs to be known. The

composition used in our work is taken from a geochemical study of neighboring loess sections of Batajnica and Stari Slankamen [22]. Most abundant constituents are quartz (SiO_2) 70%, alumina (Al_2O_3) 15% and quicklime (CaO) 10%, while others include Fe_2O_3 , MgO , TiO_2 , K_2O ,... Inaccuracy of our knowledge of the soil chemical composition should not strongly affect our results since, at relevant energies, dominant energy loss mechanism for muons is ionization which, according to Bethe–Bloch formula depends mostly on $\langle Z \rangle / \langle A \rangle$. Soil density profile is probed during laboratory construction. It varies slowly with depth and average density is found to be $(2.0 \pm 0.1) \text{ g/cm}^3$.

In the simulation, the effective area and angular acceptance of different modes of asymmetric muon telescope (single, coincident and anticoincident) are taken into account.

According to Dorman [12], response function can be parametrized as:

$$W(E) = \begin{cases} 0, & \text{if } E < E_{th}; \\ a \cdot k \cdot \exp(-aE^{-k}), & \text{otherwise;} \\ \frac{a \cdot k \cdot \exp(-aE^{-k})}{E^{(k+1)}(1 - aE_{th}^{-k})}, & \end{cases} \quad (4)$$

with the high energy asymptotics: $W(E) \approx a \cdot k \cdot E^{-(k+1)}$.

3.1. Ground level

Calculated response function for ground level muon detector is presented on Fig. 2, together with fitted Dorman function (4).

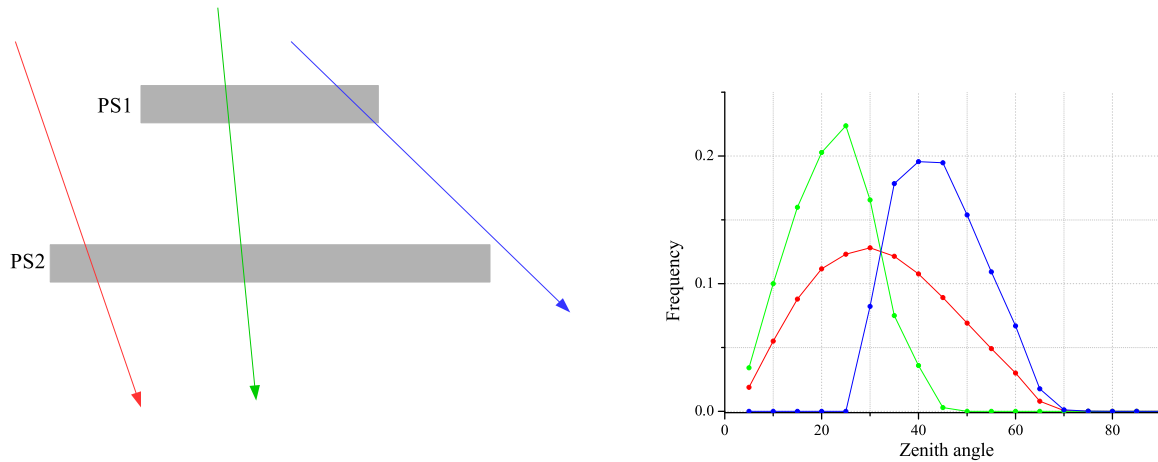


Fig. 4. Left: Schematic view of the asymmetric muon telescope; PS1 — plastic scintillator detector 1, PS2 — plastic scintillator detector 2. Right: angular distribution of detected muons in single mode (red), coincident mode (green) and anticoincident mode (blue), normalized to number of counts in each mode. (For interpretation of the references to color in this figure legend, the reader is referred to the web version of this article.)

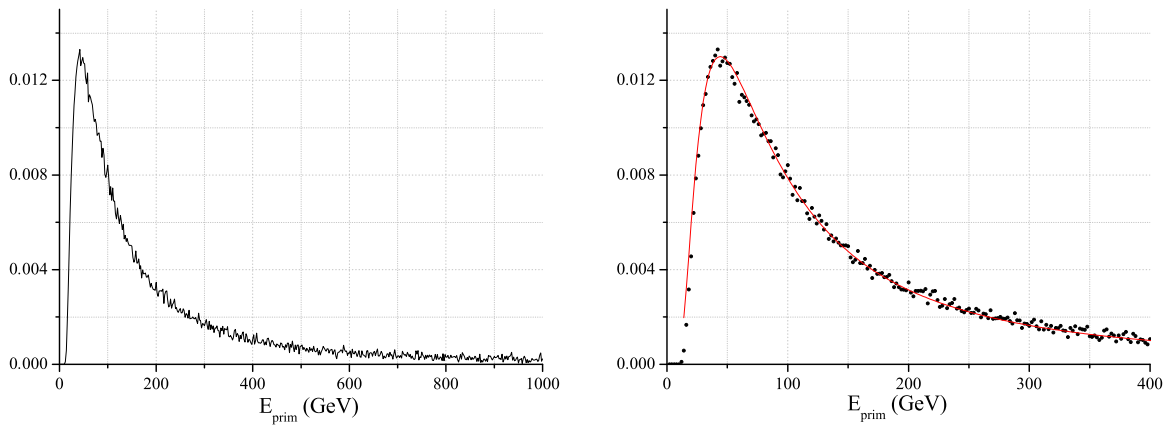


Fig. 5. Response function of single mode of ASYMUT in the UL to galactic cosmic rays. On the right panel the energy interval of interest is enlarged and Dorman function fit is plotted (red line). (For interpretation of the references to color in this figure legend, the reader is referred to the web version of this article.)

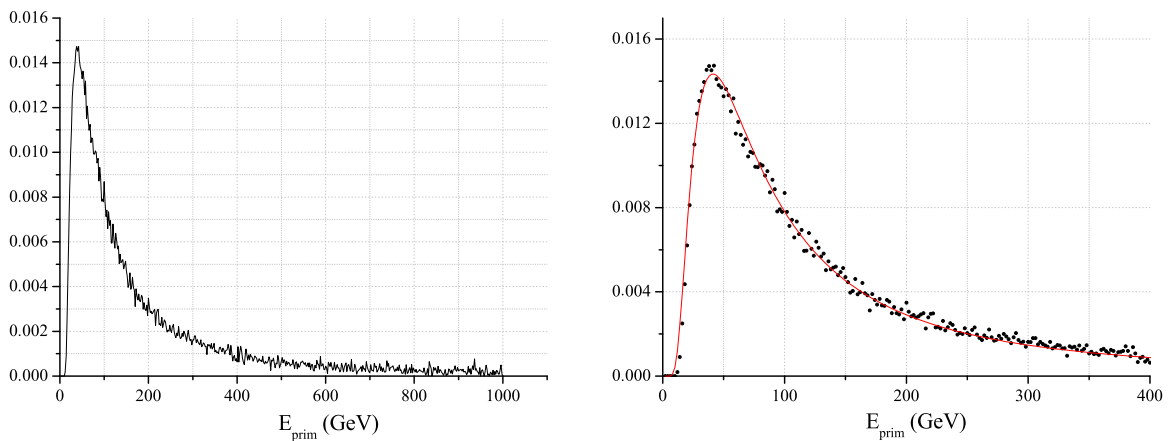


Fig. 6. Response function of coincident mode of asymmetric muon telescope in the UL to galactic cosmic rays. On the right panel the interesting energy interval is enlarged and Dorman function fit is plotted (red line). (For interpretation of the references to color in this figure legend, the reader is referred to the web version of this article.)

3.2. Underground

3.2.1. Multi-muon events

Count rate of multi-muon events underground turned out to be too low for the above mentioned array detector experiment to be feasible in our laboratory. To collect enough events for construction of the response function (Fig. 3), allowed muon separation is 200 m, fairly

exceeding laboratory dimensions. Under these conditions calculated median energy is 270 GeV.

3.2.2. ASYmmetric MUon Telescope (ASYMUT)

Asymmetric muon telescope is an inexpensive detector, constructed from components already available in the laboratory. It consists of two plastic scintillators of unequal dimensions. The lower is identical to the

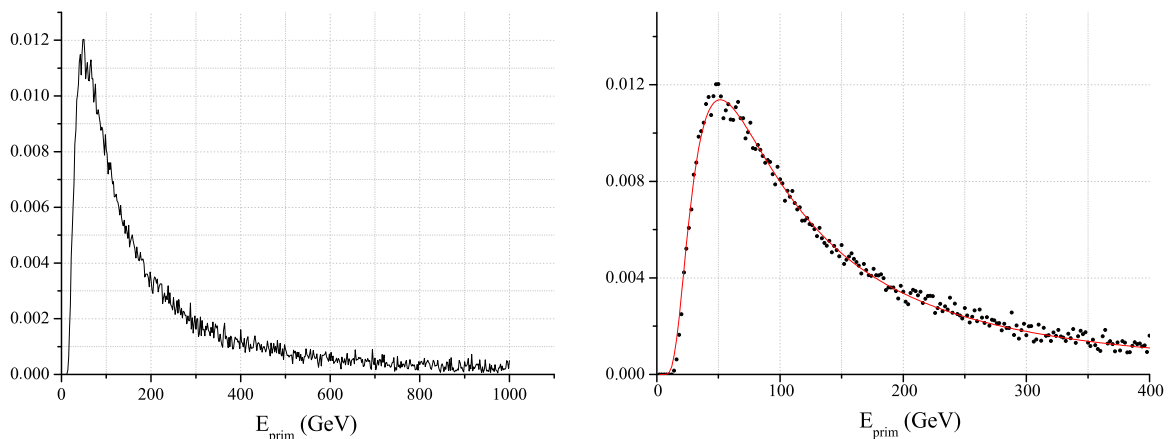


Fig. 7. Response function of anticoincident mode of asymmetric muon telescope in the UL to galactic cosmic rays. On the right panel the interesting energy interval is enlarged and Dorman function fit is plotted (red line). (For interpretation of the references to color in this figure legend, the reader is referred to the web version of this article.)

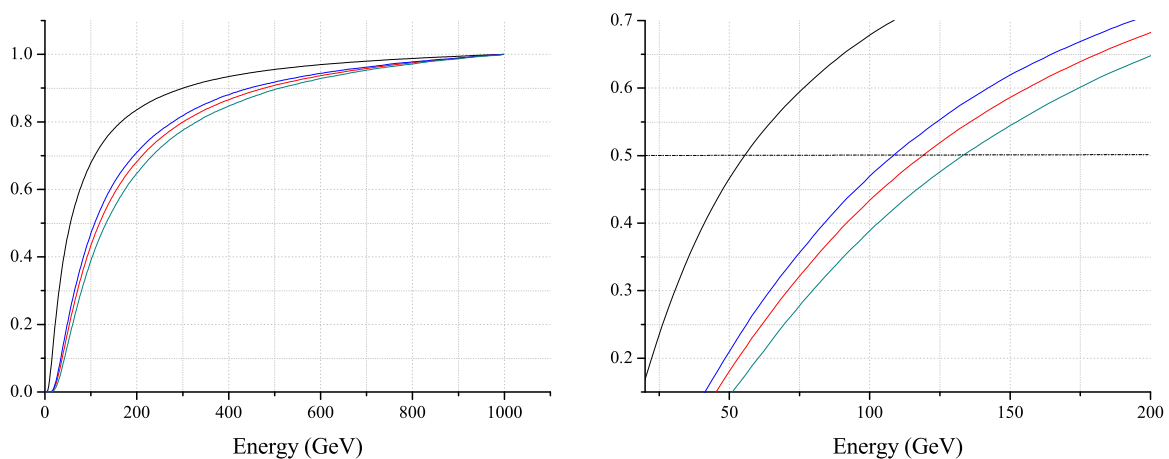


Fig. 8. Cumulative response function to galactic cosmic rays of different muon detectors in the Belgrade CR station: black curve — GLL; red curve — single UL; green curve — CC mode and blue curve — ANTI CC mode of asymmetric muon telescope. The 0.5 level corresponds to median energy. Cumulative response function with enlarged region around this level is shown in the right picture. (For interpretation of the references to color in this figure legend, the reader is referred to the web version of this article.)

one located in the GLL ($100 \times 100 \times 5$ cm) and upper one is $50 \times 46 \times 5$ cm. Detectors are separated vertically by 78 cm, as depicted in Fig. 4, to have roughly the same count rate in the coincident and anticoincident mode. Lower detector in single mode operates in the same manner as the one in the GLL, with wide angular acceptance. The coincident mode is composed of the events registered in both upper and lower detector. In the anticoincident mode, muons passing through the upper but not the lower detector are counted. Therefore, the later mode favors inclined muon paths. Different angular distribution means different path length of muons registered in three modes of ASYMUT (right part of Fig. 4) and also different energy distribution of parental primary particles.

The response functions to GCR of three modes of ASYMUT are shown on Figs. 5–7 and respective cumulative response functions are shown on Fig. 8.

Important parameters describing shapes of response functions are summarized in Table 1. The most often used characteristics of a detector system is its median energy E_{med} . Primary particles with the energy below E_{med} give 50% contribution to detector count rate. The energy interval $(E_{0.05}, E_{0.95})$ is responsible for 90% of registered events. Fitted value of the parameter k from Dorman function (Eq. (4)) is also presented. The parameters $E_{0.05}$ and E_{med} are determined with 1 GeV accuracy, while the uncertainty of $E_{0.95}$ is much higher due to small number of very high energy events and is conservatively estimated as 10%.

Table 1

Sensitivity of Belgrade CR detectors (GLL — ground level; UL — underground based ASYMUT single mode; CC — ASYMUT coincident mode; ANTI — ASYMUT anticoincident mode) to GCR primary particles. Primaries with the energy below $E_{0.05}$ (and above $E_{0.95}$) contribute with 5% to the count rate of a corresponding detector. E_{med} is median energy, E_{th} threshold energy and k is Dorman parameter.

det	E_{th} (GeV)	$E_{0.05}$ (GeV)	E_{med} (GeV)	$E_{0.95}$ (GeV)	k
GLL	5	11	59	915	0.894(1)
UL	12	31	137	1811	0.971(4)
CC	12	27	121	1585	1.015(3)
ANTI	14	35	157	2031	0.992(4)

3.3. Conclusions

Usefulness of our setup for solar modulation studies is tested on the example of investigation of a Forbush decrease of 8 March 2012. In the first half of March 2012 several M and X class solar flares erupted from the active region 1429 on the Sun. The strongest were two X class flares that bursted on March 7. The first one is the X5.4 class flare (peaked at 00:24 UT) and the second one is the X1.3 class flare (peaked at 01:14 UT). The two flares were accompanied by two fast CMEs, one of which was Earth-directed [23]. Several magnetic storms were also registered on Earth, and a series of Forbush decreases is registered. The most pronounced one was registered on March 8. Characteristics of this event as recorded by various neutron monitors and our detectors are compared.

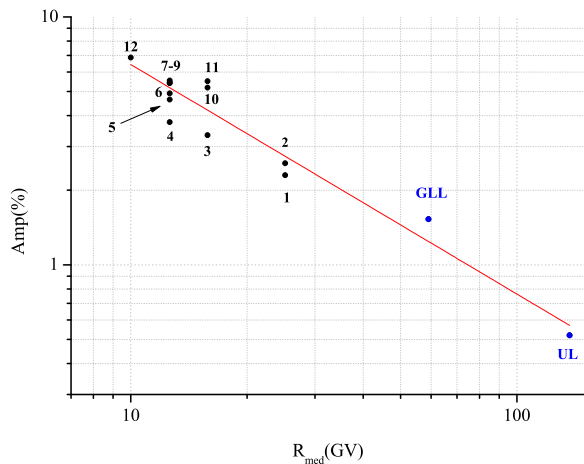


Fig. 9. Rigidity spectrum of FD from 12 March 2012. Black points represent the amplitude of the event as seen by twelve NMs: 1 — Athens, 2 — Mexico City; 3 — Almaty, 4 — Lomnický štít; 5 — Moscow; 6 — Kiel; 7 — Yakutsk; 8 — Apatity; 9 — Inuvik; 10 — McMurdo; 11 — Thule; 12 — South Pole. Blue points are from Belgrade CR station: GLL — ground level and UL — underground. (For interpretation of the references to color in this figure legend, the reader is referred to the web version of this article.)

Amplitude of a Forbush decrease is one of its main characteristics. Dependence of FD amplitude on median rigidity (or energy) is expected to follow the power law: $\Delta N/N \sim R^{-\gamma}$ [12].

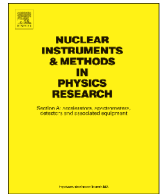
For investigation of rigidity spectrum of mentioned FD data from 12 NMs are combined with the data from our two detectors (GLL and UL) that were operational at the time of the event. Neutron monitor data in the period between 1 March 2012 and 1 April 2012 are taken from the NMDB database (www.nmdb.eu) [24]. The exponent of the rigidity spectrum of this FD γ is obtained by the least-square fitting of the data with the power function (Fig. 9) and found to be $\gamma = 0.92 \pm 0.18$. Presented analysis illustrates applicability of our setup for studies of consequences of CR solar modulation process in the energy region exceeding sensitivity of neutron monitors.

Acknowledgments

We are very grateful to late Prof. Ivan Aničin for his enthusiastic contributions, deep insights and valuable advice not just regarding work presented in this paper but also for being a real spiritus agens of our lab. We acknowledge the NMDB database (www.nmdb.eu), founded under the European Union's FP7 programme (contract no. 213007) for providing NM data. The present work was funded by the Ministry of Education, Science and Technological Development of the Republic of Serbia, under the Project No. 171002.

References

- [1] J.A. Simpson, The cosmic ray nucleonic component: The invention and scientific uses of the neutron monitor, *Cosmic Rays Earth* (2000) 11–32.
- [2] J.W. Bieber, Neutron monitoring: Past, present, future, in: Jonathan F.O. (Ed.) AIP Conference Proceedings, vol. 1516, No. 1, 2013.
- [3] M.L. Duldig, Muon observations, in: *Cosmic Rays and Earth*, Springer, Netherlands, 2000, pp. 207–226.
- [4] S. Cecchini, M. Spurio, Atmospheric muons: experimental aspects, *Geosci. Instrum. Methods Data Syst. Discuss.* 2 (2012) 603–641.
- [5] K.-H. Kampert, A.A. Watson, Extensive air showers and ultra high-energy cosmic rays: a historical review, *Eur. Phys. J. H* 37 (3) (2012) 359–412.
- [6] A. de Angelis, O. Mansutti, M. Persic, Very-high energy gamma astrophysics, *Riv. Nuovo Cimento* 31 (4) (2008) 187–246. <http://dx.doi.org/10.1393/ncr/i2008-10032-2>.
- [7] F. Arqueros, J.R. Hörandel, B. Keilhauer, Air fluorescence relevant for cosmic-ray detection — review of pioneering measurements, *Nucl. Instrum. Methods A* 597 (2008) 23–31. <http://dx.doi.org/10.1016/j.nima.2008.08.055>.
- [8] J.A. Lockwood, W.R. Webber, The 11 year solar modulation of cosmic rays as deduced from neutron monitor variations and direct measurements at low energies, *J. Geophys. Res.* 72 (23) (1967) 5977–5989.
- [9] I.G. Usoskin, G.A. Bazilevskaya, G.A. Kovaltsov, Solar modulation parameter for cosmic rays since 1936 reconstructed from ground-based neutron monitors and ionization chambers, *J. Geophys. Res.* 116 (2011) A02104. <http://dx.doi.org/10.1029/2010JA016105>.
- [10] A. Duperier, The meson intensity at the surface of the earth and the temperature at the production level, *Proc. Phys. Soc. A* 62 (11) (1949) 684.
- [11] P.M. Blackett, On the instability of the barytron and the temperature effect of cosmic rays, *Phys. Rev.* 54 (11) (1938) 973.
- [12] L. Dorman, *Cosmic Rays in the Earth's Atmosphere and Underground*, Springer Science + Business Media, LLC., New York, 2004.
- [13] G. Hausser, Cosmic ray-induced background in ge-spectrometry, *Nucl. Instrum. Methods B* 83 (1–2) (1993) 223–228.
- [14] A. Dragić, V. Udovičić, R. Banjanac, D. Joković, D. Maletić, N. Veselinović, M. Savić, J. Puzović, I.V. Aničin, The new setup in the Belgrade low-level and cosmic-ray laboratory, *Nucl. Technol. Radiat. Prot.* 26 (3) (2011) 181–192. <http://dx.doi.org/10.2298/NTRP1101064N>.
- [15] T. Kalliokoski, L. Bezrukov, T. Enqvist, H. Fynbo, L. Inzhechik, P. Jones, J. Joutsenvaara, J. Karjalainen, P. Kuusiniemi, K. Loo, B. Lubsandorzhiev, V. Petkov, T. Rih, J. Sarkamo, M. Slupecki, W. Trzaska, A. Virkajrvi, Can EMMA solve the puzzle of the knee? *Prog. Part. Nucl. Phys.* 66 (2011) 468–472.
- [16] W.H. Fonger, Cosmic radiation intensity-time variations and their origin. II. Energy dependence of 27-day variations, *Phys. Rev.* 91 (2) (1953) 351.
- [17] E.E. Brown, Neutron yield functions for the nucleonic component of cosmic radiation, *Il Nuovo Cimento* (1955–1965) 6 (4) (1957) 956–962.
- [18] L. Dorman, *Cosmic Ray Variations*, State Publishing House for Technical and Theoretical Literature, 1957.
- [19] E.O. Fluckiger, et al., A parameterized neutron monitor yield function for space weather applications, in: *Proceedings of the 30th International Cosmic Ray Conference*, Mexico City, Mexico, vol. 1 (SH), 2008, pp. 289–292.
- [20] M. Zazyan, A. Chilingarian, Calculations of the sensitivity of the particle detectors of ASEC and SEVAN networks to galactic and solar cosmic rays, *Astropart. Phys.* 32 (2009) 185–192.
- [21] K. Nakamura, et al., 24. Cosmic rays, *J. Phys. G* 37 (2010) 075021.
- [22] B. Bugle, B. Glaser, L. Zoller, U. Hambach, S. Markovic, I. Glaser, N. Gerasimenko, Geochemical characterization and origin of Southeastern and Eastern European loesses (Serbia, Romania, Ukraine), *Quat. Sci. Rev.* 27 (2008) 1058–1075.
- [23] NASA Goddard Space Weather Research Center, Summary of the space weather event associated with the X5.4 and X1.3 flare on March 7.
- [24] H. Mavromichalaki, et al., Applications and usage of the real-time Neutron Monitor Database, *Adv. Space Res.* 47 (12) (2011) 2210–2222.



On the omnipresent background gamma radiation of the continuous spectrum



R. Banjanac, D. Maletić, D. Joković*, N. Veselinović, A. Dragić, V. Udovičić, I. Aničin

Institute of Physics, University of Belgrade, Pregrevica 118, 11080 Belgrade, Serbia

ARTICLE INFO

Article history:

Received 19 June 2013

Received in revised form

30 January 2014

Accepted 30 January 2014

Available online 7 February 2014

Keywords:

Gamma spectroscopy

Cosmic-ray induced radiation

Terrestrial radiation

ABSTRACT

The background spectrum of a germanium detector, shielded from the radiations arriving from the lower and open for the radiations arriving from the upper hemisphere, is studied by means of absorption measurements, both in a ground level and in an underground laboratory. The low-energy continuous portion of this background spectrum that peaks at around 100 keV, which is its most intense component, is found to be of very similar shape at the two locations. It is established that it is mostly due to the radiations of the real continuous spectrum, which is quite similar to the instrumental one. The intensity of this radiation is in our cases estimated to about 8000 photons/(m²s · 2π · srad) in the ground level laboratory, and to about 5000 photons/(m²s · 2π · srad) in the underground laboratory, at the depth of 25 m.w.e. Simulations by GEANT4 and CORSIKA demonstrate that this radiation is predominantly of terrestrial origin, due to environmental gamma radiations scattered off the materials that surround the detector (the “skyshine radiation”), and to a far less extent to cosmic rays of degraded energy.

© 2014 Elsevier B.V. All rights reserved.

1. Introduction

After many comprehensive studies of background spectra of germanium detectors [1,2], it has become common knowledge that the main contributors to these spectra are the gamma radiations of discrete spectrum, that originate from naturally occurring radioactive isotopes dispersed in the environment and in the materials that surround the detector, as well as the complex radiations of mixed composition whose origin can be traced to cosmic rays. Gamma radiations of discrete energies produce the line spectrum but are also partially responsible for the continuum, composed of the Compton distributions of discrete energies that escape total detection. Due to the intrinsically high peak-to-Compton ratio, this continuum is in germanium detectors much lower than in other types of detectors. Vicinity of significant quantities of new lead may be also contributing to the continuum due to the presence of ²¹⁰Pb [3].

Cosmic-ray muons by direct interactions produce the continuous spectrum of energy losses that, for all detector sizes but for the thinnest ones, peaks at high energies, well beyond the region where the spectrum is usually of interest. The muon secondaries, however, contain significant quantity of low-energy radiations

that contribute to the continuum in its portion relevant to spectroscopy. The soft, electromagnetic component of cosmic rays by its scattered and degraded radiations also contributes to the continuous part of the background spectrum, mostly at lower energies, within the region of interest to practical spectroscopy. Neutrons, mostly of cosmic-ray origin, contribute the continuous spectrum of recoils that diverges at lowest energies, though usually of very low intensity. The only spectral line that is attributed to cosmic rays is the annihilation line.

All these results in the instrumental background spectrum that is characteristic of the detector size, shape and the dead layers. The prominent feature common to all instrumental background spectra, however, is that the greatest part of the spectral intensity lies in the low-energy continuum that, depending primarily on the detector size, peaks at around 100 keV. It is an empirical fact that in the background spectra of unshielded High Purity Germanium (HPGe) detectors, depending on their size, the total intensity in the lines makes only some 10–20% of the total intensity in this low-energy continuum. The cause for the particular shape of the continuum is usually found in the similarly shaped energy dependence of detection efficiency curves on germanium detectors. The intensity of the continuum is already by an educated guess well over the expected intensity of all the Compton distributions taken together, what suggests that at least some part of the continuum must be of some other origin, unaccounted for by conventional considerations. To check this, in this work we

* Corresponding author. Tel.: +381 11 3713 172; fax: +381 11 3162 190.

E-mail address: yokovic@ipb.ac.rs (D. Joković).

study by means of absorption measurements the background radiations that arrive from the upper hemisphere, which may be suspected responsible for the part of this continuum, with the aim of determining its intensity and origin. This assumption is justified by the fact that majority of germanium detectors are vertically oriented and are by virtue of their construction already of very low detection efficiency for low-energy radiations arriving from the lower hemisphere, e.g. Ref. [4].

2. The experiment

The measurements were performed with a vertically oriented 35% efficiency coaxial type radio-pure HPGe detector mounted in the 1.5 mm thick magnesium housing (of the ORTEC GEM30 type). It was shielded from the radiations coming from the lower hemisphere by the lower half of a heavy lead castle and completely open to those arriving from the upper hemisphere. The cylindrical shield around the detector has the thickness of 12 cm, while that of the layer of lead bricks on which the Dewar vessel sits is 10 cm (Fig. 1).

The same setup was used in both the ground level and in the underground laboratory situated at the depth of 25 m of water equivalent (m.w.e.). The detector is usually used in coincidence/anticoincidence with the 1 m² plastic scintillator, and is dedicated to the study of the features that cosmic rays contribute to the background spectra of heavily shielded detectors. The laboratories where the current measurements are performed are described in some detail in Ref. [5]. A set of measurements is performed with lead absorbers of increasing thickness positioned so as to block the way to the radiations coming from above (Fig. 1). The background spectra from such measurements are presented in Fig. 2. Absorber thicknesses range from 0.04 mm (45 mg/cm²) to 4.5 mm (5 g/cm²), and are marked in the figures. The figures are presented in two different scales; in the figures on the left to show the general change of spectra upon absorption, and in the figures on the right to emphasize the particularly indicative details around the X-rays of lead.

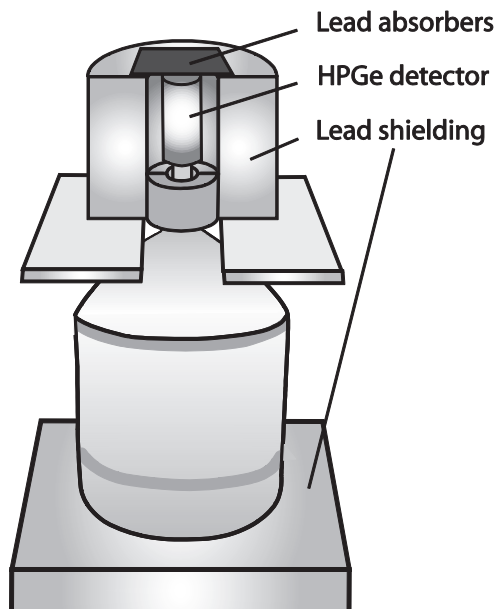


Fig. 1. Detector assembly used in this study.

3. The results and discussion

Visual inspection of the absorption spectra presented in Fig. 2 leads to a number of interesting qualitative conclusions:

1. The spectra taken on the ground level and in the underground exhibit great similarity, the integral intensity of the continuum in the underground being about 1.75 times smaller. At the same time the intensity of cosmic-ray muons in the underground is about 3.5 times smaller [6].
2. The energy, which carries maximum intensity in the continuum, increases with absorber thickness, what is typical of continuous spectra, and is known as the “hardening of the spectrum”.
3. The discontinuity in the absorption spectra on the energy of K_p X-rays of lead (K-absorption edge) reflects the fact that the instrumental continuous spectrum is mostly due to the radiations of the same continuous spectrum, and not due to incomplete detection of radiations of higher discrete energies. If it were due to the distributions of Compton scattered gamma rays of higher energies that have escaped detection, the incoming gamma rays would have been absorbed only weakly by Compton scattering in the absorbers, what would not produce the discontinuity in the spectrum of radiations that reach the detector.
4. Initial increase of the intensity of fluorescent X-rays of lead with absorber thickness again witnesses that the incoming radiation is absorbed by the photoelectric effect. This suggests that the real spectrum of this radiation is similar to the instrumental one, at least up to the energies of about 200 keV, where the photoelectric effect in lead dominates over the Compton effect.
5. Some apparent differences in absorption character of the spectra taken on the ground level and in the underground are to be expected on account of necessarily different composition of the radiations and their different angular distributions at the two locations. The detector in the ground level laboratory virtually has no overhead material, except 1 mm of iron that constitutes the roof of the container, while in the underground laboratory it is surrounded by 30 cm of concrete, that constitutes the walls, the floor and the ceiling of the cavern.

These qualitative conclusions are supported by quantitative analyses of absorption curves at different energies of the continuum. As an illustration, Fig. 3 presents the absorption curves for the count in the channel in the continuum that corresponds to the energy of 89 keV, close to the K-absorption edge in lead. The two well-defined components of very different absorption properties are found. On the surface, the much more intense and less penetrating one by its absorption coefficient corresponds within the errors to the energy close to 90 keV, while the same component in the underground appears of slightly different absorption properties, due to necessarily different composition of the radiations and their different angular distributions. The much less intense and much more penetrating component, both on the surface and in the underground, roughly corresponds to the energy of about 500 keV. The first component thus represents the radiation of the same energy at which it appears in the spectrum, which belongs to the continuum, while the second one represents the sum of Compton distributions of all radiations of higher energies that escape full detection. This last component thus manifests absorption properties of the radiation of an average energy that in our case appears to be around 500 keV.

Since the low-energy component is practically fully absorbed by 1 mm of lead, subtracting the spectrum that corresponds to the absorber of that thickness from the spectrum of the open detector

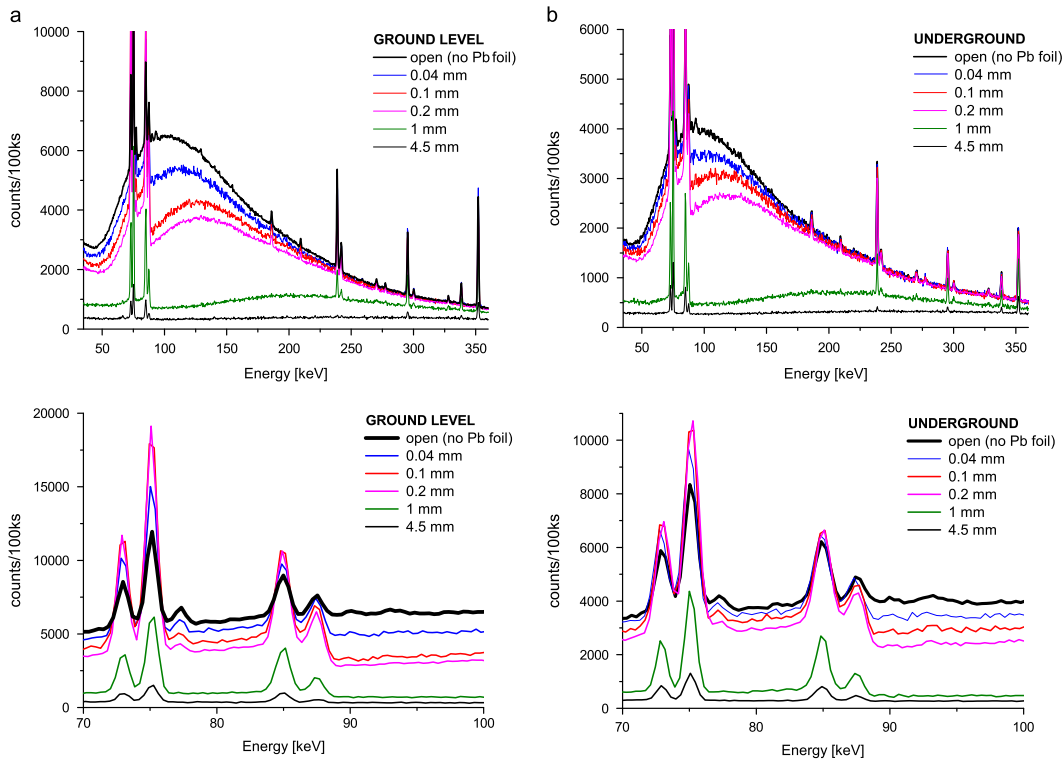


Fig. 2. Experimental low-energy portions of background spectra of the HPGe detector completely shielded from the radiations coming from the lower hemisphere, with a set of lead absorbers of different thicknesses positioned so as to intercept the radiations arriving at the detector from the upper hemisphere: (a) ground level laboratory, (b) underground laboratory at 25 m.w.e. All spectra are normalized to the measurement time of 100 ks.

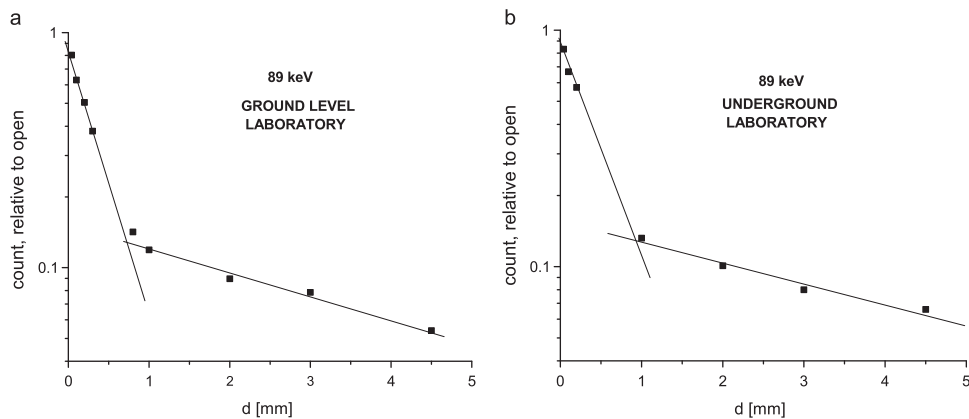


Fig. 3. Absorption curves for the count in the continuum that corresponds to the energy of 89 keV, in the ground-level laboratory (left) and in the underground laboratory at 25 m.w.e. (right). Two distinct components are seen; the first much more intense corresponds rather well to this energy of 89 keV, while the other, much weaker and much more penetrating, approximately corresponds to an average energy of about 500 keV.

would leave predominantly the spectrum of the radiations of the genuinely continuous spectrum, as seen by a given detector. The thus obtained approximate shapes of these instrumental spectra of background radiations arriving at the HPGe detector open towards the upper hemisphere are presented in Fig. 4.

The integrals of these spectra, corrected for absorption in the detector housing and the detector dead layers, yield for the fluxes of these radiations the values of about 8000 photons/($m^2s \cdot 2\pi \cdot srad$) on the surface, and about 5000 photons/($m^2s \cdot 2\pi \cdot srad$) in the underground. An important property of these spectra is that the maximum of intensity at around 100 keV, as well as the dip of intensity at energy of about 40 keV, is an essential property of the true spectrum of the incoming radiations, and is only partly due to the drop of detection efficiency at these energies. It also seems that the steep increase of

intensity below the dip is an intrinsic property of all these spectra. We could not reach this region but there is ample evidence in background spectra taken at other places that this is also their ubiquitous property [7].

All these conclusions are corroborated by the detailed simulations of the experimental situations that might be held responsible for these spectra, using the Monte Carlo simulation packages Geant4 and CORSIKA [8,9]. Two possible contributions to these spectra were considered. The first is the contribution of environmental natural radioactivity via the scattering of discrete energy gamma rays off the air, the walls, and the ceiling, that thus produce the so-called skyshine radiation, which is known to be of spectral shape similar to that of our Fig. 4 [10]. For this simulation, the as realistic as possible distribution of radioactivities in the environment was assumed, in accord with relative

intensities of spectral lines in the experimental spectra. Configuration of the HPGe detector assembly was taken into account in detail, according to the manufacturer's technical data specifications. The result of this simulation of very low efficiency is, for the setup in the underground laboratory, presented in Fig. 5 (equivalent of 4000 h of single CPU time went into the production of this figure). Similarity of the continuous low-energy parts of the simulated and experimental spectra (Fig. 2) is obvious, but absolute intensities are, due to the unknown exact distribution of activities, difficult to compare.

On the other hand, the cosmic rays represent a source of background of constant and well-known parameters, and may consequently be used for absolute comparison of simulated and experimental background spectra. Fig. 6 presents the result of the simulation of all the contributions due to cosmic rays to the background spectrum in the underground (recent work by Solc et al. [11] does not pay special attention to the low-energy part of this spectrum). The composition and energy and momentum distributions of cosmic rays at the observation plane at the surface of the Earth were simulated by CORSIKA, while the interactions in the overburden soil and the detector spectrum, were obtained by Geant4 based simulation. It is seen that the shape of the simulated spectrum follows that of the experimental spectrum, though not as closely as the simulated skyshine spectrum. The portion of the

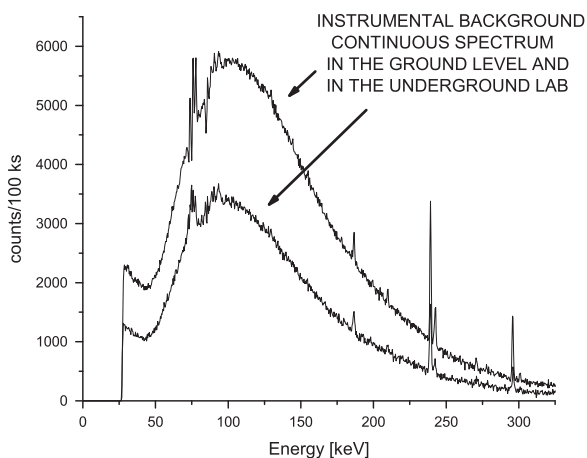


Fig. 4. Instrumental spectra of background radiations of the continuous spectrum arriving at the HPGe detector open towards the upper hemisphere in a ground-level laboratory (upper spectrum) and in an underground laboratory at 25 m.w.e. (lower spectrum). The peaks are residuals due to effects that are unessential here. Integral count rates in these spectra are 21 cps and 12 cps respectively.

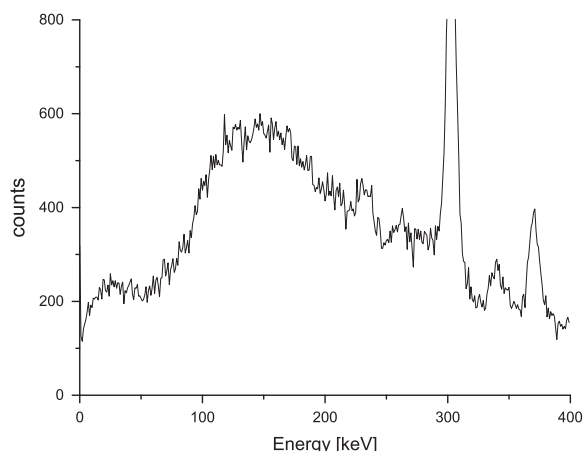


Fig. 5. The simulated "skyshine" radiation spectrum due to environmental radioactivity in the underground laboratory.

spectrum above the 2614 keV line, which is mostly due to cosmic rays, now allows for the normalization of the simulated spectrum to the experimental one. The integration of the thus normalized experimental and simulated spectra in the region of up to 500 keV shows that the cosmic rays at the depth of 25 m.w.e. contribute to the background radiations of the continuous spectrum only about one part in 250 of the scattered environmental radiations.

Finally, we performed the same procedure for the case of the detector setup in the ground level laboratory. Fig. 7 presents the simulated spectrum of cosmic ray contributions normalized to the high-energy portion of the experimental background spectrum for the detector situated in the ground level laboratory. Integration of the spectra shows that at the ground level the cosmic rays contribute to the low energy continuous background spectrum about 60 times less than the skyshine radiation.

Earlier studies implicitly offer controversial arguments as to the nature of this spectrum. For instance, the results of Tsutsumi et al. [4], which nicely reproduce the experimental background spectrum by the inclusion of natural radioactivities only, suggest that the contributions of skyshine radiation greatly overcome that of cosmic rays. On the other hand, the study by Semkow et al. [12], who measured the background spectrum of an unshielded detector in open space, demonstrates that the same shape of the continuum is obtained when only the genuine skyshine radiation,

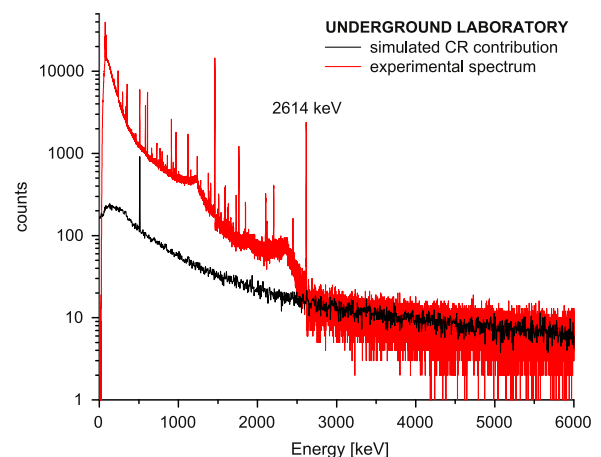


Fig. 6. The simulated contribution of all radiations of cosmic ray origin to the low-energy part of the background spectrum of the detector setup in the underground laboratory, normalized to the high-energy portion of the experimental background spectrum.

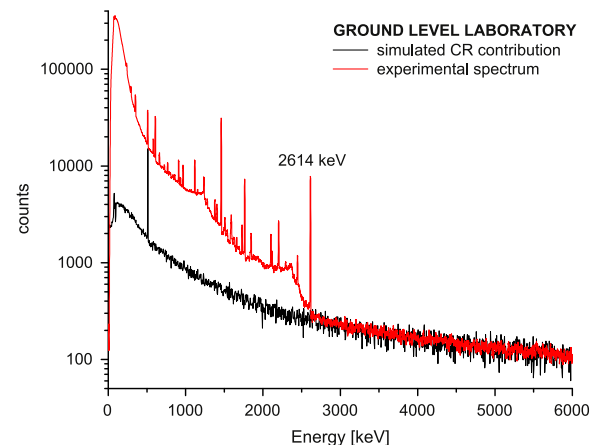


Fig. 7. The simulated contribution of all radiations of cosmic ray origin to the low-energy part of the background spectrum of the detector setup in the ground level laboratory, normalized to the high-energy portion of the experimental background spectrum.

scattered off the open air, is present, as when the detector is situated in the heavily walled building, what now speaks in favor of the non-negligible contribution of cosmic rays. In a comparatively recent study Mitchell et al. [13] find that the cosmic ray contribution constitutes about 1/10 of the skyshine contribution. In their case, however, the results may be prone to systematic error due to possibly high activity of the NaI spectrometer itself. On the basis of our findings we side with the results that support the view that skyshine radiation greatly dominates over the cosmic ray contributions.

4. Conclusion

We have established that the low-energy continuous part of background spectra of germanium detectors open to the upper hemisphere, that peaks around 100 keV, is in greatest part absorbed by 1 mm of lead and that can in a good approximation be considered as being due to the radiations of the similar true continuous spectrum arriving at the detector from the upper hemisphere. This holds true both in a ground level and in the underground laboratory at 25 m.w.e. The origin of this radiation is in the particular situations that we studied found to be predominantly of terrestrial origin. Relative contributions of the radiations of terrestrial and cosmic-ray origin to this spectrum would, however, greatly differ from place to place and from an environment to the other, depending on the quantity and distribution of

natural radioactivity in the surroundings of the detector, as well as on the geographic latitude and altitude, which determine the cosmic-ray contribution. It would in this respect be instructive to study the radiations of this continuous spectrum in largely different environments and at different spaces underground.

Acknowledgments

This work is supported by the Ministry for Education, Science and Technological Development of Serbia under the Project OI171002.

References

- [1] G. Heusser, *Annu. Rev. Nucl. Part. Sci.* 45 (1995) 543.
- [2] H. Neder, G. Heusser, M. Laubenstein, *Appl. Radiat. Isot.* 53 (2000) 191.
- [3] D. Mrda, et al., *Nucl. Instrum. Methods Phys. Res. Sect. A* 572 (2007) 739.
- [4] M. Tsutsumi, et al., *J. Nucl. Sci. Technol.* 38 (2001) 1109.
- [5] A. Dragić, et al., *Nucl. Technol. Radiat. Prot.* 26 (2011) 181 (arXiv:1203.4607).
- [6] A. Dragić, et al., *Nucl. Instrum. Methods Phys. Res. Sect. A* 591 (2008) 470.
- [7] D. Budjaš, et al., *Proceedings of the XIV International Baksan School, 2007*. INR RAS, Moscow 2008. ISBN 978-5-94274-055-9, pp. 233–238; arXiv:0812.0768.
- [8] S. Agostinelli, et al., *Nucl. Instrum. Methods Phys. Res. Sect. A* 506 (2003) 250.
- [9] D. Heck, et al., *Forsch. Karlsru. FZKA* 6019 (1998).
- [10] J. Swarup, *Nucl. Instrum. Methods* 172 (1980) 559.
- [11] J. Solc, P. Kovar, P. Dryak, *Radiat. Phys. Chem.* 95 (2014) 181.
- [12] T.M. Semkow, et al., *Appl. Radiat. Isot.* 57 (2002) 213.
- [13] A.I. Mitchell, R.T. Kouzes and J.D. Borgardt, *PNNL-18666* (2009).



ELSEVIER

Contents lists available at ScienceDirect

Applied Radiation and Isotopes

journal homepage: www.elsevier.com/locate/apradiso

Variations of gamma-ray background in the Belgrade shallow underground low-level laboratory

Radomir Banjanac^{1,*}, Aleksandar Dragić, Vladimir Udovičić, Dejan Joković, Dimitrije Maletić, Nikola Veselinović, Mihailo Savić

Institute of Physics, University of Belgrade, Belgrade 11080, Serbia

HIGHLIGHTS

- Time variability of Ge detector background was measured in two laboratories.
- Variations of cosmic ray intensity and radon concentration were tested.
- Advantage of an underground laboratory compared to a ground level one was proved.

ARTICLE INFO

Available online 1 December 2013

Keywords:

Underground low-level laboratory
Cosmic rays
Radon variability

ABSTRACT

During the last three years we investigated the variations of background simultaneously in two laboratories, the ground level (GLL) and the underground laboratory. The Forbush-like effect from March 2010 was observed in the GLL using a Ge detector and plastic veto scintillator. The underground plastic scintillator saw the same effect but the coincident veto spectrum did not detect the decrease of cosmic-ray intensity. Using a time series analysis of prominent post-radon lines, a significant radon daily variability was detected in the Ge detector background spectrum, but only in the GLL.

© 2013 Elsevier Ltd. All rights reserved.

1. Introduction

Any long and even short-term gamma-ray background measurement is subject to certain temporal variations due to time variability of two prominent contributors to background—cosmic-ray intensity and radon concentration. The duration of background measurements may be anything from one day to several months, depending on the wanted final statistical accuracy of the envisaged measurements. These measurements, however, yield only average values of the background, what in principle may lead to systematic errors in later measurements, especially of NORM samples.

Radon concentrations are known to vary considerably, depending on many parameters that determine this concentration in every particular case. This includes the deposition of radon progenies on the walls of lead castles and detectors themselves, what makes even the traditional radon suppression method by flushing the interior of the sample chamber with nitrogen potentially ineffective.

On the other side, effective protection of Ge detectors from cosmic-rays is provided by active veto shielding using convenient large area detectors, although all significant periodic and aperiodic variations of cosmic ray intensity can usually be neglected since contributions to background, apart from the annihilation line, lie in the continuum.

2. Description of the laboratories and equipment

The Belgrade underground low-level laboratory (UL), located at a depth of 25 m. w. e (meter water equivalent) is equipped with ventilation system which provides low radon concentration of 13 (5) Bq/m³, the mean value being obtained from more than two years long-term measurement. The UL is presented in more detail by Antanasijević et al. (1999), and the especially designed ventilation system for radon reduction in the laboratory has been described by Udovičić et al. (2009). This system consists of two “radon shields”—the passive and the active one. The passive shield consists of 1 mm thick aluminum foil which completely covers all the wall surfaces inside the laboratory, including floor and ceiling. It is hermetically sealed with a silicon sealant to prevent diffusion of radon from surrounding soil and concrete walls of the laboratory. As the active radon shield the laboratory is continuously ventilated with fresh air, filtered through one rough filter for dust elimination

* Corresponding author. Tel.: +381 11 3161274.

E-mail address: banjanac@ipb.ac.rs (R. Banjanac).

¹ Postal address: Pregrevica street, number 118, 11080 Belgrade, Serbia.

followed by active charcoal filters (cross-section of 60 cm × 60 cm, weight of 40 kg) for radon adsorption.

The UL has an area of 45 m² and volume of 135 m³ what required the rate of air inlet adjusted to 800 m³/h. This huge amount of fresh air contributes to greater temperature variations and the long-term mean value of temperature inside the UL is 19 (4)°C. On the other side the rate of air outlet (700 m³/h) was adjusted to get an overpressure of about 2 hPa over the atmospheric pressure, what prevents radon diffusion through eventual imperfections in the aluminum layer. The pressure buffer corridor to the laboratory (18 m²) ensures almost constant value of this overpressure. Relative humidity is controlled by a dehumidifier device, what provides that the relative humidity in the underground laboratory does not exceed 60%.

All the measurements presented in this work which were performed in the underground laboratory were performed in the ground level laboratory (GLL) as well. The GLL is air-conditioned and represents a typical ground level laboratory. This laboratory is situated in two joined standard transportation containers with iron sheet walls, but furnished with quality thermal insulation. The GLL has an area of 30 m² and volume of 75 m³. It is air-conditioned (average radon concentration of 50(30) Bq/m³).

The low-level background detector system in the UL includes an intrinsically low-radioactivity level Ge detector (35% relative efficiency, named Ge1) and a plastic veto scintillator (1 m², named PS1) situated coaxially above the Ge1 detector. Comparative background study is performed in the GLL which is equipped with a Ge detector (18% relative efficiency and not intrinsically low-radioactivity level, named Ge2) and a small plastic scintillator (0.125 m², named PS2) in veto position.

Radon monitoring inside the laboratories was performed by radon monitor, model RM1029 manufactured by Sun Nuclear Corporation, NRSB approval-code 31822. The device consists of two diffused junction photodiodes as a radon detector, and is furnished with sensors for temperature, barometric pressure and relative humidity. The user can set the measurement intervals from half an hour to 24 h. The device has no online option (direct access to data) but the data are stored in the internal memory of the device and transferred to the personal computer after the measurement interval. The data obtained from the radon monitor (RM) for the temporal variations of the radon concentrations over a long period of time enable the study of the short-term periodical variations simultaneously with Ge detectors (Bossew, 2005).

Two flash analog to digital converters (FADC), made by C.A.E.N (type N1728B), which sample at 10 ns intervals into 2¹⁴ channels were used to analyze spectra from Ge detectors. User-friendly software was developed to analyze the C.A.E.N data with the possibility to choose the integration time for further time-series analysis that correspond to integration time of the radon monitor.

3. Results and discussion

For routine measurements of NORM samples the simplest arrangement of a Ge detector system is required due to frequent samples exchanges.

As the emphasis was on realistic conditions of radon and cosmic-ray influences on the Ge background neither any additional radon suppression method nor the full (2 π coverage) veto arrangement were applied.

3.1. Cosmic-ray influence on the Ge detector background spectrum

The periodicities in cosmic-ray intensity variations (1-day and 27-days) are known to have small amplitudes. The Ge detectors can not see these variations neither in the annihilation line nor in the entire spectrum, mostly due to their small active area. Aperiodic

variations of cosmic-ray intensity have greater amplitudes like a Forbush effect which typically lasts for several days. During simultaneously background measurements using two veto shielded Ge detectors the most intensive cosmic-ray variation occurred in March 2010. The decrease of cosmic-ray intensity, which lasted about four days, was very similar to characteristic decrease during a real Forbush effect, hence this event is appointed as a Forbush-like effect. Characteristic variation (decrease) of cosmic-ray intensity remains after cosmic-ray data correction on pressure variation (real Forbush effect) or vanishes after this correction (Forbush-like effect). A Ge detector does not recognize the cause of these cosmic-ray variations but it can detect them. The Forbush-like effect from March 2010 was registered in both single PS2 and single PS1 detectors inside the GLL and the UL, respectively. The cosmic-ray intensity decrease was relatively small, about 4% in the GLL and 2.5% as measured in the UL. Even small, it seems that a certain variation in number of coincidences between PS2 and Ge2 was registered, and both spectra followed each other during four days (Fig. 1). Integration time in the time series of the coincidence spectrum was chosen to be 6 h to emphasize the similarity between the two spectra. Strictly speaking it is only the time variation of the well-defined annihilation line, mostly caused by cosmic-ray pair-production, that can reflect the cosmic-ray changes, but its count rate is too low. Similarly, statistics is poor even for the high-energy continuous part of the Ge spectrum. The coincidence veto spectrum in Fig. 1 has no energy cuts and includes all gamma-ray lines what corresponds to the real condition of background measurement without a priori selected energy intervals. The single cosmic-ray spectrum was not corrected for atmospheric pressure and temperature because this represents the realistic situation in a typical ground level laboratory, which is probably without a veto shield.

The big plastic scintillator PS1 inside the UL registered the same Forbush-like effect, but the coincidence spectrum does not show any corresponding changes, Fig. 2. At a depth of 25 m.w.e, the mean energy of cosmic-ray muons is about 5 GeV higher than that of ground level muons, which is why they feel all solar modulation effects far less than the cosmic-rays particles on the ground level.

3.2. Radon influence on the Ge detector background spectrum

The significance of the other time variable background component was tested in simultaneous measurements of radon concentration by RM and gamma-ray background by the Ge detector. Inside the sample chamber (SC) of the Ge detector, in the space between the lead shield and the detector, radon concentration is influenced by the radon distribution outside the SC, when the SC is

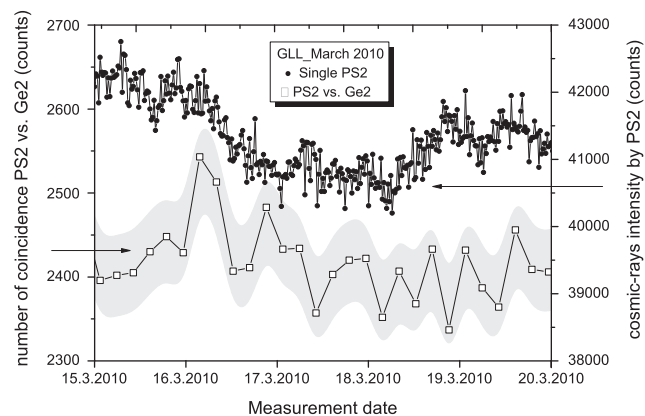


Fig. 1. Single cosmic-ray spectrum (circles) of PS2 and coincidence veto spectrum between PS2 and Ge2 (squares) inside the GLL during the Forbush-like effect in March 2010. The coincidence spectrum includes the error bars (1 σ -B-spline).

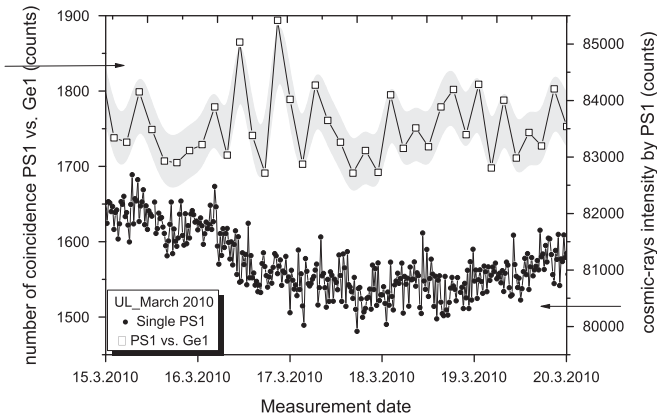


Fig. 2. Single cosmic-ray spectrum (circles) of PS1 and coincidence veto spectrum between PS1 and Ge1 (squares) inside the UL during the Forbush-like effect in March 2010. The coincidence spectrum includes the error bars (1σ -B-spline).

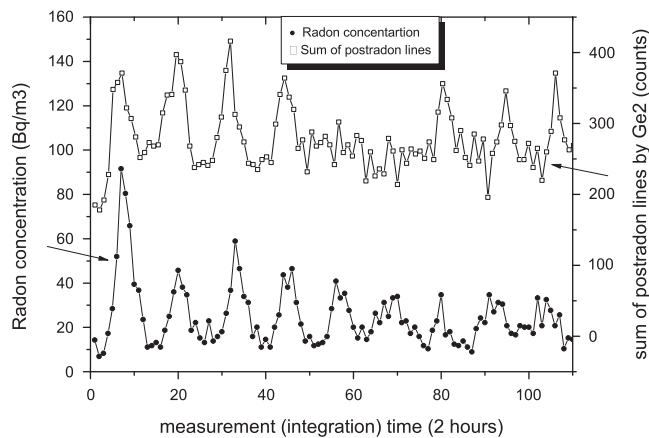


Fig. 3. Variability of radon concentration measured by RM inside the sampling chamber of the Ge2 detector (circles) and the sum of four post-radon lines (squares) measured by Ge2 inside the GLL.

not hermetically sealed. The Ge detector can see the radon daughters (^{214}Pb and ^{214}Bi) not only from the air inside SC but also from surface depositions on the detector and its passive shield.

Fig. 3 presents how the summed intensity of the four most prominent radon daughter lines (295.2 keV and 351.9 keV from ^{214}Pb , 609.3 keV and 1120.3 keV from ^{214}Bi) varies with time, as

seen by the small shielded Ge detector (Ge2) inside the air-conditioned GLL. This follows closely the readings of the radon monitor positioned inside the SC (air volume of 1 dm^3). Here, we used the summed intensity of post-radon lines since the detector is small, but for high-efficiency detectors every single line should manifest the same behavior.

The radon monitor recorded radon and atmospheric parameters readings every 2 h and the integration in the time series of post-radon lines was chosen accordingly. This is sufficient to show clearly the one-day radon periodicity (Fig. 3).

Inside the UL, the radon concentration is kept at the low value under stable atmospheric parameters. The variability of radon concentration in the fresh air on the ground level is maximally suppressed in the UL by the ventilation system. The value of the summed post-radon lines inside the UL is almost constant as well as is the radon concentration.

The issue of stability of the gamma-ray background requires special attention when low-level ^{226}Ra measurements are performed by Ge detectors due to radon variability in ground level laboratories and sampling chambers of Ge detectors. Even a small Ge detector can see significant changes of background, if the mean radon concentration in ambient air is of the order or above 10 Bq/m^3 and some kind of radon suppression method inside a sample chamber must be applied (Neumaier et al., 2009).

Acknowledgements

The authors wish to thank Prof. Ivan Aničin for constant interest and support.

This work is supported by the Ministry of Education, Science and Technological Development of Republic of Serbia under project OI 171002.

References

- Antanasijević, R., Aničin, I., Bikit, I., Banjanac, R., Dragić, A., Joksimović, D., Krmpotić, D., Udovičić, V., Vuković, J., 1999. Radon measurements during the building of a low-level laboratory. *Radiat. Meas.* 31, 371–374.
- Bossev, P., 2005. A very long-term HPGe-background gamma spectrum. *Appl. Radiat. Isot* 62, 635–644.
- Neumaier, S., Wojcik, M., Dombrowski, H., Arnold, D., 2009. Improvements of a low-level gamma-ray spectrometry system at the underground laboratory “UDO”. *Appl. Radiat. Isot* 67, 726–730.
- Udovičić, V., Grabež, B., Dragić, A., Banjanac, R., Joković, D., Panić, B., Joksimović, D., Puzović, J., Aničin, I., 2009. Radon problem in an underground low-level laboratory. *Radiat. Meas.* 44, 1009–1012.

CORRELATIVE AND MULTIVARIATE ANALYSIS OF INCREASED RADON CONCENTRATION IN UNDERGROUND LABORATORY

Dimitrije M. Maletić*, Vladimir I. Udovičić, Radomir M. Banjanac, Dejan R. Joković, Aleksandar L. Dragić, Nikola B. Veselinović and Jelena Filipović
Institute of Physics, University of Belgrade, Pregrevica 118, 11080 Zemun, Serbia

*Corresponding author: maletic@ipb.ac.rs

The results of analysis using correlative and multivariate methods, as developed for data analysis in high-energy physics and implemented in the Toolkit for Multivariate Analysis software package, of the relations of the variation of increased radon concentration with climate variables in shallow underground laboratory is presented. Multivariate regression analysis identified a number of multivariate methods which can give a good evaluation of increased radon concentrations based on climate variables. The use of the multivariate regression methods will enable the investigation of the relations of specific climate variable with increased radon concentrations by analysis of regression methods resulting in ‘mapped’ underlying functional behaviour of radon concentrations depending on a wide spectrum of climate variables.

INTRODUCTION

Radon is considered to be the main source of human exposure to natural radiation. By the World Health Organization, the greatest exposure is due to the inhalation of indoor short-lived decay products of radon⁽¹⁾. They contribute for about 55 % to the annual effective dose received by the general population. Indoor radon concentrations vary significantly due to a large number of factors. The focus of this work is only on climate parameters by investigating the possible correlation of short-term variations of climate parameters and radon concentrations.

Low Background Laboratory in the Institute of Physics, Belgrade consists of the Ground level laboratory and the Underground level (UL) laboratory, placed 12 m underground. Laboratory is described in details elsewhere⁽²⁾. During normal working operations, the UL laboratory has an operating ventilation system, which serves two purposes: first one is to exchange air in the laboratory with the outdoor one and the second purpose is to create over-pressurised air in the laboratory in order to help stopping the radon incursion into the laboratory. The ventilation system is constantly switched on, but in some special cases, for a short period of time, like in the case of the study presented in this work, the ventilation system was switched off. In the case of non-over-pressurised and no air exchange conditions in the UL, there is an increase of the radon concentrations. This is a very good condition to look into relations of climate variables and increased radon concentrations.

The goal in this study is a use of the multivariate analysis approach in finding the relations of climate variables and increased radon concentrations in the UL. The first tests of correlative and multivariate

analysis of variations of indoor radon concentrations with climate variables were published elsewhere⁽³⁾.

When the ventilation system in the UL is switched off, radon concentrations increase rapidly, indicated by starting activities from $<20 \text{ Bq m}^{-3}$. After a few days, the rapid increase of radon concentrations becomes steady, with values of radon activities reaching as much as 900 Bq m^{-3} , and also, the variability of radon concentrations is much more pronounced. Additional interesting property of the conditions in the UL, while taking into account radon activity measurements, is that during the measurement time, the laboratory is practically not accessed, so air exchanges cannot explain the changes of radon concentrations. This fact alone will improve the chances of finding the stronger correlation of climate variables with radon concentrations. Radon tends to concentrate in enclosed spaces such as underground mines or houses. Soil gas infiltration is recognised as the most important source of residential radon⁽¹⁾. Conditions in the UL with the ventilation system switched off are a close match for such enclosed spaces.

The search for an appropriate analysis method resulted in the selection of multivariate methods. Many multivariate methods and algorithms for classification and regression are already integrated into the analysis framework ROOT⁽⁴⁾, more specifically, into the Toolkit for Multivariate Analysis (TMVA)⁽⁵⁾.

In the present analysis 12 variables based on outdoor climate variables were used. The outdoor climate variables are temperature, pressure and humidity, the temperatures of ground at two depths of 20 and 50 cm and wind speed. The additional variables are atmospheric pressure, air temperature and humidity measured with a radonmeter measuring system and the differences of

these values with outdoor measured ones. The analysis starts with comparing the multivariate methods in order to find out which one is best suited for classification (division) of radon concentrations into what would be considered acceptable and what would be considered increased concentration in UL.

EXPERIMENTAL DATA

For measurement of radon concentrations, air temperature, atmospheric pressure and humidity in the UL the SN1029 radon monitor (manufactured by the Sun Nuclear Corporation, NRSB approval-code 31822) is used. This device consists of two diffused junction photodiodes as a radon detector. The radon monitor was used for measuring radon concentration, air temperature, atmospheric pressure and humidity at 2-h intervals during the September and October of 2013.

RESULTS

The results of MVA classification and regression methods are commented.

The start of MVA method-based analysis is done by using the events consisting of one set of all climate variables and the corresponding measured radon activity. For classification methods, all events are split into signal events—a set of events where the measured radon activity is greater than some predefined value (200 Bq m^{-3}) and background ones, the set of events with values less than the predefined value. After the process of training of MVA methods, comparison of their performance in properly splitting the whole set of events into signal and background events is performed. The graph presenting the ‘receiver operating characteristic’ (ROC) for each multivariate method (Figure 1) may be considered as the most indicative in comparing the different methods used for classification of radon concentrations using climate variables. On this graph one can read the dependence of background rejection on signal efficiency. The best method is the one that holds the maximum value of background

rejection for highest signal efficiency, i.e. the best method has an ROC curve closest to the upper right corner on the graph presented in Figure 1.

From Figure 1 it can be seen that the selected 12 MVA methods can very efficiently classify all events into signal and background ones. For all MVA classifiers, the signal efficiency is $>85\%$ for practically 100% background rejection. The best performing MVA methods are BDT and MVA methods. The response function of the best classifier is shown in Figure 2. From this figure it can be seen that the signal and background events are separated very good.

Classifiers can be very useful, especially from a radiation protection aspect in connection with radon measurements. In radon measurements one can use either long-term measurements or expensive short-term ones. This way, by training the classifiers, it will be achievable to predict short-term variations, which are considered as increased radon activity ($>200 \text{ Bq m}^{-3}$), which will otherwise be blended (invisible) in long-term measurements.

Regression

The next step was to try to get more information from MVA methods by trying to ‘map’ a functional behaviour of radon vs. input climate variables. This is done by using the MVA regression methods. During the tests, the observation was made that not all MVA methods give good evaluation of radon concentrations. In Figure 3 the authors present the initial and corrected values of evaluation of radon concentration for one of the MVA methods.

The distribution of measured radon activities and MVA regression evaluations is shown in Figure 4. From this plot, it is clear that the distribution of MVA evaluations are in good agreement with the experimental values. This also means that it is now possible to calculate the errors of MVA evaluation which is presented in Figure 5. One can see that for the high values of radon concentrations, such as in the UL, the

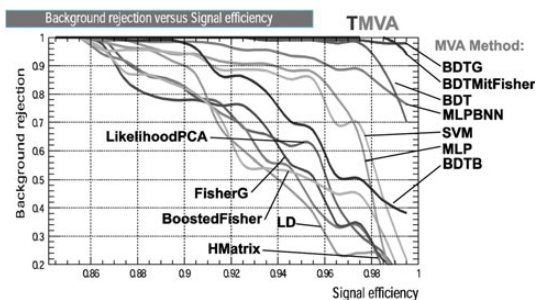


Figure 1. ROC for all multivariate methods used for classification of radon concentration using climate variables.

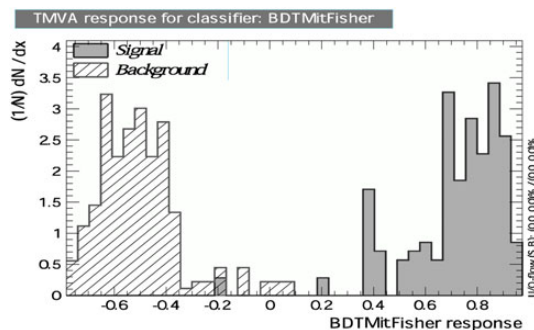


Figure 2. TMVA response for classifier for best performing MVA classifier, a method based on boosted decision trees.

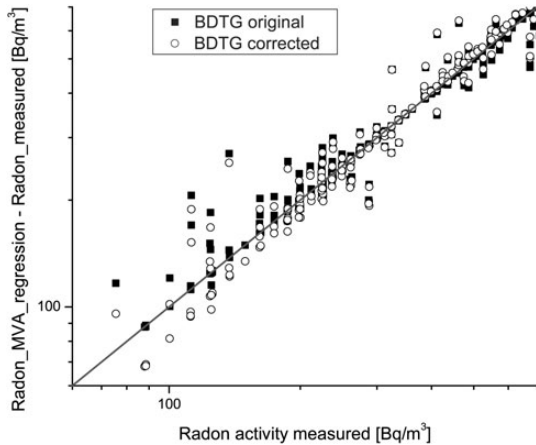


Figure 3. Initial and corrected evaluations of radon activity. After corrections, the difference between measured and corrected evaluation is closer to 0 for a whole range of radon activities.

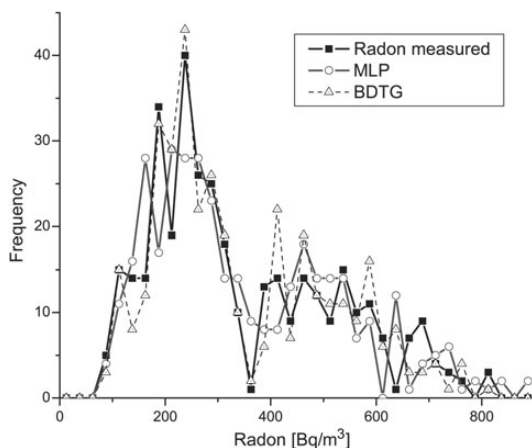


Figure 4. Distribution of the values of radon activity for measured (radon) and MVA regression methods' evaluation values (MLP and DBT methods).

evaluation is better. The error of evaluation is estimated to be $\sim 6\%$.

CONCLUSION

The results of analysis of relation of increased radon concentrations in UL and climate variables using multivariate classification and regression methods, as developed for data analysis in high-energy physics and implemented in the TMVA software package are presented. These methods enabled the investigation of the relations of a wide spectrum of climate variables with increased radon concentrations in the UL. Multivariate

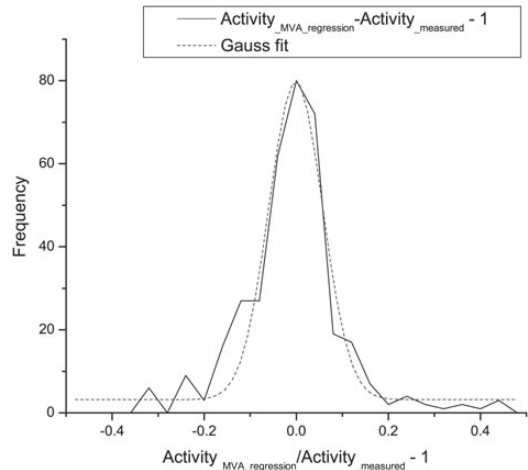


Figure 5. Calculation of relative variations of MVA evaluated values from measured radon activities.

regression analysis gives a possible choice of several good multivariate methods which can be used for evaluation of increased radon concentration in the UL, with input events based on climate variables. The analysis performed showed that there is a significant relation of climate variables and increased radon concentrations in the UL. As a result of the analysis presented in this work, there is now MVA regression 'mapped' underlying functional behaviour of radon concentrations depending on a wide spectrum of climate variables. Having 'mapped' the functional behaviour of radon concentrations enables analysis with the possibility of exclusion of the inter-correlations of climate variables, which presents one with a new advantage in the analysis of radon concentration relations with climate variables.

ACKNOWLEDGEMENT

This paper was realized within the project "Nuclear Methods Research of Rare Processes and Cosmic Rays" (No. OI171002) financed by the Ministry of Education and Science of the Republic of Serbia (2011–2014).

REFERENCES

1. WHO. *Handbook on Indoor Radon. A Public Health Perspective*. World Health Organisation (2006).
2. Dragić, A., Udovičić, V., Banjanac, R., Joković, D., Maletić, D., Veselinović, N., Savić, M., Puzović, J. and Aničin, I. V. *The new setup in the Belgrade low-level and cosmic-ray laboratory*. Nucl. Technol. Radiat. Prot. **26**, 181–192 (2011).
3. Maletić, D. M., Udovičić, V. I., Banjanac, R. M., Joković, D. R., Dragić, A. L., Veselinović, N. B. and

RADON CONCENTRATION IN UNDERGROUND LABORATORY

- Filipović, J. Z. *Comparison of multivariate classification and regression methods for the indoor radon measurements*. Nucl. Technol. Radiat. Prot. **29**(1), 17–23 (2014).
4. Brun, R. and Rademakers, F. *ROOT—an object oriented data analysis framework*. Nucl. Inst. Methods Phys. Res. A **389**, 81 (1997).
5. Hoecker, A., Speckmayer, P., Stelzer, J., Therhaag, J., von Toerne, E. and Voss, H. *TMVA—toolkit for multivariate data analysis*. In: PoS ACAT 040, XI International Workshop on Advanced Computing and Analysis Techniques in Physics Research, April 23-27 2007, Amsterdam, the Netherlands (2007). arXiv:physics/070303.

DAILY AND SEASONAL RADON VARIABILITY IN THE UNDERGROUND LOW-BACKGROUND LABORATORY IN BELGRADE, SERBIA

V. Udovičić*, J. Filipović, A. Dragić, R. Banjanac, D. Joković, D. Maletić, B. Grabež and N. Veselinović
Institute of Physics Belgrade, University of Belgrade, Pregrevica 118, Belgrade 11080, Serbia

*Corresponding author: udovicic@ipb.ac.rs

Radon time-series analysis, based on the short-term indoor radon measurements performed worldwide, shows two main periodicity: daily and seasonal. The information obtained from time series of the measured radon values is the results of the complex radon dynamics that arises from the influence of the large number of different parameters (the state of the indoor atmosphere (temperature, pressure and relative humidity, aerosol concentration), the exchange rate between indoor and outdoor air and so on). In this paper we considered daily radon variability in the underground low-background laboratory in Belgrade, Serbia. The results are originated from the radon time-series analysis based on the 3 y of the continuous short-term indoor radon measurements. At the same time, we obtained the time series of the temperature, pressure and relative humidity in the laboratory. We also tried to find the correlation between different time series.

INTRODUCTION

The Low-Background Laboratory for Nuclear Physics at the Institute of Physics in Belgrade is a shallow underground laboratory. The experiments and routine measurements in the underground Low-Background Laboratory for Nuclear Physics require low levels of radon concentration with minimum temporal variations^(1, 2). Unfortunately, in the underground environments, radon level is extremely high (up to several kBq m⁻³) and temporal variations, especially the daily amplitude, might be very intensive. The radon behaviour in such specific environments is the subject of intensive research. This is confirmed by a number of scientific articles published in last years^(3–7). The radon time-series analysis, based on the 3 y of the short-term radon measurements, has shown that there are two periodicity at 1 d and 1 y. Besides the fact that the laboratory has the system for radon reduction⁽⁸⁾, there is a significant 1-d period which is the main subject of this work. The physical origin of the obtained daily variation in the underground laboratory is not straightforward. The daily variability shows the best correlation with the difference of external and internal temperature.

EXPERIMENT

The continuous short-term radon measurements were performed in the underground low-level laboratory in Belgrade. The device for the performed short-term radon measurements is SN1029 radon monitor (manufactured by the Sun Nuclear Corporation, NRSB approval-code 31822) with the following characteristics: the measurement range from 1 Bq m⁻³ to 99.99 kBq m⁻³, accuracy equal to $\pm 25\%$, sensitivity of 0.16 counts hour per Bq m⁻³. With these characteristics,

SN1029 radon monitor is defined as a high-sensitivity passive instrument for the short-term radon measurements and it is an optimal solution for radon monitoring in the underground laboratory. The measurements covered period from June 2008 to November 2011. The device has sensors for temperature, barometric pressure and relative humidity. The sampling time was set to 2 h. The data are stored in the internal memory of the device and then transferred to the personal computer. The data obtained from the radon monitor for the temporal variations in the radon concentrations over a long period of time enable the study of the short-term periodical variations. The series taken during period of 3 y were spectrally analysed by the Lomb-Scargle periodogram method. After the 2 y, after start of the measurements, the data were analysed and the obtained results were published⁽⁹⁾.

RESULTS AND DISCUSSION

The descriptive statistics on the raw radon data are shown in Table 1. The radon data from radon monitor device SN1029 for the period of 3 y are spectrally analysed. The Lomb-Scargle periodogram analysis method has been used in spectral analysis of radon time series. With the better statistics compared with the previous results⁽⁹⁾, the obtained periodogram show two periodicity, on the 1 d and 1 y.

In Figure 1, the obtained radon and the difference between outdoor and indoor temperature time series during one calendar year are presented. The results show similar behaviour of the two quantities. Figure 2 shows the correlation between radon and temperature differences.

It is relatively a good correlation and presents the results that may correspond to the previous results⁽³⁾. Also, the temperature profile defined two season, cold (winter) and hot (summer). The winter time covered the

Table 1. Descriptive statistics on the raw radon data.

	<i>n</i>	Mean	SD	Median
Radon concentration (Bq m ⁻³)	10 090	13.75	9.86	12.4

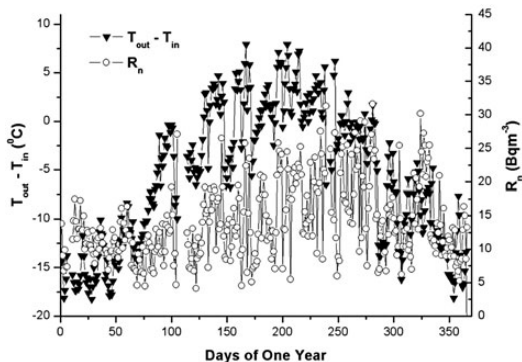


Figure 1. The radon and difference between outdoor and indoor temperature time series during one calendar year.

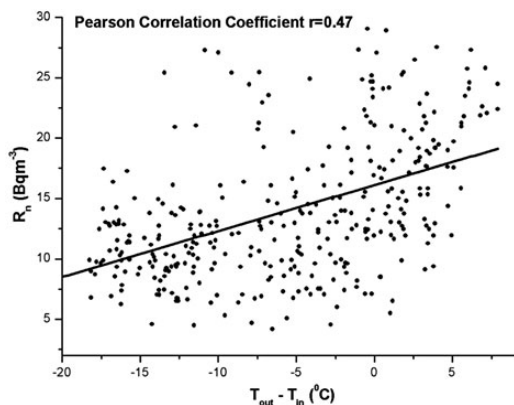


Figure 2. The correlation between radon and temperature differences.

period from December to June and the summer time is the period from June to November. According to that fact, the radon behaviour is presented in Figure 3.

The maximum radon concentration is in the August and the minimum value is in the March. The daily radon variability also has the interesting characteristic.

In Figure 4, the daily radon and the difference between outdoor and indoor temperature variability during 1 d are presented. Two quantities are shifted in phase. This means that, when the difference between the exterior and interior temperature decrease (between 4 and 13 h), the radon level decreases (between 6 and 16 h). The daily radon variability is

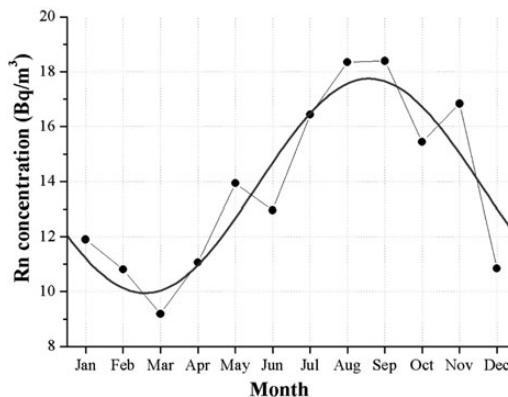


Figure 3. The radon monthly variability in the one calendar year.

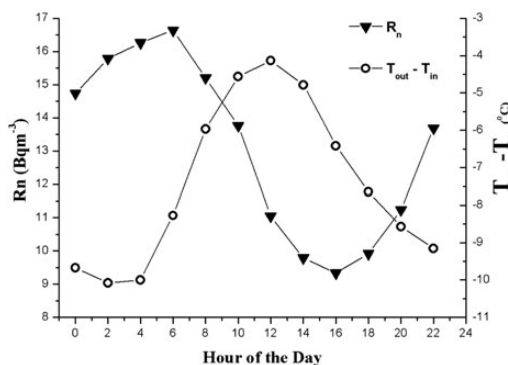


Figure 4. The daily radon and difference between outdoor and indoor temperature variability during one day.

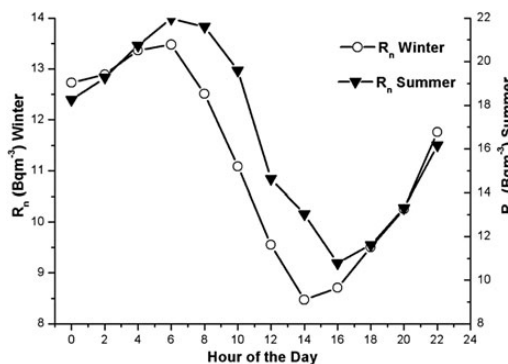


Figure 5. The daily radon variability during two periods, winter and summer.

also analysed due to different periods of the year, winter and summer.

The daily radon variability during two periods, winter and summer, is presented in Figure 5. The positions of

the peaks are almost the same, but in the summer, the daily variability is more intensive compared with the winter period.

CONCLUSIONS

It has been shown that the radon behaviour in the underground low-level laboratory in Belgrade has the similar characteristics as in the other underground environment (caves, mines, boreholes and so on), because it has the same source and the places are completely surrounded with the soil. It is also not quite understood the influence of the meteorological parameters on the radon variability. In this work, the correlation between daily radon variation and the difference of external and internal temperature in the UL is pointed out. The further theoretical and experimental research work is necessary to explain physical mechanisms by which the temperature gradient is correlated with radon variations in the underground environments.

FUNDING

This work is supported by the Ministry of Education, Science and Technological Development of Republic of Serbia under project number III 43002.

REFERENCES

1. Dragić, A., Joković, D., Banjanac, R., Udovičić, V., Panić, B., Puzović, J. and Aničin, I. *Measurement of cosmic ray muon flux in the Belgrade ground level and underground laboratories*. Nucl. Instrum. Methods Phys. Res. **A591**, 470–475 (2008).
2. Dragić, A., Udovičić, V., Banjanac, R., Joković, D., Maletić, D., Veselinović, N., Savić, M., Puzović, J. and Aničin, I. *The new set-up in the Belgrade low-level and cosmic-ray laboratory*. Nucl. Technol. Radiat. Protect. **XXVI**(3), 181–192 (2011).
3. Choubey, V. M., Arora, B. R., Barbosa, S. M., Kumar, N. and Kamra, L. *Seasonal and daily variation of radon at 10 m depth in borehole, Garhwal Lesser Himalaya, India*. Appl. Radiat. Isotopes. **69**(7), 1070–1078 (2011).
4. Viñas, R., Eff-Darwich, A., Soler, V., Martín-Luis, M. C., Quesada, M. L. and de la Nuez, J. *Processing of radon time series in underground environments: Implications for volcanic surveillance in the island of Tenerife, Canary Islands, Spain*. Radiat. Meas. **42**, 101–115 (2007).
5. Barbosa, S. M., Zafir, H., Malik, U. and Piatibratova, O. *Multiyear to daily radon variability from continuous monitoring at the Amram tunnel, southern Israel*. Geophys. J. Int. **182**, 829–842 (2010).
6. Marušiaková, M. and Hulka, J. *Estimates of the annual average indoor radon concentration in Teleci in the Czech Republic*. Radiat. Prot. Dosim. **145**(2–3), 145–149 (2011).
7. Vaupotič, J. *Nanosize radon short-lived decay products in the air of the Postojna Cave*. Sci. Total Environ. **393**(1), 27–38 (2008).
8. Udovičić, V., Grabež, B., Dragić, A., Banjanac, R., Joković, D., Panić, B., Joksimović, D., Puzović, J. and Aničin, I. *Radon problem in an underground low-level laboratory*. Radiat. Meas. **44**, 1009–1012 (2009).
9. Udovičić, V., Aničin, I., Joković, D., Dragić, A., Banjanac, R., Grabež, B. and Veselinović, N. *Radon time-series analysis in the underground low-level laboratory in Belgrade, Serbia*. Radiat. Prot. Dosim. **145**(2–3), 155–158 (2011).

Representation of Radiative Strength Functions within a Practical Model of Cascade Gamma Decay

D. C. Vu^{1),2)*}, A. M. Sukhovej^{1)**}, L. V. Mitsyna^{1)***}, Sh. Zeinalov^{1)****},
N. Jovancevic^{3)*****}, D. Knezevic^{3)*****}, M. Krmar^{3)*****}, and A. Dragic^{4)*****}

Received June 14, 2016; in final form, August 24, 2016

Abstract—A practical model developed at the Joint Institute for Nuclear Research (JINR, Dubna) in order to describe the cascade gamma decay of neutron resonances makes it possible to determine simultaneously, from an approximation of the intensities of two-step cascades, parameters of nuclear level densities and partial widths with respect to the emission of nuclear-reaction products. The number of the phenomenological ideas used is minimized in the model version considered in the present study. An analysis of new results confirms what was obtained earlier for the dependence of dynamics of the interaction of fermion and boson nuclear states on the nuclear shape. From the ratio of the level densities for excitations of the vibrational and quasiparticle types, it also follows that this interaction manifests itself in the region around the neutron binding energy and is probably different in nuclei that have different parities of nucleons.

DOI: 10.1134/S1063778817020260

INTRODUCTION

At any excitation energy, parameters of the cascade gamma decay of an arbitrary high-lying nuclear level are determined exclusively by the level density ρ and the partial widths Γ with respect to electric and magnetic dipole transitions. The intensity of cascades that involve purely quadrupole transitions is negligible at nuclear-excitation energies above several MeV units. For either parity, the spins of levels that are excited by primary transitions lie in the range of $2 \leq \Delta J \leq 4$. Investigation of the gamma-decay process is of interest, first of all, for studying the dynamics of interaction of fermion and boson states

of nuclear matter. Reliable information on the subject is also necessary for more precisely describing the fission process. According to [1], the distribution of the energy between excited fission fragments depends on their level densities. However, the level densities calculated on the basis of existing models [2] deviate strongly from the most recent experimental data [3]. The reason behind this discrepancy may only be that experiments that detect the cascade of reaction products provide more information than any procedure for obtaining spectra of single gamma rays or nucleon products without employing a coincidence mode.

Since one-step gamma-ray spectra and reaction cross sections depend on the product $\rho \times \Gamma$, it is absolutely impossible to determine simultaneously reliable values of ρ and Γ from such data. This was done only in experiments that study cascades involving two sequential gamma transitions whose intensities carry information both about the nuclear excitation energy and about the energy of the emitted photon (nucleon). Only such experiments may reduce the total error in the values determined for ρ and Γ to a few tens of percent.

Since all individual levels and probabilities for transitions between them cannot be determined with the aid of modern spectrometric detectors, information about nuclear superfluidity is extractable from indirect experiments exclusively. In that case, both the level density ρ and the partial widths Γ are unknown functions in any nucleus.

¹⁾Joint Institute for Nuclear Research, ul. Joliot-Curie 6, Dubna, Moscow oblast, 141980 Russia.

²⁾Institute of Physics, Vietnam Academy of Science and Technology, 10 Dao Tan, Ba Dinh, Ha Noi, Viet Nam.

³⁾Department of Physics, Faculty of Sciences, University of Novi Sad, Trg Dositeja Obradovića 3, 21000 Novi Sad, Republic of Serbia.

⁴⁾Institute of Physics Belgrade, Pregrevica 118, 11080 Zemun, Republic of Serbia.

*E-mail: vuconghnue@gmail.com

**E-mail: sukhovej@nf.jinr.ru

***E-mail: mitsyna@nf.jinr.ru

****E-mail: zeinal@nf.jinr.ru

*****E-mail: nikola.jovancevic@df.uns.ac.rs

*****E-mail: david.knezevic@df.uns.ac.rs

*****E-mail: krmar@df.uns.ac.rs

*****E-mail: dragic@ipb.ac.rs

1. POTENTIAL OF THE PRESENT-DAY EXPERIMENT AND OF ITS MODEL SIMULATION

At a fixed primary-transition energy E_1 , the intensities $I_{\gamma\gamma}(E_1)$ of two-step cascades connecting a neutron resonance (or some other compound state) λ and some group f of low-lying nuclear levels and proceeding through arbitrary intermediate levels i are described by the set of equations

$$I_{\gamma\gamma}(E_1) = \sum_{\lambda,f} \sum_i \frac{\Gamma_{\lambda i} \Gamma_{if}}{\Gamma_{\lambda} \Gamma_i} \quad (1)$$

$$= \sum_{\lambda,f} \frac{\Gamma_{\lambda i}}{\langle \Gamma_{\lambda i} \rangle m_{\lambda i}} n_{\lambda i} \frac{\Gamma_{if}}{\langle \Gamma_{if} \rangle m_{if}},$$

where $m_{\lambda i}$ is the number of levels excited by primary transitions in the ranges between the energy of the initial level λ and the energy of an intermediate level i , m_{if} is the number of levels excited by secondary gamma transitions in the ranges between the energy of an intermediate level i and the energy of the final level f , and $n_{\lambda i}$ is the number of intermediate levels of cascades in narrow ranges of primary-transition energies. From the set of Eqs. (1), which relates the unknown number of levels, n (or m), to unknown partial widths, Γ , one determines the set of parameters p and q of the model functions $\rho = f(p_1, p_2, \dots)$ and $\Gamma = \varphi(q_1, q_2, \dots)$ with an error originating from the inconsistency of the existing theoretical ideas with experimental results. The analysis performed earlier in [4] revealed that one can even include in the model the possible relation between the values of the level density and strength functions in some narrow excitation-energy interval. Thus, we see that, at any densities of the levels λ and i , one can determine parameters of the sought functions ρ and Γ from the spectra of two-step cascades.

The analysis in [3] of experimental data on cascade intensities over the mass-number range of $28 \leq A \leq 200$ showed that experimental level densities could not be reproduced to an experimental precision on the basis of models that ignore the existence of bosonic branches of nuclear-matter states (on the basis of those where the inclusion of this branch was insufficiently correct).

The procedure developed by our group does not require invoking hypotheses not tested experimentally (such as the Porter–Thomas hypothesis [5] on the distribution of widths with respect to the emission of nuclear-reaction products, the Axel–Brink hypothesis [6, 7] that radiative-width values are independent of the energy of an excited level, or the Bohr–Mottelson hypothesis [8] on the correctness of employing the optical model of the nucleus to determine the probability for the emission of nucleon reaction

products). The Dubna model of the cascade gamma decay of compound nuclear states whose excitation energies lie in the range of $E_{\text{ex}} \approx 5\text{--}10$ MeV is based on a model of the density of n -quasiparticle levels, the balance of the changes in the entropy and energy of quasiparticle levels [2, 9, 10], and tested ideas about the shape of the energy dependence of radiative strength functions.

The systematic error of any experimental procedure for obtaining the functions ρ and Γ is always determined by large coefficients of the transfer of the errors in the measured spectrum, δS , or in the reaction cross section, $\delta\sigma$, to the errors $\delta\rho$ and $\delta\Gamma$ in the parameters being determined. The error in question may grow sizably upon the increase in the energy of the level that decays in the reaction under study. This error and the direction in which the model concepts of $\rho = f(p_1, p_2, \dots)$ and $\Gamma = \varphi(q_1, q_2, \dots)$ should be corrected can only be estimated by comparing various versions of the description of the level densities and radiative strength functions. For example, a comparison of several versions of our practical model [3, 11, 12] made it possible to reveal that the rate of the change in the vibrational level density specified phenomenologically in [11, 12] is determined partly or fully by the pairing energy Δ_0 of the last nucleon in the nucleus being considered. In all of the implemented versions of the practical model, the accuracy of the approximation of intensities remains unimpaired as one gradually reduces the number of fitted parameters; therefore, we do not present here the ultimate approximations of the spectra $I_{\gamma\gamma}$.

In contrast to what was done in [3], the proposed model version employs, instead of two parameters (the rate of the change in the nuclear entropy and the rate of the change in the energy of quasiparticle states) in the phenomenological expression for the coefficient of the collective level-density enhancement, C_{coll} [3, 10], only one fitted parameter, E_u ; that is,

$$C_{\text{coll}} = A_l \exp(\sqrt{(E_{\text{ex}} - U_l)/E_u}) - (E_{\text{ex}} - U_l)/E_u + \beta, \quad (2)$$

where A_l are the parameters of the vibrational level density above the point of break of each l th Cooper pair and U_l are the energy thresholds for the break of Cooper pairs. For deformed nuclei, the parameter $\beta \geq 1$ may differ from unity.

The effect of shell inhomogeneities in the single-particle spectrum [2, 10] was taken into account in terms of the excitation-energy-dependent level-density parameter a ,

$$a(A, E_{\text{ex}}) = \tilde{a}(1 + ((1 - \exp(\gamma E_{\text{ex}}))\delta E/E_{\text{ex}})), \quad (3)$$

or in terms of the parameter $g = 6a/\pi^2$ for n -quasiparticle states in the vicinity of the Fermi surface [9]. The asymptotic value of $\tilde{a} = 0.114A + 0.162A^{2/3}$ and the value of $\gamma = 0.054$ were taken from [2, 10]. The shell correction δE calculated [2] on the basis of mass-defect data within the liquid-drop model of the nucleus was slightly modified for the mean spacing between resonances, D_λ , to remain unchanged [3].

2. ENERGY DEPENDENCE OF STRENGTH FUNCTIONS

In the model of cascade gamma decay, the shape of the energy dependence of partial radiative widths should be specified to a high degree of precision for any excited levels and energies of emitted gamma rays.

On the basis of existing models, the strength function for a nucleus of mass number A is defined as $k = \Gamma/(A^{2/3}E_\gamma^3 D_\lambda)$, where E_γ is the gamma-transition energy. The absolute value of the sum of radiative widths for primary $E1$ and $M1$ cascade transitions (total radiative width) can usually be determined from measured reaction cross sections. The most probable form of this sum can be obtained from purely phenomenological considerations or from an extrapolation of some theoretical models to the excitation-energy range of $E_d < E_{\text{ex}} < B_n$ {here, E_d is the point of transition in Eq. (1) from known levels [13] to the level-density concept, while B_n is the neutron binding energy in the nucleus}.

It was found experimentally that a precise reproduction of cascade intensities leads to supplementing the energy dependence of the function $k(E1, E_\gamma) + k(M1, E_\gamma)$ with several peaks that have various areas, positions of the center, and shape asymmetries. But the main term in this energy dependence can be represented by a smooth distribution of strength functions from models of the type in [14] but with allowance for additional parameters whose variation generates a set of functions describing $E1$ and $M1$ transitions and taking values over a broad region (see [11, 12]). The shape of the extra peaks can be revealed and specified only empirically. For example, a description of each such peak in terms of two exponentials (as in an earlier version of our model [3, 11, 12]) is convenient in solving the set of nonlinear equations in (1), even though these exponentials are not used in the model formalism based on theoretical concepts [2].

In order to describe the shape of the peaks in the $E1$ and $M1$ strength functions, Breit–Wigner or Lorentzian functions are used. An asymmetric Breit–Wigner function was applied in theoretically analyzing the regularities of fragmentation of quasiparticle

states for their various positions with respect to the Fermi surface [15]. In employing this function, we were unfortunately unable to choose a set of parameters that would be appropriate for approximating the most probable values of $\rho = f(p_1, p_2, \dots)$ and $\Gamma = \varphi(q_1, q_2, \dots)$.

The use of an asymmetric Lorentzian curve in describing local peaks in the strength functions proved to be more straightforward. For each i th peak its parameters, such as the position of the center, E_i ; the width, Γ_i ; the amplitude, W_i ; and the asymmetry parameter, $\alpha_i = CT^2$, are similar to their counterparts in the model employed in [14]. The expression $\alpha_i(E_\gamma - E_i)/E_\gamma$ increases linearly as the excitation energy $B_n - E_i$ grows from zero at the center of the respective peak to the maximum value at B_n and decreases as the nuclear excitation energy becomes lower. Thus, the peaks of the $E1$ and $M1$ strength functions are represented in the form

$$k = W \frac{(E_\gamma^2 + (\alpha_i(E_i - E_\gamma)/E_\gamma))\Gamma_i^2}{(E_\gamma^2 - E_i^2)^2 + E_\gamma^2\Gamma_i^2}. \quad (4)$$

In approximating Lorentzian functions that describe the decay of a highly excited level, the convergence of the respective iterative process sharply becomes poorer, which creates a serious problem. Upon fitting all parameters of the functions in Eq. (4), the widths Γ_i decrease indefinitely within some segments of the iterative-process trajectory.

The need for taking into account the effect of a sharp local change in the level density on strength functions was revealed at the stage of a model-free determination of the set of random functions ρ and Γ [16]. For this purpose, the strength functions to be determined were multiplied in [4] by the ratio

$$M = \rho_{\text{mod}}/\rho_{\text{exp}}, \quad (5)$$

where ρ_{exp} is the best approximation for the iteration being considered and ρ_{mod} is a smooth model dependence that reproduces both the density of neutron resonances and the cumulative sum of known levels for which E_{ex} is lower than E_d . In order to determine ρ_{mod} , we have chosen the back-shifted Fermi gas model. In the present version of our analysis, we have employed the constraint $1 \leq \rho_{\text{mod}}/\rho_{\text{exp}} \leq 10$ [11].

3. RESULTS

Difficulties in solving the set of Eqs. (1) arise both because of a strong nonlinearity of the sought functions ρ and Γ and because of their anticorrelation. There is a probability for arriving at a spurious minimum of χ^2 , and this may lead to a sizable systematic error in the resulting values of ρ and Γ .

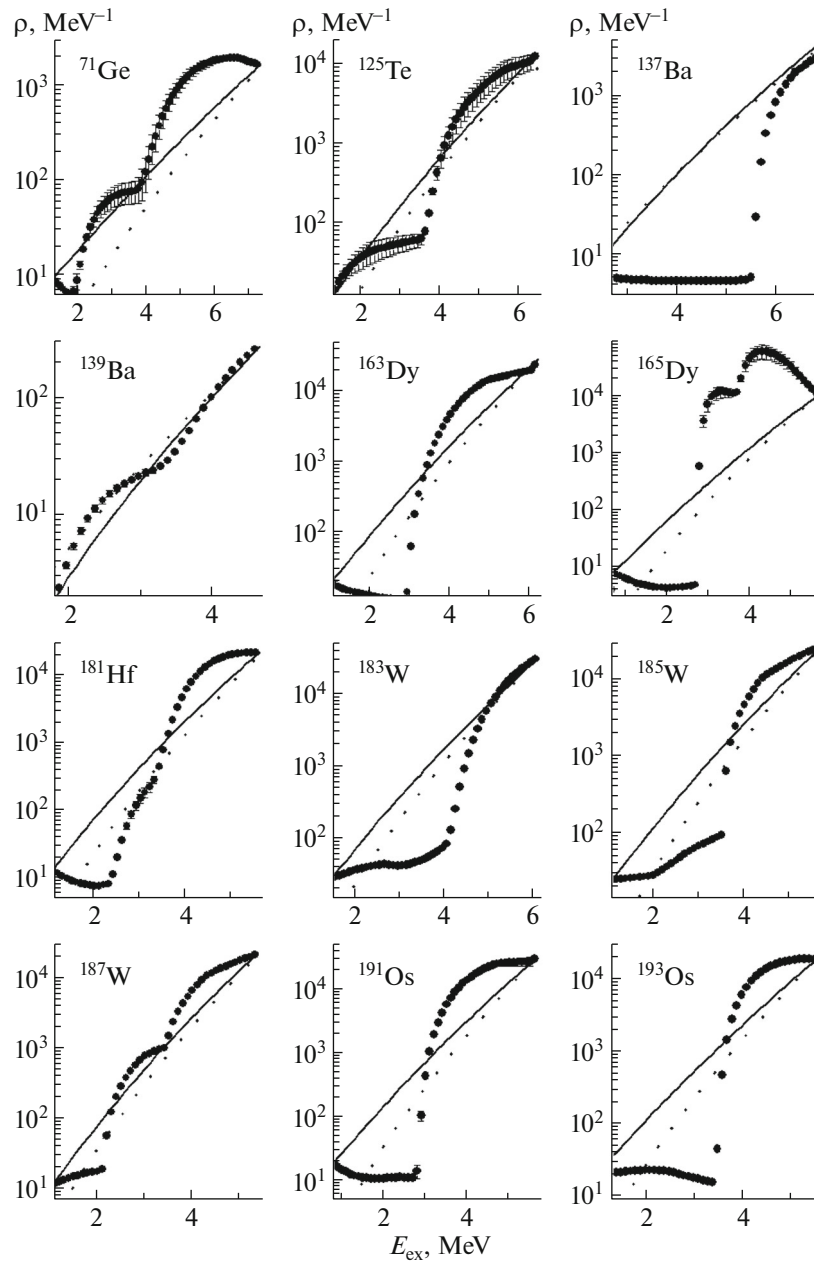


Fig. 1. Excitation-energy dependence of the mean densities of intermediate levels in two-step cascades (points with error bars) for even-odd nuclei (lowest χ^2 fits): (solid lines) data calculated in [17] and (dotted lines) results of the calculations based on the model proposed in [10].

A comparison of the results obtained within the present version of our model and within its earlier versions showed that we reached a fairly high accuracy in describing the densities of intermediate cascade levels. The discrepancies are the greatest for ^{137}Ba and ^{182}Ta . Most likely, a large error for ^{137}Ba stems from the preceding approximation version [3]. For ^{182}Ta , the energy thresholds for the break of the second and third Cooper pairs are 1.6 and 5.8 MeV within the present version; in [3], the values of the same

thresholds are 1.6 and 4.0 MeV. It follows that, even in the worst case of ^{182}Ta , the data obtained for the level density yield a picture where the uncertainties are due to the imperfections in the present-day ideas of the gamma-decay process.

One can reach the highest accuracy and reliability of the results on the basis of experiments where it is possible to single out not less than about 99% of the intensities of primary transitions among the whole array of gamma-ray cascades of the decay of the

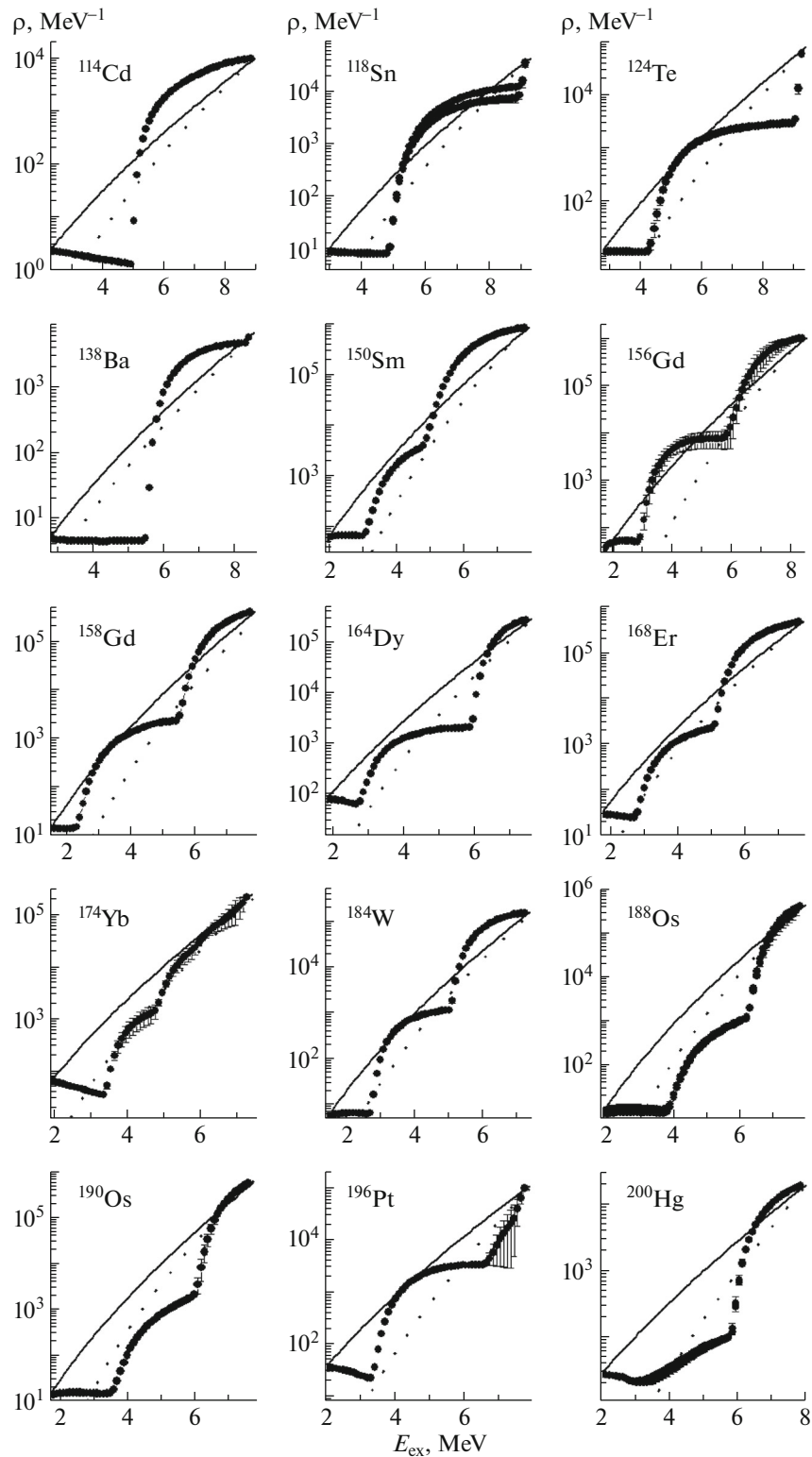


Fig. 2. As in Fig. 1, but for even-even nuclei.

compound state of any nucleus. Nevertheless, reliable information about the most probable level density and about strength functions for dipole gamma transi-

tions can be extracted even from the convolution of the spectrum of primary products of the decay of the compound state and the gamma-transition branching fractions depending on the energy of the interme-

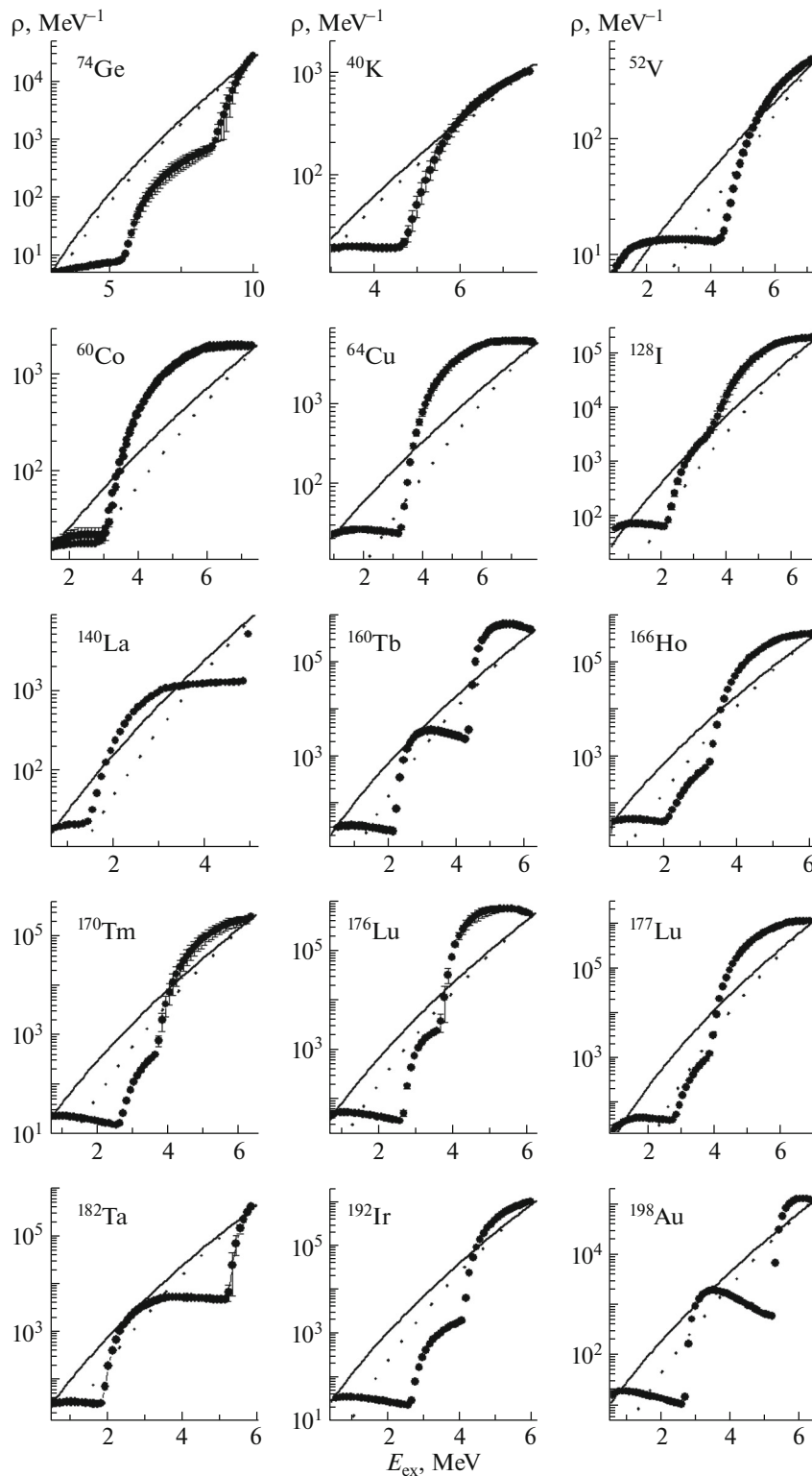


Fig. 3. As in Fig. 1, but for ^{74}Ge , ^{177}Lu , and odd–odd nuclei.

diate cascade level. This follows from a comparison of the thresholds determined for the break of three to four Cooper pairs by employing different versions of the energy dependence of ρ and Γ . In the most recent

versions of the practical model, these results change only slightly.

The level densities from the back-shifted Fermi gas model [17] and those from the model that takes

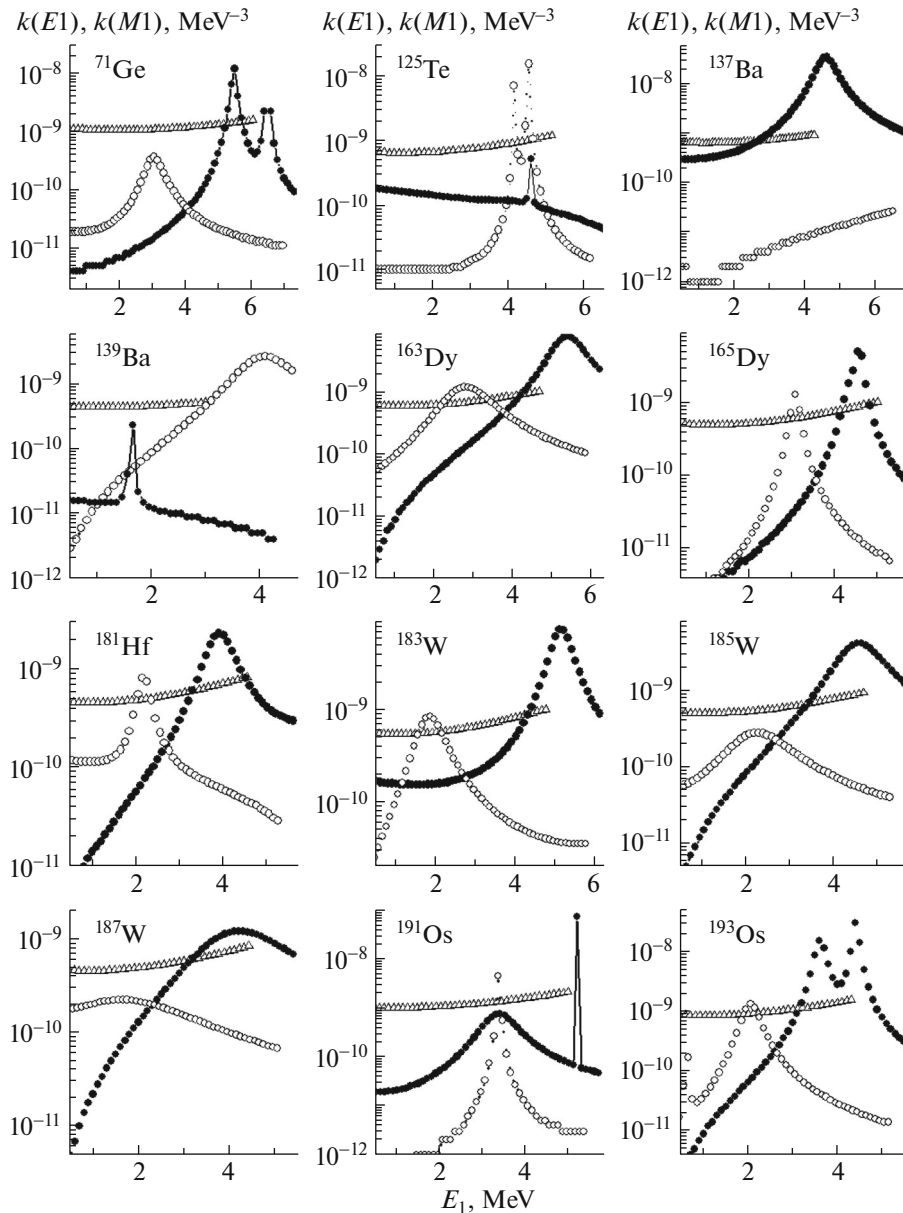


Fig. 4. Strength functions for $E1$ (closed circles) and $M1$ (open circles) transitions for even–odd nuclei versus the primary-transition energy. The open triangles stand for the sum of the values calculated on the basis of the model used in [14] and $k(M1) = \text{const}$ in the energy range of $0 < E_1 < B_n - E_d$.

into account the shell-inhomogeneities in the single-particle spectrum [10] are given in Figs. 1–3. One can see that the model from [10] reproduces the derivative $d\rho/dE_{\text{ex}}$ to a higher degree of precision than the model from [17]; however, the level densities calculated on the basis of both models deviate markedly from the respective experimental results.

The results presented for the $E1$ and $M1$ radiative strength functions (Figs. 4–6) and their sums (Figs. 7–9) do not exhibit drastic distinctions from those published earlier in [18–20], but there remains the unresolved problem of unambiguously describing

the shape of the observed peaks in the electric and magnetic strength functions in those cases where the use of exponential functions [3] and the modified Lorentzian function (3) leads to close values of χ^2 .

It is worth noting that the data in Figs. 4–9 do not require including any additional pygmy resonance in the strength functions being considered. In order to interpret the process in question, it is sufficient to develop theoretical ideas of the coexistence of vibrational and quasiparticle levels in any nucleus and their fragmentation as E_{ex} grows.

In many nuclei (see Fig. 7–9), the sum of the

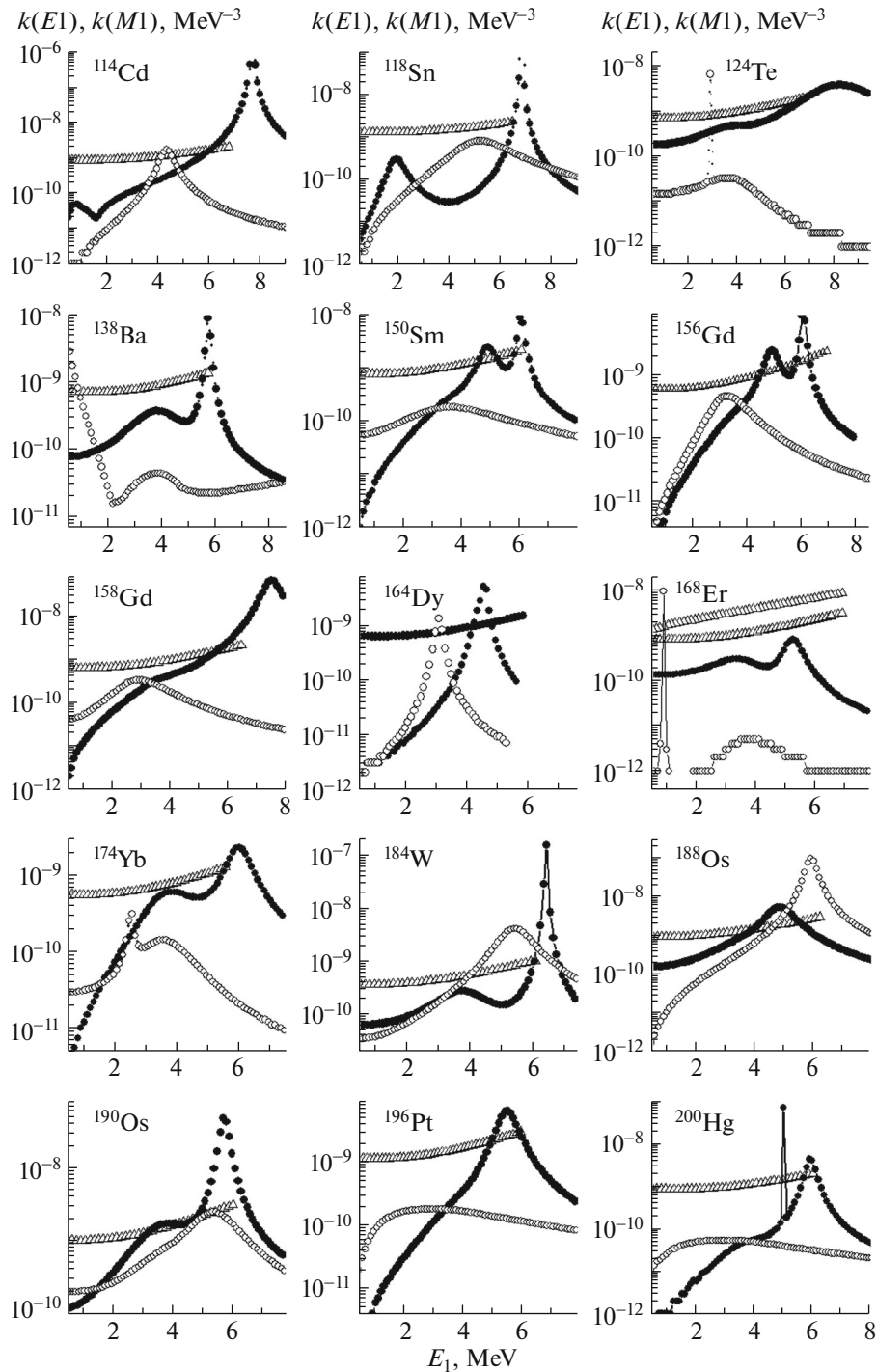


Fig. 5. As in Fig. 4, but for even–even nuclei.

strength functions for $E1$ and $M1$ transitions develops a plateau that agrees with the sum of the values calculated within the model used in [14] and $k(M1) = \text{const}$ normalized to the experimental ratios $k(M1)/k(E1)$. The strength functions for primary transitions whose energy lies in the range of $E_1 < 0.5B_n$ decrease regularly as the energy becomes lower. A significant decrease in the

sum $k(M1) + k(E1)$ for moderately small gamma-transition energies is observed for all versions of the description of radiative strength functions. At the same time, there are no asymptotic zero values of the sums of strength functions [14]. We cannot rule out the possibility of a sizable increase in the $E1$ or $M1$ strength functions in the vicinity of and above B_n because of the fragmentation of n -quasiparticle nu-

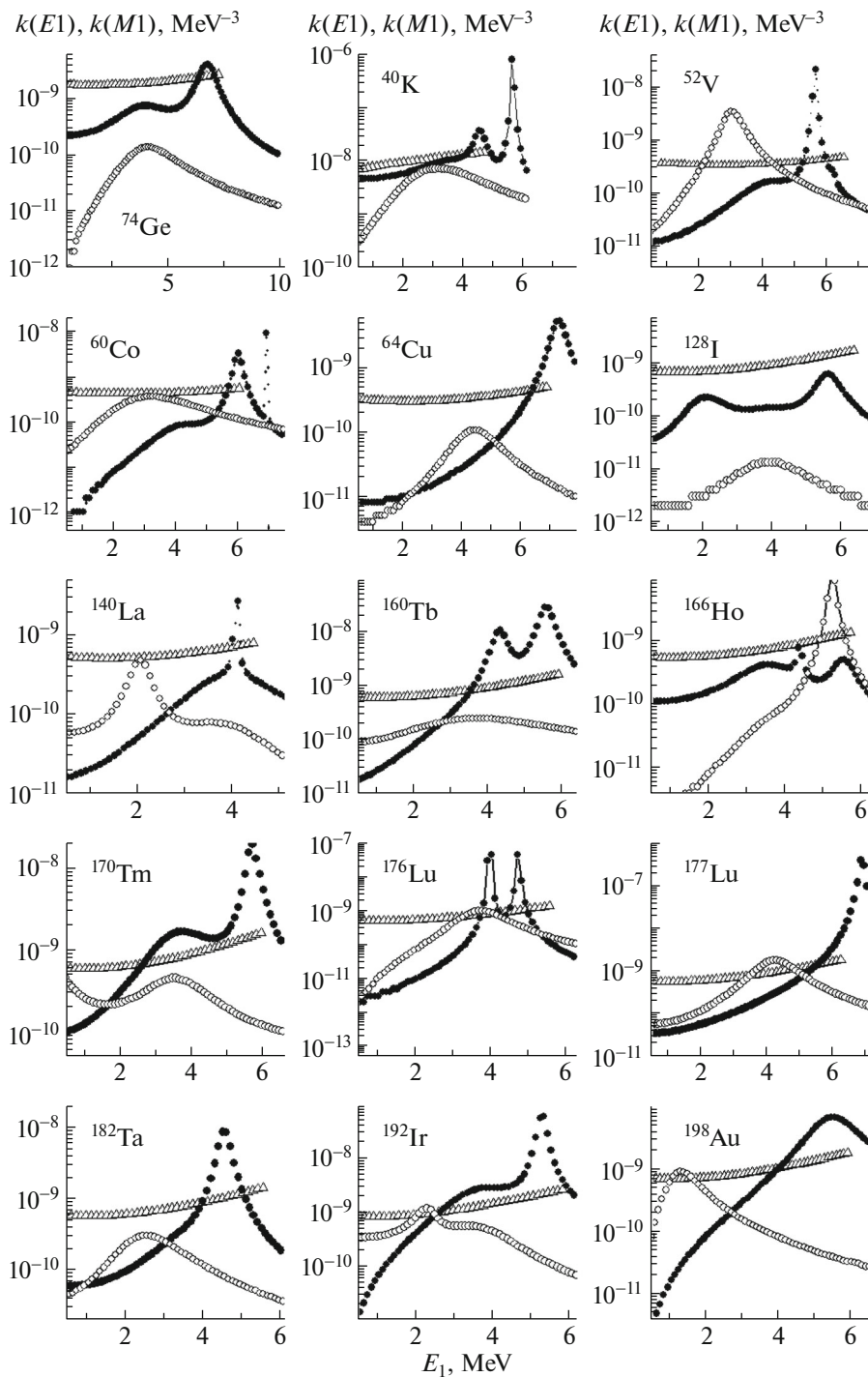


Fig. 6. As in Fig. 4, but for ^{74}Ge , ^{177}Lu and odd-odd nuclei.

clear states if the threshold for the break of a Cooper pair lies in the region of the neutron binding energy. Therefore, the radiative strength functions cannot be a mere extrapolation of giant resonances. This contradicts radically the Axel-Brink hypothesis [6, 7], which is used in dealing with gamma spectra.

Figure 10 gives the mass-number dependence of

the energy thresholds for the break of the second and third Cooper pairs. Since these quantities are different for nuclei in which the numbers of nucleons have different parities and depend on the mean pairing energy, they are shown separately in this figure and are compared with B_n/Δ_0 (in just the same way as in [3]). One can see that the thresholds for the break of

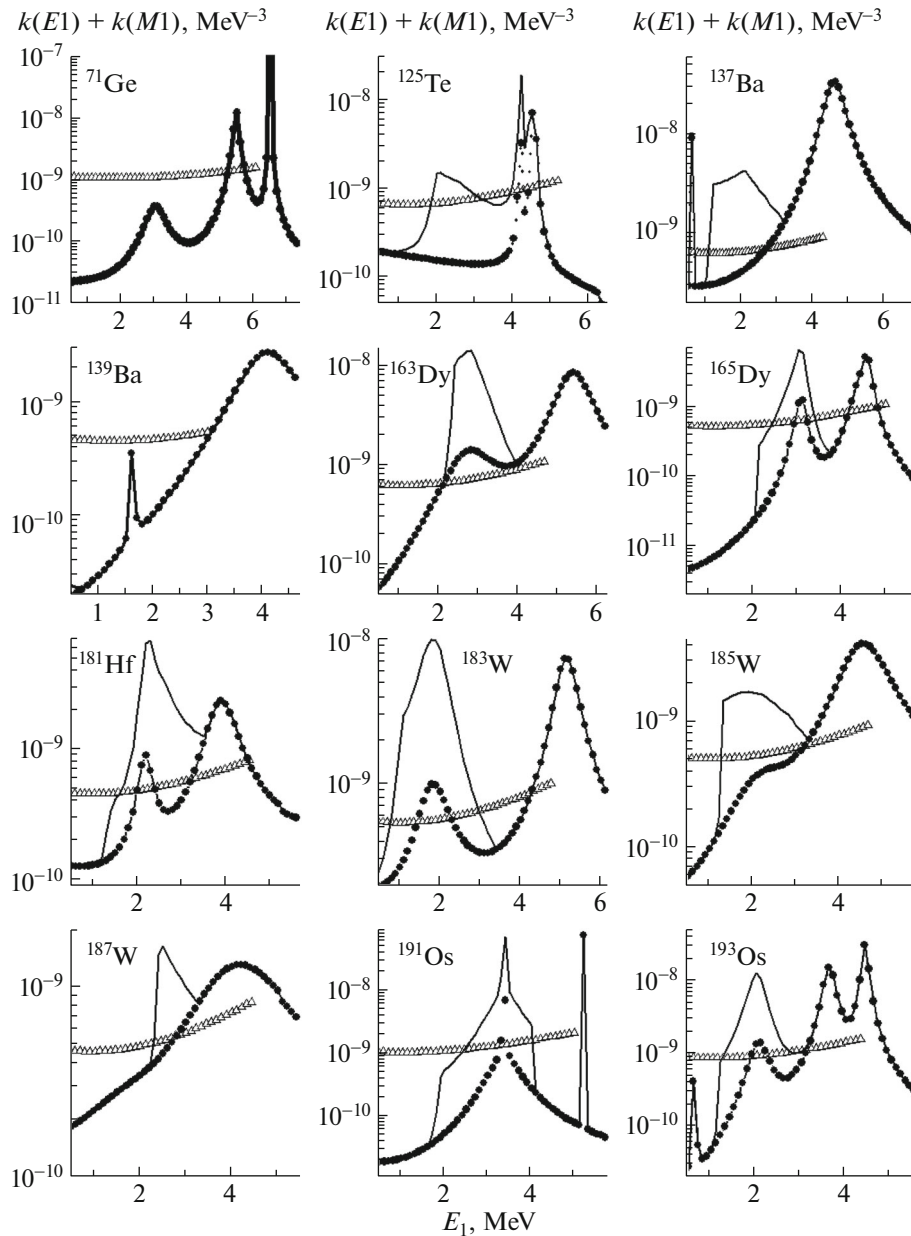


Fig. 7. Sums of strength functions for $E1$ and $M1$ transitions (closed circles) for even-odd nuclei versus the primary-transition energy. The solid lines represent the results fitted with allowance for the correction in Eq. (5). The open triangles stand for the sum of the values calculated on the basis of the model used in [14] and $k(M1) = \text{const}$ in the energy range of $0 < E_1 < B_n - E_d$.

pairs depend only slightly on the shape of the strength functions. This means that, in experiments detecting two-step cascades, the actual correlation of ρ and Γ is insignificant.

Figure 11 shows the results obtained by approximating the parameter E_u . Its values almost perfectly comply with the mean pairing energy Δ_0 of the last nucleon for approximately 30 nuclei. The spread of the remaining values of E_u may be due to the errors in the normalization of experimental values of $I_{\gamma\gamma}$ because of the fact that the model used in [11, 12]

disregards the possibility of the break of proton pairs simultaneously with or instead of the break of neutron pairs, the inaccuracy of the phenomenological part of the model, or fluctuations of the experimental values of Δ_0 [21]. In addition, we cannot rule out the possibility of different weights of quasiparticle and phonon components in the wave function for the resonance that determines the cross section for thermal-neutron capture by any stable (long-lived) target nucleus.

In currently used models [2], the total level density is represented as the sum of the level densities for

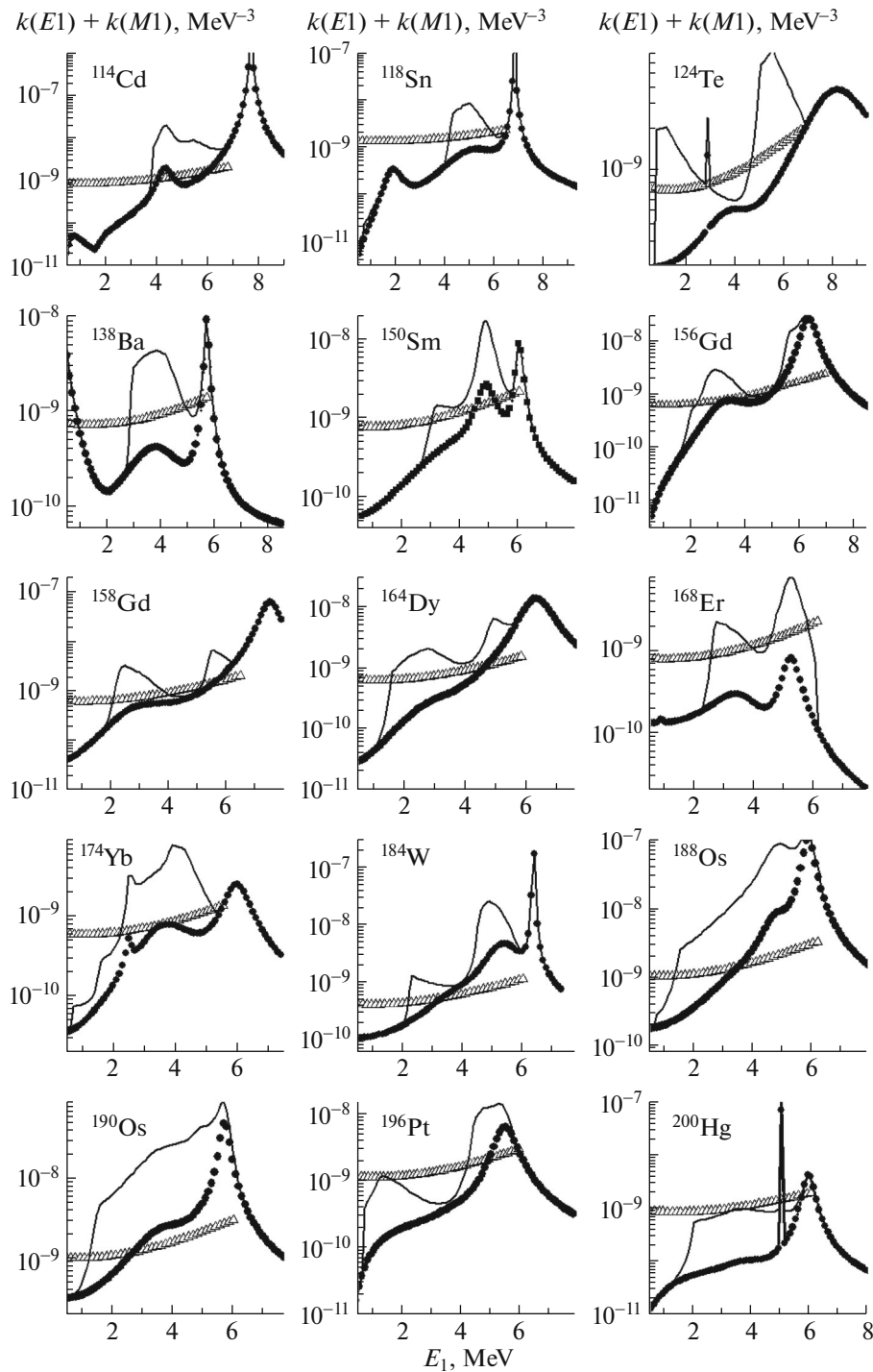


Fig. 8. As in Fig. 7, but for even–even nuclei.

quasiparticle and collective excitations. Figure 12 gives the ratio of the collective (only vibrational in actual practice) level density to the total level density. In the region around B_n , this ratio has close values for nuclei in which the numbers of nucleons have different parities, but, at the energy E_d , the ratio in question is substantially smaller for even–even nuclei than

for even–odd and odd–odd ones. No version of the Dubna model gives grounds to assume the presence of sharp changes in the nuclear structure at the point $E_{ex} = B_n$. On the basis of the data in Fig. 12, it would be legitimate to assume that neutron resonances may preserve various types of the wave-function structure (dominated by quasiparticle or phonon components)

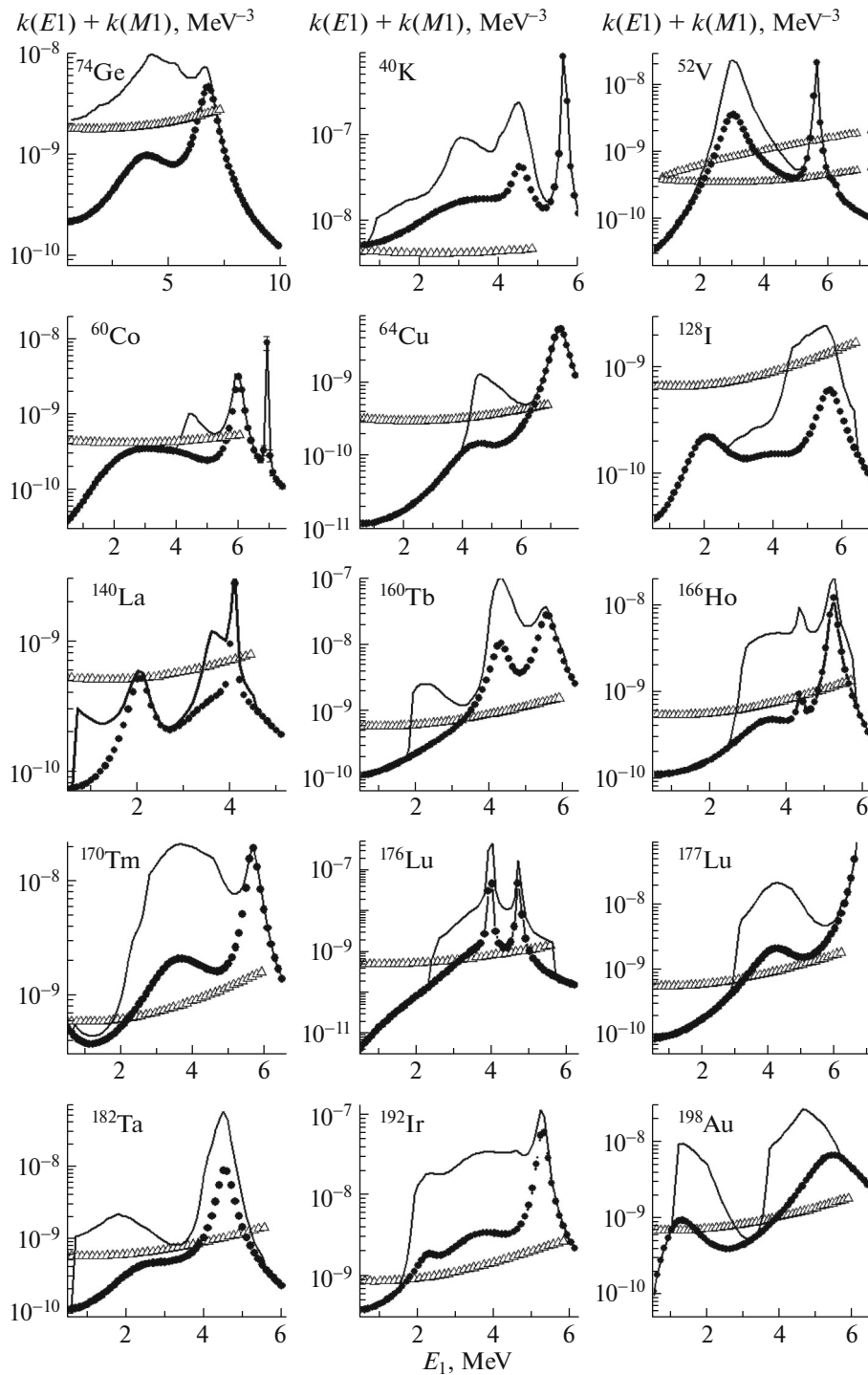


Fig. 9. As in Fig. 7, but for ^{74}Ge , ^{177}Lu , and odd-odd nuclei.

and belong to several different distributions of reduced neutron and total radiative resonance widths.

The distribution of reduced neutron and total radiative widths of neutron resonances were approximated in [22]. In the respective analysis, it is assumed that the experimental set of these widths is represented as the sum of several (up to four) distributions

whose widths and peak positions are varied. For the total radiative widths in nuclei featuring not less than 170 resonances, the mean fractions of two distributions that are the most intense are 44 and 34% of the summed distribution of total radiative widths (this is close to a 40% fraction of vibrational levels). Thus, two experiments that are methodologically indepen-

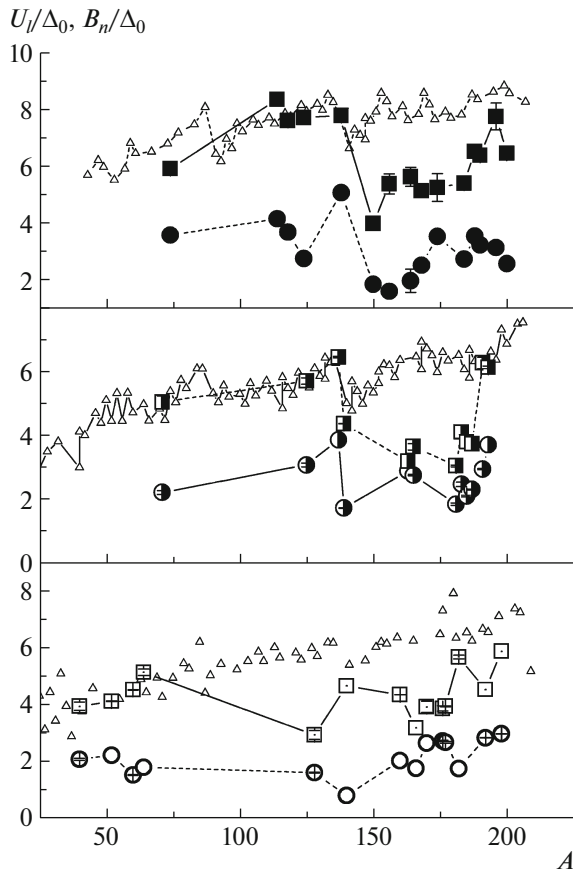


Fig. 10. Mass-number dependence of the energy thresholds for the break of the (circles) second and (boxes) third Cooper pairs. The closed, half-closed, and open symbols represent these results for, respectively, even–even, even–odd, and odd–odd compound nuclei. The open triangles correspond to the mass-number dependence of B_n/Δ_0 .

dent are indicative of the difference in the structure of the wave functions for neighboring levels over a broad range of stable target nuclei up to an energy of or somewhat higher than B_n .

There is some discrepancy between the values obtained here for the $E1$ and $M1$ strength functions (see Fig. 4–9) and the results reported in [3], which is due most likely to different degrees of the effect that the shape of the partial widths of the additional peaks (4) in the strength functions exert on χ^2 values in the region of small values of the energy dependences used. The observed variations in the shape of the sums of $E1$ and $M1$ strength functions (see Fig. 7–9) cannot be interpreted as their unquestionable distinction without ruling out the possible existence of levels of different structure at excitation energies of about 5 to 10 MeV.

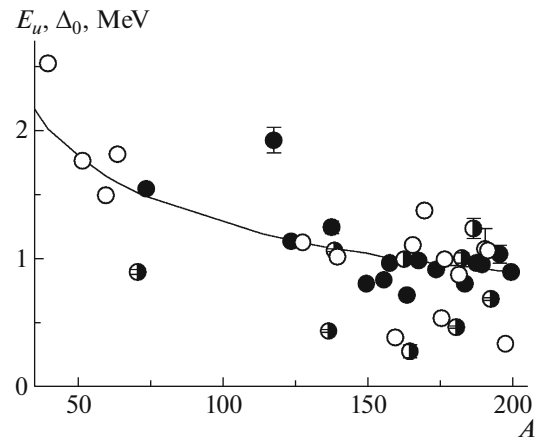


Fig. 11. Mass-number (A) dependence of the parameter $E_u(2)$ for (closed circles) even–even, (half-closed circles) even–odd, and (open circles) odd–odd compound nuclei. The curve represents the mean pairing energy Δ_0 of the last nucleon in a nucleus of mass number A [21].

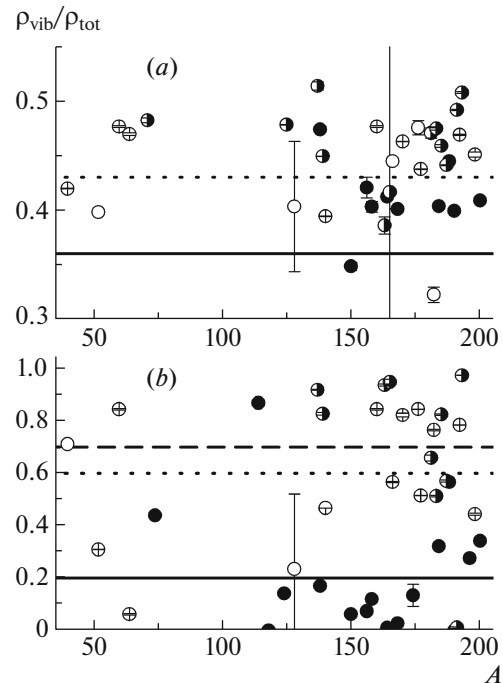


Fig. 12. Ratio of the vibrational level density to the total level density in the region around the neutron binding energy B_n (a) and at the point E_d (b). The closed, half-open, and open circles represent these results for, respectively, even–even, even–odd, and odd–odd nuclei. The solid, dashed, and dotted lines stand for the mean values in, respectively, even–even, even–odd, and odd–odd nuclei.

4. CONCLUSIONS

We have obtained experimental information about the dynamics of the break of three to four Cooper pairs of nucleons. The systematic error in determining the

break thresholds does not exceed a value of about 1 MeV for the bulk of nuclei that are accessible to study.

The set of data obtained by employing (i) the model of the density of n -quasiparticle levels from [9] for describing the sequential break of three to four Cooper pairs at an energy not higher than 5 to 10 MeV above the ground state of the nucleus being considered; (ii) the phenomenological concepts specified by Eq. (2), which concern the energy dependence of the vibrational level density in the same energy range; and (iii) combinations of phenomenological and/or theoretical ideas of the shape of the energy dependences of widths with respect to gamma-ray emission gives sufficient grounds to assume that the dynamics of the interaction of fermion and boson nuclear-matter states depends on the shape of the nucleus being studied.

REFERENCES

1. K. H. Schmidt and B. Jurado, *Phys. Rev. C* **83**, 014607 (2011).
2. *Reference Input Parameter Library RIPL-2, Handbook for Calculations of Nuclear Reaction Data*, IAEA-TECDOC (IAEA, 2002).
3. A. M. Sukhovej, L. V. Mitsyna, N. Jovancevic, *Phys. At. Nucl.* **79**, 313 (2016).
4. N. Jovancevich, A. M. Sukhovej, W. I. Furman, and V. A. Khitrov, in *Proceedings of the 20th International Seminar on Interaction of Neutrons with Nuclei, Dubna, May 2012*, Preprint JINR No. E3-2013-22 (Joint Inst. Nucl. Res., Dubna, 2013), p. 157. <http://isinn.jinr.ru/past-isinns.html>.
5. C. F. Porter and R. G. Thomas, *Phys. Rev.* **104**, 483 (1956).
6. P. Axel, *Phys. Rev.* **126**, 671 (1962).
7. D. M. Brink, PhD Thesis (Oxford Univ., Oxford, 1955).
8. A. Bohr and B. R. Mottelson, *Nuclear Structure*, Vol. 1: *Single-Particle Motion*, (Benjamin, New York, 1969).
9. V. M. Strutinsky, in *Proceedings of the International Congress on Nuclear Physics, Paris, France, 1958*, p. 617.
10. A. V. Ignatyuk, Report INDC-233(L) (IAEA, Vienna, 1985).
11. A. M. Sukhovej, *Phys. At. Nucl.* **78**, 230 (2015).
12. A. M. Sukhovej and L. V. Mitsyna, in *Proceedings of the 22nd International Seminar on Interaction of Neutrons with Nuclei, Dubna, May 2014*, Preprint JINR No. E3-2015-13 (Joint Inst. Nucl. Res., Dubna, 2015), p. 245. <http://isinn.jinr.ru/past-isinns.html>.
13. <http://www-nds.iaea.org/ENDSF>.
14. S. G. Kadenskii, V. P. Markushev, and V. I. Furman, *Sov. J. Nucl. Phys.* **37**, 165 (1983).
15. L. A. Malov and V. G. Solov'ev, *Sov. J. Nucl. Phys.* **26**, 384 (1977).
16. E. V. Vasileva, A. M. Sukhovej, and V. A. Khitrov, *Phys. At. Nucl.* **64**, 153 (2001).
17. W. Dilg, W. Schantl, H. Vonach, and M. Uhl, *Nucl. Phys. A* **217**, 269 (1973).
18. A. M. Sukhovej and V. A. Khitrov, Preprint JINR No. E3-2005-196 (Joint Inst. Nucl. Res., Dubna, 2005).
19. A. M. Sukhovej and V. A. Khitrov, *Phys. Part. Nucl.* **36**, 359 (2005).
20. A. M. Sukhovej and V. A. Khitrov, *Phys. Part. Nucl.* **37**, 899 (2006).
21. V. A. Kravtsov, *Atomic Masses and Nuclear Binding Energies* (Atomizdat, Moscow, 1965) [in Russian].
22. A. M. Sukhovej and V. A. Khitrov, *Phys. At. Nucl.* **76**, 68 (2013).

COMPARISON OF MULTIVARIATE CLASSIFICATION AND REGRESSION METHODS FOR THE INDOOR RADON MEASUREMENTS

by

***Dimitrije M. MALETIĆ, Vladimir I. UDOVIČIĆ*,
Radomir M. BANJANAC, Dejan R. JOKOVIĆ, Aleksandar L. DRAGIĆ,
Nikola B. VESELINOVIĆ, and Jelena Z. FILIPOVIĆ***

Institute of Physics, University of Belgrade, Belgrade, Serbia

Scientific paper
DOI: 10.2298/NTRP1401017M

We present the results of a test usage of multivariate methods, as developed for data analysis in high-energy physics and implemented in the toolkit for multivariate analysis software package, in our analysis of the dependence of the variation of indoor radon concentration on climate variables. The method enables the investigation of the connections of the wide spectrum of climate variables with radon concentrations. We find that multivariate classification and regression methods work well, giving new information and indications, which may be helpful in further research of the variation of radon concentration in indoor spaces. The method may also lead to considerable prediction power of the variations of indoor radon concentrations based on the knowledge of climate variables only.

Key words: radon, multivariate analysis, climate parameter

INTRODUCTION

Radon is a unique natural element since it is a gas, noble and radioactive in all of its isotopes. As noble gases, radon isotopes are mobile and can travel significant distances within the ground and through the atmosphere. Being radioactive, radon makes for about 55% of the annual effective dose received by average non-professional. Indoor radon concentrations vary significantly due to a large number of factors, which include the local geology, soil permeability, building materials and lifestyle characteristics, climate parameters and the exchange rate between indoor and outdoor air. Since both the climate parameters and air exchange rates may significantly vary during a day, it is important to investigate their correlation with short-term variations of indoor radon concentrations. In the past somewhat unusual climate parameters, such as wind speed and cloud cover, were occasionally considered, using a multivariate method [1-3]. We start this analysis with the maximum of 18 climate parameters and use and compare 12 different multivariate methods.

Variations of radon concentration were studied in our laboratory [4] in many details since 1999 [5-8].

Several climate variables, like air temperature, pressure, and humidity were considered [8, 9]. We now make further advance and try to use all publicly available climate variables monitored by, in our case, nearby automatic meteorological station (Automatic Meteorological Station Belgrade-south, Banjica-Trošarina, 44°45'16"N, 20°29'21"E). We want to find the appropriate method out of the wide spectrum of multivariate analysis methods that are developed for the analysis of data from high-energy physics experiments to analyze our measurements of variations of radon concentrations in indoor spaces.

FORMULATION OF THE PROBLEM

The demand for detailed analyses of large amount of data in high-energy physics resulted in wide and intense development and usage of multivariate methods. Many of multivariate methods and algorithms for classification and regression are already integrated into the analysis framework ROOT [10], more specifically, into the toolkit for multivariate analysis (TMVA) [11]. We use these multivariate methods to create, test and apply all available classifiers and regression methods implemented in the TMVA in order to find the method that would be the most appropriate

* Corresponding author; e-mail: udovicic@ipb.ac.rs

and yield maximum information on the dependence of indoor radon concentrations on the multitude of climate variables.

The first step is to calculate and rank the correlation coefficients between all the variables involved, what will help in setting up and testing the framework for running the various multivariate methods contained in the TMVA. Although these correlation rankings will later be superseded by method-specific variable rankings, they are useful at the beginning of the analysis.

The next step is to use and compare the multivariate methods in order to find out which one is best suited for classification (division) of radon concentrations into what would be considered acceptable and what would be considered increased concentration in indoor spaces. Main aim is to find out which method can, if any, on the basis of input climate variables only, give an output that would satisfactorily close match the observed variations of radon concentrations. This would enable the creation of the "radon alarm" using only the multivariate classification of the now widely available records of climate variables. Towards this aim, this work should be considered a preliminary one, for the number of specific cases that should be studied in this way should be much larger, to comprise the multitude of possible representative situations that occur in real life.

In order to be able to use the multivariate classification, the set of input events (values for climate variables for each measurement) used, have to be split into those that correspond to the signal (the radon concentrations that are considered increased) and to the background (consisting of radon concentrations that are declared acceptable). This splitting of the set of input events is for the purposes of this preliminary analysis performed at the limiting value of 40 Bq/m^3 . This value is used for most of the analyses, and is selected because this splitting ensures maximum employment of multivariate comparison methods, and this particular value reflects the fact that in our test case the statistics on higher radon concentration values are lower. For the purposes of setting of a sort of a "radon alarm", the value of radon concentration that should be used for splitting of input events is the value for radon concentration recommended by World health organization of 100 Bq/m^3 . The method of multivariate regression, however, does not require preliminary splitting of input events, and is therefore a more general one.

EXPERIMENTAL DATA

There are many methods available for measurement of radon concentrations in air. According to the integrating measurement time, these may be divided into the long-term and short-term ones. The first are mostly performed with passive integrating measuring

devices based on nuclear track detectors, which are due to their low cost, simplicity, and wide availability well suited for simultaneous collection of data from a large number of measurement points and are thus used in large radon mapping projects. The second group comprises the methods that are performed with more complex and more expensive passive or active (with pumped air sampling) devices. For the short-term measurements of radon concentration in a single-family dwelling house in Belgrade, Serbia, we use the SN1029 radon monitor (manufactured by the Sun Nuclear Corporation, NRSB approval-code 31822). The device consists of two diffused junction photodiodes as a radon detector, and is furnished with sensors for temperature, barometric pressure and relative humidity. The user can set the measurement intervals from 30 minutes to 24 hours. It was set to record simultaneously the radon concentration, temperature, atmospheric pressure and relative humidity.

The selected house to measure the temporal variations of radon concentration is a typical one-family detached dwelling house built with standard construction materials such as brick, concrete, and mortar. The house is thermally insulated with Styrofoam. During the period of measurements (summer), the house was naturally ventilated and air conditioning was used during the hottest days. The indoor radon measurements were performed in the living room, where family spends anything from 16 up to 24 hours during the working days of the week. Radon monitor was measuring radon concentration, temperature, pressure, and humidity at 2 hour intervals, starting from the 3rd of June till the 3rd of July and from the 18th of July till the 11th of August 2013.

The values of climate variables, which will be correlated with radon monitor results, are obtained from a modern automatic meteorological station located some 400 m (GPS coordinates) away from the house where the radon monitor was placed. The wide set of climate variables were used, for the measurements of which were performed at 5 minute intervals during June, July, and August 2013. The fifteen climate parameters used are: outdoor air temperature, pressure and humidity, solar irradiance, wind speed at the height of 10 m above the ground, precipitation, evaporation, and underground temperature and humidity at the depths of 10-30 and 50 cm.

The second site used for the tests is our own ground level laboratory [1], which is air-conditioned and only rarely accessed, thus having much more stable indoor conditions than the dwelling house described. The measurements were performed during September and October 2012. Measurements of climate parameters that will be combined with radon measurements in this case come from the different, and somewhat older automatic metrological station, located about 4 km from the laboratory where the radon monitor was taking data.

MULTIVARIATE METHODS

The TMVA provides a ROOT-integrated environment for the processing, parallel evaluation and application of multivariate classification and multivariate regression methods. All multivariate methods in TMVA belong to the family of “supervised learning” algorithms. They make use of training events, for which the desired output is known, to determine the mapping function that either describes a decision boundary (classification) or an approximation of the underlying functional behavior defining the target value (regression). All MVA methods see the same training and test data. The correlation coefficients of the input variables are calculated and displayed, and a preliminary ranking is derived (which is later superseded by method-specific variable rankings). For standalone use of the trained classifiers, TMVA also generates lightweight C++ response classes that do not depend on TMVA or ROOT, neither on any other external library. As will be demonstrated, the two most important multivariate methods for our purposes are the boosted decision trees (BDT) and the artificial neural networks (ANN) methods.

Boosted decision trees

BDT has been successfully used in high energy physics analysis for example by the MiniBooNE experiment [12]. In BDT, the selection is done on a majority vote on the result of several decision trees. Decision tree consists of successive decision nodes, which are used to categorize the events in sample as either signal or background. Each node uses only a single discriminating variable to decide if the event is signal-like “goes right” or background-like “goes left”. This forms a tree like structure with “baskets” at the end (leave nodes), and an event is classified as either signal or background according to whether the basket where it ends up has been classified as signal or background during the training. Typically, BDT is constructed of a forest of such decision trees. The (final) classification for an event is based on a majority vote of the classifications done by each tree in the forest. However, the advantage of the straightforward interpretation of the decision tree is lost. In many academic examples with more complex correlations or real life examples, the BDT often outperform the other techniques. More detailed information about training can be found in [11].

Artificial neural networks

An artificial neural network (ANN) [13] is most generally speaking any simulated collection of interconnected neurons, with each neuron producing a certain response at a given set of input signals. By apply-

ing an external signal to some (input) neurons the network is put into a defined state that can be measured from the response of one or several (output) neurons.

ANN in TMVA belong to the class of multilayer perceptrons (MLP), which are feed-forward neural networks. The input layer contains as many neurons as input variables used in the MVA. The output layer contains a single neuron for the signal weight. In between the input and output layers are a variable number of k hidden layers with arbitrary numbers of neurons.

All neuron inputs to a layer are linear combinations of the neuron output of the previous layer. The transfer from input to output within a neuron is performed by means of an “activation function”. In general, the activation function of a neuron can be zero (deactivated), one (linear), or non-linear. The ANN used for our purposes uses a sigmoid activation function. The transfer function of the output layer is usually linear.

RESULTS

We comment on the results of our analyses divided into cases that differ by the size of the set of climate parameters used, by the indoor space studied, and by the methods of analysis used.

First, we intercompare the multivariate methods used for classification of radon concentrations by using the full set of climate variables as described in previous sections.

We are using the input events (set of climate variables for each measurement) to train, test and evaluate the 12 multivariate methods implemented in TMVA. The graph presenting the receiver operating characteristic (ROC) for each multivariate method (fig. 1) may be considered as the most indicative in comparing the different methods used for classification of radon concentrations using climate variables. On this graph one can read the dependence of background rejection on signal efficiency. The best method is the one that holds maximum value of background rejection for highest signal efficiency, *i. e.* the best method has ROC curve closest to the upper right corner on the graph presented in fig. 1. It turns out that the method best suited for our purpose is the BDT method. This means that BDT gives most efficient classification of input events. This is seen in fig. 2, which shows the distribution of BDT classification method outputs for input signal and background events. The second best method is the implementation of ANN MLP.

In fig. 3, one can see the values of signal and background efficiency and significance. Significance, calculated as

$$\frac{N(\text{signal})}{\sqrt{N(\text{signal}) N(\text{background})}}$$

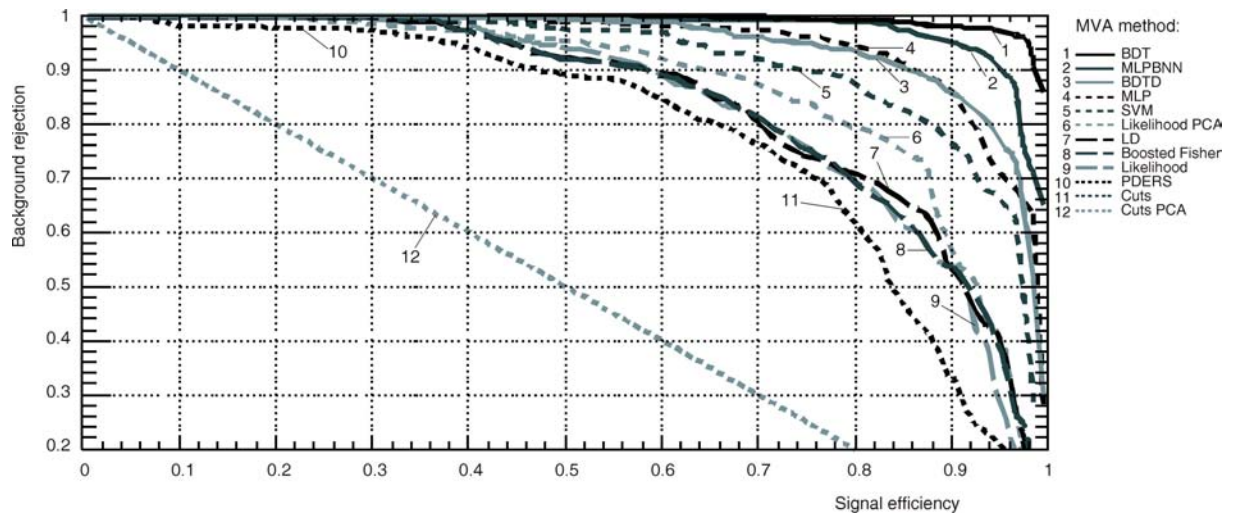


Figure 1. ROC for all multivariate methods used for classification of radon concentration using climate variables

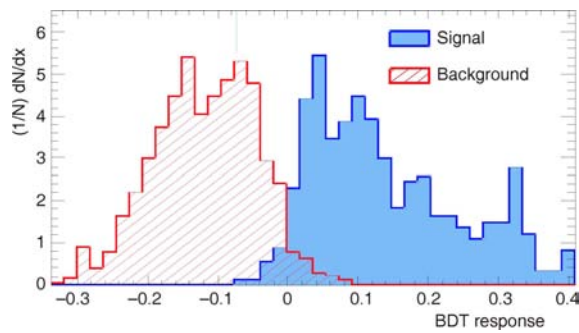


Figure 2. Distribution of BDT classification method outputs for input signal and background events

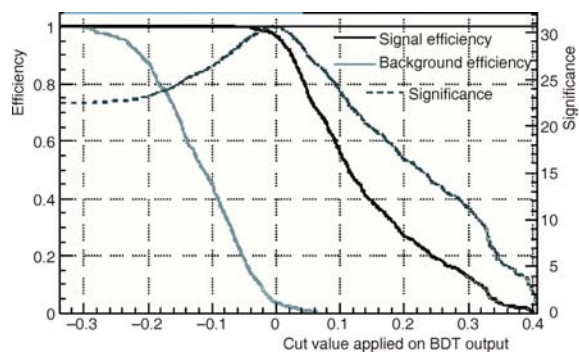


Figure 3. Cut efficiency and optimal cut value of BDT classification MVA method

can be used as the value for comparison of various multivariate methods, and also for comparison of method efficiencies for different sets of input variables. The significance of the BDT method with full set of input climate variables turns out to be 30.6. Ranking of the BDT input variables (tab. 1.) is derived by counting how often the variables are used to split decision tree nodes, and by weighting each split occurrence by the separation it has achieved and by the num-

ber of events in the node. As seen from tab. 1, temperature of the soil at the depth of 10 cm appears to be by far the most important variable.

Now we compare the multivariate methods for classification of radon concentration by using the minimum set of climate variables that would give similar results as when using the full set. While searching for the best multivariate method for radon classification indoors in this situation, we found that the BDT method again gives the best result, with the significance of 29.6 as compared to 30.6, when all the available climate variables for training and testing of multivariate methods are used. The climate variables chosen for training and testing in this case were: outdoor air temperature, humidity and pressure, outdoor soil temperature at the depth of 10 cm, differences of

Table 1. Ranking of BDT input variables

Variable	Variable importance
Temperature of soil at depth of 10 cm	1.37e-01*
Outside air temperature	7.40e-02
Evaporation	7.16e-02
Outside air pressure	7.16e-02
P (outside) – P (radon monitor)	6.51e-02
Outside air humidity	6.40e-02
H (outside) – H (radon monitor)	6.12e-02
T (outside) – T (radon monitor)	5.79e-02
Humidity of soil at depth of 10 cm	5.74e-02
Solar irradiance	5.16e-02
Temperature of soil at depth of 20 cm	4.99e-02
Temperature of soil at depth of 50 cm	4.68e-02
Temperature of soil at depth of 30 cm	4.46e-02
Humidity of soil at depth of 20 cm	4.31e-02
Wind speed at height of 10 m	3.87e-02
Humidity of soil at depth of 30 cm	3.41e-02
Humidity of soil at depth of 50 cm	3.13e-02
Precipitation	0.00e+00

*1.37e-01 read as $1.37 \cdot 10^{-1}$

outdoor and indoors temperature, and the indoors humidity and pressure. One important caveat is in place here. It concerns the possibility that the two sets of instruments (for indoor and outdoor measurements) are not identically calibrated, what may especially be the case when two different groups or institutions conduct the indoor and outdoor measurements. It is estimated that these instrumental effects do not influence significantly the results of this study. In the case of calibration of MVA classification method, we need radon monitor apparatus indoors and apparatus for P, H, and T measurements outdoors and an apparatus for measurement of the outdoor soil temperature with the sensor positioned at the soil depth of 10 cm. While aiming at setting a “radon alarm” in this case, we thus have to have two apparatuses for P, H, and T measurements, indoor and outdoor, and an apparatus for measurement of outdoor soil temperature with the sensor positioned at the depth of 10 cm.

Next we compare the uses of multivariate methods for classification of radon concentration indoors when using the simplest possible set of climate variables. The climate variables used for training and testing were: outdoor air temperature, pressure and humidity, and differences of outdoor and indoor temperature, pressure and humidity. That means that we need to have two devices for measurement and recording of temperature, pressure and humidity, both indoors and outdoors at the same time. For calibration and testing of multivariate methods, in case of using this set of climate variables we would need one radon monitor indoors, and an apparatus for measurement of P, H, and T outdoors. For the purpose of setting the radon alarm, we would need to have two apparatuses for P, H, and T measurement. The best multivariate method for radon classification indoors in this case is also BDT method. The resulting significance is 28.2 as compared to 30.6 what we get when using the full set of available climate variables for training and testing of multivariate methods. This testifies that when we drop out many climate parameters in this case of analysis the resulting significance decreases notably, but still leaving MVA classification work good.

We also compared the multivariate methods for classification of radon concentration using the simplest set of climate variables in our Ground level laboratory, which is, as said, an air-conditioned and only seldom accessed space. The climate data are provided by the 4 km away and somewhat older automatic meteorological station. The methods are still found to work satisfactorily – the resulting significance of the BDT method now being 27.6 as compared to 28.2, obtained with the simplest set of variables in the case of the actively inhabited dwelling. The climate variables, requirements for training and testing are the same as in the previous case.

We also tested the simple set of only outdoor measured climate variables consisting of the outdoor

air temperature, pressure and humidity, and the outdoor soil temperature at the depth of 10 cm. This means that the devices for measurement and recording of outdoor temperature, pressure and humidity as well as the device for measurement and recording of the outdoor soil temperature at depth of 10 cm are required. The resulting significance is now 27.2 as compared to 30.6 when using the full set of available climate variables, and 28.19 when using the two apparatuses for P, H, and T measurements.

Comparison of multivariate methods for classification of radon concentration indoors

The difference between this case and the previous one with the full set of climate variables is that input events are now split at the value of radon concentration of 100 Bq/m³, which is the recommended limiting value between the acceptable and increased radon concentration by the World Health Organization (WHO). Previous method had a cut on the value of 40 Bq/m³, which was found to insure maximum employment of multivariate classifications. This particular value reflects the fact that the statistics on higher radon concentrations are getting progressively lower. In tab. 2, we present the significance and the signal and background efficiency for several best multivariate classifier methods. Again, the BDT (and BDT decorrelated) multivariate method shows the best performance in classifying the events into the categories of increased and acceptable concentrations.

Figure 4 shows the distribution of BDT classification method outputs for input signal and background events. These figures again demonstrate that classification methods work well *i. e.*, that the separation of signal and background works very good. Also, the significance value for BDT is higher for higher cut values for splitting of input events. Interestingly, it appears that other multivariate methods also give better results under these new conditions.

Regression methods

Regression is the approximation of the underlying functional behavior defining the target value. We tried to find the best regression method that will give

Table 2. Significance, signal, and background efficiency for several best multivariate classifier methods in the case of imposed limiting value of 100 Bq/m³

Classifier	S/sqrt(S + B)	EffSig	EffBkg
BDT	31.1	0.97	0.01
BDTD	30.9	0.98	0.03
MLPBNN	30.6	0.95	0.02
MLP	30.0	0.93	0.04
SVM	29.6	0.93	0.05

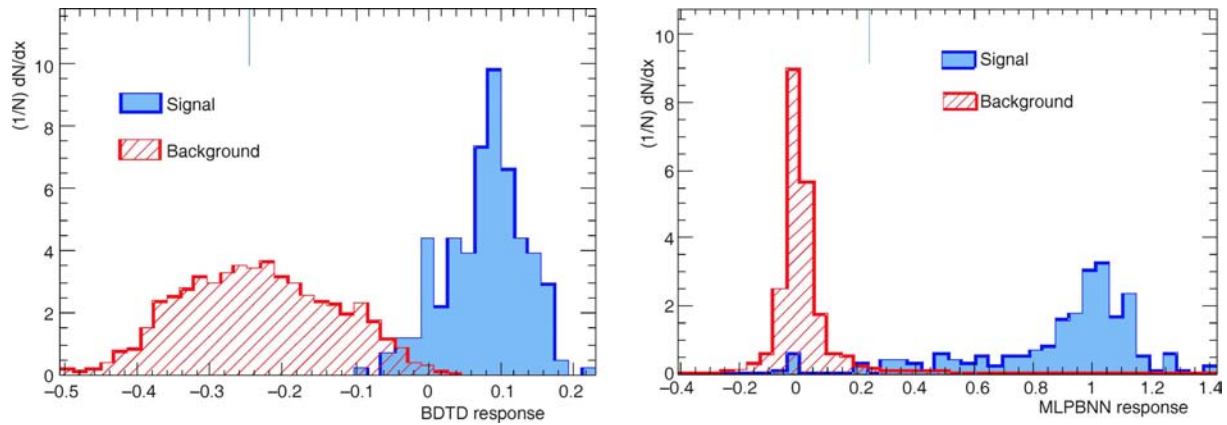


Figure 4. Distribution of BDT and ANN MLP classification method outputs for input signal and background events

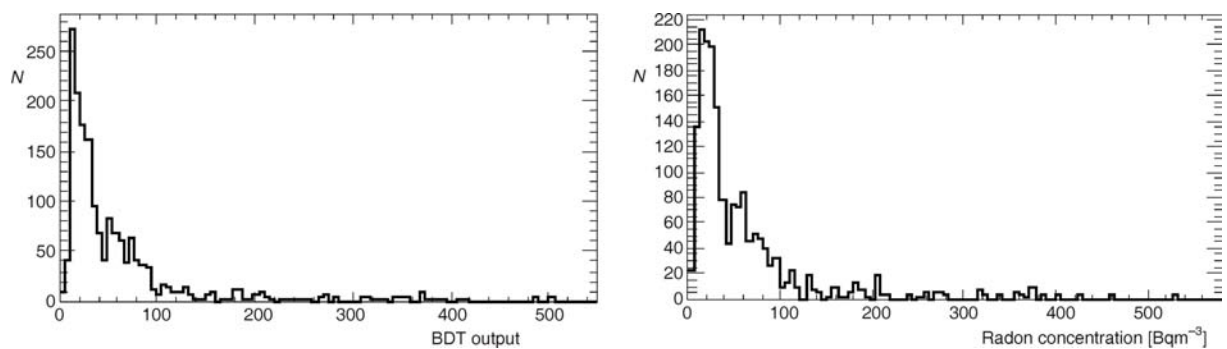


Figure 5. Distribution of radon concentrations and outputs from BDT multivariate method for regression of radon concentration using all climate variables

output values (predicted radon concentration) closest to the actual radon concentration that corresponds to specific input climate variables. The best multivariate regression method is found to be BDT, and the second one is MLP, same as in case of multivariate classifiers. Figure 5 presents the distribution of radon concentrations and outputs from the BDT multivariate method from regression of radon concentration using all climate variables.

To best way to estimate the quality of the method is to look at the differences between the output values from BDT multivariate regression method and the values of measured radon concentrations (fig. 6). The figure indicates the satisfactory predictive power of multivariate regression methods as applied for prediction of variations of indoor radon concentrations based on the full set.

CONCLUSIONS

The first test of multivariate methods developed for data analysis in high-energy physics and implemented in the TMVA software package applied to the analysis of the dependence of indoor radon concentra-

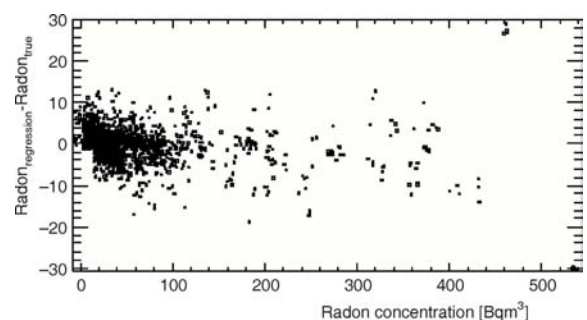


Figure 6. Difference of outputs from BDT multivariate regression method and radon concentrations, vs. radon concentration

tion variations on climate variables demonstrated the potential usefulness of these methods. It appears that the method can be used with sufficient reliability for prediction of the increase of indoor radon concentrations above some prescribed value on the basis of monitored set of climate variables only. Surprisingly, this set of climate variables does not have to include too many of those which are nowadays widely available. To confirm these promising preliminary findings more case studies of similar character are required.

ACKNOWLEDGEMENT

The authors wish to thank Prof. Ivan Aničin for constant interest and support. This work is supported by the Ministry of Education, Science and Technological Development of the Republic of Serbia under project numbers III 43002 and OI171002.

AUTHOR CONTRIBUTIONS

The idea for this paper came as a result of discussions of V. I. Udovičić, R. M. Banjanac, D. R. Joković, and D. M. Maletić. Gathering climate data and MVA analysis was done by D. M. Maletić. V. I. Udovičić performed indoor radon measurements. Writing of the paper was done by D. M. Maletić and V. I. Udovičić. A. L. Dragić gave idea about using MVA methods in cosmic and radon measurements. N. B. Veselinović analyzed and validated climate data. J. Z. Filipović helped with MVA analysis. D. R. Joković helped with data analysis and paper technical preparation.

REFERENCES

- [1] Baciu, A. C., Radon and Thoron Progeny Concentration Variability in Relation to Meteorological Conditions at Bucharest (in Romania), *Journal of Environmental Radioactivity*, 83 (2005), 2, pp. 171-189
- [2] Simon, E., et al., Estimation and Prediction of the Outdoor ^{222}Rn and ^{220}Rn Progeny Concentrations Using Meteorological Variables, *Rom. Journ. Phys.*, 58 (2013), Suppl., pp. S262-S272
- [3] Cuculeanu, V., et al., Dynamics, Deterministic Nature and Correlations of Outdoor ^{222}Rn and ^{220}Rn Progeny

- Concentrations Measured at Baciu, *Journal of Environmental Radioactivity*, 102 (2011), 7, pp. 703-712
- [4] Dragić, A., et al., The New Setup in the Belgrade Low-Level and Cosmic-Ray Laboratory, *Nucl Technol Radiat*, 26 (2011), pp. 181-192
- [5] Antanasijević, R., et al., Radon Measurements During the Building of a Low-Level Laboratory, *Radiat. Meas.*, 31 (1999), 1-6, pp. 371-374
- [6] Banjanac, R., Indoor Radon Measurements by Nuclear Track Detectors: Applications in Secondary Schools, *Facta Universitas, Series: Physics, Chemistry and Technology*, 4 (2006), 1, pp. 93-100
- [7] Udovičić, V., et al., Radon Problem in an Underground Low-Level Laboratory, *Radiat. Meas.*, 44 (2009), 9-10, pp. 1009-1012
- [8] Udovičić, V., Radon Time-Series Analysis in the Underground Low-Level Laboratory in Belgrade (in Serbian), *Radiation Protection Dosimetry*, 145 (2-3), (2011), pp. 155-158
- [9] Mihailović, D. T., et al., A Complexity Measure Based Method for Studying the Dependence of ^{222}Rn Concentration Time Series on Indoor Air Temperature and Humidity, *Applied Radiation and Isotopes*, 84 (2014), pp. 27-32
- [10] Brun, R., Rademakers, F., ROOT – An Object Oriented Data Analysis Framework, *Nucl. Inst. Meth. in Phys. Res.*, A 389 (1997), 1-2, pp. 81-86
- [11] Hoecker, A., et al., TMVA Users Guide – Toolkit for Multivariate Data Analysis, PoS ACAT 040 (2007), <http://arxiv.org/abs/physics/070303>
- [12] Yang, H.-J., Roe, B. P., Zhu, J., Studies of Boosted Decision Trees for MiniBooNE Particle Identification, *Nucl. Instrum. Meth.*, A555 (2005), 1-2, pp. 370-385
- [13] Rojas, R., Neural Networks, Springer-Verlag, Berlin, 1996

Received on September 23, 2013

Accepted on March 10, 2014

**Димитрије М. МАЛЕТИЋ, Владимир И. УДОВИЧИЋ, Радомир М. БАЊАНАЦ,
Дејан Р. ЈОКОВИЋ, Александар Ј. ДРАГИЋ, Никола Б. ВЕСЕЛИНОВИЋ,
Јелена З. ФИЛИПОВИЋ**

ПОРЕЂЕЊЕ МУЛТИВАРИЈАНТНИХ МЕТОДА ПРИ КЛАСИФИКАЦИЈИ И РЕГРЕСИЈИ РЕЗУЛТАТА МЕРЕЊА РАДОНА У ЗАТВОРЕНИМ ПРОСТОРИЈАМА

Представљамо резултате тестирања коришћења мултиваријантних метода, развијених за анализу података у физици високих енергија и имплементираних у програмском пакету за мултиваријантну анализу – у нашем проучавању зависности варијација концентрације радона у затвореним просторијама и климатских варијабли. Мултиваријантни методи омогућавају испитивање повезаности широког спектра климатских варијабли и концентрације радона, и онда када међу њима нема значајних корелација. Показали смо да мултиваријантни методи за класификацију и регресију раде добро, дајући као резултат нове информације и индикације које би могле бити корисне у даљем изучавању варијација концентрације радона у затвореним просторијама. Коришћењем ових метода, моћи ће да се дође до релативно добре моћи предвиђања концентрација радона, користећи само податке климатских варијабли.

Кључне речи: радон, мултиваријантна анализа, климатски параметар

Prompt fission γ -ray data from spontaneous fission and the mechanism of fission-fragment de-excitation

Stephan Oberstedt^{1,a}, Aleksandar Dragic^{1,2}, Angelique Gatera^{1,b}, Alf Gök¹, Franz-Josef Hambsch¹, and Andreas Oberstedt³

¹ European Commission, Joint Research Centre, Directorate for Nuclear Safety and Security, Unit G.2 Standards for Nuclear Safety, Security and Safeguards, 2440 Geel, Belgium

² Institute of Physics, Pregrevica 118, 11080 Belgrade, Serbia

³ Extreme Light Infrastructure - Nuclear Physics (ELI-NP) / Horia Hulubei National Institute for Physics and Nuclear Engineering (IFIN-HH), Bucharest-Magurele 077125, Romania

Abstract. The investigation of prompt γ -ray emission in nuclear fission has a great relevance for the assessment of prompt heat generation in a reactor core and for the better understanding of the de-excitation mechanism of fission fragments. Some years ago experimental data was scarce and available only from a few fission reactions, $^{233,235}\text{U}(n_{th}, f)$, $^{239}\text{Pu}(n_{th}, f)$, and $^{252}\text{Cf}(sf)$. Initiated by a high priority data request published by the OECD/NEA a dedicated prompt fission γ -ray measurement program is being conducted at the Joint Research Centre Geel. In recent years we obtained new and accurate prompt fission γ -ray spectrum (PFGS) characteristics (average number of photons per fission, average total energy per fission and mean photon energy) from $^{252}\text{Cf}(sf)$, $^{235}\text{U}(n_{th}, f)$ and $^{239,241}\text{Pu}(n_{th}, f)$ within 2% of uncertainty. In order to understand the dependence of prompt fission γ -ray emission on the compound nuclear mass and excitation energy, we started a first measurement campaign on spontaneously fissioning plutonium and curium isotopes. Results on PFGS characteristics from $^{240,242}\text{Pu}(sf)$ show a dependence on the fragment mass distribution rather than on the average prompt neutron multiplicity, pointing to a more complex competition between prompt fission γ -ray and neutron emission.

1. Introduction

Some years ago new interest was shown in the measurement of prompt fission γ -ray spectra (PFGS). This was motivated by requests for new precise values especially for γ -ray multiplicities and average photon energy release per fission in the thermal-neutron induced fission on ^{235}U [1] and ^{239}Pu [2]. Improvements of nuclear data have now become possible due to advances in scintillator materials, as used e.g. in lanthanide halide detectors. They offer a superior combination of intrinsic peak efficiency, energy and timing resolution, as already demonstrated in a number of recent experiments on $^{252}\text{Cf}(sf)$ [3–5], $^{235}\text{U}(n_{th}, f)$ [4, 6] and $^{241}\text{Pu}(n_{th}, f)$ [4, 7].

A first parametrization to describe systematic trends of PFGS characteristics was made by T.E. Valentine [9], where he introduced a somewhat arbitrary functional dependence of PFGS characteristics on the compound nucleus' mass and atomic numbers as well as its prompt fission neutron multiplicity to account for the competition between the two de-excitation channels of prompt γ -ray and neutron emission. In this early work only $^{252}\text{Cf}(sf)$ and thermal-neutron induced fission were considered. The parameters obtained back then need an adjustment due to recently published experimental results as shown in Refs. [10, 11], and JRC Geel started measurements on

spontaneously fissioning actinides other than ^{252}Cf . We obtained first results on PFGS characteristics from the spontaneous fission of ^{240}Pu and ^{242}Pu [8].

2. Experiment and data treatment

The prompt fission γ -ray measurements on ^{240}Pu and ^{242}Pu formed part of a series of experiments, which originally aimed at the precise measurement of their neutron-induced fission cross-sections, in response to a high-priority request published through the OECD/NEA [12, 13]. In preparation of these measurements a precise determination of the spontaneous fission half-life of each isotope was achieved [14]. For this proceedings we will summarize briefly the experimental setup and the achieved results. More details may be found in Ref. [8].

A pre-requisite for such measurements is the availability of high-quality targets with a high isotopic purity. The preparation of such targets was achieved at the EC-JRC Geel [15]. The plutonium targets had an isotopic purity of 99.89 and 99.96%. Thin targets of ^{240}Pu (92.94 μg) and ^{242}Pu (6716 μg) were placed back-to-back at the central cathode position inside a cylindrical twin Frisch-grid ionization chamber. The fission rates were 0.044/s and 0.54/s for ^{240}Pu and ^{242}Pu , respectively. In coincidence with the fission fragments γ -rays were measured with one coaxial $\text{LaBr}_3:\text{Ce}$ scintillation detector of size 76.2 mm \times 76.2 mm (diameter \times length).

^a e-mail: stephan.oberstedt@ec.europa.eu

^b The European Commission is gratefully acknowledged for providing a PhD fellowship to one of the authors (A. Gatera).

Table 1. Average prompt fission γ -ray spectrum characteristics for the spontaneous fission of ^{240}Pu and of ^{242}Pu from this work compared with corresponding results from thermal-neutron induced fission on $^{239,241}\text{Pu}$ from Refs. [7,22] and from systematic trends established in Ref. [9].

$(^A\text{X})_{CN}$	Δt (ns)	\overline{M}_γ (/fission)	$\overline{\epsilon}_\gamma$ (MeV)	$\overline{E}_{\gamma,tot}$ (MeV)	Reference
^{242}Pu	± 10	6.72 ± 0.07	0.843 ± 0.012	5.66 ± 0.06	this work
^{242}Pu		6.5 ± 0.5	0.93 ± 0.07	6.05 ± 0.03	[9]
$^{242}\text{Pu}^*$	± 3	8.21 ± 0.09	0.78 ± 0.01	6.41 ± 0.06	[7]
^{240}Pu	± 10	8.2 ± 0.4	0.80 ± 0.07	6.6 ± 0.5	this work
^{240}Pu		6.4 ± 0.5	0.95 ± 0.07	6.07 ± 0.03	[9]
$^{240}\text{Pu}^*$	± 10	7.23	0.94 ± 0.05	6.81 ± 0.3	[22]

The pulse-height of the γ -rays was calibrated with standard radioactive sources with decay energies between 81 keV and 4.44 MeV, using ^{133}Ba (81 keV–356 keV), ^{137}Cs (662 keV), ^{60}Co (1173 keV, 1333 keV), ^{232}Th (583 keV and 2614 keV) and AmBe (decay of the first excited state in ^{12}C ; $E_\gamma = 4.44$ MeV). The low-energy threshold during the PFGS measurements was set to 100 keV.

Due to the DAQ the timing resolution was about 7 ns (FWHM). This was still sufficient to discriminate prompt fission γ -rays from photons created in (n, n') reactions of fission neutrons by their time-of-flight relative to the instant of a fission event. With the γ -ray detector placed at a distance of 4082 mm relative to the fission source all neutrons with energies below 6.5 MeV were discriminated. The corresponding background-corrected numbers of prompt fission γ -rays measured in coincidence with a fission fragment were 888 and 8210.

3. PFGS characteristics from $^{242}\text{Pu}(\text{sf})$

To extract an emission spectrum from the measured one, the response function of the detector must be determined and unfolded. The usual procedure is to simulate, by means of Monte-Carlo simulations, the response of the detector to mono-energetic γ -rays accounting for the geometrical efficiency and the experimental set-up. The resulting spectra are then adjusted to the measured spectrum (for details see Ref. [3]). Due to the limited number of events at energies above 3 MeV, an exponential was fitted to the experimental data above 1.8 MeV. When extracting the spectral characteristics the uncertainty of the coefficients of the exponential function were properly taken into account.

The resulting prompt fission γ -ray spectrum is depicted in Fig. 1 by the red line. For comparison we show the emission spectrum obtained previously for the thermal-neutron induced fission on ^{241}Pu [7]. Both spectra agree very well with each other. The effect of the extra excitation energy in neutron-induced fission seems to be reflected in a surplus of photons at energies below 500 keV. The spectral characteristics, integrated from $0.1 \text{ MeV} \leq E_\gamma \leq 7 \text{ MeV}$, are summarized in Table 1.

4. PFGS characteristics from $^{240}\text{Pu}(\text{sf})$

In the case of $^{242}\text{Pu}(\text{sf})$ we were able to perform the *standard* unfolding of the measured PFGS. This was not possible in the present study in the case of $^{240}\text{Pu}(\text{sf})$ due to the poor counting statistics of less than 1000 events). Instead we followed here a different approach, based upon

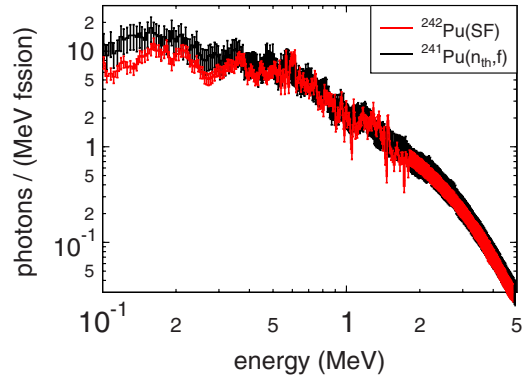


Figure 1. Prompt γ -ray spectrum for $^{242}\text{Pu}(\text{sf})$ in photons per MeV and per fission (red line); the corresponding spectrum for $^{241}\text{Pu}(n_{th}, f)$ [7] is shown for comparison (black line). The data are depicted in logarithmic energy scale to emphasize the low-energy region.

the definition of a so-called *transformation function* as detailed in the following.

The method of applying a transformation function is motivated by the fact that we measured both spectral data from two samples in essentially the same position relative to the γ -detector. Therefore, the response should be identical in both cases reported here. In addition, both measured spectra have to exhibit a very similar shape as we may observe in the case of $^{242}\text{Pu}(\text{sf})$ when compared to that from $^{241}\text{Pu}(n_{th}, f)$. Hence, we define a *transformation function* as ratio between the emission spectrum and the measured spectrum:

$$ES(E_{\gamma,i}) = TF(E_{\gamma,i}) \times MS(E_{\gamma,i}) / N_{fission}. \quad (1)$$

Here, $ES(E_{\gamma,i})$ denotes the emission spectrum, $MS(E_{\gamma,i})$ the measured one and $TF(E_{\gamma,i})$ a transformation function. The latter was determined from the experiment on $^{242}\text{Pu}(\text{sf})$. The energies $E_{\gamma,i}$, for which $TF(E_{\gamma,i})$ was calculated, correspond to the energies of the unfolded spectrum, to which the measured spectrum was interpolated to by using the Aitken-Neville method [18]. The transformation function contains both the statistical uncertainty from the measured spectrum as well as the uncertainties of the emission spectrum from the unfolding of the response function.

Prior to applying this transformation function to the measured prompt fission γ -ray spectrum from this work, new values and their uncertainties for matching energies were interpolated again. Finally, we obtain an emission spectrum as depicted as full (blue) line in Fig. 2. The error bars include the statistical uncertainties from the

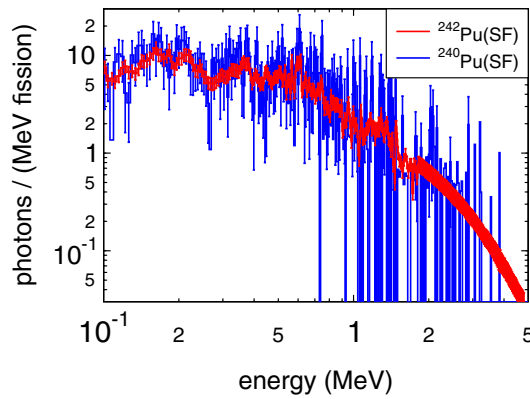


Figure 2. Prompt γ -ray spectra for $^{240}\text{Pu}(\text{sf})$ and $^{242}\text{Pu}(\text{sf})$ from this work depicted as full red and blue lines, respectively. The data are shown in logarithmic energy scale to emphasize the low-energy region.

measured spectrum and uncertainties in the transformation function. For comparison the PFGS for $^{242}\text{Pu}(\text{sf})$ is shown as full (red) line. The spectral characteristics, integrated from $0.1 \text{ MeV} \leq E_\gamma \leq 4 \text{ MeV}$, are summarized in Table 1. In Fig. 2 we show the spectra with a logarithmic energy scale to provide a better view on the low-energy part below 1 MeV. The excellent agreement between both emission spectra is obvious, which implies that also the measured spectra have the same shape indeed and, hence, one of the conditions for the meaningful application of a transformation function is fulfilled.

5. Results and discussion

Since we present here the first prompt fission γ -ray data from spontaneously fissioning ^{240}Pu and ^{242}Pu , we compare our results in Table 1 with spectral characteristics drawn from the above mentioned trend established by T.E. Valentine [9]. For a detailed decomposition of the uncertainties we refer to Ref. [8].

In the case of $^{242}\text{Pu}(\text{sf})$ the agreement is very reasonable, taking into account that the trend is based on a few experimental data available back then. The mean energy per photon, ϵ_γ , is close to 0.8 MeV. From our previous measurements we have evidence that the average energy per photon shows only weak dependence on the compound system and even on the incident neutron energy. That the multiplicity is somewhat higher, is in line with our findings in $^{252}\text{Cf}(\text{sf})$ [3–5], $^{235}\text{U}(\text{n}_{\text{th}}, \text{f})$ [4,6] and $^{241}\text{Pu}(\text{n}_{\text{th}}, \text{f})$ [4,7]. This is understandable when remembering that the low-energy threshold in our measurements is in most cases lower than in measurements conducted in the past. The different average multiplicity, \overline{M}_γ , observed between spontaneous and neutron-induced fission of ^{242}Pu scales well with the average total prompt neutron multiplicity for both fissioning systems, $\overline{\nu}_{\text{sf}} = 2.134(6)$ and $\overline{\nu}_{\text{th}} = 2.946(6)$ [19]. The influence of the different widths of the prompt time window, Δt (cf. Table 1), may be neglected, because $\Delta t \geq 1.43 \text{ FWHM}_t$ in both cases.

In case of $^{240}\text{Pu}(\text{sf})$, \overline{M}_γ appears on first sight pretty high, definitely when comparing with the predictions drawn from Valentine's trend. The differences may be regarded as significant despite the much larger uncertainty. However, our value for the average energy per photon,

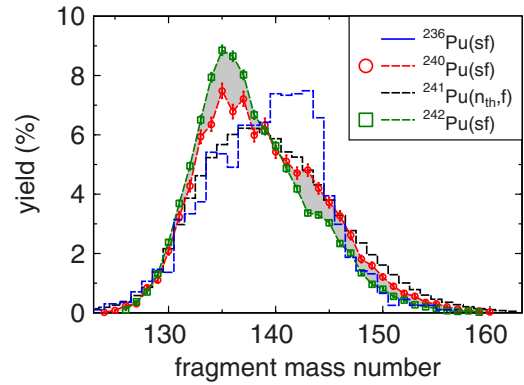


Figure 3. Pre-neutron fission-fragment yield distribution from $^{236,240,242}\text{Pu}(\text{sf})$ and $^{241}\text{Pu}(\text{n}_{\text{th}}, \text{f})$ in the heavy fragment mass region [20].

$\epsilon_\gamma = 0.8 \text{ MeV}$, is well in agreement with all our other results, providing us with confidence in our new PFGS data for $^{240}\text{Pu}(\text{sf})$ as well as in the underlying data analysis.

Systematic measurements of pre-neutron mass distributions from different spontaneously fissioning plutonium isotopes have revealed significant changes in fission fragment yield distribution as a function of neutron number of the compound nucleus [20]. Starting from ^{236}Pu , the maximum yield of heavy fragments, A_h , is around 142 u (Fig. 3). This position moves down to $A_h \approx 135$ u for ^{242}Pu , i.e. increasing the fraction of less-deformed fragments being close to the doubly magic isotope ^{132}Sn . One might, therefore, argue that in case of $^{240}\text{Pu}(\text{sf})$ the dominant fraction of deformed fragments leads to an enhanced multiplicity due to higher level densities manifesting in a higher \overline{M}_γ .

However, one must not forget that for both spontaneously fissioning isotopes $\overline{\nu}_{\text{sf}}$ is essentially the same with $\delta \overline{\nu}_{\text{sf}}(^{240}\text{Pu}, ^{242}\text{Pu}) < 0.4\%$ [19]. In Ref. [20] we find that the average total kinetic energy, $\overline{TK E}$, is lower for $^{240}\text{Pu}(\text{sf})$ by almost 2 MeV. This small amount of more excitation energy, depending on the Q-value of the reaction, does not seem to lead to an enhanced average neutron multiplicity, but may account for the excess observed for \overline{M}_γ .

6. Conclusion

PFGS characteristics from the spontaneous fission of ^{240}Pu and of ^{242}Pu were measured for the first time with reasonable statistical accuracy. This was possible in the case of ^{240}Pu by applying a transformation function on the measured spectrum in order to deduce the emission spectrum from a measured spectrum instead of a proper unfolding procedure by a response function. The transformation function was obtained from $^{242}\text{Pu}(\text{sf})$ measured with sufficient statistics under exactly the same conditions. This procedure seems to work well as long as reference spectra exist, that have a very similar shape, which is the case here. Hence, this technique should be considered as an alternative, if recorded spectra are obtained from a low number of events (see Ref. [8] and Refs. therein).

The results presented in this work fit well into the trend established by Valentine [9] and recently revised

in Refs. [10,11]. They may be regarded as the first step to enlarge the data base from which new systematic trends as a function of incident neutron energy are established.

The significantly enhanced average multiplicity in case of $^{240}\text{Pu}(\text{sf})$ points to a possible correlation of prompt γ -ray emission with the distinct shape of the fission fragment distribution. To fully understand the underlying physics more data is needed. Exchange with theoreticians is highly encouraged. In particular PFGS measurements on $^{244}\text{Pu}(\text{sf})$ and different spontaneously fissioning curium isotopes are recommended. For the latter also measurements of pre-neutron fragment distributions $Y(A, \text{TKE})$ will be indispensable.

A PFGS measurement on the reaction $^{239}\text{Pu}(n_{\text{th}}, f)$ to be compared with $^{240}\text{Pu}(\text{sf})$ in analogy to the presented ^{242}Pu case is subject of an on-going campaign.

References

- [1] Nuclear Data High Priority Request List of the NEA (Req. ID: H.4), www.oecd-nea.org/dbdata/hprl/hprlview.pl?ID=422
- [2] Nuclear Data High Priority Request List of the NEA (Req. ID: H.3), www.oecd-nea.org/dbdata/hprl/hprlview.pl?ID=421
- [3] R. Billnert, F.-J. Hamsch, A. Oberstedt, and S. Oberstedt, Phys. Rev. C **87**, 024601 (2013)
- [4] R. Billnert, T. Belgia, T. Bryś, W. Geerts, C. Guerrero, F.-J. Hamsch, Z. Kis, A. Oberstedt, S. Oberstedt, L. Szentmiklosi, K. Takács, and M. Vidali, Phys. Proc. **59**, 17 (2014)
- [5] A. Oberstedt, R. Billnert, F.-J. Hamsch, and S. Oberstedt, Phys. Rev. C **92**, 014618 (2015)
- [6] A. Oberstedt, T. Belgia, R. Billnert, R. Borcea, T. Bryś, W. Geerts, A. Göök, F.-J. Hamsch, Z. Kis, T. Martinez, S. Oberstedt, L. Szentmiklosi, K. Takács, and M. Vidali, Phys. Rev. C **87**, 051602(R) (2013)
- [7] S. Oberstedt, R. Billnert, T. Belgia, T. Bryś, W. Geerts, C. Guerrero, F.-J. Hamsch, Z. Kis, A. Moens, A. Oberstedt, G. Sibbens, L. Szentmiklosi, D. Vanleeuw, and M. Vidali, Phys. Rev. C **90**, 024618 (2014)
- [8] S. Oberstedt, A. Gatera, A. Göök, F.-J. Hamsch and A. Oberstedt, Phys. Rev. C **93**, 054603 (2016)
- [9] T.E. Valentine, Ann. Nucl. Energy **28**, 191 (2001)
- [10] A. Oberstedt, R. Billnert and S. Oberstedt, Proceedings of NEMEA-7 The 7th Workshop on Nuclear Measurements, Evaluations and Applications, November 5–8, 2013, Geel, Belgium, OECD Nuclear Science NEA/NSC/DOC **13**, 199 (2014)
- [11] A. Oberstedt, R. Billnert, and S. Oberstedt, manuscript to be submitted
- [12] Nuclear Data High Priority Request List of the NEA (Req. ID: H.37), www.oecd-nea.org/dbdata/hprl/hprlview.pl?ID=457
- [13] Nuclear Data High Priority Request List of the NEA (Req. ID: H.39), www.oecd-nea.org/dbdata/hprl/hprlview.pl?ID=457
- [14] P. Salvador-Castifeira, T. Bryś, R. Eykens, F.-J. Hamsch, A. Moens, S. Oberstedt, G. Sibbens, D. Vanleeuw, and M. Vidali, Phys. Rev. C **88**, 064611 (2013)
- [15] G. Sibbens, A. Moens, R. Eykens, D. Vanleeuw, F. Kehoe, H. Kühn, R. Jakopic, S. Richter, A. Plompen, Y. Aregbe, J. Radioanal. Nucl. Chem. **299**, 1093–1098 (2014)
- [16] www.mesytec.com/datasheets/MPR-1.pdf
- [17] <http://www.keysight.com/en/pd-1184897-pn-U1065A/acqiris-10-bit-high-speed-cpci-digitizers?&cc=BE&lc=dut>
- [18] I.N. Bronstein, K.A. Semendjajew, G. Musiol, H. Mühlig, Taschenbuch der Mathematik mit Multiplattform-CD-ROM, 5. Edition, Verlag Harri Deutsch, Frankfurt am Main, ISBN: 978-3-8171-2017-8 (2000)
- [19] F. Gönnewein, in: C. Wagemans (editor), The Nuclear Fission Process, CRC press (1991), ISBN 0-8493-5443-X, Chapter 11, 514
- [20] L. Demattè, C. Wagemans, R. Barthelemy, P. D'Hondt, A. Deruytter, Nucl. Phys. A **614**, 331 (1997)
- [21] R. Gold, An Iterative Unfolding Method for Response Matrices, Argonne National Laboratory, ANL-6984 (1964)
- [22] V.V. Verbinski, Hans Weber, and R.E. Sund, Phys. Rev. C **7**, 1173 (1973)

Utilization of a shallow underground laboratory for studies of the energy dependent CR solar modulation

N. Veselinović, A. Dragić, M. Savić, D. Maletić, D. Joković, R. Banjanac, V. Udovičić,
Institute of physics, University of Belgrade, Serbia

The aim of the paper is to investigate possibility of utilizing a shallow underground laboratory for the study of energy dependent solar modulation process and to find an optimum detector configuration sensitive to primaries of widest possible energy range for a given site. The laboratory ought to be equipped with single muon detectors at ground level and underground as well as the underground detector array for registration of multi-muon events of different multiplicities. The response function of these detectors to primary cosmic-rays is determined from Monte Carlo simulation of muon generation and propagation through the atmosphere and soil, based on Corsika and GEANT4 simulation packages. The simulation predictions in terms of flux ratio, lateral distribution, response functions and energy dependencies are tested experimentally and feasibility of proposed setup in Belgrade underground laboratory is discussed.

1. INTRODUCTION

Cosmic rays (CR) are energetic particles, arriving at the Earth from space after interaction with the heliosphere. The interaction of these, primary CRs, with the atmosphere leads to production of a cascade (shower) of secondary particles: hadrons, electrons and photons, muons, neutrinos. CR research has been undertaken at almost every location accessible to humans – from the outer space to deep underground [1].

At the low energy part of the spectrum, lower than 100 GeV, CRs are affected by the solar magnetic field. Modulation effects are energy dependent and have been studied extensively by the neutron monitors, sensitive up to about 10 GeV. Muon detectors at the ground level are sensitive to higher energy primaries [2], and the muons detected underground correspond to even higher energies. The possibility to further extend the sensitivity to higher energies with the detection of multi-muon events underground is the intriguing one. The idea was exploited with the EMMA underground array [3]. For a shallow underground laboratory, exceeding the energy region of solar modulation would open the possibility to study CR flux variations of galactic origin.

2. BELGRADE CR STATION

The Belgrade cosmic-ray station is situated at the Laboratory for Nuclear Physics at the Institute of Physics. Its geographic position is: latitude $44^{\circ} 51' N$ and longitude $20^{\circ} 23' E$, altitude of 78 m a.s.l., with geomagnetic latitude $39^{\circ} 32' N$ and geomagnetic vertical cut-off rigidity 5.3 GV. It is composed of two sections, the underground lab (UL) with useful area of 45 m^2 , dug at the 12-meter shallow depth (equivalent to 25 m.w.e) and the ground level lab (GLL). At UL depth, practically, only the muonic component of the atmospheric shower is present.

The cosmic-ray muon measurements in Belgrade CR station are performed by means of the plastic scintillation detectors, placed both in the GLL and in the UL. With the previous set-ups, monitoring is continuous from 2002.

Measured cosmic-ray intensity data were thoroughly analysed, yielding some results on the variations of the cosmic-ray intensity [4,5,6].

Time series (pressure and temperature corrected) of these measurements can be accessed online at http://cosmic.ipb.ac.rs/muon_station/index.html.

In addition to single muon detectors, a small-scale test setup for multi-muon events is installed underground. It consists from three scintillators: one large detector (100cm x 100cm x 5cm) and two small detectors (50cm x 23cm x 5cm) which are placed horizontally on their largest sides. Their mutual position is adaptable. The data acquisition system is based on fast 4-channel flash analog-to-digital converters (FADC), made by CAEN (type N1728B), with 100 MHz sampling frequency. The events are recorded in the list mode. For each event from every input channel the timing and amplitude are saved, together with auxiliary information such as the result of pile-up inspection routine. From this list a time series of single or coincident events could be constructed. The experimental set-up is sketched in Figure 1.

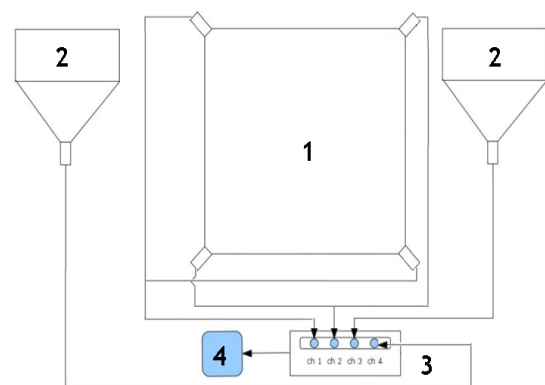


Figure 1 : Sketch of the experimental set-up for the cosmic-ray measurements:

1) Large scintillation detector, 2) small scintillation detectors, 3) flash analog-to-digital Converter (FADC), 4) experiment control and data storage computer

With simultaneous operation of several detector systems, as described, a single facility with the same rigidity cut-off would be used for investigation of solar modulation at different energies. Further integration with the Neutron Monitors data would be beneficial [7, 8, 9].

3. SIMULATION DETAILS AND RESULTS

Simulation of the CR shower dynamics up to the doorstep of GLL and UL has been done using Monte Carlo simulation packages CORSIKA and Geant4 [10, 11]. The cosmic-ray muon spatial and momentum distribution at 78m a.s.l. is of our interest. The output of CORSIKA at ground level is used as the input for Geant4 based simulation of particle transport through the soil and simulation of detector response. For this purpose soil analysis is done beforehand. The mean density is found to be (2.0 ± 0.1) g/cm³ and soil type is loess with the assumed composition of Al₂O₃ 20%, CaO 10% and SiO₂ 70%. For the simulation of underground detector system only those muons with energy sufficient enough to survive passage through soil are taken into consideration (Figure 2).

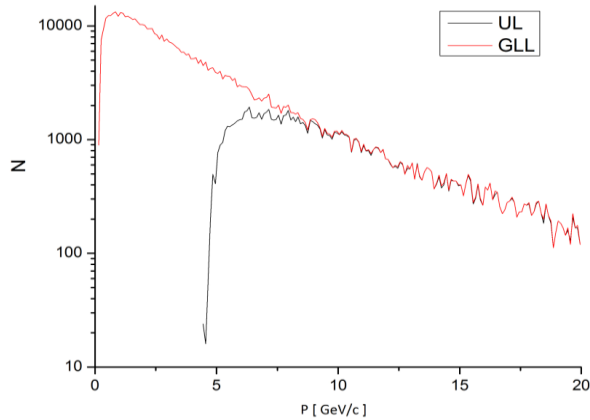


Figure 2: Surface momentum distribution for muons at GLL and muons reaching UL at Belgrade CR station based on GEANT4 and CORSIKA

At lower energies, protons make ~85% of CR, so primary particles used in the simulation were protons. The number of muons reaching UL is not linearly proportional to energy of the primary particle, especially for energies lower than 200 GeV which is energy range of interest, as showed in Figure 3. This correspond to similar work done elsewhere [12]. Probability that a registered event corresponds to a primary particle of certain energy is inferred from the simulation for every detection system:

- Single muon detector at ground level
- Single muon detector underground
- Two-fold muon coincidences underground
- Muon coincidences of higher multiplicity

For these response functions, simulation use 23 million primary protons with energy range from 5 GeV to 10^{16} eV

with zenith angle between (0° , 70°) and with power law energy spectrum with the exponent -2.7 .

Shift toward higher energies is evident for transition from GL to UL and to the events of higher multiplicities.

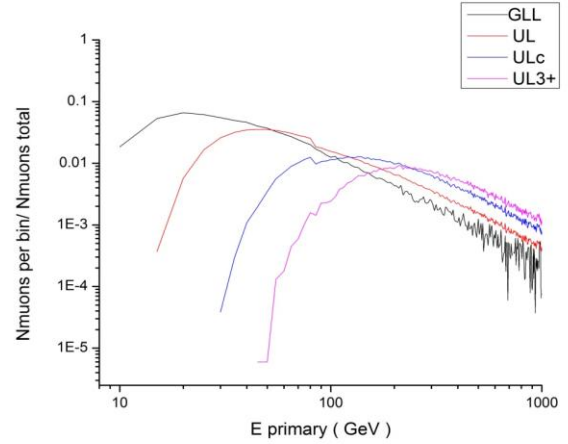


Figure 3: Differential response functions of muon detectors in GLL and UL based on simulation for: single muons at ground level (GLL), underground level (UL), coincident muons at underground level (ULc) and triple and higher multiplicity coincident muons at underground level (UL3+) normalized to total number of muons respectively.

For all relevant quantities of the muon flux is given at Table 1. Equivalent depth was found using ratios of integral fluxes of muons at different shallow depth [13].

Table 1: Properties of the flux of the primary particles at Belgrade CR station based on simulation for: ground level (GLL), underground level (UL), coincident muons at underground level (ULc) and triple and more coincident muons at underground level (UL3+).

Primary protons	GLL	UL	ULc	UL3+
Energy cut-off	5 GeV	12.3 ± 0.7 GeV	30 ± 4 GeV	55 ± 14 GeV
Equivalent depth	0 m.w.e. GLL Belgrade	25 m.w.e.	40 m.w.e.	66 m.w.e.
Peak energy	20 GeV	45 GeV	125 GeV	200 GeV
Median energy	62 GeV	122 ± 5 GeV	296 ± 8 GeV	458 ± 18 GeV

Cut-off energy at the ground level is due to geomagnetic cut-off rigidity at Belgrade CR station. For the

underground level, the 25 m.w.e. of soil overburden is the cause of the higher cut-off underground. All the relevant quantities: cut-off, peak and median energies are higher underground and for the events with higher multiplicity. This, in principle, creates a possibility to investigate the CR flux and its variations at different energies of primaries, exceeding the energies relevant to neutron monitors, the most frequently used instrument for study of the low energy side of the CR spectrum. This vindicates the aim of the simulation to investigate possibility of utilizing a shallow underground laboratory for the study of energy dependent solar modulation process and to find an optimum detector configuration sensitive to primaries of different energy range for a given site.

4. DISCUSION ON FEASIBILITY

It is needed, however, to address the questions of reliability of simulation. On the graph 3, the discontinuity at energy of 80 GeV of primary protons is visible, especially muon in UL and muons in UL in coincidence. CORSIKA, by default, uses GHEISHA 2002d particle generator to calculate the elastic and inelastic cross-sections of hadrons below 80 GeV in air and their interaction and particle collisions and for higher energies QGSJET 01C routine is used. Also it is important to know whether sufficient statistics of multi-muon events could be achieved in the limited laboratory space. For this purpose, the flux of single muons is measured at ground level and underground, the rate of double coincidences as a function of detector distance is simulated also. In addition, the rates of double and triple coincidences are also measured for several detector arrangements.

The muon flux is calculated, from simulation, by finding ratio between the number of muons reaching depth of UL (for single and muons in coincidence) and numbers of muons generated from CORSIKA at the surface and multiplying by experimentally measured value of integrated muon surface flux which is 137(6) muons per m^2s [14]. The experimental value of integrated flux, compared with number of muons from simulation, is also used to find physical time needed to generate same number of muons at the site as the simulation.

Absolute muon fluxes measured at the site for surface and shallow underground is well reproduced by the simulation (Table 2).

Table 2: Ratio of muon fluxes at Belgrade CR station based on measurements and simulation for: ground level (GLL), underground level (UL), coincident muons at underground level (ULc) and triple and more coincident muons at underground level (UL3+)

Muon flux ratio	Measured GLL/UL	Simulation GLL/UL	Simulation UL/ULc	Simulation UL/UL3+
	3.17(8)	3.06(3)	1.86(4)	2.68(6)

Recently with new detector arrangement, the scintillators in Belgrade CR station measured coincident events and triple coincident events at two distances of the detectors: 1.5m and 6m, in UL part of the laboratory. Number of coincidences per unit area of the detector, based on simulation for these distances is 80 and 66 muon coincidences per m^2 per day respectively. Experimental values are higher for closer (~350 coincidences a day) and ~60 coincidences per day for farther arrangement. The ratio of single/coincidence events underground is well reproduced for greater distance of the detector. At shorter distances the measured ratio is higher than predicted by simulation, further study will show is it due to contribution from local EM showers and knock-on electrons. Numbers of measured triple coincidences at same distances are the order of magnitude smaller.

When upgraded, the detector arrangements will cover the whole area of the UL with muon detectors it should provide, based on the simulation, approximately 61k coincidences per day thus allowing to observe ~ 1.2% fluctuation of the CR flux with 3σ certainty originated from Solar modulation (e.g. Forbush decreases) thus allowing possibility to study solar modulation on three different energy ranges of the primary particles and at higher energies then regular energies detected with NM. To prevent miss-identification of muons, additional methods of sorting muons is needed (lead shielding, hodoscopes...) or to measure only coincidences that occur on reliable distances between detectors, larger then 6m, allowing observation of higher fluctuations (~2.5%) with same certainty.

In principle, larger shallow depth laboratories [15] can be used to investigate solar modulation and extreme solar events on different energies of primary particles, using rate of detected muons on different detectors in coincidence but present small detection area at Belgrade CR station can also give some valuable insight.

5. CONCLUSION

The possibility of utilizing a shallow underground laboratory for the study of energy dependent solar modulation of CR is investigated, by means of computer simulation based on CORSIKA and GEANT packages, combined with the experiment. On the experimental part, the muon flux is measured at ground level and underground at the depth of 25 mwe. In the present feasibility study, the flexible test setup for detection of multiple muons is installed underground in an attempt to achieve sensitivity to higher energy primaries. The rates of double and triple coincidences are measured for several detector distances. The simulation revealed the response functions of each experimental setup. The experimental fluxes are compared with those arising from simulation (Table 2). For single muons, the experimental ratio of

fluxes GLL/UL agrees with the simulated one. The experimental ratio of single/coincident events underground is well reproduced by simulation if the detector distance is greater than 6m. At shorter distances the measured ratio is higher than predicted by simulation, mainly due to contribution from local EM showers and knock-on electrons. When upgraded, the detector arrangements will cover almost the entire area of the UL with muons detectors resulting in expected approximately 61k coincidence per day. One day of measurements will be sufficient to observe $\sim 1.2\%$ fluctuation of the flux at 3σ significance for CRs with several hundred GeV of energy. Together with the single muon measurements at GLL and UL we will have simultaneous measurements centered on three different energies, under the same atmospheric and geomagnetic conditions. Any difference in time series behavior could be attributed to energy dependent response to the forcing. The rate of triple coincidences is too low to be effectively exploited in our conditions.

Acknowledgments

The present work was funded by the Ministry of Education and Science of the Republic of Serbia, under the Project No. 171002. .

References

- [1] L.I. Dorman, Cosmic-rays in the Earth's Atmosphere and Underground, Kluwer, Dordrecht, (2004)
- [2] I. Braun, J. Engler, J.R. Hörandel, J. Milke, Forbush decreases and solar events seen in the 10 - 20GeV energy range by the Karlsruhe Muon Telescope, ADVANCES IN SPACE RESEARCH 43(4):480-488, (2008)
- [3] Kalliokoski ,L. Bezrukov, T. Enqvist, H. Fynbo, L. Inzhechik, P.J. Jones, J. Joutsenvaara, J. Karjalainen, P. Kuusiniemi, K. Loo, B. Lubsandorzhev, V. Petkov, T. Rähkä, J. Sarkamo, M. Slupecki, W.H. Trzaska, A. Virkajärvi, Can EMMA solve the puzzle of the knee?, Progress in Particle and Nuclear Physics 66, 468-472, (2011)
- [4] A.Dragić, V.Udovičić, R.Banjanac, D.Joković, D.Maletić, N.Veselinović, M.Savić, J.Puzović, I.Aničin, The new set-up in the Belgrade low-level and cosmic-ray laboratory, Nucl. Technol. Radiat. 26, 181-192 , (2011)
- [5] A.Dragić, R.Banjanac, V.Udovičić, D.Joković, J.Puzović, I.Aničin, Periodic Variations of CR Muon Intensity in the Period 2002-2004 , Proceedings of the 21st European cosmic-ray Symposium, Košice, Slovakia ,368-373, (2008)
- [6] N. Veselinović, A. Dragić, D. Maletić, D. Joković, M. Savić, R. Banjanac ,V. Udovičić and I. Aničin, Cosmic rays muon flux measurements at Belgrade shallow underground laboratory, AIP Conf. Proc. 1645, 421 (2015); <http://dx.doi.org/10.1063/1.4909614>
- [7] S.N.Karpov ,Z.M. Karpova, A.B. Chernyaev, Multiplicity, yield and response functions for Baksan EAS-arrays and Muon Detector in comparison with similar functions of Neutron Monitors, Proceedings of the 29th International Cosmic Ray Conference, Pune, India, (2005)
- [8] D. Maurin, A. Cheminet, L. Derome, A. Ghelfi, G Hubert, Neutron Monitors and muon detectors for solar modulation studies: Interstellar flux, yield function, and assessment of critical parameters in count rate calculations, Advances in Space Research 55 (1) 363 (2015)
- [9] J.M. Clem and L.I. Dorman, Neutron monitor response functions, Space Science Reviews, Volume 93, Issue 1, pp 335-359,(2000)
- [10] D. Heck et al., CORSIKA: a Monte Carlo code to simulate extensive air showers, Report FZKA 6019, Forschungszentrum Karlsruhe, (1998)
- [11] S. Agostinelli et al., the Geant4 collaboration, Nucl. Instrum. Meth. A 506, 250-303, (2003)
- [12] A. Bogdanov, A. Dmitrieva, R. Kokoulin, A. Petrukhin, D. Timashkov, E. Yakovleva, Coupling functions for primary cosmic rays and ground-level muons at various zenith angles, Proceedings of the 21st European Cosmic Ray Symposium, pp341-346L, (2008)
- [13] N. Bogdanova, M. G. Gavrilov, V. N. Kornoukhov, A. S. Starostin, Cosmic muon flux at shallow depths underground, Phys.Atom.Nucl. 69 , 1293-1298, (2006)
- [14] A. Dragić et al., Measurement of cosmic ray muon flux in the Belgrade ground level and underground laboratories,Nucl. Instrum. Meth. A 591, 470-475, (2008)
- [15] F. Suarez for the Pierre Auger Collaboration, The AMIGA muon detectors of the Pierre Auger Observatory: overview and status, 33rd international cosmic ray conference, (2013)

Effect of pressure and temperature corrections on muon flux variability at ground level and underground

M. Savic, A. Dragic, N. Veselinovic, V. Udovicic, R. Banjanac, D. Jokovic, D. Maletic
Institute of Physics, Belgrade, Pregrevica 118, Serbia

In Low Background Laboratory at Institute of Physics Belgrade, plastic scintillators are used to continuously monitor flux of the muon component of secondary cosmic rays. Measurements are performed on the surface as well as underground (25 m.w.e depth). Temperature effect on muon component of secondary cosmic rays is well known and several methods to correct for it are already developed and widely used. Here, we apply integral method to calculate correction coefficients and use GFS (Global Forecast System) model to obtain atmospheric temperature profiles. Atmospheric corrections reduce variance of muon flux and lead to improved sensitivity to transient cosmic ray variations. Influence of corrections on correlation with neutron monitor data is discussed.

Belgrade Low Background Laboratory (LBL) is located at Institute of Physics, Belgrade and consists of two interconnected spaces, a ground level laboratory (GLL) and a shallow underground one (UL) [Fig. 1]. GLL is at 75 meters above sea level while UL is dug under a 10 meter cliff and has a 12 meters of loess soil overburden (25 meters of water equivalent) [1]. Geographic latitude for the site is 44.86 and longitude is 20.39 while geomagnetic rigidity cutoff is 5.3 GV.

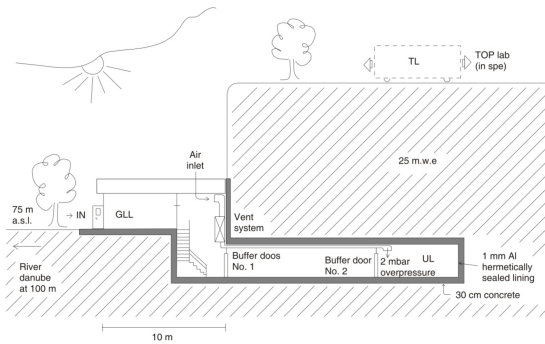


FIG. 1: Layout of the Low Background Laboratory.

Experimental setup consists of two identical sets of detectors and read out electronics, one situated in GLL and the other in UL. Each setup utilizes a plastic scintillator detector with dimensions 100cm x 100cm x 5cm (Amcryst-H, Kharkov, Ukraine) equipped with 4 PMTs (Hamamatsu R1306) directly coupled to the corners [Fig. 2]. Flash ADC (CAEN type N1728B) with 10ns sampling are used for read out [1].

Preamplifier outputs of two diagonally opposing PMTs are summed and fed to a single FADC input thus engaging two inputs of the FADC for two such diagonal pairings. Signals recorded by the two inputs are coincided in offline analysis, resulting in coincidence spectrum which is then used to determine the integral count [Fig. 3]. This procedure almost completely eliminates low-energy environmental background leaving only events induced by cosmic ray muons and muon related EM showers [1].

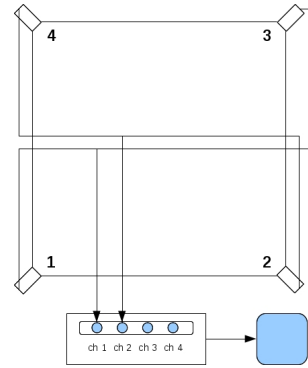


FIG. 2: Experimental setup scheme.

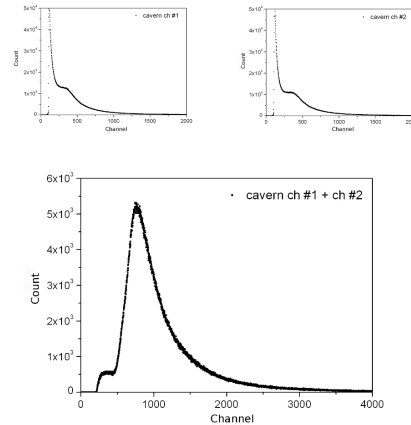


FIG. 3: Single summed diagonal and coincidence spectra.

I. SIGNIFICANCE OF METEOROLOGICAL EFFECTS

Meteorological effects on muon component of secondary cosmic rays are well known, with pressure and temperature effect being most dominant [2]. Correcting for these effects noticeably increases data usefulness, especially increasing sensitivity to periodic and aperiodic variations of non-atmospheric origin (vari-

ations of primary cosmic rays, different heliospheric processes, etc.)

In Belgrade Low Background Laboratory continual measurements utilizing described setup started in April of 2008 for the GLL and in November of 2008 for the UL, and with some interruptions are still ongoing. Base time resolution for integrated count is 5 minutes but time resolution of 1 hour is also often used in analysis. Link to Belgrade cosmic ray station can be found on the following address: <http://www.cosmic.ipb.ac.rs/>.

A. Pressure effect

Barometric effect is defined by the following equation:

$$\left(\frac{\delta I}{I}\right)_P = \beta \cdot \delta P \quad (1)$$

where $\frac{\delta I}{I}$ is the normalized variation of muon flux intensity, β is barometric coefficient and δP is pressure variation. Pressure variation is calculated as $\delta P = P - P_B$, where P is current pressure and P_B is base pressure value [4].

Since no in situ pressure measurement was performed prior to 2015, current pressure values have mostly been acquired from official meteorological measurements performed by Republic Hydrometeorological Service of Serbia as well as from Belgrade airport meteorological measurements. In all, data from 5 different stations were used. All pressure data was normalized to Belgrade main meteorological station. Stations were sorted according to geographical proximity and consistence of data. Unique pressure time series was composed by using data from the first station with available pressure entries for a given hour. Linear interpolation was then performed and pressure values were sampled with 5 minute step. Normalized variation of muon flux intensity vs. pressure variation was plotted for each year. Only data for the 5 geomagnetically most quiet days of each month were taken into account (selected from International Quiet Days list). Barometric coefficient for each year was determined from linear fits of these plots [Fig. 4].

B. Temperature effect

Temperature effect on hard muons is well known [2] and there are several methods developed to describe and correct for it. Method we used was integral method, where normalized variation of muon flux dependence on temperature variation is described as:

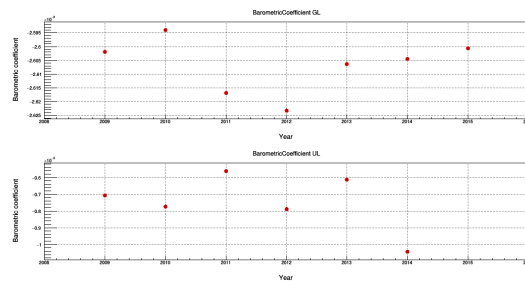


FIG. 4: Yearly values for barometric coefficient for GLL and UL.

$$\left(\frac{\delta I}{I}\right)_T = \int_0^{h_0} \alpha(h) \cdot \delta T(h) \cdot dh \quad (2)$$

$\alpha(h)$ being temperature coefficient density and temperature variation calculated as $\delta T = T - T_B$, where T is current temperature and T_B is base temperature value [3].

To correct for temperature effect using formula above it is necessary to have most complete information about atmospheric temperature profile for a given geographical location as well as to know temperature coefficient density function. Temperature profile measurements performed by local meteorological service are not done on consistent basis but more detailed information is available from meteorological models. One such model is GFS (Global Forecast System) that, among other data, provides temperatures for 25 isobaric levels for a given geographical location with latitude/longitude precision of 0.5 degrees [3].

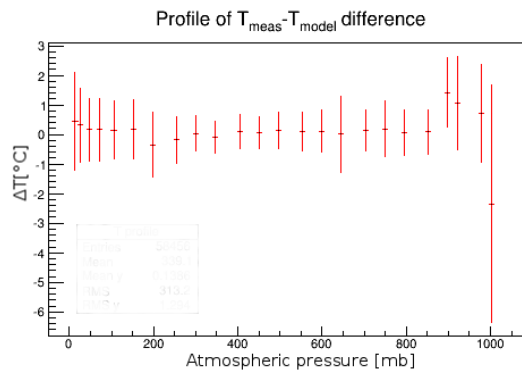


FIG. 5: Distribution of difference between modelled temperatures and temperatures measured by meteorological balloons above Belgrade (where such data was available).

Measured and modelled values seem to be in fairly good agreement [Fig. 5] except for the lowest isobaric level. That is why for this level temperature from local meteorological stations was used, treated in the same manner as described for local pressure data. Time

resolution for modelled temperatures is 6 hours so interpolation was performed using cubic spline [3] and temperature values were sampled in 5 minute steps.

Temperature density functions [Fig. 6] are calculated according to procedure described in [2].

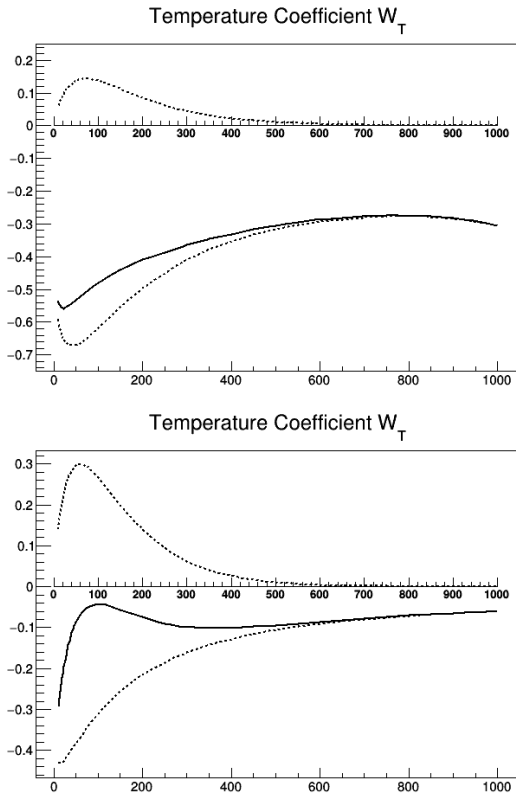


FIG. 6: Temperature coefficient density functions for ground level (above) and depth 25 m.w.e. (below).

II. RESULTS

A. PT corrected time series

It would seem that pressure correction successfully removes aperiodic pressure induced fluctuations while temperature correction most significantly affects annual variation induced by atmospheric temperature variations [Fig. 7].

B. Spectral analysis

Spectral analysis can give us more insight into effect of temperature correction on annual variation of muon count (presented for GLL data in [Fig. 8])

After temperature correction, peak related to annual periodicity in power spectrum appears to be significantly reduced relative to nearby peaks.

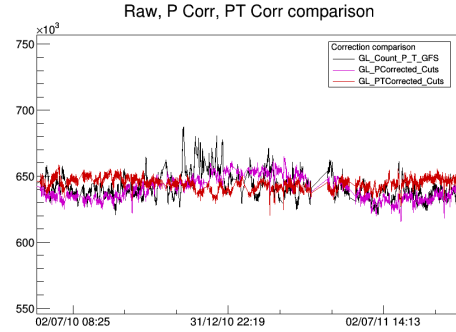


FIG. 7: GLL raw (black), pressure corrected (magenta) and PT corrected (red) muon count time series for a selected period.

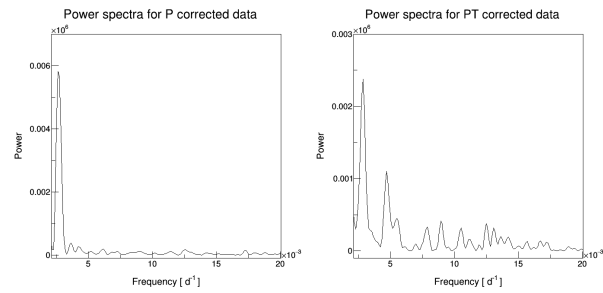


FIG. 8: Power spectra for pressure corrected and temperature and pressure corrected data.

C. Neutron monitor correlation

Possible validation for correction procedure would be agreement of pressure/temperature corrected muon count time series with neutron monitor data. BAK-SAN neutron monitor was selected as a possible reference [Fig. 9].

III. CONCLUSIONS

Corrections for temperature and pressure effect are essential for muon data gathered at Belgrade LBL. Atmospheric temperature profile for Belgrade seems to be adequately modeled by GFS. Temperature correction utilizing integral method seems to give acceptable results (while quality can still be further improved). Also, other methods could be applied and results compared. Muon flux data after pressure and temperature corrections has increased sensitivity to periodic and aperiodic effects of non-atmospheric origin. Preliminary comparison with neutron monitor data supports this claim with more detailed correlation analysis to follow in the future.

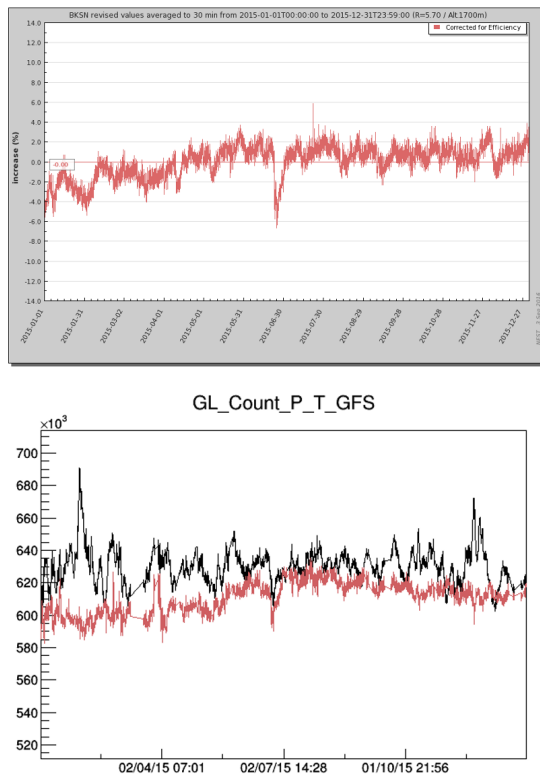


FIG. 9: BAKSAN neutron monitor (above) and GLL raw and pressure/temperature corrected data (below in red) comparison for year 2015.

IV. ACKNOWLEDGEMENTS

The present work was funded by the Ministry of Education and Science of the Republic of Serbia, under the Project No. 171002. The Belgrade Laboratory bears the name of Dr. Radovan Antanasijevic, in honour of its early deceased founder and first director.

V. REFERENCES

- [1] The new set-up in the Belgrade low-level and cosmic-ray laboratory Nucl. Technol. Radiat. 26 (2011) 181-192. A.Dragic at all
- [2] Dorman, Cosmic Rays in the Earths Atmosphere and Underground
- [3] M. Berkova , A. Belov, E. Eroshenko, and V. Yanke, Temperature effect of muon component and practical questions of how to take into account in real time, Astrophys. Space Sci. Trans., 8, 41-44, 2012
- [4] R. R. S. De Mendona, J. -P. Raulin, E. Echer, V. S. Makhmutov, and G. Fernandez, Analysis of atmospheric pressure and temperature effects on cosmic ray measurements. JOURNAL OF GEOPHYSICAL RESEARCH: SPACE PHYSICS, VOL. 118, 14031409, doi:10.1029/2012JA018026, 2013

PAPER • OPEN ACCESS

Pressure and temperature effect corrections of atmospheric muon data in the Belgrade cosmic-ray station

To cite this article: M Savi *et al* 2015 *J. Phys.: Conf. Ser.* **632** 012059

View the [article online](#) for updates and enhancements.

Related content

- [Temperature effect correction for muon flux at the Earth surface: estimation of the accuracy of different methods](#)
A N Dmitrieva, I I Astapov, A A Kovylyayeva et al.
- [Temperature effect correction for the cosmic ray muon data observed at the Brazilian Southern Space Observatory in São Martinho da Serra](#)
C R Braga, A Dal Lago, T Kuwabara et al.

Pressure and temperature effect corrections of atmospheric muon data in the Belgrade cosmic-ray station

M Savić, D Maletić, D Joković, N Veselinović, R Banjanac, V Udovičić, A Dragić
Institute of Physics, University of Belgrade
Pregrevica 118, 11080 Belgrade, Serbia

E-mail: yokovic@ipb.ac.rs

Abstract. We present results of continuous monitoring of the cosmic-ray muon intensity at the ground and shallow underground level at the Belgrade cosmic-ray station. The cosmic-ray muon measurements have been performed since 2002, by means of plastic scintillation detectors. The scintillator counts are corrected for atmospheric pressure for the whole period of measurements and, as well, for vertical temperature profile for the period of the last six years. The results are compared with other correction methods available. One-hour time series of the cosmic-ray muon intensity at the ground level are checked for correlation with European neutron monitors, with emphasis on occasional extreme solar events, e.g. Forbush decreases.

1. Introduction

The Belgrade cosmic-ray station, situated in the Low-level Laboratory for Nuclear Physics at Institute of Physics, Belgrade, have been continuously measuring the cosmic-ray intensity since 2002. The station is at near-sea level at the altitude of 78 m a.s.l.; its geomagnetic latitude is 39° 32' N and geomagnetic vertical cut-off rigidity is 5.3 GV. It consists of two parts: the ground level lab (GLL) and the underground lab (UL); the UL is located at a depth of 12 metres below the surface, i.e. 25 metre water equivalent. At this depth practically only the muonic component is present. The cosmic-ray muon measurements are performed by means of plastic scintillation detectors, a pair of which is, along with instrumentation modules for data acquisition, placed in both the GLL and the UL. The set-up is quiet flexible, as the scintillators could be arranged in different ways, which allows conducting different experiments. The analyses of the measurements yielded some results on variations of the cosmic-ray muon intensity and on precise values of the integral muon flux at the ground level and at the depth of 25 m.w.e. [1,2,3,4].

2. Experimental set-up

The experimental set-up in both the GLL and the UL consists of a large plastic scintillation detector (rectangular shape, 100cm x 100cm x 5cm) and a data acquisition system (DAQ). The scintillator is polystyrene based UPS-89, with four 2-inch photomultiplier tubes attached to its corners, so that each PM tube looks at the rectangle diagonal. Preamplifier signals from two PM tubes looking at the same diagonal are summed in one output signal, thus two output signals are led to the DAQ from each scintillator.

The summed signals from the PM tubes on the same diagonal of the detectors are stored and digitized by the DAQ, which is based on 4-channel flash analog-to-digital converters (FADC), made by CAEN (type N1728B), with 100 MHz sampling frequency. The FADCs are capable of operating in



the event-list mode, when every analyzed event is fully recorded by the time of its occurrence and its amplitude. This enables the correlation of events, both prompt and arbitrarily delayed, at all four inputs with the time resolution of 10 ns. Single and coincident data can be organized into time series within any desired integration period. The FADCs can also be synchronized with each other for the additional coinciding of the events in the GLL and the UL.

For both the GLL and the UL detector, two input channels on the corresponding FADC are reserved for events recorded by each of detector's diagonals. The cosmic-ray events recorded by a single diagonal are drawn in the background. Coinciding of the prompt events from two diagonals within a narrow time window gives the resulting experimental spectrum of the plastic scintillator, which is the energy deposit (ΔE) spectrum of the cosmic-ray particles (figure 1). Interpretation of the experimental spectra and their features as well as their calibration have been done using Geant4 based Monte Carlo simulation [4,5]. The spectra peak at ~ 11 MeV and have the instrumental thresholds at ~ 4 MeV. Comparing the spectra of the GLL detector and the UL detector one can notice the obvious difference in their shape, especially in the low-energy part below ~ 6 MeV. This difference points to the contribution of the cosmic-ray electrons and gammas (electromagnetic component) to the ΔE spectra at the ground level, which is absent in case of the underground detector.

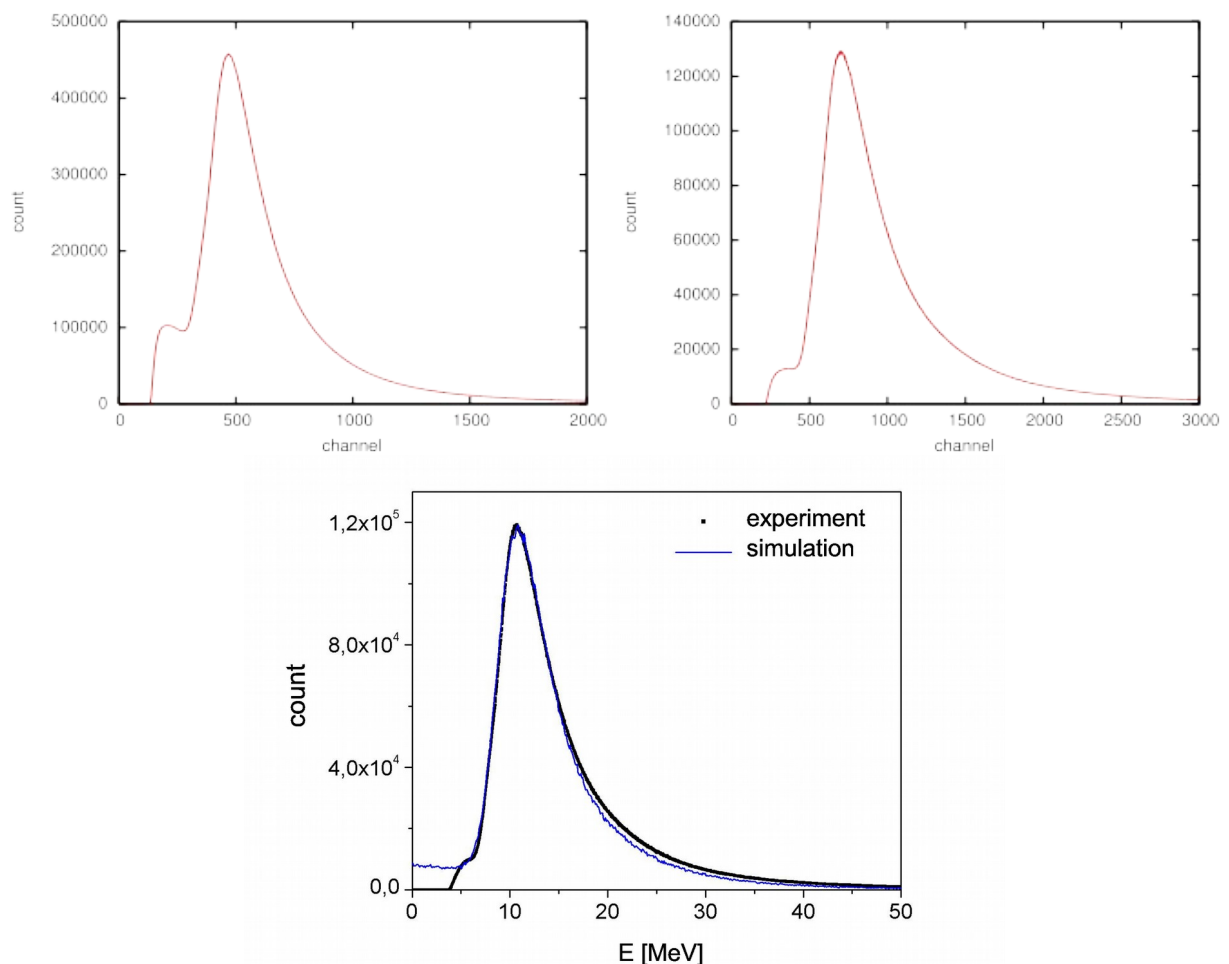


Figure 1. The cosmic-ray ΔE spectra of the GLL detector (top left) and the UL detector (top right). Experimental and simulated ΔE spectra of the UL detector (bottom).

3. Results and discussion

The cosmic-ray intensity data are automatically processed, using a web-based “robot” developed for this purpose, and published online at www.cosmic.ipb.ac.rs/muon_station. The online available data are raw scintillator counts in time series with resolution of 5 min or 1 h. Time series of the raw data are corrected for pressure and temperature effect; pressure corrections have been done for the whole data taking period and temperature effect corrections have been done for the the time period of the last six years.

3.1. Efficiency corrections

The first data corrections are related to detector assembly efficiency. As mentioned, the instrumental thresholds cut the spectra at ~ 3 MeV. However, the thresholds may vary, thus changing the initial spectrum and resulting in fluctuations of the integral spectrum count. Related to this, the necessary correction has been done by means of constant fraction discriminator (CFD) function (figure 2); with use of the CFD cut the spectrum fluctuations decreased significantly. The CFD is based on cut on chosen height as a percentage of peak height where the spectrum is cut. The simulation tells us that, for the underground detector, $\sim 6\%$ of muon events is also cut (figure 1).

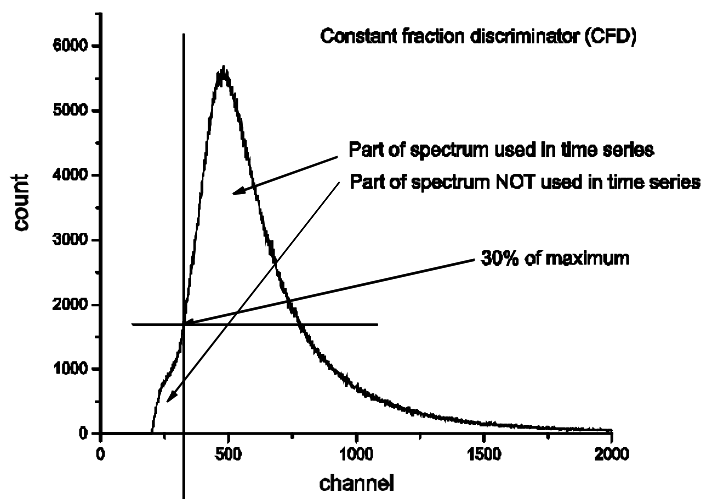


Figure 2. Constant fraction discriminator (CFD) applied in efficiency corrections. The obtained truncated spectrum is used for calculating time series.

The next step in the efficiency corrections is a correction of 5-min count values that are clearly lower than a mean 5-min count in surrounding time intervals. This undershoot comes at the beginning/end of runs, where events are not collected for all 5 min of measurement. The last and smallest correction is a correction of fluctuations of spectrum due to fluctuation in amplification which influence the cut on diagonals and efficiency of coincidence of two diagonals. We found that the CFD cut is proportional to efficiency of coincidence.

3.2. Corrections for atmospheric pressure and for temperature

Significant part of variation of cosmic ray muon component intensity can be attributed to meteorological effects. Here, two main contributors are barometric and temperature effect [6].

Barometric effect is caused by variation of the atmospheric mass above the detector. These pressure corrections are done by finding the linear regression coefficient, using only International Quiet Days, i.e. time series data from periods with more or less constant intensity of galactic cosmic rays, for creation of the distribution of scintillator counts vs. atmospheric pressure. Atmospheric pressure data are available due to on-site continuous measurement.

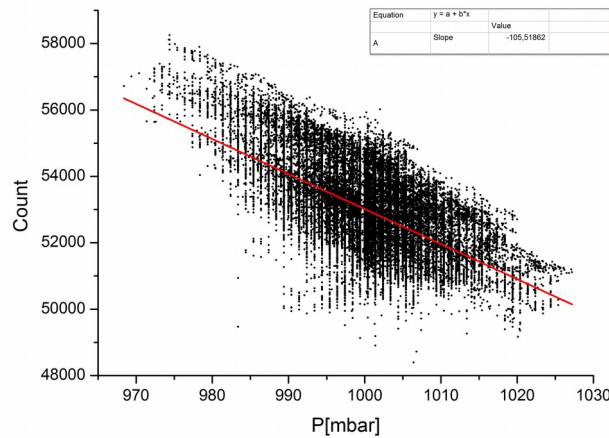


Figure 3. Dependence of 5-min counts on atmospheric pressure.

The temperature effect is related to the variation of the atmospheric temperature profile. The effect is two-fold, as it affects pion decay (positive contribution) as well as muon ionization losses and possible decay (negative contribution). To correct for these effects, integral correction method was applied [6,7]. The variation of the muon intensity due to temperature variations is calculated by using the formula:

$$\delta I_T = \int_0^{h_0} \alpha(h) \cdot \delta T(h) \cdot dh$$

where δI_T is the variation of the muon intensity due to the temperature effect, $\delta T(h)$ is the variation of the atmospheric temperature, which is calculated in reference to the mean temperature value for a given time period (denoted by index M): $\delta T(h) = T_M(h) - T(h)$, where h is atmospheric depth. Temperature coefficient densities $\alpha(h)$ are calculated according to [6].

Available meteorological models make it possible to have hourly atmospheric temperature profiles for 17 standard isobaric levels at the geographic position of the Belgrade muon station, necessary for application of formula shown above. The procedure used here is as described in [7]. Temperature profiles have been obtained from ftp://cr0.izmiran.rssi.ru/COSRAY!/FTP_METEO/blgd_Th/, courtesy of IZMIRAN laboratory.

3.3. Time series of the cosmic-ray intensity

In Figure 4 the count rate time series is shown for all corrections. First, the corrected count rate for efficiency corrected data is shown. Also, the atmospheric pressure and combined atmospheric pressure and temperature corrections time series of count rates are shown.

One-hour time series of the cosmic-ray muon intensity at the ground level are checked for correlation with European neutron monitors (NM), with emphasis on occasional extreme solar events, e.g. Forbush decreases.

In Figure 5 the comparison of time series of pressure corrected and pressure and temperature corrected count rates for the Belgrade muon station and Jungfraujoch, Rome, Baksan and Oulu neutron monitors is presented for Forbush candidate in March 2012. The count rates of neutron monitors are shifted to be close to each-other for visibility. The count rate for the Belgrade station is shown in percentages with additional shift down for visibility. The count rate drop for the neutron monitors is clearly more pronounced than for Belgrade muon monitor.

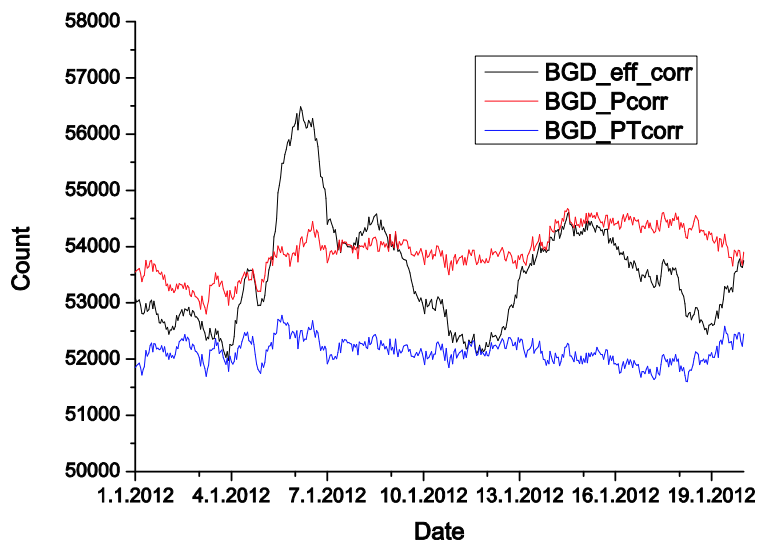


Figure 4. Time series of efficiency corrected, pressure corrected and pressure and temperature corrected counts.

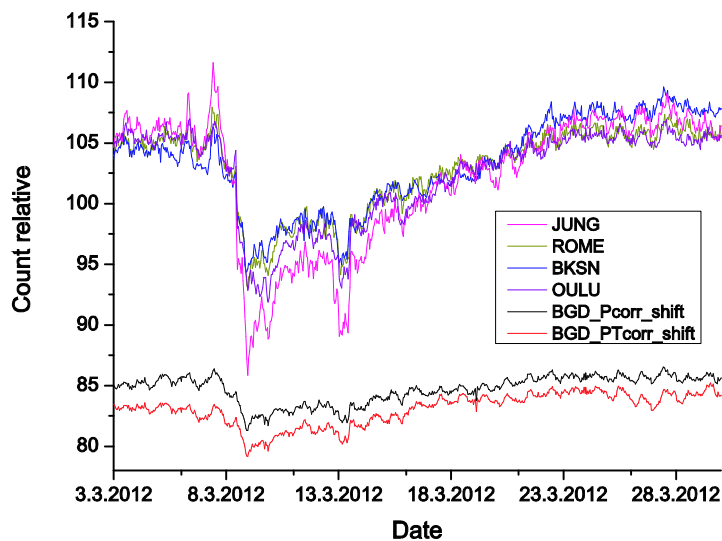


Figure 5. Comparison of time series of pressure corrected and pressure and temperature corrected count rates for the Belgrade muon monitor station and neutron monitors. Count rates are shifted for comparison.

In Figure 6 the comparison of time series of pressure corrected count rates for the Belgrade muon station Jungfrauoch, Rome, Baksan and Oulu neutron monitors is presented. The count rates of neutron monitors are shifted to be close to each-other for visibility. The count rate for Belgrade station is scaled in the way that the drop in count rate is similar to most of the stations (except Jungfrauoch, which is at high altitude). The visual comparison shows the good correlation of the count rates of Belgrade muon monitor and neutron monitors, previously noticed using correlative analyses of count rates. The pressure corrected count rates from Belgrade muon monitor is only dataset used for visual comparison, since neutron monitor data are also only pressure corrected. This was also observed previously using correlative analyses of count rates.

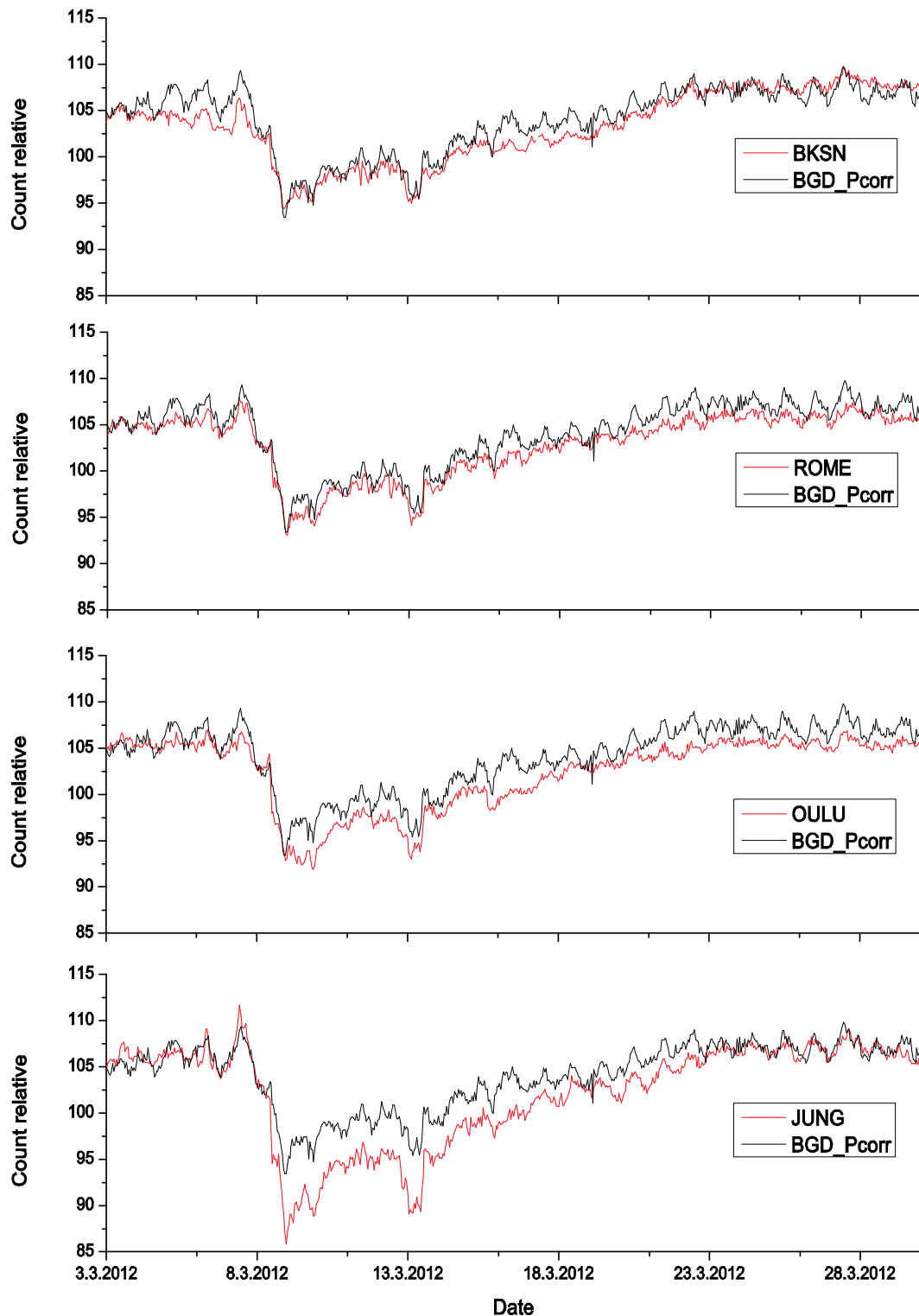


Figure 6. Comparison of time series of pressure corrected count rates for the Belgrade muon monitor station and neutron monitors. Count rates are shifted and scaled for comparison.

4. Conclusions

The results of continuous monitoring of the cosmic-ray muon intensity at the ground and shallow underground level at the Belgrade cosmic-ray station are presented. The scintillator counts are corrected for atmospheric pressure for the whole period of measurements and, as well, for vertical temperature profile for the period of the last six years. The results are compared with other correction methods available and showed excellent agreement. One-hour time series of the cosmic-ray muon intensity at the ground level are checked for correlation with European neutron monitors, with emphasis on occasional extreme solar events, e.g. Forbush decreases. As a result of correlative analysis, the Forbush candidate in March 2012 is the best choice to be used for visual comparison presented in this work. The comparison showed high correlation of the Belgrade muon monitor with neutron monitors, especially geographically closer neutron monitors such as Rome NM. In some specific time periods, like during the Forbush candidate in March 2012, we showed that our muon measurement system has sensitivity comparable to European neutron monitors in this period, but still not as efficient as NM with better geographical position (at high altitude), e.g. Jungfraujoch in the Swiss Alps.

5. Acknowledgements

This work is supported by the Ministry of Education, Science and Technological Development of Republic of Serbia, project no. OI171002. We acknowledge the NMDB database (www.nmdb.eu), founded under the European Union's FP7 programme (contract no. 213007) for providing data. We acknowledge the Department of Physical Sciences, University of Oulu, Finland, as the source of data used in publications. Jungfraujoch neutron monitor data were kindly provided by the Cosmic Ray Group, Physikalisches Institut, University of Bern, Switzerland. We acknowledge the ROME neutron monitor data. SVIRCO NM is supported by IFSI/INAF-UNIRoma3 collaboration. We acknowledge the Baksan Neutrino Observatory of Institute for Nuclear Research of Russian Academy of Science, Moscow, for providing data.

6. References

- [1] Dragić A, Banjanac R, Udovičić V, Joković D, Aničin I and Puzović J 2005 *Int. J. Mod. Phys. A* **20** 6953
- [2] Dragić A, Banjanac R, Udovičić V, Joković D, Puzović J and Aničin I 2008 *Proc. 21st European Cosmic Ray Symposium (Košice, Slovakia)* p 368
- [3] Dragić A, Banjanac R, Udovičić V, Joković D, Aničin I and Puzović J 2009 *Proc. 31st Int. Cosmic Ray Conf. (Lodz, Poland)*
- [4] Dragić A, Joković D, Banjanac R, Udovičić V, Panić B, Puzović J and Aničin I 2008 *Nucl. Instrum. Meth. A* **591** 470
- [5] Joković D, Dragić A, Udovičić V, Banjanac R, Puzović J and Aničin I 2009 *Appl. Radiat. Isot.* **67** 719
- [6] Dorman L.I. 2004 *Cosmic Rays in the Earth's Atmosphere and Underground* (Berlin: Springer)
- [7] Berkova M, Belov A, Eroshenko E and Yanke V 2012 *Astrophys. Space Sci. Trans.* **8** 41



Cosmic rays muon flux measurements at Belgrade shallow underground laboratory

N. Veselinović, A. Dragić, D. Maletić, D. Joković, M. Savić, R. Banjanac, V. Udovičić, and I. Aničin

Citation: [AIP Conference Proceedings](#) **1645**, 421 (2015); doi: 10.1063/1.4909614

View online: <http://dx.doi.org/10.1063/1.4909614>

View Table of Contents: <http://scitation.aip.org/content/aip/proceeding/aipcp/1645?ver=pdfcov>

Published by the [AIP Publishing](#)

Articles you may be interested in

[A comprehensive comparison for simulations of cosmic-ray muons underground](#)

[AIP Conf. Proc.](#) **1549**, 227 (2013); 10.1063/1.4818114

[Measurements of cosmic-ray correlated events at the Soudan underground laboratory](#)

[AIP Conf. Proc.](#) **1549**, 177 (2013); 10.1063/1.4818103

[Cosmic-ray Muon Flux In Belgrade](#)

[AIP Conf. Proc.](#) **899**, 543 (2007); 10.1063/1.2733284

[Laboratory study of the cosmic-ray muon lifetime](#)

[Am. J. Phys.](#) **53**, 542 (1985); 10.1119/1.14235

[Cosmic-ray muon flux and the W particle](#)

[Phys. Today](#) **24**, 17 (1971); 10.1063/1.3022428

Cosmic Rays Muon Flux Measurements at Belgrade Shallow Underground Laboratory

N. Veselinović ^{a)}, A. Dragić, D. Maletić, D. Joković, M. Savić, R. Banjanac, V. Udovičić, I. Aničin

Institute of Physics, University of Belgrade, Pregrevica 118, Belgrade, Serbia

^{a)} Corresponding author: veselinovic@ipb.ac.rs

Abstract. The Belgrade underground laboratory is a shallow underground one, at 25 meters of water equivalent. It is dedicated to low-background spectroscopy and cosmic rays measurement. Its uniqueness is that it is composed of two parts, one above ground, the other below with identical sets of detectors and analyzing electronics thus creating opportunity to monitor simultaneously muon flux and ambient radiation. We investigate the possibility of utilizing measurements at the shallow depth for the study of muons, processes to which these muons are sensitive and processes induced by cosmic rays muons. For this purpose a series of simulations of muon generation and propagation is done, based on the CORSIKA air shower simulation package and GEANT4. Results show good agreement with other laboratories and cosmic rays stations.

Belgrade Cosmic Rays Station

Cosmic rays are energetic particles from outer space that continuously bombard Earth atmosphere, causing creation of secondary showers made of elementary particles. For last hundred years, after Hess' discoveries, cosmic rays (CR) has been studied at almost every location accessible to research, from deep underground to above atmosphere [1]. Low-level and cosmic-ray lab in Belgrade is dedicated to the measurement of low activities and CR muon component. One of the objectives is also intersection of these two fields, namely, muon-induced background in gamma spectroscopy. Belgrade lab is relatively shallow underground laboratory [2] located at the right bank of river Danube on the ground of Institute of Physics in Belgrade. It is located at near-sea level at the altitude of 78 m a.s.l. and its geographic position is 44° 51' N and longitude 20° 23' E with geomagnetic latitude 39° 32' N and geomagnetic vertical cut-off rigidity 5.3 GV. The lab has two portions, ground level portion (GL) is situated at the foot of the vertical loess cliff. Other portion, the underground level (UL) is dug into the foot of the cliff and is accessible from the GL via horizontal corridor as can be seen at Fig.1. Working area of UL has three niches for independent experiments.

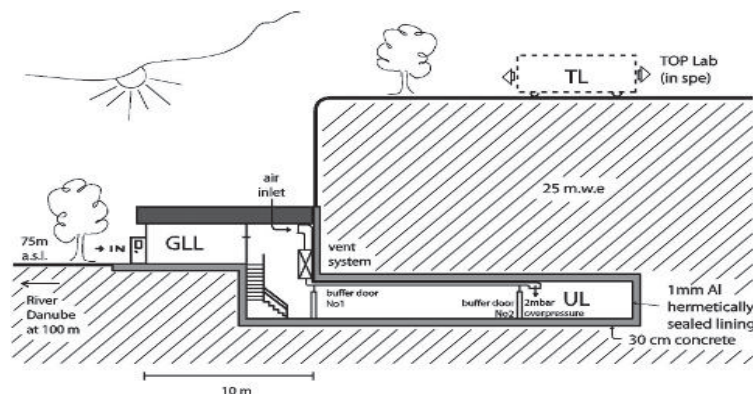


FIGURE 1. Scheme of low-level and CR laboratory at Institute of Physics, Belgrade

The overburden of the UL is about 12 meters of loess soil, which is equivalent to 25 meters of water. The walls are made of 30 cm thick reinforced concrete and covered with the hermetically sealed Al lining 1 mm thick, to

prevent the radon from the soil to diffuse into the laboratory. The low-level laboratory is equipped with an air ventilation system which keeps 2 mbar overpressure in the UL, in order to minimize radon diffusion through eventual imperfections in the Al lining.

Experimental Set-up

The equipment of the lab consists of two identical set of detectors and analyzing electronics. One set is situated in the GL and other in the UL. Each set is composed of gamma spectrometer and muon detectors. For muon measurements a pair of plastic scintillator detectors is used. One of the detectors is small, 50 cm x 23 cm x 5 cm plastic scintillator detector, with a single PMT looking at its longest side via a Perspex light guide tapering to the diameter of a PMT, made by JINR, Dubna, Russia, and assembled locally. The other, larger one has dimensions of 100 cm x 100 cm x 5 cm, equipped with four PMT directly coupled to the corners beveled at 45°, made by Amcrys-H, Kharkov, Ukraine. The smaller detector may serve as a check of stability of the muon time series obtained from the larger detector, which is important for long term measurements. It can also be used (in coincidence with the larger detector) for measurements of the lateral spread of particles in CR showers and decoherence. Plastic scintillation detectors are also employed for active shielding of gamma spectrometers. In the UL, a 35% efficiency radio-pure p-type HPGe detector, made by ORTEC, 12 cm thick cylindrical lead castle is deployed around the detector. One of the set-ups is presented at Fig.2. Another HPGe detector, of 10% efficiency, is placed in GL.



FIGURE 2. Detectors in the underground laboratory. Large scintillator detector is placed above HPGe and small scintillator can change position.

Data acquisition system is identical both in UL and GL and it has two flash analog to digital converter (FADC), one in each laboratory, made by CAEN (type N1728B). These are versatile instruments, capable of working in two modes, energy histogram mode when performing as digital spectrometers or, in the oscillogram mode, when they perform as digital storage oscilloscopes. In both modes, they sample at 10 ns intervals into 2^{14} channels in four independent inputs. The full voltage range is ± 1.1 V. They are capable of operating in the list mode, when every analyzed event is fully recorded by the time of its occurrence and its amplitude. This enables the correlation of events, both prompt and arbitrarily delayed, at all four in puts with the time resolution of 10 ns. Single and coincident data can be organized into time series within any integration period from 10 ns up. The two N1728B units are synchronized, enabling coincidence/correlation of the events recorded in both of them. The flexible software encompassing all above said off-line analyses is user-friendly and entirely homemade. The preamplifier outputs of the PMT of the larger detectors are paired diagonally. Signals from these paired inputs are later coincided off-line and their amplitudes added to produce the single spectra. This procedure suppress low-energy portion of the background spectrum (up to some 3 MeV), mostly environmental radiation, leaving only high-energy loss events due to CR muons and EM showers that peak at about 10 MeV, shown at Fig 3. The output of the PMT of the smaller detector is fed to the third input of FADC. [3]

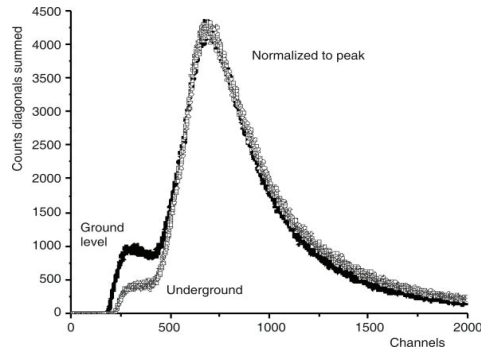


FIGURE 3. The sum spectra of two diagonals of the large plastic detectors in the UL and GLL. For comparison, the spectra are normalized for the peaks to coincide. Channel 650 corresponds to the muon energy loss of 10 MeV.

Simulation and Results

The experimental set-up is rather flexible, thus allowing different studies of the muon and electromagnetic components of cosmic rays at the ground level and at the shallow depth underground. The cosmic-ray muon flux in the underground laboratory has been determined from data taken from November 2008 till June 2013 (there were some small gaps in recording data during this period). These measurements yielded the precise values of the integral cosmic ray muon flux at the location of Belgrade. Measured muon flux is: $137(6) \text{ m}^{-2}\text{s}^{-1}$ at the ground level and $45(2) \text{ m}^{-2}\text{s}^{-1}$ at the underground level [4]. Different analyses of time series of these measurements have also been performed. Interpretation and calibration of the experimental spectra has been done using Monte Carlo simulation packages CORSIKA and Geant4 [5, 6]. CORSIKA simulates extensive air showers generated by the primary cosmic-rays in interactions with air nuclei at the top of the atmosphere. It gives spectra of the secondary cosmic-rays at the preferred observation level. These secondary particles, their energy and momentum direction distribution, obtained by CORSIKA, are then used as an input for the Geant4 based simulation of the detectors. In this simulation, particles first traverse through soil and infrastructure of the UL lab before hitting the detector. Then the response of the plastic scintillation detectors is simulated. For the UL scintillators, the simulated spectra are shown in Fig. 4.[7]

They agree very well with the experimental ones, except in the low-energy part where the ambient gamma radiation is mostly present and where the cuts are applied. We also used these simulation packages to simulate different experimental set-ups and to obtain information about lower cut-of energy of primary cosmic rays at our site and for single muons and muons in coincidence. Energy of the primary particles from which detected muons originate increases for UL compared to GL but also for muons in coincidence compared with single detected muons.

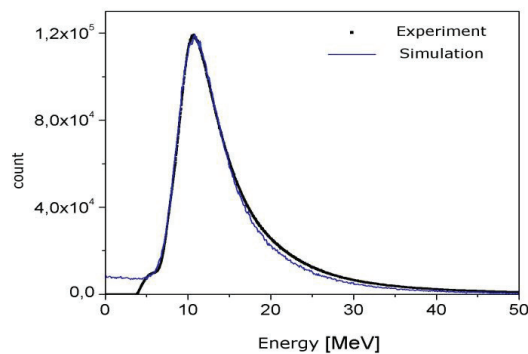


FIGURE 4. Experimental vs simulated spectrum of large plastic scintillator detector at UL

These measurements allow us to study fluctuations in muon flux intensity during the rising phase of Solar Cycle 24 and to make five-minutes or one-hour time series of the flux. The scintillator counts are corrected for atmospheric pressure for the whole period of measurements and, as well, for vertical temperature profile for the period of last six years. The results are compared with other correction methods available. One-hour time series of the cosmic ray muon intensity at the ground level are checked for correlation with European neutron monitors (NM), with emphasis on occasional extreme solar events, e.g. Forbush decreases (FD) in order to investigate claims of influence of cosmic-rays on cloud formation and climate [8,9] In some specific time periods, like during the FD in March 2012, we showed that our muon measurement system has sensitivity comparable to European neutron monitors in this period, but still not as efficient as NM with better geographical position (at high altitude), e.g. Jungfraujoch in the Swiss Alps. These results are presented at Fig. 5. Due to fact that muons detected underground originate from primary particles with energy around and above the limit for solar modulation time series from UL are less sensitive to these Solar events.



FIGURE 5. Time series for March 2012 recorded at NM at Jungfraujoch compared to time series obtained at Belgrade cosmic-rays station

Acknowledgement

The present work was funded by the Ministry of Education and Science of the Republic of Serbia, under the Project No. 171002.

References

- [1] L.I. Dorman, *Cosmic-rays in the Earth's Atmosphere and Underground*, Kluwer, Dordrecht, 2004.
- [2] S. Niese, *Underground laboratories for low-level radioactivity measurements. Analysis of Environmental Radionuclides*, 209-240, (2008) P.P. Povinec, ed., Elsevier, Amsterdam.
- [3] A. Dragić, V. Udovičić, R. Banjanac, D. Joković, D. Maletić, N. Veselinović, M. Savić, J. Puzović, I. Aničin, *The new set-up in the Belgrade low-level and cosmic-ray laboratory*, Nucl. Technol. Radiat. 26 (2011) 181-192
- [4] A. Dragić, D. Joković, R. Banjanac, V. Udovičić, B. Panić, J. Puzović, I. Aničin, *Measurement of cosmic ray muon flux in the Belgrade ground level and underground laboratories*, Nuclear Instruments and Methods in Physics Research A 591 (2008) 470-475.

- [5] D. Heck, *CORSIKA: a Monte Carlo code to simulate extensive air showers*, Report FZKA 6019, Forschungszentrum Karlsruhe, 1998.
- [6] S. Agostinelli et al., *the Geant4 collaboration*, Nucl. Instrum. and Meth. A 506 (2003) 250-303
- [7] A.Dragić, R. Banjanac, V. Udovičić, D. Joković, J.Puzović, I Aničin, I., *Periodic Variations of CR Muon Intensity in the Period 2002-2004* Proceedings of the 21st European cosmic-ray Symposium, Košice, Slovakia (2008) 368-373.
- [8] A.Dragić, I.Aničin, R.Banjanac, V.Udovičić, D.Joković, D.Maletić, J.Puzović, *Forbush decreases - clouds relation in the neutron monitor era*, Astrophys. Space Sci. Trans. 7 (2011) 315-318.
- [9] H. Svensmark, *Cosmoclimatology: a new theory emerges*, Astron. Geophys. 48 (2007) 1.18-1.24.

CORRELATIVE AND PERIDOGRAM ANALYSIS OF DEPENDENCE OF CONTINUOUS GAMMA SPECTRUM IN THE SHALLOW UNDERGROUND LABORATORY ON COSMIC RAY AND CLIMATE VARIABLES

**Dimitrije Maletić, Radomir Banjanac, Dejan Joković, Vladimir Udovičić,
Aleksandar Dragić, Mihailo Savić, Nikola Veselinović**

Institute of Physics University of Belgrade, Serbia

Abstract. *The continuous gamma spectrum, Cosmic ray intensity and climate variables; atmospheric pressure, air temperature and humidity were continually measured in the Underground laboratory of Low Background Laboratory in the Institute of Physics Belgrade. Same three climate variables for outside air were obtained from nearby meteorological station. The obtained gamma spectrum, measured using HPGe detector, is split into three energy ranges, low, intermediate and high ending with energy of 4.4 MeV. For each of the energy intervals periodogram and correlative analysis of dependence of continuous gamma spectrum on cosmic ray intensity and climate variables is performed. Periodogram analysis is done using Lomb-Scargle periodograms. The difference of linear correlation coefficients are shown and discussed, as well as the differences in resulting periodograms.*

Key words: *gamma spectroscopy, surface air, underground laboratory, correlative analysis, periodogram analysis.*

1. INTRODUCTION

The low-level and cosmic-ray laboratory in the Low-Background laboratory for Nuclear Physics in the Institute of Physics Belgrade is dedicated to the measurements of low activities and to the studies of the muon and electromagnetic components of cosmic rays at the ground level and at the shallow depth underground, and in particular to the detailed studies of the signatures of these radiations in HPGe spectrometers situated shallow underground. The ground level part of the laboratory (GLL), at 75 m above sea level, is situated at the foot of the vertical loess cliff, which is about 10 meters high. The underground part of the laboratory (UL), of the useful area of 45 m², is dug into the foot of the cliff and is accessible from the GLL via the 10 meters long horizontal corridor, which serves also as a pressure buffer for a slight overpressure in the UL (Fig.1). The overburden of the UL is about 12m of loess soil, equivalent to 25 meters of water. [1]

In the UL laboratory the gamma spectrum is recorded using HPGe detector and fast ADC unit made by CAEN, and analysed using software developed in our laboratory. Besides HPGe measurements the air pressure, temperature and humidity were recorded in UL also. Values for temperature, pressure and humidity of outside air was taken from publicly available web site. The time period from which the

measurements were used in this analysis is from beginning of December 2009 till end of April 2010.

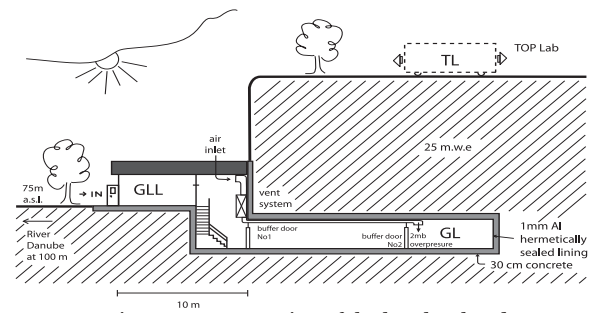


Figure 1. Cross-section of the low-level and CR laboratory at IOP, Belgrade, 44°49'N, 20°28'E, vertical rigidity cut off 5.3 GV.

Continuous Cosmic rays' (CR) spectrum measurements by means of a pair of small plastic scintillators [(50x25x5)cm] started in the GLL and UL back in 2002 and lasted for about 5 years. It agrees to the spectrum of relatively shallow underground laboratories worldwide [2]. These measurements yielded the precise values of the integral CR muon flux at the ground level and underground level laboratory, at the location of Belgrade [3]. Different analyses of the time series of these measurements have also been performed [4, 5]. Since the UL is completely lined with the hermetically sealed 1 mm thick aluminum lining, and the ventilation system keeps the overpressure of 2 mbars of doubly filtered air, the concentration of radon is kept at the low average value of about 10 Bq/m³.

Measurements and analysis of periodicity of gamma-rays in underground laboratory had been reported [6-7], and also for Radon measurements and periodicity [8-9] including advanced Multivariate Analysis techniques [10-11].

Most recent research done in our laboratory [12] addresses the question of determination of origin of low energy gamma-rays detected by HPGe detector, which are coming either from environmental radiation or from CR. In this paper the correlative analysis is used to address the same question of composition of low-energy gamma-rays spectrum, thus giving us the new approach to the research done in [12].

The correlative analysis in this paper was done using Toolkit for Multivariate Analysis TMVA[13] package as part of the ROOT[14] software, widely used in analysis, especially for High Energy Physics experiments. The TMVA was used for analysis extensively in our laboratory, and it was the natural choice to use the software for correlative analysis also. Lomb-Scargle periodograms were produced using software developed in Low-Background laboratory.

2. EXPERIMENTAL SETUP

In the UL 35% efficiency radiopure HPGe detector, made by ORTEC, is used. The HPGe is surrounded by 12 cm thick cylindrical lead castle. Cosmic ray setup consists of a single [100x100x5]cm plastic scintillator detector equipped with four PMTs directly coupled to the corners beveled at 45°, made by Amcrys-H of Kharkov, Ukraine. The signals from HPGe detector and plastic scintillators give output to fast ADC unit with four independent inputs each, made by CAEN, of the type N1728B. CAEN units are versatile instruments capable of working in the so-called energy histogram mode, when they perform like digital spectrometers, or/and in the oscillogram mode, when they perform like digital storage oscilloscopes. In both modes they sample at 10 ns intervals, into 2^{14} channels. The full voltage range is $\pm 1.1V$.

CAEN units are capable of operating in the list mode, when every analyzed event is fully recorded by the time of its occurrence over the set triggering level, and its amplitude, in the same PC, which controls their workings. This enables to off-line coincide the events at all four inputs, prompt as well as arbitrarily delayed, with the time resolution of 10 ns, as well as to analyze the time series not only of all single inputs, but also of arbitrary coincidences, with any integration period from 10 ns up. The flexible software that performs all these off-line analyses is user-friendly and is entirely homemade.

The preamplifier outputs of the PMTs of detectors are paired diagonally, the whole detector thus engaging the two inputs of the CAEN unit. The signals from these inputs are later off-line coincided and their amplitudes added, to produce the singles spectra of these detectors. Offline coincidence allows that the high intensity but uninteresting low energy portion of the background spectrum of this detector (up to some 3 MeV), which is mostly due to environmental radiations, is practically completely suppressed, leaving only the high energy-loss events due to CR muons and EM showers that peak at about 10 MeV, as shown in Figure 2.

Since event of HPGe gamma spectrum and Cosmic rays consists of time-stamp and the amplitude, off-line analysis is used to create time series of arbitrary time window with selection of specific part of gamma spectrum as well as the time series of Cosmic ray flux in UL (Figure 3.). This enables that whole gamma spectrum can be divided into energy ranges, and analyze each energy range separately. The spectrum separation is done on channel numbers, and after the energy calibration, the energy ranges used in our analysis are 180-440 keV, 620-1330 keV and 1800-4440 keV. The full gamma spectrum is recorded in range of 180-6670 keV. The part of gamma spectrum of the HPGe is shown in Figure 4.

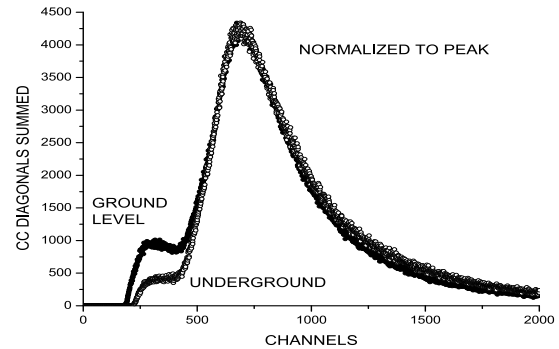


Fig. 2. The sum spectra of two diagonals of big plastic detectors in the UL and GLL .

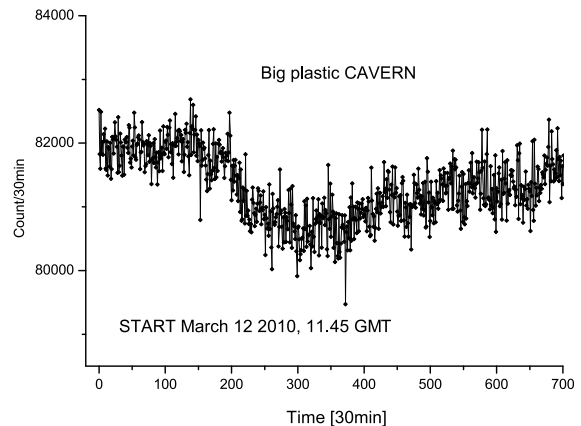


Fig. 3. The time series of the CR muon count of the big plastic detector in the UL.

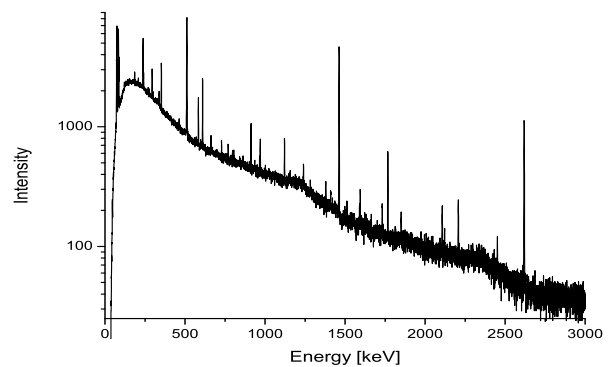


Figure 4. Gamma spectrum of the HPGe detector in 12cm lead castle in the Underground laboratory.

3. RESULTS AND DISCUSSIONS

The analysis starts with correlation analysis. The software for correlative analysis is a part of TMVA package. Hourly time series of variables, atmospheric pressure P, temperature T, and humidity H for UL (P_R, T_R, H_R), and outside (P,T,H) are used, Cosmic ray time series (CR) as well as T (DT) and H (DH) difference of UL and outside values make the number of nine input variables. The table summarizing the linear correlation coefficients is shown in Table 1. We can see correlation between each input variable and HPGe gamma spectrum for full energy range in Table 1 also.

DH	-10	69	-9	-86	57	-22	51	-25	-64	100
DT	7	-98	7	60	-30	10	-24	42	100	-64
CR	-14	-42	-65	36	-14	-52	13	100	42	-25
H_R	-2	30	-44	-1	42	-59	100	13	-24	51
P_R	14	-13	80	-8	-22	100	-59	-52	10	-22
T_R	1	43	-16	-41	100	-22	42	-14	-30	57
H	10	-63	-15	100	-41	-8	-1	36	60	-86
P	11	-9	100	-15	-16	80	-44	-65	7	-9
T	-6	100	-9	-63	43	-13	30	-42	-98	69
HPGe	100	-6	11	10	1	14	-2	-14	7	-10
	HPGe	T	P	H	T_R	P_R	H_R	CR	DT	DH

Table 1. Summary table of linear correlation coefficient for all 9 input variables' 1 hour time series and 1 hour time series of HPGe gamma spectrum for full energy range.

Correlation analysis was done also for three mentioned energy ranges, the Table 2. summarizes the results.

	180-6670 keV	180-440 keV	620-1330 keV	1780-4440 keV
T	-0.070	-0.045	-0.041	-0.096
P	+0.111	+0.124	+0.033	+0.010
H	+0.106	+0.056	+0.047	+0.101
T _{UG}	+0.013	-0.029	+0.014	-0.012
P _{UG}	+0.149	+0.111	+0.091	+0.061
H _{UG}	-0.029	-0.068	-0.030	+0.028
CR	-0.140	-0.179	-0.030	+0.036
T _{UG} -T	+0.076	+0.043	+0.046	+0.100
H _{UG} -H	-0.105	-0.083	-0.055	-0.072

Table 2. Linear correlation coefficients in % for full and three narrower energy ranges.

All the correlation of HPGe gamma spectrum hourly time series and input variables are not significant. The biggest correlation coefficient with HPGe time series is pressure time series measured underground followed by Cosmic ray time series. It is interesting to notice the change of correlation coefficients with HPGe for atmospheric pressure and Cosmic rays time series. While pressure correlation coefficients tend to drop going towards higher gamma energies, Cosmic rays' correlation coefficients are increasing from negative sign to positive one. This observation is in agreement with the fact that the Cosmic rays are contributing

more to the the gamma spectrum of higher energies, as it was shown in [12]. Since Cosmic rays and pressure are anti-correlated with correlation coefficient of -65%, as can be seen in Table 1, increase in atmospheric pressure will give negative correlation coefficient of HPGe and Cosmic rays' time series. This can be explained by having in mind that Cosmic rays are contributing insignificantly to gamma spectrum on lower energies [12] behaving like constant in low energy range, while increase in pressure increases the air density, thus more gamma scattering events are contributing to low energy gamma spectrum.

In the periodogram analysis the Lomb-Scargle periodograms were produced for atmospheric variables P, T, H and HPGe gamma spectrum. The periodograms show only daily periodicity of T, H time series as shown on figures 5 and 6. The P periodogram on Figure 7. Shows expected daily and mid-daily periodicity. It is noticeable that the periodogram for P has lowest spectral powers, which means that periodicity of P is less noticeable. Also, the unexpected 1/3 day periodicity is with low spectral power. The periodogram analysis showed that there is no significant periodicity in HPGe gamma spectrum time series, as shown on Figure 8.

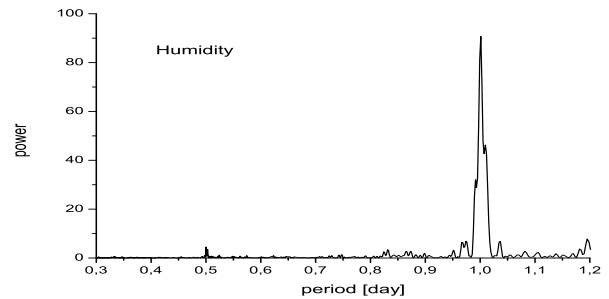


Figure 5. Lomb-Scargle periodogram of air humidity.

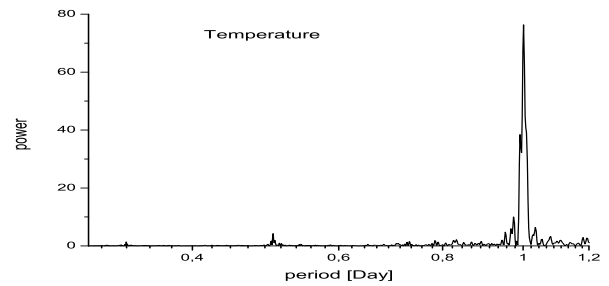


Figure 6. Lomb-Scargle periodogram of air temperature.

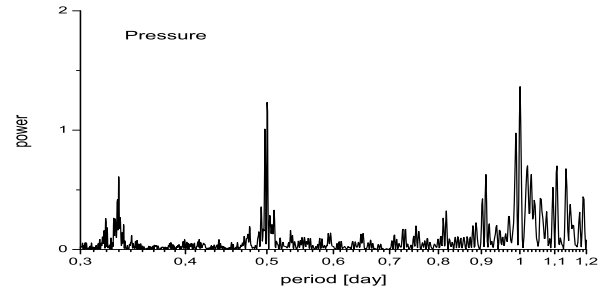


Figure 7. Lomb-Scargle periodogram of air pressure.

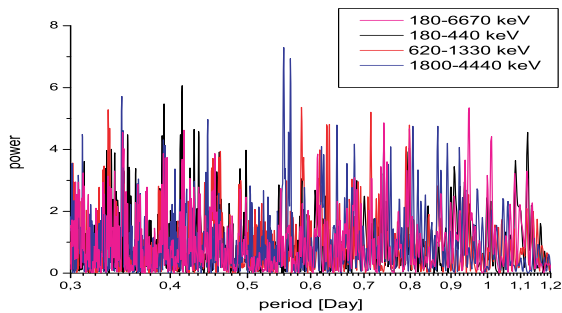


Figure 8. Lomb-Scargle periodogram of full and three different energy range HPGe gamma spectrum time series.

CONCLUSION

In the Underground laboratory of Low Background Laboratory in the Institute of Physics Belgrade the continuous HPGe gamma spectrum, Cosmic ray intensity and climate variables were continually measured in the period from beginning of December 2009 till the end of April 2010. The HPGe gamma spectrum is split into three energy ranges, low, intermediate and high. For each of the energy intervals periodogram and correlative analysis of dependence of continuous gamma spectrum on cosmic ray intensity time series and climate variables time series is performed. Periodogram analysis is done using Lomb-Scargle periodograms. The correlation coefficient between air pressure and Cosmic rays is -65%. The correlation coefficients between HPGe gamma spectrum and input variables are not significant. The decrease of values of correlation coefficients of gamma spectrum and air pressure is present. The increase of values of correlation coefficients of gamma spectrum and Cosmic rays is present also. Increase in atmospheric pressure is resulting in negative correlation coefficient between HPGe and Cosmic rays' time series for low energy gamma spectrum. The more significant contribution of Cosmic rays in high energy gamma spectrum, as opposite to insignificant contribution of Cosmic rays to low energy gamma spectrum is evident. Lomb-Scargle periodograms showed daily periodicity for air temperature and humidity, and additional mid-daily periodicity for air pressure. There is no noticeable periodicity for each of energy ranges of gamma spectrum.

Acknowledgement: *The paper is a part of the research done within the project "Nuclear research methods of rare events and cosmic radiation" (No. 171002) financed by the Ministry of Education, Science and Technological Development of the Republic of Serbia (2011-2015).*

REFERENCES

1. Dragic Aleksandar, Udovicic Vladimir I, Banjanac Radomir M, Jokovic Dejan R, Maletic Dimitrije M, Veselinovic Nikola B, Savic Mihailo, Puzovic Jovan M, Anicin Ivan V "The New Set-Up in the Belgrade Low-

- Level and Cosmic-Ray Laboratory", NUCLEAR TECHNOLOGY & RADIATION PROTECTION, vol. 26, br. 3, pp. 181-192, 2011
2. S. Niese, "Underground laboratories for low-level radioactivity measurements", Analysis of Environmental Radionuclides, Ed. P.Povinec, Elsevier, Amsterdam, pp.209-239, 2008
3. A.Dragić, D.Joković, R.Banjanac, V.Udovičić, B.Panić, J.Puzović and I.Anićin, "Measurement of cosmic ray muon flux in the Belgrade ground level and underground laboratories", Nucl. Instr. and Meth. in Phys. Res. A591, pp. 470 – 475, 2008
4. A. Dragić, R. Banjanac, V. Udovičić, D. Joković, I. Anićin and J. Puzović, "Comparative study of power spectra of ground and shallow underground muon data", Int. Journal of Modern Physics A, Vol. 20 pp. 6953-6955, 2005
5. A. Dragić, R. Banjanac, V. Udovičić, D. Joković, J. Puzović, I. Anićin, "Periodic Variations of CR Muon Intensity in the Period 2002-2004", Proc. 21st European Cosmic Ray Symposium, Košice, Slovakia, pp.368-373, 2008.
6. Banjanac Radomir M, Udovicic Vladimir I, Dragic Aleksandar, Jokovic Dejan R, Maletic Dimitrije M, Veselinovic Nikola B, Grabez Bojana S "Daily Variations of Gamma-Ray Background and Radon Concentration", ROMANIAN JOURNAL OF PHYSICS, vol. 58, br. , pp. S14-S21, 2013
7. Banjanac Radomir M, Dragic Aleksandar, Udovicic Vladimir I, Jokovic Dejan R, Maletic Dimitrije M, Veselinovic Nikola B, Savic Mihailo "Variations of gamma-ray background in the Belgrade shallow underground low-level laboratory", APPLIED RADIATION AND ISOTOPES, vol. 87, br. , pp. 70-72, 2014
8. V. Udovičić, B. Grabež, A. Dragić, R. Banjanac, D. Joković, B. Panić, D. Joksimović, J. Puzović, I. Anićin, "Radon problem in an underground low-level laboratory", Radiation Measurements 44 pp. 1009-1012. 2009
9. V. Udovičić, I. Anićin, D. Joković, A. Dragić, R. Banjanac, B. Grabež, N. Veselinović, "Radon Time-series Analysis in the Underground Low-level Laboratory in Belgrade, Serbia", Radiation Protection Dosimetry 145 (2-3) pp. 155-158, 2011
10. Maletic Dimitrije M, Udovicic Vladimir I, Banjanac Radomir M, Jokovic Dejan R, Dragic Aleksandar L, Veselinovic Nikola B, Filipovic Jelena Z "Comparison of Multivariate Classification and Regression Methods for the Indoor Radon Measurements", NUCLEAR TECHNOLOGY & RADIATION PROTECTION, vol. 29, br. 1, pp. 17-23 (2014)
11. Maletic Dimitrije M, Udovicic Vladimir I, Banjanac Radomir M, Jokovic Dejan R, Dragic Aleksandar L, Veselinovic Nikola B, Filipovic Jelena Z "Correlative and Multivariate Analysis of Increased Radon Concentration in Underground Laboratory", RADIATION PROTECTION DOSIMETRY, vol. 162, br. 1-2, pp. 148-151, 2014
12. Banjanac Radomir M, Maletic Dimitrije M, Jokovic Dejan R, Veselinovic Nikola B, Dragic Aleksandar, Udovicic Vladimir I, Anicin Ivan V "On the omnipresent background gamma radiation of the continuous spectrum", NUCLEAR INSTRUMENTS & METHODS IN PHYSICS RESEARCH SECTION A, vol. 745, br. , str. 7-11, 2014.
13. R. Brun and F. Rademakers, "ROOT - An Object Oriented Data Analysis Framework", Nucl. Inst. Meth. in Phys. Res. A 389, 81, 1997
14. A. Hoecker, P. Speckmayer, J. Stelzer, J. Therhaag, E. von Toerne, and H. Voss, "TMVA - Toolkit for Multivariate Data Analysis", PoS ACAT 040 (2007), arXiv:physics/070303

BACKGROUND SPECTRUM CHARACTERISTICS OF THE HPGE DETECTOR LONG-TERM MEASUREMENT IN THE BELGRADE LOW-BACKGROUND LABORATORY

Radomir Banjanac, Vladimir Udovičić, Dejan Joković, Dimitrije Maletić, Nikola Veselinović, Mihailo Savić, Aleksandar Dragić, Ivan Aničin

Institute of Physics, Belgrade, Serbia

Abstract. The Belgrade low-level background laboratory, built in 1997, is shallow (25 m.w.e) underground space (45m²) which is constantly ventilated with fresh air against radon. The muon intensity (about 3.5 times less than at ground level), radon concentration (suppressed to averaged value of 15 Bqm⁻³), as well as gamma-ray background are monitoring for more than eight years. After long-term measurement using the radiopure HPGe detector with 35% relative efficiency, the measured data includes radionuclide concentration of detector surroundings, estimation of background time variation due to radon and cosmic-rays as well as MDA values for typical samples of water matrix. The detailed characteristics of gamma-ray background spectra are here presented.

Key words : Underground laboratory, Low-level background, long-term gamma-ray measurement

1. INTRODUCTION

Various experiments which strive for the detection of very rare events require the lowest possible background radiation which can be achieved only in a deep underground laboratory. Some of recent the most interesting are double beta-decay experiments, [1] and dark matter searches, [2]. In any applied measurements of low activities, a goal that is pursued by all gamma spectroscopist is to lower the minimum detectable activity (MDA) of their detection system obtaining more statistical evidence in less time.

But, any long and even short-term gamma-ray background measurement is subject to certain temporal variations due to time variability of two prominent contributors to background, cosmic-rays and radon. The most of the low background laboratories that deal with low activity measurements have developed routine measurements of background. The duration of these measurements may be from one day to even a month and they are designed to produce results with sufficiently low statistical errors for the envisaged measurements. These measurements yield only average values of the background, what in principle may lead to systematic errors in later measurements, especially of NORM samples.

The averaged values of the background, gamma lines and continuum, nuclide concentrations or MDA presenting a "personal card" of used detector system for certain samples in any low-level background laboratory, [3]. Here is attempt to present our low-level background laboratory in a similar way. First of all, the detailed description of the laboratories and used detector system are described.

2. DESCRIPTION OF THE LABORATORIES AND EQUIPMENT

The Belgrade underground low-level laboratory (UL), built in 1997 and located on the right bank of the river Danube in the Belgrade borough of Zemun, on the grounds of the Institute of Physics. The overburden of the UL is about 12 meters of loess soil, equivalent to 25 meters of water. It is equipped with ventilation system which provides low radon concentration of 15(5) Bq/m³. The "passive" shield consists of 1 mm thick aluminum foil which completely covers all the wall surfaces inside the laboratory, including floor and ceiling. As the active radon shield the laboratory is continuously ventilated with fresh air, filtered through one rough filter for dust elimination followed by active charcoal filters for radon adsorption. The UL has an area of 45m² and volume of 135m³ what required the rate of air inlet adjusted to 800m³/h. This huge amount of fresh air contributes to greater temperature variations and the long-term mean value of temperature inside the UL is 19(4)°C. The rate of air outlet (700m³/h) was adjusted to get an overpressure of about 200 Pa over the atmospheric pressure, what prevents radon diffusion through eventual imperfections in the aluminum layer. Relative humidity is controlled by a dehumidifier device, what provides that the relative humidity in the underground laboratory does not exceed 60%. The muon intensity (which is about 3.5 times less than at ground level), radon concentration and gamma-ray background are monitoring for more than eight years. Comparative background study is performing in the GLL (at ground level) which is equipped with a Ge detector (13% relative efficiency and not intrinsically low-radioactivity level, named SGe) and a big plastic scintillator (1m², named BPS) in veto position. The GLL is air-conditioned (average radon concentration of

50(30) Bq/m³) has an area of 30m² and volume of 75m³. The Fig. 1 presents veto arrangement of the HPGe detector (BGe, in 12cm lead shield) and big plastic scintillator, inside the UL.

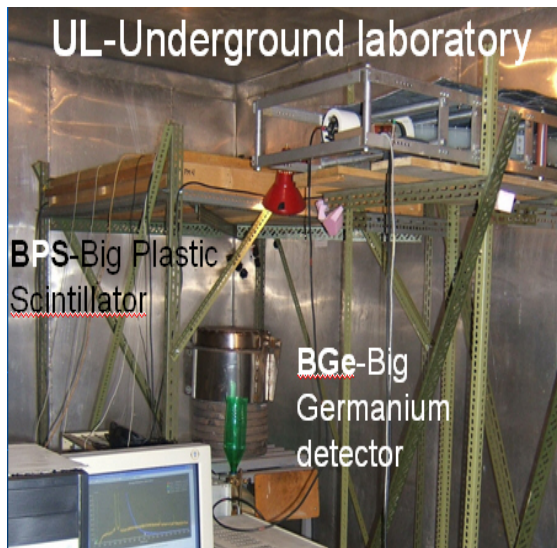


Fig. 1 Veto arrangement of the HPGe detector (BGe) and big plastic scintillator inside the UL

3. DESCRIPTION OF DETECTOR SYSTEMS IN THE UL

The low-level background detector system in the UL includes an intrinsically low-radioactivity level p-type Ge detector (35% relative efficiency, named BGe) and another plastic veto scintillator (1m², named BPS) situated coaxially above the BGe detector. The BGe is a GEM30 model (made by ORTEC) in LB-GEM-SV cryostat configuration with magnesium end cap. The energy resolution at 1332.5keV, measured by analog data acquisition system, is 1.72keV, 0.65keV at 122keV as well as the Peak to Compton ratio at 1332.5keV has value of 68. The cylindrical lead shielding of the BGe, with a wall thickness of 120 mm and an overall weight of about 900kg, was cast locally out of scratch plumbing retrieved after the demolition of some old housing. Radon monitoring inside the laboratories was performed by radon monitor, model RM1029 manufactured by Sun Nuclear Corporation. The device consists of two diffused junction photodiodes as a radon detector, and is furnished with sensors for temperature, pressure and relative humidity. A pair of plastic scintillator detectors is used for CR muon measurements at both laboratories. One of them is a larger (100cmx100cmx5cm) detector (BPS), equipped with four PMT directly coupled to the corners beveled at 45°, made by Amcryst-H, Kharkov, Ukraine. The other, a smaller 50cmx23cmx5cm plastic scintillator detector, with a single PMT looking at its longest side via a Perspex light guide tapering to the diameter of a PMT, made by JINR, Dubna, Russia, and assembled locally. The smaller detector may serve as a check of stability of the muon time series obtained from the larger detector, which is important for long term measurements. Two flash analog to digital converters (FADC), made by C.A.E.N (type N1728B), which sample at 10 ns intervals into 214 channels were used

to analyze spectra from Ge detectors as well as corresponding BPS. User-friendly software was developed to analyze the C.A.E.N data with the possibility to choose the integration time for further time-series analysis that corresponds to integration time of the radon monitor. The performances of digital acquisition system as well as software developed for analysis were described in detail, [4].

4. THE RESULTS OF BACKGROUND MEASUREMENTS IN THE UL

Additional to intrinsically low-radioactivity level of the BGe itself, environmental radioactivity is low, too. The UL was built from low activity concrete about 12 Bq/kg of U-238 and Th-232, and of 23 Bq/kg and 30 Bq/kg of surrounding soil, respectively. Radioactivity of aluminum wall-lining is negligible. Pb-210 activity of used lead shield of 30Bq/kg is measured. After long-term cosmic-ray, [5], radon concentration, [6] and gamma-ray background measurements, no significant long-term time variations of gamma background was found, [7]. After several years of almost continuously background measurements, the integral background rate in the region from 40keV to 2700keV has mean value of about 0.5 cps. The lines of Co-60 are absent in the background spectrum, while the line of Cs-137 with the rate of 1×10^{-4} cps starts to appear significantly only if the measurement time approaches one month. Fukushima activities, though strongly presented in our inlet air filters samples, did not enter the background at observable levels, in spite of the great quantities of air that we pump into the UL to maintain the overpressure, and it seems that the double air filtering and double buffer door system, along with stringent radiation hygiene measures, is capable of keeping the UL clean in cases of global accidental contaminations. No signatures of environmental neutrons, neither slow nor fast, are present in direct background spectra.

The Fig. 2 shows a characteristic shape of background spectrum obtained in the UL after about 6 months of measuring, with distinctive Pb X-ray lines at the beginning of the spectrum, annihilation line, and lines from ⁴⁰K and ²⁰⁸Tl (2614.5keV) at the end of the spectrum with a lot of post-radon lines between them.

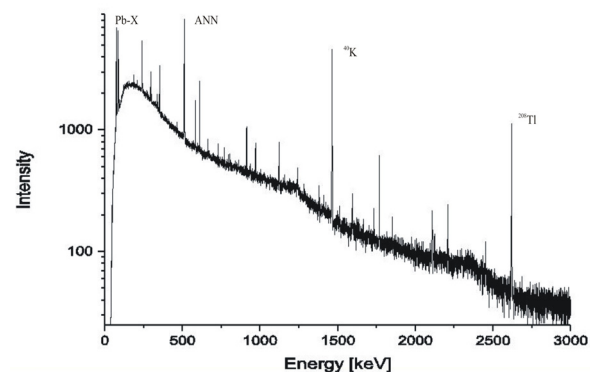


Fig. 2 Background spectrum of the HPGe detector (BGe) inside the UL after about 6 months of measuring

The table 1 in the third column presents gamma-ray background values of typical spectrum measured in

the UL using the BGe in direct (no veto) mode. The measurement time was about 6 months.

Table 1 The background characteristics of the BGe inside the UL

Line/ region (keV)	Radionuclide/ series/ nuclear reaction	Intensity (10^{-3} s^{-1})	MDA (mBq) for 100ks Water matrix
40-2700	-	500	-
46.5	Pb-210/U-238	0.38(11)	1500
53.2	U-234	-	9400
63.3	Th-234	-	700
72.8	Pb-X-K α_2	3.1(1)	-
75	Pb-X-K α_1	6.2(1)	-
84.9	Pb-X-K β_1	4.2(1)	-
87.3	Pb-X-K β_2	1.49(6)	-
92.5	Th-234	-	100
143.8	U-235	-	20
163.4	U-235	-	110
200.3	U-235	-	100
238.6	Pb-212/Th-232	0.83(4)	40
242	Pb-214/U-238	0.20(2)	-
295.2	Pb-214/U-238	0.71(4)	40
338.3	Ac-228/Th-232	0.15(2)	-
351.9	Pb-214/U-238	1.26(5)	30
477.6	Be-7	-	40
510.8+511	Tl-208/Th-232/ANN	7.0(1)	-
583.2	Tl-208/Th-232	0.30(3)	56
609.2	Bi-214/U-238	1.08(5)	60
661.7	Cs-137	0.10(5)	9
727.3	Bi-212	-	200
803.3	Pb-206 (n,n γ) Pb-206	0.11(2)	-
911.2	Ac-228/Th-232	0.25(2)	110
969	Ac-228/Th-232	0.11(2)	80
1001	Pa-234m	-	1300
1120.4	Bi-214/U-238	0.28(3)	-
1173.2	Co-60	-	19
1332.5	Co-60	-	11
1238.1	Bi-214/U-238	0.09(2)	-
1460.8	K-40	3.27(9)	850
1764.6	Bi-214/U-238	0.49(3)	230
2103.7	2614.5SE/Tl-208	0.13(2)	-
2204.2	Bi-214/U-238	0.15(2)	-
2614.5	Tl-208/Th-232	1.05(5)	-

The fourth column of the same table presents minimum detectable activity (MDA) calculated for predicted measurement time of 100000 seconds (approximately one day) for cylindrical sample (volume of 120cm³) situated on the top of the detector. Efficiency calibration was obtained by GEANT4 simulation toolkit as well as experimentally using appropriate standard. The difference between the two efficiency calibration curves is less than 5% for sample of water matrix, which MDA is here presented. MDA values are calculated as $MDA=L_D/(t \times \text{Eff} \times p)$, where the $L_D=2.71+4.65B^{1/2}$ is detection limit. B is background at the energy of gamma-ray line with

absolute detection efficiency Eff and emission probability p. If the predicted measurement time t is valued in seconds then MDA values have Bq unit. The obtained MDA values are presented for water matrix cylindrical samples in bottles with volume of 120cm³.

With the BPS currently positioned rather high over the detector top, at a vertical distance of 60cm from the top of the lead castle, in order to allow for the placing of voluminous sources in front of the vertically oriented detector, the off-line reduction of this integral count by the CR veto condition is only about 18%. Up to a factor of two might be gained if the veto detector were to be positioned at the closest possible distance over the BGe detector. This configuration requires some changes of the lead shield including introducing a sliding lead lid. Such a new shielding and veto configuration would be additionally reduce gamma-ray background up to the same factor that corresponds to factor of reduction expected for cosmic rays.

We do not insist on the lowering of statistical errors which depend on background levels solely and are difficult to reduce further with available means, but rather emphasize its stability due to the low and controlled radon concentration in the laboratory. This is essential, especially in NORM measurements, and makes our system virtually free of systematic errors as compared to systems which operate in environments where radon is not controlled. In that systems the reduction of post-radon background activities is achieved by flushing the detector cavity with liquid nitrogen vapor, where the transient regimes during sample changes and possible deposition of radon progenies may introduce systematic uncertainties which are difficult to estimate.

Acknowledgement: The paper is a part of the research done within the projects OI171002 and III43002.

REFERENCES

1. W.G. Kang, *et al.*, "Ultra-low gamma-ray measurement system for neutrinoless double beta decay", *Appl. Radiat. Isot.* (2013), vol. 81, pp. 290–293.
2. G. Angloher, *et al.*, "Results from 730 kg days of the CRESST-II Dark Matter search", *Eur. Phys. J.* (2012), vol. C72, pp. 1971
3. L. Dragounová and P. Rulík, "Low level activity determination by means of gamma spectrometry with respect to the natural background fluctuation", *Appl. Radiat. Isot.* (2013), vol. 81, pp. 123–127
4. A. Dragić *et al.*, "The new set-up in the Belgrade low-level and cosmic-ray laboratory", *Nucl. Techn. Radiat. Prot.* (2011), vol. 26/3, pp. 181-192
5. A. Dragić *et al.*, "Variations of CR-muon intensity in the declining phase of the 23rd solar cycle in ground and shallow underground data", 29th International Cosmic Ray Conference, Pune (2005), vol. 1, pp. 249-252
6. V. Udovičić *et al.*, "Daily and seasonal radon variability in the underground low-background laboratory in Belgrade, Serbia", *Radiation Protection Dosimetry* (2014), vol. 160, Issue 1-3, pp. 62-64
7. R. Banjanac *et al.*, "Variations of gamma-ray background in the Belgrade shallow underground low-level laboratory", *Applied Radiation and Isotopes*, (2014), vol. 87, pp. 70-72

RELATION BETWEEN DAILY GAMMA-RAY BACKGROUND AND RADON VARIABILITY IN THE UNDERGROUND LOW-LEVEL LABORATORY IN BELGRADE

R. Banjanac, V. Udovičić, J. Filipović, D. Joković, D. Maletić, M. Savić, N. Veselinović, P. Kolarž, A. Dragić

Institute of Physics, Belgrade, Serbia

Abstract. *The most important background source in low-level gamma-ray spectrometry is radon which additionally causes background variability. Intensive daily radon variation at the same time with daily variation of gamma-ray background was already measured in our ground level laboratory. The new simultaneously measurements of radon concentration and gamma-ray background performed in the underground laboratory and correlation between them in a wide range of radon concentration was analyzed.*

Key words: *gamma-ray background, radon variability, underground laboratory*

1. INTRODUCTION

Correlation between diurnal variation of radon concentration and intensities of postradon background lines measured simultaneously in a surface laboratory was already analyzed, [1]. Daily variation of postradon gamma-ray lines intensity is important as a source of systematic error in low-level NORM-sample measuring, containing Ra-226. Background measurement in the underground laboratory, as well radon monitoring, [1], did not show obvious neither radon progenies nor radon daily periodicity but the new measurements inside the underground laboratory were done.

Description of laboratories, measuring techniques and used detectors is shown in detail in [1,2].

Radon concentration is known to vary considerably, depending on many parameters, but one of the most important is ventilation rate. For indoor spaces is known that depending of ventilation rate, equilibrium factor between radon concentration and its progenies is expecting to vary from 0.3 to 0.7. The UL is equipped with ventilation system which provide a low value of radon concentration due to, among other factors, constant exchange rate of fresh air thus radon monitoring should be preferably performed together with atmospheric parameters.

2. PRELIMINARY MEASUREMENTS

In order to prepare a new setup of „radon vs. postradon“ measurement inside the UL, the results from several different radon measurements proved useful.

Radon measurement using track detectors at several positions within the UL was done, during ventilation was switched on. Preliminary results show significant inhomogeneity in spatial distribution of radon concentration after 6 months of track detectors exposition. For this long time period a single value of radon concentration obtained by each track detector can not see diurnal radon variability inside the UL (air volume of 135 m³).

For the last six years, radon concentration inside the UL was measured several times during transition ventilation regime. From the low averaged value (about 10 Bqm⁻³) with ventilation on mode, radon concentration rised lineary after ventilation was switched off up to saturated value. Rising time lasted for several days (3 to 4) while mean saturated value of radon concentration varied from 300 Bqm⁻³ up to 900 Bqm⁻³, which strongly depends on ambiental parameters and eventually on season. Obviously, diffusion rate of radon from 4pi surrounding soil and concrete must be measured precisely. For radon progenies spatial distribution is very important deposition rate of radon progenies on the walls of lead shielding as well on the detector itself. Relationship between deposition and attachment rates in Jacobi room model, [3], can be tested in order to explain spatial radon progenies distribution in the UL.

Additional preliminary result obtained using radon monitor (RM) positioned in front of one fresh-air inlet inside the UL, for ten days. The measured values of radon concentration have been often below detection level of the instrument, detecting a zero value, which confirms that radon-free air enters to the lab.

Finally, radon was simultaneously measured using a Rad7 detector for inside and RM for outside positions of lead shielding of the germanium detector (VGe). That measurements were conducted in ventilation „on“

regime, as well when ventilation was switched off. After a month of measurement there was no difference in radon concentration measured between two radon detectors, figure 1. The sampling time of both detectors was set to 12 hours during ventilation on mode in order to minimize statistical errors, and only 2 hours after ventilation was switched off.

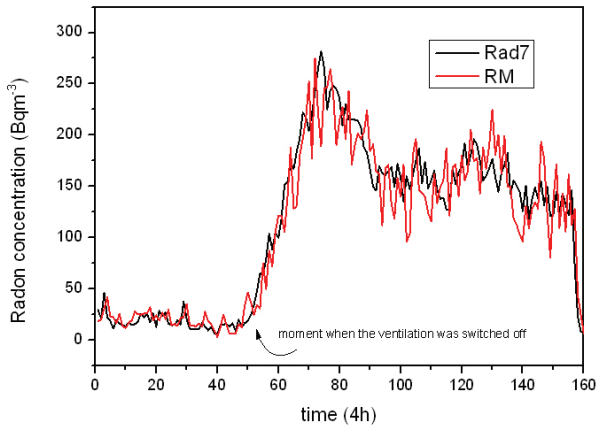


Fig. 1 Radon measurement inside and outside the lead shielding of the VGe detector

3. MEASUREMENTS AND RESULTS

The gamma-ray background was measured simultaneously using two germanium detectors, VGe (35% relative efficiency) and MGe (13%), both without any passive shielding. The germanium detectors were mutually separated about 4 meters while the MGe was positioned near wall, the VGe was about 1.5 meters far of the side walls. The both with vertical dipstick of cryostat configuration stayed on the ground with active detector volume positioned about 80cm above the ground. In the same time, RM has monitored radon in position close to the VGe, figure 2.

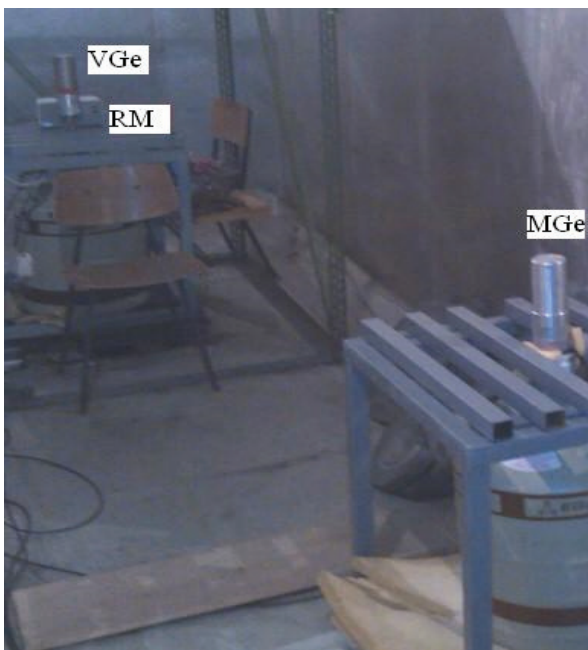


Fig. 2 Positions of detectors inside the UL

The RM, model SN1029, is used by readings on every thirty minutes, which was the same time chosen for intensities of postradon lines in time series of germanium detectors.

Correlation between radon concentration and postradon line intensities during ventilation on and off regimes was analyzed. One cycle of two consecutive ventilation regimes, on then off, presented on figure 3. Here are presented just two most intensive ones at 352keV from Pb-214 and at 609keV from Bi-214.

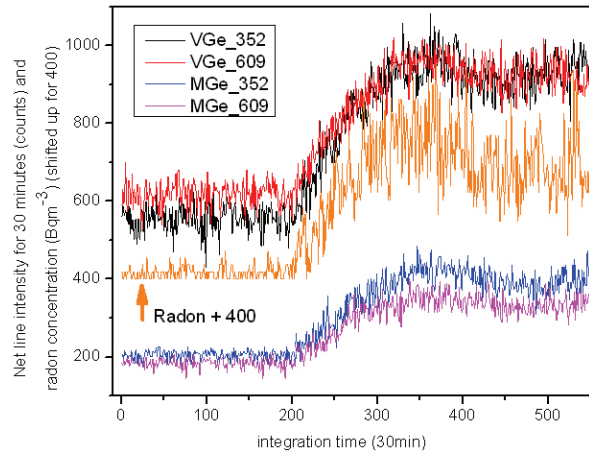


Fig. 3 Radon concentration and postradon line intensities variations inside the UL

On the figure 3, radon concentration values are shifted up for 400 to emphasize similarity of variations, especially between radon and radon progenies measured by VGe. Due to smaller detection efficiency of smaller MGe detector, one can expect better correlation between the VGe and the RM, additionally because of spatial radon distribution and separated positions of germanium detectors. The other postradon lines which have smaller intensities do not show obvious variation even in rising part of radon, during a tree days after ventilation was switched off.

When the ventilation was switched on, both radon concentration and postradon line intensities had almost constant values. For the chosen sampling time of 30 minutes, detection sensitivity of the RM is too low to register non zero values, when the ventilation is on and the mean value of radon concentration is only about 10 Bq·m⁻³.

When the ventilation was in “on” regime there was no significant variation in radon and postradon measured values. From the figure 2 is obvious that postradon values follows each other, more for the same germanium detectors, and less comparing to radon data. When radon concentration achieved saturation in “off” regime, expected daily variation of both values can not be proved using even sophisticated Lomb-Scargle periodogram analysis, [2], because of a short measuring period. A poor statistics is reason, too, why any time lag effect between 609 keV (from Bi-214) and 352 keV (from Pb-214) did not registered.

Pearson correlation coefficient (Pcc) determined for every combination of variables in rising part of ventilation “off” regime, table 1.

Table 1 Pcc for every combination of variables in rising part of ventilation “off” regime

Pcc	Radon	VGe	VGe	MGe	MGe
		352	609	352	609
Radon	1	0.78	0.77	0.70	0.69
VGe-352	0.78	1	0.88	0.76	0.79
VGe-609	0.77	0.88	1	0.78	0.80
MGe-352	0.70	0.76	0.78	1	0.76
MGe-609	0.69	0.79	0.80	0.76	1

Slightly smaller correlation coefficient for radon and MGe lines combination compared to that between radon and VGe lines can be caused by difference in radon concentration on the two different positions of germanium detectors. On the contrary, there is a strong correlation for the same postradon line detected by both Ge detectors. Similarly, the Pcc value for 352 vs. 609 combination of the MGe detector is slightly smaller than that of the VGe detector, which can be caused by the same reason mentioned above. Obviously, there is a need for further investigations for getting better explanation with better statistics.

In another ventilation “on/off” cycle after short period in ventilation “off” regime, radon concentration drops down immediately when ventilation was switched on. Then, the surfaces of both germanium detectors was cleaned thoroughly by alcohol, but in a new cycle the differences in postradon line intensities did not detected. As the both germanium detectors were in lead shielding before, for a long time period, we can conclude indirectly that attachment rates of aerosol particles on detector surfaces, measured via postradon progenies, have small values.

4. CONCLUSIONS

Correlation between daily gamma-ray background and radon variability was tested in the underground low-level laboratory in Belgrade using two unshielded germanium detectors and single radon monitor.

Pearson correlation coefficients are determined for every combination of variables in rising part of ventilation “off” regime. Daily variations in radon and postradon lines did not registered in ventilation “on” regime, as well as in saturated radon atmosphere during ventilation “off” regime. Hence, there is a need for further investigations for getting better statistics to explain radon behavior inside the underground laboratory.

The majority of commercial available active radon detectors have sensitivity threshold of radon detection about 10 Bqm^{-3} . Radon atmosphere inside the underground laboratory with long-term low radon concentration seems to be suitable place for some kind of radon chamber.

Acknowledgement: This work is supported by the Ministry of Education, Science and Technological

REFERENCES

1. R. Banjanac *et al.*, “Daily variations of gamma-ray background radiation and radon concentration”, Rom. Journ. Phys., Vol. 58, Supplement, P. S14–S21, Bucharest, 2013
2. V. Udovičić *et al.*, “Radon problem in an underground low-level laboratory”, Radiat. Meas. , Volume 44, Issues 9–10, October–November 2009, Pages 1009–1012, Proceedings of the 24th International Conference on Nuclear Tracks in Solids
3. N. Stevanovic, V.M. Markovic, D. Nikezic, “Relationship between deposition and attachment rates in Jacobi room model”, Journal of Environmental Radioactivity 101 (2010) 349-352

GAMMA-2 Scientific Workshop on the Emission of Prompt Gamma Rays in Fission and Related Topics

Some peculiarities of digital gamma-ray spectroscopy with germanium detectors performed in presence of neutrons

N. Veselinović^{a*}, D. Maletić^a, D. Joković, R. Banjanac^a, V. Udovičić^a,
M. Savić^a, J. Puzović^b, I.V. Aničin^a and A. Dragić^{a+}

^a*Institute of Physics, Pregrevica 118, 11080 Belgrade, Serbia*

^b*Faculty of Physics, Studentski trg 12, 11000 Belgrade, Serbia*

⁺*on leave at Joint Research Centre, Geel, Belgium*

Abstract

We measured the time-differentiated spectrum of the ²⁵²Cf source as seen by an high-purity germanium detector triggered by the NE213 liquid scintillator detector. The detectors are off-line coincided from the event-by-event list formed with 10 ns resolution by the quad FADC unit of the CAEN N1728B type. The signatures of the processes induced by fast and slow neutrons, both within the detector itself and in its environment, appear completely separated. The processes induced by fast neutrons are found in the prompt part of the time spectrum and those induced by thermal neutrons in the long tail of delayed coincidences. We analyse the time behaviour of spectral structures at 692 keV, which are the signatures of inelastic neutron scattering on Ge-72, and comment on its suitability for determination of the fast neutron flux in general, and in the digital gamma-ray spectroscopy in particular.

© 2014 The Authors. Published by Elsevier B.V. This is an open access article under the CC BY-NC-ND license (<http://creativecommons.org/licenses/by-nc-nd/3.0/>).

Selection and peer-review under responsibility of Guest Editor: Mr. Stephan Oberstedt - stephan.oberstedt@ec.europa.eu

Keywords: background spectra; neutrons; germanium; Cf-252

* Corresponding author: Tel.: +381 113713000
Email-address: veselinovic@ipb.ac.rs

1. Introduction

Neutrons induce a number of nuclear reactions on stable isotopes of germanium, which produce characteristic signatures in the spectra of germanium detectors. These have been studied in great detail with the aim to either improve on the knowledge of background spectra of germanium detectors, or for determination of neutron fluxes at the position of the detector (Stelson et al., 1972; Škoro et al., 1992; Wordel et al., 1996; Fehrenbacher et al., 1996, 1997; Gete et al., 1997; Siiskonen and Toivonen, 2005; Ljungvall and Nyberg, 2005; Abt et al., 2007; Ataç et al., 2009; Jovančević et al., 2010). Some of the studies dealt with environmental neutrons of cosmic-ray origin while some used different neutron sources, mostly with the fission spectrum. The findings were quite similar, irrespective of the origin of the neutrons. We undertook the time-differentiated study of some of these processes induced by ^{252}Cf fission neutrons in order to gain some insight into the dynamics of neutron-induced background in the detectors themselves, as well as in their usual environments.

2. The experiment

Our experimental setup consists of a small volume (2 litres) liquid scintillator (NE213) detector placed in a steel container and a 15% efficiency coaxial high-purity germanium (HPGe) detector, positioned as schematically presented in Fig. 1.

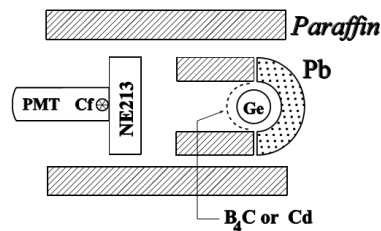


Fig. 1. The layout of the experiment (view from above)

The materials, which surround the detectors in the experiments, include lead, paraffin (hydrogen), boron, cadmium, aluminium and iron. The encapsulated ^{252}Cf source had a strength of about 2000 neutrons in 4π sr/s. On their way towards the HPGe detector the neutrons traverse the 7 cm thick layer of NE213. The distance between the end-cap of the NE213, which faces the HPGe detector, and the closest point of the HPGe detector is 10 cm. Fast neutrons with energies higher than 1 MeV, which leave the NE213 detector towards the HPGe detector, take less than 10 ns to reach this detector, while the neutrons which start as thermal take about 50 μs . Majority of neutrons, which slow down on their way towards the detector, take something in between these two values, but certainly closer to the lower one. The preamplifier outputs of both detectors are fed to the two out of four identical inputs of the flash ADC unit of the CAEN N1728B type. It can perform like a digital spectrometer capable to operate in the list, or the event-by-event mode. For every analysed event the time of its appearance over the triggering level is recorded with 10 ns resolution, while its amplitude is digitized and recorded in one of the available 32 k channels. This enables to off-line coincide the events of given amplitudes with 10 ns resolution. The software that produces and analyses the time spectra, which are equivalent to hardware TAC spectra, is entirely homemade.

3. The results

The singles spectrum of NE213 serves practically only as a trigger for the HPGe spectrum. The singles spectrum of the in this case lightly shielded germanium detector consists of the correspondingly rich environmental background spectrum, of the gamma rays given off by the californium source, and of the different features induced by fission neutrons of californium in the HPGe detector and in the surrounding materials. It stretches up to some 8 MeV. We shall here deal only with some interesting portions of this spectrum that are coincident with different delay times with the NE213 spectrum.

3.1. Effects in the environment

The time structure of the signatures of the effects, which neutrons induce in surrounding materials in our HPGe spectra, is particularly simple and illustrative. All the effects induced by fast neutrons which we see (mostly the inelastic scattering) tend to fall into the prompt peak of our time spectrum, while the effects induced by slow neutrons (mostly capture reactions) fall into the (very long) tail of delayed coincidences. The completeness of this separation is perhaps best illustrated by the cases of boron and iron. Fig.2a presents the portion of the HPGe spectrum that contains the 478 keV Doppler–widened line from the (n,α) reaction on ^{10}B , while Fig.2b depicts the part of the spectrum with the 847 keV line from (n, n') reaction on ^{56}Fe (found mostly in the NE213 casing). The first reaction has the high cross section for thermal neutrons, while the second is induced by neutron energies higher than about 1 MeV. The difference between the two cases is striking; the 478 keV structure is present only in the spectrum of delayed coincidences and on its place in the prompt spectrum the weak lines from the decay of californium appear, while the strong line of 847 keV exists only in the prompt spectrum and is completely absent in the delayed spectrum.

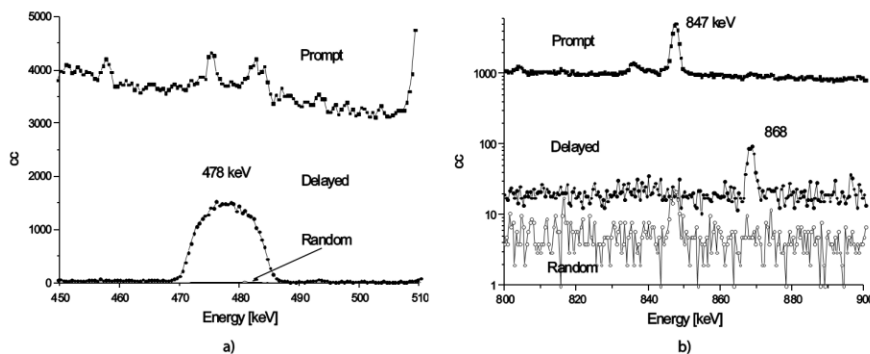


Fig. 2. The prompt, delayed (up to 1 μs) and random coincidence spectra of the 478 keV line from the reaction on boron (a), and of the 847 keV line from the reaction on iron (b). The line at 868 keV is from neutron capture on ^{73}Ge . Note that the first scale is linear while the second one is logarithmic.

Now the case of cadmium becomes instructive. Figure 3 is same as Fig. 2, but for the portion of the spectrum containing the most prominent line of 558 keV from the assumed thermal neutron capture on ^{113}Cd .

The prompt line is much more intense than the delayed one, implying that for the somewhat harder neutron spectrum, which we have in this case as compared to the one in the case when the boron absorber is present, the (n, n') reaction on ^{114}Cd contributes much more to the intensity of the 558 keV line, than the commonly assumed neutron capture by ^{113}Cd . The ratio of the prompt and delayed intensities could thus in principle serve as a simple estimate of the relative hardness of the neutron spectrum.

3.2. The structure at $E_\gamma = 692$ keV

The quasi-triangular structure starting at 692 keV, which is due to inelastic neutron scattering on the first excited state of ^{72}Ge , has been studied many times and in greatest detail [3-6]. The 692 keV state is an isomeric state, with a half-life of 444 ns, and the depopulating radiation is pure E0, meaning that detection efficiency for the 692 keV radiation is practically always 100%. This transition energy sums with the recoil energy from neutron scattering, which depends on the incident neutron energy and the scattering angle, and is reduced by the pulse-height defect. The shape of the resulting spectral distribution has been studied in detail, mostly because the intensity of this distribution has been frequently used to estimate the fast neutron flux at the position of the detector (Škoro et al., 1972; Wordel et al., 1996; Fehrenbacher et al., 1996; Jovančević et al., 2010).

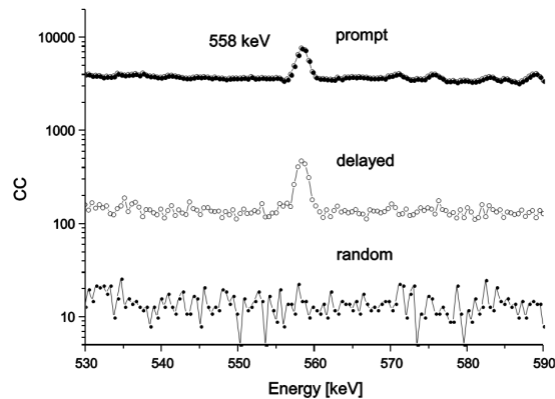


Fig. 3. Same as Fig. 2, but for the 558 keV line induced by neutrons on ^{113}Cd

The time structure of the 692 keV distribution can be seen in Fig. 4. It is seen that in the prompt spectrum, where the spectral background is quite high, the time interval narrow and the intensity of the 692 keV radiation consecutively low, the structure is barely discernible. On the other hand, in the delayed spectrum (here up to 1 μs), where the spectral background is virtually absent, the structure has the pronounced and typical triangular form.

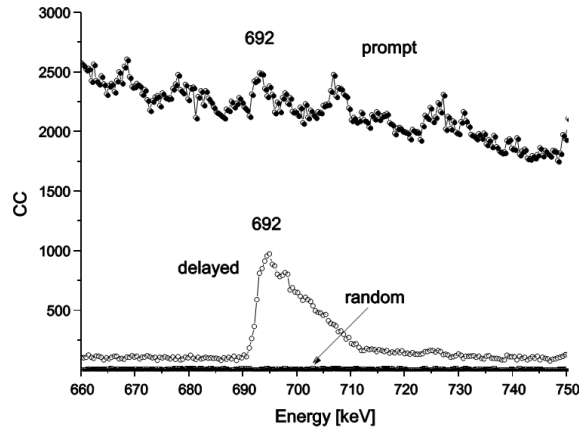


Fig. 4. Spectra of prompt, delayed, and random coincidences (practically negligible) containing the structure of 692 keV from inelastic neutron scattering on ^{72}Ge

Now, if we take the 30 keV-wide software gate, so as to fully embrace this structure (cf. Fig. 5), and find the corresponding time spectrum of coincidences with the entire NE213 spectrum, we obtain the time spectrum presented in Fig. 6a. The time spectrum is corrected for amplitude walk according to the procedure described in (Puzović and Aničin, 2007). The fit through the nicely exponential tail of delayed coincidences (Fig. 6b) yields at the 68% CL the half-life of 459(11) ns, which compares satisfactorily with the established value of 444 ns. This justifies the use of the intensity of this distribution for fast-neutron flux estimation in the case of digital spectroscopy as well. The treatment of the below-the-triggering-level pulses in a given digital spectroscopy system is essential in this respect. The condition is that the threshold is high enough, to let all the recoil pulses sum with the 692 keV pulses.

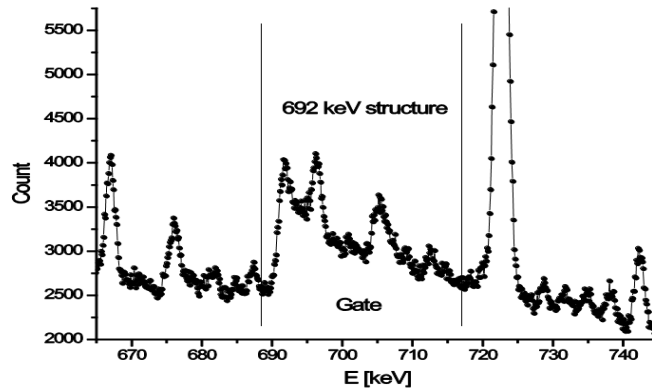


Fig. 5. The “triangular” structure at $E_\gamma = 692$ keV in the non-gated HPGe spectrum from the inelastic neutron scattering on ^{72}Ge . The position of the 30 keV-wide software gate, which is used to produce the time spectrum, shown in Fig. 6, is also shown.

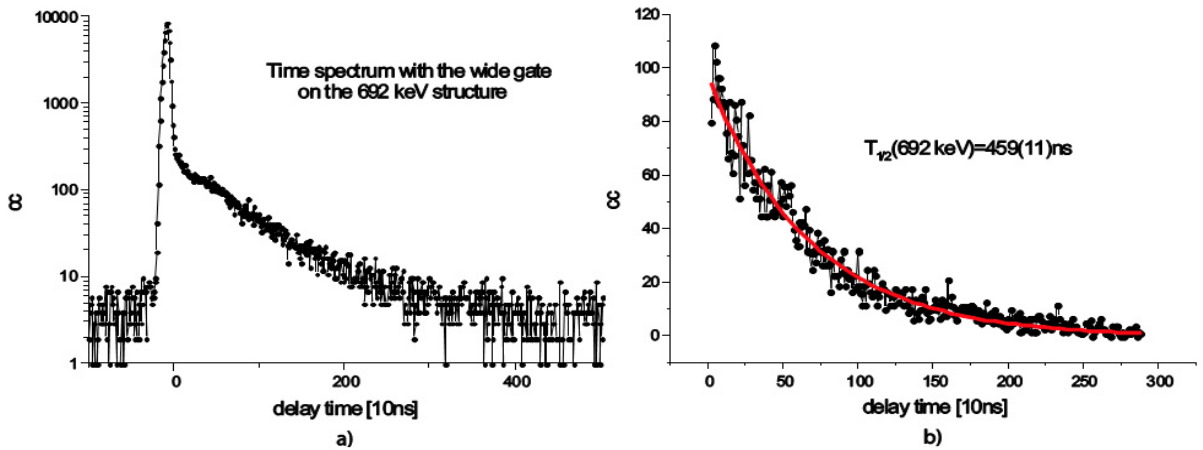


Fig. 6. Time spectrum of delayed coincidences of the 692 keV structure within the gate shown in Fig. 5 with the entire NE213 spectrum (a), which yields the half-life of the 692 keV state of 459(11) ns as shown in (b).

Finally, we took and analysed the direct HPGe californium spectrum in the so-called oscillogramme mode, when the pulses are sampled at 10 ns intervals, starting at the given number of points before the defined trigger level. To illustrate, we present in Fig. 7 the pulse with the amplitude that corresponds to 692 keV, preceded by its corresponding recoil pulse. Firstly, we produced the distribution of time intervals between the appearance of the recoil and 692 keV pulses.

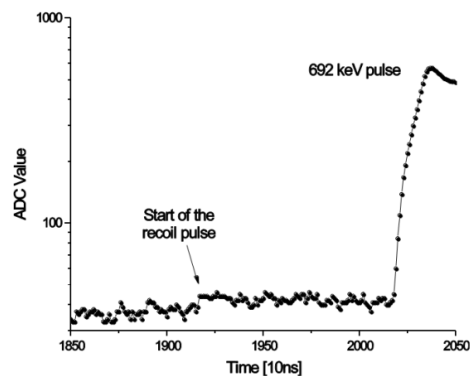


Fig.7. The joint pulses due to the recoil of the excited ^{72}Ge and the de-exciting 692 keV radiation, separated on the average for the mean lifetime of the 692 keV state. The distribution of these time intervals yields 442 to 446 ns for the half-life of this state, in excellent agreement with the accepted value.

We produce the spectrum in the 692 keV region, by the algorithm that defines the baseline after subtracting the corresponding recoil pulse. This, for the first time, produces the normal line at 692 keV, instead of the common summing structure (Fig.8, to be compared with Fig.5). The integral of the line equals the integral of the structure, This additional analysis validates our earlier conclusions concerning the suitability of the 692

keV structure for the determination of the fast neutron flux at the position of the detector.

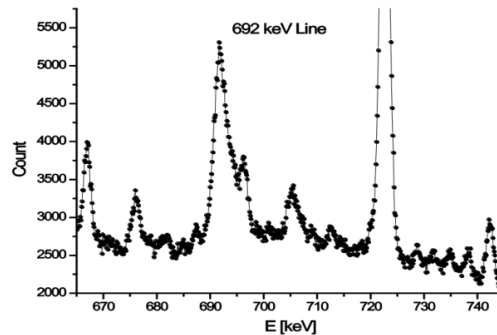


Fig. 8. The spectral line at 692 keV, from the de-excitation of the first excited state of ^{72}Ge , obtained by subtraction of the adjoined recoil pulses. This compares with the structure in Fig. 5, which results from the standard digital spectroscopy algorithm for baseline correction. In both cases the integral of the distributions contains all the events induced by fast neutrons on ^{72}Ge .

4. Conclusion

We measured the time-differentiated spectrum of the ^{252}Cf source as seen by an HPGe detector triggered by the NE213 liquid scintillator detector. The detectors were off-line coincided from the event-by-event list formed with 10 ns resolution by the quad FADC unit of the CAEN N1728B type. We tested the workings of the system on a number of effects generated by neutrons and found the time resolution satisfactory for the purpose. The signatures of the processes induced by fast and slow neutrons, both within the detector itself and in its environment, appear completely separated. The processes induced by fast neutrons are found in the prompt part of the time spectrum and those induced by thermal neutrons in the long tail of delayed coincidences. We find the intensity of the structure at 692 keV structure remains suitable for this purpose even in digital spectroscopy, if the threshold is higher than some 25 to 30 keV, and the germanium recoil pulses are let to sum with the 692 keV pulses.

Acknowledgments

The work is supported by the Ministry of “Education, Science and Technological Development” of the Republic of Serbia, under the Project No. 171002.

References

- Abt, I. et al., arXiv:0711.2255v1 [nucl-ex] 14 Nov 2007
- Ataç, A. et al., Nucl. Instr. Meth. A607 (2009) 554.
- Fehrenbacher, G., Meckbach, R. and Paretzke, H.G., Nucl. Instr. Meth. A372 (1996) 239.
- Fehrenbacher, G., Meckbach, R. and Paretzke, H.G., Nucl. Instr. Meth. A377 (1997) 391.
- Gete, E. et al., Nucl. Instr. Meth. A388 (1997) 212.
- Jovančević, N. et al., Nucl. Instr. Meth. A612 (2010) 303.
- Ljungvall, J. and Nyberg, J., Nucl. Instr. Meth. A550 (2005) 379.
- Puzović, J. and Aničin, I., Nucl. Instr. Meth. A572 (2007) 926.
- Siiskonen, T. and Toivonen, H., Nucl. Instr. Meth. A540 (2005) 403.
- Škoro, G. et al., Nucl. Instr. Meth. A316 (1992) 333.

Stelson, P.H. et al., Nucl. Instr. Meth. 98 (1972) 481.
Worzel, R. et al., Nucl. Instr. Meth. A369 (1996) 557.



GAMMA-2 Scientific Workshop on the Emission of Prompt Gamma Rays in Fission and Related Topics

Shape-isomer studies with resonance neutron capture

A. Dragić^{a,**}, G. Nyman^b, A. Oberstedt^b, S. Oberstedt^a^aEuropean Commission, DG Joint Research Centre (IRMM), 2440 Geel, Belgium^bFundamental Fysik, Chalmers Tekniska Högskola, 41296 Göteborg, Sweden**Abstract**

An experiment searching for formation of super-deformed shape isomers in odd uranium isotopes following neutron capture is designed at the GELINA neutron source of IRMM. We focus on neutron energies around the so-called intermediate structure in the fission cross-section, where the coupling between compound states above the first and the second minimum is largest. The experimental arrangement is described. The results of a feasibility study on the population of the shape isomer in ^{235}U , using a ^{234}U target, together with the results from first run with a ^{238}U target are presented.

© 2014 The Authors. Published by Elsevier B.V. This is an open access article under the CC BY-NC-ND license

(<http://creativecommons.org/licenses/by-nc-nd/3.0/>).

Selection and peer-review under responsibility of Guest Editor: Mr. Stephan Oberstedt - stephan.oberstedt@ec.europa.eu

Keywords: shape isomer; neutron capture; neutron resonances; intermediate structure;

1. Introduction

Introduction of microscopic shell corrections into macroscopic liquid drop model (Strutinski V.M., 1967) led to the picture of doubly-humped barrier in actinide nuclear binding energy. The concept successfully explained intermediate structure in sub-threshold fission cross sections as well as the existence of shape isomers.

Many research effort since 1960s resulted in the discovery of various shape isomers and in the characterization of their fission barriers. A (relatively) recent review lists 35 shape isomers (Singh et al., 2002). However, data for shape isomers of odd-N uranium isotopes are still lacking. Since the pioneering work on ^{239}U of Oberstedt and Günsing (Oberstedt and Günsing, 1998) and on ^{235}U of Oberstedt et al. (Oberstedt et al., 2007) no new results are published. It is our intention to study shape isomers of ^{239}U and ^{235}U by means of (n, γ) reaction. We plan to investigate the γ -decay of the shape isomer back to the normal ground state by γ -spectroscopic methods. In order to study the feasibility of our concept we conducted two test experiments with the two named uranium isotopes, and the results are presented in this paper.

* On leave from Institute of Physics, Pregrevica 118, Belgrade, Serbia.

** Corresponding author.

E-mail address: aleksandar.dragic@ec.europa.eu

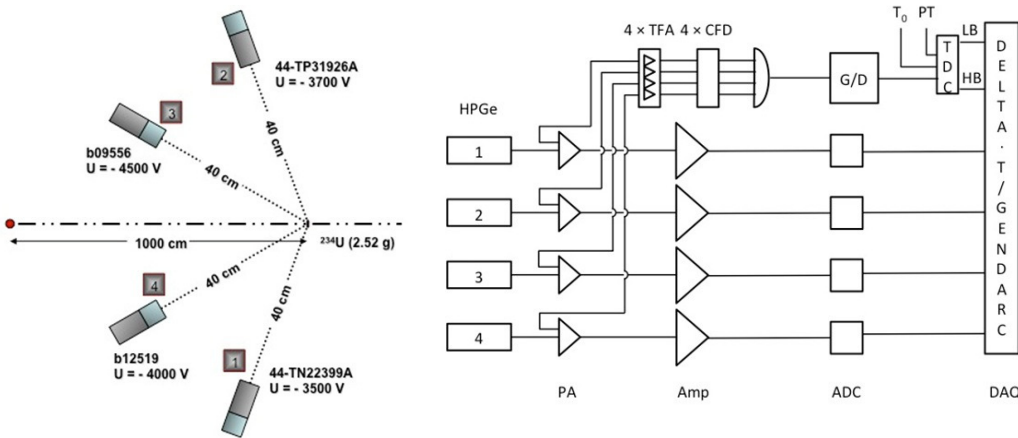


Fig. 1. (a) Detector setup and; (b) data acquisition system.

2. Experimental details

Both the ^{234}U and ^{238}U measurements are performed at the GELINA pulsed white energy neutron source of the Institute for Reference Materials and Measurements (IRMM) in Geel, Belgium. The host measurement station is at 10 m nominal distance from the neutron production target. Our detector system consists of four n-type coaxial HPGe detectors of 45% relative efficiency. Two detectors are produced by (Canberra, 2007) and two by (Ortec, 2004). All detectors are electrically cooled. The energy resolution at $E_\gamma = 1332.5 \text{ keV}$ (^{60}Co) ranges from 2.1-2.4 keV, measured with $2\mu\text{s}$ shaping time.

The data acquisition system is based on a *Delta-T* data-acquisition (DAQ) system (Send GmbH, 2000) and the GENDARC on-/off-line data analysis software, which was developed at IRMM (Figure 1). One output from the detector preamplifier (PA) is used to determine the amplitude of the signal. After amplification and shaping (Amp) the signal is digitized (ADC) and fed into the DAQ. The second PA output is used for obtaining the neutron time-of-flight information. The signal is fed into a timing filter amplifier (TFA) and constant fraction discriminator (CFD) for accurate timing. During the feasibility study timing problems were enhanced due to noise, appearing with the frequency of the linac electron beam.

For neutron time-of-flight (TOF) determination we use the signal, t_0 , which comes from the electron burst just before impinging on the mercury-cooled uranium target used for neutron production, as start signal. The stop signal is generated from any HPGe detector which has registered an event. The difference of both signals is the TOF, from which the neutron energy may be calculated. To avoid the γ -flash triggering the DAQ a $10\mu\text{s}$ anti-coincidence gate following the t_0 signal is applied.

3. Results

3.1. ^{234}U run

Experimental setup for the ^{234}U run has been described in the previous section and schematically represented on Fig. 1. The experiment has been performed in the frame of the EUFRAT trans-national access programme at IRMM (Euftrat, 2011). The ^{234}U target was a 3.0 cm disc made from 2.1285(1) g of ^{234}U (99.077%, ^{235}U : 0.076%, ^{236}U : 0.057%, ^{238}U : 0.79%). The major difficulty in the experiment stems from the high intrinsic activity of the target ($5.8 \times 10^8 \text{ Bq}$). Total count rate in the detector system is 10^4 cps , even in beam-off condition. With the neutron beam on the target the experimental spectrum is still dominated by the target activity, arising mainly from the presence of the isotope ^{232}U with $T_{1/2} = 68 \text{ y}$ and, therefore, very high specific activity. Two isotopes from ^{232}U decay chain are

Table 1. List of observed neutron resonances in the ^{234}U time-of-flight spectrum. The two resonances at 59 and 142.2 eV could not be attributed to any isotope present in the target or set-up, yet.

TOF (μs)	$E_n(\text{eV})$ (calibrated)	$E_n(\text{eV})$ (tabulated value)	TOF (μs)	$E_n(\text{eV})$ (calibrated)	$E_n(\text{eV})$ (tabulated value)
144.4	29.5	31.13	61.5	187.8	187.52
116.5	46.4	48.56	58.0	214.0	208.4
106.2	59.0	-	55.8	233.8	237.8
93.2	75.0	77.38	53.2	261.1	258.3
84.9	91.9	94.29	49.9	302.6	307.5
80.2	103.9	106.13	46.1	363.2	359.1
78.5	108.9	111.06	43.6	416.3	412.6
69.8	142.2	-	42.9	431.8	436.3
69.0	144.8	146.25	40.8	485.9	489.0
67.7	151.1	152.16	40.0	511.9	511.0
63.2	176.1	176.18	39.4	529.9	526.2
62.4	181.5	182.49			

responsible for the majority of γ -lines in the spectrum: ^{208}Tl and ^{212}Po . Observed γ -lines from these two isotopes are listed here:

- ^{208}Tl : 485.95 keV, 510.77 keV, 583.19 keV, 650.10 keV, 763.13 keV, 821.20 keV, 860.56 keV,
927.60 keV, 982.60 keV, 1093.90 keV, 1282.80 keV, 1592.5 keV, 2103.51 keV, 2614.51 keV.
- ^{212}Po : 727.33 keV, 893.39 keV, 952.12 keV, 1078.63 keV, 1109.7 keV,
1512.8 keV, 1620.74 keV, 1679.45 keV, 1806.0 keV.

In the time-of-flight spectrum resonant structures are observed and attributed to capture resonances in ^{234}U (see Table 1). In addition to the tabulated ^{234}U resonances, two resonances at energies 59 eV and 142 eV are observed in the time-of-flight spectrum.

Although resonances are present, spectra produced with cuts on resonant part of TOF curve does not differ significantly from spectra obtained from the non-resonant part. Prospects for observation of shape isomer population are not favourable without allowing for longer measurement time and without setup improvement.

3.2. ^{238}U run

A test measurement with ^{238}U target was performed for a live time of 320270 s. The target is a disk of 11.1 cm radius, made from depleted uranium (0.2% of ^{235}U). Four HPGe detectors are arranged similarly as in the ^{234}U run, at 40 cm distance from the target. Two detectors are positioned at 90° and the two others at 115° with respect to the neutron beam. Recorded spectra are highly complex, with more than 200 γ -lines arising from natural background, radiation from the target, and neutron-induced radiation in the accelerator wall, detectors or other materials present in the laboratory. A summary of all γ -lines identified in the spectrum together with the corresponding count rate is given below. Some lines which should be present in the spectra but were not found are indicated as "below detection limit" (below DL).

3.2.1. Radiation from the target

- ^{234m}Pa : 258.2 keV (0.44 cps), 742.8 keV (0.84 cps), 766.4 keV (3.12 cps), 921.7 keV (below DL),
1001.03 keV (4.98 cps), 1237.3 keV (0.30 cps), 1737.7 keV (0.11 cps), 1831.5 keV (0.07 cps),
1867.7 keV (0.06 cps), 1875.5 keV (0.04 cps).
- ^{234}Pa : 569.3 keV (below DL), 926.4 keV (0.14 cps).

3.2.2. Environmental radiation

^{238}U decay chain (other than ^{234m}Pa and ^{234}Pa)

^{214m}Bi : 609.3 keV(below DL), 665.5 keV(0.04 cps), 806.2 keV(below DL), 1120.3 keV(0.62 cps),
1377.7 keV (below DL), 1408.0 keV (0.15 cps), 1764.5 keV (0.63 cps), 1847.4 keV (0.02 cps),
2204.2 keV (0.33 cps), 2447.9 keV (0.1124 cps).

^{214}Pb : 351.9 keV(below DL).

^{232}Th decay chain

^{228m}Ac : 338.3 keV(0.60 cps), 726.9 keV(below DL), 755.3 keV (0.10 cps), 795.0 keV (0.21 cps)
911.2 keV (0.91 cps), 969.0 keV(0.54 cps), 1588.2 keV(below DL), 1630.6 keV (0.05 cps).

^{212}Pb : 238.6 keV (2.44 cps).

^{212}Bi : 727.2 keV(below DL), 1620.6 keV(below DL).

^{208}Tl : 277.4 keV (0.85 cps), 583.2 keV (1.24 cps), 860.6 keV (0.21 cps), 2614.5 keV (1.01 cps).

^{40}K : 1460.8 keV (6.08 cps)

3.2.3. Neutron induced radiation

In detectors. Many γ -lines arising from neutron capture on Ge isotopes are visible, but not lines from neutron inelastic scattering, indicating absence of fast neutrons in the fly path. Lines from $^{115}\text{In}(n, \gamma)$ reaction are found in Ortec detectors only.

$^{73}\text{Ge}(n, \gamma)$: 492.9 keV (1.01 cps), 595.9 keV(8.10 cps), 608.4 keV (below DL), 638.8 keV (0.03 cps),
701.5 keV (0.31 cps), 867.9 keV (2.50 cps), 961.05 keV(below DL), 1033.1 keV (0.02 cps),
1131.4 keV (0.16 cps), 1204.2 keV (1.41 cps), 1267.7 keV (0.04 cps), 1471.6 keV (0.16 cps),
1489.3 keV (0.11 cps), 1942.0 keV (below DL), 2073.7 keV (0.12 cps), 2368.2 keV (0.02 cps).

$^{70}\text{Ge}(n, \gamma)$: 283.3 keV (0.16 cps), 391.4 keV (0.24 cps), 500.0 keV (4.22 cps), 708.1 keV (1.95 cps),
747.1 keV (0.51 cps), 808.1 keV (below DL), 831.3 keV (1.07 cps), 1026.4 keV (0.09 cps),
1095.5 keV(below DL), 1096.1 keV(below DL), 1139.2 keV (0.70 cps), 1298.6 keV (0.89 cps),
1378.7 keV(below DL), 1416.0 keV (0.07 cps), 1598.5 keV (0.31 cps), 1743.4 keV (0.07 cps),
1965.0 keV (0.29 cps), 2032.7 keV (0.09 cps), 2351.0 keV (0.14 cps), 2534.4 keV (0.12 cps),
2675.8 keV (0.06 cps).

$^{72}\text{Ge}(n, \gamma)$: 297.2 keV (2.83 cps), 1250.1 keV (0.05 cps).

$^{74}\text{Ge}(n, \gamma)$: 253.0 keV (2.34 cps), 575.0 keV (0.66 cps), 632.4 keV (0.32 cps), 2138.7 keV (0.01 cps).

$^{115}\text{In}(n, \gamma)$: 272.9 keV (0.47 cps), 385.1 keV (0.13 cps), 416.9 keV (1.42 cps), 818.6 keV (0.27 cps),
1293.4 keV (1.81 cps), 2112.1 keV (0.44 cps), 2390.1 keV (0.20 cps), 2801.0 keV (0.04 cps).

In concrete walls. Typical concrete contains oxygen, silicon, hydrogen, calcium, aluminium, magnesium, iron etc. In accelerator walls, neutron shielding materials, such as boron are also present. Some of the most intense γ -lines in the spectrum are generated in neutron interactions with wall material.

$^{28}\text{Si}(n, \gamma)$: 1273.3 keV(below DL), 1867.3 keV(below DL), 2092.9 keV(below DL), 2425.5 keV (0.04 cps).

$^1\text{H}(n, \gamma)d$: 1711.9 keV (0.81 cps), 2223.1 keV (10.39 cps).

$^{40}\text{Ca}(n, \gamma)$: 1942.6 keV (below DL), 2001.6 keV (0.11 cps), 2009.8 keV (0.09 cps).

$^{27}\text{Al}(n, \gamma)$: 983.0 keV (0.16 cps), 1013.7 keV (0.09 cps), 1526.1 keV (0.06 cps), 1778.6 keV (4.61 cps), 2271.6 keV (0.05 cps), 2282.7 keV (0.10 cps), 2577.7 keV (0.06 cps), 2590.0 keV (0.09 cps), 2821.9 keV (0.0858 cps).

$^{56}\text{Fe}(n, \gamma)$: 352.4 keV (below DL), 366.7 keV (0.26 cps), 569.9 keV (below DL), 692.0 keV (0.80 cps), 884.7 keV (0.32 cps), 898.3 keV (0.37 cps), 920.8 keV (below DL), 1019.0 keV (0.32 cps), 1197.3 keV (below DL), 1358.7 keV (0.09 cps), 1612.8 keV (0.57 cps), 1674.6 keV (0.02 cps), 1810.5 keV (0.25 cps), 2066.2 keV (0.17 cps), 2091.8 keV (below DL), 2129.5 keV (below DL), 2721.2 keV (0.10 cps).

$^{10}\text{B}(n, \alpha)^7\text{Li}$ 477.7 keV (52.62 cps)

In other lab material. Among other materials found in the laboratory, noticeable contribution to spectrum comes from cadmium, used as overlap filter, and chlorine, since certain amounts of PVC are always present.

$^{113}\text{Cd}(n, \gamma)$: 558.4 keV (2.85 cps), 1364.3 keV (0.13 cps), 1660.4 keV (0.09 cps), 2660.1 keV (0.04 cps).

$^{35}\text{Cl}(n, \gamma)$: 786.3 keV (below DL), 788.4 keV (below DL), 1164.8 keV (0.86 cps), 1951.1 keV (below DL), 1959.3 keV (below DL), 2863.8 keV (0.12 cps).

3.3. Coincidences

A time-to-amplitude converter was operated between detectors 3 and 4 (cf. Figure 1). Lines present in summed spectrum with a cut on the peak in TAC curve are listed in Tab. 2.

The majority of coincident γ -lines occurs as consequence of interactions of neutrons, backscattered from the target, with the detectors.

3.4. Neutron resonances

The integral time-of-flight spectrum is presented in the left part of Fig. 2. In there three characteristic regions are indicated, (I) γ -flash, (II) resonance region and (III) far delayed non-resonant region below the lowest resonance at 6.671 eV.

Calibration of TOF curve yields the list of observed neutron resonances. Resonances important for class-II states: 173.18 eV and 721.58 eV are not observed due to long dead system time after γ -flash. Summed γ -ray spectrum from all four detectors with the gate on 6.671 eV resonance compared to background spectrum is shown on Fig. 3.

4. Conclusions

The purpose of the presented feasibility study was to test functionality of the present setup and to provide us with guidance on how to improve it. Several important conclusions can be drawn. First, it is necessary to install properly designed shielding against different background components. The most deteriorating impact comes from the γ -flash during neutron production. Due to the proximity of our measurement laboratory to the neutron target hall, the intensity of the γ -flash is high. It extends the detector dead time, preventing us from reaching the interesting part of the TOF spectrum in ^{238}U . As a consequence of the long decay time of HPGe preamplifiers ($\approx 50 \mu\text{s}$), all other pulses sum with γ -flash pulse, which leads to lower resolution, distorted peak shape and peak shifting. The energy distribution

Table 2. Coincident spectrum between detectors 3 and 4.

No	Energy(keV)	FWHM(keV)	Net count	Identification
1	272.7	2.07	157	$^{115}\text{In}(n, \gamma)$
2	324.9	1.08	192	$^{70}\text{Ge}(n, \gamma) + ^{72}\text{Ge}(n, \gamma)$
3	416.8	2.13	508	$^{115}\text{In}(n, \gamma)$
4	478.7	0.89	692	$^{10}\text{B}(n, \alpha)^7\text{Li}$
5	492.9	1.87	145	$^{73}\text{Ge}(n, \gamma)$
6	500.1	2.62	245	$^{70}\text{Ge}(n, \gamma)$
7	511.2	3.87	2303	ANN
8	558.8	1.02	80	$^{113}\text{Cd}(n, \gamma)$
9	595.9	2.37	2519	$^{73}\text{Ge}(n, \gamma)$
10	608.5	1.99	416	$^{73}\text{Ge}(n, \gamma)$
11	701.5	0.93	104	$^{73}\text{Ge}(n, \gamma)$
12	708.3	1.08	134	$^{70}\text{Ge}(n, \gamma)$
13	818.8	0.63	82	$^{115}\text{In}(n, \gamma)$
14	867.9	3.07	852	$^{73}\text{Ge}(n, \gamma)$
15	960.7	2.07	189	$^{73}\text{Ge}(n, \gamma)$
16	1000.8	0.58	73	^{234m}Pa
17	1096.8	2.18	243	$^{115}\text{In}(n, \gamma) + ^{70}\text{Ge}(n, \gamma) + ^{70}\text{Ge}(n, \gamma)$
18	1203.6	2.24	187	$^{73}\text{Ge}(n, \gamma)$
19	1293.4	2.18	396	$^{115}\text{In}(n, \gamma)$
20	2223.3	1.69	277	$^1\text{H}(n, \gamma)d$

of γ -flash is rather broad, centered around 250 keV (Plompen et al., 2010). A good compromise for attenuation of as much of γ -flash radiation as possible and non-attenuation of neutron flux would be 2 cm lead shield installed close to the neutron production target well behind the wall.

Another source of background are neutrons, present even with closed shutter on the flight path. They amount to about 15% of neutrons in the interesting energy range, but carry no timing information. Neutron induced radiation in the accelerator wall results in many γ -lines in all parts of the spectrum. These background components could be treated by graded shield consisting of a moderator (such as paraffin or polyethylene), a neutron absorber (made from material with high capture cross section) and a γ -shielding (typically lead). If placed close to the detector, lead can serve also as a shield against environmental radiation.

Usefulness of coincident spectrum would be significantly enhanced if additional shield from target-scattered neutrons is placed in front of the detectors. Low-Z, low density material with high neutron scattering cross-section is ideal.

Transition from analog to digital data acquisition would further improve the setup. It would allow to employ pulse shape analysis to further suppress the impact of the γ -flash.

References

- Canberra, <http://www.canberra.com/products/detectors/pdf/REGe-Detector-SS-C40432.pdf>
- EUFRAT, Special Support Action, 7th Framework Programme of the European Atomic Energy Community, Nov. 1 (2008) to Oct. 31 (2012)
- Oberstedt S. and Günsing F. 1998. Evidence for low-energy γ -decay above the shape isomer in ^{239}U . Nucl. Phys. A 636, 129-138.
- Oberstedt A., Oberstedt S., Gawrys M. and Kornilov N. 2007. Identification of a shape Isomer in ^{235}U . Phys. Rev. Lett. 99, 042502.
- Ortec, <http://www.ortec-online.com/Solutions/RadiationDetectors/semiconductor-photon-detectors.aspx>
- Ene, D et al., Nucl. Inst. Method A618 (2010) 54.
- Send GmbH, Hamburg (2000).
- Singh B., Zywna R. and Firestone R.B. 2002. Nuclear Data Sheets 97, 241.

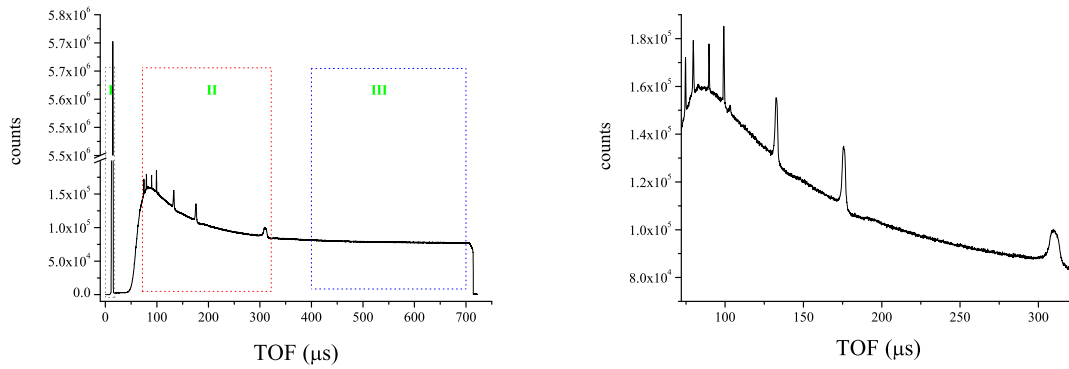


Fig. 2. Left part: TOF spectrum with marked regions: I - γ -flash region, II - resonant region and III - far delayed region and; Right part: zoom into region II

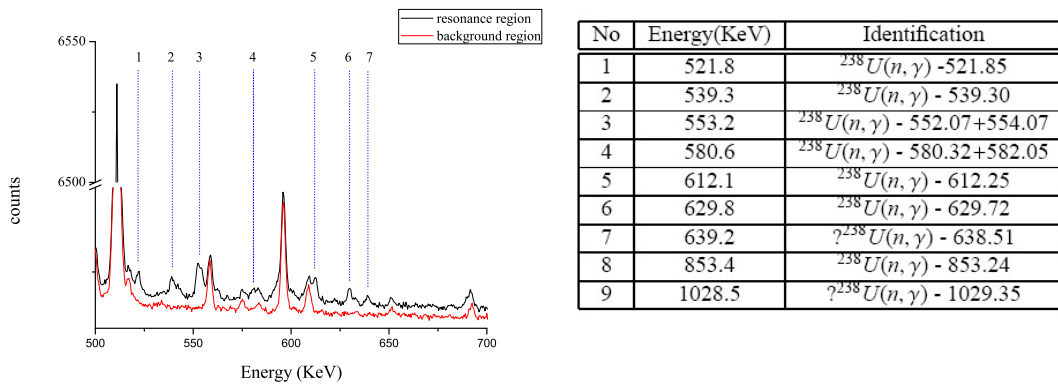


Fig. 3. Right part: the identified γ -lines from neutron capture in ^{238}U in the resonant region not visible in the non-resonant TOF region; Left part: Identified γ -lines in ^{239}U as indicated in the spectrum shown to the left.

Strutinsky V.M., 1967.Shell effects in nuclear masses and deformations energies. Nucl. Phys. A 95, 420-442.

12. J. T. Duffý, J. S. Madden, G. M. Mackin, A. T. McGarry, P. A. Colgan: A reconnaissance survey of radon in show caves in Ireland, *Environment International*, 22(1), 415-423, (1996)
13. N. Kávási, T. Vigh, T. Kovács, J. Vaupotić, V. Jobbágy, T. Ishikawa, H. Yonehara: Dose estimation and radon action level problems due to nanosize radon progeny aerosols in underground manganese ore mine, *Journal of Environmental Radioactivity*, 102(9), 806-812, (2011)
14. N. Kávási, J. Somlai, T. Kovács, C. Németh, T. Szabó, Z. Gorjanacz, A. Várhegyi, J. Hák: Difficulties in radon measurements at workplaces, *Radiation Measurements*, 41, 229-234, (2006)
15. SSI (Swedish Radiation Protection Institute): Radon Legislation and National Guidelines, Akerblom, G: ISSN 0282-4434, (1999)

INFLUENCE OF VENTILATION SYSTEMS ON INDOOR RADON VARIABILITY

Vladimir Udovičić, Aleksandar Dragić, Radomir Banjanac, Dejan Joković,
Dimitrije Maletić, Nikola Veselinović, Jelena Filipović

University of Belgrade, Institute of Physics, Belgrade, Serbia

Abstract

Indoor radon concentration varies daily and seasonally, mainly due to the changes of the atmospheric parameters (temperature, atmospheric pressure) and the exchange rate between indoor and outdoor air. Because the short-term variation during a day may be extreme, it is important to investigate short-term variations of indoor radon. The physical origin of the variation on the indoor radon concentration is not straightforward. In this paper, we pointed out the influence of ventilation systems on changes of indoor radon concentration in different environments.

Introduction

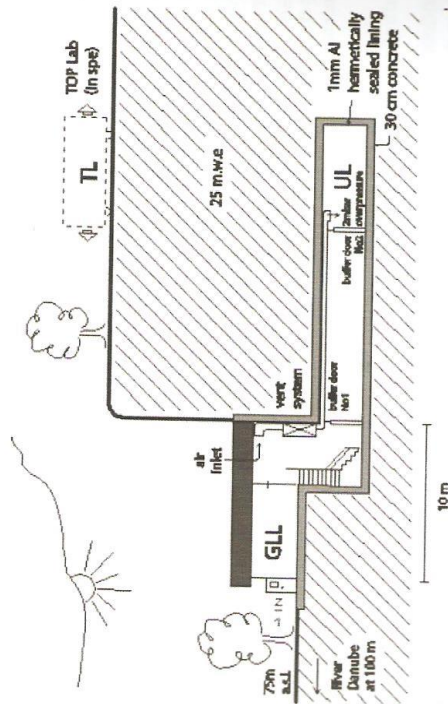
The indoor radon behaviour is affected by large number of factors. As a result, the indoor radon concentration varies (mostly within one day or a year) with different amplitudes. In this paper, we pointed out the influence of ventilation systems on changes of indoor radon concentration in different environments. For this purpose, we choose two laboratories (the Underground Low-Level [ULL] and Ground Level Laboratory [GLL] of the Low-Background Laboratory for Nuclear Physics at the Institute of Physics in Belgrade [IPB]) and two typical family houses with different type of ventilation systems (natural and air-conditioning). Based on the obtained results, some of general conclusions can be found.

Experiment

All radon measurements were done using active continuous radon monitor device: Sun Nuclear - model 1029 (manufactured by the Sun Nuclear Corporation, NRSB approval-code 31822). The device consists of two diffused junction photodiodes and is furnished with sensors for temperature, barometric pressure and relative humidity. The time sampling of 0.5, 1, 2, 4, 8, 12, 16, 20 or 24-hour intervals is selectable by user. The duration of the countings measurements is limited by the device memory which can store the data of 720 measurements. We selected the 2 hours sampling time with measurements lasting of several days.

The Low-Background Laboratory for Nuclear Physics⁽¹⁾ at the Institute of Physics in Belgrade is a shallow underground laboratory (*Figure*). The laboratory was built in the loamy loess cliff on the bank of the river Danube with the overburden of 12 m of soil. It has an active area of about 45 m² (135 m³). The experiments and routine

measurements in the underground Low-Background Laboratory for Nuclear Physics require low levels of radon concentration with minimum temporal variations. Cross section of the ULL and GLL laboratories at IPB is shown in the 1. figure.



1. figure: Cross section of the ULL and GLL laboratories at IPB

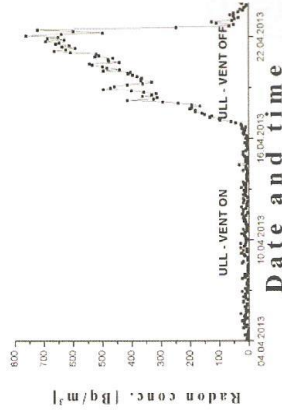
Also, for the indoor radon measurements two typical family houses with different (natural and air-conditioning) type of ventilation systems were chosen.

Results and discussion

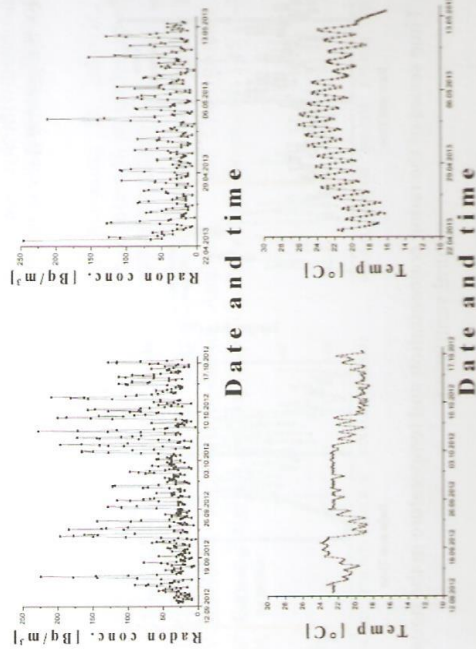
The description of the radon reducing system, and the results of the three years of the continuous short-term radon measurements in the ULL are presented in the work³ (2015). Comparison of radon concentrations when the ventilation system is switched on and off in the ULL, demonstrates that the ventilation system is a crucial stage in the radon reduction system in our underground laboratory (2. figure). This highlights the need for the ventilation systems to reduce the radon problem in the underground environments.

Similar type of indoor radon measurements were done in the GLL, which is only air-conditioned. This laboratory is situated in two joined standard transportation containers with iron sheet walls, but furnished with quality thermal insulation. The GLL has area of 30 m² and volume of 75 m³. In spite of quality wall insulation of the GLL, influence of radon through the ground floor is intensive. We tested the effects of air-conditioning on radon concentration in the GLL, under the conditions of stabilized temperature by one air-conditioning unit. The air-conditioner (12 kBTU) is adjusted to automatically provide temperature of 22(2) °C. Time series of the radon concentrations and temperature in the GLL with the air conditioning on (<Rn> (sd)= 54(44) Bqm⁻³)

and off (<Rn> (sd)= 41(34) Bqm⁻³) are shown in 3. figure. The obtained results show slightly higher average value of the radon concentration with air conditioning switched on compared with situation when the air conditioning is switched off. Also, the daily difference between maximum and minimum radon concentrations is decreasing when the air-conditioning system is not active.

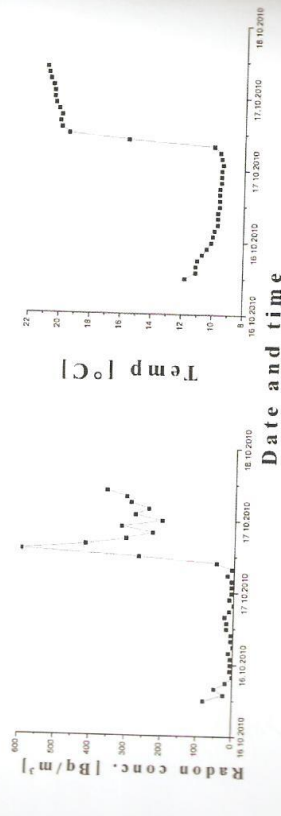


2. figure: Time series of radon concentration in the ULL with the ventilation system switched on and off



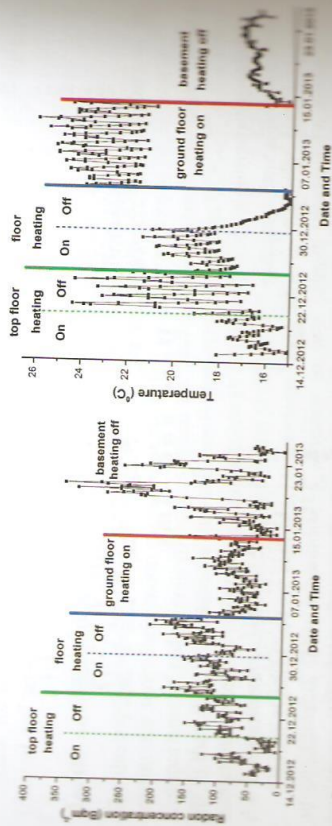
3. figure: Time series of the radon concentrations and temperature in the GLL, with the air conditioning on, <Rn> (sd)= 54(44) Bqm⁻³ (left) and off, <Rn> (sd)= 41(34) Bqm⁻³ (right)

The selected house is a typical one-family house with standard construction materials such as blocks of brick, concrete, mortar. The house is thermally insulated with Styrofoam (depth of 5 cm). Air conditioning device is used during the hottest part of summer, and also for the heating in the autumn. The graphs present the effect of air condition switch on, on indoor radon and temperature (4. figure).



4. figure: Time series of the radon concentrations and temperature in the house with air-conditioning system (heat mode)

The second house is, also a typical one-family house with three floors. The house is thermally insulated with Styrofoam (depth of 10 cm). In the selected time of the year (winter time), the ground floor is ventilated every day for about 15 min (5. figure).



5. figure: Time series of the radon concentration and temperature in the house with natural ventilation

Time series of the radon concentrations and temperature in the house with natural ventilation are presented in 5. figure. Despite the fact that the radon measurements are done in the winter time (usually it is the period of the higher indoor radon concentration

due to the seasonally radon variability) and the trend of the increasing of the indoor radon values from the top to the ground floor, the obtained results show quite different effect. The decreasing in the radon concentration on the ground floor is reached only with the usage of natural ventilation, opening windows for 15 min, every day during the period of the indoor radon measurements.

Conclusions

Ventilation system is a crucial stage in the radon reduction system in the underground environments. In dwellings and workplaces air conditioning systems are more commonly used. Unfortunately, it appears that usage of air conditioning systems may increase the levels of indoor radon. The natural ventilation is the first and simplest radon mitigation technique.

Acknowledgements

This work is supported by the Ministry of Education, Science and Technological Development of Republic of Serbia under project number III 43002.

References

1. A. Dragić, V. Udovičić, R. Banjanac, D. Joković, D. Maletić, N. Veselinović, M. Savić, J. Puzović, I. V. Aničin: The new setup in the Belgrade low-level and cosmic-ray laboratory. Nuclear Technology and Radiation Protection, 26(3), 181–192, (2011)
2. V. Udovičić, B. Grabež, A. Dragić, R. Banjanac, D. Joković, B. Pamić, D. Joksimović, J. Puzović, I. Aničin: Radon problem in an underground low-level laboratory. Radiation Measurements 44, 1009–1012, (2009)
3. V. Udovičić, I. Aničin, D. Joković, A. Dragić, R. Banjanac, B. Grabež, N. Veselinović: Radon Time-Series Analysis in the Underground Low-Level Laboratory in Belgrade, Serbia, Radiation Protection Dosimetry 145 (2-3), 155–158, (2011)

COMPARATIVE STUDY OF GAMMA-RAY BACKGROUND AND RADON CONCENTRATION INSIDE GROUND LEVEL AND UNDERGROUND LOW-LEVEL LABORATORIES

R. Banjanac, A. Dragić, V. Udovičić, D. Joković, D. Maletić,
N. Veselinović, M. Savić

Institute of Physics, University of Belgrade, Serbia

Abstract

Radon concentration is known to vary considerably depending on many parameters which influence to time variability of germanium gamma-ray background spectra. Besides atmospheric these parameters include the deposition of radon progenies on the walls of lead castles and Ge detectors themselves. It makes even the traditional radon suppression method by flushing the interior of the sample chamber with liquid nitrogen vapor potentially ineffective. Simultaneously measurements of Ge gamma-ray background and radon concentration were performed inside the Belgrade air-conditioned ground level and ventilated underground low-level laboratories. The obtained results confirmed the advantage of the complex ventilated system providing stability of Ge gamma-ray background inside the underground laboratory.

Introduction

A short-term gamma-ray background measurement is subject to certain temporal variations due to time variability of radon concentration. The duration of these background measurements may be anything from one day to several months, depending on the wanted final statistical accuracy of the envisaged measurements. Radon concentration is known to vary considerably depending on many parameters which influence to time variability of germanium gamma-ray background spectra. These parameters include the deposition of radon progenies on the walls of lead castles and detectors themselves, what makes even the traditional radon suppression method by flushing the interior of the sample chamber with liquid nitrogen vapor potentially ineffective. The aim of this work was to experimentally prove the advantage of the complex ventilated system providing stability of germanium gamma-ray background inside the underground laboratory. Hence, the simultaneous measurements of germanium gamma-ray background and radon concentration were performed inside the Belgrade air-conditioned ground level and ventilated underground low-level laboratories.

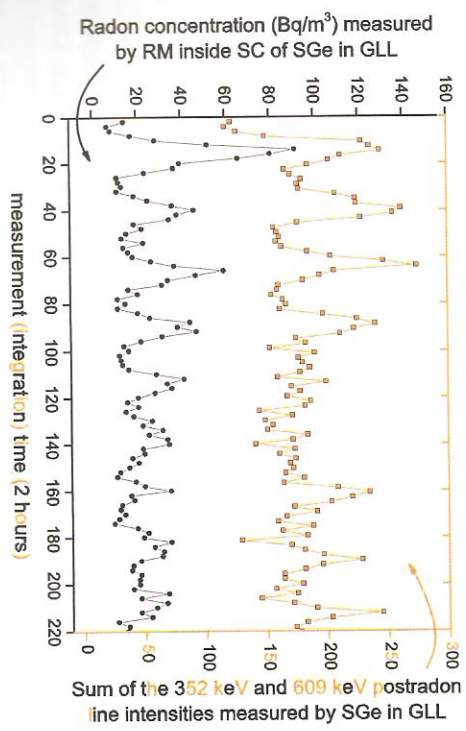
Descriptions of the laboratories

The Belgrade underground low-level laboratory (UL, 25 meters of water equivalent) is equipped with ventilation system which provides low radon concentration. The initial value of radon concentration, when the ventilation system is turned off, is more than 1000 Bq/m³ was reduced up to 80 times when the ventilation system is turned on obtained the mean value of 13(5) Bq/m³ after very long-term measurement. This system consists of two "radon shields" the passive and the active. The passive shield consists of the 1 mm aluminum sheet which completely covers all the wall surfaces inside the laboratory (4pi coverage). It is hermetically sealed with a silicon sealant to prevent diffusion of radon from surrounding soil and concrete walls of the laboratory. As the active radon shield the laboratory is continuously ventilated with fresh air, filtered through one rough filter for dust elimination followed by the active charcoal filters for radon adsorption. The UL is equipped with the intrinsically low-radioactivity level germanium detector, 35% of relative efficiency, here named BGe. For comparative background study the ground-level laboratory (GLL) is used. It is air-conditioned (average radon concentration of 50(30) Bq/m³) and equipped with the Ge detector, 18% of relative efficiency, here named SGe. Radon monitoring inside the laboratories was performed by radon monitor (RM), model RM1029, made by Sun Nuclear Corporation. Analyzing devices for both Ge detectors are flash analog to digital converters (FADC), made by C.A.E.N (type NI1728B), which sample at 10 ns intervals into 2¹⁴ channels. User-friendly software was developed and dedicated to C.A.E.N analyzer data with the possibility to choose integration time for further time-series analysis corresponding to time of readings of the radon monitor.

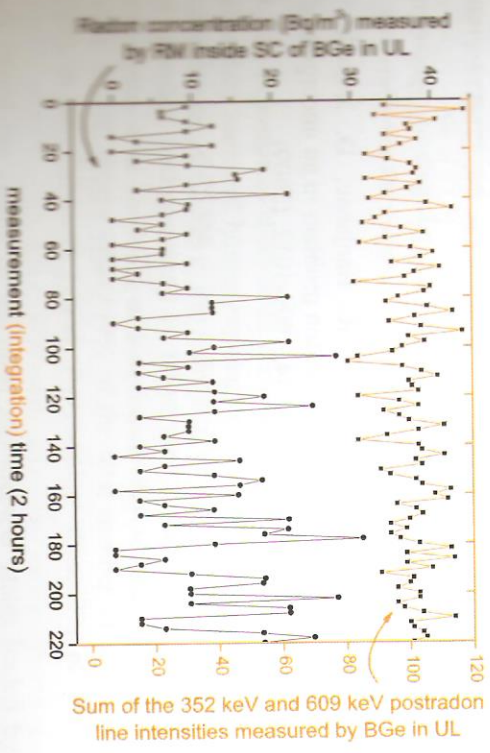
Results

Inside a sample chamber (SC) between the SGe and lead SGe shielding of 10cm, the RM was situated. Simultaneously measurements of radon concentration by RM and gamma-ray background by SGe were performed. The 1. figure presents strong correlation due to prominent daily radon and consequently daily post-radon lines variability.

The sum of two most intensive post-radon gamma-ray lines was used to emphasize small SGe efficiency. The RM recorded radon and atmospheric parameters readings every 2 hours and the integration in the time series of post-radon lines was chosen accordingly. The 2. figure presents the results of the same quantities from the measurements inside the UL but the values of the sum of two most intensive post-radon lines was shifted up for 50 counts to avoid overlapping. Neither evident daily radon concentration periodicity nor daily variability of post-radon lines intensities is present.



1. figure: Variability of radon concentration inside the SC of the SGe detector (circles) and the sum of two post-radon lines (squares) inside the GLL



2. figure: Variability of radon concentration inside the SC of the BGe detector (circles) and the sum of two post-radon lines (squares) inside the UL

Conclusion

Comparative study of daily radon variability inside the GLL and the UL was achieved by simultaneously measurements of radon concentration and gamma-ray background. The ventilation system installed inside the UL provides low radon concentration (the mean value of 13(5) Bq/m³) as well as low daily variation of post-radon line intensities. On the contrary, inside the air-conditioned GLL (the mean value of 50(30) Bq/m³) prominent daily variation of radon concentration and consequently post-radon line intensities can cause systematic errors of intensities in Ra-226 NORM samples obtained by low-level gamma-ray spectrometry.

Acknowledgements

The authors wish to thank prof. Ivan Aničin for constant interest and support. This work is supported by the Ministry of Education, Science and Technological Development of Republic of Serbia under project III 43002.

References

1. R. Antanasijević, I. Aničin, I. Bikit, R. Banjanac, A. Dragić, D. Joksimović, D. Krmpočić, V. Udovičić, J. Vuković: Radon measurements during the building of a low-level laboratory, *Radiation Measurements*, 31, 371-374, (1999)
2. P. Bossew: A very long-term HPGe-background gamma spectrum, *Applied Radiation and Isotopes*, 62, 635-644, (2005)
3. V. Udovičić, B. Grabež, A. Dragić, R. Banjanac, D. Joković, B. Panić, D. Joksimović, J. Puzović, I. Aničin: Radon problem in an underground low-level laboratory, *Radiation Measurements*, 44, 1009-1012, (2009)

RADON EXPOSURE IN THE NORTH-EAST REGION OF ROMANIA

Irina-Anca Popescu¹, Andreea Teodor¹, Catalin Borcia², Alexandra Cucu³

¹National Institute of Public Health (NIPH) – Regional Centre of Public Health Iasi – Radiations Laboratory

²Al. I. Cuza University of Iasi – Faculty of Physics

³NIPH - Regional Centre of Public Health Bucharest - Radiations Laboratory

Abstract

The paper presents the annual effective doses estimated for the population of the North-East Region of Romanian due to inhaled airborne radon and thoron progeny (Radon-²²²Rn and Thoron-²²⁰Rn). The exposure from ²²²Rn and ²²⁰Rn was assessed by sampling campaigns measurements of their individual concentrations, in indoor and outdoor air by an active technique. The method for dose estimation was specific to radon radiation source, using the conversion coefficients published in UNSCEAR Reports and ICRP Publications. The maximum value actually measured in urban houses was two times higher than the previous reported data for the same countries. Only in the air of urban houses from three counties (27.9% from total region surveyed) the annual effective doses were over the annual admitted limit of 1mSv/year for the general population, with an exceedingly value of 18.08 mSv/year. The reported radionuclides concentrations will be used for preparing a systematic campaign for estimating the exposure and perform the risk assessment and the mapping of the region.

Introduction

The population exposure to short-lived decay products (²²²Rn and ²²⁰Rn progeny) is the most important source of human exposure to ionizing radiation through inhalation, having a contribution of 52.5% to the individual annual effective dose (1.26 mSv) in the natural radiation background (2.40 mSv/year)⁽¹⁾. Radon is considered to be the second main cause, after smoking, of lung cancer development, being reported with approximately 20,000 deaths yearly (9% of the total number of deaths produced by lung cancer) in the European Union, representing about 2% of overall cancers deaths⁽²⁾.

Romania joined the efforts of the other EU member states leaded by the Joint Research Centre of the European Commission in order to establish a comprehensive mapping of radon levels, especially in homes and public buildings (schools, kindergartens)⁽³⁾.

A SIMPLE MONTE CARLO SIMULATION METHOD FOR ESTIMATING RADON INDUCED BACKGROUND OF GERMANIUM DETECTORS

Dejan Joković¹, Vladimir Udovičić¹, Radomir Banjanac¹, Dimitrije Malečić¹, Aleksandar Dragić¹, Nikola Veselinović¹, Bojana Grabež¹, Jovana Nikolov²

¹*Institute of Physics, University of Belgrade, Serbia*
²*Department of Physics, University of Novi Sad, Serbia*

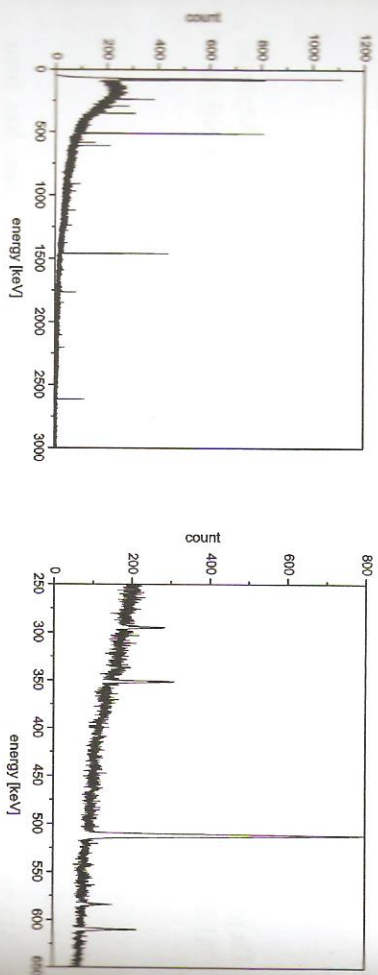
Abstract

Monte Carlo simulation method, based on Geant4 simulation package, has been developed to obtain background spectra of HPGe detectors. In this paper the emphasis was on radon induced background, while other sources of background were treated elsewhere. In the simulation, primary photons are uniformly randomly generated in the air surrounding the detector, with uniformly randomly momentum directions in 4π space. Energies of photons are those of characteristic peak lines in the HPGe spectra; their relative intensities are given by relative intensities seen in experimental spectra. The simulation gives a detector response to primary photons and their secondary particles, i.e. spectrum of the HPGe detector. The obtained results for radon concentration are then compared with experimental ones.

Introduction

The Low-Background Laboratory for Nuclear Physics at the Institute of Physics in Belgrade has an underground facility with a 12 m of earth overburden (25 m.w.e.). The laboratory is described in detail in⁽¹⁾. The lab room is hermetically sealed with 1 mm thick aluminium lining, and the ventilation system keeps the overpressure of about 15 Bqm⁻³. Thus the concentration of radon is kept at a low average value of about 15 Bqm⁻³. Some interesting behaviour of this concentration throughout the years has been reported previously^(2,3). In the laboratory operates one coaxial germanium detector (ORTEC, type GEM30); its active volume is 148.9 cm³ and relative efficiency is 35%. It is shielded with a 12 cm lead castle. The underground position of the detector, together with the passive lead shield, yields a good background reduction, with a count rate of less than 0,5 counts per second in the energy range of 100 keV. The main contribution to the background of the germanium detector comes from radon and its progeny. Characteristic energy lines induced by radon progeny, as well as from other contributors, can be seen in the background spectra of the detector (Figure).

Monte Carlo simulation, based on Geant4 simulation package⁽⁴⁾, has been developed to obtain response of germanium detectors and which, hopefully, could reproduce the experimental spectra of detectors as good as possible. In this case, the application is to estimate radon induced background of our HPGe detector.



1. Figure: Experimental background spectrum of the germanium detector, measured for $2.1 \cdot 10^6$ s (left). Section of spectrum of interest, showing peak lines at 295 and 352 keV ($Pb-214$), 511 keV (annihilation), 583 keV (Tl-208) and 609 keV (Bi-214) (right)

Simulation

In the simulation, the germanium detector, together with the whole detector assembly, is constructed in great detail, according to manufacturer's data specifications. Basically, it consists of a cylindrical germanium crystal as a sensitive detector volume, a copper holder on which the detector is mounted, and a magnesium housing. Inactive germanium layers and a hole drilled inside the crystal are also taken in account. The sensitive germanium volume has 58.5 mm diameter and 56.4 mm length, and the hole in the crystal has 9 mm diameter and 42.9 mm length. The inactive germanium layer is 0.7 mm thick. The copper holder has a length of 94 mm and is 0.76 mm thick. All this gives an active detector volume of 148.9 cm^3 . Surroundings of the detector are included in order to account for scattered photons. The whole detector assembly is placed inside 10 cm thick lead shield, at the position of 10 cm below the upper side of the shield.

Primary photons are generated in the air surrounding the detector (sample chamber within the lead castle), with uniformly random positions and momentum directions in full space (4π strad). Energies of photons are those of radon induced lines in the HPGe spectra (295, 352, 609 keV). Each photon then undergoes interaction processes and deposits energy in the detector or it traverses the detector (or the whole system) without interaction. All electromagnetic processes are considered and taken into account, using low-energy data packages. As a result, distribution of deposited energies gives the detector response, i.e. spectrum. From simulated spectrum one can obtain simulated full peak intensities, and from this derive simulated detector efficiency for a given energy.

A Simple Monte Carlo Simulation Method for Estimating Radon Induced Background of Germanium Detectors

Results

With detector efficiency calculated by simulation and with measured full peak intensity from the experimental spectrum, radon concentration is determined. For each energy, radon concentration as activity per unit volume is calculated using equation $A = I / (eff \cdot V)$, where I is measured full peak intensity, eff is simulated detector efficiency, p emission probability and V sample chamber volume. Results are given in the 1. table. They were compared with radon concentration obtained by radon monitor, which was found to be $13(5) \text{ Bq m}^{-3}$. Higher values of activities are due to radon progeny deposited on the walls of the lead castle and the detector, which is not taken in account here. It is shown that this activity is $\sim 1/4$ of the total. Also, it is expected that at higher energies some activity would come from radon outside the lead castle.

1. table: Radon concentration calculated from full peak intensities in the background spectrum of the HPGe detector. Sample chamber volume is 6.2 dm^3

E [keV]	I [$\cdot 10^{-3} \text{ s}^{-1}$]	p	eff	A [Bq m $^{-3}$]
295	0.428	0.19	0.0247	15(3)
352	0.906	0.36	0.0212	19(4)
609	0.654	0.47	0.013	17(4)

Acknowledgements

The authors wish to thank prof. Ivan Aničin for constant interest and support. This work is supported by the Ministry of Education, Science and Technological Development of Republic of Serbia under project III-43002.

References

1. A. Dragić, V. Udovičić, R. Banjanac, D. Joković, D. Maletić, N. Veselinović, M. Šavij, J. Puzović, I. V. Aničin: The new setup in the Belgrade low-level and some-ray laboratory, Nuclear Technology and Radiation Protection, 26, 181-192 (2011)
2. V. Udovičić, B. Grabez, A. Dragić, R. Banjanac, D. Joković, B. Panić, D. Joksimović, J. Puzović, I. Aničin, Radon problem in an underground low-level laboratory, Radiation Measurements, 44, 1009-1012, (2009)
3. V. Udovičić, I. Aničin, D. Joković, A. Dragić, R. Banjanac, B. Grabez, N. Veselinović, Radon time-series analysis in the underground low-level laboratory in Belgrade, Serbia, Radiation Protection Dosimetry, 145, 155-158, (2011)
4. S. Agostinelli et al., Geant4 – a simulation toolkit, Nuclear Instruments and Methods, A 506, 250-303, (2003)

12. J. T. Duffy, J. S. Madden, G. M. Mackin, A. T. McGarry, P. A. Colgan: A reconnaissance survey of radon in show caves in Ireland, *Environment International*, 22(1), 415–423, (1996)
13. N. Kávási, T. Vigh, T. Kovács, J. Vaupotič, V. Jobbágy, T. Ishikawa, H. Yonehara: Dose estimation and radon action level problems due to nanosize radon progeny aerosols in underground manganese ore mine, *Journal of Environmental Radioactivity*, 102(9), 806–812, (2011)
14. N. Kávási, J. Somlai, T. Kovács, C. Németh, T. Szabó, Z. Gorjanacz, A. Várhegyi, J. Haki: Difficulties in radon measurements at workplaces, *Radiation Measurements*, 41, 229–234, (2006)
15. SSI (Swedish Radiation Protection Institute): Radon Legislation and National Guidelines, Åkerblom, G: ISSN 0282–4434, (1999)

INFLUENCE OF VENTILATION SYSTEMS ON INDOOR RADON VARIABILITY

Vladimir Udovičić, Aleksandar Dragić, Radomir Banjanac, Dejan Joković,
Dimitrije Maletić, Nikola Veselinović, Jelena Filipović

University of Belgrade, Institute of Physics, Belgrade, Serbia

Abstract

Indoor radon concentration varies daily and seasonally, mainly due to the changes of the atmospheric parameters (temperature, atmospheric pressure) and the exchange rate between indoor and outdoor air. Because the short-term variation during a day may be extreme, it is important to investigate short-term variations of indoor radon. The physical origin of the variation on the indoor radon concentration is not straightforward. In this paper, we pointed out the influence of ventilation systems on changes of indoor radon concentration in different environments.

Introduction

The indoor radon behaviour is affected by large number of factors. As a result, the indoor radon concentration varies (mostly within one day or a year) with different amplitudes. In this paper, we pointed out the influence of ventilation systems on changes of indoor radon concentration in different environments. For this purpose, we choose two laboratories (the Underground Low-Level [ULL] and Ground Level Laboratory [GLL] of the Low-Background Laboratory for Nuclear Physics at the Institute of Physics in Belgrade [IPB]) and two typical family houses with different type of ventilation systems (natural and air-conditioning). Based on the obtained results, some of general conclusions can be found.

Experiment

All radon measurements were done using active continuous radon monitor device: Sun Nuclear - model 1029 (manufactured by the Sun Nuclear Corporation, NRSB approval-code 31822). The device consists of two diffused junction photodiodes and is furnished with sensors for temperature, barometric pressure and relative humidity. The time sampling of 0.5, 1, 2, 4, 8, 12, 16, 20 or 24-hour intervals is selectable by user. The duration of the continuous measurements is limited by the device memory which can store the data of 720 measurements. We selected the 2 hours sampling time with measurements lasting of several days.

The Low-Background Laboratory for Nuclear Physics⁽¹⁾ at the Institute of Physics in Belgrade is a shallow underground laboratory (*1 figure*). The laboratory was built in the loamy loess cliff on the bank of the river Danube with the overburden of 12 m of soil. It has an active area of about 45 m² (135 m³). The experiments and routine

RADON EQUILIBRIUM MEASUREMENT IN THE AIR

Sofija Forkapić, Dušan Mrđa, Miroslav Vesković, Nataša Todorović, Kristina Bikit,
Jovana Nikolov, Jan HANSMAN

Department of Physics, Faculty of Sciences, Novi Sad, Serbia
Corresponding author: sofija@df.uns.ac.rs

This paper presents the exact method of radon equilibrium measuring in the air and determining the radon progeny concentrations. The method is based on simultaneous sampling of air through the filter paper and alpha spectrometry measurement of radon activity concentration in the air. This paper derived a mathematical formula to calculate the initial concentrations of radon progenies ^{218}Po , ^{214}Pb and ^{214}Bi in the air at the start of sampling based on the detected count rate of postradon gamma lines in the sample of filter paper. Such a model containing the radioactive decay corrections during the time of sampling, cooling and measurement can be applied in other nuclear analysis where the half-life of the source has the same order of magnitude as the available recording time.

DAILY VARIATION OF GAMMA-RAY BACKGROUND AND RADON CONCENTRATION

R. Banjanac¹, V. Udovičić¹, A. Dragić¹, D. Joković¹,
D. Maletić¹, N. Veselinović¹, J. Puzović²

¹*Institute of Physics, University of Belgrade, Pregrevica 118, Belgrade, Serbia*
²*Faculty of Physics, University of Belgrade, Studentski trg 12-16, Belgrade, Serbia*
Corresponding author: banjanac@ipb.ac.rs

Reducing gamma-ray background contributes to the reduction of statistical errors of low activity measurements, while reducing time variation of gamma-ray background achieves lower systematic errors. The sources of time variation of gamma-ray background in a typical measurement of low activity, when the measurement time is only several days, are daily (periodic) variations of radon concentration and aperiodic variations of cosmic rays intensity. In this study we investigated the conditions that contribute to variations of gamma-ray background and radon concentration, by analyzing of their simultaneously measured time series in a typical ground level and shallow underground laboratories.

Effects of the Air Conditioning System Usage on the Indoor Radon Variability

Vladimir Udovičić, Aleksandar Dragić, Radomir Banjanac, Dejan Joković,
Dimitrije Maletić, Bojana Grabež, Jelena Filipović

Low-Background Laboratory for Nuclear Physics, Institute of Physics Belgrade,
Pregrevica 118, Belgrade, 11080, Serbia

udovicic@ipb.ac.rs

The air conditioning system usage in the dwellings and the workplaces is increasing, due to climate change, worldwide. Also, there is a need to increase energy efficiency regarding general energy problem, which leads to changes in the standards for the construction of new residential and commercial buildings. On the other hand, all this changes leads to significantly altered behavior of indoor air and consequentially the indoor radon dynamics. In this paper, the effects of the application of air conditioners in the dwellings and the workplaces to the indoor radon variability are investigated. The obtained results show increase in the average indoor radon concentration and difference between minimum and maximum value during one day, when the air conditioner is used.

Requirements on Indoor Radon with Indoor VOC

Christine Daeumling¹, Bernd Hoffmann², Ma

¹ II 1.3, Umweltbundesamt, German Federal Environ
Berlin, 14195, Germa

² SW 1.1, Bundesamt für Strahlenschutz, K
Berlin, 10318, Germa

³ Bundesanstalt für Materialforschung und -prüf
Berlin, 12205, Germa

christine.daeumling@u

While ratifying the upcoming European Basic S
ting radiation protection, some member states among
the "new" tasks how to implement legal and statutor
radon concentrations at work and at home. The ques
on Radon - from soil as well as from building produ
side of the legal framework for radiation protection m
in three European Countries (France, Germany, Belgi
demanding materials emissions tests to prove the sui
a healthy indoor environment. In Germany, some gro
comply with requirements on VOC (volatile organic co
scheme for approval. The tests are carried out in emis
and nature of the VOC emissions are taken into acco
conditions as defined in FprCEN/TS 16516 and ISO
connected way of quality evaluation can also be the de
lation from building products by use of these chambers
First results in a research project are promising but quite
still to be resolved. The use of the broader framework c
has been discussed recently. To include radon as a carc
will surely reveal some technical challenges.

Daily Radon Variability in the Underground Low-Background Laboratory in Belgrade, Serbia

Vladimir Udovičić, Jelena Filipović, Aleksandar Dragić, Radomir Banjanac, Dejan Joković, Dimitrije Maletić, Bojana Grabež

Low-Background Laboratory for Nuclear Physics, Institute of Physics Belgrade, Pregrevica 118, Belgrade, 11080, Serbia

udovicic@ipb.ac.rs

Radon time series analysis, based on the short-term indoor radon measurements performed worldwide, shows two main periodicity, daily and yearly. The information obtained from time series of the measured radon values is the results of the complex radon dynamics which arises from the influence of the large number of different parameters (the state of the indoor atmosphere (temperature, pressure and relative humidity, aerosol concentration), the exchange rate between indoor and outdoor air...). In this paper we considered daily radon variability in the underground low-background laboratory in Belgrade, Serbia. The results are originated from the radon time series analysis based on the three years of the continuous short-term indoor radon measurements. In the same time, we obtained the time series of the temperature, pressure and relative humidity in the laboratory. Also, we tried to find the correlation between different time series. It has been shown that the radon behavior in the underground low-background laboratory in Belgrade has the similar characteristics as in the other underground environment (caves, mines, boreholes...).

Diurnal Variation of Radon in Dwellings in Central Poland

Magdalena Piekarczyk

Central Laboratory for Radiological Protection, Institute of Nuclear Physics, Warsaw, 03-194, Poland

piekarz@clor.waw.pl

Due to the fact, that radon has high contribution from natural sources, it is important to monitor its concentration in dwellings.

The most important source of radon in buildings is radon from building material. Other sources have smaller contribution. The concentration of radon is seasonal and daily variable. The highest concentration of radon in buildings is observed in the ground floors of rooms is limited, but not in each case. Diurnal variations of radon concentration are related with the lifestyle of people and what is related with, opening windows. In some cases diurnal variations of radon concentration have significant impact.

The aim of the experiment was to examine the diurnal variation of radon concentration during long-time measurement and to find a correlation of radon concentration with conditions such as temperature, humidity and barometric pressure.

The continuous radon measurements (1-2 weeks) were performed in central Poland. The conditions were various. The measurements were performed on the ground floors in single-family houses, flats in block flats. During the measurements windows and door were closed and no ventilation was used.

Radon measurements were performed using calibrated radon monitor (Genitron Instruments GmbH, Germany).

The concentration of radon was very small, therefore the dependence of radon concentration on building material was not observed. The smallest values of radon were observed in flats with wooden floor. In some dwellings it was possible to observe diurnal variations of radon concentration.

MONITORING BERYLLIUM-7 AND TRITIUM IN RAINWATER IN DAEJEON, KOREA AND ITS SIGNIFICANCE

Kyeong Ja Kim, Yire Choi, Yoon-Yeol Yoon

KIGAM

Beryllium-7 ($T_{1/2} = 53.22$ days) and Tritium ($H-3$, $T_{1/2} = 12.32$ years) nuclides are produced by cosmic ray interactions in upper atmosphere with atmospheric constituents. The concentrations of Be-7 and H-3 of rainwater in Daejeon, Korea ($36.32^{\circ}N$, $127.41^{\circ}E$) were investigated for seven months during 2007-2008. We extracted Be-7 and H-3 as well as stable nuclides in a sufficient large volume of monthly rain collector (ID=55.4 cm, H=51.8 cm) installed on a roof of a three-story building. The amount of rainwater collected each month varied up to 120 liters depending on the weather of each month. The rainwater was filtered to remove dust then run through an ion exchange filter to collect Be-7 and Na. The concentrations of Be-7, H-3, and stable isotopes were measured using High-Purity Germanium gamma-ray detector, electrolytic enrichment device, and ICP-AES, respectively.

The results of our study demonstrate that the concentration of Be-7 in rainwater is inversely proportional to sodium amount and proportional to the rainwater amounts. It was found that both Be-7 and H-3 data have a trend associated with rainwater amount and air mixing time of the stratosphere in spring. Both isotopes show their peaks during fall and spring season. The trend of H-3 variation appeared to be shifted about a month compared to that of Be-7. This could be due to the different residence time between H-3 and Be-7 in the atmosphere. Interestingly, Kim et al. 1998 [1] shows that the variations of Be-7 and Pb-210 (a decay product from Rn-222) of rain samples in Korean Yellow Sea coast are appeared as a similar pattern to each other. This could be due to the fact that both Be-7 and Pb-210 nuclides precipitate as atmospheric aerosols after their productions in the atmosphere. Kim et al. 1998 [1] also demonstrated that wet depositional fluxes of Be-7 and Pb-210 are higher in spring and summer than the rest of the year due to higher amounts of precipitation.

The detection efficiency uncorrected Be-7 concentrations in Daejeon, Korea show lower values than the reference values of both New Zealand ($0.5-4.3 \times 10^7$ atoms/kg) [2] and Japan [3]. The H-3 concentrations of this study ranged from 4.8 ± 0.10 and 18.62 ± 0.27 (TU). This range is well compared to the H-3 concentration of the Northern Hemisphere ($10-20$ TU). Also, sodium variation of the rainwater is found to be inversely proportional to the concentrations of Be-7. There are not sufficient published Be-7 data of rainwater measured in the region of the Korean Peninsula. The Be-7 data of this study will be an important data set of rainwater for future studies associated with geological applications with Be-7 and Be-10 in Korea.

Reference: [1] S. H. Kim et al. The Yellow Sea, 4, 58-68 (1998); [2] I. Graham et al. Geochimica et Cosmochimica Acta 67(3) 361-373 (2003); [3] Y. Maejima et al. Geoderma 126, 389-399 (2005).

Corresponding author's email address: kjkim@kigam.re.kr

LONG-TERM BACKGROUND MEASUREMENTS IN THE BELGRADE LOW-LEVEL UNDERGROUND LABORATORY

R. Banjanac, D. Joković, D. Malešić, V. Udovičić, N. Veselinović, M. Savić, A. Dragić

Institute of Physics, University of Belgrade, Serbia

In the Belgrade low-level underground laboratory (UL, 25 m.w.e) all components of background radiations are continuously monitored for a period of more than ten years now. Laboratory space is lined with a hermetically sealed aluminum lining and is furnished with the two-stage ventilation system that constantly keeps an over-pressure of 2 mbar. This keeps the radon concentration at the low average value of about 1.5 Bq m^{-3} . The continuous background measurements include the spectral measurements of the cosmic-ray flux with a system of large plastic scintillators, the measurements of radon concentration with a radon monitor, and the measurements of the background spectrum of a passively and actively shielded radio-pure HPGe detector. Temperature, pressure and humidity are also constantly monitored and recorded at regular time intervals, in the period from 2008 to 2014 the cosmic-ray flux and the HPGe detector spectra were performed by using a C.A.E.N. flash AD converter in the event-by-event mode with a 10 ns resolution time stamp, to collect and analyze the spectra off-line. The 1 m^2 plastic scintillator, positioned as a veto shield over the HPGe detector, provides the cosmic-ray data either as a single data or in coincidence-anticoincidence with the HPGe gamma-ray background measurement, using the same C.A.E.N. device. The user-friendly software was developed to analyze the C.A.E.N. data with the possibility to choose an arbitrary integration time for the time-series analysis of any part of the collected spectra. This allows the formation of time-series of different features in the spectra – the spectral lines from pre-radon and post-radon isotopes in the HPGe spectra as well as of any other part of this spectrum, and the time series of any part of the cosmic-ray spectra. The system is set up to enable the correlative and multi-variate regression studies of different features of all our spectra with the parameters extraneous to our measurements – primarily the different meteorological, geophysical and heliospheric data. Here we present the results of the correlative and multi-variate regression analysis of some of the interesting features of our spectra. The correlative studies are used in order to select the most responsive extraneous variables, while multi-variate analysis helps in choosing the best multi-variate method to be used for our purposes and the “mapped” function of time-series dependence on extraneous variables.

Corresponding author's email address: banjanac@ipb.ac.rs



VARIATION OF MUON COSMIC RAY FLUX RECORDED BY BELGRADE COSMIC RAY STATION DURING DECEMBER 2015 AND COMPARISON WITH EUROPEAN NEUTRON FLUX MONITORS

**Dimitrije Maletic, Dejan Jokovic, Radomir Banjanac,
Vladimir Udovicic, Aleksandar Dragic, Nikola Veselinovic,
Mihailo Savic**

Institute of Physics, University of Belgrade, Belgrade, Serbia

The Solar activity in rather quiet 24th Solar cycle had it's maximum in 2014. The year 2015 is the year of declining Solar activity, and still interesting variation of Cosmic ray flux are evident. In this paper we present the results of measurements of muon flux variations in the second part of year 2015, especially December's variations. The Cosmic ray flux is continually monitored at the Belgrade Muon Cosmic Ray station in the Low background Laboratory in the Institute of Physics Belgrade. The measurement of Muon flux is compared with measured neutron flux, also originating from Cosmic rays, which was recorded at several European Neutron monitor stations. The Belgrade data correlates very well with Neutron monitors measurements. The significant variations in Cosmic ray flux are discussed. Additionally, December event was discussed in the light of Solar activity during the current 24th and previous two Solar cycles.

Long-term indoor radon measurements in a family house – a case study in Serbia

Vladimir Udovicic¹, Dimitrije Maletic¹, Jelena Zivanovic¹, Aleksandar Dragic¹, Radomir Banjanac¹, Dejan Jokovic¹, Sofija Forkapic²

¹ Low-Background Laboratory for Nuclear Physics, Institute of Physics, University of Belgrade, Pregrevica 118, Belgrade, 11 080, Serbia

² Department of Physics, Faculty of Science, University of Novi Sad, Trg Dositaja Obradovica 3, Novi Sad, 21 000, Serbia

udovicic@ipb.ac.rs

The indoor radon behavior has complex dynamics due to the influence of the large number of different parameters: the state of the indoor atmosphere (temperature, pressure and relative humidity), aerosol concentration, the exchange rate between indoor and outdoor air, construction materials and living habits. As a result, the indoor radon concentration shows a variation, with the usually periodicity of one day and one year. It is also well-known that the seasonal variation of the radon concentration exists. Besides, it is particularly interesting to investigate indoor

radon variation at the same measuring location and time period, year after year, due to estimation of individual annual dose from radon exposure. In that sense, we performed long-term indoor radon measurements in a typical family house in Serbia. Measurements were taken during the 2014, 2015 and 2016, in February and July, every year. We used the following measuring techniques: active, passive and charcoal canisters methods. Detail analysis of the obtained results is presented in this paper.